AEM2023

3-7 September 2023
Fitzroy Island, QLD, Australia

8th International Airborne Electromagnetics Workshop

Extended Abstracts

PROUDLY SPONSORED BY

Xcalibur — Kimberlite Sponsor

GEOTECH AIRBORNE GEOPHYSICAL SURVEYS — Nickel Sponsor

SKYTEM — Gold Sponsor

Graphite Sponsor

NRG — Award Sponsor

CGG — Social Event Sponsor

CO-HOSTED BY

Australian Society of Exploration Geophysicists

CSIRO

Conference committee

Role	Name	Employer
Co-chair / Treasurer	Andrew Fitzpatrick	IGO
Co-chair	James Reid	Mira Geoscience
Technical	Aaron Davis	CSIRO
Sponsorship	Tim Munday	CSIRO
ASEG Liaison	Astrid Carlton	GSNSW
Conference Liaison	Lisa Worrall	Protean Geoscience
Indigenous Liaison	Torres Webb	CSIRO
Proceedings	David Annetts	CSIRO

Technical committee		
	Aaron Davis	CSIRO
	James Macnae	CT3D / RMIT
	Yusen Ley Cooper	GA
	Andrew King	CSIRO
	Shane Mule	CSIRO
	Tania Dhu	NTGS

Conference organisation		
	Nell Harrison	TAS
	Gary Bender	TAS
	Bettina Newton	TAS

Program key	
Session	Chair
Keynote	Presenter
Presentation	Name
Break	

Monday 4 September			
09:00	09:10	Welcome to particpants and opening comments	Andrew Fitzpatrick
09:10	09:30	Welcome to country	TBA
AEM Systems 1			Andrew Fitpatrick
09:30	09:50	Design of BIPTEM: an airborne B field IP and TEM system	James Macnae
09:50	10:10	Helitem^2 – System Updates for Broadband AEM Data	Duane Griffith
10:10	10:30	New helicopter-borne TEM system HoriZOND for effective exploration	Alexey Trusov
10:30	11:00	Morning tea	
AEM Systems 2			Aaron Davis
11:00	11:20	The Development of the TEMPEST AEM System	Andy Green
11:20	11:40	The last five years of Tempest System Development	Teo B Hage
11:40	12:00	TEMPEST electromagnetic transmitters with multiple loops and multistep waveforms	Andrew Sunderland
12:00	12:20	Noise Considerations for TEMPEST Data	Peter Wolfgram
12:20	13:20	Lunch	
AEM Data processing 1			Andrew King
13:20	13:40	Perspectives on AEM processing for geophysical exploration in Canada and worldwide	Magdel Combrinck
13:40	14:00	Estimating noise in AEM data	Aaron Davis
14:00	14:20	Supervised stacking to improve the signal-to-noise ratio of AEM data	Pierre-Alexandre Reninger
14:20	14:40	Analysis of the self-interference model and compensation methods in airborne electromagnetics	Evgeny Karshakov
14:40	15:10	Afternoon Tea	
Regional Data Acquisition, Calibration And Interpretation			Lisa Worrall
15:10	15:30	Reconciling the previously incompatible through the continental scale AusAEM survey	Yusen Ley-Cooper
15:30	15:50	Australian continental-scale multilayered chronostratigraphic interpretation of airborne electromagnetics	Sebastian C.T. Wong
15:50	16:10	The HydroGeosITe for AEM mapping: characterization through joint inversion of AEM, ground EM and DCIP data	Alessandro Signora
16:10	16:30	Free AEM data over NSW, Australia	Astrid Carlton
16:30	End		

Tuesday 5 September			
AEM Data Processing 2			James Macnae
09:00	09:20	Lessons learned from a decade of AIP modelling	Andrea Viezzoli
09:00	09:40	A Forward Model Study to Investigate 25, 12.5 and 6.25Hz AEM System responses to IP and SPM Effects in the Regolith	Rodney Paterson
09:00	10:00	Joint Inversions of AEM modelling AIP effects: Helicopter-borne, Ground IP and Fixed-Wing systems	Francesco Dauti
10:00	10:20	Modelling induced polarization effects in frequency-domain data	Dmitry Khliustov
10:00	10:50	MORNING TEA	
Mineral System Studies			Magdel Combrinck
10:00	11:10	Use of Airborne Electromagnetics for Mineral Exploration and Mining	Katherine McKenna
11:00	11:30	Some comparisons of AEM systems for specific mineral exploration problems	Michael Whitford
11:00	11:50	Going the extra mile - Julimar, a case study from Western Australia	Camilla Sørensen
11:00	12:10	An Airborne Heterodyne Sulphide Exploration Test at Kempfield	James Macnae
12:00	12:30	The Valen Prospect: It's SPM,... No it's not,... Yes it is!.. No wait....	Tim Munday
12:00	13:30	Lunch	
Geological Settings And Mineral Systems 1			James Reid
13:00	13:50	Enhanced Weathering and Oxidation Modelling in Coals by Integration of ATEM Results with Standard Coal Geoscience Data at Peak Downs Mine, Queensland, Australia	Geoffrey Peters
13:00	14:10	Investigating volcanic systems via multi-scale electromagnetic imaging	Paul A Bedrosian
14:00	14:30	AEM imagery down to one kilometer depth: New constraints for geological and hydrogeological modeling in volcanic contexts	Pierre-Alexandre Reninger
14:00	14:50	ZTEM Airborne Natural Field EM-Magnetics and Mineral Targeting Results over the Berg Porphyry Copper Project, near Houston, British Columbia.	Jean M Legault
14:00	15:10	Passive and active airborne electromagnetics – separate and combined technical solutions and applicability	Alexander Prikhodko
15:00	15:40	Afternoon Tea	
UAVS			Lindsey Heagy
15:00	16:00	Geotechnical ground investigations with a small airborne TEM prototype system	Andi Pfaffhuber
16:00	16:20	Developing a fully airborne drone TEM system	Nicklas S. Nyboe
16:20	16:40	An early time semi-airborne loop source TEM system	Esben Auken
16:60	End		

Wednesday 6 September			
09:00	09:20		
09:20	09:40		
09:40	10:00		
10:00	10:20		
10:20	10:50	Morning Free	
10:40	11:10		
11:00	11:30		
11:20	11:50		
11:40	12:10		
12:00	12:30		
12:30	13:30	Lunch	
Hydrology / Hydrogeology 1			Richard Kellet
13:30	13:50	BGR helicopter-borne frequency-domain EM – past, present, future	Bernhard Siemon
13:50	14:10	AEM survey of the Neretva Delta (Croatia): a case study for hydrogeology	John Moilanen
14:10	14:30	AEM-derived watersheds in crystalline domain under volcanic cover	Damien Ciolczyk
14:30	14:50	Quantifying salinity in the layered coastal aquifers underlying and adjacent to Delaware Bay USA using AEM-derived resistivity	Lyndsay Ball
14:50	15:10	Using regional airborne electromagnetic conductivity data to characterise surface water groundwater interaction in the Cooper Creek floodplain in arid central eastern Australia	Neil J Symington
15:10	15:40	Afternoon Tea	
Hydrology / Hydrogeology 2			Yusen Ley-Cooper
15:40	16:00	An AEM experience in Northern Italy. Innovative and multidisciplinary approach for a modern ground-water and land management	Matteo Gisolo
16:00	16:20	Integration of airborne transient electromagnetic models with ground geophysics and borehole data for groundwater mapping in Hawkes Bay region, New Zealand	Richard Kellett
16:20	16:40	System-scale airborne electromagnetic surveys in the lower Mississippi River Valley support multi-disciplinary applications	Burke Minsley
16:40	17:00	California's Statewide AEM Surveys: Project Implementation and Next Steps	Katherine Dlubac
17:00	End		

Thursday 7 September			
Indigenous Engagement			Tim Munday
09:00	09:20	Indigenous Knowledge and Methodologies to Inform Science and Data Capture	Bradley Moggridge
09:20	09:40	Round Table discussion on approaches to indigenous engagement/involvement with Airborne EM acquisition & application	Paul Bedrosian, Yusen Ley Cooper, Maïwenn Herpe, Tim Munday
09:40	10:00	POSTER SESSION	
10:00	10:30	MORNING TEA	
MI & AI: Joint Inversion			Andi Pfaffhuber
10:30	11:00	Deep Learning for the Inversion of Airborne EM Data	Eldad Haber
11:00	11:20	Automated data processing of a large-scale airborne time-domain electromagnetic survey by a deep learning expert system	Muhammad Rizwan Asif
11:20	11:40	Finding Geology Structures in Depth Sections from Airborne Geophysics: Automatic workflows	Simge Ayfer
11:40	12:00	Airborne magnetics as structural guide in the 3D inversion of Airborne EM data	Carsten Scholl
12:00	12:20	Thoughts on layered inversions	Andrew King
12:20	13:20	Lunch	
Open Source Codes			Katherine McKenna
13:20	13:40	Advances in open-source software for 3D electromagnetics using SimPEG	Lindsey J Heagy
13:40	14:00	Closing the gap between galvanic and inductive methods: EEMverter, a new 1D/2D/3D inversion tool for Electric and Electromagnetic data with focus on Induced Polarization	Gianluca Fiandaca
14:00	14:20	HiQGA: Open source deterministic and probabilistic AEM inversion	Anandaroop Ray
14:20	14:40	Toward Open Science: Introducing the Geophysical Survey (GS) Data Standard and GSPy Toolbox	Stephanie R James
14:40	15:00	EEMstudio: an open-source freeware QGIS plugin for processing, modelling and inversion of electric and electromagnetic data	Nicole Anna Lidia Sullivan
15:00	15:30	Afternoon Tea	
Close Of Workshop			Andrew Fitzpatrick
15:30	15:45	Paper awards	
15:45	16:05	Next Venue - 9th International Workshop	
16:05	16:25	Closing Remarks	
16:25	End of Workshop		

Posters

Title	Author
Using airborne electromagnetics to improve depth to bedrock estimates in Wisconsin	Burke Minsley
Adaptive correction for airborne electromagnetic measurements	Evgeny Karshakov
Airborne electromagnetics: dealing with the aircraft speed	Evgeny Karshakov
Targeting epithermal Au-Ag using helicopter TDEM, magnetic, and radiometric data at Lawyers Project, North-Central BC, Canada.	Jean M Legault
Beyond conductive targets: Characterizing lithium-prospective lacustrine evaporite mineral systems of North America's Basin and Range Province with regional-scale AEM	Lyndsay Ball
Airborne electromagnetic imaging for critical-minerals resource assessment	Paul Bedrosian
An overview of SkyTEM surveys in New Zealand: data acquisition, community engagement, and results from Northland	Maïwenn Herpe
Automated integration of A EM data, VES and borehole logs	Stefano Galli
TEMPEST Data System Bandwidth Comparisons	Nirocca Devkurran
AEM base frequency and depth of investigation	Magdel Combrinck
Combined ground-UAV TDEM survey over gold prospect in Baikal-Patom Highlands (eastern Russia) with detection of AIP effect	Vladislav Kaminski

Oral Presentations

Poster Presentations

Author Index

Automated data processing of a large-scale airborne time-domain electromagnetic survey by a deep learning expert system

Muhammad Rizwan Asif*, M. Andy Kass, Anders Vest Christiansen
HydroGeophysics Group, Department of Geoscience
Høegh-Guldbergs Gade 2, Aarhus C, Denmark
rizwanasif@geo.au.dk

Zara Rawlinson, Rogier Westerhoff
GNS Science
114 Karetoto Road, Taupo, New Zealand
Z.Rawlinson@gns.cri.nz

SUMMARY

The new generation of airborne electromagnetic (AEM) surveys yield large data sets of thousands of line kilometres. Parts of these data are often contaminated by noise from various sources, e.g. fences, power lines, which corrupts the data to a degree that it can no longer be used. The problem intensifies in urban areas where the risk of data corruption is highest due to dense infrastructure. The inversion of corrupted data risks interpreting spurious subsurface features and flawed geological interpretations. Therefore, in many cases, the corrupted data is identified and culled prior to inversion. This process of culling corrupted data is generally a manual task requiring specialists to examine the data in detail, which is an extremely complex and time-consuming process.

Recently, we proposed a deep learning expert system to automate the complex AEM data processing workflows. The proposed method uses a deep convolutional auto-encoder to identify corrupted data, and was trained such that it generalises to diverse geological conditions and various survey areas. In this study, we investigate the generalisation capabilities of our deep learning method on a large AEM survey area in Northland, New Zealand. Our approach takes ~ 600 s to process 3984 line kilometres of data and displays strong spatial correlation for the data identified as corrupted. The inversion results show very few potential anomalies in the model space which are being inspected by a manual operator. In general, the proposed approach is generalisable and displays high-quality data processing within short amounts of time, which requires minimal further quality inspection.

Key words: airborne electromagnetics, data processing, deep learning, anomaly detection.

INTRODUCTION

Modern AEM systems collect large data sets of thousands of line kilometres in short amounts of time for the purposes of geological mapping, mineral exploration, and environmental and engineering investigations (Smith, et al. 2004). The data from AEM systems is often contaminated by noise from various sources, e.g. electrical fences and power lines, which corrupts the data to a degree that it can no longer be used. When corrupted by noise sources, the data from AEM surveys are typically culled to avoid misrepresentation of the subsurface. The identification and culling of corrupt data is mainly a manual task, which requires highly trained specialists to examine the data in detail. The manual data processing workflows are subjective, difficult to reproduce and time-consuming. The problem increases dramatically in urban areas where the risk of data corruption is highest due to dense infrastructure. Nevertheless, neglecting these workflows may create increased risk of inferring spurious subsurface features, flawed interpretations, and incorrect conclusions.

Recently, we proposed a deep learning expert system (Asif, et al. 2022) to automate the complex AEM data processing workflows. We stressed that the proposed deep learning method is readily applicable to various geological conditions and survey areas due to its training conditions. As such, our model has been trained on a huge ensemble of geophysical resolvable 1-D subsurface models (Asif, et al. 2023) which is different than standard deep learning methods that utilises the data from existing survey areas to identify corrupt data, resulting in a bias to local geological conditions (Andersen, et al. 2016).

In this study, we apply our deep learning expert system off-the-shelf on a large-scale AEM survey carried out in the south of Northland, New Zealand. The survey was collected over 17 days and consists of 3984 line kilometres of data having ~ 830,000 soundings. As expected, the automated processing shows a high degree of spatiotemporal correlation for the corrupted data. We also present the 1-D inversion results of the automated processing, which shows few to no anomalies, indicating that no or minimal quality inspection is further required. The manual quality inspection is time-consuming and is in process at the time of submission, but the results for the automated and the manual processing will be included in the presentation.

METHOD AND RESULTS

The proposed deep learning expert system makes use of an unsupervised learning strategy, specifically auto-encoders, where the most relevant aspects of the data are encoded into a compact representation by dimensionality reduction. The encoded features of the data are then decoded back to identify any spurious data patterns. This approach of auto-encoders for the processing of AEM data is discussed in detail in our previous work (Asif, et al. 2022), where we show that the proposed approach successfully identifies spurious features in AEM data and displays high-quality data processing.

In this study, we investigate the performance of the proposed deep learning expert system on a survey area in Northland, New Zealand. The survey was flown with the SkyTEM306HP system (Gisselø and Nyboe 2017) with ~200 m line spacing and 3984 line kilometres of data, which were acquired in 284 lines.

The survey flight lines are shown in Figure 1 that consist of ~830,000 point locations of the soundings. It can be observed in Figure 1 that some major infrastructure, e.g. the state highway, runs in the middle of the survey area from Northwest to Southeast.

Figure 1. AEM survey lines for Northland, New Zealand shown on top of the Google Earth image.

Our expert system is applied off-the-shelf on the low moment (LM) and high moment (HM) data of the raw AEM soundings. It takes ~305 s to process the LM and ~307 s to process the HM data. The automated processing keeps ~92% and rejects ~7% of all LM soundings. The remaining 1% of the LM soundings are marked as partially corrupted. In the context of HM data, ~90% of the soundings are marked as clean while ~8% are marked as corrupted. In addition, ~2% soundings are marked as partially corrupted.

The processing results of our automated approach are shown in Figure 2. The blue points in Figure 2 represent the data marked as clean and therefore, kept for inversion. The data locations with yellow points exemplify the soundings where the late times are affected by noise and a part of the sounding is removed. Furthermore, the orange points represent the data completely removed in the automated processing. Since the LM and HM waveforms are significantly different from each other, we observe several instances where only one of the moment of the data is corrupted to noise. We also note that there is a strong spatial relationship between the data marked as corrupted or partially corrupted, especially for the HM data.

We also show the LM and HM processing results of the most northwest flight line from the survey area in Figure 3. The drastic change in the signal amplitude at the beginning and at the end of the line is due to the transition zone between the land and the sea, where the data over the seawater results in high

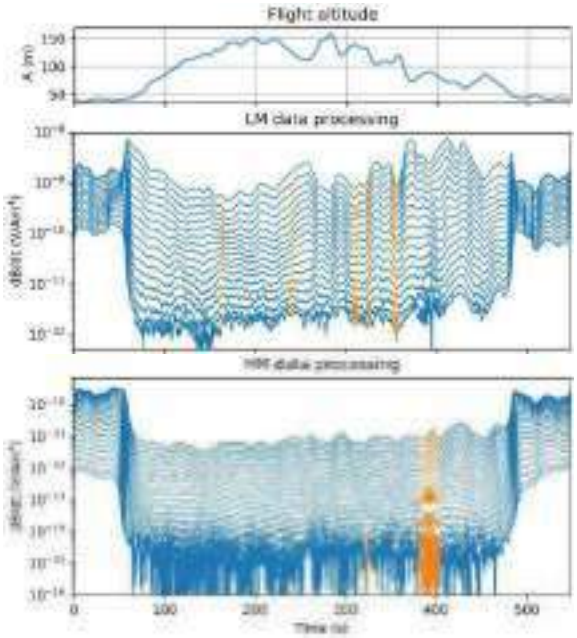

Figure 3. Data processing results of the most northwest line of the survey area. The orange marked data represents data culled by the automated processing.

signal amplitudes. The data marked as corrupted by the automated processing is represented by orange, while the data marked as ready for inversion is shown in blue.

The survey area is inverted with the 1-D spatially constrained inversion algorithm (Viezzoli, et al. 2009) using AarhusInv (Auken, et al. 2015). We apply the commonly used settings with a 30-layer smooth model discretisation with the starting layer boundary at 3 m and the last layer boundary at 350 m. The inversion takes a total of 22 iterations and results in a data misfit of 1.02. A misfit of one corresponds to a fit just within the standard deviation assigned to the data. The inversion results are shown in Figure 4 in the form of mean resistivity maps of depth slices from 40 m to 50 m, and 240 m to 280 m. A visual inspection on the mean resistivity maps shows some anomalies in the model space for the transition zone between the land and sea, which could be due to 2-D or 3-D effects. Few anomalies in the form of conductive blobs are also observed, which could be due to the corrupted data mimicking a geological response, however; a detailed analysis by a manual operator will reveal further details, which will be discussed in the presentation.

CONCLUSIONS

We show that the proposed deep learning expert system is generalisable and readily applicable for the data processing of large-scale survey areas. The preliminary results on the data

from Northland, New Zealand indicate a strong spatial relationship between the data marked as corrupted by our automated approach. Additionally, the inversion results show little to no immediate anomalies in the model space. However, the processed data are being examined thoroughly for quality control and to further comment on the automated data processing results. Regardless, our results show that the proposed approach is a significant step forward to completely automating the data processing workflows and minimise the need for highly skilled specialists.

ACKNOWLEDGMENTS

The authors would like to acknowledge Ngāi Takoto iwi, Ngāti Kuri iwi, Te Aupōuri iwi, Te Rarawa iwi, landowners, the ratepayers association, Far North district Council, and Northland Regional Council for their contributions as part of the Te Hiku Water Project team. The SkyTEM project was funded by Kānoa Regional Economic Development and Investment Unit (part of the New Zealand Ministry of Business, Innovation and Employment), Northland Regional Council, Far North District council, GNS Science Groundwater Strategic Science Investment Fund, Te Aupōuri iwi and Ngāi Takoto iwi.

This work was supported in part by Innovation Fund Denmark (IFD) through the Project "MapField" under Grant 8055-00025B and in part by "SuperTEM" under Grant 0177-00085B.

REFERENCES

Andersen, K.K., Kirkegaard, C., Foged, N., Christiansen, A.V., and Auken, E., 2016, Artificial Neural Networks for Removal of Couplings in Airborne Transient Electromagnetic Data. Geophysical Prospecting 64, 741-52.

Asif, M.R., Foged, N., Bording, T., Larsen, J.J., and Christiansen, A.V., 2023, DL-RMD: A Geophysically Constrained Electromagnetic Resistivity Model Database for Deep Learning Applications. Earth Syst. Sci. Data Discuss. 2022, 1-17.

Asif, M.R., Maurya, P.K., Foged, N., Larsen, J.J., Auken, E., and Christiansen, A.V., 2022, Automated Transient Electromagnetic Data Processing for Ground-Based and Airborne Systems by a Deep Learning Expert System. IEEE Transactions on Geoscience Remote Sensing 60, 1-14.

Auken, E., Christiansen, A.V., Kirkegaard, C., Fiandaca, G., Schamper, C., Behroozmand, A.A., Binley, A., Nielsen, E., Effersø, F., and Christensen, N.B., 2015, An Overview of a Highly Versatile Forward and Stable Inverse Algorithm for Airborne, Ground-Based and Borehole Electromagnetic and Electric Data. Exploration Geophysics 46, 223-35.

Gisselø, P. and Nyboe, N., Skytem High Power Systems–a New Generation of Airborne Tem Transmitters. Second European Airborne Electromagnetics Conference, 1-5.

Smith, R.S., O'Connell, M.D., and Poulsen, L.H., 2004, Using Airborne Electromagnetics Surveys to Investigate the Hydrogeology of an Area near Nyborg, Denmark. Near Surface Geophysics 2, 123-30.

Viezzoli, A., Auken, E., and Munday, T., 2009, Spatially Constrained Inversion for Quasi 3d Modelling of Airborne Electromagnetic Data–an Application for Environmental Assessment in the Lower Murray Region of South Australia. Exploration Geophysics 40, 173-83.

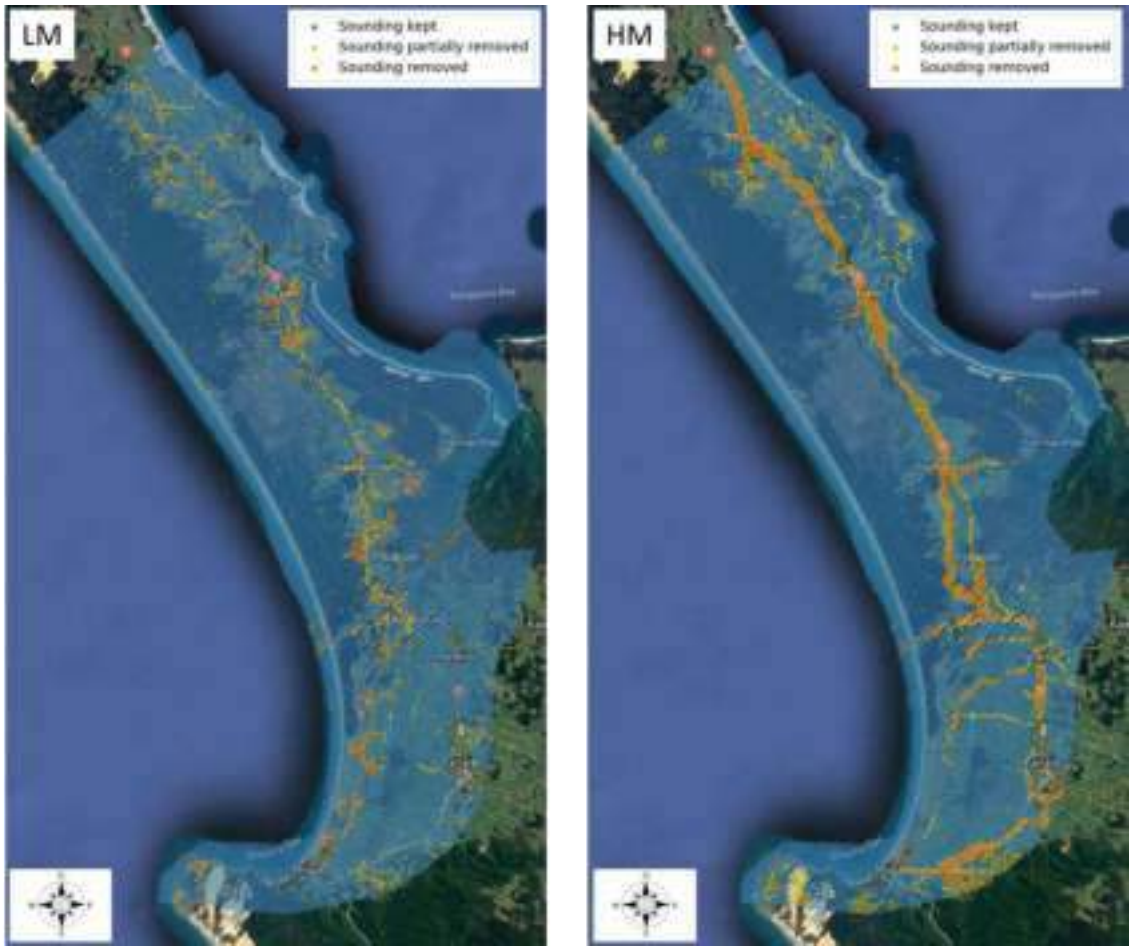

Figure 2. Data processing results for the LM and the HM data indicating the locations where the soundings are marked as corrupted, partially corrupted and clean and therefore, has been removed, partially removed or kept for inversion respectively.

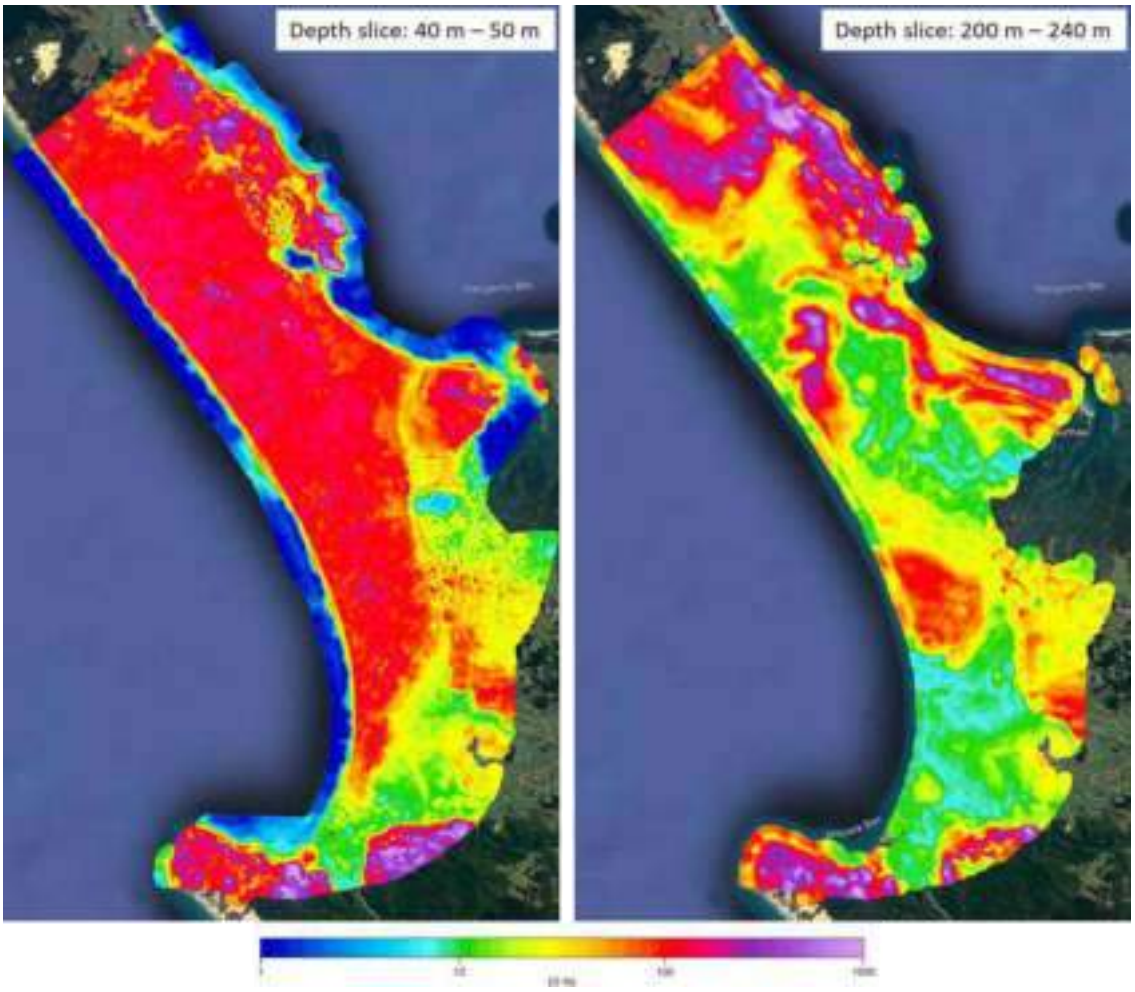

Figure 4. Mean resistivity maps with depth slices of 40 m to 50 m, and 200 m to 240 m.

An early time semi-airborne loop source TEM system

Esben Auken*
Aarhus GeoInstruments,Denmark
ea@aarhusgeoinstruments.dk

Pradip K. Maurya
Aarhus GeoInstruments, Denmark
pm@aarhusgeoinstruments.dk

Anders Vest Christiansen
Aarhus University, Denmark
anders.vest@geo.au.dk

Lichao Liu
Aarhus University, Denmark
lichao@geo.au.dk

Jacob Juul Naundrup
Aalborg University, Denmark
jnpe@es.aau.dk

Anders la Cour-Harbo
Aalborg University, Denmark
alc@es.aau.dk

Michael Juul Nielsen
Aalborg University
mjn@es.aau.dk

**Presenting author asterisked*

SUMMARY

We present a new semi-airborne transient electromagnetic (TEM) system, dTEM, for subsurface imaging. The dTEM system is designed for both imaging of groundwater and mineral resources. The system uses a large ground loop for transmitting energy into the ground. It's a dual moment system with peak current up to 30 A for high moment and 1-2 A for low moment. The fast LM turn off time is around 8 µs from the beginning of the turn-off ramp. The receiver coil is a high frequency, low noise, open air coil carried by the drone as a slung load. The high accuracy synchronisation between the transmitter and the receiver is achieved by GPS, within less than 50 ns. The drone is equipped with two lasers for determination of the attitude and real-time image processing has been developed to measure and control the movement of the receiver coil with the drone in the airspace. Data from all sensors are continuously streamed to the ground station.

The system can be used for mapping of deep targets. However, as the current waveform and system bandwidth is well defined also more shallow layered targets can be mapped. The latter makes it possible to use the system to map shallow ground water aquifers in terrains inaccessible for traditional ground-based TEM systems.

Key words: TEM, semi-airborne, Hydrogeophysics, mineral exploration, drone

INTRODUCTION

The development of semi-airborne electromagnetic systemshas been subject for numerous publications in the later years. Making a search on Google Scholar reveals not less than 292 publications since 2019 with the word "semi-airborne" in the title. Much of the research focus on systems with a large, grounded dipole transmitter and a lightweight receiver carried by a drone. With a few exceptions the research is made in the Chinese research environment.

Semi-airborne systems are in general simple systems compared to helicopter systems because the heavy source is not carried together with the receiver. However, once a 3D mineralisation target has been identified, the semi-airborne systems give a superior resolution because the offset between transmitter and receiver is varying from the centre of the transmitter loop to 3 - 4 times the loop side length.

dTEM is still under heavily research and development but the system will be presented including real survey data at the time of the AEM2023 conference.

We focus on developing a system with a well-defined and constant transmitter waveform and a receiver system with a very high frequency bandwidth. The purpose of the system is to give unbiased data from 10 µs after turn-off of the primary current in the transmitter loop so the system can be used for 3D mineralisation targets as well as layered Earth groundwater targets. The source is a single turn ground loop. The receiver is carried by a lightweight drone and the movement of the receive coil is monitored by real time image recognition.

METHOD AND RESULTS

The dTEM system consists of a transmitter, receiver, and a drone. In the following we describe the specifications and performance of each of these components. The transmitter and receiver electronics is based on the newly developed SuperTEM platform.

Transmitter: The transmitter is capable of transmitting up to 30 A with a 36 V power supply and about 1.1 ohm resistance in the transmitter loop. A 1-ohm transmitter loop can be made of a 40 x 40 m 2.5 mm^2 wire or a 100 x 100 m 6 mm^2 wire. The transmitter operates at two alternating transmitter moments, 1) a low and fast alternating moment of typically 1 Amp yielding a very fast turn-off of a ~8 µs and 2) a high and more slowly alternating moment with a longer turn-off but with maximum current output. The transmitter is water cooled with a weight of only 6 kg. The power supply can be made by 3x12 V lithium batteries in series. The current and temperature of the transmitter is kept strictly at fixed predefined values giving a completely non-varying transmitter waveform. The timing is made by a 4 MHz clock synchronised by the GPS PPS signal.

Receiver: The receiver has two channels with a bandwidth of about 1 MHz. The sampling frequency is 4 MHz, 18 bit and it has a variable gain which can be added typically after 100 µs of sampling. Data can be streamed to the instrument PC attached with internet or they can be gated with up to 1024 gates in the FPGA. It is standard to acquire 512 logarithmic spaced square gates, and during data processing use low pass filtering to

remove vibration noise from the receiver coil and then create tapered gates with a density of 8 - 10 gates/decay in time (Larsen *et al.*, 2021). Besides square gating, the FPGA controls timing, A/D converters and if attached to a transmitter it controls the pulse timing and receives current and temperatures. As for the transmitter the timing is made by a 4 MHz clock synchronised by the GPS PPS signal. Data are stored on the instrument PC and only stacked data are transferred by internet to terminal for real-time display. The noise level of the receiver board with shortened inputs is as low as 0.1 nV/√Hz.

Receiver coil: The differential receiver coil has a bandwidth of about 500 kHz with an area of 20 m^2 and a diameter of only 75 cm. The total weight of receiver electronics, battery power supply and receiver coil are just around 2 kg.

Drone: The drone is a lightweight drone of type DroneVolt Hercules 20. We chose this drone because it can carry a slung load of about 6 kg with a flight time of up to 30 min. Very important, the autopilot is based on PX4 and is open source and easily accessible. This allows us to control the drone movement in real-time which is important for controlling the oscillations of the receiver coil 5-10 m below the drone to a minimum. The drone is equipped with two laser altimeters and a downfacing camera. The camera is used to track the movement of the receiver coil and determine the relative position with respect to the GNNS position of the drone itself. The tether system can change the pitch of the receiver coil to always keep it level. The drone also has an onboard computer and radio for direct access to the receiver unit.

Figure 1. The picture shows a prototype of the drone and receiver coil flying at the Aalborg University drone test facility.

System verification: Several verifications tests has been made to verify that the system can measure unbiased low noise data. Results are not shown here but they can be summarised as: 1) Transmitter, receiver and receiver coil has been verified independently. The boards have also been built into one instrument and this instrument has been verified to be capable of reproducing the Aarhus TEM test site (Foged *et al.*, 2013) 2) It has been verified that the noise from the electronic systems on the drone does not induce noise in the receiver board itself and it does not cause increased noise in the receiver coil. 3) and finally, we verified that transmitter induced noise in the drone does not couple into the receiver coil placed at 7-10 m below the done.

All these verifications have proven that the system can receive high quality bias free data from 10 µs measured from begin of the turn-off ramp until 13 ms.

Figure 1 shows an early version being flown by a DJI M600 for aerodynamic trials.

CONCLUSIONS

dTEM is still under heavily research and development but the complete system will be presented including real survey data at the time of the AEM2023 conference.

dTEM is a semi-airborne TEM system with a well-defined transmitter waveform in the ground loop, high frequency bandwidth receiver and a unique drone carrier system. The system uses a relatively small and cheap drone, open-source auto pilot, and with a real time image processing to monitor the movement of the receiver coil. High quality bias free data begin at 10 µs measured from begin of the turn-off ramp until 13 milli second.

The system can be used not only to map deep 3D mineralisation targets but also more shallow groundwater type targets.

ACKNOWLEDGMENTS

We like to acknowledge the Innovation Fond Denmark and the Poul Due Jensen | Grundfos Foundation which under contract number 0177-00085B, SuperTEM project, supportes the research.

REFERENCES

Foged, N., Auken, E., Christiansen, A.V. & Sørensen, K.I., 2013. Test site calibration and validation of airborne and ground based TEM systems, Geophysics, 78, E95-E106.

Larsen, J.J., Pedersen, S.S., Foged, N. & Auken, E., 2021. Suppression of very low frequency radio noise in transient electromagnetic data with semi-tapered gates, Geosci. Instrum. Method. Data Syst., 10, 81-90.

Finding Geology Structures in Depth Sections from Airborne Geophysics: Automatic workflows

Desmond FitzGerald
Intrepid Geophysics
des@intrepid-geophysics.com

Simge Ayfer
Intrepid Geophysics
simge@intrepid-geophysics.com

SUMMARY

The explosion in new airborne electro-magnetic surveys is creating the need for less cutting of corners, better honouring of the known physics in the algorithms, proper use of all the system monitors.

The importance of a "good" starting model in a deterministic, iterative, non-linear inversion, such as that provided by the 2.5D Moksha code, has been recognised for many years.

This study touch bases on two project scale examples that collected by the same aircraft. Clearly in the context of an emerging continent wide AEM campaign to acquire prospective surveys the implications fort these developments are critical, in that these tools can also manage complete surveys, no matter what line length are involved. This concentration of predicting geology structures in depth sections has demonstrated the ability to identify possible exploration targets and map steeply dipping and folded geology in a deformed terrane. Equally important is then to create workflows and visualization toolkits to help interpreters, no matter what scale, or which aspect of geology or rock properties they wish to interrogate.

The lase-fare situation of accepting sub-optimal methods for estimating potential field gradients has plagued, and held back, the successful use of potential field geophysics for too many years now. Almost all interpretation methods are based upon estimating these gradients.

Key words: airborne electromagnetic, inversion, targeting, prospective survey.

INTRODUCTION

Significant breakthroughs are made by not cutting corners. 2.5D Inversion (FWI, 2D-geology, 3D-sources) formulations of Maxwell's equations leads to inversion of airborne electromagnetic (AEM) data.

Our approach with the Moksha application:

1. Links solving Maxwell's equations numerically.
2. Takes into account all of the measured secondary components (X, Y & Z)
3. Uses an adaptive noise estimation.
4. Considers topography.
5. Allows prior geology models, as well as a resistive half space as a starting model.
6. Automatically optimises the formation of the system of global equations, formulated in the complex frequency domain.
7. Is based upon a forward model algorithm for the above, that also can include both Induced Polarization and SPM.

Unlike 1D inversion methods, there is no need for applying a late time smoothing filter or using a sample-to-sample averaging process. The vertical plane approximation used in Moksha, is the canvas on which an adaptive 2D finite element mesh, is created.

All of this is hosted in a common earth 3D geology workbench environment. The setup for any survey, involves creating a system file, and a Wizard multi-panel visualization set of tools, to examine all aspects of the survey data, including decay curves, and aides for leading the operators to what part of the signal is consistent, and what part drops into the noise floor.

This has evolved (hundreds of surveys) into an established practice on any/all AEM datasets This is, hosted in the GeoModeller workbench to collate and create direct interpretation sections in their 3D context. This also includes an evolving API, based upon the GOOGLE protobuf messaging technology, that leads to optimization, audit trails, re-usable workflows, partitioning parts of the process across a set of complimentary tools, that can be deployed, via the Docker packaging, on any modern hardware (Except Fujitsu).

A second breakthrough applies to aeromagnetic datasets. Well known, but ignored till now, Cauchy derivative by integration theory stabilises the field measurements. In the last 12 months, extensive R&D and calibration work has been undertaken to verify the application of this theory to exploration geophysics datasets. This allows for higher order gradients to be computed that remain coherent, up to order 7 or better. Downwards continuation follows, allowing the creation of depth sections. Given a second high resolution depth section, the established ideas about joint inversion involving magnetics and AEM are being questioned.

The Dugald River case study, (North Queensland) demonstrates the ability of 2.5D AEM Inversion to image steeply dipping and folded geology. Simultaneously Aeromagnetic data collected in the same survey, is used to show the magnetic field projected far below the surface, also imaging some of the same, but also other aspects of the geology.

METHOD AND RESULTS

Merging the disciplines of AEM, TMI geophysics and 3D structural geology continues to challenge software engineering. Full geophysical survey data, structural geology field data and processed and inverted depth sections are to be rapidly linked, created model space and rendered in a 3D context. The support

of the implicit volume, potential field-based calculation engine used in GeoModeller, gives added influence on any gradients derived from the geophysics (Guillen et.al., 2008)

The new demonstrated workflow automatically takes any airborne observed dataset and creates a 3D project and then best fit vertical sections on a line-by-line basis. Not only AEM but TMI, Falcon, gravity, all make use of this automation.

- TMI downward continued
- EM_X & EM_Z, FWI processed,

Case Study: Dugald River VTEM Survey

In 2017 Geoscience Australia contracted Geotech to acquire approximately 15,000 line-km of VTEM Airborne EM data in Mt Isa district, Queensland. The subset of these regional survey flight lines, covering the Dugald River geological syncline are shown in Figure 1.

It is a historic and present-day mining district and also includes the Lady Loretta strata bound Zn Pb Ag deposit, and the Mount Oxide and Capricorn (Mount Gordon) fault-bound breccia and replacement copper deposits (Hutton and Wilson, 1985).

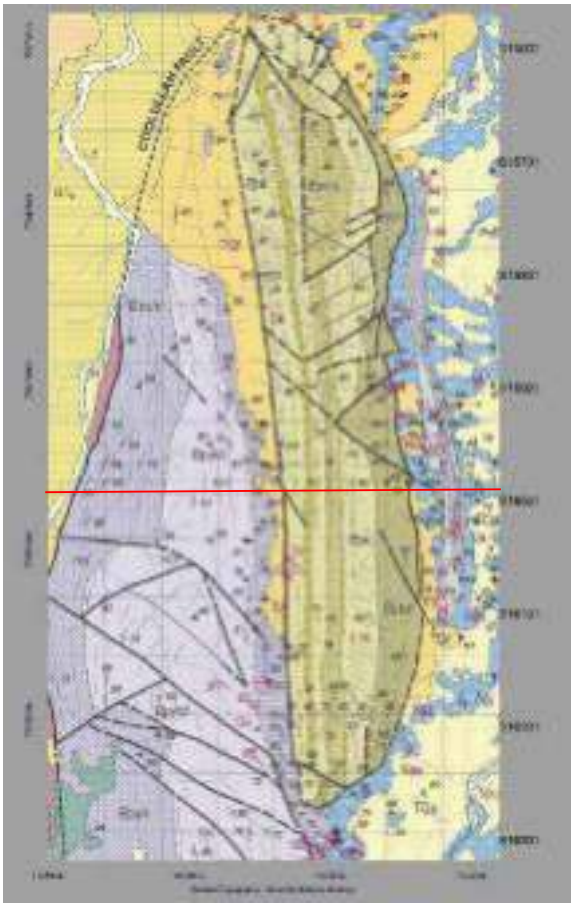

Figure 1. Dugald River area showing the Airborne EM VTEM Plus survey lines overlain. Data acquired by Geoscience Australia in 2017

Inversion result is presented for line number 16101 in Figure 1. The Moksha FWI take account of variable receiver-transmitter geometry and make use of the recorded receiver pitch channel as well as the vertical, along line and across line transmitter-receiver separation. (Silic et al, 2018, Paterson, 2020, FitzGerald et al, 2018)

Once completed, a process of presentation of the inversion results as sections in the 3D common earth geology model for the prospect are shown in Figure 2. A section is created for each survey line and then used to show each AEM geoelectric prediction, as well as the new style TMI downwards continued sections.

In this part of Australia, there is a conductive regolith, which hampers the ability to penetrate much below 400m. Compare this with areas in Canada and Europe, where depths greater than 1000m are more routinely achieved.

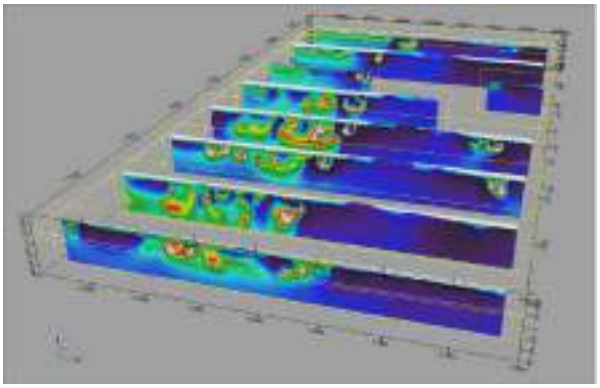

Figure 2. Dugald River Full Waveform inversion for the Log Conductivity property (units: mS/m) shown in a 3D Perspective.

For comparison, a 1D inversion was also performed on the same line. The results for Line 16101 are shown on Figure 3 along with the near-coincident geological cross section.

The FWI, using all the measured components of the B field decays, improves the definition of steep conductors, and produces a much cleaner section geometry at greater depths through the higher sensitivity of a joint inversion using both X and Z components. The adaptive noise model strategy also allows for final fine details to be teased out at depth.

Downward Continuation Method applied to Dugald River Case Study

Figure 4 shows the TMI DC responses for the same airborne survey line. The results are showing some detail that AEM does not see, some thin deeper dipoles to the west. In the location of the known synclines, the black shales may well be remnant, as positive/negative responses can be brought out via image enhancements on the limbs.

Relatively shallow positive susceptibility contrast with a polarity flip at depth (~250m asl). The plane on which the change from positive (red) to negative (blue) may be interpreted as the lower extent of the source, so we suggest this is a relatively high susceptibility body, compact in the lateral and vertical dimensions. The bottom of the source is roughly coincident with the conductive body imaged on the EM inversion.

Interpreted as sub-vertical positive susceptibility source with considerable depth extent (i.e. no change in polarity at depth). This feature aligns with the dipping eastern edge of the highly conductive EM response.

Similar in character to Feature 1, except the shallow low suggests a negative susceptibility contrast with a polarity flip to positive at depth (~250m asl). The plane on which the change from negative (blue) to positive (red) may be interpreted as the lower extent of the source. We interpret this as a relatively low susceptibility body, compact in the lateral and vertical dimensions. The bottom of is slightly offset from the eastern edge of the conductive body imaged on the EM inversion.

Figure 5 shows both the TMI and Log Conductivity sections properly co-registered. It indicates the synclines, and the more resistive quartz rocks. The TMI downward continued results show similar, and also different aspects of the geology. The dipole anomaly responses in the magnetics, are not just reflecting the inducing field, but also responding to the geometry and remanence of the black shales.

Signal enhancements are a critical enabler for the non-specialist to grasp the implied geological context. For AEM, the property shown is the electrical conductivity rock property, so units of microSeimens, while then taking its log. The dynamic range is usually 0 to 3. For the TMI work, the signal remains magnetic intensity, so the units are nano-Teslas. What is shown, derives from histogram stretching and a pseudo-colour lookup. However, a cube root is also an appropriate enhancement, as both positive and negative numbers are involved.

CONCLUSIONS

While this case study is at a relatively small scale, it still effectively shows the contrasts between the AEM/**FWI** results compared to the TMI/Cauchy Downward Continuation results. The depth sections that directly reflect structures that show Hot-Spots, folds, faults, in a way that a geologist can directly appreciate, and also test by drilling, is a major improvement and cost saver.

In the near surface conductive terrain of North Queensland, FWI still manages to see through cover and estimate both depth, geology gradients and geometry.
This collection of predicting geology structures in depth sections has demonstrated the ability to identify possible exploration targets and map steeply-dipping and folded geology in a deformed terrane. Equally important is then to create workflows and visualization toolkits to help interpreters, no matter what scale, or which aspect of geology or rock properties you wish to interrogate.

ACKNOWLEDGMENTS

The authors acknowledge George Cottew, Jeff Thurston and Ed Biegert for assistance in the development of the Cauchy workflows. Jovan Silic and, Rod Paterson made significant contributions to the practical implementation of Moksha.

REFERENCES

Cooper, G., 2004. The stable downward continuation of potential field data. Exploration Geophysics 35, 260–265.

Fedi, M., and G. Florio, 2002, A stable downward continuation by using the ISVD method, Geophys. J. Int., 151, 146–156.

FitzGerald, D., Silic, J., and Paterson, R., 2.5D AEM and Geology: 80th EAGE Conference 2018.
"Cauchy integral", *Encyclopedia of Mathematics*, EMS Press, 2001 [1994]

Guillen, A., Calcagno, P., Courrioux, G., Joly, A., Ledru, P. 2008, Geological modelling from field data and geological knowledge Part II. Modelling validation using gravity and magnetic data inversion. Physics of the earth and planetary interiors.

Hutton, L., and Wilson, I., 1985: 1:100 000 Geological Map Commentary, Mammoth Mines Region, Queensland, Bureau of Mineral Resources and Geological Survey of Queensland, Australian Government Publishing Service, Canberra.

Silic, J., Paterson, R., and FitzGerald, D., 2.5D vs 1D Forward and Inversion Methods at a Survey Scale: A Case Study: ASEG Extended Abstracts 2018 (1) 1-8.

Paterson, R. 2.5D Airborne electromagnetic inversion: A review of the benefits of moving to a higher dimension: ASEG Preview 33-47., August 2020.

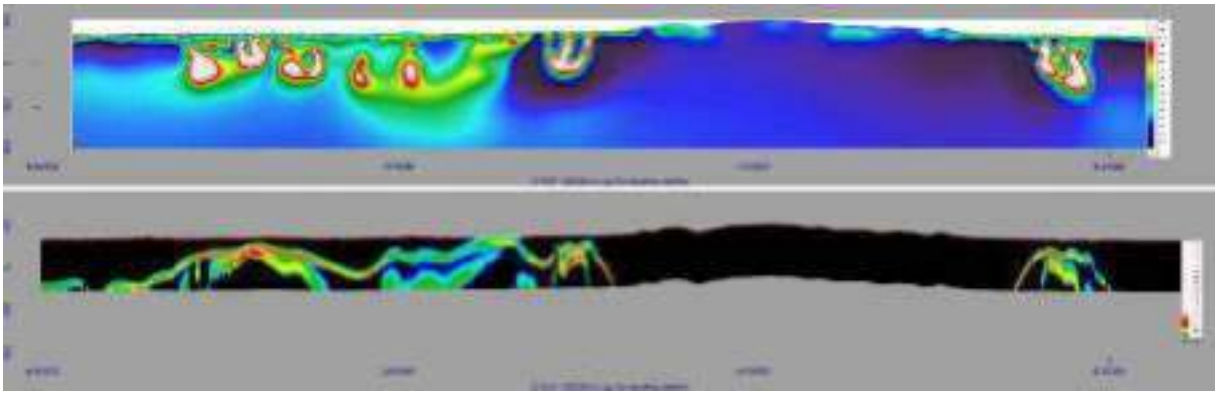

Figure 3. Dugald River Full Waveform inversion and CDI results for Line 16101 in 900m depth level.

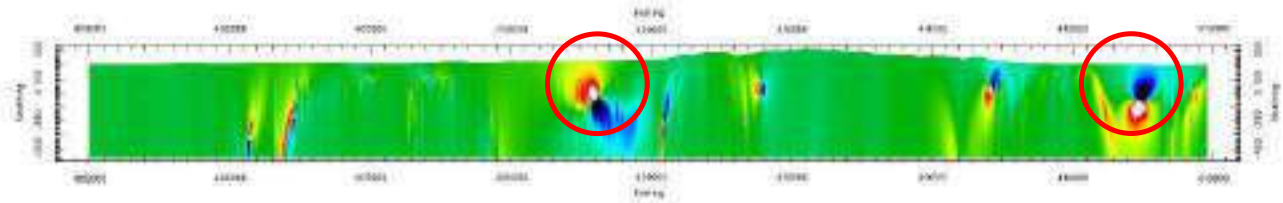

Figure 4. Dugald River Downward Continuation Dipoles, line 16101

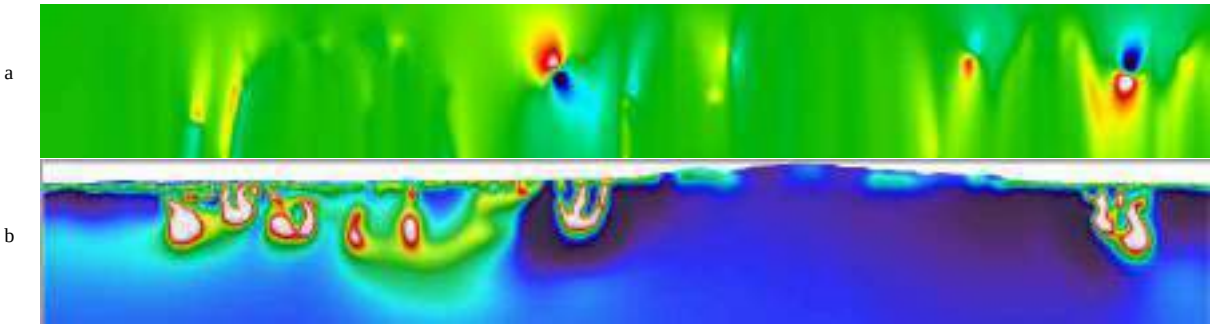

Figure 5. Dugald River a) Downward Continuation and b) Airborne VTEM 2.5D Inversion results

Quantifying salinity in the layered coastal aquifers underlying and adjacent to Delaware Bay USA using AEM-derived resistivity

Lyndsay B. Ball
U.S. Geological Survey
Denver, Colorado, USA
lbball@usgs.gov

Burke J. Minsley
U.S. Geological Survey
Denver, Colorado, USA
bminsley@usgs.gov

Gavin S. Wilson
U.S. Geological Survey
Denver, Colorado, USA
gswilson@usgs.gov

Holly A. Michael
University of Delaware
Newark, Delaware, USA
hmichael@udel.edu

Douglas A. Burns
U.S. Geological Survey
Troy, New York, USA
daburns@usgs.gov

Mark R. Nardi
U.S. Geological Survey
Dover, Delaware, USA
mrnardi@usgs.gov

Emmanuel G. Charles
U.S. Geological Survey
Lawrenceville, New Jersey, USA
echarles@usgs.gov

SUMMARY

Airborne electromagnetic (AEM) methods are particularly well suited to coastal aquifer salinity studies, yet the quantitative translation from bulk resistivity to fluid salinity carries uncertainty that can impact mapped salinity distributions and interpretations of the freshwater-saline interface and hydrostratigraphic layers. A recent AEM survey of the region near the Delaware Bay, USA highlights several challenges common to coastal hydrogeologic settings that may influence both qualitative and quantitative interpretation. We use a Bayesian inversion to estimate geophysical parameter uncertainty, and results are integrated with hydrogeologic measurements to develop quantitative interpretations of salinity across the freshwater-saline interface in stacked aquifers.

Key words: airborne electromagnetic, salinity, uncertainty, saltwater interface, coastal aquifers

INTRODUCTION

Coastal regions are among the most densely populated parts of the world, and increasing coastal development is placing higher pressure on the water resources of these regions. Groundwater salinity can limit the beneficial uses of water, impacting groundwater availability, and the salinity of groundwater-surface water exchange also plays an important role in estuary and marine ecosystems. The dynamics of the freshwater-saline water interface (FSI) in coastal aquifers is influenced by multiple stressors, including groundwater pumping, land modifications, tidal flooding and storm surge, and changes in hydrologic boundary conditions from regional inland groundwater systems and rising sea levels. Large fluid density contrasts across the FSI can lead to particularly challenging groundwater modelling conditions, while salinity distributions are difficult to measure at the spatial resolution needed to characterise the FSI (10s of meters) at scales relevant to potential hydrologic stressors (many kilometers). An improved understanding of the current location of the FSI and a better understanding of the hydrogeologic framework of coastal aquifer systems are critical to the development of useful groundwater flow and transport models, to establish baseline conditions that can be used to assess changing conditions in the future, and to inform management of ecological and water resources (Michael *et al.*, 2017; Stein *et al.*, 2023).

Groundwater is an important component of the fresh water supply of the Northern Atlantic Coastal Plain of the eastern United States, representing 10-20% of total water withdrawals in New Jersey and Delaware (Dieter *et al.*, 2018). The relative importance of salinity distributions to modelling and managing this critical aquifer system has motivated an AEM survey of the Delaware Bay and surrounding near-shore environment as part of the U.S. Geological Survey's (USGS) Next Generation Water Observing System implementation in the greater Delaware River Basin. One objective of this program is to foster innovation and development of water monitoring methods to support modern water prediction and decision support systems.

AEM surveys have a number of advantages to mapping salinity distributions in coastal aquifers. While well data are fundamental to directly measuring salinity, wells can be difficult to install and maintain in the marshy intertidal zones where the most dynamic salinity conditions are expected to occur, leaving substantial lateral and vertical gaps between point observations. Electromagnetic methods are well suited to estimating salinity distributions between wells, due to the inherent sensitivity to conductive bodies, the strong dependency between fluid conductivity and total dissolved solids concentrations, and the relatively high salinity gradients encountered across the FSI. The airborne platform is uniquely suited to acquiring continuous data across land, tidal, and open water environments with minimal disturbance to sensitive ecosystems, while covering large areas in a relatively short time period. However, coastal aquifers present distinct methodological challenges, including abrupt resistivity contrasts and sensitivity limitations underlying strongly conductive layers. Consideration of geophysical parameter uncertainty in the context of specific hydrogeologic interpretations is key to accurate salinity transforms and to advancing the use of AEM methods in coastal aquifer research and resource management.

METHOD AND RESULTS

AEM data acquisition over and adjacent to the Delaware Bay was conducted with the SkyTEM 304M system in July 2022 (Figure 1). The survey extends from the Atlantic Coast to the mouth of the Delaware River and encompasses both Delaware and New Jersey shores. The survey was designed with 500 m line separation in intertidal and near-shore regions where the FSI is anticipated to occur, generally extending from 500 m landward of the transition from the intertidal zone to dry land, approximated by a 2 m land surface elevation contour, to 2 km seaward of the shoreline. Flight lines traversing the Delaware Bay occur at 3 km line separation where more gradual salinity transitions were expected and to minimise overwater flights. Additional lines extend inland following major river corridors and selected inland bays.

The Delaware Bay survey presents several hydrogeologic scenarios that lead to challenging inverse modelling and reduced sensitivity zones that can impact the accuracy in defining the FSI, quantifying groundwater salinity distributions, and constraining important hydrostratigraphic boundaries. These non-uniform sensitivity variations are inherently tied to high-contrast conductivity layering and are not fully captured by readily available depth-of-investigation estimates or sensitivity estimates from regularized deterministic inversions (Christiansen and Auken, 2012; Auken *et al.*, 2015). The introduction of seawater at the surface in the intertidal and near-tidal zones results in a strong surface conductor in numerous locations (Figure 2 A), with reduced sensitivity to underlying parameters. The FSI commonly occurs in the intertidal zone and below this surface conductor, and defining the relative uncertainty of transformations to total dissolved solids or chloride concentrations is fundamental to quantitative integration with groundwater models. Similar sensitivity challenges occur in the underlying confined systems (Figure 2 B) and below the strongly conductive Delaware Bay itself, where variations in subseafloor salinity is of particular interest (Figure 2 C). In some locations, interruptions in the modelled lateral extent of moderately conductive layers associated with clay-rich regional confining units correlate with the presence of thin surficial saline layers, such as tidal stream channels, making interpretations of the continuity of these units questionable (Figure 2 D). Additionally, tidal inundation changes throughout the period of data collection, resulting in potential shifts in shallow conductivity structure.

To evaluate the interpretational impacts of these various sources of uncertainty, we are using a Bayesian inversion approach (Minsley, 2021) utilising the open-source code GeoBIPy (Foks and Minsley, 2020) to develop depth-distributed resistivity probability distributions and layer interface likelihoods. This probablistic approach is integrated with groundwater and surface water salinity measurements, lithologic records, borehole geophysical logs, and tide gauge data to constrain resistivity-salinity relationships and refine the hydrostratigraphic framework. A combination of probabilistic categorical scenarios and lateral and vertical resistivity gradients are being explored to develop interpretations of the FSI reflective of the geophysical and interpretational uncertainty of this challenging coastal environment.

.

Figure 1. Map showing location of AEM flight lines for the Delaware Bay survey along the eastern coastal plain of the United States.

ACKNOWLEDGEMENTS

This work is funded by the U.S. Geological Survey's (USGS) Next Generation Water Observing System with supplemental funds from Delaware's Project WiCCED (Water in the Changing Coastal Environment of Delaware, National Science Foundation EPSCoR OIA1757353). AEM data were collected by SkyTEM ApS and Livewire Aviation under contract to USGS through Woolpert; Doug Garrie, Steve Sartor, Amir Soltanzadeh, Greg Roman, and Urbano Jaimes, Chase Olsen and Alan Stack were instrumental to the collection of these data. Any use of trade, firm, or product names is for descriptive purposes only and does not imply endorsement by the U.S. government.

REFERENCES

Auken E, Christiansen A, Kirkegaard C, Fiandaca G, Schamper C, Behroozmand A, Binley A, Nielsen E, Effersø F, Christensen N, et al. 2015. An overview of a highly versatile forward and stable inverse algorithm for airborne, ground-based and borehole electromagnetic and electric data. *Exploration Geophysics* **46** (3): 223–235 DOI: 10.1071/EG13097

Christiansen AV, Auken E. 2012. A global measure for depth of investigation. *GEOPHYSICS* **77** (4): WB171–WB177 DOI: 10.1190/geo2011-0393.1

Dieter CA, Maupin MA, Caldwell RR, Harris MA, Ivahnenko TI, Lovelace JK, Barber NL, Linsey KS. 2018. Estimated use of water in the United States in 2015. U.S. Geological Survey Circular 1441. U.S. Geological Survey, Reston, VA. DOI: 10.3133/cir1441

Foks NL, Minsley BJ. 2020. Geophysical Bayesian Inference in Python (GeoBIPy) Available at: https://doi.org/10.5066/P9K3YH9O [Accessed 17 December 2020]

Michael HA, Post VEA, Wilson AM, Werner AD. 2017. Science, society, and the coastal groundwater squeeze. *Water Resources Research* **53** (4): 2610–2617 DOI: 10.1002/2017WR020851

Minsley BJ. 2011. A trans-dimensional Bayesian Markov chain Monte Carlo algorithm for model assessment using frequency-domain electromagnetic data. *Geophysical Journal International* **187** (1): 252–272 DOI: 10.1111/j.1365-246X.2011.05165.x

Stein S, Shalev E, Sivan O, Yechieli Y. 2023. Challenges and approaches for management of seawater intrusion in coastal aquifers. *Hydrogeology Journal* **31** (1): 19–22 DOI: 10.1007/s10040-022-02575-5

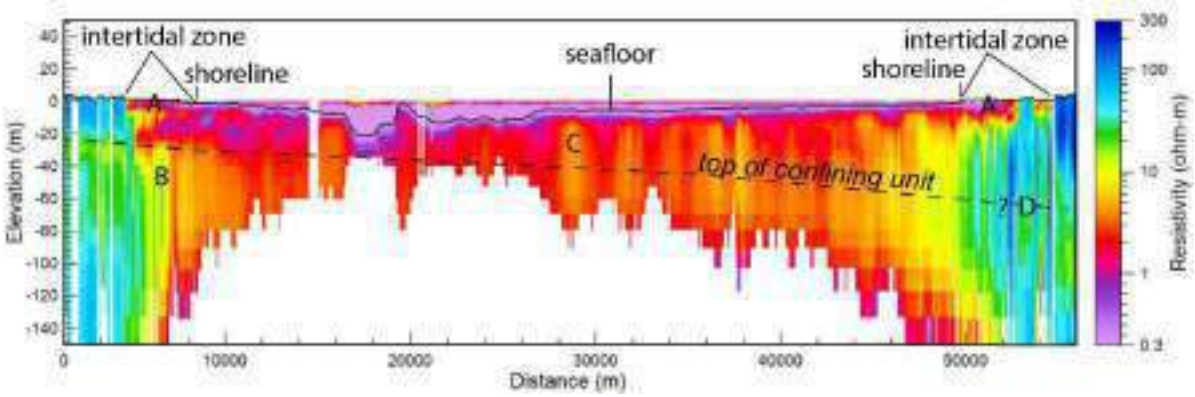

Figure 2. Example of a deterministic laterally constrained inverted resistivity section across the Delaware Bay highlighting some of the sensitivity challenges to salinity mapping in coastal aquifers. Letters indicate features described in the text.

Imaging volcanic systems via multi-scale electromagnetic imaging

Paul A Bedrosian*
U.S. Geological Survey
Denver, Colorado, USA
pbedrosian@usgs.gov

Carol A Finn
U.S. Geological Survey
Denver, Colorado, USA
cfinn@usgs.gov

Jade Crosbie
U.S. Geological Survey
Denver, Colorado, USA
jcrosbie@usgs.gov

Dana E Peterson
U.S. Geological Survey
Denver, CO, USA
dpeterson@usgs.gov

Jim Kauahikaua
U.S. Geological Survey
Hilo, HI, USA
jimk@usgs.gov

Patricia MacQueen
U.S. Geological Survey
Denver, CO, USA
pmacqueen@usgs.gov

**presenting author*

SUMMARY

Electromagnetic imaging provides a wealth of information about the structure, composition, and processes within volcanic systems. While deep-sensing techniques such as magnetotellurics (MT) focus on the magmatic system, airborne electromagnetics (AEM) is capable of mapping active hydrothermal cells and their alteration products, faults, lava flows, water-saturated zones, and perched aquifers. All these components are important to improving volcanic hazard assessments and understanding magmatic and hydrothermal processes at work beneath active volcanoes.

We present two recent AEM studies at Yellowstone and Kīlauea volcanoes. At Yellowstone, AEM studies map conduits that connect heat and deep thermal fluids to surface thermal features. We further identify a distinct electrical signature over hydrothermal domes which sheds light on their formation and potential for hydrothermal explosions. At Kīlauea, AEM models image the structural backbone of this complex volcano, including elevated conductivity over the summit lava lake, along faults accommodating collapse of the volcano's south flank, and along both the flanking rift zones that have sourced lavas from fissure eruptions over the past two centuries. Work at both volcanoes is ongoing of merging AEM and MT data sets to image these systems from the base of the crust to the surface.

Key words: airborne electromagnetic, volcanic systems, magnetotellurics, Yellowstone, Kīlauea

INTRODUCTION

Active volcanoes present a range of eruptive and non-eruptive hazards (lava flows, pyroclastic flows, phreatic explosions, lahars, etc.) yet these systems are notoriously hard to image geophysically due to their large extent, steep and unstable terrain, and general inaccessibility. To understand and mitigate volcanic hazards requires detailed understanding of 1) the structure of the volcanic edifice including faults, fractures and collapse scars, 2) the three-dimensional distribution of subsurface water and alteration, and 3) the location and volume of subsurface magmas.

Relative to most areas, volcanic systems are lithologically homogeneous and offer a generally resistive 'background' for imaging the effects of water saturation, hydrothermal alteration, and melt, all of which serve to decrease bulk resistivity. Electromagnetic (EM) methods also offer the opportunity for true multi-scale imaging – with the combination of AEM and MT methods providing a complete picture of a volcano's hydrothermal and magmatic system from 10s of meters to 10s of kilometers.

The U.S. Geological Survey (USGS) has been imaging active volcanic systems using AEM for over two decades. Early studies focused on slope stability and lahar potential at Mounts Rainier and Adams in the Washington Cascades volcanic arc, USA by mapping water-saturated zones and regions of hydrothermal alteration (e.g., Finn et al., 2001, 2007). AEM models have also been used to constrain snow and ice thickness, providing estimates of the amount of water that could be mobilised during lahars or debris flows (Finn et al., 2012). These early studies utilised frequency-domain EM systems and were limited to the volcanic summits; more recent studies at Mounts St. Helens and Iliamna (Peterson et al., 2021) employ time-domain EM systems and cover the entire volcanic edifice.

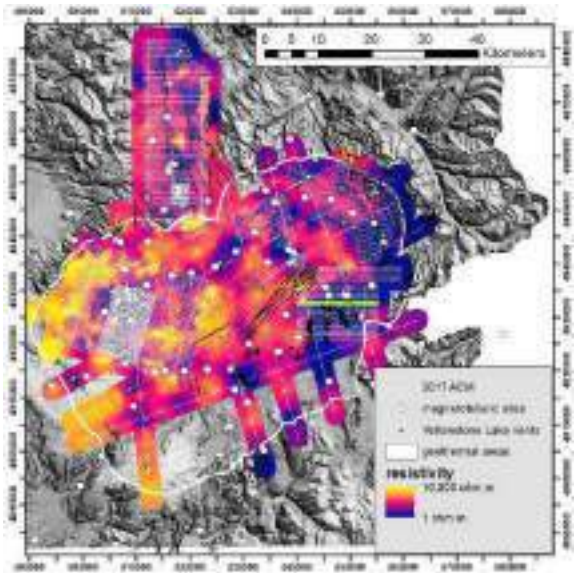

Figure 1. Electromagnetic surveys over Yellowstone volcano (2016-2022). Background color represents resistivity at 100 m depth from a kriged voxel of the (1D) inverted AEM data. Regional faults in black; caldera margin in white. Green line marks the location of cross-section in Figure 3.

Past investigations were all at arc stratovolcanoes and, except for Mount St. Helens, are limited to the shallowest parts of the volcanic system (≤100 m). We focus here on two new studies at hotspot volcanoes – the mafic Kīlauea shield volcano in Hawaii and the silicic Yellowstone volcano in Wyoming, USA.

Yellowstone volcano, one of the largest silicic calderas on Earth, drives more than 10,000 thermal features including a variety of geysers, mud pots, hot pools, and fumaroles. The primary volcanic hazard at Yellowstone comes not from magmatic eruptions but from hydrothermal explosions generated during rapid decompression of confined thermal fluids. An AEM survey was flown to image the subsurface plumbing that links heat and fluids at depth to surface features as well as to understand the structure, controls, and triggers for hydrothermal explosions. Through the addition of MT data collected throughout the caldera (Figure 1), we seek to further map the connection between the shallow hydrothermal systems (<1-2 km depth) and the underlying heat source (silicic magmas at 6-10 km depth) that drive them.

Kīlauea volcano is one of the most active volcanoes in the world, erupting nearly continuously for more than 100 years. Fissure eruptions in 2018 along the Lower East Rift Zone (LERZ), accompanied by collapse of the summit crater (Neal et al., 2018), motivated AEM and MT surveys to provide a post-eruptive 'snapshot' of the system and to image structural connections between the summit area, the LERZ, and Southwest Rift Zone (SRZ) (Figure 2). The completed AEM survey and ongoing MT surveys cover the same area and, when combined, will image Kīlauea from ~10 m to 10+ km depth.

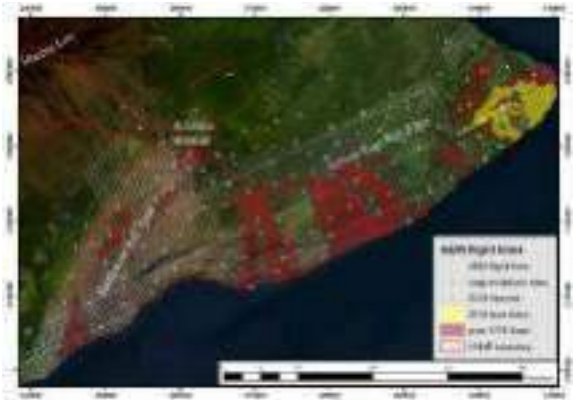

Figure 2. Electromagnetic surveys over Kīlauea volcano. HVNP = Hawaiian Volcanoes National Park.

METHOD AND RESULTS

At Yellowstone and Kīlauea, 4,200 and 2,100 line-kms of AEM data were acquired in 2016 and 2022, respectively, using a SkyTEM 312 time-domain helicopter EM system (Finn et al., 2022a; Bedrosian et al., 2022). The surveys were designed to capture the entirety of each of these large volcanic systems. A series of tightly spaced lines were flown over the major thermal basins at Yellowstone, augmented by widely spaced reconnaissance lines spanning the entire caldera (Figure 1). At Kīlauea, flight lines encompassed the SRZ, the summit crater (which hosted an active lava lake at the time of flying), and the LERZ (where fissure eruption occurred during the 2018 eruption) (Figure 2).

One-dimensional electrical resistivity models were estimated using Aarhus Workbench laterally and spatially constrained inversions (Auken et al. 2015). Early-time system response data were modelled at both volcanoes to enhance imaging of near-surface structure. Stochastic inversions (Minsley et al., 2021) were also carried out to better understand uncertainty and depth-of-investigation of the resulting models. Specific to Yellowstone, spatially constrained inversion was carried out beneath Yellowstone Lake where detailed lake bathymetry was used as prior information in the starting models to estimate sub-lake resistivity structure more accurately.

The processing and inversion of the Kīlauea AEM data are challenging and require considerable manual editing. The high resistivity of fresh lava flows and challenging terrain, particularly near the summit area, result in extremely low signal levels, sometimes with only a handful of time gates rising above background noise. In addition, one of only a handful of worldwide VLF transmitters is on the nearby island of Oahu and resulted in some degradation of the data. These data are also challenging from an inversion perspective; the vast majority of flight lines (Figure 2) transition from saltwater intrusion near the coastline (~1 Ωm) to highly resistive lava flows (~10,000 Ωm). Such strong contrasts present challenges to laterally and spatially constrained inversions - both in terms of generating meaningful start models and with inversion convergence.

Yellowstone: faults, fluids, and explosion craters

The distribution of thermal features at Yellowstone is non-uniform, with their locations, until recently, thought to be controlled primarily by the edges of relatively impermeable rhyolite flows, where water flowing laterally from distal sources can emerge. The AEM models have instead shown that most thermal areas are localised above regions of low resistivity (and low magnetic susceptibility) that are in turn associated with regional and caldera margin faults, and extensive fracture networks (Finn et al., 2022b). These spatial relations are evident when examining subsurface resistivity in relation to regional faults and surface geothermal features (Figure 1). The models further show evidence for mixing of thermal fluids, which tend to be more electrically conductive, and local groundwater. The balance of heat and fluid flux is a function of groundwater elevation, which together influence the nature and chemistry of the resulting thermal fluids (acid sulphate vs neutral chloride). Ultimately, it is the combination of the rhyolite heat source beneath the caldera, active faults that present permeable fluid pathways, and surface elevation that control Yellowstone's thermal features.

The northeast corner of the caldera is where rhyolite melts are shallowest and heat flow is highest. This is also where the highest concentration of hydrothermal explosion craters (HECs) are found, including the world's largest known HEC at Mary Bay (2.5 km diameter). HECs are considered one end member of a hydrothermal system where energy, typically

dissipated through convection, surface boiling and discharge, is limited by a low-permeability cap. Hydrothermal domes (which have been speculated to be incipient HECs) and craters are common beneath Yellowstone Lake due to the added confining pressure of the water column, resulting in elevated fluid temperatures (more energy in the system), higher heat flux (larger ΔT at the lake bottom), and accelerated alteration rates. Hydrothermal explosions may be triggered by perturbations to the system such as earthquakes or a sudden drop in lake-level.

AEM models beneath Yellowstone Lake reveal important aspects of these systems. There is abundant evidence for doming from parabolic conductors imaged within glacial sediment and debris beneath the lake (Figure 3). These domes are co-located with vents along their limbs and further aligned with deep-seated faults that are mapped or inferred from magnetic data. Many of the imaged hydrothermal domes have moderate resistors at their centers that are interpreted to reflect less altered rock within a steam or vapor-dominated reservoir. Independent evidence for vapor-dominated zones beneath the lake comes from vent fluid temperature and chemistry in addition to the type of alteration products on the lake bottom (Fowler et al., 2019). The electrical signature of these domes is like that of nearby Mud Volcano (Figure 1), where a vapour-dominated system has been confirmed through drilling (White et al., 1971).

Structure and alteration at Kīlauea volcano

Modelling of the Kīlauea AEM data is ongoing, but observations can be made from map slices of the measured data. Signal amplitudes at 25 µs (Figure 4a), corresponding to depths of 10-30 m, are elevated due to high conductivity from saltwater intrusion along the coastline (1). High conductivity is also suggested in the northwest survey area (2) that was blanketed by ash layers from explosive eruptions more than 2,000 years ago (Uwekahuna ash). The summit crater (3) is also conductive due to the ~300-acre lava lake and adjacent areas of hydrothermal alteration exposed in the crater wall. High amplitudes are also present along the chain of craters that mark the LERZ (4), including at Pu`u O`o, the source of the longest and most voluminous outpouring of lava in the last 500 years along the LERZ (1983-2018). Finally, several linear features south of the summit area are marked by high amplitudes that follow faults of the Hilina Fault System (5), a series of extensional faults accommodating progressive collapse of Kīlauea's south flank.

At 225 µs decay time, corresponding to ~200 m depth, saltwater intrusion (1) is more pronounced, extending 5+ km inland along the entire coastline. The summit area (2) remains conductive, where nearly 400 m of lava have filled the summit crater since the 2018 summit collapse. Elevated conductivity is also suggested by several linear tracks of high signal amplitude along the LERZ (3) and SRZ (4). These features underlay the source regions for nearly all lava flows since 1780 and may reflect alteration halos surrounding the sheeted dike complexes that feed fissure eruptions along the two rift zones.

An inverted cross section (Figure 5) crossing the LERZ provides a more detailed window into the volcano. A relatively flat lava delta is imaged near the coast, transitioning inland to a thick package of resistive lava flows. Layering can be seen within these lavas, possibly reflecting debris flows or more extensive weathering during interflow periods. Saltwater intrusion can be traced inland for more than 5 km before resolution is lost beneath ~600 m of overlying flows. Conductive pore waters further illuminate the composite nature of the lava flows, revealing thin layering when saturated. Finally, the cross-section is disrupted by a conductive zone, 2-5 km in width that projects 300-400 m above the background structure and aligns with the axis of the LERZ. As speculated above, this may reflect hydrothermal alteration peripheral to the sheeted dikes that feed fissure eruptions along the rift axis.

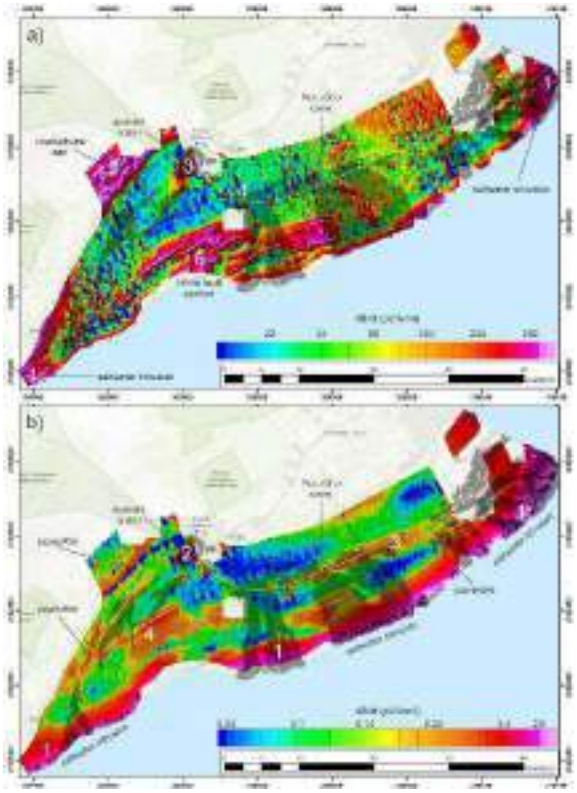

Figure 4. Secondary magnetic field amplitude at (a) 25 and (b) 225 µs after current turn-off. High (low) amplitudes are in pink (blue). Shaded regions show post-1778 lava flows. Black dashed line indicates cross-section in Figure 5.

CONCLUSIONS & OUTLOOK

AEM surveys over two high-profile volcanoes provide unprecedented views into their near-surface structure. At Yellowstone, fluid pathways have been imaged for the first time and highlight the importance of faults and vertical fluid flow in driving surface thermal features. Electrical models over Yellowstone Lake image vapour-dominated hydrothermal domes and provide clues as to the processes leading to their formation and their demise through hydrothermal explosions. At Kīlauea, structures in the AEM data connect the summit to the flanking rift zones, where all recent fissure eruptions have occurred. Additionally, a clear electrical signature is observed along faults interpreted to accommodate collapse of Kīlauea's south flank. Finally, models over the summit crater may provide important constraints on the volume of the evolving lava lake.

All of these findings are the result of imaging volcanic systems from the surface to ~500 m depth. These depths are too shallow, however, to image a volcano's magmatic system or to capture the roots of the hydrothermal system. MT imaging is required to study the critical connection between magmatic and hydrothermal systems. MT modelling of the upper 500 m is challenging due to the high station density needed to constrain these depths as well as issues of static shifts — a type of bias in MT data caused by near-surface electric-field distortion. These limitations can be overcome by marrying the two methods. At Yellowstone, we have used the AEM models to generate a voxel of the upper 500 m which can then be embedded as prior information into a three-dimensional MT inversion. Figure 1 shows a slice through the voxel generated for Yellowstone. Through this and other approaches approach we hope to achieve the first truly multi-dimensional models through a complex volcanic system.

ACKNOWLEDGMENTS

These studies were funded through the USGS Volcano Hazards and Mineral Resources Programs. The Kīlauea studies are funded by 2019 Kīlauea Disaster Supplemental Funding. All airborne geophysical data were acquired by SkyTEM through competitive open solicitations. We thank SkyTEM personnel and the staff at Yellowstone and Hawaiian Volcanoes National Parks for invaluable assistance in executing these surveys. Any use of trade, firm, or product names is for descriptive purposes only and does not imply endorsement by the U.S. government.

REFERENCES

Auken, E., A. V. Christiansen, C. Kirkegaard, G. Fiandaca, C. Schamper, A. A. Behroozmand, A. Binley, et al. 2015. "An Overview of a Highly Versatile Forward and Stable Inverse Algorithm for Airborne, Ground-Based and Borehole Electromagnetic and Electric Data." *Exploration Geophysics* 46 (3): 223–35. https://doi.org/10.1071/EG13097.

Bedrosian, P.A., Finn, C.A., Crosbie, J., Bloss, B.R., Holbrook, W.S., and Auken, E., 2022, Airborne Electromagnetic Survey Processed Data and Models Data Release, Yellowstone National Park, Wyoming, 2016: U.S. Geological Survey data release, doi: 10.5066/P9LVAU7W.

Finn, C.A., Bedrosian, P.A., Bloss, B.R., Holbrook, W.S., and Auken, E., 2022a, Airborne Electromagnetic and Magnetic Survey, Yellowstone National Park, 2016 - Minimally Processed Data: U.S. Geological Survey data release, doi: 10.5066/P9MCJ9B6.

Finn, C.A., Bedrosian, P.A., Holbrook, W.S., Auken, E., Bloss, B.R., Crosbie, J. 2022b. Geophysical imaging of the Yellowstone hydrothermal plumbing system. Nature, 603(7902), 643–647, doi: 10.1038/s41586-021-04379-1.

Finn, C.A., Deszcz-Pan, M. and Bedrosian, P.A. 2012. Helicopter electromagnetic data map ice thickness at Mount Adams and Mount Baker, Washington, USA, J. Glaciol., 58 (212), 1433-1443.

Finn, C.A., Deszcz-Pan, M., Anderson, E.D. and John, D.A. 2007. Three-dimensional geophysical mapping of rock alteration and water content at Mount Adams, Washington: Implications for lahar hazards, J. Geophys. Res., 112, B10204, doi:10.1029/2006JB004783.

Finn, C.A., Sisson, T. W. and Descsz-Pan, M. 2001. Aerogeophysical measurements of collapse-prone hydrothermally altered zones at Mount Rainier Volcano, Washington: Nature, v. 409, p. 600-603.

Fowler, A.P.G., Tan, C., Cino, C., Scheuermann, P., Volk, M.W.R., Shanks, W.C.P. III and Seyfried, W.E. Jr. 2019. Vapor-driven sublacustrine vents in Yellowstone Lake, Wyoming, USA, Geology, 47, 223–226, doi: 10.1130 /G45577.1.

Minsley, B.J., Foks, N.L., and Bedrosian, P.A. 2021. Quantifying model structural uncertainty using airborne electromagnetic data, Geophys. J. Intl., 224, 590-607, doi: 10.1093/gji/ggaa393.

Neal, C. et al. 2018. The 2018 rift eruption and summit collapse of Kīlauea Volcano, Science, 363(6425), 367-374, doi:10.1126/science.aav7046.

Peterson, D. E., Finn, C. A. and Bedrosian, P. A. 2021. Airborne geophysical imaging of weak zones on Iliamna Volcano, Alaska: Implications for slope stability. Journal of Geophysical Research: Solid Earth, 126, e2020JB020807. doi: 10.1029/2020JB020807.

White D. E., Muffler, L. J. P. and Truesdell, A. H. 1971. Vapor-dominated hydrothermal systems compared with hot-water systems: Econ. Geol., 66, 75-97.

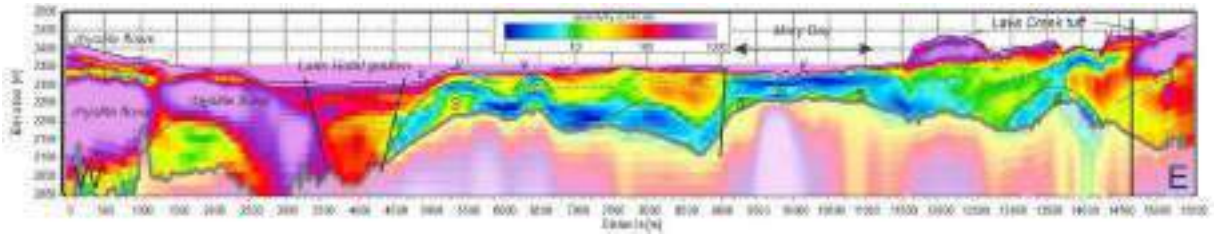

Figure 3. Resistivity cross-section through Yellowstone Lake. Profile location shown in Figure 1. Vertical exaggeration of 5:1. S= steam-dominated zone; V=lake-bottom vent. Thick black lines indicate mapped or inferred faults. Thin black lines denote hydrothermal domes; dashed lines are interpreted contacts.

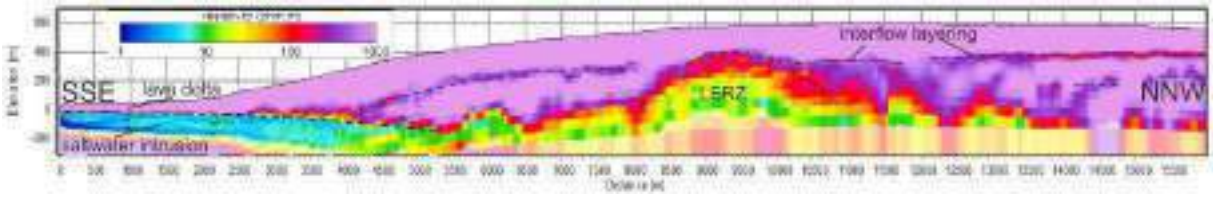

Figure 5. Resistivity cross-section across Kīlauea's LERZ. Profile location shown in Figure 4. Vertical exaggeration of 2:1. Dashed lines are interpreted contacts.

Helitem^2 – System Updates for Broadband AEM Data

Darren Burrows*
Xcalibur Multiphysics
Mississauga, Ontario, Canada
darren.burrows@xcaliburmp.com

David Murray
Xcalibur Multiphysics
Mississauga, Ontario, Canada
dave.murray@xcaliburmp.com

Graham Konieczny
Xcalibur Multiphysics
Mississauga, Ontario, Canada
graham.konieczny@xcaliburmp.com

**presenting author asterisked*

SUMMARY

In the last 5 years, advances in receiver suspension and receiver construction have made airborne electromagnetic low-base frequency operation possible and greatly improved the ability to explore in conductive environments. We discuss the changes made to the Xcalibur Helitem^2, helicopter time domain EM, system to enable low base frequency operation - first at 15 / 12.5 Hz, and then at 7.5 / 6.25 Hz.

The transmitter has also been redesigned to now use a square input waveform at 50% duty cycle, with a rapid turn-off. At low base frequencies this results in a long, high powered transmitter pulse that still creates high frequency signal.

Various data examples will be shown to illustrate the practical advantages of the system updates. This includes an example from Nevada where various Helitem^2 system configurations were flown over a line of ground TDEM data at different heights, as well as a Nickel exploration project.

Key words: Time Domain Electromagnetics, Low base frequency, Coil motion, Mineral exploration

INTRODUCTION

Increasingly, mineral exploration is targeting deeper deposits in areas under cover and geophysical methods are being used as a first pass screening tool. There is value in an airborne EM system that is able to penetrate conductive cover and is sensitive to deeper deposits so that large areas can be explored quickly and with greater confidence. However, it would be foolish to ignore the response from near surface targets, or targets in resistive host rocks.

Additionally, system upgrades have also been targeted at specific commodities, such as Nickel Sulphides (NiS) and Lithium brines (Li). The extreme conductivity of massive NiS can cause the decay constant of a potential resource to be very large (Smiarowski and Macnae, 2013), necessitating low-base frequency or ground EM surveys. Exploration for saline groundwater that is enriched in dissolved lithium faces a similar challenge. Unlike airborne acquisition, ground EM surveys can be time-consuming, very costly, and suffer in difficult to access terrain.

GOALS FOR SYTEM UPGRADES

In general, the team responsible for the Helitem system has endeavoured to increase the system bandwidth. Initially, this resulted in the Helitem MultiPulse system, which employed a short (1 ms), low moment square pulse at the end of the standard half-sine offtime. The increase in high frequency power above 2 kHz can be seen in Figure 1. This overlapped with the lowering of the transmitter base frequency from 30 / 25 Hz to 15 / 12.5 Hz to be the first step in achieving generally broadband data from AEM systems.

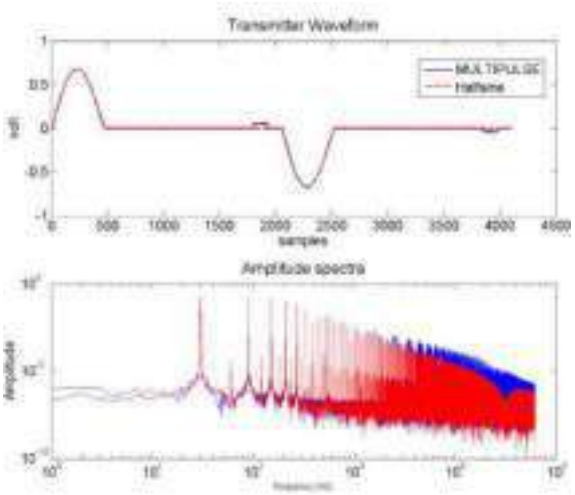

Figure 1. Current waveform for a halfsine-only pulse (red) and MultiPulse (top panel) and their calculated power spectra (bottom). At low frequencies, the power spectra are the same but at high frequencies (> 2 kHz) the MultiPulse waveform has significantly more power.(Smiarowski, et al, 2018)

More recent developments have used further refinements in the receiver suspension system to decrease the base frequencies even further to 7.5 / 6.25 Hz. This can be seen in Figure 2, where the receiver corner frequency has been moved from 25 Hz to 6 Hz, and general electronic noise has also been reduced.

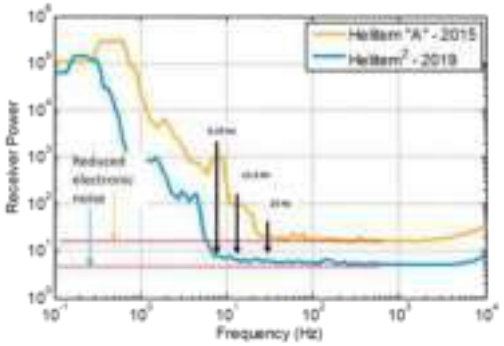

Figure 2. Receiver power spectra collected with the transmitter off for Helitem generations from 2015 (orange line) and 2019 (blue line).

In conjunction with this the transmitter waveform has been redesigned to now use a square input waveform at 50% duty cycle, with a rapid turn-off. At low base frequencies this results in a long, high powered transmitter pulse that still creates high frequency signal amplitude.

FORRESTANIA REPEAT LINE

The Forrestania EM test range is situated approximately ~350 km east of Perth. Two discrete bedrock conductors were defined during previous geophysical exploration – drilling intersected barren, disseminated to semi-massive pyrrhotite and pyrite bodies hosted in granite. We will concentrate on the western conductor (IR2) which is of limited areal size (<75 m x 75 m), shallow depth (<100 m), high conductance (>7000 S) and moderate dip (30-40 degrees). This conductor is well defined by surface and downhole EM and makes for an interesting airborne EM target (Gilgallon et al, 2019).

Figure 3 compares the EM response measured before and after the system changes and contrasts data collected over the Forrestania test site, 7 years apart. The system changes can be summarised as follows:

Helitem generation	**2012**	**2019**
Base frequency	25 Hz	12.5 Hz
Transmitter pulse	6 ms half sine	20 ms square
Offtime	14 ms	20 ms
Peak dipole moment	1500 kAm²	560 kAm²

The dramatic difference in noise level is clear at the left-side of each profile; this is made possible from changes to the receiver coil itself as well as its suspension system. The anomaly in the centre of the profile is due to sulphide mineralisation. The response at the right side of the profile is due to conductive overburden. A subtle difference between the profiles is the relative amplitude between the central anomaly and the overburden response. The central anomaly is relatively larger for the system using a longer energisation pulse (right-side image). A longer pulse maximises the response from the very conductive target. This is critical for detecting targets at depth or in conductive overburden.

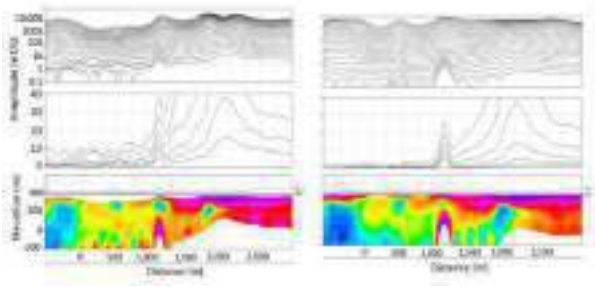

Figure 3. Log and linear-scale EM Z dB/dt response (top and middle, respectively) with a Conductivity-Depth Image shown in the bottom panel. Left column shows result from a 25 Hz survey flown in 2012 while right image shows a result from a 12.5 Hz survey flown in 2019

NEVADA TEST LINE

An acquisition program in Nevada required two different Helitem² system configurations to be flown over a test line for verification purposes. The test line also had ground TDEM soundings to be used as a calibration. The two system configurations tested can be summarised as follows:

Helitem transmitter	**35 m loop**	**21 m loop**
Base frequency	7.5 Hz	30 Hz
Transmitter pulse	33 ms square	5 ms square
Offtime	33 ms	12 ms
Peak dipole moment	560 kAm²	100 kAm²
Turn off ramp	450 µs	50 µs

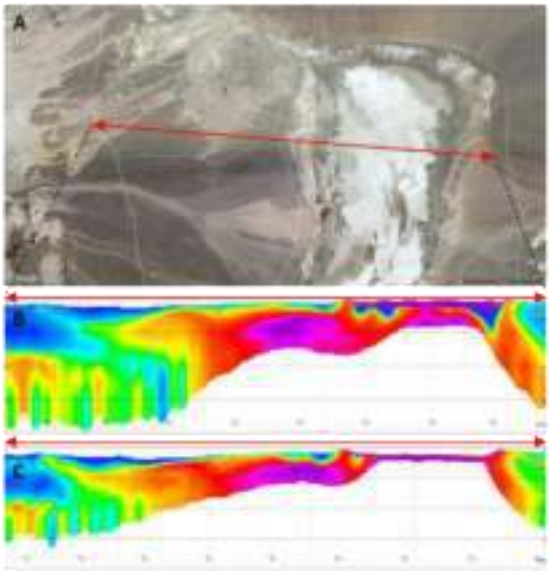

Figure 4. A) Satellite image of test line location in Nevada, USA. B) 35 m loop differential conductivity section. C) 21 m loop differential conductivity section. Both sections B and C use the same linear colour scale, and extend to 500 m depth (125 m scale divisions shown)

The test line contained features with a wide variety of conductivity and depth ranges and, in general, provided a good comparison of the imaging capability for the two systems. The system specifications were designed to focus on opposite ends of the depth / bandwidth spectrum. The 35 m configuration was imaging deep features and the 21 m configuration was imaging shallow features.

Comparing the Differential Conductivity images in Figure 4, the 35 m system was able to penetrate through some portions of a conductive playa in the eastern portion of the test line, while also detecting a subtle feature in the resistive western portion of the line. The lower moment 21 m system did not penetrate as deeply, especially in the conductive portions of the test line. However, due to its very rapid transmitter turn-off (50 µs) the near surface content of this data is greatly improved, as is the ability to map moderately conductive features in the western portion of the line.

NICKEL EXPLORATION

The Julimar Complex is located within an inferred 1200 x 100 km Ni-Cu-PGE province that follows the western margin of the Yilgarn Craton about 70 km north east of Perth. It is a mafic-ultramafic layered intrusive complex, the structure of which has been delineated with high-resolution regional airborne magnetics in an area of poor exposure. The Helitem^2 survey was designed to test for conductors within and proximal to the Julimar State Forest associated with magmatic Nickel Sulphides. The survey successfully imaged the known mineralization, and the outlined three new extensive EM anomalies within the Julimar State Forest – Hartog, Baudin and Jansz.

In September 2020 a 6.25 Hz Helitem^2 survey was flown in an attempt to understand the conductive response of the Gonneville discovery, and to identify similar mineralized zones. As can be seen in Figure 5, a large conductive zone extends directly north of Gonnville, termed the Hartog anomaly. The conductive Hartog anomaly is offset 500 m to 1,000 m west of the magnetic anomaly, and is coincident with Ni-Cu-Pd anomalism in soil sampling that is comparable to Gonneville. The amplitude of the EM response of the Hartog anomaly is almost double that of Gonneville, and once permission is obtained to access the state forest the anomaly will be drill tested.

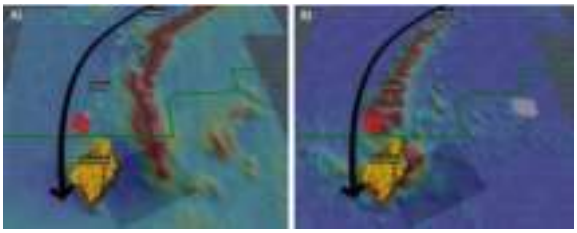

Figure 4: Perspective view looking north of, A) Gonneville mineralisation with magnetic data background, B) Gonneville mineralisation with EM data background.

CONCLUDING REMARKS

The redesigned Helitem system, now called Helitem^2, has allowed for an increase in the general bandwidth of the system. The ability to operate at low base frequencies is possible due to a complete receiver system redesign, including the receiver suspension system. Additionally, the ability to accurately control the waveform allows the transmitter turn off time to be chosen based on the near surface sensitivity required.

The advancement of airborne EM systems to collect data at ever lower base frequencies has been occurring for some time and will likely continue. This advancement fits with the exploration for deeper, under cover deposits, and to some extent for very conductive Nickel Sulphides.

REFERENCES

Gilgallon, K., Tomlinson, A., and Mortimer, R., 2019. The Forrestania and Nepean electromagnetic test ranges, Western Australia – a comparison of airborne systems, ASEG Extended Abstracts, 2019:1, 1-4

Smiarowski, A., Macnae, J., 2013. Detection of a perfect conductor with an airborne electromagnetic system: The Gemini Field Test, Geophysics (2013) 78 (5): E249.

Smiarowski, A., Miles, P., and Konieczny, G., 2018. CGG'S New Helitem-C AEM Systems, ASEG Extended Abstracts, 2018:1, 1-4,

Free AEM data over NSW, Australia

Astrid Carlton
Geological Survey of NSW
516 High St, Maitland 2320
astrid.carlton@regional.nsw.gov.au

SUMMARY

The Geological Survey of New South Wales (GSNSW) in the Department of Regional NSW, Mining Exploration & Geoscience, has an online application, called MinView, which allows users to view and download geoscientific data, including airborne electromagnetic (AEM) survey data and inversion sections. Much of the AEM data are from surveys acquired in collaboration with Geoscience Australia and other NSW state government departments. Other surveys were acquired by exploration companies. Exploration companies are required to submit geophysical data to the government. After 5 years the data can be made publicly available.

Data is free to download and its use is covered by CC-BY copyright, which gives the users the right to use distribute, adapt, remix or build upon so long as attribution is given to the author. This abstract provides the reader with instructions on how to access AEM data on MinView.

Key words: AEM, airborne electromagnetic, MinView, NSW.

INTRODUCTION

MinView is a leading, world-class online application that is easy and free to use. It contains more than 500 layers of geoscience-related layers, including geophysical data and images. GSNSW is the custodian of 190 AEM surveys. Open-file AEM data can be accessed through MinView. There are:

- 16 government-acquired surveys (totalling 78 GB) that cover large areas with widely spaced lines, and
- 30 GB of open-file company AEM data, that cover smaller areas with closely spaced lines.

VIEW AEM SURVEY AREAS IN MINVIEW

Navigate to https://minview.geoscience.nsw.gov.au/. On the left-hand side of the screen is a blue 'Add layers' panel that has a white right-facing arrow. Click on the white arrow and a new panel will appear with a search bar at the top. Type 'aem' into the search bar and the list of layers will reduce to those that contain AEM data, such as 'Geophysical imagery' and 'Geophysical surveys'. On the 'Geophysical surveys' layer click on the down arrow. Survey data is separated into 'Company geophysics' and 'Government geophysics'. Click on the down arrow on either option to reveal 'Airborne electromagnetic' (Figure 1). Click on the square blue button with a white plus sign to add the survey areas to MinView map (Figure 2).

DOWNLOAD AEM DATA FROM MINVIEW

Use the steps in the previous section to add AEM survey areas to the map view. Then click on an AEM survey area. A window with survey details will open (Figure 3). If the data is open-file there will be a blue link in the column named 'Data availability'.

Click on the link and a new window will open. The file size is displayed with a download link in blue text (Figure 4). Click on the blue text to start the download. Some of these files are very large so ensure you have a good internet connection before starting a download.

Generally, an AEM download includes a zip file that contains folders with standard names such as grids, images, located data, vectors and reports (these are logistics, acquisition and or processing reports). The data in open-file exploration company surveys is as it was submitted to the government.

VIEW AEM SECTIONS IN MINVIEW 3D

Recently acquired government AEM surveys have geolocated AEM sections available for viewing in MinView when in 3D mode. 3D sections are called 'curtains' and are not available for download. To view curtains search for 'aem' in the 'Layers' panel and under the 'Geophysical imagery' drop down menu, add a set of AEM curtains to the map (Figure 5). The curtains are displayed above the ground as MinView does not support underground data. Each set of curtains is displayed with vertical exaggeration to best display the curtain, so each section can be seen with minimal overlap (Figure 6). Inversion methods and colour keys are unique to each survey. To view the colour-key move the mouse to the map layers panel, where the name of the survey curtains is displayed. Click on the arrow to the right of the text (it points to the right) to reveal a panel with metadata and the colour-key. The arrow changes direction after it has been clicked on. To remove the new panel from the view, click on the arrow that now points left.

Tip: to tilt the display press 'ctrl' and left mouse button and drag the mouse.

USEFUL LAYERS TO MINVIEW FOR AEM INTERPRETATION

There are over 500 layers available in MinView. Many are useful in AEM interpretation such as those for drill holes, waterbores, NSW Seamless Geology (Figure 7), mineral occurrences, other geophysical imagery, infrastructure layers, watercourses and soil maps.

CONCLUSIONS

The GSNSW has 108 GB of open-file AEM data that is freely available through MinView. MinView is a powerful application for NSW geoscience data, that allows you to view and download AEM data. A 3D function in MinView enables users to view recent government-acquired AEM sections alongside 500 other layers.

Figure 1 Screen capture of MinView showing AEM layer selection.

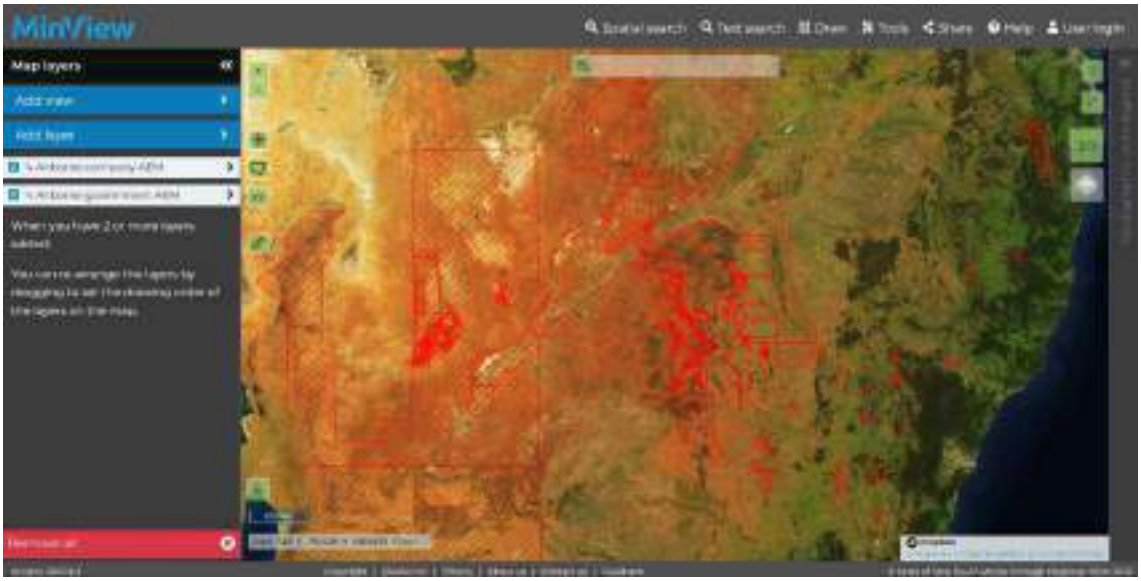

Figure 2 Screen capture showing company and government acquired AEM surveys.

Figure 3 MinView window showing available AEM surveys and their details.

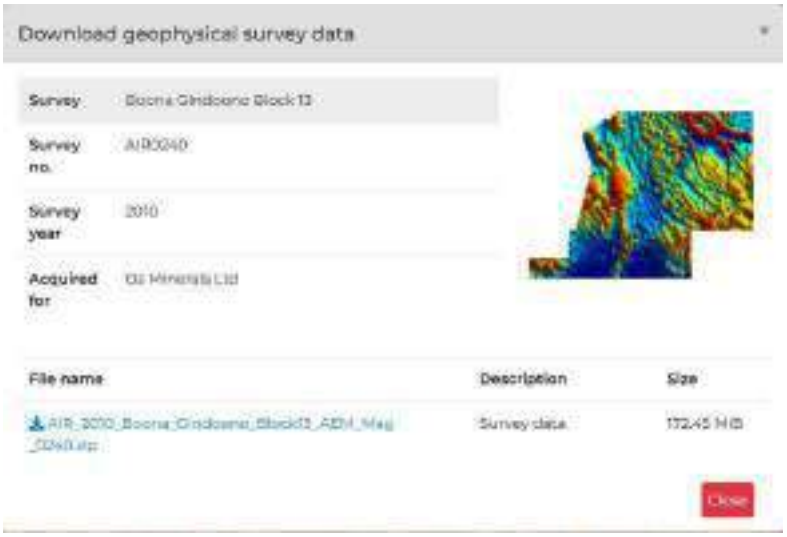

Figure 4 Download window with download link in blue text.

Figure 5 AEM survey curtains, in 2D mode.

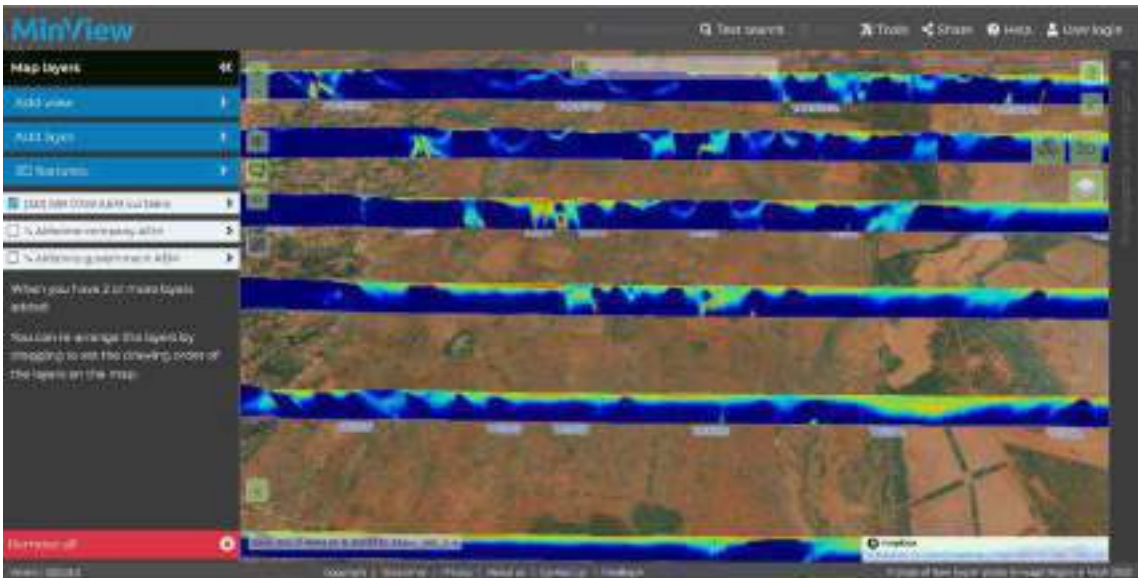

Figure 6 AEM curtains in MinView 3D, zoomed in to an area with a pipeline, with the view tilted.

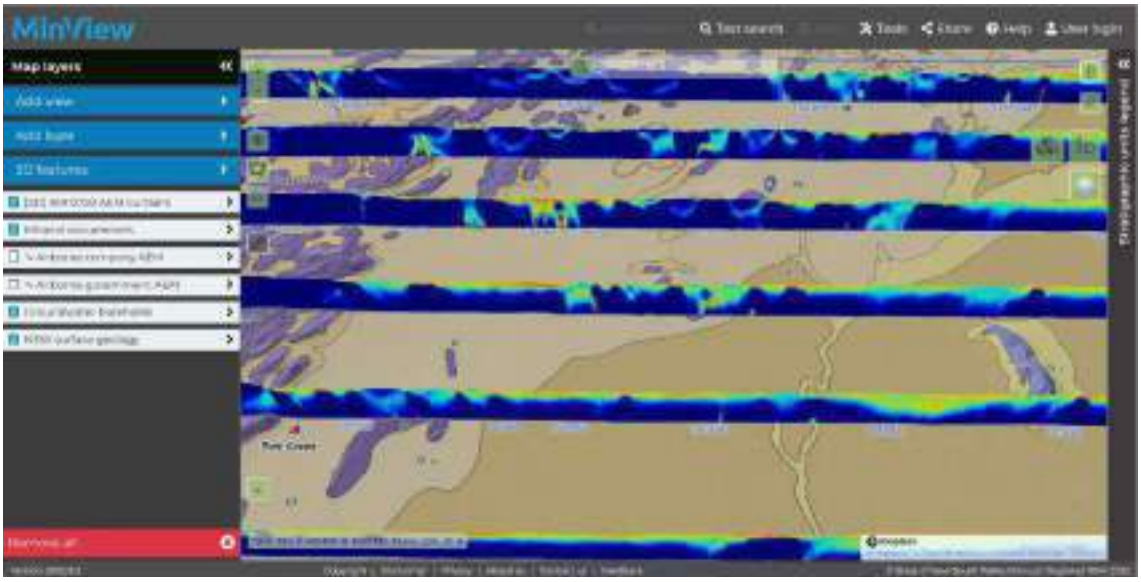

Figure 7 AEM curtains with NSW Seamless Geology.

AEM-derived watersheds in crystalline domain under volcanic cover

Damien Ciolczyk*
BRGM, UCA-CNRS-IRD-OPGC-LMV
3 avenue Claude Guillemin
45000, Orléans, France
d.ciolczyk@brgm.fr

Pierre-Alexandre Reninger
BRGM
3 avenue Claude Guillemin
45000, Orléans, France
pa.reninger@brgm.fr

Clotilde Bertin
BRGM
12 avenue des landais
63170 Aubière, France
c.bertin@brgm.fr

Julien Bernard
BRGM
3 avenue Claude Guillemin
45000, Orléans, France
j.bernard@brgm.fr

Anne Raingeard
BRGM
3 avenue Claude Guillemin
45000, Orléans, France
a.raingeard@brgm.fr

Pierre Belle
Danone Waters, Water Institute by Evian
11 avenue du Général Dupas - BP 87
74503 Evian-Les-Bains Cedex
pierre.belle@danone.com

Lydie Gailler
UCA-CNRS-IRD-OPGC-LMV
F-63000 Clermont-Ferrand
France
lydie.gailler@uca.fr

Philippe Labazuy
UCA-CNRS-IRD-OPGC-LMV
F-63000 Clermont-Ferrand
France
philippe.labazuy@uca.fr

Guillaume Martelet
BRGM
3 avenue Claude Guillemin
45000 Orléans, France
g.martelet@brgm.fr

Olivier Merle
UCA-CNRS-IRD-OPGC-LMV
F-63000 Clermont-Ferrand
France
o.merle@opgc.fr

SUMMARY

In the Chaîne des Puys (CdP, France), volcanic edifices and their emissions cover the weathered conductive low-permeable basement and fill the paleo-valleys, hiding the groundwater flows. The 3D delineation of such buried watersheds can be achieved studying variations of conductivity related to primary geological contrasts as well as secondary weathering-induced contrasts.

We used AEM data to delineate the geometry of the undercover volcanism-basement interface in the northern part of the CdP and derived watersheds. Despite the highly resistive volcanic cover, our processing allowed structural imaging up to a depth of investigation of 330 meters in average.

The processing and inversion of AEM data highlights the interface between a strongly resistant volcanic cover (~10^4-10^5 Ω.m) and a decametric conductive weathered horizon at the top of the basement (30-300 Ω.m).

We picked the weathered horizon of the basement on several resistivity profiles, to build an elevation model of its top. The newly derived watersheds noticeably differ from the ones proposed in literature.

Key words: AEM, Electromagnetics, Volcanism, Chaîne des Puys, Hydrogeology

INTRODUCTION

The Chaîne des Puys (CdP, center of, France) is a North-South alignment of about 80 volcanic edifices including cinder cones, lava domes and maars (purple in Figure 1). Outcropping volcanic formations are young (~100 ka to ~6.7 ka) and preserved from alteration (Boivin *et al.*, 2017). They lay on a Variscan granito-gneissic basement (beige and brown in Figure 1), strongly faulted and weathered (Merle et al. 2023 and references therein). Alluviums and colluviums of the plateau and tertiary sedimentary rocks of the Limagne Basin (East of studied area) are referred to as "sediments" in Figure 1.

The CdP is an important ground water reservoir for various usages, but suffer from climate change, as precipitations decrease. In this context, a good resource management requires a structural knowledge. Because of the high permeability of the volcanic formations and the relatively low permeability of the top of the basement, the geometry of the volcanism-basement interface constraints water flows. Therefore, several authors have recognized its importance to derive realistic watershed geometries (Joux 2002; Aumar 2022).

We use airborne electromagnetics (AEM) to image this interface within the Northern part of the CdP. The geo-electrical configuration is appropriate for AEM (i.e. a rather conductive layer overlain by a resistive layer as commonly inferred in such volcanic context). However, the very important resistivity of the cover makes the valorisation of the AEM data challenging, as the signal decreases extremely quickly. Acquisition parameters were thus optimized and a rigorous processing was performed.

The structures of the CdP have been investigated by ground geophysics, mainly at local scale using electrical resistivity tomography providing heterogeneous information density. Geo-electrical context was thenceforth established. Volcanic layers show high resistivity (~10^4-10^5 Ω.m), magnetic susceptibility (~10^{-2} SI) and great permeability. Basement is less resistive, especially its weathered horizon (~10^2 Ω.m) almost amagnetic (~10^{-4} SI) except for monzonitic intrusion (referred as "magnetic basement" in Figure 1) and with a comparatively very low permeability due to its weathered surface.

METHOD

Data

BRGM (the French Geological Survey) has conducted a helicopter-borne multi-physic survey operated by SkyTEM Surveys ApS over the Northern part of the CdP. Transient electromagnetic, magnetic and gamma-spectrometric data were acquired along 1018 km of flight lines, located in Figure 1.

Regarding AEM, the SkyTEM 304 system (Sorensen and Auken, 2004) was used. SkyTEM systems have the particularity of emitting two different magnetic moments, a low moment (LM) and a high moment (HM), in order to characterize the near-surface and greater depths respectively. The LM and HM parameter are given Table 1. The duration of the sequence had been reduced, and the stack size, increased, to adapt the survey the expected high resistivity of the volcanic cover.

Parameter	LM	HM
Magnetic moment	3,000 Am²	145,000 A.m²
On-time duration	800 µs	2.500 ms
Off-time duration	533 µs	4.167 ms
Stack size	300	180
Number of gates	22	22
First gate center time	0.535 µs	72.7 µs
Last gate center time	428.5 µs	3.642 ms

Table 1: Acquisition parameters for the low moment (LM) and the high moment (HM)

Processing & inversion

We only used AEM and magnetic data in this study and we focus on the AEM data in the following. We processed AEM data following the procedure described in Reninger *et al.* (2020). In order to remove the remaining noises from the dataset, we complete the processing by a manual editing.

We invert AEM data using Aarhus Workbench (HydroGeoPhysics Group). We used Spatially Constrained Inversion (SCI) described in Viezzoli *et al.* (2008) to invert data considering very early times (from 2 µs), thanks to system response modelling procedure implemented in the Workbench. 1D soundings imaging the resistivity variations with depth were obtained. Each 1D sounding is defined by 40 layers whose the thickness increases logarithmically with depth from 2 m to 80 m, for a total thickness of 880 m. Lateral smoothness constraints were function of altitude.

RESULTS

Average depth of investigation, as defined in Christiansen and Auken (2012), is above 330 m for the whole survey and more than 400 m in volcanic context, which is more than the expected thickness of volcanic products.

Figure 2 shows a typical resistivity profile acquired over the volcanic formations (located in Figure 1). The volcanic cover displays resistivities ranging from a few thousands up to one hundred thousand ohm-meter (max: ~79 kΩ.m for the cross-section shown in Figure 2). The weathered layer at the top of the basement stands at about a hundred ohm-meter. Underneath basement shows a wide range of resistivity and numerous structures such as faults or contacts between lithologies that are beyond the scope of this paper. Thus, AEM allowed clearly imaging the expected volcanic-basement interface, as seen on Figure 2, under most of the volcanic cover.

We manually picked this interface on the different resistivity profiles, resulting in about 4000 sampling points of the interface on resistivity soundings within the volcanic area. We always consider the top of the conductive layer as top of the basement. This seems consistent to us for most of the survey as this conductive layer is continuous with limited thickness variation and is interpreted as the weathered horizon as observed in wells and underground gallery. However, a few picked points might locally require a different interpretation; especially under volcanic edifices where the shape of the conductive anomaly changes (see sub-volcanic structures, Figure 2) and might be due to other processes.

We interpolated the picked points with minimum curvature in the volcanic area and we extended the interface outside volcanism using a Digital Elevation Model (DEM, RGE ALTI 5m, IGN). Figure 3 displays the elevation model of the interface and the derived watershed limits (red) compared to those usually considered so far in the literature (in blue, from Livet *et al.* (2009)). Some watershed in crystalline domain are the results of edge effects and should not be compared (white hatched limits). The interpretation of conductive anomalies under some volcanic (generally basic) edifices would lead to lower altitude estimation of the basement, then, to different watershed limits, mainly between Volvic and Argnat as East of the black ellipse is under an alignment of cones (northern black ellipse on Figure 3). Elsewhere, those anomalies are not local crests, so they have very little impact on watershed limits.

There is no consensus about watersheds limits in the area and another model is proposed by Aumar (2022) based on ground spontaneous potential measurements and field observations.

As we provide a new image of the substratum topography, we consequently define new drainage divides. As remarkable examples, the limit between Tiretaine watershed and Nohanent-Durtol watershed is strongly modified, and so is the triple point between Volvic, Argnat and Louchadière & Côme (southern black dashed ellipses in Figure 3). These evolutions are yet to be confronted to hydrogeological data such as specific flowrate. Ground water flows will be updated as well, constrained by the new interface, allowing revising the vulnerability of the aquifer to pollutions.

CONCLUSION

AEM allowed us to image underground resistivity contrasts between basement and the volcanic cover and inside the

bedrock itself. We the obtained the geometry of the contact between the two formations. The buried volcanism-basement interface clearly displays paleo-thalweg, which were filled by lava flows (Figure 3). The only clue that remains of these paleo-thalwegs at the outcrop are often the direction of the lava flows themselves. This shows the necessity of geophysical method to investigate and to constraint actual ground water flows and watersheds.

With these results, we show that AEM, with an appropriate processing, is a suitable method in volcanic context to delineate the clay-rich conductive horizon of weathered basement, even under very highly resistive and thick lavas with an average thickness of 103 m and often more than 200 m. In addition, AEM allows imaging a very complex basement with strong lateral and vertical resistivity contrasts highlighting discontinuities, structures and faults.

The results we present are part of an on-going PhD thesis, and are submitted to evolution. An uncertainty is yet to be defined on the obtained interface. Furthermore, modelling the contrast of petromagnetic properties of the basement and volcanic rocks will be used to better interpolate the interface and estimate the error on its depth/altitude.

ACKNOWLEDGMENTS

We thanks FEDER-FSE Auvergne-Rhône-Alpes, which supported the data acquisition. We are grateful to Clermont Auvergne Metropole (CAM) and Société des Eaux de Volvic (SEV) which, together with BRGM, support this on-going PhD.

REFERENCES

Aumar, C. 2022. Modélisation de la topographie anté-volcanique de la Chaîne des Puys. PhD thesis, Université Clermont Auvergne.

Boivin P., J.C. Besson, D. Briot, C. Deniel, A. Gourgaud, P. Labazuy, E. Langlois, F.D. de Larouzière, M. Livet, C. Merciecca, E. Médard, J. Mergoil, D. Miallier, L.M. Morel, J.C. Thouret, and G. Vernet (2017). Volcanologie de la Chaîne des Puys Massif Central Français. 6e édition, bilingue. Carte 1/25 000. p.200 p., Édition PNRVA.

Christiansen, A. V., and E. Auken. 2012. A Global Measure for Depth of Investigation. *GEOPHYSICS* 77 (4): WB171–77. https://doi.org/10.1190/geo2011-0393.1.

Joux, M. 2002. Structure et fonctionnement hydrogéologique du système aquifère volcanique des eaux minérales de Volvic. PhD thesis, Université d'Avignon et des Pays de Vaucluse.

Livet, M., H. Tachrift, and C. Bertin. 2009. Bilan de la ressource hydrogéologique des bassins de la Chaine des Puys. RP-57092-FR. Centre d'Etudes Techniques de l'Equipement.

Merle, O., C. Aumar, P. Labazuy, C. Merciecca, and S. Buvat. 2023. 'Tertiary and Quaternary structural evolution of the Plateau des Dômes (Chaîne des Puys, Massif central, France)'. *Géologie de la France*, no. 1: 1–22.

Reninger, P.-A., G. Martelet, J. Perrin, and M. Dumont. 2020. Processing Methodology for Regional AEM Surveys and Local Implications. *Exploration Geophysics* 51 (1): 143–54. https://doi.org/10.1080/08123985.2019.1680249.

Sorensen, K. I., and E. Auken. 2004. SkyTEM–a New High-Resolution Helicopter Transient Electromagnetic System. *Exploration Geophysics* 35 (3): 194–202. https://doi.org/10.1071/EG04194.

Viezzoli, A., A. V. Christiansen, E. Auken, and K. Sørensen. 2008. Quasi-3D Modeling of Airborne TEM Data by Spatially Constrained Inversion. *GEOPHYSICS* s73 (3): F105–13. https://doi.org/10.1190/1.2895521.

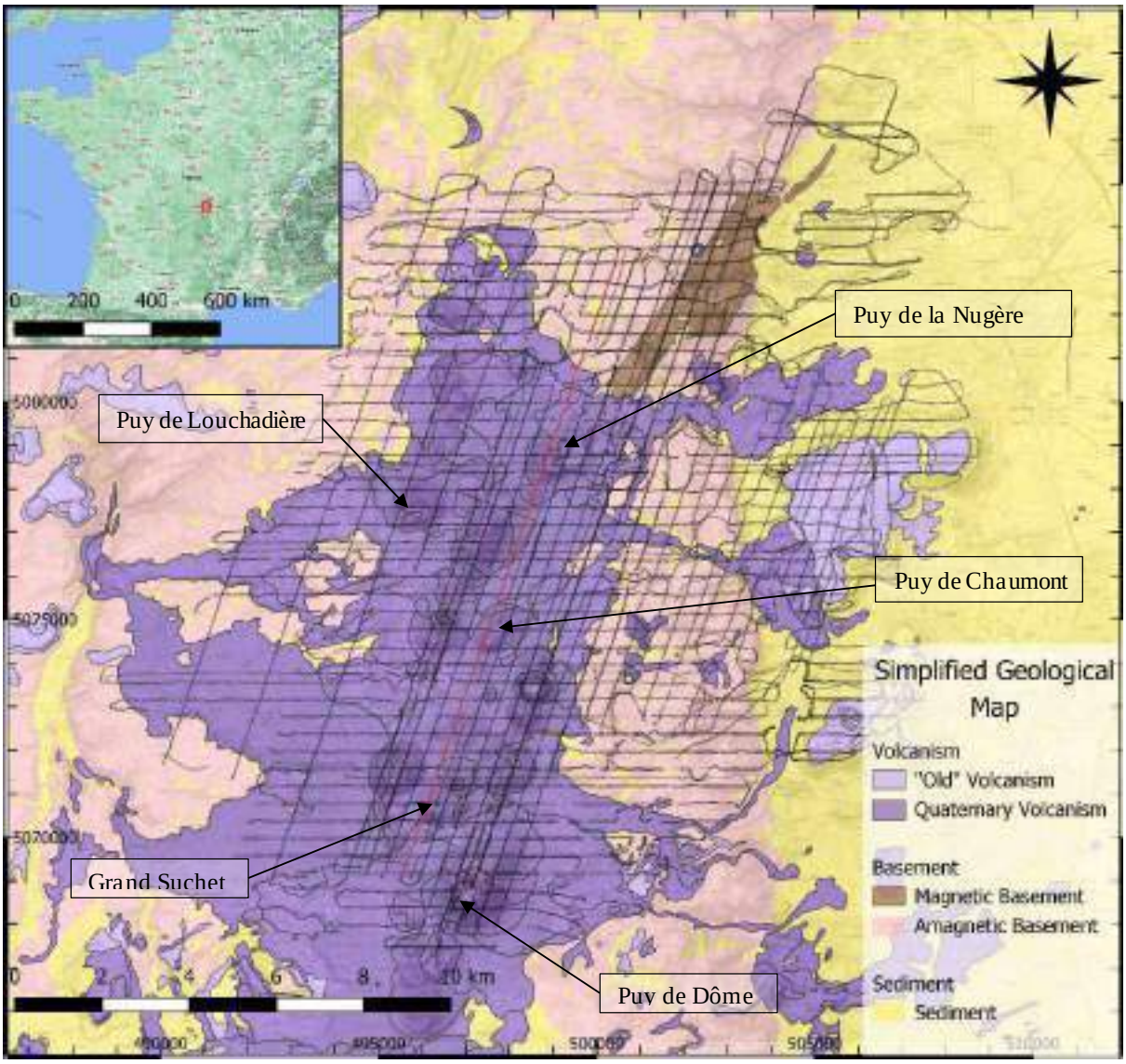

Figure 1 : Location of the studied area: a) Location at France scale; red box limits map b. Background: Google Terrain Hybrid; b) Lines flown on a simplified geological map (based on BRGM 1:50000 map). Red flight line locates cross-section in Figure 2. Background: Plan IGN v2, DEM: RGE ALTI 5m (IGN). Coordinates are in meter (WGS84/UTM31N).

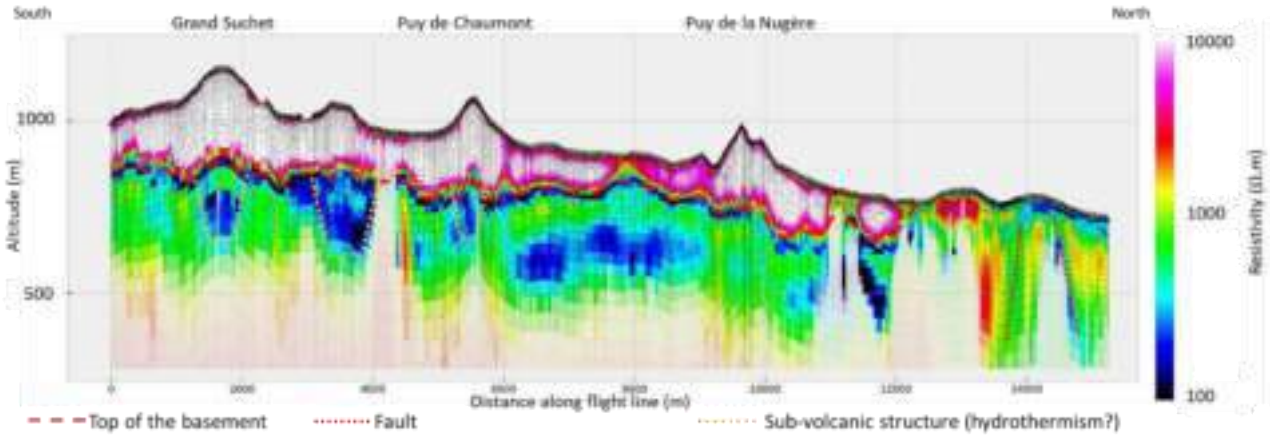

Figure 2 : South-North cross-section, located in Figure. Red dashed line highlights the contact between basement and volcanic cover. We interpret the thin low resistivity layer (dark blue) that underlies highly resistive volcanism as weathered (clay-rich) basement.

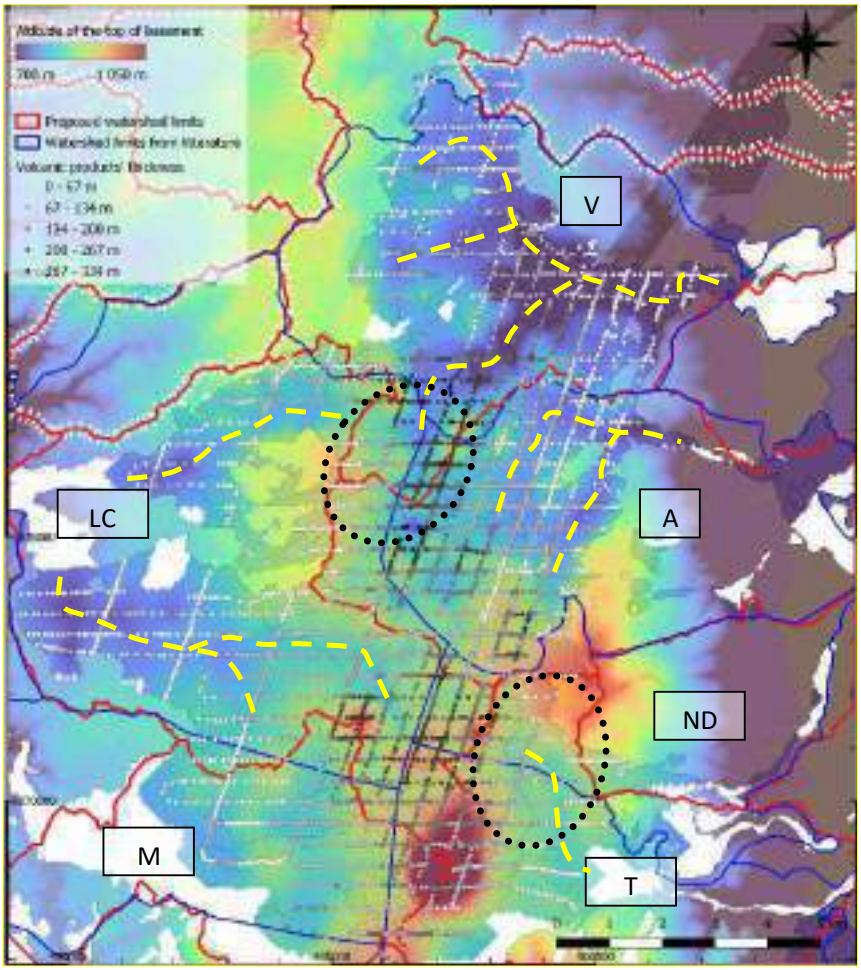

Figure 3 : Altitude of the top of the basement interpreted from AEM data and limits of the derived watersheds compared (red) compared to previously proposed watershed (blue). White hatcher watershed limits are DEM derived and affected by edge effect. Points along flight lines show where we picked interface and their color shows the thickness of the volcanic cover (black: thick; white: thin). Yellow dashed lines highlight paleo-thalwegs and dashed ellipses highlights zones where the main differences arise. Ticks refer to the names of the watershed: V: Volvic; LC: Louchadière & Côme; A: Argnat; ND: Nohanent-Durtol; M: Mazaye; T: Tiretaine

Perspectives on AEM processing for geophysical exploration in Canada and worldwide

Magdel Combrinck
New Resolution Geophysics (NRG)
Unit 1, Stand 98, Tijger Vallei Office Park
Silver Lakes Rd, Pretoria
magdel.combrinck@nrgex.co.za

SUMMARY

Acquiring and processing AEM data in different regions of the world require different approaches and procedures to deliver the best data. Four case histories are discussed to illustrate the effect of jungles, mountains, electrical and magnetic storms on AEM and ancillary data. Lesson learned as well as current approaches to deal with challenges in this region are presented. There is no "on-size-fits-all" processing workflow and critical evaluation of data an survey conditions are required to deliver the best data.

Key words: AEM, data processing, noise.

INTRODUCTION

NRG has acquired and processed Xcite AEM data from many different parts of the world, including Canada, Southern and Central Africa, Australia, and Southern Asia.

Even though the systems have the same designs and the laws of physics apply equally across continents, different regions of the world each bring their own challenges for operations, acquisition, and data processing. Vegetation, topography, electrical storms, magnetic storms, climate, and anthropogenic noise all influence AEM data.

With modern data science trending more and more to automated and artificial intelligence (AI) applications, it is important to incorporate training environments and models that are representative of all the varieties of noise that are encountered in the world.

CASE HISTORIES

Case history 1

Location: Central Africa
Challenge: Jungle

In central Africa we were confronted with the most impressive jungle environment. AEM data interpretation is very strongly dependent on accurate altitude measurements, and this proved to be the biggest challenge in this region. The trees there are up to 50m tall and dense understory vegetation fills the gaps between them. The Xcite system is equipped with a GPS and laser altimeter on the transmitter frame as well as a GPS and stronger laser altimeter mounted on the helicopter. The two GPS's and altimeters allow for correlation between instruments as a continuous control on accuracy, and provide redundancy if one of the instruments happen to fail during a flight.

With the range of sensors available the transmitter frame (and receiver) altitude above ground is measured directly using the frame-altimeter (Alt_F) ans also calculated as:

$$Alt_{F\_C} = Alt_H - (GPS_{H\_Z} - GPS_{F\_Z}),$$

where,

Alt_F: Frame Altitude Measured
Alt_{F_C}: Frame Altitude Calculated
Alt_H: Helicopter Altitude Measured
GPS_{H_Z}: Helicopter GPS Elevation above mean sea level
GPS_{F_Z}: Frame GPS Elevation above mean sea level

Performing this calculation, and accounting for any offsets in sensor placements on the helicopter, Alt_F and Alt_{F_C} values should exhibit the same trends and vary in absolute value by the vertical offset of the frame from the helicopter.

Additionally, two sets of pseudo-altitudes can be calculated as:

$$PseudoAlt_F = GPS_{F\_Z} - SRTM, \text{ and}$$
$$PseudoAlt_H = GPS_{H\_Z} - SRTM.$$

These two channels should coincide with the respective laser altimeter readings and is used as an external control on altitude and GPS measurements. In the calculations SRTM refers to the Shuttle Radar Topography Mission data acquired and published by NASA (NASA JPL, 2013).

Dense vegetation cause inaccurate laser altimeter readings when the signal is reflected off the tree canopy instead of the ground. This is not an uncommon occurrence in the world and we use filters that pick the largest values as indicative of ground response and cull the lowest values (tree top reflections) to process altimeter data when vegetation is present. SRTM data are used as a control measurement under the assumption that the lower radar frequencies are more reliable in penetrating vegetation cover than laser altimeters, even though lateral resolution is significantly less.

Following standard altimeter calibrations we commenced the survey, yet the altimeter and GPS data from the initial flights did not seem to make sense (Figure 1). Under normal conditions the pseudo-altimeter data would match the filtered laser altimeter data very closely when averaged over a line. In this case, there was a large difference, averaging close to 25 m, which is by far not accurate enough for an AEM survey. The puzzling aspect was that the laser altimeters seemed to have better penetration through the trees than the radar.

It turned out that in extremely dense jungles SRTM data are in fact not reliable (Bourgine and Baghdadi, 2005), and that high

sampling and proper filtering of the laser altimeters gave more accurate results than the SRTM and GPS combination.

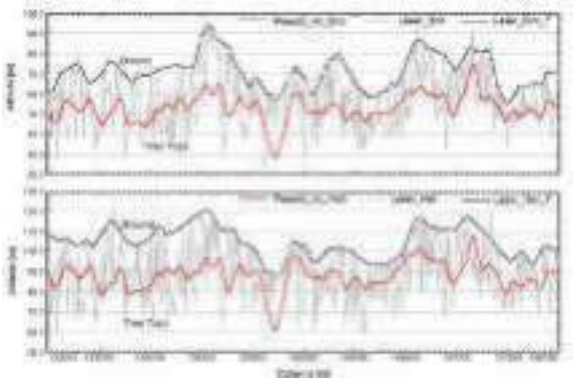

Figure 1. Laser altimeter data (grey), filtered laser altimeter data (black) and pseudo-altimeter data (red) for frame(top) and helicopter(bottom) sensors.

Case history 2

Location: Southern Asia
Challenge: Mountains

Helicopter flying characteristics vary significantly between steep ascents and descents, with the ascents being generally more stable. Draping to nominal heights of 30m - 40m is never realistically achieved in rugged terrain. On steep slopes the realized altitudes, as well as frame orientation, vary greatly along lines and between adjacent lines. In addition to the aviation challenges, mountainous regions tend to be very resistive, resulting in weak AEM responses even at nominal altitudes.

From a processing perspective, levelling this type of data presents a real challenge, because we know that data from adjacent lines with sharply varying altitudes should *not* have the same amplitudes (as opposed to principles we use for levelling in flat topographic regions), but we do not have an efficient process to determine what these values *should* be.

One approach to test for proper levelling is to use conductivity grids calculated from CDI or 1D inversion algorithms and require that these grids be smooth, i.e., without linear artefacts visible along flight lines.

In collaboration with Des Fitzgerald (Intrepid Geophysics) and Jovan Silic (Jovan Silic & Associates) I have performed model studies to test whether this approach is an effective way of evaluating AEM data in rugged terrains. The process was straightforward, and consisted of applying CDI (Combrinck, 2008) and GALEI 1D inversion (Brodie, 2016) algorithms to forward modelled responses generated with 2.5D modelling software (Silic et al. 2015; Silic et al., 2016). The models were based on an actual recorded survey flight path, but with simple halfspace and two-layer earth models substituted for the true conductivity distribution. Even with all parameters explicitly known and specified, including altitude, tilt and system description, the 1D algorithms could not recover the conductivity models without introducing flight line artefacts. Strong correlations between deviations from the true model data and topographic regions (highs, lows and slopes) confirmed that in areas with rugged topography, CDIs and 1D inversions are not sufficient to recover true conductivity models, or to be used as a test for levelling efficiency (Figures 2 and 3). 2.5D or 3D inversions are needed to account for AEM responses originating from rugged terrain.
One option that has shown some promise in conductive regions is to level data based on decay constants correlation rather than AEM response values.

Case history 3

Location: Central and Southern Africa
Challenge: Electrical storms

Depending on the location and time of year electrical storms generate spheric noise and have a significant effect on AEM data.

When the spherics frequency is less than the stacking width post-stack de-spiking filters are sufficient to deal with spheric noise. However, if spherics affect data at more frequent intervals the stacked noise responses overlap and non-linear and low-pass filters fail to effectively remove the noise signatures. (Figures 4 and 5).

I have developed an in-house filtering procedure that operates on a combination of stacked and pre-stacked data to remove spherics noise. This procedure is very effective and has allowed us to continue with production even in afternoons which typically would not have been an option in the past due to increased electrical storm activity.

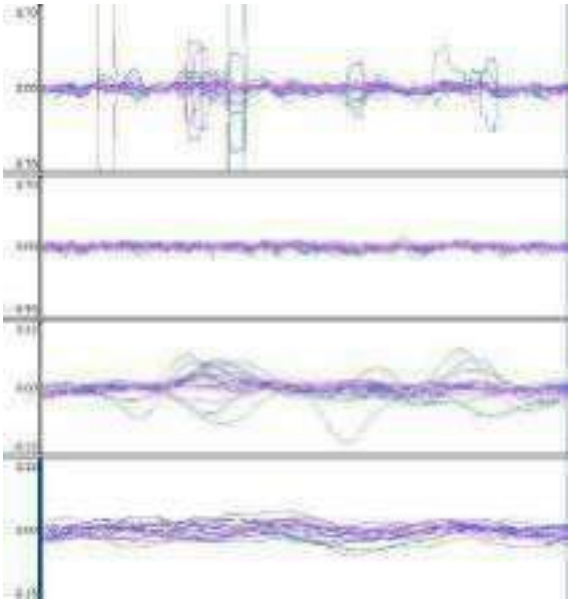

Figure 4. Late time dBdt-X [pV/(Am^4)] channels over a 350m horizontal distance. Panel 1: Pre-filtered, stacked data with spheric noise spikes occurring more frequently than the stacking width results in overlaps. Panel 2: Data with spheric events filtered out using an in-house procedure. Panel 3: Data from panel 1, filtered with standard despike (non-linear and low-pass combination) filter. Panel 4: Data from panel 2, filtered with standard despike (non-linear and low-pass combination) filter.

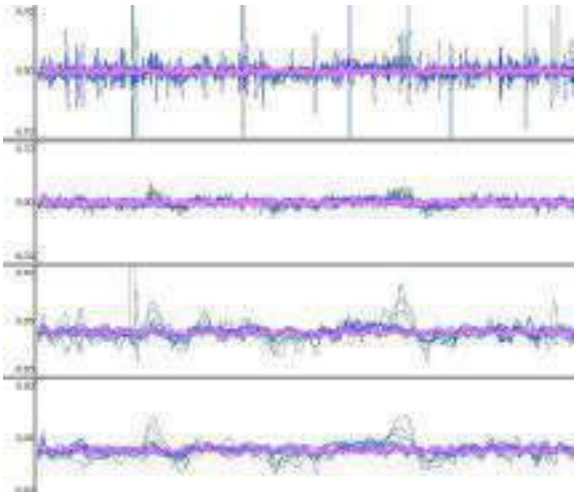

Figure 5. The same combinations of data as in Figure 4, presented over a horizontal distance of 3000m, illustrating the effective removal of noise while preserving small anomalies.

Case history 4

Location: Canada
Challenge: Geomagnetic storms

The final example is from Northern Saskatchewan in Canada. This survey presented an interesting combination of 60Hz powerlines and a level G3 magnetic storm. The storm was so intense that the local power grid was shut down for three days.

At the time of the magnetic storm the Xcite AEM and magnetic survey had to be paused because of increased late time noise and because the magnetic diurnal data variation was out of specification. We also got some very interesting results around the powerlines (Figure 6). No amount of filtering could get rid of the enormous response due to the magnetic storm. The only option was to wait it out and then we had a few bonus flights while the power grid was still down and where we could measure signatures of an inactive powerline. Building a database of signatures for different types of noise is necessary in the drive for more automated processing and interpretation

CONCLUSIONS

Depending on the geographic location and time of year AEM surveys are performed, different challenges are encountered to provide high quality data. There is not a one-size fits all processing workflow that will always results in the best data. Critical analysis of the data and survey conditions are required to pick the best processing options, and often design new ones, in order to deliver the best results.

ACKNOWLEDGMENTS

Thank you to Forum Energy Metals Corp for using their data and to Jovan Silic (Jovan Silic & Associates) and Des Fitzgerald (Intrepid Geophysics) for providing 2.5D forward models.

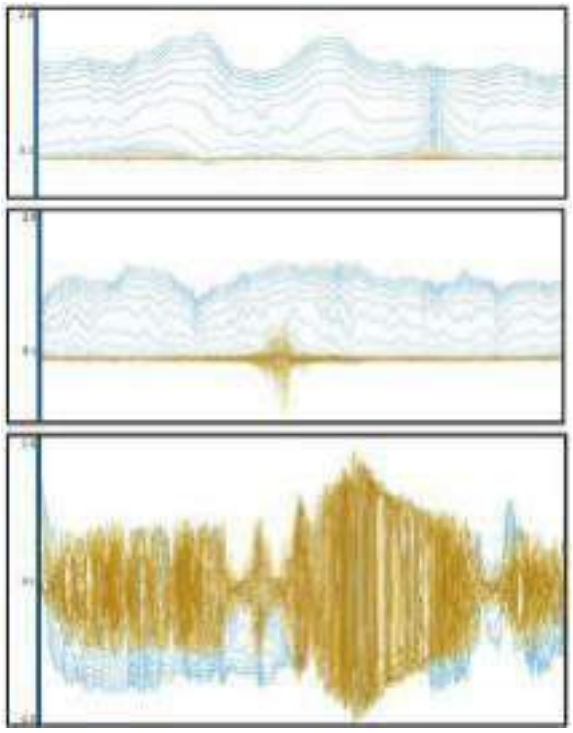

Figure 5. dBdt-Z data [pV/(Am^4)] with a powerline response during grid blackout (top), powerline response during normal operations (middle) and powerline response during G3 magnetic storm. Horizontal extent of 5,000 m is shown.

REFERENCES

Bernard Bourgine, Nicolas Baghdadi, 2005. Assessment of C-band SRTM DEM in a dense equatorial forest zone. *Comptes Rendus Geoscience*, 337: 225-1234

Brodie, RC., 2016. User Manual for Geoscience Australia's Airborne Electromagnetic Inversion Software. Geoscience Australia.

Combrinck, M., 2008, Calculation of conductivity and depth correction factors for the S-layer differential transform: *Exploration Geophysics*, 39, 133–138.

NASA JPL (2013). NASA Shuttle Radar Topography Mission Global 1 arc second [Data set]. NASA EOSDIS Land Processes DAAC.

Silic, J., Paterson, R., FitzGerald, D. and Archer, T., 2015. Comparing 1D and 2.5D AEM inversions in 3D geological mapping using a new adaptive inversion solver: Extended Abstracts 14th International Congress of the Brazilian Geophysical Society, Brazil.

Silic, J., Paterson, R., and FitzGerald, D., 2016. Improved Structural Mapping and Conductive Targeting Delivered by a new 2.5D AEM Inversion Solver: ASEG Extended Abstracts 2016, 1-8

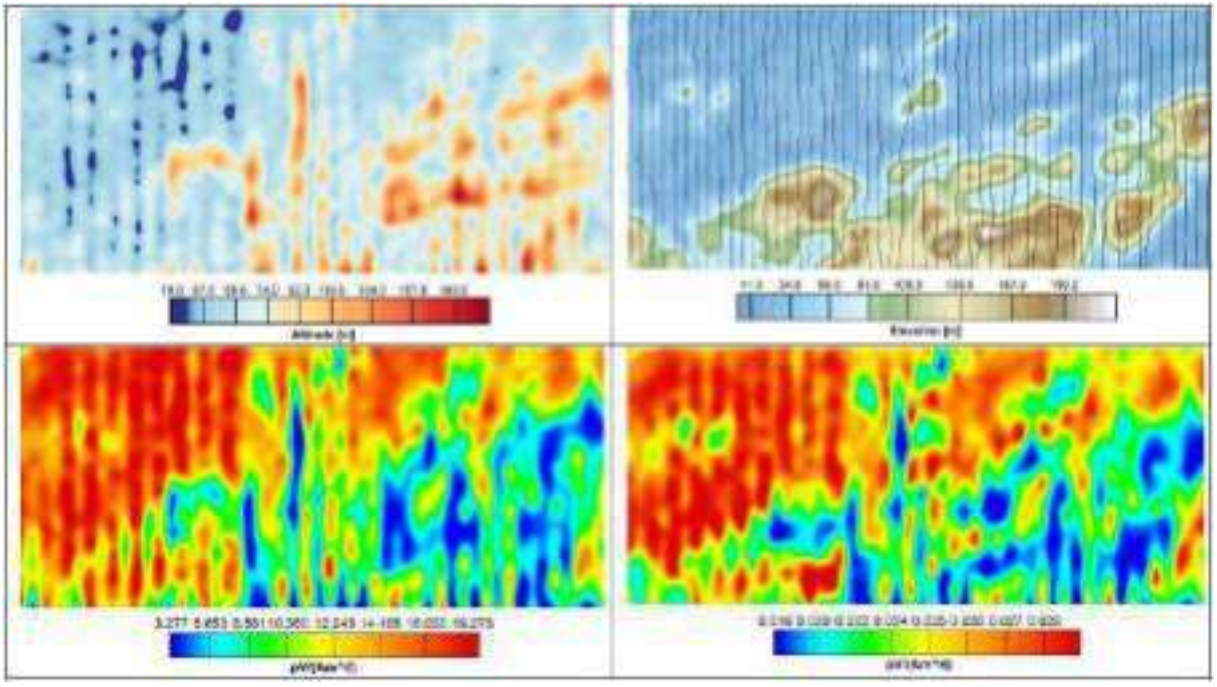

Figure 2. The receiver/transmitter altitude (top left) and digital terrain model (DTM) (top right). The black lines on the DTM represent the flight path and the dBdt-Z[10] (0.065 ms) and dBdt-Z[38] (2.67 ms) grids for the HS_100 model are displayed on the bottom left and bottom right respectively.

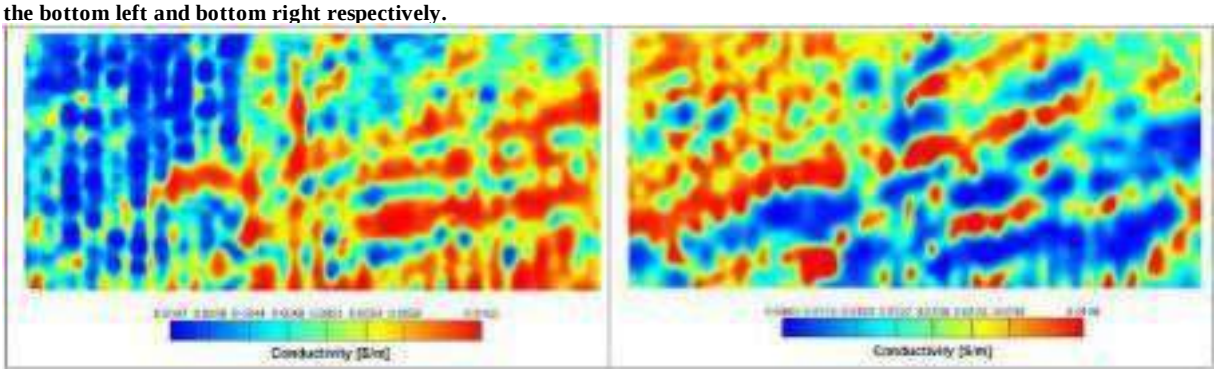

Figure 3. Conductivity-depth slices calculated with GALEI at 50 m depth (left) and S-layer differential transform at 150 m depth (right) for the HS_100 model.

An AEM experience in Northern Italy. Innovative and multidisciplinary approach for a modern groundwater and land management

Matteo Gisolo
A2A S.p.A.
Brescia (IT)
matteo.gisolo@a2a.eu

Luca Spagnoli*
A2A S.p.A.
Brescia (IT)
luca.spagnoli@a2a.eu

Silene Cresseri
A2A S.p.A.
Brescia (IT)
silene.cresseri@a2a.eu

Andrea Viezzoli
Emergo s.r.l.
Pisa (IT)
andrea.viezzoli@aarhusgeo.com

SUMMARY

Climate changes are strongly affecting water supply all around the world and Northern Italy does not make exception to this. In addition, pollutant contamination due to human, both industrial and farming, activities is increasingly spreading in the high Po Plain region and its lateral valleys. Hence, in 2021 an AEM survey has been conducted, aiming at the identification of unknown water reservoirs, on an area of about 200 km^2 located West of the Garda Lake. A time-domain transient EM system (SkyTEM) has been used to perform airborne measurements.

To address the complex depositional environments typical of the subalpine region, the resulting geophysical data, joint with lithological data collected from wells in the last decades, have been interpreted through a cognitive approach.

Where neither electromagnetic nor lithological data were available, a number of ground TDEM tests has been performed to cover the lack of knowledge.

The 3D geological model has been constructed manually as a voxel model with lithofacies attributes supplemented by several bounding surfaces. Two different modelling methods have been combined, namely smooth and sharp, allowing to get the geological complexity.

Starting from the geological model and based on an *ad hoc* piezometric campaign, carried out in the meanwhile on the same area, two 3D FEM flow models has been developed, namely a steady-state one and a transient one.

These achievements have allowed us to understand complex operational situations and to manage them with robust awareness.

In the light of these promising results, we have decided to extend the investigation on a wider area, covering further 1700 km^2.
The whole activity will provide a detailed database, from which impressive multidisciplinary applications can be inferred. Amongst them, priority will be given in kettling drought effects, assessing groundwater vulnerability and evaluating geotechnical phenomena, such as saturated loose sand liquefaction.

Key words: airborne, cognitive approach, geological model, flow model, operational managing.

INTRODUCTION

"*Ensure availability and sustainable management of water and sanitation for all*". This statement introduces the 6th goal claimed by United Nations in the Sustainable Development Goals for 2030. Facing this goal requires, firstly, the identification of new water reservoirs for future generations. But this is not enough. The same importance does take the assessment of impacts arising from current land management, in terms of traditional and emerging pollutants, and the ability to predict how climate change scenarios could affect the hydrogeological cycle.

On all these themes depends not only drinking water availability, but also sanitation, hygiene and water-related ecosystems survival. Hence, the major scopes of the present work.

The region we live in, located between the Alps' piedmont district and the high Po Plain region, suffers from pollution induced by industrial activity, large-scale agriculture and intensive livestock farming. In addition, in the last years a lack of groundwater recharge during the fall and winter seasons is observed. This phenomenon can be related to the modified rainfall characteristics, since the usual long-duration moderate precipitations are increasingly replaced by short-duration intense events. In such situation, a numerical groundwater flow model becomes fundamental for a water public utility.

Usually, hydrogeological assessments and predictions are made on the basis of boreholes from wells. Even if hundreds of data from wells are available in the study area, they mainly concentrate near residential zones, along the Chiese river, hence large extensions of land are lacking information and, due to the peculiar complex geological structure, additional data within the deficient portions of land are needed.

We find that investigations by airborne electromagnetism of the time-domain type could be the more appropriate, detailed, time-saving and money-saving method to gain this target, following the remarkable examples all around the world (Auken et al., 2017; Ley-Cooper & Richardson, 2019; Munday, 2013; Kang et al. 2022; Knight et al., 2018).

As pioneering experience in our province, we conducted a first campaign in 2021, when 212 km^2 were flown in less than 15 days (Figure 1). This has led to a great amount of data, processed and interpreted by a cognitive approach, which involved a multidisciplinary team made of geophysicists, geologists and hydrogeologists.

As a result, we have got 120 thousand geophysical models (60 thousand with smooth inversion and 60 thousand with sharp one). From them a 3D geological model and two 3D flow models, for steady-state regime and transient one as well, have been obtained. These first results have provided insightful explanations of well-known operational problems, unresolved till now.

Given these promising achievements, a second campaign has been started in March 2023, covering further 1.717 km^2 in 97 days. This new survey aims at even more challenging targets, deemed essential for a sustainable and responsible management of land and geo-resources use. Hence, present and future efforts are oriented towards drought effects mitigation by

artificial recharge of shallow aquifers (San-Sebastián-Sauto et al., 2018; Sendrós et al., 2020; Teatini et al., 2020) and groundwater protection (Thomsen et al., 2004). Geotechnical applications are in our sights as well, such as landslides mapping (Thiery et al., 2021; Pfaffhuber et al., 2010), seismic bedrock tracking (Christensen et al., 2015), evaluation of waste bodies conditions (Hammack et al., 2010) and liquefaction hazard assessment.

METHOD

Time Domain Electro-Magnetic method

To obtain information at basin scale and high depths, a helicopter electromagnetic survey was carried out, with the SkyTEM system (Sørensen & Auken, 2004). This is a time-domain helicopter electromagnetic system (TEM) designed for hydrogeophysical, environmental and mineral investigations (Viezzoli et al., 2012).

With the time-domain method, the signal amplitude is measured as a function of time. The system mainly consists of a transmitter coil (Tx) and a receiver loop (Rx). A current is transmitted in the Tx loop and is abruptly turned off. This generates an electromagnetic field, which induces an electrical current in the surroundings, which in turn induces a secondary magnetic field. The receiver coil records a series of voltages related to the change in the secondary magnetic field over time (dB/dt), which provide information on the electrical conductivity of the ground. The voltages are recorded through time windows (gates).

The sampling approach is based on using the same number of gates per decade of time. The gates have a width increasing logarithmically with time, a configuration called log-gating (Munkholm & Auken, 1996).

The raw data acquired in 2021 were processed and inverted by EMergo, who has been asked to develop two different geophysical models, in order to achieve the most reliable geological modelling, by means of two different inversion methods: *smooth* and *sharp*.

By the *smooth inversion* the half-space is discretised in several layers whose thickness logarithmically increases with depth. This inversion strategy gets the solution that involves a gradual variation of model parameters in space.

Figure 2a shows an example of *smooth inversion*. In the magnified boxes, the gradual transition between two different layers is shown: a shallower resistive layer (~ 200 Ω·m) and deeper conductive layer (~ 1 Ω·m). The resistivity of these two layers ranges gradually from 200 Ω·m to 1 Ω·m. Generally speaking, this condition is satisfied in sedimentary environments, with parallel sub-plane geometries, where facies exhibit broad lateral continuity and an effective vertical gradual variation.

The *sharp inversion* (Vignoli et al., 2014) promotes the reconstruction of blocky solutions, using a parametrisation characterised by several layers (like smooth inversion strategy), by minimising the volume where the spatial model variation is non-vanishing. *Sharp inversion* reconstructs electrical subdomains in which parameters are free to change under a certain threshold. This approach ensures that the results are consistent with the measured data while favouring, at the same time, the retrieval of horizontal abrupt changes. In addition, the focusing regularization can also be applied in the horizontal direction, in order to promote the reconstruction of lateral boundaries such as faults (Vignoli et al., 2014).

Figure 2b shows an example of *sharp inversion*. The magnified boxes show how the transition between two bodies can be defined, when a sharp contrast in electrical properties characterises them.

In general terms, this inversion strategy is more suitable than *smooth inversion* when the layer has an effective sharp spatial variation of model parameters. For example, it applies suitably where structural elements or magmatic intrusions do prevail in the investigation area.

Data cognitive interpretation and overall framework

The geological model is developed with a cognitive approach, in which all available data (AEM data surface geological map, stratigraphic boreholes, etc.) and the overall conceptual geological knowledge are combined and translated into a manually interpreted 3D model (e.g., Sapia et al. 2015, Høyer et al., 2015, Jørgensen et al., 2013).

For the overall model construction, we used the software package GeoScene3D (https://geoscene3d.com/). This software promotes the visualisation of data by cross sections, horizontal sections, map views and 3D view (Jørgensen et al., 2015).

As stated by Jørgensen et al. (2015), the cognitive layer model is developed as a framework model consisting of layers that are defined as bodies between surfaces. These last are, in turn, controlled by interpretation points defined in space and manually digitised and attached to cross sections, horizontal sections, boreholes, geophysical sections, etc., according to the modeller's geological interpretations. Most interpretation points are attached to cross sections that were gradually moved through the model space and checked against perpendicular moveable cross sections. The interpretation points are instantaneously interpolated into surface grids, providing an instant overview of the surface or boundary being modelled.

In addition to the cognitive approach, the geological model takes its robustness upstream of the process, during the AEM survey itself. During the 2021 campaign, the continuous interaction between A2A geologists and EMergo geophysicists made possible to cope with the many difficulties inherent in the study area and to better plan the acquisition of the following days.

The information interchange between geologist and geophysicist during the survey has led to the best geological interpretation, achievable from the numerical processing of raw data. This interaction resulted in a good knowledge of the subsurface, which was used as a basis for geological modelling.

Groundwater model with FeFlow

Three-dimensional numerical modelling was performed using FeFlow 7.4 software (*Finite Element subsurface Flow system - WASY GmbH*), based on the finite element method (FEM). The

Darcy's equation of flow is solved within a grid-discretised domain (mesh).

The choice of the FeFlow code is justified considering the complex geometries of the subsurface in the study area. With a finite element software, it is possible to implement a groundwater model without making simplifications to the geometries elaborated during the geological modelling phase.

In a first phase of the work, we set up a 3D-type problem in which a steady-state flow was simulated. In a second phase of the work the 3D-type problem considered a transient flow. Both models were implemented by considering a flow without mass and/or heat transport, within a saturated aquifer under unconfined conditions, considering a free water table surface.

For the implementation and calibration of the steady-state model, we used the piezometric values collected during the 2021 monitoring campaign. The hydraulic properties of the aquifer were defined from literature data and field tests, while the conductance of the riverbed was defined from literature values only (e.g., Chen et al., 2013; Naganna et al., 2017; Stewardson et al., 2016; Tang et al., 2018).

The transient model was implemented from the calibrated steady-state model, where the hydraulic conductivity of the aquifer and the conductance of the riverbed were automatically calibrated by a PEST analysis (J.E Doerthy & R.J. Hunt, 2010).

The transient modelling was carried out in two phases. In the first phase, the hydrological dynamics for the year 2020 was modelled, based on the time series coming from hydrological model returned by the software TOPKAPI. The purpose of this phase was to calibrate the model so that the groundwater recharge dynamics could be optimally reproduced. For the calibration, four representative reference points have been considered. In particular, the Pearson correlation coefficient (r) and the root mean square deviation (RMSE) were assumed as statistical criteria.

Whitin the second phase, three future climate scenarios models (RPC8.5, RPC4.5 and RPC2.6) was developed, for the years between 2071 and 2080, assuming as a starting point for the boundary conditions the time series modelled by TOPKAPI.

RESULTS

3D geological model

The 3D geological model, developed by the AEM data, is shown in Figure 3.

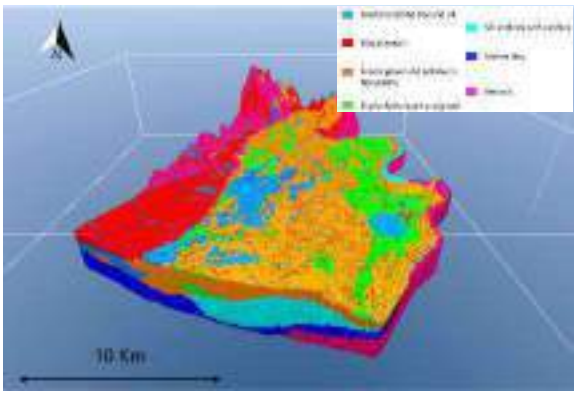

Figure 3. 3D geological model.

By developing the 3D geological model, we could identify two different geological domains: fluvial domain and glacial domain (Figure 3).

The glacial domain, covering the Eastern portion of the study area, is characterised by an alternation of heterogeneous deposits due to the presence of glacial depositional environments. The overall thickness is quantified in approximately 300 m and lays on the bedrock.

The fluvial domain, pertaining to the western portion of the area, is characterised by the recent fluvial deposits of the Chiese River, mainly composed of coarse gravels and pebbles, delimited in depth by deep fine deposits.

It is worth noting that, from the geological model, the two domains appear to be separated, due to bedrock rising. The only portion where the two domains come into contact is the southernmost part of the model where they overlap in angular unconformities.

Finally, by reconstructing the geometries of the glacial domain, we have observed that on the coast of Garda Lake (eastern limit of the geological model) the slope of the glacial deposits and the rise of the bedrock ensure that no interconnection between the lake and the aquifer is possible.

Groundwater model results

The fluvial deposits of the Chiese River represent the main aquifer in the study area, therefore the 3D groundwater flow simulation focused on the recent and current fluvial deposits.

The 3D steady-state groundwater model has been initially calibrated manually by *trials and errors* and, successively, by an automatic procedure with PEST.

The achieved results return a RMSE of 0.53 m and an average absolute error of 0.42 m (Figure 4). The piezometry from the model and the data collected during the piezometric campaigns show a very good agreement. Moreover, the model is able to take into account the effects given by the geometry of the fluvial aquifer, by the external inputs related to surface water (Chiese River, percolation and lateral flow) and by the lateral inputs from the carbonate bedrock (West side of the studied area).

The 3D transient model was calibrated using *trials and errors*. Groundwater levels from the 2020 time series in the 4

observation wells were used as comparison data (Figure 5). The final calibration of the model resulted in an RMSE of 1.91 m and an average correlation coefficient (r) equal to 0.73. In particular, the model is able to reproduce the different recharge dynamics in the areas identified during the hydrogeological characterisation phase.

After this calibration phase, the three future climate scenarios were applied. Scenario RPC2.6 is considered the optimal scenario, close to the current meteo-climatic values. Scenario RPC8.5 represents the most unfavourable case, while the scenario RPC4.5 is intermediate between the two previous ones. As far as the modelled water balance volumes are concerned, variations consistent with the meteoclimatic forecasts are observed. In particular, for all three scenarios a negative aquifer storage (loss) is observed. The order of magnitude is approximately 10^3 m^3/day. A 35% increase in loss between the RPC2.6 and RPC8.5 scenarios is obtained. This is mainly due to the reduction in volumes exchanged between the river and the aquifer (with a 10.5% reduction in the river's contribution) and between the bedrock and the aquifer (with a 3% reduction in the lateral water supply).

SURVEY 2023

The recent campaign, started in March, has covered the major part of the district area (Figure 6). Inside it, we have distinguished four different compartments, according to different geo-lithological and structural peculiarities.

Figure 6. District under investigation: province of Brescia, in Northern Italy (modified from www.originalmap.it).

This new survey does not represent a mere aerial expansion of the previous one. In fact, thanks to progressive expertise, acquired in progress, we could focus on the several applications that deserve attention (Figure 7).

In the mountain zone, efforts are devoted to the identification of proper sites for perforating new drinking water wells in fractured rock masses.

In the Western Garda Lake area, opportunities for new enhancements in recent neotectonics activity come to the fore. In the plain portion, artificial recharge of shallow aquifers and groundwater protection are priority targets.

The southernmost part of the Po Plain, apart from drought problems affecting agriculture, suffers from poor geotechnical characteristics and coseismic effects, like loose sand liquefaction.

At present, all these targets are in progress. Hence, *in itinere* preliminary results will be presented.

CONCLUSIONS

Starting from this pioneering experience for Italy, a great amount of work is in progress and an even greater quantity awaits us for the future.
The only conclusion, up to now, is that AEM methods together with cognitive interpretation for geological modelling do represent the most promising tool in facing environment-related problems and climate changes. From them, technicians, georesources managers and politicians can no longer escape.

AKNOWLEDGMENTS

We acknowledge all the people involved in this project. First of all, Dr. Roberta Perico for her essential contribution in flow modelling. We also acknowledge the cute and competent EMergo team, headed by Dr. Antonio Menghini; Prof. Gianluca Fiandaca and his students from University of Milan. Finally, we give special thanks to Dr. Flemming Effersø and his professional staff.

REFERENCES

Auchen, E., Boesen, T. & Christensen, A.V. (2017). A Review of Airborne Electromagnetic Methods With Focus on Geotechnical and Hydrological Applications From 2007 to 2017. *Advances in Geophysics*, 58, 47-93.

Chen, X., Dong, W., Ou, G., Wang, Z., & Liu, C. (2013). Gaining and losing stream reaches have opposite hydraulic conductivity distribution patterns. *Hydrology and Earth System Sciences*, 17(7), 2569-2579.

Christensen, C.W., Pfaffhuber, A.A., Anschütz, H. & Smaavik, T.F. (2015). Combining airborne electromagnetic and geotechnical data for automated depth to bedrock tracking. *Journal of Applied Geophysics*, 119, 178-191.

Doherty, J. E., & Hunt, R. J. (2010). Approaches to highly parameterized inversion: a guide to using PEST for groundwater-model calibration (Vol. 2010). Reston, VA, USA: US Department of the Interior, US Geological Survey.

Hammack, R., Kaminski, V., Harbert, W., Veloski, G. & Lipinski, B. (2010). Using helicopter electromagnetic (HEM) surveys to identify potential hazards at coal-waste impoundments: Examples from West Virginia. *Geophysics*, 75(6), B221-B229.

Høyer, A. S., Jørgensen, F., Sandersen, P. B. E., Viezzoli, A., & Møller, I. (2015). 3D geological modelling of a complex buried-valley network delineated from borehole and AEM data. *Journal of Applied Geophysics*, 122, 94-102.

Jørgensen, F., Møller, R.R., Nebel, L. et al. (2013). A method for cognitive 3D geological voxel modelling of AEM data. *Bull Eng Geol Environ* 72, 421–432.

Jørgensen, F., Høyer, A. S., Sandersen, P. B., He, X., & Foged, N. (2015). Combining 3D geological modelling techniques to address variations in geology, data type and density–An example from Southern Denmark. *Computers & geosciences*, 81, 53-63.

Kang, S., Knight, R., & Goebel, M. (2022). Improved Imaging of the Large-Scale Structure of a Groundwater System With Airborne Electromagnetic Data. *Water Resources Research*, 58(4).

Knight, R., Smith, R., Asch, T., Abraham, J. Cannia, J., Viezzoli, A. & Fogg. G. (2018). Mapping Aquifer Systems with Airborne Electromagnetics in the Central Valley of California. *Groundwater*, 56(6), 893-908.

Ley-Cooper, A.Y. & Richardson M. (2018). Aus AEM; acquisition of AEM at an unprecedented scale. *ASEG Extended Abstracts*, 1, 1-3.

Munday, T. (2013). The role of airborne geophysics in facilitating long-term outback water solutions to support mining in South Australia. *ASEG Extended Abstracts*, 1, 1-4.

Munkholm, M. S., & Auken, E. (1996). Electromagnetic noise contamination on transient electromagnetic soundings in culturally disturbed environments. Journal of Environmental and *Engineering Geophysics*, 1(2), 119-127.

Naganna, S. R., Deka, P. C., Ch, S., & Hansen, W. F. (2017). Factors influencing streambed hydraulic conductivity and their implications on stream–aquifer interaction: a conceptual review. *Environmental Science and Pollution Research*, 24(32), 24765-24789.

Pfaffhuber, A.A., Grimstad, E., Domaas, U., Auken, E., Foged, N. & Halkjær, M. (2010). Airborne EM mapping of rockslides and tunneling hazards. *The Leading Edge*, 29(8), 956-959.

Sapia, V., Oldenborger, G. A., Jørgensen, F., Pugin, A. J. M., Marchetti, M., & Viezzoli, A. (2015). 3D modeling of buried valley geology using airborne electromagnetic data. Interpretation, 3(4), SAC9-SAC22.

San-Sebastián-Sauto, J., Fernández-Escalante, E., Calero-Gil, R., Carvalho, T. & Rodríguez-Escales, P. (2018). Characterization and benchmarking of seven managed aquifer recharge systems in south-western Europe. *Sustainable Water Resources Management*, 4, 193-215.

Sendrós, A., Himi, M., Lover, R., Rivero, L., Garcia-Artigas, R., Urruela, A. & Casas, A. (2020). *Water*, 12(12), 3455.

Sørensen, K.I. & Auken, E. (2004). SkyTEM – a new high-resolution helicopter transient electromagnetic system, *Exp. Geoph*., 35, 191-199.

Stewardson, M. J., Datry, T., Lamouroux, N., Pella, H., Thommeret, N., Valette, L., & Grant, S. B. (2016). Variation in reach-scale hydraulic conductivity of streambeds. *Geomorphology*, 259, 70-80.

Tang, Q., Schilling, O. S., Kurtz, W., Brunner, P., Vereecken, H., & Hendricks Franssen, H. J. (2018). Simulating Flood-Induced Riverbed Transience Using Unmanned Aerial Vehicles, Physically Based Hydrological Modeling, and the Ensemble Kalman Filter. *Water resources research*, 54(11), 9342-9363.

Teatini, P., Martelli, G., Comerlati, A., Paiero, G. & Zoccarato, C. (2020). Managed Versus Natural Recharge of Pre-Alpine Phreatic Aquifers. *Water Resources Research*, 56(9),

Thiery, Y., Reninger, P.A. & Nachbaur, A. (2021). Airborne Electromagnetics to Improve Landslide Knowledge in Tropical Volcanic Environments. *Applied Sciences*, 11(8), 3390.

Thomsen, R., Søndergaard, V.H. & Sørensen, K.I. (2004). Hydrogeological mapping as a basis for establishing site-specific groundwater protection zones in Denmark. *Hydrogeology Journal*, 12(5), 550-562.

Viezzoli, A., Jørgensen, F., Sørensen, C. (2012). Flawed Processing of Airborne EM Data Affecting Hydrogeological Interpretation. *Ground Water*, 51, pp. 191-202. doi: 10.1111/j.1745-6584.2012.00958.

Vignoli, G., Fiandaca, G., Christiansen, A. V., Kierkegaard, C., Auken, E. (2014). Sharp spatially constrained inversion with applications to transient electromagnetic data. *Geophysical Prospecting* (EAGE), pp.1-13.

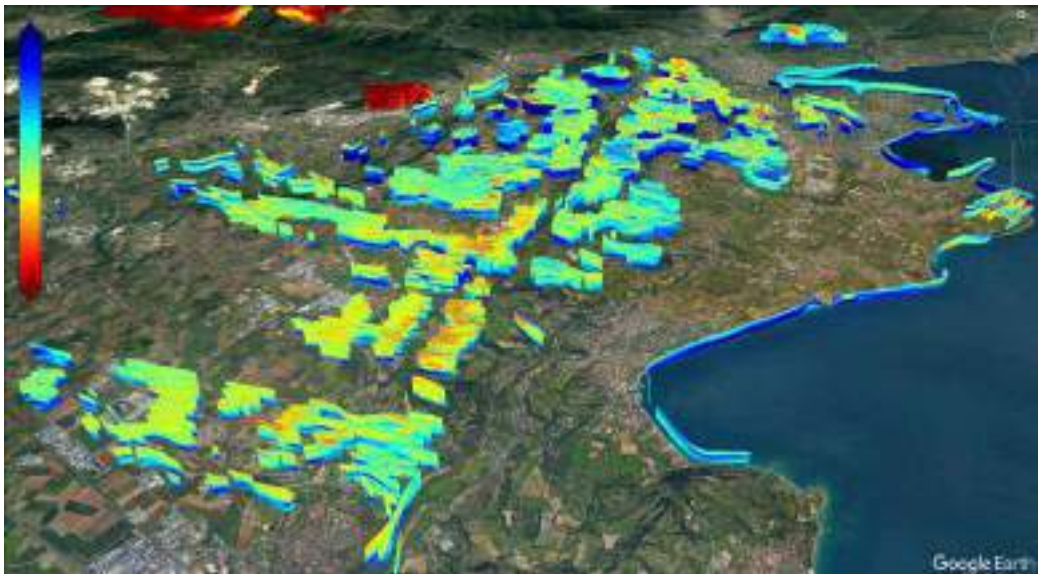

Figure 1. Aerial overview of the flight lines from 2021 survey, with contour plots of the electrical sections (from Google Earth).

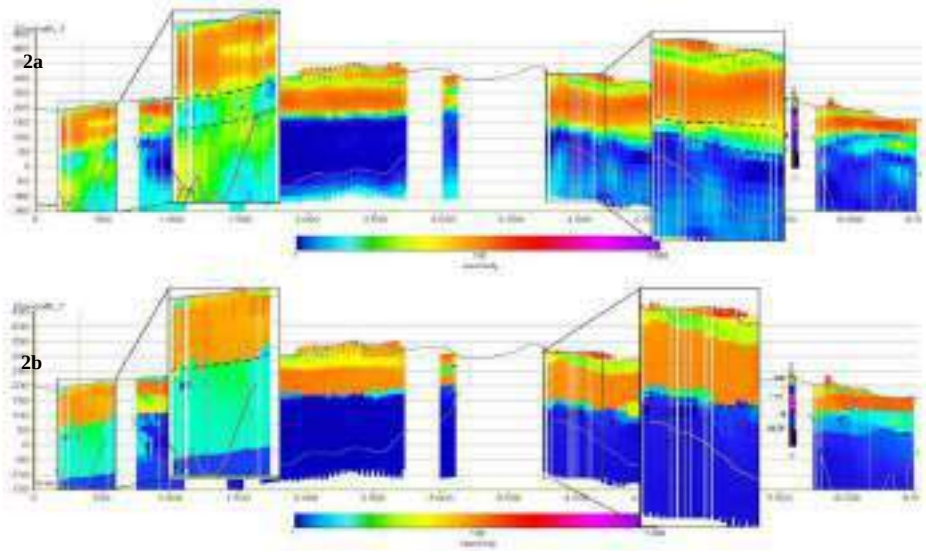

Figure 2. 2D section of smooth (a) and sharp (b) electrical model. Grey curves represent DOI (Depth of Investigation).

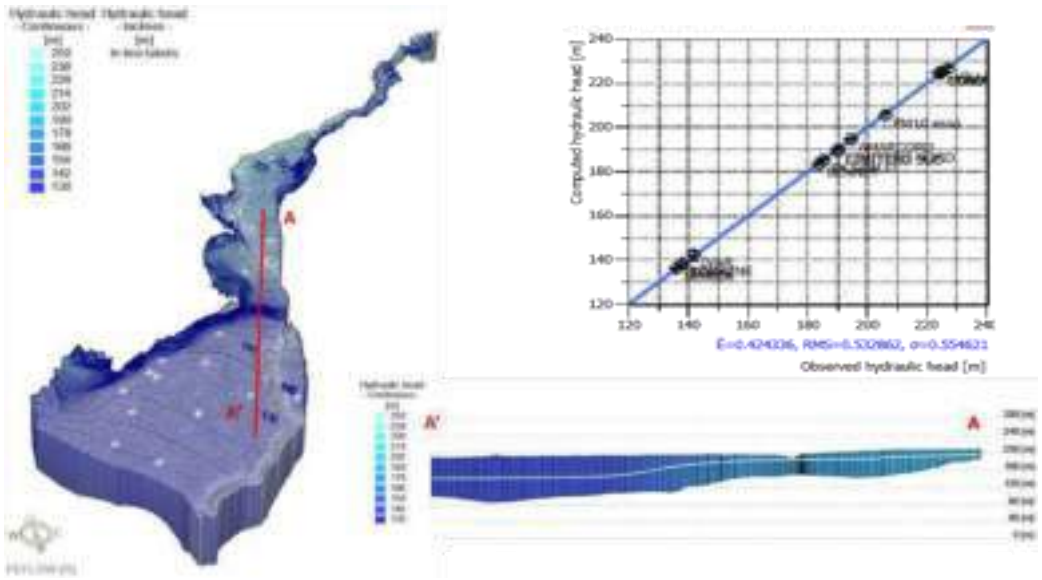

Figure 4. Results of steady-state model calibration.

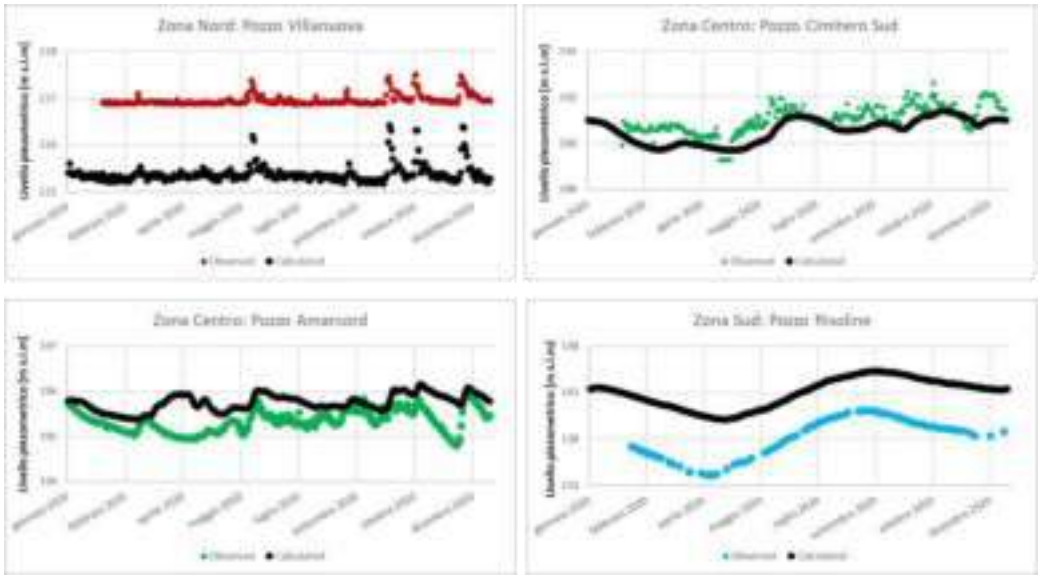

Figure 5. Comparison between observed and model-measured time series at the 4 available observation points.

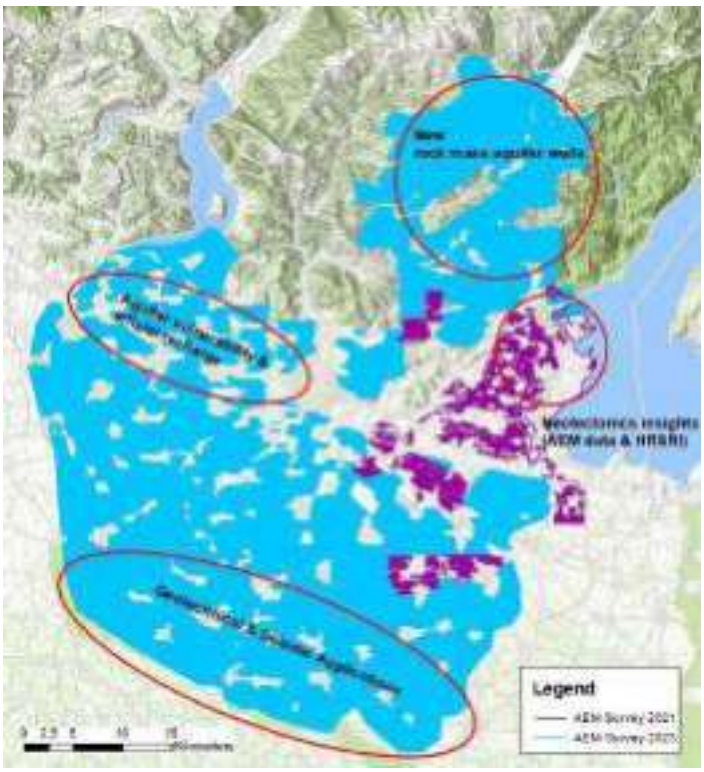

Figure 7. Survey 2023. Flight zones and specific topics to deal with.

Joint Inversions of AEM modelling AIP effects: Helicopter-borne, Ground IP and Fixed-Wing systems

Francesco Dauti
The EEM Team for Hydro & eXploration
Dep. of Earth Sciences A. Desio,
Università degli Studi di Milano,
Via Botticelli 23, Milano (Italy)
francesco.dauti@unimi.it

Andrea Viezzoli
EMergo srl,
Via XX Settembre 12, Cascina, (Pisa, Italy)
andrea.viezzoli@em-ergo.it

Gianluca Fiandaca
The EEM Team for Hydro & eXploration
Dep. of Earth Sciences A. Desio,
Università degli Studi di Milano,
Via Botticelli 23, Milano (Italy)
gianluca.fiandaca@unimi.it

SUMMARY

It is nowadays widely accepted that Induced Polarization (IP) effects can affect Airborne Electromagnetic (AEM) measurements. Modelling the AEM data with a dispersive-resistivity allow to properly retrieve the halfspace parameters avoiding high inversion misfits and wrong structures. Even if the Airborne IP (AIP) modelling it is a known and controlled practice, there are still some open questions regarding the complexities of this modelling approach. Most of this lie into the AIP sensitivity to geological targets, others in its capability in integrate with the ground IP and other more about the parametrical management during the inversion process. To contribute on the AEM-IP modelling field of research, with this work we performed two joint inversions on real data modelling AIP effects. For the first experiment we jointly inverted AEM-IP fixed-wing data with helicopter-borne data. For the other experiment, we jointly modelled ground DCIP and helicopter-borne AEM data, modelling AIP parameters. With these experiments we retrieved that inductive airborne IP can contribute, in term of sensitivity, to the ground IP modelling procedure and that fixed-wing airborne data have a good sensitivity to chargeable geological targets as well as helicopter-borne platforms. More in general, it has been seen that inductive IP contains complementary information for modelling IP effects.

Key words: Airborne Electromagnetics, Airborne IP, Fixed-Wing measurements, Ground IP measurements.

INTRODUCTION

Airborne Electromagnetic methodologies represent nowadays one of the most common and effective techniques for large scale resistivity mapping in mineral exploration and environmental issues (Flis et al., 1989; Smith, 1989; Smith and Klein, 1996; Kratzer and Macnae, 2012; Viezzoli et al., 2013). At the same time, it is recognized and subject of a growing interest, that AEM measurements are sensitive to Induced Polarization (IP) effects when acquired over a polarizable halfspace (Kratzer and Macnae, 2012; Viezzoli et al., 2013). These effects are given by the physics of polarizable materials that are able to complete a full charge and discharge cycle in a finite time interval when subject to an external electric field. The polarization ion-movement generates a polarization current that is is add, under the quasi-static approximation, to the pure EM currents induced in the ground by the AEM system. This currents interaction will inevitably manifest itself into the secondary magnetic field generated with their flow and that is recorded by the system's receiver (Flis, 1989). The IP effects are thus detectable with a typical signature in EM data: a fast decay that can culminate, if the polarization currents dominate the EM currents (opposite sign during discharging phase), to a change of sign of the EM signal. Under these conditions, the general relationships between the measured voltages versus time and depth (from which derive the correlation between the conductance and the data sensitivity) are compromised if the capacitive behaviour of the ground is not considered (Viezzoli 2017, Smith and Klein, 1996). It follows that modelling the AIP effects when they affect the AEM data is crucial to recover a correct parametrization of the investigated halfspace and to properly fit the data. The illustrated physics behaviour is model with the well-known dispersive resistivity models (such as Cole&Cole, Maximum Phase Angle, Constant Phase Angle…) typically used for galvanic DCIP data and that make the AEM data modelling effective but more complex at the same time. The modelling effectiveness is demonstrated by ground proven correct structures recovery such as cover thicknesses, conductive bodies top and bottoms, chargeable anomalies, and more (Viezzoli et al., 2017). Moreover, with a recent study (Dauti et al., 2023), it has been shown how AIP can provide significative information for exploration purposes providing airborne chargeable anomalies confirmed subsequently by ground DCIP acquisitions.

All these contributions and confirmations made the AIP interest increase in industry and in academia in the last decades.

With this work we will thus focus on AEM data modelling considering IP effects, illustrating two attempts of AEM-IP joint real data modelling. The joint inversions are carried between:

- AEM helicopter borne and galvanic DCIP data
- AEM helicopter borne and AEM fixed-wing data

Both the experiments aim to use the AEM-IP data sensitivity to increase the spectral content modelling of the acquired inductive (or galvanic) data.

For the first joint inversion, between airborne and ground IP, we wanted to verify if and how AEM-IP data are able to integrate the ground DCIP sensitivity to recover the dispersive-resistivity of the ground. As well known, the two methodologies work at different base frequencies and are considered, at this state of the art, spectrally sensitive to different and not compatible geological features (Macnae 2016). At this regard, given its spectral range, the airborne IP measurements are considered sensitive only to low time constants (quick polarization) and high chargeabilities only that, geologically speaking, is translatable to fine grained materials like clay, alterations or non-economic minerals.

Regarding the second experiment, between helicopter-borne and fixed-wing systems, we wanted to verify if the fixed-wing systems are sensitive to the same geological features of helicopter-borne platforms and are able to contribute to the model resolution. The fixed-wing systems were historically considered not able to detect IP effects, given their in-offset geometry that does not allow to uniquely relate negative voltages to IP effects (contrary to concentric loop helicopter-borne platforms), and to their bigger system footprint (lower shallow resolution). Anyway, recent studies (Viezzoli et al. 2021, Dauti et al., 2022), showed that it is possible to theoretically detect IP effects for fixed wing data and that it is satisfying model them.

With this work we thus want to contribute to the understanding of the sensitivity of the AIP spectral content in AEM data modelling.

METHOD AND RESULTS

The experiment set up and their results will be separately treated and illustrated in detail in the sections below.

Helicopter-Borne and Ground DCIP joint Inversion modelling AIP

The Airborne EM data have been acquired the last spring with the NRG XCite Time Domain 25Hz base frequency system, illustrated in black lines in figure 3. As introduced, for the same area 18 SyscalPro lines (0.125Hz of base frequency, 50% duty cycle) of ground Time Domain DCIP have been acquired.

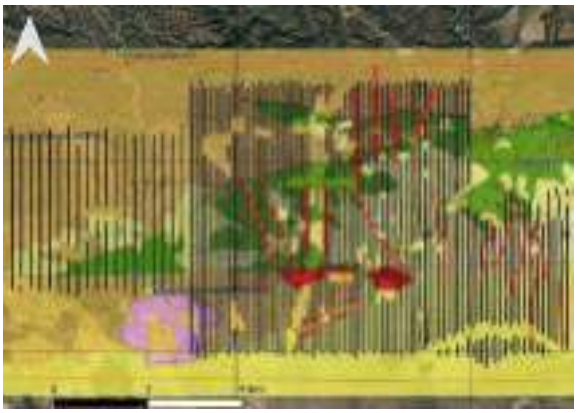

Figure 1. Survey location. In black the Airborne EM lines are displayed, in red the DCIP.

The datasets have been modelled with a consistent modelling procedure, with a 2D forward response formulation for the DCIP data (Fiandaca 2013) and 1D for the TDEM (Fiandaca 2012). The modelling approach proposed by Fiandaca allows to model the full-voltage decay (instead of the integral chargeability), the transmitter waveform and the receiver transfer function, increasing the procedure accuracy in recovering the spectral parameters. These features have been modelled both for the Airborne EM than for the Ground DCIP. Regarding the model-space parametrisation, we used the Maximum Phase Angle (MPA) Cole-Cole re-parametrisation (Fiandaca et al., 2018; Madsen et al., 2018) instead of the classical Cole-Cole model re-arranged by Pelton (1978). The MPA Cole-Cole model is a re-parametrized form of the classic Cole-Cole, where instead of m_0 and τ_ρ we used the maximum phase φ_{max} and the phase relaxation time τ_φ. The phase of the complex conductivity can be defined in terms of both *equations 1* and *2* as:

$$\varphi(\omega) = atan\left(\frac{\sigma''(\omega)}{\sigma'(\omega)}\right) = atan\left(\frac{\rho''(\omega)}{\rho'(\omega)}\right) \qquad \text{(eq. 1)}$$

The phase reaches his maximum φ_{max} at an angular frequency $\omega_\varphi \equiv 1/\tau_\varphi$ as:

$$\varphi_{max} = atan\left(\frac{\sigma''(1/\tau_\varphi)}{\sigma'(1/\tau_\varphi)}\right) = atan\left(\frac{\rho''(1/\tau_\varphi)}{\rho'(1/\tau_\varphi)}\right) \qquad \text{(eq. 2)}$$

Furthermore, the model space of the MPA Cole-Cole model can be written as:

$$m_{MPA\ Cole-Cole} = \{\rho_0, \varphi_{max}, \tau_\varphi, C\}$$

The MPA parametrisation allows to minimize the correlations between the Cole-Cole m_0 and C using the poorly correlated φ_{max} and C, and to improve the resolution retrieved from inversion IP data of the classical Cole-Cole model.

The inversions have been performed with the inversion scheme proposed by Fiandaca et al., 2023 that uses voxel model mesh to map the solved parameters via an interpolation of the forward mesh solutions. The decoupling of the model mesh and the forward mesh allows to work with more flexible and manageable spaces (forward and model) to perform joint inversions and time laps inversions. In our inversion procedure, in order to increase the parametrical resolution and the phase sensitivity in depth, we parametrized the spectral parameters (τ_φ, C) on an independent mesh respect to resistivity and phase, with different lateral constraints and vertically fixed (as proposed by Viezzoli and Fiandaca in 2021).

The inversion results for the lines on which we performed the joint modelling are presented in Figure 2. In the figure we compared the results for AEM chargeability section only, the modelled DCIP chargeability, and the joint inversion model of the two. In terms of inversion misfit, we obtained: AEM only: 1.10, DC only: 4.2, IP only: 1.2 and, for the joint inversion, AEM joint: 1.18, DC joint: 4.9, IP joint: 1.20. The misfits are thus comparable and satisfying considering the standard deviations of each dataset. As visible from the results, the joint inversion model merges the sensitivities of the two methodologies and add the information of the ground DCIP to the chargeable bodies. It is also visible how the AIP modelling add information to the joint inversion and, at the same time, accept the ground DCIP sensitivity.

Helicopter-Borne and Fixed-Wing joint Inversion modelling AIP

For our experiments we used data from a GEOTEM$_{DEEP}$ fixed-wing system (Annan, 1990) acquired in Northern Territories, Australia, in 2010 and some overlapping (Figure 3) government VTEM helicopter-borne data acquired in 2009. Geologically, the investigated area is a classical Australian environment with a conductive cover over a resistive bedrock; the aim of the investigation was the estimation of the cover thickness for exploration purposes.

From a geophysical point of view, the differences between the two systems are many and are reflected in the acquired data. The dipole moment for the fixed wing GEOTEM system is

almost the double of the VTEM one and, geometrically, the offset configuration (and a 15-year-old technology) does not allow to properly monitor and measure the receiver bird position producing strong modelling complexities. For our modelling procedure we used the theoretical bird position, with a receiver horizontal offset of 70 m and a vertical offset of 50 m respect the craft.

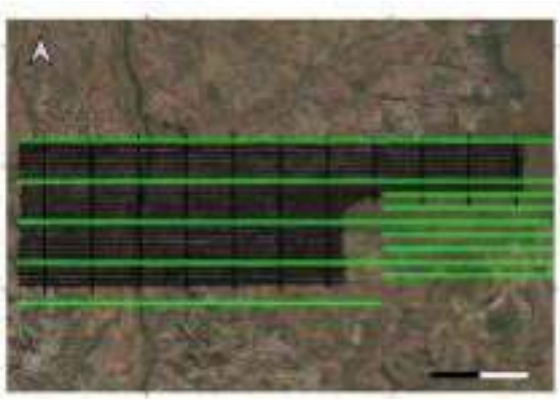

Figure 3. In black: GEOTEM's lines; in green: VTEM's lines.

As workflow, we firstly manually processed the EM data to assess the noise level for the two systems, to improve the S/N and to delete artifacts. Then we proceed with the joint inversion of the overlapping lines using, as before, the approach proposed by Fiandaca et al., 2023 and using the MPA parametrization as presented in Equations 1 and 2. In Figure 4 an example of a jointly modelled couple of lines is presented. The presented models are cropped with the depth of investigation (DOI). This is calculated as Fiandaca et al., 2015, based on an approximated covariance analysis applied to the model output from the inversion while considering the data standard deviations.

In the figure is interesting to see how the chargeability has a good resolution and follows, also in depth, the conductive shallow layer modelled in the resistivity model as expected from the geological information of the area.

CONCLUSIONS

With this contribution we shown that the AIP spectral content can significatively contribute to the dispersive-resistivity modelling when jointly modelled with other techniques (galvanic Induced Polarization) and between different airborne systems (fixed wing and helicopter borne platforms).

First, it has been demonstrated that is successfully possible to jointly model Airborne and Ground IP. In particular, it has been shown how the airborne IP contributes to the sensitivity of the modelling procedure and accepts the ground sensitivity in the inversion procedure. Important is to underly how the recovered structure not only changes (if comparing galvanic-only or inductive-only inversions) in terms of resistivity modelling but also in terms of chargeability. This importantly evidence that the spectral content of airborne data is complementary and can add information to the ground DCIP.

Regarding the airborne inversions, it is possible to jointly model helicopter borne and fixed-wing AEM data considering IP effects. The inversion process, as expected, converged to the resultant model using the different sensitivities of the two systems fitting the data. The different sensitivities are given by the different system's features (such as footprint, geometry, height of flight, dipole moment…) and the obtained results merge the features of both.

ACKNOWLEDGMENTS

We acknowledge PanGlobal resources to allow us in using ground IP and airborne IP data for our joint inversion. We acknowledge the Australian Government and Geoscience Australia for having made the VTEM data available. We also thanks Alligator Energy and John Donohoue for allowing us to present the data.

REFERENCES

Annan, A.P., GEOTEM: Fixed Wing Transient EM System, 1990, SEG Annual Meeting, San Francisco, California.

Dauti, F., Viezzoli, A., Fiandaca, G., 2022, First attempts to model AIP in fixed-wing EM data, South African Geophysical Association, Conference Paper, Sun City, South Africa.

Dauti, F., Viezzoli, A., Fernandez, I., Royall, J., Fiandaca, G, 2021. Airborne and Ground Induced Polarization integration: new insights for exploration. AEGC Conference, Brisbane.

Fiandaca, G., Fiandaca, G., Gazoty, A., Auken, E., & Christiansen, A. V., 2012. Time-domain-induced polarization: Full-decay forward modeling and 1D laterally constrained inversion of Cole-Cole parameters. Geophysics, 77, E213-E225.

Fiandaca, G., Ramm, J., Binley, J., Gazoty, A., Christiansen., A.V., Auken, E., 2013 Resolving spectral information from time domain induced polarization data through 2-D inversion, Geophysical Journal International, Volume 192, Issue 2, February 2013, Pages 631–646.

Fiandaca, G., Christiansen, A. V., Auken E., 2015, Depth of investigation for multi-parameters inversions, Near Surface Geoscience 2015 - 21st European Meeting of Environmental and Engineering Geophysics, Sep 2015, Volume 2015, p.1 – 5.

Fiandaca, G., Madsen, L.M. and Maurya, P.K. (2018), Re-parameterisations of the Cole–Cole model for improved spectral inversion of induced polarization data. Near Surface Geophysics, 16: 385-399.

Fiandaca, G., Zhang, B., Chen, J., Signora, A., Dauti, F., Galli, S., Sullivan, N.A.L., Viezzoli, A. (2023). Closing the gap between galvanic and inductive methods: EEMverter, a new 1D/2D/3D inversion tool for Electric and Electromagnetic data with focus on Induced Polarization *AEM2023 - 8th International Airborne Electromagnetics Workshop, 3-7 September 2023, Fitzroy Island, QLD, Australia*.

Flis, M.F., Newman, G.A., Hohmann, G.W., 1989, Induced-polarization effects in time-domain electromagnetic measurements, Geophysics, 54, 514-523.

James Macnae (2016) Airborne IP detects only fine-grained minerals when compared to conventional IP, ASEG Extended Abstracts, 2016:1, 1-4, DOI: 10.1071/ASEG2016ab141

Kratzer, T. and Macnae, J., 2012, Induced polarization in airborne EM, Geophysics, 77(5), E317–E327.

Smith, R.S., and J. Klein, 1996, A special circumstance of airborne induced polarization measurements, Geophysics, 61, 66–73.

Viezzoli, A., Fiandaca, G., Segio, S., Auken., E., 2013, Constrained inversion of IP parameters from Airbome EM data, ASEG-PESA Expanded abstracts, Melbourne, Australia.

Viezzoli, A., Kaminski, V., Fiandaca, G., 2017. Modeling induced polarization effects in helicopter TEM data: Synthetic case studies. (82-2) E31-E50 Geophysics.

Viezzoli, A., Dauti, F., Devkurran, N., Pitts, B., 2021. AIP effects in Airborne EM Fixed Wing Systems: a Spectrem theoretical study. AEGC Conference, Brisbane

Viezzoli, A., Fiandaca, G., 2021. Closing the gap between airborne and ground IP. AEGC Conference, Brisbane.

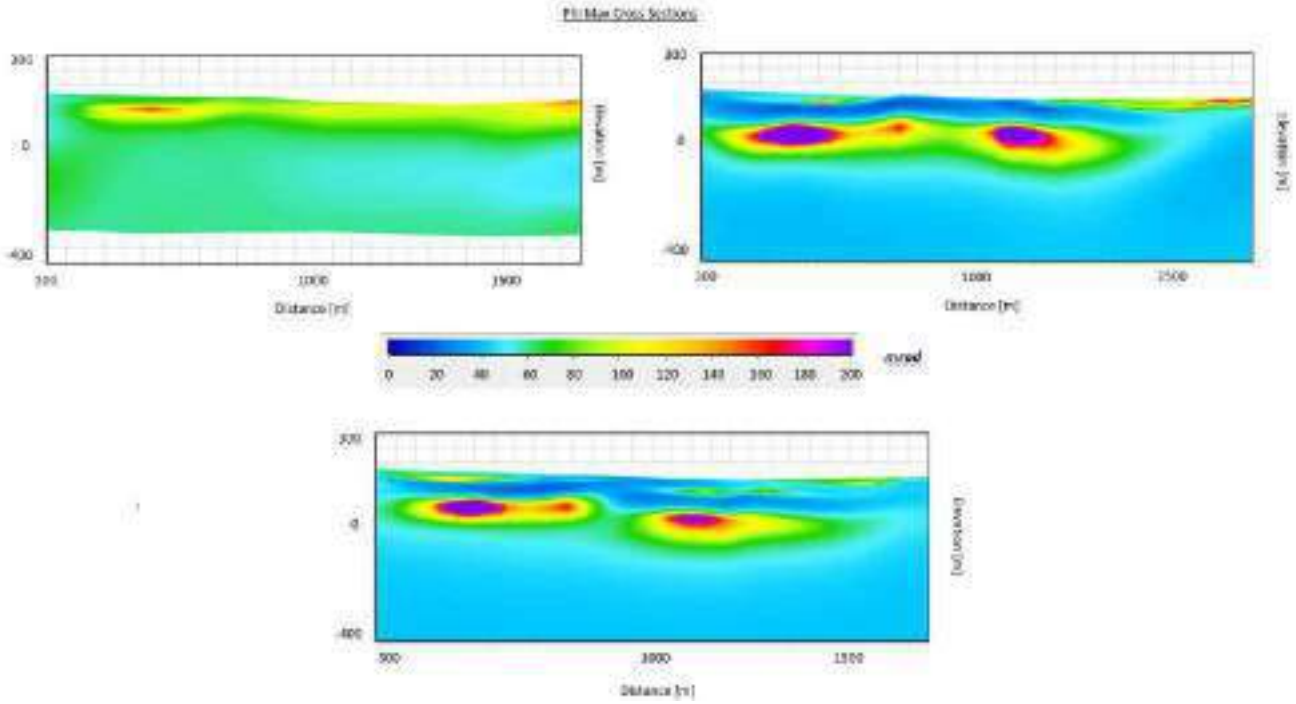

Figure 2. Top left: DCIP chargeability only. Top right: AEM chargeability model for the selected line only. Bottom: Joint inversion chargeability model of DCIP and AEM for the selected line.

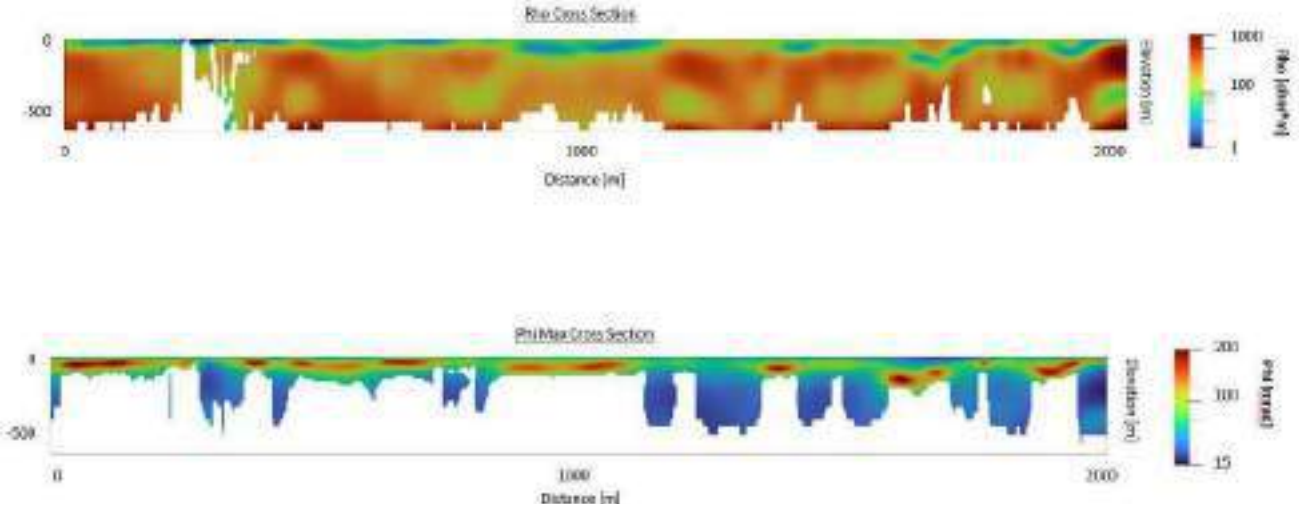

Figure 4. Top: jointly modelled resistivity cross section of two overlapping VTEM and GEOTEM lines. Bottom: jointly modelled chargeability cross section of same selected lines. Both the lines are cropped with the DOI.

Estimating noise in AEM data

Aaron Davis
CSIRO
26 Dick Perry Ave, WA, AUSTRALIA, 6151
Aaron.davis@csiro.au

SUMMARY

In this paper, I discuss a method to obtain reliable noise estimates for airborne electromagnetic (AEM) surveys based on the reversible-jump Markov chain Monte Carlo method. In addition to estimating electrical conductivity and thickness using 1D layered-earth models, the method provides estimates of the additive error required to make all measurements of a repeat line agree. The noise estimates can also be obtained from a single line where repeat line information is unavailable. The resulting additive noise estimates then can be used in a general deterministic inversion. Analysis of inversions shows that model regularisation has little effect at depths where the data is informative. This improves the reliability of the inverted models, since it is the noise-adjusted data which is informing the model.

Key words: airborne electromagnetics, noise, RJMCMC.

INTRODUCTION

The airborne electromagnetic (AEM) method was originally developed for use in mineral exploration whereby an explorer searched the survey data for signals that indicated prospective mineralisation targets. More recently, AEM is increasingly applied to near surface investigations for groundwater exploration, hazard identification and geological mapping. Products from AEM surveys for the newer applications usually include conductivity-depth inversions generated from the collected survey data. Inversion of AEM data is a complicated task due to incomplete information, the difficulty of the inverse problem to be addressed, different systems offered for service, and estimation of the utility of the data for the purpose for which the survey was flown. With increased focus on the near surface for resources such as groundwater, the inversion task needs to address resolution of conductive features in the ground.

Inversion of AEM data for electrical conductivity models involves many factors that need to be addressed. Some factors must be addressed prior to the survey being flown and are governed by such things as system availability, cost of acquisition, and the goal of the study. Other factors are part of the inversion problem itself. These include: the description of the AEM system to be modelled, discretisation of the model used to estimate conductivity, the choice of inversion algorithm, and the amount of regularisation needed to ensure reasonable convergence. Perhaps one of the most important factors that needs to be mentioned, and one that is closely tied to model regularisation, is estimates of noise in the AEM survey data. Noise is any unwanted signal that interferes with the electromagnetic signal transmitted and received by the AEM sensor. It can be generated by various sources such as man-made structures, power lines, lightning, and atmospheric disturbances, but can also be caused by the variation in the earth's natural electromagnetic fields and the geology of the survey area. Different types of noise can be present in AEM data, but they are generally classified as random and systematic noise. Systematic noise, caused by a specific source that produces a consistent pattern of interference in the AEM data, can often be corrected by identifying the source and applying appropriate correction methods. Random noise is caused by the statistical variation of the electromagnetic signal received by the AEM sensor. This noise is difficult to remove as it is not correlated with any causes.

Accurate estimation of noise levels in AEM survey data is necessary since they directly influence the accuracy and reliability of the data. This can have a profound impact on our interpretation of the subsurface geology. Despite the importance of obtaining accurate estimates of data noise, there is little in the literature that describes how we obtain them. The purpose of this paper is to address this apparent shortcoming.

DETERMINING NOISE IN AEM SURVEY DATA

It can be difficult to determine the noise characteristics of AEM survey data since the effective use of many of the systems available depends upon them being airborne to operate effectively. That is, there is little opportunity to operate them at full capacity while on the ground. To address this, many contractors now offer measurements of high-altitude data. With the transmitter operating at full capacity, the AEM system is taken to extreme altitude in the assumption that the signals measured by the receiver coils will be uninterrupted by earth responses. These measurements offer an understanding of the noise floor of the receiver assembly: the measurements of the receivers in the absence of any signal other than the system itself. This is a good first step to understanding the bias of the system. An example of high altitude noise recordings is shown with the solid lines in Figure 1.

Green and Lane (2003) suggest a different strategy for estimating noise in survey data through use of repeat lines. The assumption here is that the system should always measure the same responses over the same survey transect. They recommend characterising noise as either additive or multiplicative in nature, meaning that noise levels for a given delay time are composed of some base level of noise plus some factor multiplied by the signal itself at that delay time. This can be written as

$$\sigma_i = \sqrt{\sigma_{iadd}^2 + (\sigma_{im} \cdot d_i)^2},$$

where σ_i is the noise at delay time i, d_i is the measured data for that delay time, and σ_{iadd} and σ_{im} are the additive noise term and the multiplicative factor, respectively. It should be

noticed that the noise term σ_i enters the data misfit equations

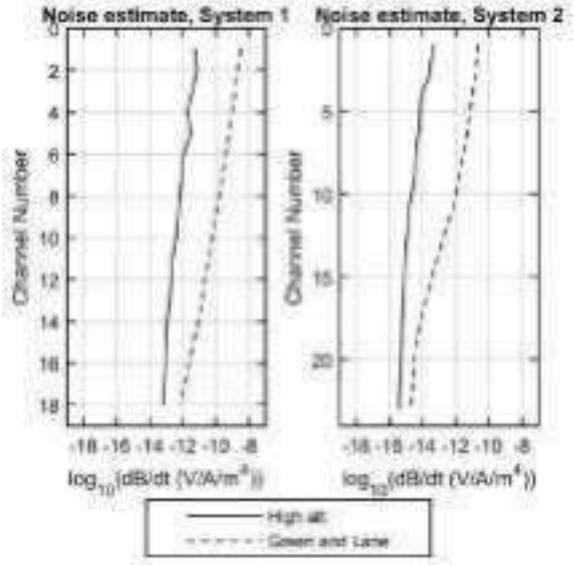

Figure 1. Noise estimates from an AEM system. Solid black lines show the high-altitude measurements, while the dashed lines show the estimates from a Green and Lane (2003) analysis of repeat lines.

as an additive term when used in this manner. An example of an additive noise estimate following this method is show with dashed lines in Figure 1.

One of the drawbacks of the method of Green and Lane (2003) is that repeat lines are impossible to replicate exactly due to the platforms being airborne. Differences in altitude can have a profound effect on the measured response. Another drawback is that many older surveys do not have repeat lines flown (or are not available as part of the delivered data); so, a compromise must be sought. In my approach, I assume that while repeat lines may not have the same measured responses due to variations in acquisition, they should have the same earth *and noise* model provided the repeat lines are flown reasonably close together. At each station of the repeat lines, differences between the recorded data and the forward response for each station can therefore be classified as 'noise'. Noise in this sense incorporates variations in measurement at each station, but also encompasses the choice of model used to determine the earth response.

Reversible-jump Markov chain Monte Carlo

To achieve estimates of electrical conductivity distribution and noise for the repeat lines, I employ the Reversible-jump Markov chain Monte Carlo (RJMCMC) method described by Green, (1995) with a few modifications similar to those employed by Minsley et al., (2021), but with some modifications.

We begin by ensuring that sampling of the repeat line data is consistent across a regular spacing along the survey line. The simplest way of doing this is by taking stations from each repeat line that are close enough that we can assume they are measuring the same volume of the earth (eg, Reid et al., 2006) or by resampling the data to a regular spacing. For every station, we create a 1D layered-earth model of variable electrical conductivity layers (and thickness) and a common noise estimate for every delay time of the system. Using $\boldsymbol{m}_s$ to describe the model at station s, the model is composed of k layers of resistivity $\boldsymbol{\rho}$ with thickness $\boldsymbol{t}$ to describe the earth, and n values of $\boldsymbol{\sigma}$ to describe the additive error applied to the n delay times for the j measurements at location s. Notice that the variables in bold are vectors.

At every iteration in the chain, a new model $\boldsymbol{m}'_s$ is proposed from the previous model $\boldsymbol{m}_s$. The new model is accepted or rejected based on the Metropolis, Hastings, Green (MHG) algorithm according to the following acceptance criterion α

$$\alpha(\mathbf{m}'_s|\mathbf{m}_s) = \min\left[1, \frac{p(\boldsymbol{m}'_s)}{p(\boldsymbol{m}_s)}\frac{p(\mathbf{d}|\boldsymbol{m}'_s)}{p(\mathbf{d}|\boldsymbol{m}_s)}\frac{q(\boldsymbol{m}_s|\boldsymbol{m}'_s)}{q(\boldsymbol{m}'_s|\boldsymbol{m}_s),}|\mathbf{J}|\right],$$

where $p(\boldsymbol{m}'_s)/p(\boldsymbol{m}_s)$ is the prior ratio of the models, $p(\mathbf{d}|\boldsymbol{m}'_s)/p(\mathbf{d}|\boldsymbol{m}_s)$ is the likelihood ratio of the data given the models, $q(\boldsymbol{m}_s|\boldsymbol{m}'_s)\backslash q(\boldsymbol{m}'_s|\boldsymbol{m}_s)$ is the proposal ratio, and $\boldsymbol{J}$ is the Jacobian governing changes between dimensions. Of special interest in this paper is the data likelihood function $p(\mathbf{d}|\boldsymbol{m}_s)$ which will change at every iteration due to choices of perturbations in $k, \boldsymbol{\rho}, \boldsymbol{t},$ or $\boldsymbol{\sigma}$. We write the likelihood function as

$$p(\mathbf{d}|\boldsymbol{m}_s) = \sum_{i=1}^{j}\frac{1}{\sqrt{2\pi|\boldsymbol{C}_d(\boldsymbol{\sigma})|}}\exp\left(-\frac{1}{2}\left((\boldsymbol{f}(\boldsymbol{\rho},\boldsymbol{t},k) - \boldsymbol{d}_{si})^T\boldsymbol{C}_d(\boldsymbol{\sigma})(\boldsymbol{f}(\boldsymbol{\rho},\boldsymbol{t},k) - \boldsymbol{d}_{si})\right)\right)$$

where $\boldsymbol{f}(\boldsymbol{\rho},\boldsymbol{t},k)$ is the predicted data given the model parameters, $\boldsymbol{d}_{si}$ is the measured data at station s for measurement i ,and $\boldsymbol{C}_d(\boldsymbol{\sigma})$ the data covariance matrix that models the error in the system responsible for the measurements. In this paper, $\boldsymbol{C}_d(\boldsymbol{\sigma})$ is assumed to be diagonal.

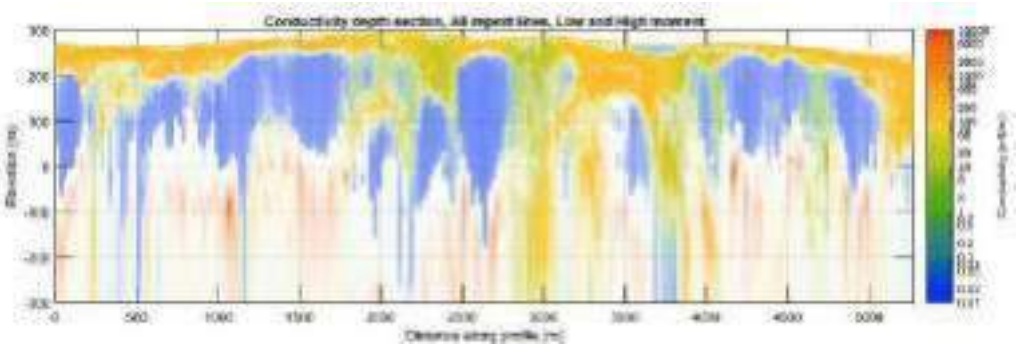

Figure 2. An example of the posterior mean conductivity section resulting from the RJMCMC process. Blanked areas are due to a wide spread of accepted models relative to the prior conductivity.

Model proposals are based on the usual choices for MHG samplers. At every iteration, we choose to: create a conductivity interface, destroy a conductivity interface, change the structure of the existing model (by creating and destroying random interfaces, or vice versa), or changing one of the n noise parameters in $\boldsymbol{\sigma}$. For each station, several chains (8) are run for many iterations (3×10^5). Several thousand models are excluded from the beginning of each of the chains, and the results are accumulated.

RESULTS

Figure 2 shows a posterior mean electrical conductivity distribution transect for the example discussed earlier. Areas that are made transparent reveal that the spread in conductivity of the accepted models is similar to the prior probability of the conductivity proposals (and, therefore, less informative). The section looks reasonable, and there is clear structure to depths of approximately 300 mAHD. Figure 3 shows the mean distributions of the marginalised noise estimates for every model in the reduced RJMCMC chains, and for every station. The distributions are shown in shaded blue, while the mean additive noise value for each delay time is marked by the solid gold line. The mean values from the gold line are chosen to represent the average additive noise values for the entire survey. Also shown are the high-altitude (black), the Green and Lane (2003) noise estimates (red), and an RJMCMC noise estimate conducted on only one line. Clearly, the RJMCMC noise estimates are consistently higher than the high-altitude noise estimates, but mostly lower than the Green and Lane (2003) estimates.

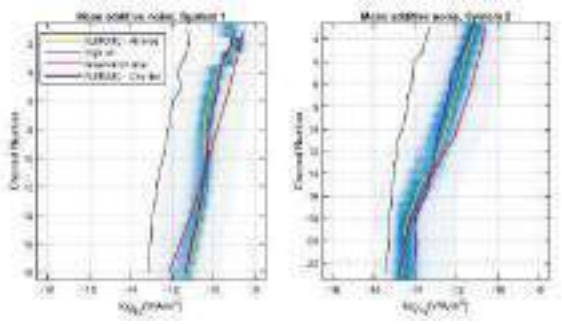

Figure 3. Estimates of additive noise for each delay time of both systems. The blue colour variations show the distributions of the noise estimates. The solid gold line shows the peak of the distributions and is taken as the average measurement noise for the entire survey. The solid black line is from high-altitude tests, the red line is the Green and Lane (2003) estimate, and the purple line is from an analysis conducted with only one repeat line.

What if you don't have repeat lines?

The purple lines in Figure 3 show the result of an RJMCMC noise analysis conducted with only one of the repeat lines. Instead of using all 4 lines to estimate noise, the chains are run using only one measurement per station. Noise is estimated from each model in the chain. We can see that the use of only one line exhibits similar noise levels, indicating this method can be used if there are no repeat lines available.

Effect on regularisation in inversion

Having determined an average noise estimate for the entire survey based on several repeat lines, it is useful to see the effect the noise estimates have on deterministic inversion. Figure 4 shows smooth 1D layered earth inversion models for a wide range of model regularisation values. In this case, an isotropic exponential regularisation with a 25 m correlation length was chosen for the model regularisation; the regularisation matrix was the same and only the weighting was changed. The prior resistivity was chosen to be 10^4 Ωm. A depth of investigation line (DOI) (Christiansen and Auken, 2012) for each inversion is shown in white. The figure shows little variation in inverted conductivity models above the DOI line. This indicates that the model regularisation has little effect in determining model structure where the models are informed by the data, which is precisely what is desired in the inversion.

CONCLUSIONS

In this paper, I have adapted the results of previous authors by using a reversible-jump Markov chain Monte Carlo method that, in addition to yielding conductivity-depth information, provides us with noise estimates for airborne electromagnetic surveys. The noise estimates are shown to be similar to the repeat line method of Green and Lane (2003) but are significantly greater than the high-altitude measurements provided. The additive RJMCMC noise estimates can be applied to the entire survey. The method can be applied when there are no repeat lines available. Analysis of the RJMCMC noise estimates show that model regularisation has little effect at depths where the signal is informative in generating electrical conductivity models.

ACKNOWLEDGMENTS

I would like to acknowledge the CSIRO Deep Earth Imaging Future Science Platform and CSIRO Mineral Resources for support in producing this work.

REFERENCES

Christiansen, A.V. and Auken, E., 2012, A global measure for depth of investigation: *Geophysics*, 77(4), WB171–WB177.

Green, A. and Lane, R., 2003, Estimating Noise Levels in AEM Data: *ASEG Extended Abstracts*, 2003(2), 1.

Green, P.J., 1995, Reversible jump Markov chain Monte Carlo computation and Bayesian model determination: *Biometrika*, 82(4), 711–732.

Minsley, B.J., Foks, N.L. and Bedrosian, P.A., 2021, Quantifying model structural uncertainty using airborne electromagnetic data: *Geophysical Journal International*, 224(1), 590–607.

Reid, J.E., Pfaffling, A. and Vrbancich, J., 2006, Airborne electromagnetic footprints in 1D earths: *GEOPHYSICS*, 71(2), G63–G72.

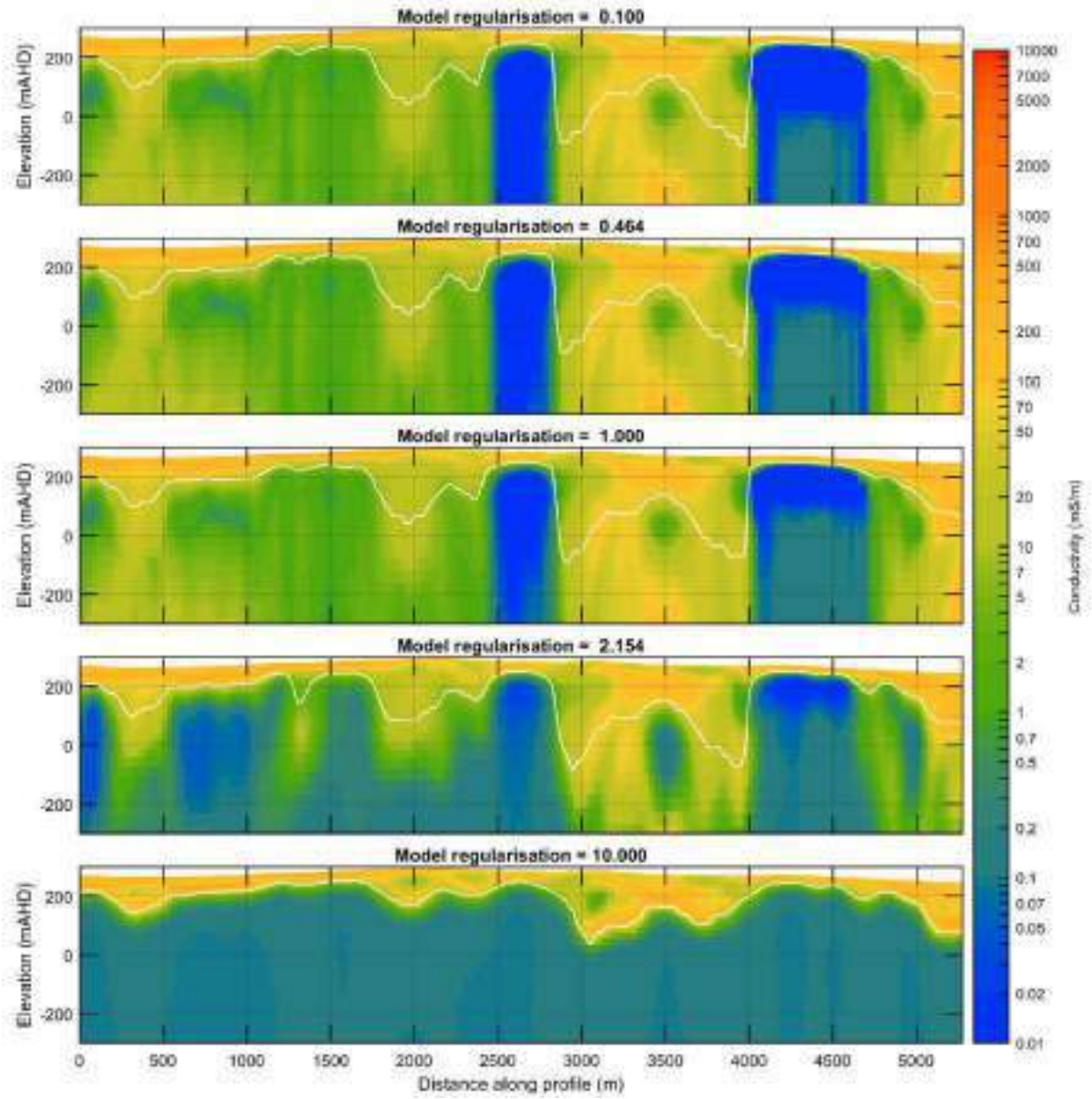

Figure 4. Inversions showing the effect of model regularisation for a wide range of regularisation weighting values. All inversion runs were initialised with the same starting model. The model regularisation structure for each is the same. A depth of investigation (DOI) line is shown in white. There is very little variation in models above the DOI.

California's Statewide AEM Surveys: Project Implementation and Next Steps

Katherine Dlubac
California Department of Water Resources (DWR)
Sacramento, CA, USA
Katherine.Dlubac@water.ca.gov

Steven Springhorn
California DWR
Sacramento, CA, USA
Steven.Springhorn@water.ca.gov

Benjamin Brezing
California DWR
Sacramento, CA, USA
Benjamin.Brezing@water.ca.gov

Ian Gottschalk
Ramboll
Tampa, FL, USA
igottschalk@ramboll.com

Paul Thorn
Ramboll
Copenhagen, DK
path@ramboll.dk

Timothy Parker
Ramboll
Sacrament, CA, USA
tkparker@ramboll.com

Chris Peterson
GEI
Sacramento, CA, USA
cpetersen@geiconsultants.com

SUMMARY

Passage of the Sustainable Groundwater Management ACT (SGMA) in California has resulted in the need for improving the understanding of groundwater aquifers to support groundwater managers in developing and implementing groundwater management plans and actions. The California Department of Water Resources (DWR) has supported this effort by implementing the Statewide AEM Survey Project, where data are collected in a reconnaissance grid across California's priority basins. Raw, processed, inverted, and interpreted AEM data as well as digitized lithology and e-logs are made publicly available and novel tools have been developed to support data accessibility.

With the Statewide AEM Surveys nearing completion, DWR is undertaking an effort to utilize the Statewide AEM Survey dataset along with other existing data (surface geophysics, lithology logs, e-logs, geologic cross sections) to provide an improved understanding of basin characteristics. To support this task, new tools are being developed that will analyse all data available to produce refined, texture and hydrogeologic models. Results will be archived in DWR's California Groundwater publication and Basin Reports and models will be available to visualize through new and innovative 3D, GIS-based tools.

To support this effort, DWR will also be conducting Pilot Studies that will include the collection of additional data with the goal of filling data gaps and addressing specific SGMA implementation questions. The first Pilot Study will be conducted on the eastern side of the San Joaquin Valley in California's Central Valley and will include the collection of infill AEM data, as well as other ground-based geophysical surveys.

Key words: AEM, California, Sustainable, Groundwater, Statewide,

INTRODUCTION

The historic passage of California's Sustainable Groundwater Management Act (SGMA) in 2014 set forth a statewide framework to help protect groundwater resources over the long-term (California Assembly Bill 1739, Senate Bill 1319, and Senate Bill 1168, 2014.). SGMA requires local agencies to form groundwater sustainability agencies (GSAs) for groundwater basin's defined as high- and medium-priority. GSAs develop and implement groundwater sustainability plans (GSPs) to avoid undesirable results and mitigate overdraft within 20 years.

DWR serves two roles to support local SGMA implementation: 1) regulatory oversight through the evaluation and assessment of GSPs and 2) providing ongoing assistance to locals through the development of best management practice guidance, financial assistance, and technical assistance.

DWR has a long history of characterizing California's groundwater basins and providing technical assistance through DWR's Basin Characterization efforts under California's Groundwater, Bulletin 118 (California Code of Regulations, California Department of Water Resources 2020b). California's Groundwater archives and documents groundwater basin characteristics, available data within the basin, and groundwater management activities through the 5-Year Update, Basin Reports, and CalGW Live.

As a part of DWR's Basin Characterization effort, DWR supports locals in improving their basin's hydrogeologic conceptual model through the collection and compilation of relevant data. Data and information that DWR collects or catalogues includes lithology and geophysical logs, location of dry wells, groundwater elevation levels, interferometric synthetic aperture radar data, extensometers, crop mapping, and drilling new wells.

In 2021, DWR's Basin Characterization data collection effort expanded to include the Statewide AEM Survey Project. The goal of the project is to improve the understanding of large-scale aquifer structures across groundwater basins and support refinement of texture models, hydrogeologic conceptual models, and groundwater flow models. As a part of the project, AEM data are collected in all high- and medium-priority groundwater basins, where data collection is feasible and all data and reports are made publicly available (California Assembly Bill 1755, 2016). To support data accessibility, DWR has developed novel tools to allow the data to be viewed online by the general public.

As the Statewide AEM Survey Project nears its completion, DWR is starting the next phase of the Basin Characterization effort where all new and existing data will be compiled and analysed to provide an improved understanding of basin characteristics.

METHOD AND RESULTS

In 2018, California Proposition 68 was passed, which provided DWR with $12 million to collect AEM data in California to support the implementation of SGMA (California Department of Water Resources, 2020). From 2018 through 2020, a set of AEM Pilot Studies was undertaken by Stanford University, the Kingdom of Denmark, local groundwater agencies, and private consulting firms to determine the optimal workflow of AEM data collection in California. Knowledge gained from the AEM Pilot Studies was used to support the development of DWR's Statewide AEM Surveys.

As a part of the Statewide Survey Project, DWR and their consultants (Ramboll, SkyTEM, Sinton Helicopters, GEI, Eclogite Consulting, and Aarhus University) are collecting AEM data in a coarse, reconnaissance grid with a line spacing of approximately 3 by 13 km. The grid was defined to allow the maximum amount of data to be collected within the defined groundwater basins while capturing the geologic heterogeneity unique to California. The survey grid was oriented to capture local geologic features and to lines were modified to cover areas of interest defined by local, state, and federal agencies. Survey lines were further modified to avoid safety and electromagnetic noise sources, like buildings and structures containing people or confined livestock, heavily trafficked highways, powerlines, vineyards, etc.

Prior to the start of the surveys, DWR undertakes a robust outreach effort to ensure the public are aware of the project and that a low-flying helicopter will be in their area. This includes meetings with local GSAs, sending notification letters to parcel owners within the vicinity of the flight path, social media announcements, and media advisories. DWR also keeps the public aware of the survey schedule through an online Survey Schedule StoryMap.

After data collection, the data are processed and inverted by the consultant. Data at all stages (raw, processed, and inverted) are provided to DWR and published on the California Natural Resources Agency Open Data Portal. Inverted AEM data can be viewed on DWR's AEM Data Viewer, an online, GIS-based tool that displays electrical resistivity values as Point Clouds, which points located within the centre of the AEM data interval. The tool allows users to zoom and view the data from various angles without the data being downloaded or the use of specialised software (Figure 1). DWR also makes the formatted Point Cloud files publicly available so that technical users can download and view the data along with other relevant datasets in a GIS-based platform.

AEM data are interpreted for coarse fraction (texture) and for an initial hydrostratigraphic cluster model through the integration of other supporting datasets, including lithology logs, e-logs, water quality, and water levels. Two lithology logs and e-logs per Public Land Survey Square Mile along a survey flight line are quality controlled (for location accuracy and lithology description) and digitized. Water quality and water level data were utilized in the interpretation only when the density and quality of data were appropriate. All digitized supporting data are made publicly available and locations and metadata can be viewed on DWR's Supporting Data Viewer.

With the Statewide AEM Surveys nearing completion, DWR is undertaking the next phase of the Basin Characterisation effort where all AEM coarse fraction data will be incorporated with other existing data (surface geophysics, lithology logs, e-logs, geologic cross sections) and analysed to provide an improved understanding of basin characteristics. To support this task, new tools are being developed that will analyse all data available within a basin to develop refined, 3D hydrogeologic and texture models. The results of these analyses will be available to visualise through new and innovative 3D, GIS-based tools, which will be updated on a regular basis as new data and tools become available.

To support Basin Characterization and the implementation of SGMA, DWR will also be conducting Pilot Studies to address SGMA implementation initiatives and fill data gaps. The Pilot Studies will include the collection of additional data based on review of the reconnaissance AEM data and local SGMA implementation initiatives, like groundwater recharge, surface water groundwater interaction, subsidence, vulnerable domestic wells, disadvantaged communities, seawater intrusion, base of fresh water, etc. Additional data collection methods may include infill AEM, t-TEM, floaTEM, NMR logging, e-logging, installing new wells or reactivating existing wells, CPT, etc.

The first Pilot Study will focus on providing information to support floodplain rehabilitation, groundwater recharge, and domestic well assistance activities. The study area is located within the Kings and Madera subbasins and concentrated on the eastern side of the San Joaquin Valley, between the Upper San Joaquin and Fresno Rivers. The Pilot Study will include AEM infill data collection followed by ground-based surveys. The results from the Pilot Study are expected to be available by Winter 2023/2024 and available to support local and state groundwater management decisions in the event of another wet water year.

Figure 1. DWR's AEM Data Viewer displaying AEM data as a Point Cloud in an online, GIS-based platform.

CONCLUSIONS

DWR's Statewide AEM Survey Project has provided high-quality AEM data across the medium- and high-priority

groundwater basins and has provided local GSAs with a unique dataset that improves the development and implementation of their GSPs and project and management actions. DWR's commitment to open access to data has resulted in the development of novel tools which has made viewing data accessible to the general public and increased the public's understanding of geophysics. The success of this project has allowed DWR to continue with the next steps of Basin Characterization and the collection of additional geophysical data and the development of new tools to improve the understanding of groundwater basins.

ACKNOWLEDGMENTS

The authors would like to thank the Department of Water Resources, Sustainable Groundwater Management Office's Deputy Director Paul, Gosselin, and the Policy and Technical Advisor to the Deputy Director, Tim Godwin, for their continued support on the development and implementation of the Statewide AEM Survey Project. The authors would also like to thank Ramboll, GEI, SkyTEM, Sinton Helicopters, Eclogite Consulting, AECOM, Woodard & Curran, SS Papadopulos and Associates, Max Halkjaer, Ahmad-Ali Behroozmand, and Peter Thomsen for their support in the collection, analysis, or interpretation of AEM data or development of data analysis tools. DWR would like to thank Rosemary Knight, Paul Gosselin, and Graham Fogg for their AEM White Paper which supported obtaining $12 million in Proposition 68 funds to implement the Statewide AEM Survey Project.

REFERENCES

California Assembly Bill 1739, Senate Bill 1319, and Senate Bill 1168, 2014. The Sustainable Groundwater Management Act (SGMA).

California Assembly Bill 1755, 2016. Open and Transparent Water Data Act.

California Department of Water Resources, 2020a. Fact Sheet to Conduct Airborne Electromagnetic Surveys.

California Department of Water Resource, 2020b. California's Groundwater, Formally Bulletin 118.

California Code of Regulations, Title 23, California Water Code, § 12924(a).

Closing the gap between galvanic and inductive methods: EEMverter, a new 1D/2D/3D inversion tool for Electric and Electromagnetic data with focus on Induced Polarization

Gianluca Fiandaca*
The EEM Team for Hydro & eXploration, Dep. of Earth Sciences A. Desio, Università degli Studi di Milano, Via Botticelli 23, Milano (Italy)
gianluca.fiandaca@unimi.it

Bo Zhang
Institute of Earth exploration, Science and Technology, Jilin University, Changchun (China)
em_zhangbo@163.com

Jian Chen
The EEM Team for Hydro & eXploration Dep. of Earth Sciences A. Desio, Università degli Studi di Milano, Via Botticelli 23, Milano (Italy)
jian.chen@unimi.it

Alessandro Signora
The EEM Team for Hydro & eXploration, Dep. of Earth Sciences A. Desio, Università degli Studi di Milano, Via Botticelli 23, Milano (Italy)
alessandro.signora@unimi.it

Francesco Dauti
The EEM Team for Hydro & eXploration, Dep. of Earth Sciences A. Desio, Università degli Studi di Milano, Via Botticelli 23, Milano (Italy)
francesco.dauti@unimi.it

Stefano Galli
The EEM Team for Hydro & eXploration Dep. of Earth Sciences A. Desio, Università degli Studi di Milano, Via Botticelli 23, Milano (Italy)
stefano.galli@unimi.it

Nicole Anna Lidia Sullivan
The EEM Team for Hydro & eXploration, Dep. of Earth Sciences A. Desio, Università degli Studi di Milano, Via Botticelli 23, Milano (Italy)
nicole.sullivan@unimi.it

Arcangela Bollino
The EEM Team for Hydro & eXploration, Dep. of Earth Sciences A. Desio, Università degli Studi di Milano, Via Botticelli 23, Milano (Italy)
arcangela.bollino@unimi.it

Andrea Viezzoli
EMergo srl, Via XX Settembre 12, Cascina, (Pisa, Italy)
andrea.viezzoli@em-ergo.it

SUMMARY

The interest on Induced Polarization (IP) in AEM data (AIP) has significantly increased in recent years, both within the research community and in the industry. However, the inversion of AIP data is particularly ill-posed, especially when spectral modelling, such as Cole-Cole modelling, is used. Furthermore, the comparison of AIP and galvanic ground IP inversion models is hindered by the fact that the IP effect is usually modelled differently in the inductive and galvanic computations.

In this study we present a new inversion software, EEMverter, which has been developed to model IP in electric and electromagnetic (EM) data within the same inversion framework. In particular, three specific goals have been identified within EEMverter's development: i) to allow multiple inversion cycles that mix, sequentially or simultaneously, 1D, 2D and 3D forward modelling, for diminishing the inversion burden; ii) to allow the joint inversion of AIP, ground EM-IP and ground galvanic IP data; iii) to allow time-lapse inversions of AIP, EM and galvanic IP data.

EEMverter has been tested on several AEM and AIP surveys, also in conjunction with ground EM and ground galvanic IP data in joint inversion. In this study, the inversion of the VTEM AIP survey over the Valen Cu-Ni deposit is presented, highlighting the improvements in model resolution when compared to standard inversion approaches.

Key words: Induced Polarization, Joint Inversion, 1D, 2D, 3D, galvanic

INTRODUCTION

The induced polarization (IP) phenomenon in airborne electromagnetic AEM data (AIP) presents a challenge to exploration in many parts of the world. It is a well-known phenomenon since Smith and Klein (1996) first demonstrated the presence of IP effects, which have been further discussed by several authors (e.g., Marchant *et al.*, 2014; Macnae, 2016; Viezzoli *et al.*, 2017). IP-affected AEM data are often interpreted in terms of the Cole-Cole model (e.g., Marchant et al., 2014; Viezzoli *et al.*, 2017; Lin *et al.*, 2019), but the inversion problem is particularly ill-posed: for a 1D inversion of a single sounding four parameters have to be retrieved for each model layer. Furthermore, AIP and ground IP modelling are usually carried out in different inversion frameworks, making difficult a direct comparison of the results. In this study we present a novel inversion software, EEMverter, specifically developed to model electric and electromagnetic data taking into account the IP phenomenon. Three distinctive features have been implemented in EEMverter: i) 1D, 2D and 3D forward modelling can be mixed sequentially or simultaneously in the iterative process within multiple inversion cycles, for diminishing the computational burden; ii) the joint inversion of AIP, ground EM-IP and ground galvanic IP data is fully supported with a common IP parameterization; iii) time-lapse inversions of AIP, EM and galvanic IP data is possible with both sequential and simultaneous approaches. In the following, the implementation of EEMverter is described, with examples of synthetic and field inversion results.

METHOD

In EEMverter the inversion parameters are defined on model meshes which do not coincide with the forward meshes used for data modelling: the link between model and forward meshes is obtained interpolating the model mesh parameters into the forward mesh discretization, as done for 1D AEM in Christensen et al. (2017), in 3D galvanic IP in Madsen et al.

(2020) and in 3D EM in Zhang et al. (2021), Engebretsen et al. (2022) and Xiao et al. (2022a). This spatial decoupling allows for defining the model parameters, e.g. the Cole-Cole ones, on several model meshes, for instance one for each inversion parameter. In this way, it is possible to define the spectral parameters, like the time constant and the frequency exponent in the Cole-Cole model, on meshes coarser than the resistivity and chargeability ones, vertically and/or horizontally, with a significant improvement in parameter resolution.

For each dataset of the inversion process, a distinct forward mesh is defined. The interpolation from the model parameters $\boldsymbol{M}$ defined on the model mesh nodes into the values $\boldsymbol{m_i}$ at the subdivisions of the i[th] forward mesh is expressed through a matrix multiplication, in which the matrix $\boldsymbol{F_i}$ holds the weights of the interpolation, which depends only on the distances between model mesh nodes and the subdivisions of the i[th] forward mesh:

$$\boldsymbol{m_i} = f_i(\boldsymbol{M}) = \boldsymbol{F_i} \cdot \boldsymbol{M} \quad (1)$$

In EEMverter 1D, 2D and 3D forward & Jacobian computations have been implemented. In particular, Transient EM data are modelled in 1D following Effersø et al. (1999); in 3D the forward solution is carried out in frequency domain, with the finite element method, both with tetrahedral elements or with the octree approach, similarly to what has been done with the time-stepping time-domain approach in Zhang et al. (2021) and Xiao et al. (2022a). The finite element approach is used also for frequency-domain galvanic computations in 2D (Fiandaca et al., 2013) and 3D (Madsen et al., 2020). The transformation to time-domain is obtained through a fast Hankel transformation (as in Effersø et al., 1999) for both the forward response and the Jacobian. In particular, the time-domain Jacobian in the i[th] forward mesh is computed as:

$$\boldsymbol{J_{m_i,TD}} = \boldsymbol{A} \cdot \boldsymbol{T} \cdot \boldsymbol{J_{m_i,FD}} \quad (2)$$

Where the matrix $\boldsymbol{T}$ holds the Hankel coefficients, the matrix $\boldsymbol{A}$ implements the effects of current waveform, gate integration and filters and the frequency-domain Jacobian $\boldsymbol{J_{m_i,FD}}$ is calculated in 1D through finite difference and in 2D/3D using the adjoint method and the chain rule as in Fiandaca et al. (2013) and Madsen et al. (2020):

$$\boldsymbol{J_{m_i,FD}} = \boldsymbol{J_{\sigma^*,i}} \cdot \frac{\partial \sigma^*}{\partial m_i} \quad (3)$$

where $\boldsymbol{J_{\sigma^*,i}}$ is the Jacobian of the i[th] forward mesh with respect to the complex conductivity $\boldsymbol{\sigma^*}$ and $\frac{\partial \sigma^*}{\partial m_i}$ is the partial derivative of the complex conductivity versus the model parameters. This approach, contrary to the time stepping approach, allows to use any parameterization of the IP phenomenon in the inversion. Finally, the Jacobian of the model space $\boldsymbol{J_M}$ is computed summing the contributions of all forward meshes up (Christensen et al., 2017; Madsen et al., 2020, Zhang et al., 2021), using the domain decomposition with a forward mesh for each sounding in 3D EM computations (Cox et al., 2010; Zhang et al., 2021):

$$\boldsymbol{J_M} = \sum_i \boldsymbol{J_{m_i}} \cdot \boldsymbol{F_i}^T \quad (4)$$

The total Jacobian is used for computing the inversion model in a Levenberg-Marquardt linearized approach as follows:

$$\boldsymbol{M_{n+1,j}} = \boldsymbol{M_{n,j}} + \left[\boldsymbol{J_{M,j}}^T \boldsymbol{C_d}^{-1} \boldsymbol{J_{M,i}} + \boldsymbol{R}^T \boldsymbol{C_{R,j}}^{-1} \boldsymbol{R_j} + \lambda \boldsymbol{I}\right]^{-1} \cdot \left[\boldsymbol{J_{M,j}}^T \boldsymbol{C_d}^{-1} \cdot \left(\boldsymbol{d} - \boldsymbol{f_{n,j}}\right) + \boldsymbol{R}^T \boldsymbol{C_{R,j}}^{-1} \boldsymbol{R_j} \cdot \boldsymbol{M_{n,j}}\right] \quad (5)$$

In equation (5) the subscript j indicates that the inversion process can be split in several inversion cycles: in each cycle j it is possible to change the forward computation for each dataset (e.g. from 1D to 3D), as well as to insert/remove data/constraints from the objective function. Figure (1) shows the 3-cycle inversion scheme for AIP inversion, in which the parameters of the Maximum Phase Angle (MPA) Cole-Cole reparameterization (Fiandaca et al., 2018) are defined in two distinct model meshes: the resistivity $\boldsymbol{\rho}$ and the phase $\boldsymbol{\varphi}$ vary both horizontally and vertically (Figure 1a), but the time constant $\boldsymbol{\tau}$ and the frequency exponent $\boldsymbol{C}$ vary only horizontally (Figure 1b), for increasing the sensitivity of the spectral parameters.

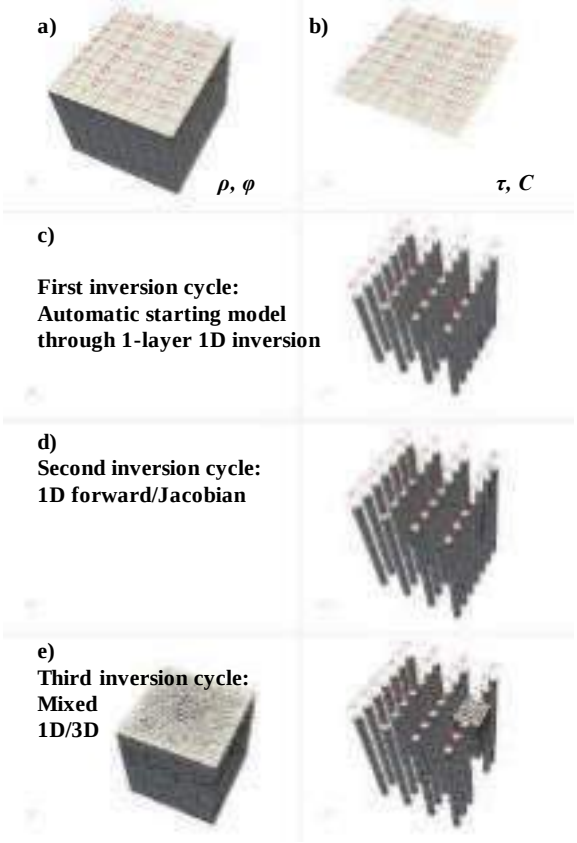

Figure 1. EEMverter multi-cycle inversion scheme for 3D AEM inversion with Induced polarization. a) Model mesh for resistivity ρ and phase φ, with depth variability, with red polygons representing AEM frames. b) Model mesh for relaxation time τ and frequency exponent C, without depth variability. c) First inversion cycle for computation of automatic starting model, with 1D forward meshes (grey bars) composed by only one layer. d) Second inversion cycle with 1D forward/Jacobian computations, with vertical discretization of the 1D forward meshes (grey bars). e) Third inversion cycle with mixed dimensionality of the forward/Jacobian meshes: 1D for the soundings with red frames and 3D for the soundings with blue frames (left: 3D Mesh; right: subset of the 3D mesh and 1D meshes)

The 3-cycle inversion comprises: i) a first cycle which finds the best starting model without vertical variability of the parameters, through the use of a single-layer 1D forward mesh (Figure 1c); ii) a second cycle with 1D forward/Jacobian computations; iii) a third cycle that switches to 3D computations the soundings in area with strong contrasts in electrical properties.

Figure 2 presents the model and forward meshes for a joint inversion, in which 1D AEM and 1D ground EM computations are combined with 2D galvanic computations.

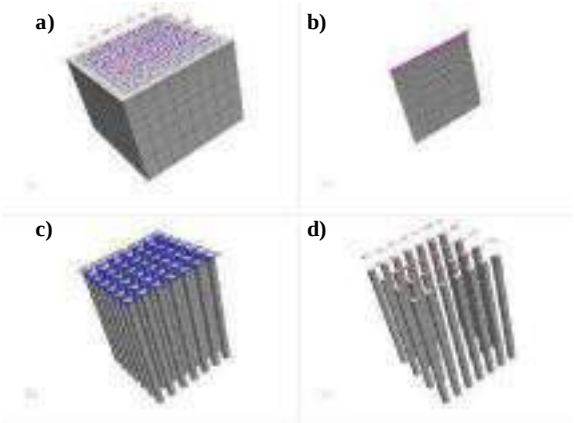

Figure 2. EEMverter multi-mesh inversion scheme for Joint inversion of inductive and galvanic data. a) Model mesh and data positions: red polygons for AEM frames; blue squares for ground TEM frames; magenta line for galvanic 2D profile. b) Galvanic 2D forward mesh. c) Ground TEM frames (blue squares) and corresponding 1D soundings (grey bars). d) AEM frames (red polygons) and corresponding 1D soundings (grey bars).

Figure (3) presents the time-lapse approach of EEMverter, in which all the models of all the time steps can be inverted at once, without the need of relocating the model meshes when the positions of the acquisitions vary among the time steps, as in Xiao et al. (2022b).

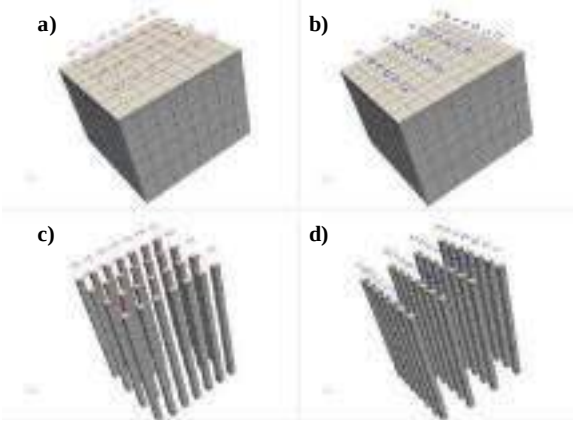

Figure 3. EEMverter multi-mesh inversion scheme for Time-Lapse inversion. a) Model mesh corresponding to the first Time-lapse acquisition (red polygons). Model mesh corresponding to the second Time-lapse acquisition (blue polygons), identical to the first model mesh despite of the different sounding positions. c) Forward meshes (grey bars) of the first acquisition (red frames). d) Forward meshes (grey bars) of the second acquisition (blue frames).

RESULTS

The joint inversion of AEM, ground EM and galvanic IP data through EEMverter is presented in Dauti et al. (2023) in applications related to mineral exploration and in Signora et al. (2023) for the characterization of the HydroGeosITe, the Italian reference and calibration site for hydrogeophysical methods under development in Brescia, Italy.

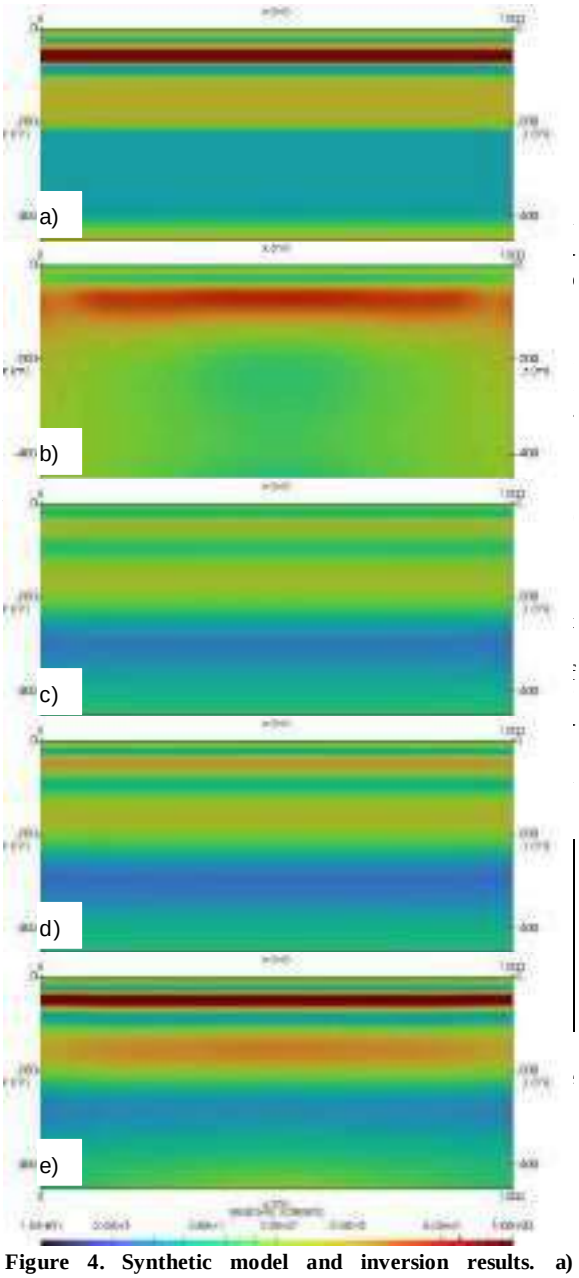

Figure 4. Synthetic model and inversion results. a) resistivity section of a MPA IP simulation of electrical properties; b) inversion model of DCIP data; c) inversion model of AEM+ground EM data; d) inversion model of AEM+ground EM+tTEM data; e) joint inversion of all inductive and galvanic data.

In both cases a unique inversion model in terms of MPA parameterization is able to describe both inductive and full-decay galvanic data, with data misfits very similar to the ones

obtained with independent inversions, in contrast to the findings of Christiansen et al. (2007). Figure 4 presents the resistivity section of a synthetic model that mimics the electrical properties (both conduction and polarization) of sand, clay and consolidated formations, based on the petrophysical relations described in Weller et al. (2015), together with the inversion model of inductive and galvanic data. In particular, four different inversion results are presented: direct current and full-decay induced polarization (DCIP) galvanic data, with 10 m electrode spacing and 2D gradient sequence; AEM + ground EM data, with sounding distance of 40 m; AEM+ground EM + tTEM data (Auken et al., 2019), with tTEM soundings every 10 m; all data together in a joint inversion scheme.

The joint inversion presents much better resolution capability, with the inductive and galvanic data complementing each other in resolving both conductive and resistive layers. The same kind of improvement is found in Signora et al. (2023) with field data. Another example of joint inversion of AEM and galvanic VES data in EEMverter, without IP modelling but with integration with resistivity logs is presented in Galli et al. (2023), where the asymmetric minimum support norm (Fiandaca et al., 2015) is used for an automated rejection of conflicting borehole information. A similar approach is implemented in EEMverter also for automatic processing of AEM data (2021).

The second EEMverter inversion presented in this study is the AIP inversion of four lines of the VTEM survey carried out on the Valen Cu-Ni deposit, in South Australia, consisting of 1108 soundings, with the approach presented in figure (1), but without the final 3D inversion cycle, which will be presented at the conference.

Table 1 presents a comparison of the sensitivities of the four Cole-Cole parameters, in terms of maximum elements of the $\boldsymbol{J_P}^T \boldsymbol{C_d}^{-1} \boldsymbol{J_P}$ matrix, for two cases: 1) no vertical variability for τ and C (i.e. τ and C defined on the mesh of Figure (1b); 2) vertical variability for τ and C (i.e. τ and C defined on the mesh of Figure (1a). Coarsening the spatial discretization of τ and C, allowing no vertical variability, causes an increase in their sensitivity more than ten-fold, with a significant improvement in resolution and decrease in correlations among parameters.

Figure 5 shows the inversion model of the four MPA parameters of the Valen data, while Figure 6 presents the fit of one line, plotted in EEMstudio (Sullivan et al., 2023). Very good fit is reached in the inversion, with the IP modelling decreasing the overall data misfit of more than 20%, when compared to the resistivity-only inversion.

Table 1. Maximum element of the matrix $\boldsymbol{J_P}^T \boldsymbol{C_d}^{-1} \boldsymbol{J_P}$, for the first iteration of the Valen inversion, without vertical variability for τ and C (Figure 1b) and with vertical variability (Figure 1a).

parameter	Max ${J_P}^T {C_d}^{-1} J_P$ value, τ and C **without** vertical variability	Max ${J_P}^T {C_d}^{-1} J_P$ value, τ and C **with** vertical variability
ρ	3.5E+03	3.5E+03
φ_{max}	2.1E+02	2.1E+02
τ	6.5E+01	5.9E+00
C	3.2E+02	1.7E+01

CONCLUSIONS

We presented EEMverter, a novel inversion software for electric and electromagnetic data with focus on induced polarization. Three distinctive features have been implemented in EEMverter: i) 1D, 2D and 3D forward modelling can be mixed sequentially or simultaneously in the iterative process within multiple inversion cycles, for diminishing the computational burden; ii) the joint inversion of AIP, ground EM-IP and ground galvanic IP data is fully supported with a common IP parameterization; iii) time-lapse inversions of AIP, EM and galvanic IP data is possible with both sequential and simultaneous approaches.

We tested EEMverter on several synthetic and field data sets, with AIP inversions alone and in joint inversion between: i) different AEM systems, ii) AEM and ground based EM data and iii) AEM, ground EM and galvanic full-decay DCIP data. In particular, the synthetic example of joint inversion of AEM, ground EM and DCIP data presented in this study shows a significant improvement in spatial resolution, with inductive and galvanic data complementing each other in an excellent retrieval of both conductive and resistive anomalies. The field example of the AIP inversion of the VTEM data acquired over the Valen Cu-Ni deposit shows a significant improvement in data fit in comparison with the resistivity-only inversion. Furthermore, the definition of the spectral Cole-Cole parameters in a separate inversion mesh without vertical variability allows to enhance significantly their resolution. We believe that EEMverter, with its common inversion environment for the IP inversion of inductive and galvanic data will help in closing the gap between electric and electromagnetic data in AEM applications.

ACKNOWLEDGMENTS

This study has been partially carried out within the Horizon Europe project SEMACRET. Thanks to CSIRO and Tim Munday for providing the AEM Valen data.

REFERENCES

Auken E., Foged N., Larsen J.J., Trøllund Lassen K.V., Maurya P.K., Dath S.M., Eiskjær T.T (2019). tTEM — A towed transient electromagnetic system for detailed 3D imaging of the top 70 m of the subsurface. *Geophysics, 84 (1), E13-E22.*

Christensen, N. K., Ferre, T. P. A., Fiandaca, G., & Christensen, S. (2017). Voxel inversion of airborne electromagnetic data for improved groundwater model construction and prediction accuracy. *Hydrology and Earth System Sciences*, *21*(2), 1321-1337.

Christiansen, A. V., Auken, E., Foged, N., & Sørensen, K. I. (2007). Mutually and laterally constrained inversion of CVES and TEM data: a case study. *Near Surface Geophysics*, *5*(2), 115-123.

Cox, L. H., Wilson, G. A., & Zhdanov, M. S. (2010). 3D inversion of airborne electromagnetic data using a moving footprint. *Exploration Geophysics*, *41*(4), 250-259.

Dauti, F., Viezzoli, A., Fiandaca, G. (2023). Joint Inversions of AEM modelling AIP effects: Helicopter-borne, Ground IP and Fixed-Wing systems. *AEM2023 - 8th International Airborne*

Electromagnetics Workshop, 3-7 September 2023, Fitzroy Island, QLD, Australia.

Effersø, F., Auken, E., & Sørensen, K. I. (1999). Inversion of band-limited TEM responses. *Geophysical Prospecting*, 47(4), 551-564.

Engebretsen, K. W., Zhang, B., Fiandaca, G., Madsen, L. M., Auken, E., & Christiansen, A. V. (2022). Accelerated 2.5-D inversion of airborne transient electromagnetic data using reduced 3-D meshing. *Geophysical Journal International*, *230*(1), 643-653.

Fiandaca, G., Auken, E., Christiansen, A. V., & Gazoty, A. (2012). Time-domain-induced polarization: Full-decay forward modeling and 1D laterally constrained inversion of Cole-Cole parameters. *Geophysics*, *77*(3), E213-E225.

Fiandaca, G., Ramm, J., Binley, A., Gazoty, A., Christiansen, A. V., & Auken, E. (2013). Resolving spectral information from time domain induced polarization data through 2-D inversion. *Geophysical Journal International*, *192*(2), 631-646.

Fiandaca, G., Doetsch, J., Vignoli, G., & Auken, E. (2015). Generalized focusing of time-lapse changes with applications to direct current and time-domain induced polarization inversions. *Geophysical Journal International*, *203*(2), 1101-1112.

Fiandaca, G., Madsen, L. M., & Maurya, P. K. (2018). Re-parameterisations of the Cole–Cole model for improved spectral inversion of induced polarization data. *Near Surface Geophysics*, *16*(4), 385-399.

Fiandaca, G., Viezzoli, A. (2021). Inversion of Airborne IP data with a multi-mesh approach for parameter definition. *Australasian Exploration Geoscience Conference AEGC2021, 13-17 September 2021, Virtual Conference.*

Fiandaca, G. (2021). Inversion-based automatic processing of AEM data. *Australasian Exploration Geoscience Conference AEGC2021, 13-17 September 2021, Virtual Conference.*

Galli, S., Shaars, F., Smits, F., Borst, L., Rapiti, A., Fiandaca G. (2023). Automated integration of AEM data, VES and borehole logs. *AEM2023 - 8th International Airborne Electromagnetics Workshop, 3-7 September 2023, Fitzroy Island, QLD, Australia*.

Lin, C., Fiandaca, G., Auken, E., Couto, M. A., & Christiansen, A. V. (2019). A discussion of 2D induced polarization effects in airborne electromagnetic and inversion with a robust 1D laterally constrained inversion scheme. *Geophysics*, 84(2), E75-E88.

Haber, E., Oldenburg, D. W., & Shekhtman, R. (2007). Inversion of time domain three-dimensional electromagnetic data. *Geophysical Journal International*, *171*(2), 550-564.

Kang, S., Oldenburg, D. W., & Heagy, L. J. (2020). Detecting induced polarisation effects in time-domain data: a modelling study using stretched exponentials. *Exploration Geophysics*, *51*(1), 122-133.

Lin, C., Fiandaca, G., Auken, E., Couto, M. A., & Christiansen, A. V. (2019). A discussion of 2D induced polarization effects in airborne electromagnetic and inversion with a robust 1D laterally constrained inversion scheme. Geophysics, 84(2), E75-E88.

Marchant, D., E. Haber, and D. Oldenburg, 2014, Three-dimensional modeling of IP effects in time-domain electromagnetic data: Geophysics, 79, no. 6, E303–E314, doi: 10.1190/geo2014-0060.1.

Madsen, L. M., Fiandaca, G., & Auken, E. (2020). 3-D time-domain spectral inversion of resistivity and full-decay induced polarization data—full solution of Poisson's equation and modelling of the current waveform. *Geophysical Journal International*, *223*(3), 2101-2116.

Signora, A., Galli, S., Gisolo, M., Fiandaca, G. (2023). The HydroGeosITe for AEM mapping: characterization through joint inversion of AEM, ground EM and DCIP data. *AEM2023 - 8th International Airborne Electromagnetics Workshop, 3-7 September 2023, Fitzroy Island, QLD, Australia*.

Sullivan, N.A.L., Viezzoli, A., Fiandaca, G. (2023). EEMstudio: an open-source freeware QGIS plugin for processing, modelling and inversion of electric and electromagnetic data. *AEM2023 - 8th International Airborne Electromagnetics Workshop, 3-7 September 2023, Fitzroy Island, QLD, Australia*.

Viezzoli, A., V. Kaminski, and G. Fiandaca, 2017, Modeling induced polarization effects in helicopter time domain electromagnetic data: Synthetic case studies. *Geophysics*, 82, no. 2, E31–E50.

Weller, A., Slater, L., Binley, A., Nordsiek, S., & Xu, S. (2015). Permeability prediction based on induced polarization: Insights from measurements on sandstone and unconsolidated samples spanning a wide permeability range. *Geophysics*, *80*(2), D161-D173.

Xiao, L., Fiandaca, G., Zhang, B., Auken, E., & Christiansen, A. V. (2022a). Fast 2.5 D and 3D inversion of transient electromagnetic surveys using the octree-based finite-element method. *Geophysics*, *87*(4), E267-E277.

Xiao, L., Fiandaca, G., Maurya, P. K., Christiansen, A. V., & Lévy, L. (2022b). Three-dimensional time-lapse inversion of transient electromagnetic data, with application at an Icelandic geothermal site. *Geophysical Journal International*, *231*(1), 584-596.

Zhang, B., Engebretsen, K. W., Fiandaca, G., Cai, H., & Auken, E. (2021). 3D inversion of time-domain electromagnetic data using finite elements and a triple mesh formulation. *Geophysics*, *86*(3), E257-E267.

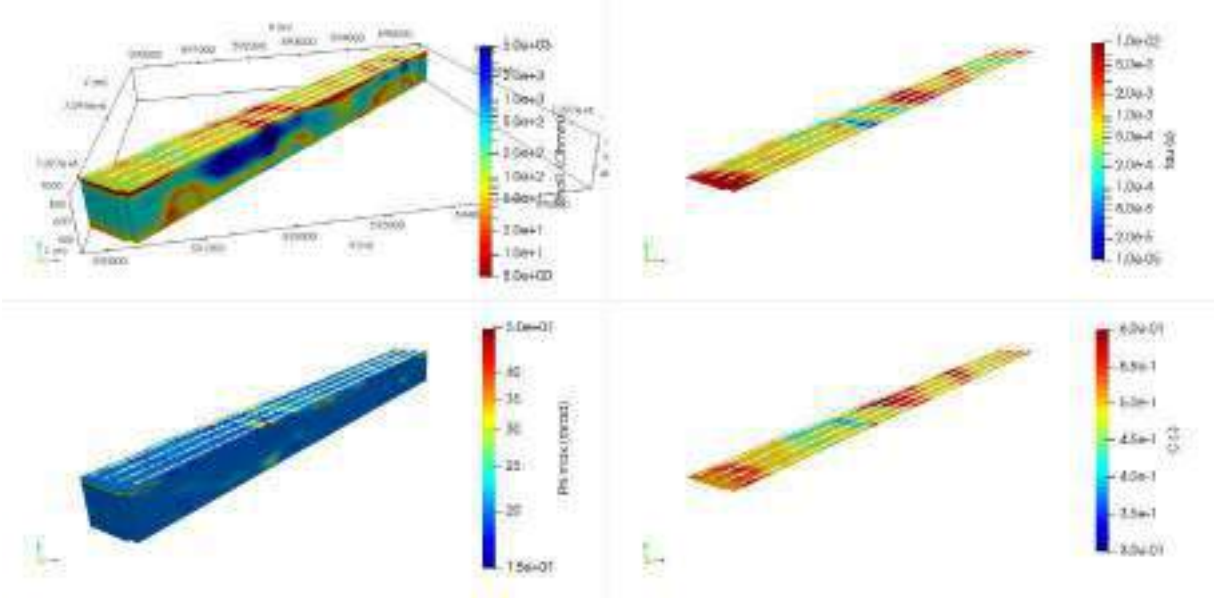

Figure 5. EEMverter inversion model of the Valen VTEM survey. Top left – resistivity model; Bottom left – chargeability (maximum phase) model; Top right –model of the time constant tau; Bottom right – model of the spectral exponent C. White lines represent the acquisition lines.

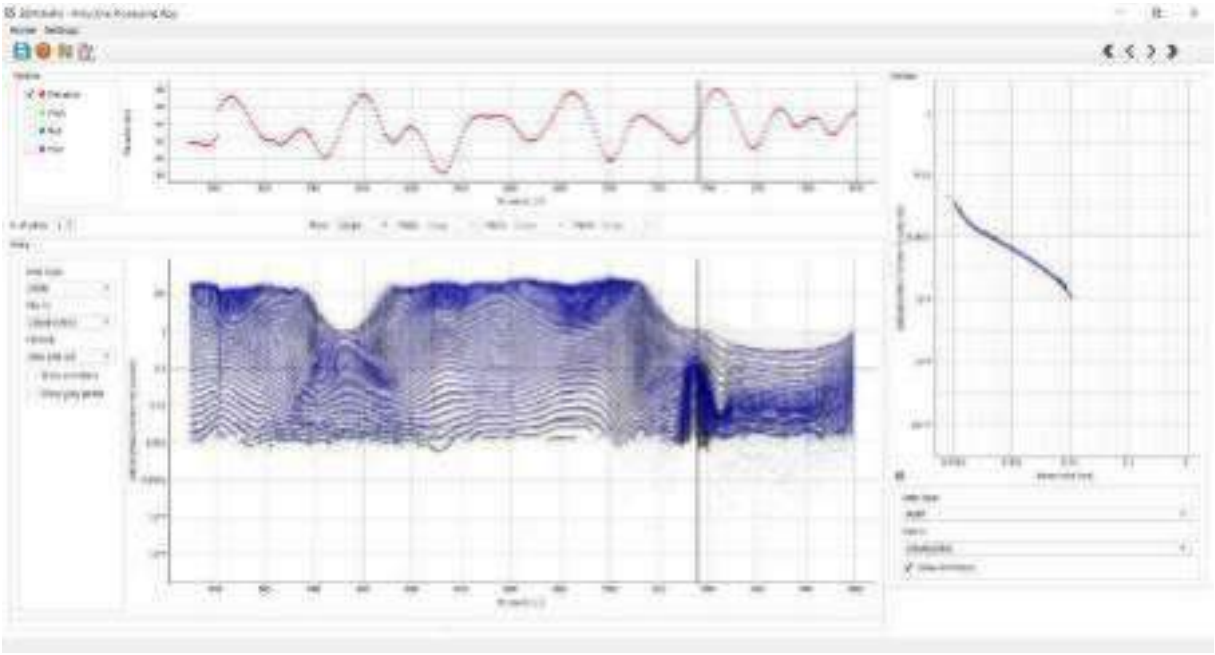

Figure 6. Fit of EEMverter inversion in correspondance to the strongest conductivity anomaly displayed through EEMstudio (Sullivan et al., 2023). Top section: flight altitude; bottom section: data (blue markers) and gate-by-gate fit (black lines); right panel: exemplary decay in correspondance to the vertical black line along the data stripe.

The Development of the TEMPEST AEM System

Andy Green*
OTBC Pty. Ltd.
8 Lawley Cres. Pymble NSW 2073
andy@corstruth.com.au

**Presenting author asterisked*

SUMMARY

TEMPEST's origins lie in the difficulty half-sine AEM systems had in mapping the Australia's dryland salinity. This resulted in the development of the SALTMAP system, a collaboration between World Geoscience Corp and CSIRO. This was a 500 Hz square wave system with excellent high frequency response, full-waveform digital acquisition, processing, calibration and bird positioning. With the advent of the CRC for Australian Mineral Exploration Technologies (CRCAMET) and an industry push for an Australian system with deeper penetration, the SALTMAP System was taken to a lower base frequency (25 Hz) and higher power while retaining as much higher frequency response as possible. The previously implemented signal processing and calibration was retained enabling a reliable conversion to Step Response for ease of interpretation.

The development history of TEMPEST is a result of collaboration between company, university and government research. Funding came from a diverse range of sources, government grants, collaborative industry funds and WGC.

However, like most other fixed-wing systems, it was caught up in the consolidation and subsequent decadal changes in ownership that started after TEMPEST first became operational. But the consolidation was good for TEMPEST. At the end of 2000 it was operating on a platform that had limited power and an airframe that constrained the bird to a shape that made coil motion noise difficult to reduce. The merger with Geoterrex brought new aircraft, better coil suspension and extensive operational experience that took TEMPEST to another level of operational efficiency.

Key words: TEMPEST, AEM, History

A HISTORY

TEMPEST is Australia's first home-grown Fixed Wing AEM system. Yet it has its origins, as do most AEM systems, in Canada. The story starts with World Geoscience Corporation's (WGC) purchase of Questor, the holder of one of the two licences for Tony Barringer's half-sine INPUT system in 1987. The other licence was held by Geoterrex and competition was inevitable.

When WGC brought Questem to Australia in 1989 (Cunneen, 2022) that competition was manifest in two areas, traditional massive sulphide search and salinity mapping. Based in WA, with its increasingly recognized dryland salinity problems, WGC saw the opportunity to capture market share using its local knowledge and contacts. But it soon became clear that neither Questem nor Geotem (the Geoterrex system) was suited to a problem where the users were demanding near surface information. Looking back, arguments about whose first off-time channel was the best seem overwrought.

This led WGC to propose a new fixed wing system with improved high frequency performance. The opportunities for new technology were obvious. Questem (like Geotem) was now (1990) a digital system and it was clear that there were more opportunities to take advantage of new technology that could monitor and thus compensate for system variables such as aircraft orientation and transmitter current,

SALTMAP, a collaborative effort with CSIRO funded by a $1.7 million government grant, was the result. It was a 500 Hz always-on square wave with 10 µs switching giving a bandwidth of 50 kHz. The sensor, made by CSIRO, was a three-component coil set using printed circuit board construction techniques. High bandwidth digitization at ~100 kHz (tweaked to avoid VLF contamination), streamed data for pre-stack noise (especially sferic) rejection before stacking was implemented. The coil suspension was very rudimentary and the bird was long and thin to fit under the only available aircraft, a Britten Norman Trislander.

Processing included wavelet-based sferic rejection, stacking, Fourier domain calibration and deconvolution of the transmitter waveform and corrections for aircraft orientation and bird position. Transformation to step response was the final stage.

Through the early 90's SALTMAP flew a number of surveys for land management applications and competed against the DIGHEM system but although the high frequency performance was excellent it was not enough. Even for the groundwater applications, a wider band-width was necessary.

By 1993 the pressure also increased for deep probing AEM. BHP and Aberefoyle were supporting Geoterrex in the development of a high power, low base-frequency system. It was felt that competition was needed and AMIRA proposed that there be a CRC to address the issue of AEM in Australia and, as a component, support the development of a competitive system. The CRC for Australian Mineral Exploration Technologies (CRCAMET) was proposed and won funding in the first round of the new scheme. The participants were AMIRA, CSIRO, WGC, Macquarie University, Curtin University, Geoscience Australia (GA) and GSWA.

CRCAMET set up programs in AEM for Geological/Regolith Mapping/Salinity, AEM Auto-interpretation and AEM

Systems. The objectives of the AEM Systems program were to transform SALTMAP into a system which provided:

- Geological mapping of both the regolith and fresh rock.
- Detection of targets of economic interest to depths of about 300 m.
- A dramatic increase in the cost-effectiveness of AEM by cutting the data acquisition cost for each line km.

And, because there was no funding for a new, more powerful aircraft, to do most of this by reducing noise, calibrating and system monitoring!

To do all this the transmitter waveform was changed to lower frequency (25 Hz minimum) and went to a 50% duty cycle square-wave with 38 µs turn-off operating at much higher power. This was enabled by the availability of IGBT devices to replace the older, less suitable (and thus more complex) MOSFET technology. The insertion of an off-time was necessary for the system to carry a magnetometer.

The sensor system evolved as well. The CSIRO team in Sydney built a two component (X and Z) bird (Y was added later) with aluminium coils and a centre-of-mass suspension. The coil set was still long and thin to fit the cigar-shaped shaped bird under the Trislander.

The signal processing from SALTMAP was extended by including corrections for airframe response and increasing attention for primary field removal. Because the primary field removal involves an extrapolation of the data to zero frequency or, equivalently, infinitely late time, there was always a model, either explicit or implied, for the ground response in conductive environments. This is always be a problem for on-time EM methods and it forces us focus attention on the problems of noise at low frequency. Something that was difficult given the constraints on bird design.

But technical challenges were not the major consideration, money or rather the lack of it, was a serious constraint in the early days of the CRC. The grant for CRCAMET was ~$8.3 million over seven years was spread among the two universities CSIRO and WGC. It did not allow for a big expansion in existing capability. This changed in 1997 when WGC won a $9 million grant for Project CERBERUS which planned to include TEMPEST in a multi-sensor airborne geophysics platform. This enabled the expensive phase of flight testing and debugging of the system and brought Richard Lane on as AEM Systems Program leader at a critical time.

The publication of the first substantial paper on the TEMPEST system (Lane et. al. 2000) marked a hinge point in the system development. The CRCAMET was wound up and World Geoscience merged with Geoterrex inside Furgo.

But this consolidation was good for TEMPEST. At the end of 2000 it was operating on a platform that had limited power and an airframe that constrained the bird design in ways that made coil motion noise difficult to reduce. The merge with Geoterrex brought new aircraft, better coil suspension and extensive operational experience that took TEMPEST to another level of operational efficiency.

From a performance perspective a big change was the improvement in low frequency/late time performance that was achieved by integrating the Geoterrex bird configuration and coil suspension. This improved late-time noise by a factor of five. Other technical improvements followed with more accurate position and orientation sensing for the bird.

After the Trislander TEMPEST operated on a Skyvan (2001 – 2016) and a CASA 212 (2007 to 2017). Generally, operation was with a single turn loop but two surveys have been conducted in SuperTEMPEST mode with two transmitters each driving a separate two turn loop. In South Africa TEMPEST was migrated to a Cessna 208B where it operated from 2004 to 2015. It came back to Australia in its current form on a C208B Supervan 900. There are three systems installed with more under construction.

The end of the CRCAMET also saw the start of an operational phase where TEMPEST was used for increasingly large surveys for land management and then, gradually, for the UNCOVER initiative for "unlocking Australia's hidden mineral potential". It was here that the inclusion of GA in the CRCAMET paid benefits for the TEMPEST technology. Richard Lane moved to GA and it became a strong supporter of regional AEM surveys, providing supervision for most surveys and developing new inversion software suitable for these regional surveys.

CONCLUSIONS

TEMPEST is one of the few fixed wing AEM systems still in active use, if intensity of use is a measure of success it is certainly that. Helicopter systems have occupied much of the market for sulphide detection and detailed environmental mapping while TEMPEST has occupied (you might even say made) a niche for regional scale surveys. This happened, in part, because it's origins in salinity mapping demanded wide bandwidth, careful signal processing and cost effectiveness. But it would not have achieved success so quickly without the incorporation of technology that came with the worldwide consolidation of AEM systems. It had its heritage in Canada, it's conception in Australia and gained it's maturity in South Africa. It is, in the end, the product of an international effort.

ACKNOWLEDGMENTS

This paper could not have been compiled without the input of people who were closely involved in the TEMPEST system. Special thanks must go to the following people.

Pat Cunneen, Don Pridmore, Andrew Duncan, Greg Street, Guy Roberts, Phil Pik, Chis Golding, Mark Stacey, Andy Gabell, Teo Hage, Ross Brodie, Tim Munday and Ray Lockwood

REFERENCES

Cunneen, P. 2022, A short journey through Aerodata and World Geoscience, A personal memoir by Pat Cunneen, https://www.aseg.org.au/sites/default/files/A Journey Through Aerodata and World Geoscience.pdf

Lane, R., Green, A., Golding, C., Owers, M., Pik, P., Plunkett, C., Sattel, D. and Thorn, 2000 R., An example of 3D conductivity mapping using the TEMPEST airborne electromagnetic system Exploration Geophysics v31, 162-172.

.

Deep Learning for the Inversion of Airborne EM Data

Eldad Haber
The University of British Columbia
Dept of EOAS, UBC, Vancouver, BC.
ehaber@eoas.ubc.ca

Christoph Schwarzbach
Computational Geoscience Inc
christoph@compgeoinc.com

SUMMARY

In the recent decade Deep Learning have revolutionised fields such as computer vision and image understanding. However, its use for the solution of inverse problems have been limited. In this work we examine the use of deep learning for the processing and inversion of airborne EM data. Preliminary results show that by incorporating deep learning it is possible to eliminate many of the artefacts that are commonly observed in airborne inversion allowing us to obtain much more reliable inversions that fit not only the data, but also our a-priori information.

Key words: Airborne EM, deep learning, ADMM, priors.

INTRODUCTION

Airborne electromagnetic (EM) is a commonly used technique to obtain images of the subsurface over large volumes of land. The ability to fly large areas in a short time make airborne EM one of the most common method for mineral exploration, mapping of underground aquifers, and understanding near surface geology, Visoly et-al (2009).

Airborne EM data is highly challenging to invert in 3D. This is because it requires the solution of many forward problems in 3D. However, in recent years, big strides have been made that allow for such an inversion. As a result, 3D inversions of airborne EM are possible, leading to much more reliable 3D models that can be interpreted by geologists, Haber et-al (2014).

Nonetheless, inversion of EM data has some major drawbacks. In particular, any inversion tends to have some undesired artefacts. 1D inversions are known to smear 3D objects in an effect sometimes refers to as pant-legs while 3D inversion of conductive targets in a very resistive background tend to generate rings. These artefacts are due to the fact that airborne EM is an ill-posed problem. As such there are many solutions that fit the data and therefore, the inversion algorithm needs to navigate itself to a region that yields geologically reasonable models. Standard regularization techniques have difficulties in doing so. Therefore, we aim to derive a data driven regularization that yields models with some desired characters.

To this end, we use deep learning (see LeCun (2015)) to learn a data driven regularization that yields models that not only fit the data, but also have some desired properties. Our inversion algorithm is based on the Alternating Direction Methods of Multipliers (ADMM), Sun et-al (2016) that allows us to separate the data fit from the regularization. Initial results demonstrate our ability to obtain feasible models that fit the data with much less artefacts compared with standard inversions

METHOD

We consider the a common AEM survey where we write the forward problem in a generic form as

$$F_i(m) + \epsilon = b_i i = 1, \dots, n_s \qquad (1)$$

Here F is the electromagnetic forward problem, m is the (log) conductivity ϵ is noise and b are the data. We assume to have n_s sources, each yields us data that is measured over some time channels.
A model is typically obtained by approximately solving a regularized optimization problem of the form

$$\frac{1}{2}\sum|F_i(m) - b_i|\vee^{2} + R(m) \qquad (2)$$

The objective function is devised of two parts. The first is the data fit and the second is the regularization. Since the problem is ill-posed, different regularization yields different inversion results. While it is possible to solve the optimization problem using many different methods, in this work we use the ADMM method. The advantage of the method is that is allows the separation of the optimization into two main parts. The first is simply fitting the data and the second is "correcting" the model such that it is more geological. Each iteration of the algorithm can be written as follows

1. Approximately solve the problem for m by approximately minimizing $\frac{1}{2}\sum|F_i(m) - b_i|\vee^{2}$ starting from $m=z$, obtaining m_f
2. Set $z_f = 2m_f - z$
3. Approximately solve for m by minimizing $R(m)$ starting from z_f.
4. Set $z = z_f + m - m_f$

We focus our attention of the third step in the algorithm. Standard inversion techniques that involve smoothness typically use a combination of derivatives to compute the regularization R and its derivatives.

Deep learning allow for a whole new family of regularisers. In particular, we aim to use deep convolutional network as a regulariser.

We focus our attention on regularisers such as UNet and Resnet. Both methods take in z_f and return an approximate model m. Both networks contain typically millions of parameters to be learned.

In order to learn the parameters we start from a known model *m*, and use the algorithm with a network that is used as a regulariser in step 3. We then compare the results of the inversion to the "true" solution. The parameters of the regularization function are then changed in order to better recover the true model. In order to not over-fit one particular model we require to have many models to train on. This requires some model builder that is based on geo-statistics or other technique for model building. After training the model, one obtains a regularisation that does the best work in recovery of the true model given the data and the a priori information that is encoded in the training data. During the training one typically uses a validation set to estimate the performance of the training and to avoid over-fitting the data.

RESULTS

Our model problem is made of a simple example where data is collected above a thin highly conductive plate embedded within a very resistive background in 3D. The data is then inverted in 3D obtaining a model that presents ringing. Such artefacts are very common when inverting highly conductive targets in highly resistive background and they are an artefact of the reduced sensitivity just below the transmitter.

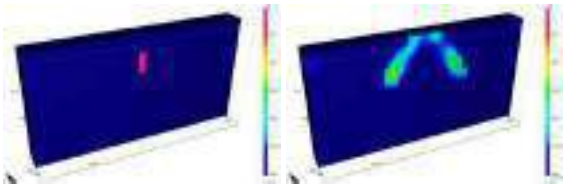

Figure 1. The simple model used to demonstrate the artefacts that can be observed when attempting to invert a 3D model using smoothness type regularisation. Left, the true model, right, the recovered one

We show the ringing effect by observing a 2D slice from the model at a depth of 50 meters in Figure 2.

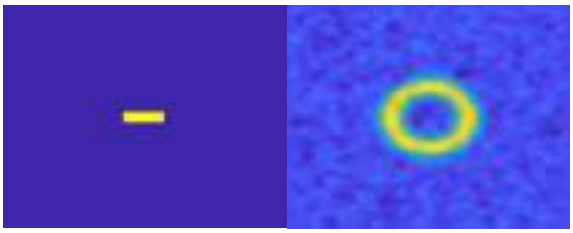

Figure 2. Horizontal slice through the simple model that demonstrate the ringing. Left, the true model, right, the recovered one.

After using a deep learning regularizer we obtain the model in Figure 3. This model have completely eliminated the ringing effect yielding a much more geologically feasible model.

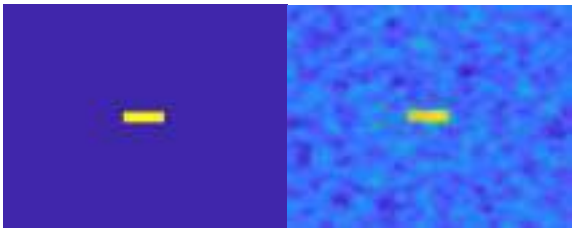

Figure 3. Horizontal slice through the simple model that demonstrate the ringing. Left, the true model, right, the recovered one using deep learning.

CONCLUSIONS

In this abstract we have presented preliminary studies for the incorporation of deep learning in airborne inversion. We have seen that using regularisation that is based on deep learning can yield much more geological results eliminating some of the well known artefacts that are commonly observed in the inversion of airborne data.

REFERENCES

E. Haber and C. Schwarzbach and R. Shekhtman., 2014. Parallel inversion of large-scale airborne time-domain electromagnetic data with multiple OcTree meshes. *Inverse Problems*, 30.

LeCun, Yann and Bengio, Yoshua and Hinton, Geoffrey., 2015. Deep learning, Nature, 521: 436--444.

A. Viezzoli and E. Auken and T. Munday, 2009. Spatially constrained inversion for quasi 3D modeling of airborne electromagnetic data - an application for environmental assessment in the Lower Murray Region of South Australia *Exploration Geophysics* 40: 173--183.

Sun, Jian and Li, Huibin and Xu, Zongben, 2016. Deep ADMM-Net for compressive sensing MRI, Advances in neural information processing systems, 29.

Zhou, B., 1988. Crosshole resistivity and acoustic velocity imaging: 2.5-D Helmholtz equation modelling and inversion. PhD thesis, University of Adelaide.

The last five years of Tempest System Development

Teo Hage*
Xcalibur Multiphysics
10 Compass Road
Jandakot, Perth
Western Australia
teo.hage@xcaliburmp.com

Eric Steele
Xcalibur Multiphysics
10 Compass Road
Jandakot, Perth
Western Australia
eric.steele@xcaliburmp.com

Peter Wolfgram
Xcalibur Multiphysics
10 Compass Road
Jandakot, Perth
Western Australia
peter.wolfgram@xcaliburmp.com

SUMMARY

Over the last five years, TEMPEST development efforts have centred around extending bandwidth, improving system geometry measurements, improving the signal processing and making the system more robust, integrating additional instruments on the platform, modernising hardware and building additional TEMPEST systems.

Pioneered by Geoscience Australia's AUSAEM project, global demand for regional and country scale Airborne EM has increased significantly. The data is being used for a broad range of applications, with geophysical mapping to improve the understanding of geology at regional scale and mapping the thickness and character of the regolith remaining popular use of the data. However, increasingly TEMPEST data is being used for groundwater resource assessment, -evaluation of the effectiveness of in-fill EM in particular areas and by some innovative companies and individuals to aid in the search for critical minerals.

This paper presents a summary of the improvements currently in development and/or implemented on the TEMPEST system since the AEM 2018 conference and how these efforts were designed to improve the platforms utility as a cost effective and capable regional Airborne EM mapping system.

Key words: TEMPEST, Regional Mapping, System Improvements

INTRODUCTION

Until recently, only a single TEMPEST system was available for commercial deployment. Whilst this limitation no longer applies as additional platforms have, and continue to be built, the TEMPEST development program designed five years ago had not anticipated this increase in system availability. Consequently, the R&D plan contemplated that each improvement would be a standalone project whose success and failure had few or no interdependencies and could be implemented quickly in order to minimise system downtime.

Extending the bandwidth of the system was considered a priority to address the growing demand for regional aquifer delineation and the anticipation that explorers are looking deeper in their quest to find in-demand natural resources. Historically, improving near surface resolution or increasing the depth of penetration would require design trade-offs that usually traded one of these improvements for the other. For a multi-utility system, these compromises could no longer be made. This necessitated that we combine the use of great engineering and innovative new ideas so that these choices were avoided wherever possible.

In keeping with the compartmentalised approach to R&D, these bandwidth extension efforts were broken into 4 projects :

- New coil suspension system for robust operation below 25Hz,
- Purpose-built data acquisition and timing system for highspeed sampling and real time processing, a
- Receiver coil-set with improved high frequency response and low noise amplifiers
- New (patented) concept in Transmitter design.

As demonstrated by Brodie et al. (2023) measurement of the System Geometry, especially when the AEM transmitter and receiver are not co-planar, is an essential ingredient to obtaining accurate conductivity inversions. Multiple GPS receivers and Inertial Measurement Units (IMU) were implemented to accomplish this task. Conceptually simple, the precise synchronisation of data that is needed, a requirement to avoid conductive surfaces or magnetic material near the receiver coils and the need to transmit some of this data from the bird proved to be an engineering challenge.

With some exceptions, the majority of the TEMPEST signal processing being developed in the late 1990's and early 2000's included algorithms that were appropriate and practical at the time. New spheric rejection techniques (not based on wavelets), VLF noise suppression and more robust system response deconvolution have been implemented, both in the real time and post mission software. Whilst noise levels improvements can be noted, the new software allows for complete flexibility of ADC sample rates and a framework for the relatively simple addition and selection of new signal processing algorithms.

Finally, the addition of peripheral sensors to complement the usual Magnetics and (sometimes) Radiometrics flown with regional EM is becoming a client driven necessity. This includes the addition of an iCORUS-X strap-down gravimeter as the most important addition, with a gyro-stabilised frame camera and a variable sampling rate laser altimeter as standard peripherals. Ensuring the synchronisation of the data is now accomplished using PTP and NTP protocols in an Internet of Things (IOT) network aboard the aircraft.

SYSTEM IMPROVEMENTS

Bandwidth extensions to the TEMPEST system target a reduction of the base frequency of operation and an increase in

the useable high frequency end, without comprising signal to noise at either end of the spectrum.

Supported by numerous papers on the effect of base frequency on skin depth, a reduction in base frequency was an early endeavour. In the case of most EM systems, the reduction in base frequency is limited by the ability to filter out coil motion noise from the signal induced by the transmitter. Whilst there are numerous ways to accomplish this, a mechanical isolator has proven to be the most effective and reliable method over the last few decades, with inertial suspension systems being our choice. However, in contrast to Helicopter EM Systems which have fewer receiver size restrictions, the space within a Fixed Wing Towed Bird is considerably more limited, and using a derivative of a Roberts Linkage mechanism was not an option for very low base frequencies. In conjunction with UWA (Sunderland et al, 2017), and over a couple of Australian Research Council grants, we have a new suspension system that has operated successfully at 12.5 and 6.25 Hz. Some challenges remain, as we would like to include direct gyroscopic measurements of coil velocity, but the concept has been proven and system commercialisation is well underway. Figure 1 shows the TEMPEST Spherical/Rotational Isolator

Figure 1 : UWA-Xcalibur Spherical Isolator

The extension of the system bandwidth into higher frequencies required a number of developments, each of which would provide an incremental system improvement, but only collectively would they provide the necessary uplift required by the design objectives i.e. to significantly improve TEMPEST's ability to resolve conductivity contrasts in the near surface.

Considering that Skin Depth is inversely proportional to the square root of frequency, increasing the system bandwidth at the top end should improve the TEMPEST's performance in the near surface. Less obvious was the benefits of "Broadband" versus "Narrowband" TEMPEST to the depth of investigation as shown in Figure 2, the forward modelling having been performed more than a decade ago. However, the necessary electronics, high speed 24 bit Analogue to Digital Converters, FPGA devices capable of synchronising timing signals in the MHz range and the timing precision needed wasn't readily available until a few years ago.

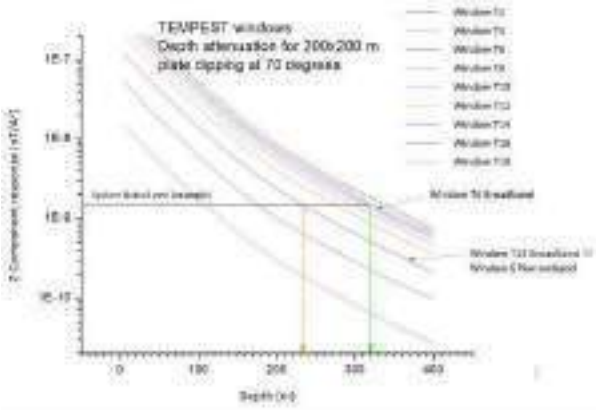

Figure 2 : An example of a set of depth attenuation curves. System noise level is shown at the black horizontal line. The vertical orange line shows when the response of a narrowband system window 6, or broadband window T14 drops below the noise level with the corresponding depth of investigation.

High speed data acquisition also provided a visual confirmation that the transmitted waveform exhibited a number of "nulls", areas of poor Signal-to Noise ratios as predicted for a 50% duty cycle square-wave with a 36 µS ramp time as implemented on TEMPEST. These nulls do not shift with reduced base frequency as shown in Figure 3 below.

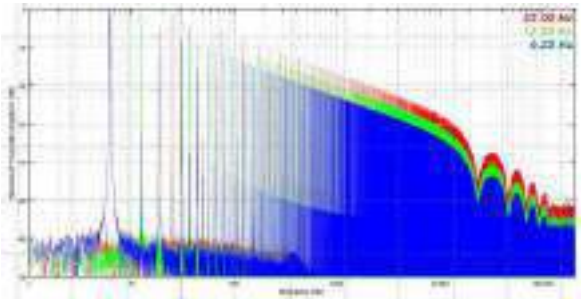

Figure 3 : Power Spectra of Tempest Transmitter "Nulls" characteristic of a 50% duty cycle transmitter waveform

Decreasing the ramp time, i.e., increasing the transmitter switching time and/or using a complex waveform allows us to tailor the transmitted power at higher frequencies by reducing the prevalence of "nulls" within the bandwidth of interest. Figure 4 illustrates the effect of faster transmitter switching time on the power spectra at the high frequency end of the bandwidth of interest.

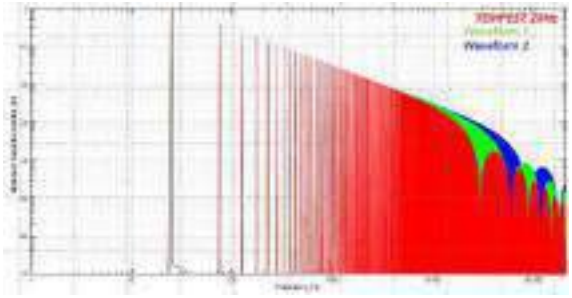

Figure 4 : Theoretical power spectra of TEMPEST waveform with faster switching

In keeping with the incremental approach to system upgrades, two methods of increasing the switching speed were/ are being pursued. The first is an engineering approach, where we use higher voltages across the transmitter loop during switching time. This necessitated the use of higher voltage electronic devices, but provided an incremental, albeit small, improvement at relatively low risk.

The second approach, inherently riskier, spawned the second ARC project with UWA and is the subject of a recently lodged patent (Sunderland, Steele etc al). Called Multi-Step, this innovative concept calls for a complex waveform whose power spectra closely matches that of TEMPEST (albeit with different phase characteristics). This criterion was imposed to ensure that the systems response deconvolution remained a stable operation. The multi-step waveform is shown in Figure 5, noting that a 3-level implementation would be equivalent to TEMPEST in its current implementation and that 7 and 9 level implementations are practically implementable. Using smaller, faster steps allows for considerable flexibility in improving the transmitted power at the high frequency end without compromising the low frequency SNR.

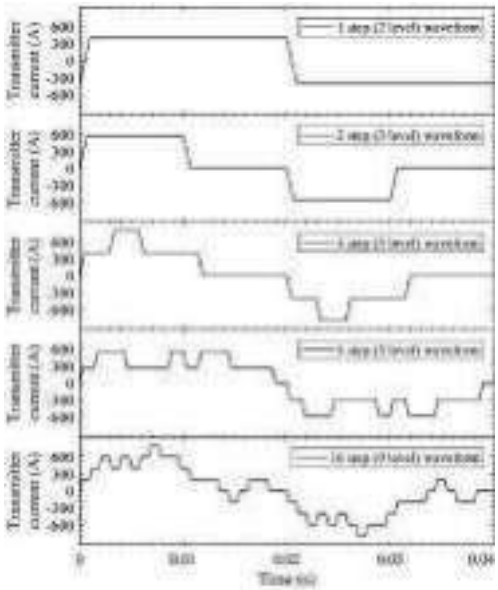

Figure 5 : Various Multi-Step Waveforms

Considerable effort over the last year has been expended on improving the TEMPEST Signal Processing, with the view of real time implementation where possible and streamlining the post-processing workflow.

Spheric rejection operates on the raw (high speed) data stream and uses a robust statistical method which does not rely on tuning parameters.

Post stacking, the previous deconvolution result has been augmented with the variance at the various transmitter frequencies obtained from the high-altitude reference line. Figure 6 illustrate the weights derived from the variance.

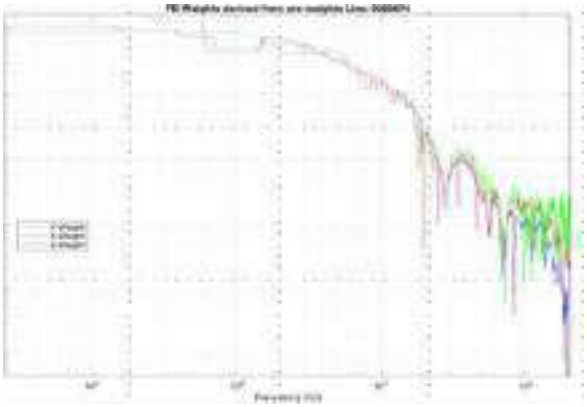

Figure 6 : Tikhonov Regularisation used during Deconvolution of TEMPEST System Response

Improvements have also been made to our Coil Motion correction and HPRG correction algorithms.

In order to improve the efficiency of TEMPEST operations, a signal processing technique has been developed to replace the necessity for a high-altitude reference line at the start of each survey flight. This approach still requires a high-altitude reference to be collected at the start of a survey and possibly at regular intervals, but the daily requirement is replaced with a low altitude repeat line. Whilst not an advantage during clear sky operations, this technique allows for a survey flight to proceed when weather prevents the aircraft from flying at the requisite 3000 feet Above Ground Level for the calibration. Figure 7 shows the minimal differences observed when using a repeat line reference compared to one acquired at high-altitude.

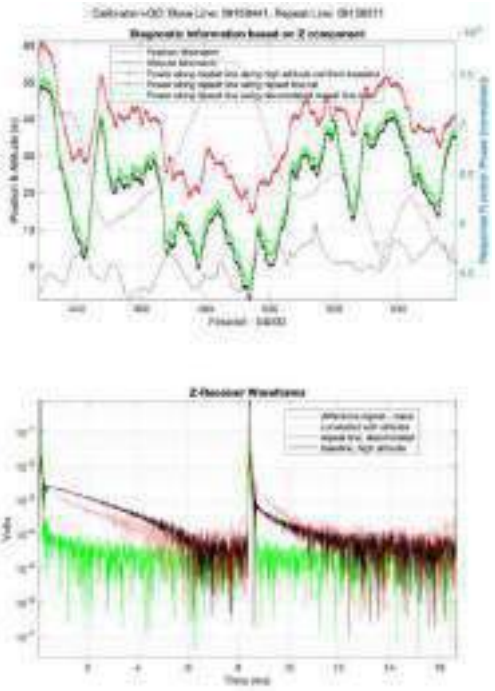

Figure 7 : QC Plot from the USGS 2020 Tempest data comparing High Altitude Reference to Repeat Line Calibration data . The de-correlated transfer function clearly gives a good match with the ideal signal power.

As TEMPEST is primarily a regional mapping tool, the concurrent acquisition of magnetics and radiometrics (when required) are standard requests. Measuring the magnetic field in the presence of the perturbating EM field can be challenging and requires attention during upgrade programs. From Mid-2023, the iCORUS-X strap-down gravimeter is a standard add-on to the TEMPEST system. This instrument provides <1 mGAL noise levels for long wavelength gravity measurements (100 second filter) as a complement to the regional EM data.

In order to provide the flexibility and ability to accomplish many of these upgrade projects, it was necessary to develop a new Data Acquisition system (DAQ). Based on High End Commercial Off the Shelf the Linux Based machine, provides a modern interface for our onboard operators as well as allowing remote login by support technicians to assist with diagnostic on the ground or in flight where internet connection is available. In addition to the application specific, hand tailored code required for the EM system, the DAQ additionally hosts an Internet of Things (IOT) server using an application called Node-Red which allows for the simple integration of inexpensive environmental sensors as necessary and system operation from a mobile phone/tablet if convenient. With precise timing being provided by a separate GPS Disciplined NTP/PTP server, the tight synchronisation of peripheral data is maintained. Wi-Fi access is available for the interfacing of remote, lower data rate sensors. Sensors supported in this IOT environment include a gyro stabilised HD (1920 x 1080 pixel), wide angle still frame camera (1 to 4 Hz), Inertial Measurement Units, GNSS Sensors, a 10-50 Hz Laser Altimeter, and any commercial sensor support by Node-Red. Figure 8 shows a screen grab from the new data acquisition system.

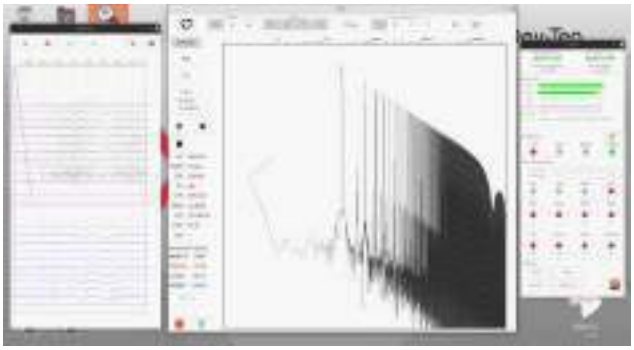

Figure 8 : TEMPEST Linux Based Data Acquisition System – An enabler for many of the technologies implemented or still in development.

With 5 TEMPEST systems under construction, primarily to meet the demand for regional EM mapping projects, Tempest developments will benefit by having an increasing number of platforms to validate new developments and bring them to market in a timely manner. With the original single system constraint, this will almost certainly result in an increased pace of innovation.

CONCLUSIONS

The five years since AEM 2018 have been an active period for various Tempest system developments. With a continued push to extend bandwidth above and below current capability, and by various other system improvements we are hopeful that the TEMPEST EM system will have increased utility for country scale regional mapping projects, with applications in Mineral Exploration, Ground Water Resources, and environmental management.

ACKNOWLEDGMENTS

The authors would like to thank A. Sunderland and the UWA Department of Physics for their valuable contribution.

REFERENCES

Brodie, R., and Mule, S., 2023, Enhancements to deterministic AEM inversion through better geometry constraints and a bunch-by-bunch algorithm. Extended Abstracts, AEGC: 2023 Breaking New Ground, Brisbane, Australia.

Sunderland, A., Lockwood, R., Blair, D., Low-frequency rotational isolator for airborne exploration. *Geophysics*, 82 No 2, 1942-2156

Sunderland, A., Steele, E., SSystem and Method for Airborne Electromagnetic Surveying: Australian Patent Application No. 2022900685.

Advances in open-source software for 3D electromagnetics using SimPEG

Lindsey J. Heagy
University of British Columbia, Geophysical Inversion Facility
lheagy@eoas.ubc.ca

Johnathan Kuttai
University of British Columbia, Geophysical Inversion Facility
jkutt@eoas.ubc.ca

Devin Cowan
University of British Columbia, Geophysical Inversion Facility
dcowan@eoas.ubc.ca

Joseph Capriotti
University of British Columbia Geophysical Inversion Facility
jcapriot@eoas.ubc.ca

Seogi Kang
Department of Geophysics, Stanford University
sgkang09@stanford.edu

Dominique Fournier
Mira Geoscience, Vancouver, BC
dominiquef@mirageoscience.com

Douglas W. Oldenburg
University of British Columbia, Geophysical Inversion Facility
doug@eoas.ubc.ca

SUMMARY

Open-source software is increasingly being adopted by the geophysics community. Their emergence has greatly reduced the time required for students and researchers to be able to implement and explore new ideas, and having new developments implemented in an open-source project facilitates technology transfer and collaboration between research and commercial organizations. SimPEG is an open-source project for geophysical simulations and inversions. In this abstract, we provide an overview of the capabilities and recent advancements in SimPEG that are relevant to the airborne electromagnetics community.

Key words: Numerical simulations, inversion, computational methods, software.

INTRODUCTION

There are now a number of simulation and inversion codes that are open-source and allow use and adaptation by academic and commercial groups. An open-source model of development and dissemination of scientific software facilitates reproducibility and extension of the code to new applications, reducing start-up time for students and researchers. These codes can also be valuable to groups with established codes, as they can be an additional tool for testing, or for extending functionality. Werthmueller, *et al.*, (2020) provides an overview of 4 open-source codes for simulating 3D electromagnetic (EM) problems. SimPEG is one such code that supports forward simulation and inversion of time and frequency domain EM data, including for controlled and natural sources (Cockett *et al.*, 2015). The SimPEG project was started in 2013 with the aim of accelerating research by building a modular, open-source code-base, and importantly, by fostering a community of researchers interested in solving inverse problems with geophysical data.

SimPEG supports a variety of data types, including gravity, magnetics, DC resistivity, induced polarization and electromagnetics. Methods for solving 3D EM forward and inverse problems were implemented 3D EM early in the project (Heagy *et al.*, 2017), but much progress has been made in recent years to improve the efficiency and expand the functionality of the codebase. In this abstract, we highlight the advances relevant to the airborne EM community. Using an example of a synthetic Z-Axis Tipper survey, we illustrate the forward simulation and inversion capabilities of SimPEG and compare the results to those obtained with UBC-GIF Fortran software.

ELECTROMAGNETICS IN SIMPEG

SimPEG provides a framework for forward simulation and gradient-based inversion of geophysical data. With respect to EM methods, it contains functionality for simulating and inverting Maxwell's equations in 1D and 3D (and for some problems, 2D).

The 1D forward simulations in time and frequency are based on semi-analytic solutions in the wavenumber-frequency domain and leverage empymod for the digital filters (Werthmüller, 2017). Inversions can be laterally or spatially constrained and use standard L2 norms or sparse / compact L1 or L0 norms. For a recent example, see Kang *et al.* (2022).

For 3D simulations and inversions, SimPEG uses a staggered-grid finite volume approach to discretize Maxwell's equations in space. Supported mesh types include tensor, cylindrical, and OcTree meshes as well as curvilinear meshes. Tetrahedral meshes are currently being developed. The meshing and finite volume operators are contained in the discretize package, which is a part of the SimPEG project. For both the frequency and time domain simulations, there are multiple formulations that can be used. The E and B formulations discretize the electric field on edges and the magnetic flux density on faces, while the H and J formulations discretize the magnetic field on edges and the current density on faces. Table 1 provides a summary of the different implementations. Having multiple implementations has proven valuable for testing of the code, as it enables us to check for internal consistency. Further, some discretizations are better-suited for a given problem than others. For example, if simulating or inverting with fully anisotropic physical properties, the choice of formulation and physical property (conductivity or resistivity) matters; we would use conductivity with the E-B formulation and resistivity with the H-J formulation to avoid the need to invert the physical property matrix, which becomes dense when properties are anisotropic. All implementations use a right-handed coordinate system with z-positive up.

In contrast to codes that are provided as an executable where the user interacts with the code primarily through input and output files (possibly through a graphical interface), SimPEG is provided as a Python library where the user has access to all components of the simulation and inversion programmatically.

For example, in EM, this enables the user to access and visualize fields and fluxes for a given simulation. This ability has proven to be valuable for understanding the physics in research and educational applications (Oldenburg *et al.*, 2021).

Table 1: Summary of the E-B and H-J formulations of Maxwell's equations.

Formulation	Time domain equations	Frequency domain equations	Boundary conditions	Physical properties	Fields, fluxes
E-B	$\nabla \times \vec{e} = \frac{-\partial \vec{b}}{\partial t}$ $\nabla \times \mu^{-1}\vec{b} - \sigma\vec{e} = \vec{J_s}$	$\nabla \times \vec{E} = -i\omega\vec{B}$ $\nabla \times \mu^{-1}\vec{B} - \sigma\vec{E} = \vec{J_s}$	$\vec{b} \times \vec{n} = 0\|_{\partial\Omega}$ $\vec{B} \times \vec{n} = 0\|_{\partial\Omega}$	σ, μ^{-1} : cell-centers	$\vec{e}, \vec{E}$: edges $\vec{b}, \vec{B}$: faces
H-J	$\nabla \times \rho\vec{j} = -\mu\frac{\partial \vec{h}}{\partial t}$ $\nabla \times \vec{h} - \vec{j} = \vec{J_s}$	$\nabla \times \rho\vec{J} = -i\omega\mu\vec{H}$ $\nabla \times \vec{H} - \vec{J} = \vec{J_s}$	$\vec{j} \times \vec{n} = 0\|_{\partial\Omega}$ $\vec{J} \times \vec{n} = 0\|_{\partial\Omega}$	ρ, μ : cell-centers	$\vec{j}, \vec{J}$: faces $\vec{h}, \vec{H}$: edges

Accessing the full flexibility of SimPEG requires that the user be comfortable working with Python code. However, commercial groups have developed graphical interfaces that can be used to run the codes, making them more accessible to a wider community of users. The open-source MIT license facilitates commercial use and adaptation; as a project, we encourage collaboration and participation from commercial and academic groups.

Our initial implementation efforts focussed on developing the modular framework and structure of the codebase to facilitate research. As such, flexibility, and ease of extending the code are priorities. The codebase has matured with usage and contributions from the community, and in conjunction, there have been advances in the Python ecosystem that can be leveraged to improve efficiency. In particular, SimPEG now has capabilities to be parallelized using a domain-decomposition approach similar to that described in Yang *et al.* (2014). The forward simulation is broken up so that it can be run on a collection of smaller meshes that cover a subset of the survey, while the set of parameters we invert for are still represented on a global mesh as shown in Figure 1. Frequency domain problems can also be parallelized over frequency. We leverage parallelization frameworks in Python, such as Dask (Rocklin, 2015), to enable distributed computing on a cluster or on the cloud.

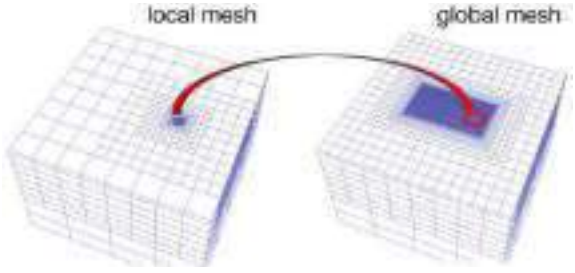

Figure 1. Domain decomposition approach where we invert for a model on the global mesh but solve the forward problem and compute sensitivities on the local mesh.

In the sections that follow, we describe the time, frequency, and natural source codes implementations in SimPEG, highlighting advancements relevant to the AEM community. Following this, we provide a synthetic example of an airborne Z-Axis Tipper EM (ZTEM) simulation and inversion. We compare the SimPEG results with those obtained using the UBC Fortran code E3DMT version 2 (https://e3dmt.rtfd.io). Finally, we conclude with a discussion of next steps for the SimPEG 3D EM codes.

Controlled Source Time Domain EM

The time domain implementation uses a backward Euler discretization in time. The user provides the time discretization. Sources can be airborne, on the ground or positioned in boreholes, and they can be inductive or galvanic sources. For wires or large-loop sources, the wire path can be provided. There are also other simple source types such as dipoles and circular loops that are implemented. The default simulation uses a step-off waveform, but the user can specify different source waveforms. Receivers can measure electric field, db/dt or magnetic fields, and these receivers can have arbitrary orientations.

Controlled Source Frequency Domain EM

Similar to the time-domain code, in the frequency domain code, the source can be galvanic or inductive, and again sources and receivers can be positioned arbitrarily. Relevant to AEM surveys, receivers can be at any orientation, which enables TMI data to be used, such as in SAM-type surveys. Receivers can measure total or secondary fields, such as for DIGHEM or RESOLVE surveys.

Natural source frequency domain EM

The natural-source EM code leverages the same forward simulation engine as the controlled source FDEM codes. The natural source EM code uses a primary-secondary approach, with a 1D primary field. A total field implementation, which uses boundary conditions to capture the effects of the inducing field is in progress. For natural source methods, the data are transfer functions. SimPEG includes common transfer functions such as MT or Tipper data and the ability to support

arbitrary transfer functions. This includes surveys with many B-field measurements and a few E-field measurements, which is relevant to AEM surveys, as well as surveys with many E-field measurements and a few B-field measurements, which might be collected as a part of a DCIP survey. Note that since the same simulation code is shared for all frequency domain methods, it is straightforward to use a controlled source with data that are transfer functions, for example in a CSAMT survey where the wire location is known.

Inversion

We formulate the inverse problem as an optimization problem where we minimize a data misfit and model norm term

$$\min_m \phi(m| \quad) = \phi_d(m) + \beta\phi_m(m) s.t. \phi_d \leq \phi_d$$

SimPEG contains classes for defining the data misfit (ϕ_d) and regularization (ϕ_m; options for the regularization include standard L2 norms, as well as capabilities for sparse and compact norms (Fournier & Oldenburg, 2019). SimPEG also contains routines for performing optimization and updating parameters such as the trade-off parameter β during the inversion. We generally use second-order optimization methods, such as Inexact Gauss Newton, or Projected Gauss Newton when bound constraints are imposed on the model. To use such methods requires that we compute products of the sensitivity and its adjoint with a vector. For the EM simulations implemented in SimPEG, we have the ability to form and store the sensitivity matrix, which is useful for problems that are sufficiently small or when domain-decomposition is used to break up the problem. Alternatively, in memory-limited applications, we can opt not to form the sensitivity matrix and instead compute products of the sensitivity and its adjoint with a vector. With these pieces, we can then go ahead and perform an inversion.

EXAMPLE

Setup

As an example, we use the L-block model shown in Figure 2. The block is 1 Ωm and it is embedded in a 100 Ωm half-space, it extends from 400m to 1200m depth. We discretize the model using an OcTree mesh with core cells of size 200m x 200m x 100m. We consider a ZTEM survey with frequencies 10 Hz, 50 Hz, and 200 Hz. The data locations are indicated by the white dots in Figure 2.

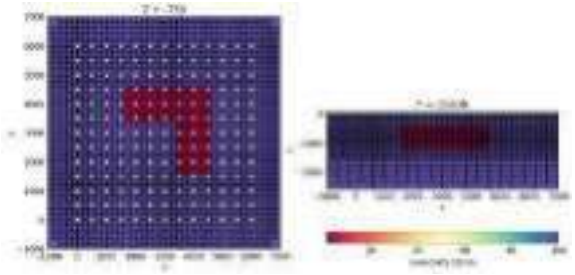

Figure 2. Model of a conductive L-shaped block in a halfspace. The block is 1 Ωm and the background is 100 Ωm. The block extends vertically from a depth of 400 m to 1200 m.

Forward Simulation

The forward simulation is performed using a primary-secondary approach with the E-formulation; a 1D primary is computed using a 100 Ωm halfspace. With SimPEG, users can choose to access the fields and fluxes that are computed as a part of the forward simulation. In Figure 3, we show the current density and anomalous magnetic field due to the conductive target for the at 10 Hz for a single source polarization. Currents are concentrated in the conductive target, producing an anomalous magnetic field, which is reflected in the data that we measure.

Figure 4 shows the simulated data. On the left we show the real and imaginary components of both Tzx and Tzy at 10 Hz; on the right, we show a corresponding profile of data at all three frequencies. The dashed lines show the data computed using the UBC E3DMT code. Both codes discretize electric fields on edges and magnetic flux density on faces. The exact same mesh and model were used in both codes. We can see the solutions are in good agreement.

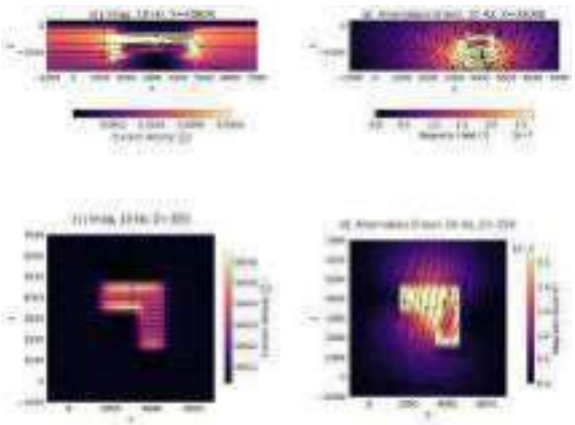

Figure 3. (a) Cross section of the imaginary part of the current density along the line Y=4000N for a single source polarization; (b) orthogonal cross section of the real part of the anomalous magnetic flux density along X=2500E. (c) Depth slice of the imaginary part of the current density and (d) depth slice of the magnetic flux density.

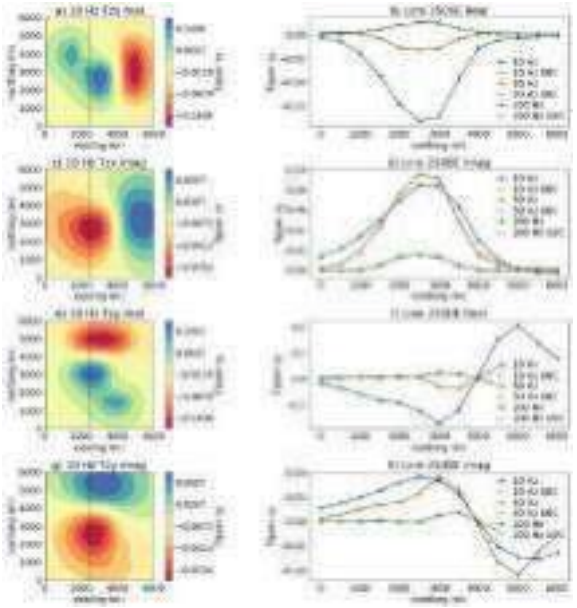

Figure 4. Simulated tipper data for the L-block model. Panels on the left show the 10 Hz data while panels on the right show a profile of data for all 3 frequencies. The colored lines show the SimPEG results while the black dashed lines show the UBC E3DMT simulation results.

Inversion

We invert the simulated data using both SimPEG and E3DMT. There are 2028 data total. A 5% relative error is assigned to all frequencies, a floor of 0.01 is used for the 10 Hz and 50 Hz data, while a floor of 0.005 is used for the 200 Hz data. We use a standard L2-norm regularization with smallness and first-order smoothness applied in each direction (α_s=2.5e-5; α_x = α_y= 1; α_z = 0.25). We use the same β-cooling schedules in both codes, starting with a value of 0.01 and decreasing by a factor of 5 every 3 iterations. The reference and starting models are a 100 Ωm half-space.

Both inversions converged to comparable misfits. The SimPEG inversion converged in 7 iterations to a final χ-factor of ϕ_d/ϕ_d = 0.47. The UBC E3DMT inversion converged in 8 iterations to a χ-factor of 0.55. The SimPEG inversion ran with the simulation parallelized over frequencies using Python's built-in multiprocessing library. It completed in 15 minutes. The UBC inversion was parallelized over frequencies using MPI and it took 11 minutes.

Figure 5 shows the inversion results obtained using SimPEG (left) and the UBC E3DMT code (right). The recovered models are comparable, resolving a smoothed version of our L-shaped target, as is expected.

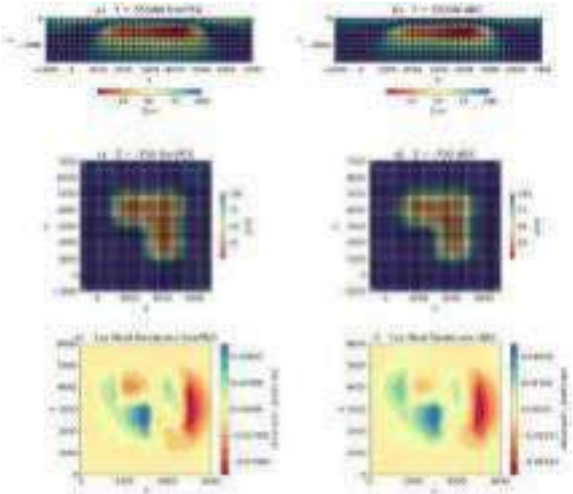

Figure 5. Recovered models obtained by inverting the synthetic ZTEM data using (a, c) SimPEG, and (b, d) the UBC E3DMT Fortran code. Panels (e), (f) show the data residual for the real part of Tzx for the SimPEG and UBC models, respectively.

CONCLUSIONS & NEXT STEPS

Work continues to advance the capabilities and efficiency of the SimPEG EM codes. Future releases of SimPEG will include support for multiple parallelization frameworks (e.g. Dask, MPI, and others) and utilities to support breaking up large simulations so that subsets can be run in parallel. Other areas of research include incorporating petrophysical and geologic information into the inversion as well as the joint inversion of multiple geophysical data sets. In conjunction, we are developing a suite of forward simulation and inversion examples that compare SimPEG results with those from the UBC GIF Fortran codes. These have proven to be valuable for testing and validating both codes and identifying areas where both code bases can be improved. Importantly, we are also taking steps to improve the usability of SimPEG. This includes an emphasis on the development of documentation and tutorials. Our hope is that by making 3D EM codes available and accessible, it will increase the use and value of EM geophysical data in solving geoscientific problems.

ACKNOWLEDGMENTS

The authors are grateful to members of the SimPEG community; those who use, contribute to, and support the project are critical to its success.

REFERENCES

Cockett, R., Kang, S., Heagy, L.J., Pidlisecky, A., Oldenburg, D.W., 2015. SimPEG: An open source framework for simulation and gradient based parameter estimation in geophysical applications. Computers & Geosciences 85, 142–154. https://doi.org/10.1016/j.cageo.2015.09.015

Fournier, D., Oldenburg, D.W., 2019. Inversion using spatially variable mixed Lp norms. Geophysical Journal International 218, 268–282. https://doi.org/10.1093/gji/ggz156

Heagy, L.J., Cockett, R., Kang, S., Rosenkjaer, G.K., Oldenburg, D.W., 2017. A framework for simulation and inversion in electromagnetics. Computers and Geosciences 107, 1–19. https://doi.org/10.1016/j.cageo.2017.06.018

Kang, S., Knight, R., Goebel, M., 2022. Improved Imaging of the Large-Scale Structure of a Groundwater System With Airborne Electromagnetic Data. Water Resources Research 58, e2021WR031439. https://doi.org/10.1029/2021WR031439

Oldenburg, D.W., Heagy, L.J., Kang, S., 2021. Geophysical electromagnetics: A retrospective, DISC 2017, and a look forward. The Leading Edge 40, 140–148. https://doi.org/10.1190/tle40020140.1

Rocklin, M., 2015. Dask: Parallel Computation with Blocked algorithms and Task Scheduling. Presented at the Python in Science Conference, Austin, Texas, pp. 126–132. https://doi.org/10.25080/Majora-7b98e3ed-013

Werthmüller, D., 2017. An open-source full 3D electromagnetic modeler for 1D VTI media in Python: empymod. GEOPHYSICS 82, WB9–WB19. https://doi.org/10.1190/geo2016-0626.1

Werthmüller, D., Rochlitz, R., Castillo-Reyes, O., Heagy, L., 2021. Towards an open-source landscape for 3D CSEM modelling. Geophysical Journal International 1–18. https://doi.org/10.1093/gji/ggab238

Yang, D., Oldenburg, D.W., Haber, E., 2014. 3-D inversion of airborne electromagnetic data parallelized and accelerated by local mesh and adaptive soundings. Geophysical Journal International 196, 1492–1507. https://doi.org/10.1093/gji/ggt465

Toward Open Science: Introducing the Geophysical Survey (GS) Data Standard and GSPy Toolbox

Stephanie R. James
U.S. Geological Survey
Denver, CO, USA
sjames@usgs.gov

Nathan Leon Foks
Inalab Consulting
Contracted to U.S. Geological Survey
Denver, CO, USA
nfoks@contractor.usgs.gov

Burke J. Minsley
U.S. Geological Survey
Denver, CO, USA
bminsley@usgs.gov

SUMMARY

The diverse field of geophysics comprises many data formats and archival conventions, often separated by specialty (e.g., electromagnetic, seismic, potential fields). Airborne geophysical methods exemplify this complexity, with critical auxiliary information on survey and system parameters, required to fully utilize and understand the data, often detailed separately throughout dense reports. An open, portable, self-describing data standard is needed to increase the interoperability, comprehensibility, and long-term archival of geophysical data. Here, we propose a new Geophysical Survey (GS) data standard that uses the NetCDF file format, in conjunction with extensions to the established Climate and Forecasts (CF) metadata convention. We have also developed an accompanying open-source Python package, GSPy, to provide methods for producing and interacting with GS-standardised files. We utilise the advantages of the NetCDF format to attach metadata directly to the data, and organise distinct, but related, datasets into groups within a hierarchical structure while leveraging the binary format to produce smaller file sizes. A root *Survey* group contains global metadata about the geophysical survey, and all data groups are located within the *Survey*. To simplify operations, data are categorised based on geometry as either *Tabular* (unstructured) or *Raster* (structured) datasets. Community development and adoption of a NetCDF-based data standard can greatly improve how these complex geophysical datasets are shared and utilised, increasing the accessibility and impact of geophysical surveys.

Key words: data standards, NetCDF, open-source software, geophysics, airborne geophysics

INTRODUCTION

The storage and documentation of scientific data are critical factors guiding how the data are ultimately used, shared, and understood. Within the field of geophysics, there is an abundance of data formats varying both within and across subdisciplines and methods (e.g., electrical, magnetic, seismic, electromagnetic, radiometric, and gravity). At a basic level, geophysical datasets share the common features of recorded measurement values, system information, coordinate information, and auxiliary metadata. However, the structure and complexity of data varies widely by method, instrumentation, acquisition design, and the specific measurement modalities (e.g., frequency-domain or time-domain electromagnetics). Due to this diversity, many different file formats and documentation protocols are in use across the geophysical community, none of which meet the FAIR (Findability, Accessibility, Interoperability, and Reuse) principles, include key metadata directly with the data in a single file, or organise data in an architecture that facilitates transferability between open-source software, web services, and geospatial systems. Establishing a community-supported open data standard that meets all these criteria for geophysical data formatting and organisation could greatly simplify the management and usability of these valuable datasets.

Airborne geophysical surveys are in particular need of standardisation, as these datasets exemplify the challenges discussed, with a multitude of systems, instrumentation, survey design, and data types. Furthermore, auxiliary information about the dataset and survey are often necessary for accurate processing and interpretation, and yet they are most often contained in separate supplementary files or contractor's reports and not directly accessible with the data values. This fundamental metadata includes information on the survey equipment, spatial positioning, timing, as well as details about acquisition parameters, instrument characteristics, and post-processing details. Past efforts to standardise airborne data formats include the national geophysical database (GERDA) format developed by the Geological Survey of Denmark and Greenland (GEUS) (Møller et al. 2009) and the Australian Society of Exploration Geophysicists (ASEG) General Data Format (ASEG-GDF2) (Dampney, Pilkington, and Pratt 1985; Pratt 2003). Both formats have advantages; GERDA uses a well-organized structured relational database, while ASEG-GDF2 is an open ASCII-based data structure for general point and line data with accompanying metadata files. However, neither meet all the criteria outlined above (open, transferable, self-describing). Additionally, gridded data and products often accompany airborne datasets and come in many binary and ASCII raster formats (e.g., TIF/GeoTIFF, ARC/INFO, GXF, Geosoft GRD, Surfer GRD, etc.); some are compatible with open software tools while others are proprietary formats that require paid software subscriptions.

As demand for and usage of airborne surveys continue to grow, an open, communal data standard is needed to handle the complexity of these datasets while ensuring maximum accessibility and interoperability. To this end, we present the newly developed Geophysical Survey (GS) data standard based on the Network Common Data Form (NetCDF) file format and the Climate and Forecast (CF) metadata convention (Unidata 2023; Eaton et al., 2022), along with the GSPy Python toolbox to facilitate creation and handling of GS standardised files.

METHOD AND RESULTS

In James, Foks, and Minsley (2022), we first introduced the GS data model and GSPy software tool with the primary goals of assimilating geophysical data from a variety of file formats, geometries, and geophysical methods into a common and open data structure that can be broadly shared and utilised. We chose

the NetCDF file format as the foundation for the GS data model due to the advantages NetCDF offers for 1) efficient metadata documentation attached to datasets, 2) joint storage of related datasets, 3) space-saving binary files with additional packing and compression options, 4) scalability for large-scale computing, and 5) accessibility and transferability to other software and web services. NetCDF was first established in 1989, but Unidata continues to provide development and support for newer NetCDF versions and related software (Unidata 2023), with the latest version (NetCDF-4) built on the HDF5 (Hierarchical Data Format) storage layer (Rew et al. 2006). As such, use and support of NetCDF is steadily increasing, especially as datasets are becoming larger and more complex, e.g., "big data" approaches (Ramapriyan and Leonard 2021; Sun et al. 2022).

GS Data Standard

In the GS data model, geophysical data, metadata, and survey information are stored within a single, self-describing, NetCDF file (Figure 1). Multiple related datasets (such as raw data, processed data, and derived models and products) are attached to a survey as separate groups within a hierarchical structure. Each file contains a root *Survey* group containing key metadata information about the survey and enclosed datasets (i.e., the who, what, where, why, and when). All data groups are attached to the *Survey* group and are categorised by the nature and geometry of the values to ease data handling. The *Tabular* data group contains unstructured data, such as scattered points or lists of values, i.e., airborne data collected along flight-lines. Conversely, the *Raster* group contains structured, i.e., gridded data. Multiple datasets attached to *Tabular* and *Raster* groups are indexed (e.g., /survey/tabular/0 and /survey/tabular/1) (Figure 1). Metadata is attached as general attributes to each group, as well as directly to individual dimensions, coordinates, and data variables. The GS standard follows the Climate and Forecast (CF) Metadata Conventions (Eaton et al. 2022) to ensure maximum portability, but also adds custom metadata components specific to the needs of geophysical datasets. Lastly, all groups share a "spatial_ref" coordinate variable defining the coordinate reference system of the data that allows datasets to be accurately visualized within geospatial software (e.g., QGIS or ArcPro).

GSPy: Python toolbox

The open-source Python package, GSPy, serves as a basic toolkit to build, explore, and export GS-standardised datasets (Foks, James, and Minsley 2022). The extensive Xarray Python package provides the primary architecture of DataArrays and Datasets upon which all GS groups are constructed (Hoyer and Hamman 2017). Each individual data variable, or *Survey* metadata component, form a DataArray, which is a labelled, multi-dimensional array containing 1) "data": a multi-dimensional array of data values, 2) "coords": a dictionary of the data coordinates, 3) "dims": the dimensions for each axis of the data array, and 4) "attrs": an attribute dictionary of key metadata (e.g., names, units, null values) (Figure 1). Variables are combined into Xarray Datasets, which have dimensions and coordinates that reflect those of the DataArrays, as well as metadata attributes that describe the collection. In the GS structure, each group (*Survey*, all *Tabular* and *Raster* groups), are individual Xarray Datasets. Since the *Survey* group is strictly metadata, its data variables (DataArrays) only contain attributes (no numerical data, coordinates, or dimensions).

The current GSPy functionality focuses on data conversion, with methods to read multiple input data formats (CSV, ASEG-GDF2, and GeoTIFF) and output a GS-structured NetCDF file. Metadata is passed to GSPy through user-prepared JSON files. The Survey group is created directly from its associated JSON file, whereas each data group is passed both a dataset-specific JSON file (containing the dataset attributes, variable metadata, and higher dimensions) and all associated data files to be combined into distinct Xarray Datasets. The *Survey* group's method "write_netcdf" exports the *Survey* to a single NetCDF file along with all attached datasets as indexed groups within their respective category (*Tabular* or *Raster*) beneath the *Survey* group following the GS hierarchy (Figure 1). In the example dataset presented in James, Foks, and Minsley (2022), eight input data files (four tabular CSV files and four raster GeoTIFF files) totalling 3.47 GB on disk were combined into a single, 1.93 GB, GS-standardized NetCDF file resulting in a 44% reduction in file size. The GSPy package, documentation, and example codes and datasets can be found at https://doi.org/10.5066/P9XNQVGQ, (Foks, James, and Minsley 2022). The GSPy package is intended to facilitate implementation of the GS data standard but is not required if users have other approaches to generate GS-standardised files.

CONCLUSIONS

To address the pressing need for a community-supported geophysical data standard, we developed the GS standard and accompanying GSPy open-source Python package to meet the goals of 1) defining an open-source format satisfying the requirements of FAIR data publication standards, 2) storing multiple related, self-described datasets together in a clear, standardised hierarchical structure, 3) implementing detailed documentation of dataset- and variable-specific attributes directly attached to the digital data, ensuring dataset integrity, longevity, and interoperability, 4) defining dimensions and coordinates, along with a coordinate reference system for accurate visualisation and representation, and 5) using a format that is transferable between operating systems, open-source computational software, web services, and geospatial systems.

Adoption of the GS standard for airborne geophysical data fills a particular need for an open-source, community-wide standard that ensures accurate archival of critical metadata jointly with digital datasets. Moreover, establishment of a NetCDF-based open data standard for a broad range of geophysical survey types can greatly improve how these complex datasets are shared and utilised, making the data more accessible to a broader science community and the public. The concepts and structures implemented in the GS standard are purposefully general (i.e., *Survey*, *Tabular*, *Raster* groups) to accommodate many different types of data that can be described by these broad categories. The current functionality supported by GSPy v0.1.0 is limited; however, by developing the standard and package as open source, we aim to leverage the broad geophysical community to contribute to the continued development of robust data standard requirements and tools to facilitate their use.

ACKNOWLEDGMENTS

This work was jointly supported by the USGS Water Availability and Use Science Program and the USGS Mineral Resources Program. Any use of trade, firm, or product names is for descriptive purposes only and does not imply endorsement by the U.S. Government.

REFERENCES

Dampney, C.N.G., Pilkington, G., and D.A. Pratt, 1985. ASEG-GDF: The ASEG Standard for Digital Transfer of Geophysical Data. *Exploration Geophysics* 16 (1): 123–38. https://doi.org/https://doi.org/10.1071/EG985123.

Eaton, B., Gregory, J., Drach, B., Taylor, K., Hankin, S., Blower, J., Caron, J., et al., 2022. NetCDF Climate and Forecast (CF) Metadata Conventions Version 1.11. Version. https://cfconventions.org/cf-conventions/cf-conventions.html.

Foks, N.L., James, S.R., and B.J. Minsley, 2022. GSPy: Geophysical Data Standard in Python. *U.S. Geological Survey Software Release*. https://doi.org/https://doi.org/10.5066/P9XNQVGQ.

Hoyer, S., and J. Hamman, 2017. Xarray: ND Labeled Arrays and Datasets in Python. *Journal of Open Research Software* 5 (1). https://doi.org/http://doi.org/10.5334/jors.148.

James, S.R., N.L. Foks, and B.J. Minsley, 2022. GSPy: A New Toolbox and Data Standard for Geophysical Datasets. *Frontiers in Earth Science* 10:907614. https://doi.org/10.3389/feart.2022.907614.

Møller, I., Søndergaard, V.H., Jørgensen, F., Auken, E., and A.V. Christiansen, 2009. Integrated Management and Utilization of Hydrogeophysical Data on a National Scale. *Near Surface Geophysics* 7 (5–6): 647–59. https://doi.org/https://doi.org/10.3997/1873-0604.2009031.

Pratt, D.A., 2003. ASEG-GDF2 A Standard for Point Located Data Exchange. *Australian Society of Exploration Geophysicists* 4 (0): 1–34. https://www.aseg.org.au/sites/default/files/pdf/ASEG-GDF2-REV4.pdf.

Ramapriyan, H.K., and P.J.T. Leonard, 2021. Data Product Development Guide (DPDG) for Data Producers Version 1.1. *NASA Earth Science Data and Information System Standards Office*. https://doi.org/https://doi.org/10.5067/DOC/ESO/RFC-041VERSION1.

Rew, R., Hartnett, E., and J. Caron, 2006. NetCDF-4: Software Implementing an Enhanced Data Model for the Geosciences. In *22nd International Conference on Interactive Information Processing Systems for Meteorology, Oceanograph, and Hydrology*. Vol. 6.

Sun, Z., Sandoval, L., Crystal-Ornelas, R., Mousavi, S.M., Wang, J., Lin, C., Cristea, N. et al., 2022. A Review of Earth Artificial Intelligence. *Computers and Geosciences* 159. https://doi.org/10.1016/J.CAGEO.2022.105034.

Unidata, 2023. Network Common Data Form (NetCDF) Version 4.9.1. *Boulder, CO: UCAR/Unidata Program Center*. https://doi.org/https://doi.org/10.5065/D6H70CW6.

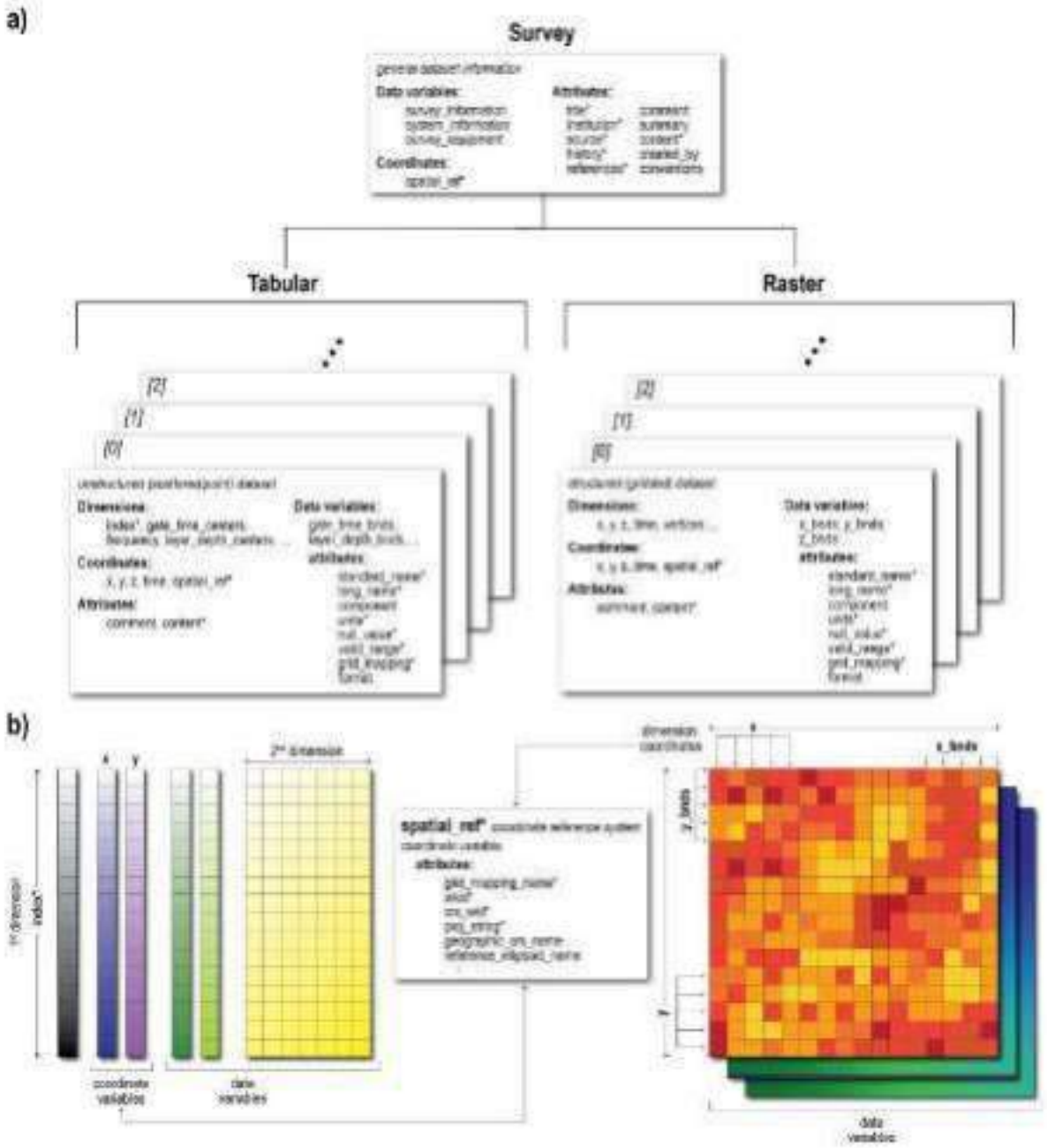

Figure 1. Geophysical Survey (GS) data standard. (a) Datasets are structured into a hierarchy composed of three fundamental groups. The *Survey* group is located at the highest level and contains general metadata about the dataset. Data groups are attached to the *Survey* and separated by geometry into either *Tabular* datasets (unstructured (scattered), such as from CSV files) or *Raster* datasets (structured (gridded), such as from GeoTIFF files). Datasets are indexed within their respective group type, and each contains general and variable-specific attributes, defined dimensions, and coordinates. (b) *Tabular* data have, at minimum, an index dimension representing individual measurements. Additional dimensions for data variables are supported, such as gate times, frequencies, or model layer depths. The x and y coordinate variables (of dimension index) provide spatial reference for the measurement locations. In *Raster* datasets, the coordinates are also the dimensions of the data. For all datasets, the coordinate variable "spatial_ref" is required and contains key elements defining the coordinate reference system and allowing the NetCDF file to be accurately displayed in geospatial software. All required components and attributes are noted with a * marker.

Combined ground-UAV TDEM survey over gold prospect in Baikal-Patom Highlands (eastern Russia) with detection of AIP effect.

Vladislav Kaminski
ISTU
Lermontova 89, Irkutsk, Russia 66407
vkaminski@geo.istu.edu

Yuri Davydenko
ISTU
,Lermontova 89, Irkutsk, , Russia 664074
dya@gelios-geo.com

Sergey Bukhalov
ISTU
Lermontova 89, Irkutsk, , Russia 664074
sbukhalov@geo.istu.edu

Ivan Goryachev
ISTU
Lermontova 89, Irkutsk, Russia 664074
ivan.goryachev@geo.istu.edu

SUMMARY

The study is describing a combined ground-UAV TDEM survey, carried out over one of the gold prospects in Eastern Russia. A drone-mounted receiver was used to measure TDEM response from ground, excited by a transient field powered line transmitter. Effect of Airborne Induced Polarization was detected in the data, so the collected data were further inverted using a Cole-Cole model approximation in order to extract the four physical parameters, which were then mapped and interpreted in an attempt to delineate mineral exploration targets.

Key words: TDEM surveys, UAV, AIP, mineral exploration, inversion, interpretation

INTRODUCTION

Study area is situated in Baikal-Patom highlands, Eastern Russia (NE part of Irkutsk region, Figure 1). From geological standpoint, the area under study is a part of Bodaibo synclinorium, known to host a black-schist pack rich in sulphides, which also include notable Au deposits and large number of Au occurrences (Figure 2, see page 4).

Figure 1. Location of the study area in NE part of Irkutsk region, Russia.

The prospect was a subject to combined ground-UAV TDEM survey aimed at delineating new potential exploration targets on the flanks of a known gold deposit (Figure 3).

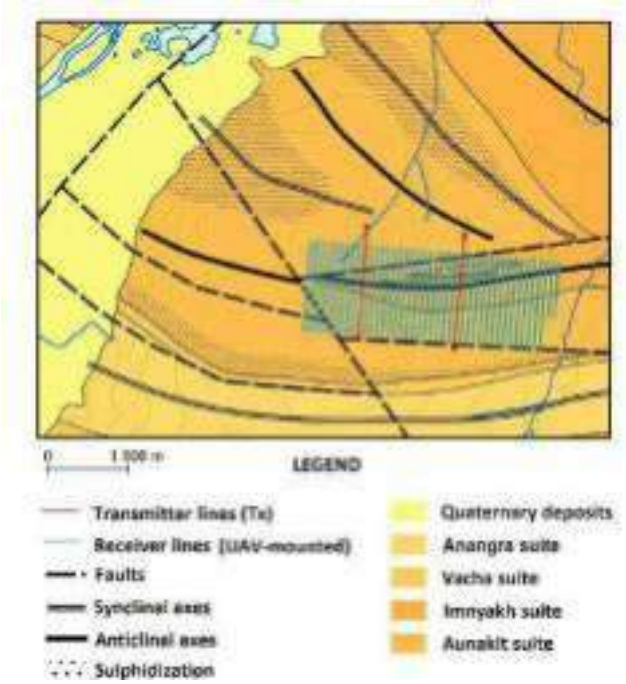

Figure 3. Geological setting and UAV flight lines over expected gold prospect.

The geological units shown in Figure 3 include mainly rifean deposits (Imnyakh, Aunakit, Vacha and Anangra suites), overlain by quaternary deposits (Tarasova et al., 2020; Chugaev et al., 2022). Imnyakh suite consists of limy shists with interbedded marbles, sandstones and limestones. Aunakit suite consists of metasandstones and carboniferous schists. Vacha suite consists of micaceous schists, clays and sandstones. All except for Imnyakh suies are hosting interbeds of carboniferous schists, which are highly conductive, as well as highly magnetic. Aunakit suite hosts intensive sulphide mineralization with rocks folded heavily at steep angles reaching 20 – 60°. The thickness of quaternary overburden does not exceed 10-20 m over the area under study.

METHOD AND RESULTS

The survey was carried out using the combined ground/UAV-TDEM technology, which employed a 1.4 km long ground transmitter (Tx) lines separated at 1.2 km between one another and a PDI-50 receiver loop with Mars 2.0.2 receiver device mounted on the UAV carrier at average 40-60 m altitude above the terrain (depending on the tree cover). The UAV used for the survey was an in-house made electric multirotor electrical apparatus, capable of carrying 4 kg of maximum load for approximately 15 minutes. The load consisted of receiver sensor and supplementary electronics with a total mass of approximately 4.5 kg (Figure 4).

Figure 4. The UAV-mounted PDI-50 TDEM receiver.

The flight line separation was 75 m. The Tx lines were powered by 1.35 to 1.85 A current operating at at 10 ms on-time and off-time intervals with a standard boxcar waveform. Off-time measurement intervals are presented in Table 1.

Gate	Start time (ms)	End time (ms)	Centre (ms)
1	0.01000	0.01697	0.01349
2	0.01587	0.02400	0.01994
3	0.02245	0.03394	0.02820
4	0.03175	0.03810	0.03493
5	0.03564	0.04276	0.03920
6	0.04000	0.05388	0.04694
7	0.05040	0.06048	0.05544
8	0.05657	0.06788	0.06223
9	0.06350	0.07620	0.06985
10	0.07127	0.08553	0.07840
11	0.08000	0.09600	0.08800
12	0.08980	0.10776	0.09878
13	0.10079	0.12095	0.11087
14	0.11314	0.13576	0.12445
15	0.12699	0.15239	0.13969
16	0.14254	0.17105	0.15680
17	0.16000	0.19200	0.17600
18	0.17959	0.21551	0.19755
19	0.20159	0.24190	0.22175
20	0.22627	0.27153	0.24890
21	0.25398	0.30478	0.27938
22	0.28509	0.34211	0.31360

23	0.32000	0.38400	0.35200
24	0.35919	0.43103	0.39511
25	0.40317	0.48381	0.44349
26	0.45255	0.54306	0.49781
27	0.50797	0.60956	0.55877
28	0.57018	0.68421	0.62720
29	0.64000	0.76800	0.70400
30	0.71838	0.86205	0.79022
31	0.80635	0.96762	0.88699
32	0.90510	1.08612	0.99561
33	1.01594	1.21912	1.11753
34	1.14035	1.36842	1.25439
35	1.28000	1.53600	1.40800
36	1.43675	1.72410	1.58043
37	1.61270	1.93524	1.77397
38	1.81019	2.17223	1.99121

Table 1. Measurement time intervals. All times are referenced to Tx current shutdown.

The measured data were processed and recorded into a database as transients, which were later subject to inversion using MARS1D software (Pesterev, 2012; Parshin et al., 2021), modelling the data dispersive electrical resistivity model (Cole-Cole parameter approach). Some transients are strongly affected by the Airborne Induced Polarization (AIP effect) with presence of negative values of measured dB/dt (EMF data). Figures 5 and 6 show examples of AIP affected transient modelling attempts using fixed and variable Cole-Cole parameters.

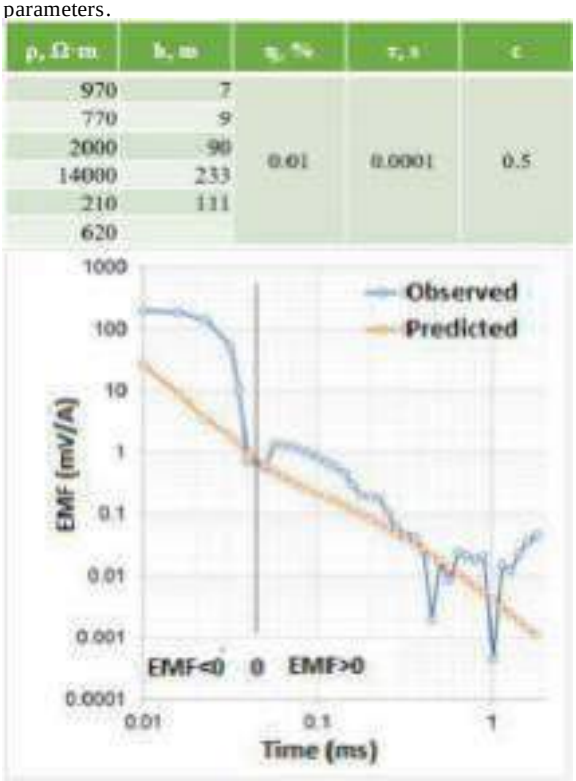

Figure 5. Inversion of a selected transient using fixed Cole-Cole parameters.

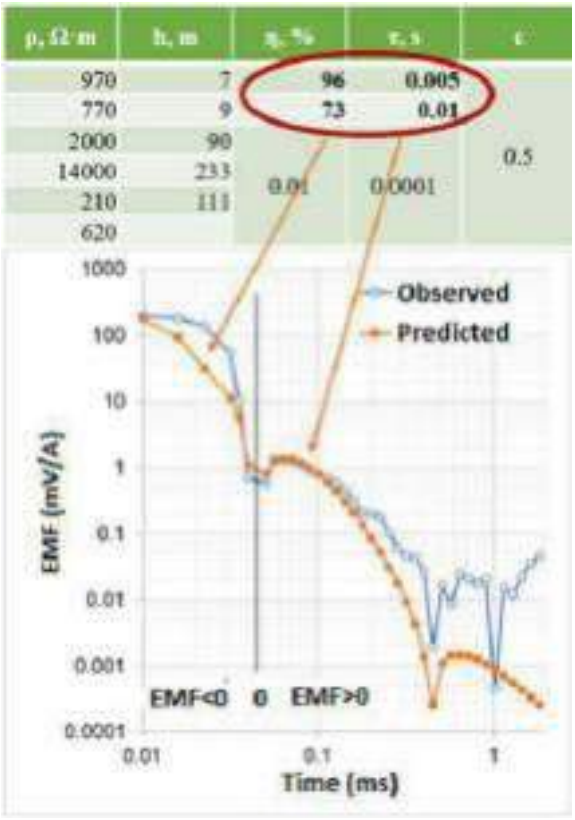

Figure 6. Inversion of a selected transient using varying Cole-Cole parameters.

.

As it is suggested by comparing figures 5 and 6, fixing some Cole-Cole parameters results in poor transient fit, especially for negative recorded voltages.

Eventually all TDEM data were inverted using the Cole-Cole model with simultaneous recovery of four Cole-Cole parameters. In current abstract we focus only on recovered resistivities and chargeabilities presented for further reference. Figure 7 shows a 3D stitched model of 1D electrical resistivity recovered from Cole-Cole inverse modelling.

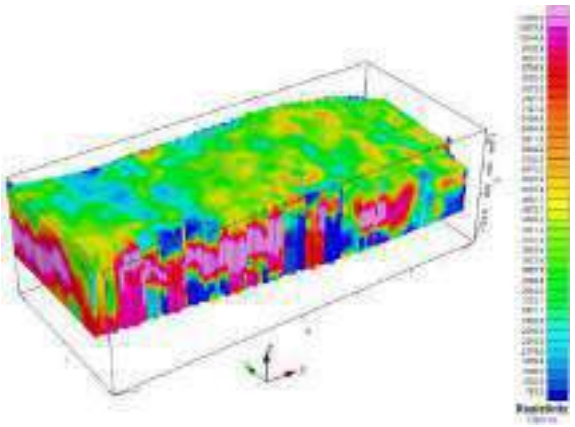

Figure 7. Electrical resistivity 3D stitched model.

The resistivity and chargeability parameters, recovered by the inversion were further used to delineate new potential prospecting areas. Figure 8 shows cross-sections of profile 12 with outlined low resistivity and high chargeability targets. It should be noted that the recovered chargeabilities show lower sensitivity to deeper objects and chargeable property recovery by means of geophysical inversion using the Cole-Cole model is mainly distributed in the top 50-70 m from surface (Figure 8).

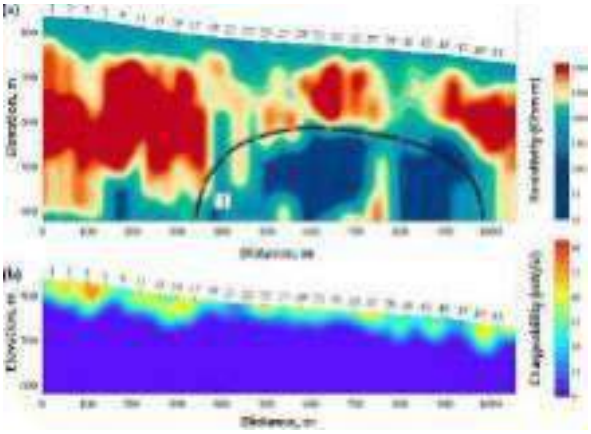

Figure 8. Cole-Cole inversion results for data recorded over profile 12. (a): Electrical resistivity. (b): Chargeability.

The anomaly example shown in Figure 8 can be followed on several neighbouring profiles, which makes it a valid exploration target. Figure 9 shows the anomaly selection in resistivity section sliced at 500 m absolute elevation.

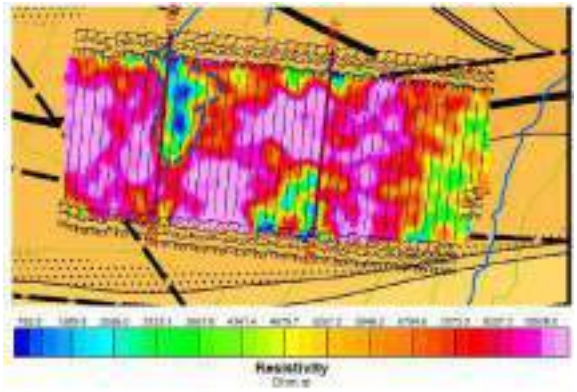

Figure 9. Electrical resistivity section with interpreted conductive anomaly (dashed line).

There are no chargeability anomalies, which can be followed to depths below 100 m below the surface (due to sensitivity issues), however there are two such anomalies interpreted in the near-surface (Figure 10) with no conductive response, which however still makes them valid exploration targets, as they are in the bedrock and may be associated with low-grade disseminated sulphidization areas. These two anomalies have been recommended for ground geochemical verification and the measured geochemical data are currently being processed.

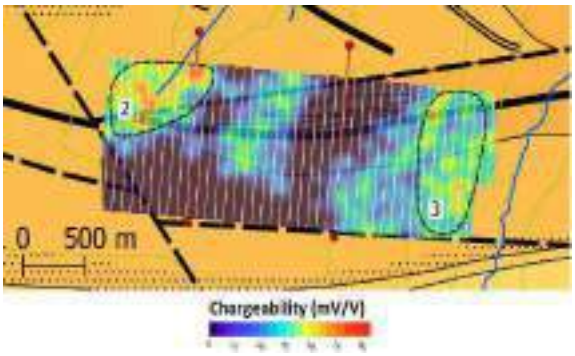

Figure 10. Chargeability depth section with interpreted conductive anomaly.

CONCLUSIONS

In conclusion it must be stated that this despite multiple combined ground-UAV surveys flown to date with the described system, this is the first example of rather strong recorded Induced Polarization (AIP) effect. Inversion and interpretation of this effect not only allows more accurate recovery of electrical resistivities (Figures 7 – 9), but also allows recovery of chargeabilities from UAV TDEM data, which may be useful in delineating valid targets for follow-up geochemical/exploration program.

ACKNOWLEDGEMENTS

The research was supported by the Russian Science Foundation grant No. 20-67-47037 "Methodological and software for processing large amounts of data from electromagnetic soundings, gravity surveying and UAV magnetic exploration based on a comprehensive solution of three dimensional inverse problems for ore delineation by geophysics".

REFERENCES

Chugaev, A.V., Budyak, A.E., Larionova, Y.O., Chernyshev, I.V., Travin, A.V., Tarasova Y..I., Gareev, B.I., Batalin, G.A., Rassokhina, I.V., Oleinikova, T.I., 2022. 40Ar-39Ar and Rb-Sr age constraints on the formation of Sukhoi-Log-style orogenic gold deposits of the Bodaibo District. *Ore Geology Reviews*. 144, 104855. DOI: 0.1016/j.oregeorev.2022.104855.

Parshin, A.V., Bashkeev, A.S., Davydenko, Y.A., Iakovlev, S.V., Buhalov, S.V., Persova, M.G., Tokareva, M.G., 2021. Lightweight Unmanned Aerial System for Time-Domain Electromagnetic Prospecting—The Next Stage in Applied UAV-Geophysics. *Applied Sciences* 11(5): 2060 DOI:10.3390/app11052060.

Pesterev, I. Y., 2012. *1D-inversion software program* (Certificate of Registration for Application Software No. 2012660743, Russian Federation ; rightholder: LLC "Gelios"). Federal Service for Intellectual Property of the Russian Federation (Rospatent)

Tarasova, Y..I., Budyak, A.E., Chugaev, A.V., Goryachev, N.A., Tauson, V.L., Skuzovatov, S.Yu., Reutsky, V.N., Abramova, V.D., Gareev, B.I., Bryukhanova, N.N., Parshin, A.V., 2020. Mineralogical and isotope-geochemical (δ13C, δ34S and Pb-Pb) characteristics of the Krasniy gold mine (Baikal-Patom Highlands): constraining ore-forming mechanisms and the model for Sukhoi Log-type deposits. *Ore Geology Reviews*. 119. 118-136. DOI: 10.1016/j.oregeorev.2020.103365.

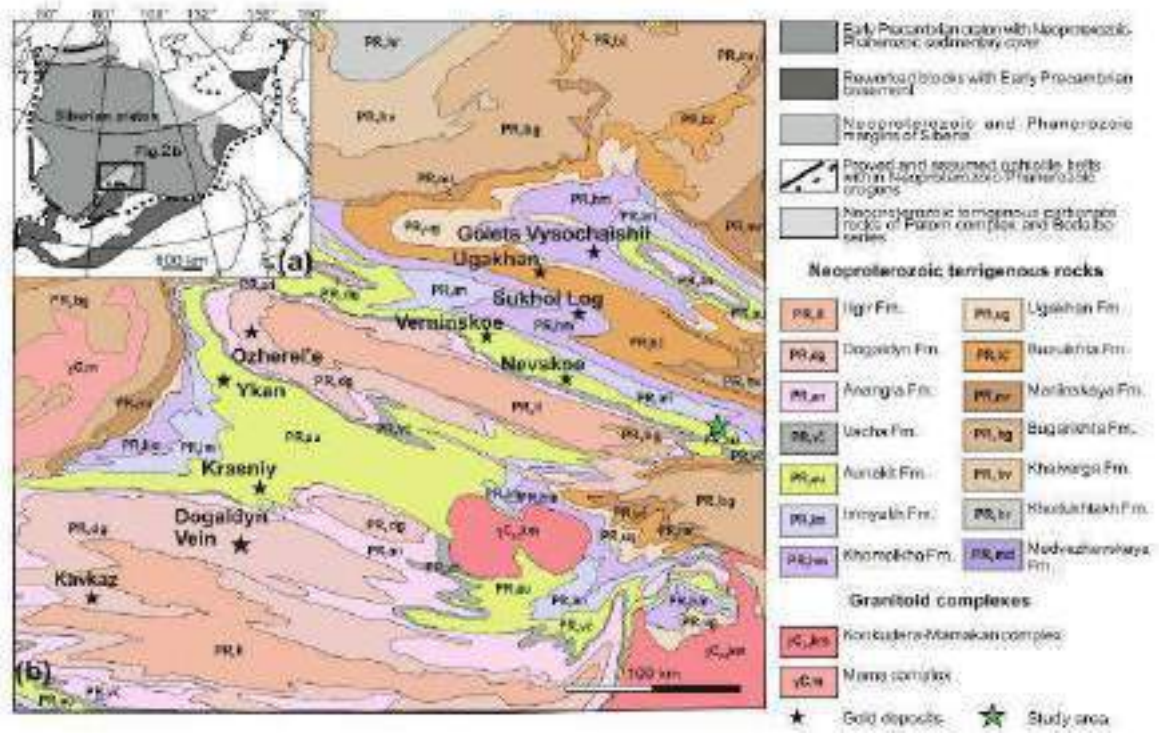

Figure 2. Geological position of study area (after Tarasova et al., 2020)

Analysis of the self-interference model and compensation methods in airborne electromagnetics

Evgeny Karshakov
Institute of Control Sciences
65, Profsoyuznaya Street,
Moscow, 117997, Russia
karshakov@ipu.ru

Ekaterina Tretyakova
Institute of Control Sciences
65, Profsoyuznaya Street,
Moscow, 117997, Russia
ekaterina_tretikova@mail.ru

Dmitry Kaplun
Aerogeophysica
19, Pohodniy driveway,
Moscow,125373, Russia
kaplun@aerogeo.ru

SUMMARY

We compare various compensation methods for the EQUATOR system and for several modifications of the airborne electromagnetic system EM4H: with a transmitter loop attached to the fuselage of Mi-8 helicopter, with a loop attached to the fuselage of An-3 aircraft, and with a loop towed by Eurocopter AS350B3. We consider two ways of the transmitter signals interference modeling: in the form of a stationary systematic component of the measurements and in the form of a stationary field vector rigidly connected to the transmitter. To implement the second approach, the EM4H and the EQUATOR use two additional dipoles to determine the relative location of the transmitter and the receiver. At high altitude, in the absence of a response from the ground, the following statistical parameters of the signals remaining after interference compensation were analyzed: the standard deviation and the difference between the minimum and the maximum values.

Key words: compensation; relative electromagnetic positioning; magnetic dipole; EM4H; EQUATOR

INTRODUCTION

Airborne electromagnetics (AEM) is one of the most popular geophysical methods used in mineral exploration around the world (Legault, 2015). Their difference lies both in the design of the transmitter and the receiver, and in the method of compensating for various interferences. Sensitivity of measuring equipment is constantly growing. Hence, it is necessary to carry out an analysis of the correspondence between data processing methods and the level of sensitivity. In this work, we determine the degree of adequacy of existing models and methods for compensating for existing interference to the modern level of equipment sensitivity.

The main source of interference are uncontrolled eddy currents that occur in the conductive elements of the carrying frame. In the case when the field sources are installed on an airplane or a helicopter, these currents can create a field that is about 1% of the primary field. This significantly complicates the further separation of the secondary field from the ground against the background of the primary one (Vovenko *et al*, 2013). The simplest method is to take into account the interference field as a constant. This method is unreliable, since the field of eddy currents depends on the changing relative position of the transmitter and the receiver of the field. The more complicated way is based on the changing geometry of the installation. To determine the relative position of the receiver and the alternating magnetic field transmitter, we solve the inverse problem. It consists in determining the parameters of the dipole according to the parameters of the field that it creates (Smith, 2001; Pavlov *et al*, 2010; Tkhorenko *et al*, 2015). The analysis was carried out using the data of the EM4H (Vovenko *et al*, 2013) and the EQUATOR (Moilanen *et al*, 2013) systems widely used in modern surveys. Being time domain system, EQUATOR also provides frequency domain data for analysis.

FORMULATION OF THE PROBLEM

Airborne electromagnetic system includes a transmitter and a receiver (Figure. 1). With the help of the former, the primary field is generated. The latter, in the case of systems, considered in the work, is located in a towed bird and registers the parameters of the secondary field. When measuring an alternating field, the eddy current field must be taken into account. It occurs in conductive structural elements of the transmitter loop (ΔM). This influence is the cause of interference ΔH, which in practice is much larger than the amplitude of the anomalous component of the field. The vector ΔM is assumed to be constant, allowing for the geometry stability of the conductive parts of the aircraft or other elements on which the loop is mounted. The vector ΔH is not constant, since the relative position of the transmitter and the receiver changes.

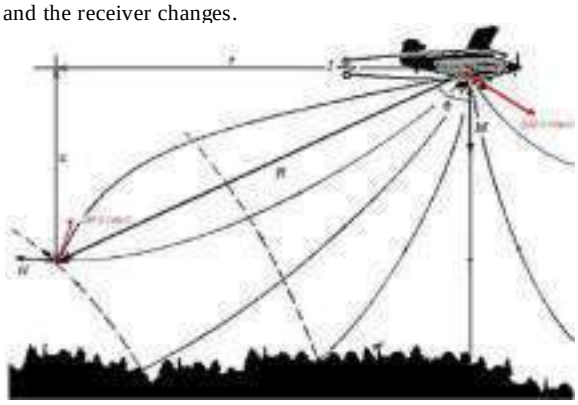

Figure 1. Airborne electromagnetic system EM4H. R - transmitter-receiver radius vector; M - vector of the magnetic moment of the exciting dipole; ΔM - vector of the magnetic moment of the eddy current field; H - magnetic field vector of the exciting dipole; ΔH – eddy current field vector.

Obviously, the effect of interference must be taken into account. For this to be done, a compensation is carried out, the essence of which is to move the system to a high altitude (700 m), where the responses from the ground can be neglected. The parameters of the eddy-current field are defined there. Next, corrections are introduced into the field measurements at the height of the survey.

We have various approaches to the compensation method. If the receiver makes small movements relative to the transmitter, we can assume that the eddy-current field strength vector is constant in the receiver coordinate system. This method, based on the subtraction of the constant component, is used in many modern systems and is called "nulling".

Another approach is based on the variability of the ΔH vector. For this an analysis of the relative spatial and angular position of the transmitter and the receiver is carried out (Vovenko *et al*, 2013).

COMPENSATION WITH REFERENCE TO THE CHANGING RELATIVE POSITION OF THE TRANSMITTER AND THE RECEIVER

In this paper, we consider electromagnetic systems, which are systems with a controlled source. Usually we can represent the primary field a field of a dipole (Smith, 2001). Pavlov *et al* (2010) and Tkhorenko *et al* (2015) wrote it in a matrix form. Let us rewrite the relations for the field in the form

$$H = \frac{1}{4\pi|R|^3}\left(3\frac{RR^T}{|R|^2} - I\right)M = \Omega(R)M \quad (1),$$

where H is the magnetic field vector, R is the position vector of the receiver relative to the transmitter, M is the vector of the magnetic moment of the dipole, I is the 3×3 identity matrix.

According to Vovenko *et al* (2013), the relation between the measured field, the generated moment, and the relative position of the transmitter and the receiver was derived. It is represented by the matrix $\Omega(R)$, which is absolutely the same for the dependence of ΔH on ΔM:

$$\Delta H = \Omega(R)\Delta M \quad (2).$$

Case with 2 additional dipoles

It is proposed to introduce two additional dipoles with moments M_1 and M_2. With their help, the magnetic moment vector of the eddy-current field ΔM can be represented as a linear combination of known vectors:

$$\Delta M = k_0 M + k_1 M_1 + k_2 M_2, k_j \in R \quad (3).$$

Applying (2) for (3), we get the same representation of the eddy-current field vector, where the coefficients will be the same as in expression (3):

$$\Delta H = k_0 H + k_1 H_1 + k_2 H_2 \quad (4).$$

The compensation step allows to determine the coefficients k_0, k_1, k_2 by the least square method. We minimize the quadrature response component and bring the in-phase response component to the same vector at all operating frequencies of the primaty field (the main sounding dipole usually excites several harmonics).

Case with 1 additional dipole

We have asked ourselves if it is possible to solve the compensation problem using only one additional dipole. Barabanova and Barabanov (2021) noted that there is a solution. Namely, the authors proposed an algorithm for solving the problem of electromagnetic positioning using the field of two dipoles. As a result, the following nonlinear expressions can be derived:

$$H'_2 = F_2(H, H_1),\ H'_1 = F_1(H, H_2) \quad (5).$$

That is, we can substitute the true dipole with a calculated vector, for example, through the vector product of two available dipoles:

$$H'_2 = \Omega(R)(M \times M_1),\ H'_1 = \Omega(R)(M \times M_2) \quad (6).$$

Using (5), we can pass to a linear combination of the eddy-current field vector by substituting the obtained dependence into expression (4).

$$\Delta H = k_0 H + k_1 H_1 + k_2(F_2(H, H_1)) \quad (7),$$
$$\Delta H = k_0 H + k_1(F_1(H, H_2)) + k_2 H_2 \quad (8).$$

As we have mentioned, the receiver is moving with respect to transmitter, which affects the measurements obtained. It is also important that the value of the spatial displacement of the receiver and the transmitter during flight usually does not exceed 10 m. This observation gives a hope that dependence (5) can be linearized, while the accuracy of the linear approximation will be sufficient to perform the compensation. Then equations (7), (8) can be rewritten as:

$$\Delta H = p_{01} H + p_1 H_1 = p_{02} H + p_2 H_2 \quad (9).$$

Therefore, it is possible to use only one additional dipole M_1 or M_2. Further, we test this hypothesis on a series of dataset of the EQUATOR system and various modifications of the EM4H systems obtained during survey flights by Geotechnologies, Aerogeophysica and by Norilsk branch of A.P. Karpinsky Russian Geological Research Institute.

COMPARISON OF COMPENSATION METHODS

The comparison of various compensation methods for several modifications of the EM4H system was carried out: with a transmitter loop attached to the fuselage of Mi-8 helicopter, with a loop attached to the fuselage of An-3 aircraft, and with a loop towed by Eurocopter AS350B3. (Figure 2).

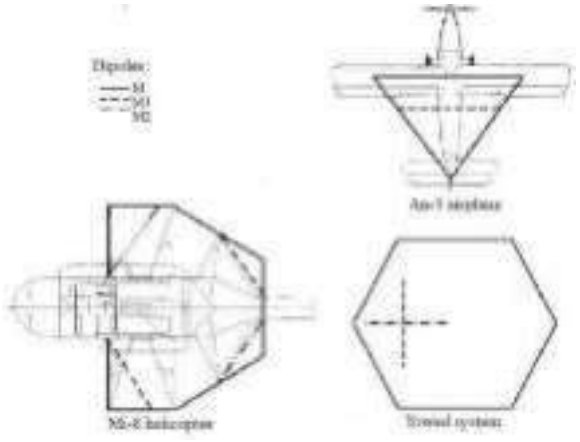

Figure 2. Loops installation for EM4H modifications.

The EQUATOR system now exists only in a towed version (Figure 3).

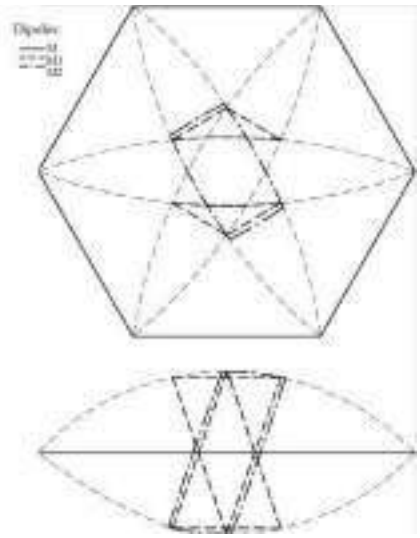

Figure 3. Loops installation for EQUATOR system.

At high altitude, in the absence of a response from the ground, we analized the following parameters of the signals remaining after interference compensation: the standard deviation and the difference between the minimum and the maximum values. The results of the comparison are shown in tables (Table 1, Table 2) and figures (Figure 4, Figure 5).

The tables contain the standard deviation (RMS) and peak-to-peak (max-min) for the quadrature component of the field. Under ideal conditions of no interference, it should be equal to zero. The values are shown after compensation of the receiver systematic offset (nulling, Figure 4B, Figure 5D, Figure 6D), also after determining the geometry parameters using the first (Figure 4A, Figure. 5B, Figure. 6B), the second (Figure 5C, Figure 6C) or two (Figure 5A, Figure 6A) additional dipoles. In the case when a fixed wing aircraft was used, the second additional dipole was absent (Figure. 4). One of the columns of the tables is the improvement factor, derived as the ratio of the corresponding values when using the nulling and the compensation using only the first additional dipole.

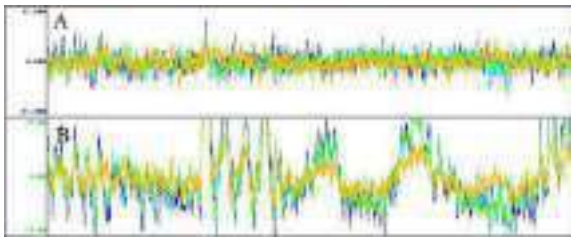

Figure 4. Quadrature component for the An-3 aircraft at 4 frequencies. A - after compensation, with using the measurements of the parameters of the additional dipole; B – nulling.

CONCLUSIONS

The best compensation result is given by an approach that takes into account the movement of the receiver relative to the field source. This is true for the EQUATOR and for all versions of the EM4H system.

For both towed systems when the transmitter is far from the helicopter fuselage, there is no eddy current field at low frequencies (77-540 Hz). However, at high frequencies (greater than 2 kHz) it is significant. Therefore, the installation geometry must be taken into account. This is also necessary for systems in the time domain, while high frequencies are associated with the early time gates.

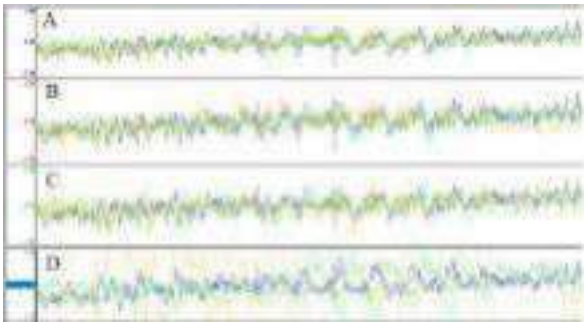

Figure 5. Quadrature component for the Mi-8 helicopter at 4 frequencies. A - after compensation, with using the measurements of the parameters of two additional dipoles; B - using the 1^{st} dipole, C - using the 2^{nd} dipole, D - nulling.

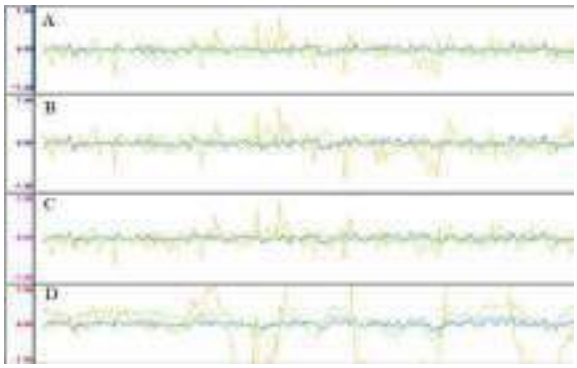

Figure 6. Quadrature component for the EQUATOR at 4 frequencies. A - after compensation, with using the measurements of the parameters of two additional dipoles; B - using the 1^{st} dipole, C - using the 2^{nd} dipole, D - nulling.

We use a linear model of the eddy current field as a function of the field of two dipoles. This is just as effective as using a full linear expansion in three dipoles. Therefore, it is possible to perform the receiver positioning described by Pavlov *et al.* (2010) with use of the field of two dipoles in a linear formulation.

REFERENCES

Barabanova, L.P. and O.O. Barabanov, 2021. Effective solution of the problem of electromagnetic positioning based on two-axial radiator. *Journal of Mathematical Sciences* 255, no. 5: 551-560.

Legault, J.M., 2015. Airborne electromagnetic systems – state of the art and future directions. *CSEG Recorder* 40, no. 6: 38-49.

Moilanen, J., Karshakov, E., and A. Volkovitsky, 2013. Time-domain helicopter EM System "Equator": resolution, sensitivity, universality. 13 th SAGA biennial and 6 th International AEM conference AEM-2013, Mpumalanga, South Africa, Expanded Abstracts: 1-4.

Smith, R.S., 2001. Tracking the transmitting-receiving offset in fixed-wing transient EM systems: methodology and application. *Exploration Geophysics* 32: 14-19.

Tkhorenko, M.Yu., Karshakov, E.V., Pavlov B.V., and A.V. Kozlov, 2015. Algorithm to position an object moving in the low-frequency electromagnetic field. *Automation and Remote Control* 76, № 11: 2033-2044.

Pavlov, B.V., Volkovitskii, A.K., and E.V. Karshakov , 2010. Low frequency electromagnetic system of relative navigation and orientation. *Gyroscopy and Navigation* 1: 201–208.

Vovenko, T., Moilanen, J., Volkovitskiy, A, and E. Karshakov, 2013. New abilities of quadrature EM systems. Papers of the 13th SAGA Biennial and 6th International AEM Conference, Mpumalanga, South Africa,Expanded Abstracts: 1-4.

Table 1. Statistics for various compensation methods at high frequencies (8 kHz – EM4H, 6kHz – EQUATOR).

	nulling	1st and 2nd dipoles	1st dipole	2nd dipole	improvement factor	
Airplane	4,53		2,17		2,1	RMS
	41,92		15,04		2,8	max-min
Helicopter Fixed	2,37	1,91	1,92	1,92	1,2	RMS
	14,97	13,01	12,76	13,16	1,2	max-min
Helicopter Towed	20,27	1,16	1,28	1,37	15,8	RMS
	92,88	8,14	8,10	9,34	11,5	max-min
EQUATOR	11,04	1,15	1,17	1,42	9,44	RMS
	53,47	9,59	10,08	10,75	5,30	max-min

Table 2.Statistics for various compensation methods at low frequencies (130 Hz – EM4H, 77 Hz – EQUATOR).

	nulling	1st and 2nd dipoles	1st dipole	2nd dipole	improvement factor	
Airplane	12,61		2,52		5,0	RMS
	121,53		21,42		5,7	max-min
HelicopterFixed	2,82	1,42	1,46	1,4	1,9	RMS
	14,18	8,42	8,29	8,62	1,7	max-min
HelicopterTowed	1,73	1,44	1,46	1,46	1,2	RMS
	10,70	10,09	9,65	9,16	1,1	max-min
EQUATOR	0,29	0,22	0,22	0,23	1,3	RMS
	1,84	1,56	1,59	1,71	1,1	max-min

Integration of airborne transient electromagnetic models with ground geophysics and borehole data for groundwater mapping in Hawkes Bay region, New Zealand

Richard Kellett* *GNS Science* *Lower Hutt, NZ* *r.kellett@gns.cri.nz*

Zara Rawlinson *GNS Science* *Wairakei, NZ* *z.rawlinson@gns.cri.nz*

Tusar Sahoo *GNS Science* *Lower Hutt, NZ* *t.sahoo@gns.cri.nz*

Angela Griffin *GNS Science* *Lower Hutt, NZ* *a.griffin@gns.cri.nz*

Maïwenn Herpe *GNS Science* *Wairakei, NZ* *m.herpe@gns.cri.nz*

Conny Tschritter *GNS Science* *Wairakei, NZ* *c.tschritter@gns.cri.nz*

Mark JF Lawrence *GNS Science* *Lower Hutt, NZ* *m.lawrence@gns.cri.nz*

Simon Harper *Hawkes Bay Regional Council* *Napier NZ* *s.harper@hbrc.govt.nz*

SUMMARY

As part of the Hawke's Bay 3D Aquifer Mapping Project (3DAMP), airborne electromagnetic data have been collected over several basins. The project was a three-year initiative (2019 – 2022) jointly funded by the Provincial Growth Fund (Kānoa Regional Economic Development & Investment Unit), Hawke's Bay Regional Council (HBRC) and GNS Science (GNS). The object of the study is to improve the hydrogeological model of the area using a resistivity model that extends to 300 m depth. The model was generated from an airborne TEM (SkyTEM) survey that covered the region at a line spacing of 170 – 250 m. A total of 7780 line-km was flown in a period of 4 weeks. Supporting data includes ground-based geophysical surveys (TEM, resistivity, and seismic reflection lines), and detailed geological data from a set of research boreholes. A total of 6800 boreholes exist in the catchments but the majority are less than 30 m deep. A set of 30 deeper boreholes across the area with more detailed geological information provide valuable control on the SkyTEM processing and modelling. The integration of a 3D model developed from the inversion of the SkyTEM data and ground geophysics data, displays the geometry of the fluvial systems (gravel), marine incursions (silt and clay), and complex faulting that affects the deposition of the sedimentary units. Work is ongoing to develop models of aquifer potential based on hydrogeological facies that will improve the understanding of the groundwater system.

Key words: Aquifers, SkyTEM, boreholes, groundwater, Hawkes Bay, New Zealand

INTRODUCTION

Groundwater is the focus of more research in New Zealand due to increasing demands on water for urban and agricultural development. Hawkes Bay is a region on the east coast of New Zealand that has a wide range of fruit, vegetable and wine production in addition to traditional farming. Additional water resources are needed to support the economic growth of region including the urban centres. The Hawkes Bay Regional Council (HBRC) has implemented a long-term plan to have better information and tools to make informed decisions on water use. Mapping the aquifers in more detail and providing subsurface geological data that can be used to improve the hydrogeological flow models.

Airborne electromagnetic mapping of the top 300 m of the subsurface over an area of 1940 km^2 was undertaken in 2020 as the main phase of geophysical investigations of the aquifer systems (Figure 1). The project follows on from several large aquifer mapping exercises undertaken over the period from 1970 to 2000 (Dravid and Brown 1997, Francis 2001). Borehole data, ground geophysics, and hydrogeological models from these earlier studies are incorporated in the current project. The processing of the SkyTEM data resulted in a dense array of one-dimensional resistivity models that were compared to the existing data and a revised 3D geological model has been produced for regions where the data are sufficiently dense. The ground-based DC resistivity, TEM, and seismic data show good correlation with the SkyTEM inversion results. The detailed lithological data from a series of research wells indicate that the SkyTEM has mapped the following targets :

1) Holocene river gravel formations (shallow aquifer)
2) Holocene marine sediments (Heretaunga only)
3) Deeper gravel fromations (Last Glacial Maximum and older)
4) Pliocene – Pleistocene limestone (bedrock)

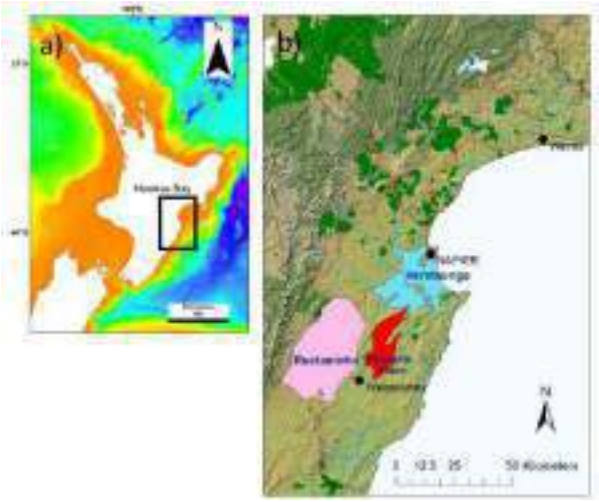

Figure 1. Location of the survey area on the eastern coast on a) North Island (NZ). The three areas are shown in b) Heretaunga, Ruataniwha, and Poukawa/Otane.

METHODOLOGY

The SkyTEM 312 is a helicopter deployed transient electromagnetic system which utilises a dual moment transmitter to provide a shallow focused transient curve (low moment) and a deep focused transient (high moment). The survey was undertaken by SkyTEM Australia. The transmitter is an octagonal loop suspended 30 m below the helicopter. The generator and receiver controller are suspended on the cable between the transmitter loop and the helicopter (Sorensen and Auken 2004). The receiver coils (horizontal and vertical) are mounted at the rear of the transmitter loop. The high moment signal is generated using a typical current of 110 A and 12 turns of the 342 m^2 transmitter loop (dipole moment is 451,000 Am^2). The low moment signal is generated using 2 turns of the loop and a smaller current of 6 A (dipole moment is 4100 Am^2). The high moment and low moment signals are interleaved with a repeat frequency of 25 Hz and 275 Hz respectively. The turn-off time of the low moment transmitter is 14 µs and the decay of the signal is measured using 27 gates over a duration of 1 ms. The high moment transient has 22 gates between 0.3 and 14 ms. By flying at 90 km/hr the transients are able to be stacked to improve signal to noise ratios, yet still yield a sounding every 17 – 25 m on the ground. The high moment data penetrate to depths of 300 m so there is significant overlap in the volume of the earth sampled at each measurement point.

The data were delivered to GNS Science in both raw format and Geosoft XYZ files. Rawlinson et al., (2021) describe the work undertaken within the AGS WorkBench to remove effects of the major sources of man-made noise (powerlines, roads, railway lines, and buildings). The Aarhus inversion algorithm (Auken et al., 2015) was used to produce a spatially constrained inversion of all of the data over each of the three study areas. The inversion was checked to ensure with the misfit was acceptable and model smoothness appropriate for both lateral and vertical changes in resistivity. Figure 2 shows the resistivity across a part of the survey area in the Heretaunga Plains, at a depth of 30 m below ground level.

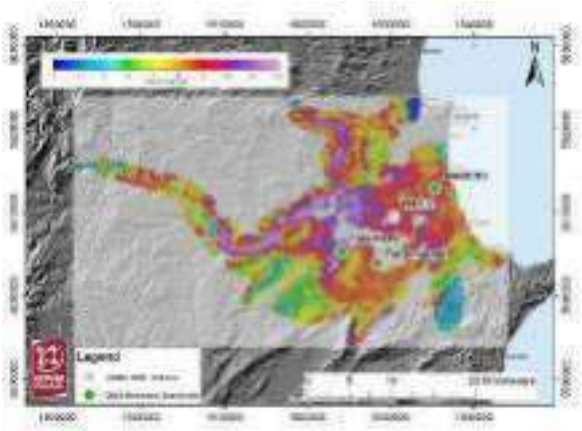

Figure 2. Average resistivity at a depth of 25-30 m below ground level. The digital elevation model and a selection of the research boreholes in Heretaunga are also shown.

BOREHOLE INFORMATION

The areas have a dense network of over 6800 water wells but the average depth of the wells is less than 35 m (Tschritter et al., 2021, 22). Each of the areas shown in Figure 1 have some existing hydrogeological models and subsurface geological data are available from research boreholes in the top 100 to 200 m. The current project included drilling three wells over 75 m deep with detailed geology and hydrogeological sampling. In the Heretaunga and Ruataniwha blocks additional deeper geological data are available from five petroleum exploration wells drilled between the 1970's and early 2000s. The research wells contained more detailed information on the lithologies, sediment ages, physical properties (density, grain-size, and natural gamma), and hydrogeological properties. Figure 3 shows a SkyTEM section through two key wells (Awatoto and Well 2) that illustrates the following :

1) The marine incursion during the Holocene produces a clay-rich layer that is seen as a shallow low resistivity layer in the SkyTEM models.
2) The Early Holocene and Late Pleistocene gravel sequence has a high resistivity.
3) The base of the gravel sequence is well imaged by the SkyTEM system and there may be a deeper aquifer present within the last interglacial or earlier Pleistocene glacial interval at 200 – 400 m depth.

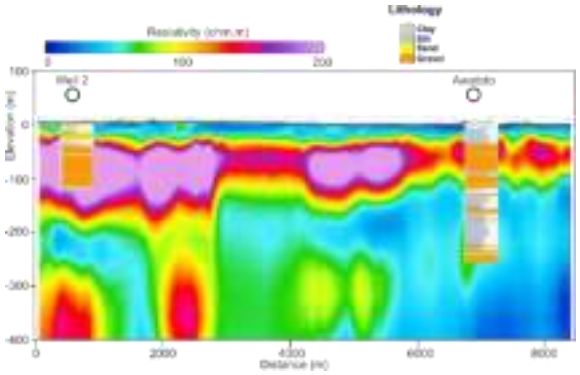

Figure 3. SkyTEM inversion models on a section through the Well 2 and Awatoto on the Heretaunga Plains (see Figure 2).

GROUND GEOPHYSICAL DATA AND INTERPRETATION

In the Heretaunga Plains, the older DC resistivity soundings (Risk 1974) have proved to be useful in supporting the interpretation of the SkyTEM data. Some of the soundings are in areas that have been covered by urban development and were not covered by the recent helicopter survey. The DC resistivity data are sensitive to the resistivity of the top 20 – 50 m and provide some independent control on the presence of high resistivity (>500 Ω.m) gravel deposits and thin low resistivity clay-rich zones. In more recent times and as part of the design phase of the SkyTEM survey, ground-based TEM data were collected in Heretaunga and Ruataniwha. The combination of Zonge TEM and NanoTEM soundings correlate well with the SkyTEM inversion models. The groundTEM models derived from sites at the research wells provide a link to the closest SkyTEM model that could be up to 500 m away based on the distribution of flight lines.

Seismic reflection data were collected as part of the petroleum exploration programs across all three areas. The seismic sections are useful for identifying the major boundaries between geological units. The Hawkes Bay region lies in the accretionary wedge of the Hikurangi subduction zone with thick Quaternary basins overlaying and incorporated into a complex fold and thrust belt that is composed of Tertiary limestone, sandstone and mudstone (Beanland et al., 1998). At the edges of the shallow basins and over some anticlinal structures within each basin, these consolidated units are within the depth of investigation of the SkyTEM system. The resistivity models reflect the changes in porosity and clay content of the bedrock (e.g. Figure 3).

Figure 4 shows a SkyTEM transect in the Ruataniwha block that crosses over a series of anticlines and synclines separated by thrust faults. Seismic reflections are produced by changes in the density and sonic velocity of the sediments. There is often a correlation between electrical resistivity and both density and velocity because of the dependence of all three properties on porosity. One limiting factor with the seismic reflection data is the poor resolution in the top 100 m due to the focus of the petroleum exploration data on deeper targets. However, the gravels that dominate the top 100 m of the unconsolidated section are apparent on the seismic as a zone of low reflectivity with a sharp base. This reflector marks the transition from high resistivity at surface to lower resistivity at depth in the SkyTEM data. The package of silt and sand, represented by low amplitude reflections and low resistivity, below the gravel unit is thicker in the synclines. The top of the Tertiary siltstone and limestone units is clearly seen in the seismic as a set of stronger and higher frequency reflections. The SkyTEM models show higher resistivity in these layers where they are thicker on the limbs of the anticlines.

CONCLUSIONS

The SkyTEM 312 system has proven to be a very effective tool in mapping a large area of Hawkes Bay (New Zealand) in support of groundwater aquifer mapping. Despite the area having several urban centres and extensive infrastructure associated with the horticultural industry, the survey produced a 3D resistivity model of the three areas surveyed with a higher level of detail than was previously known. Integrating the new SkyTEM inversion models with ground geophysical data and detailed borehole geology has helped provide some constraints on the extent of modern river gravel deposits, thick sequences of gravel laid down during the Quaternary glacial intervals, and marine incursions during the inter-glacial times that spread clay-rich sediments across coastal parts of the region. The Pliocene-Pleistocene limestone bedrock, that forms a potential deeper aquifer, was imaged on the edges of the basins. The seismic reflection data provide some regional context for the structure seen in the deeper parts of the SkyTEM inversion models. Work is ongoing to improve the transformation of the resistivity model into hydrogeological facies.

ACKNOWLEDGMENTS

This work has been funded jointly by Hawkes Bay Regional Council (HBRC) and its surrounding district councils, the Provincial Growth Fund, and Strategic Science Investment Funds from GNS Science. Rogier Westerhoff, Robert Reeves, Malcolm Arnot, and Thomas Brakenrig (GNS Science) supporting the data processing, interpretation, and field work. The team from SkyTEM Australia, Nikolaj Foged, Jesper B Pedersen and Pradip Maurya (Aarhus HGG), and Amanda Langley (ProjectHAUS) provided valuable input during the data acquisition and processing. Ollie Gibson (RDCL) supported the drilling and geophysical logging.

REFERENCES

Auken, E., A. V. Christiansen, C. Kirkegaard, G. Fiandaca, C. Schamper, A. A. Behroozmand, A. Binley, E. Nielsen, F. Effersø, N. B. Christensen et al. 2015. An overview of a highly versatile forward and stable inverse algorithm for airborne, ground-based and borehole electromagnetic and electric data. *Exploration Geophysics*. 46(3):223–235. doi:10.1071/EG13097.

Beanland, S., A. Melhuish, A. Nicol, and J. Ravens, 1998. Structure and deformational history of the inner forearc region, Hikurangi subduction margin, New Zealand. *New Zealand Journal of Geology and Geophysics*. 41(4):325–342. doi:10.1080/00288306.1998.9514814.

Dravid, P. N., and L. J. Brown, 1997. Heretaunga Plains groundwater study. Volume 1: findings. Napier (NZ): Hawke's Bay Regional Council. 254 p.

Francis, D. 2001. Subsurface geology of the Ruataniwha Plains and relation to hydrology. Lower Hutt (NZ): Geological Research Ltd. Technical Report prepared for Hawke's Bay Regional Council. 28 p.

Rawlinson, Z. J., N. Foged, R. S. Westerhoff, and R. L. Kellett, 2021. Hawke's Bay 3D Aquifer Mapping Project: Heretaunga Plains SkyTEM data processing and resistivity models. Wairakei (NZ): *GNS Science*. 90 p. Consultancy Report 2021/93. Prepared for Hawke's Bay Regional Council.

Risk, G. F., 1974. Electrical resistivity soundings on the Heretaunga Plains. Wellington (NZ): *Department of Scientific and Industrial Research, Geophysics Division*. 28 p. Report 95.

Sørensen, K. I., and E. Auken, 2004. SkyTEM – a new high-resolution helicopter transient electromagnetic system. *Exploration Geophysics* 35(3):194–202. doi:10.1071/EG04194.

Tschritter, C., R. L. Kellett, Z. J. Rawlinson, and A.G. Griffin. 2022. Hawke's Bay 3D Aquifer Mapping Project: Heretaunga Plains data and model inventory. Wairakei (NZ): *GNS Science*. 96 p. Consultancy Report 2021/113.

Tschritter, C., M. Herpe, R. L. Kellett, Z. J. Rawlinson, M. J. Arnot, and A. G. Griffin, M. J. F. Lawrence. 2022. Hawke's Bay 3D Aquifer Mapping Project: Ruataniwha Plains data and model inventory. Wairakei (NZ): GNS Science. 111 p. Consultancy Report 2022/76.

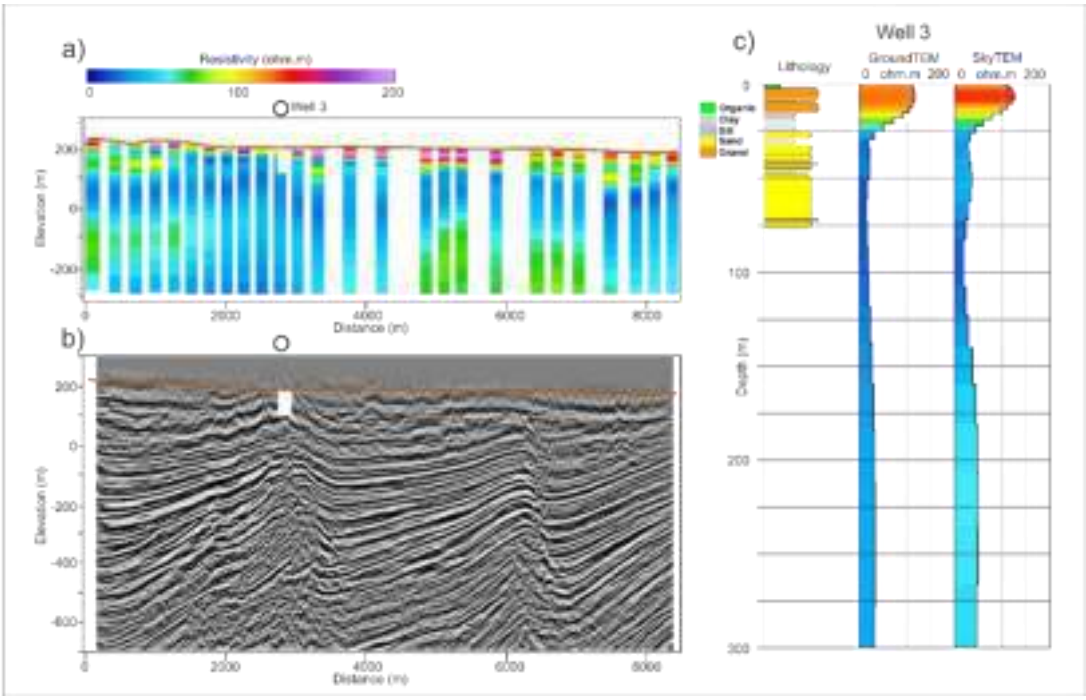

Figure 4. SkyTEM inversion models (a) on a section parallel to seismic line IP332-99-301 (b). Well 3 is shown in part (c) with the lithology, GroundTEM and SkyTEM models. The ground surface is shown on both sections by the brown horizon.

Modelling induced polarization effects in frequency-domain data

Evgeny Karshakov
Institute of Control Sciences
65, Profsoyuznaya Street,
Moscow, 117997, Russia
karshakov@ipu.ru

Dmitry Khliustov
Institute of Control Sciences
65, Profsoyuznaya Street,
Moscow, 117997, Russia
hlustov.d@gmail.com

SUMMARY

Induced polarization (IP) effects may have significant impact on airborne electromagnetic (AEM) data. They lead to dependence of apparent resistivity on the frequency of the signal. The classic approach to modelling IP consists in deriving analytical models of frequency dependent resistivity of each layer of the model. However, the amount of parameters for such model grows fast with the number of layers. Hence the problem of numerical inversion becomes intractable due to high dimensionality and ill conditioning.

This work suggests an approach to overcoming this problem. We show that the effects of IP are concentrated in relatively small number of layers and propose a simple algorithm for finding them. The results of inverting real data showing strong IP are presented.

Key words: inversion, airborne electromagnetics, frequency domain, Cole-Cole model.

INTRODUCTION

Over the past few years the induced polarisation (IP) effects have become a subject of intensive research in the field of airborne electromagnetics (AEM) data processing (Kaminski and Viezzoli, 2016). The reason for it is that in many practical applications not taking IP into account leads to problems in fitting parameters of the model.

There exist several explanations for this phenomenon. One point of view is that IP should be attributed to properties of minerals under study. Several works are devoted to construction of materials which possess the property of charge conservation (Gurin *et al*., 2019). The experiments conducted in laboratory suggest that in the presence of inhomogeneity (such as granular structure) the environment may show frequency-dependent conductivity. Another point of view is that IP effects are caused by purely geometric properties of the surface.

One of the main practical indicators of IP is the presence of negative response in time domain or, equivalently, negative in-phase response in frequency domain (Karshakov and Moilanen, 2019). In the first part of our work we show that IP model based on Cole-Cole approach can produce results having this property. After this, we derive an inversion methodology which provides a compromise between number of parameters and explanatory power. Finally, we show results of fitting this model to real data and compare them to non-chargeable model.

All computations are done in the frequency domain. Parameters of the system (frequencies, typical altitudes, relative position of emitter and receiver) correspond to those of a real AEM system EQUATOR (Moilanen *et al*., 2013).

METHOD AND RESULTS

Model formulation

In problems which require computing equivalent resistivity it is customary to use horizontally layered model (Zhdanov, 2009). This simplification leads to reduced amount of computations while providing good explanatory power. The model enables one to derive the response to the field of vertical magnetic dipole explicitly. Namely, for a given frequency ω the vertical component of the response is

$$H_z(\omega) = \int_0^\infty u(n_0, z, h_T, \omega) J_0(n_0 r)\, n_0^2 dn_0,$$

where J_0 is the zero-order Bessel function of the first kind, r is the horizontal shift of the receiver with respect to the dipole axis, h_T is the altitude of the dipole above the ground, z is the altitude of the receiver. Here u is the two-dimensional spectrum of the potential of the secondary field:

$$u(n_0, z, h_T, \omega) = \frac{M \exp\left(-n_0(z+h)\right)}{2} \frac{n_1 - n_0 R^*}{n_1 + n_0 R^*},$$

where M is the amplitude of the dipole moment and R^* is the reduced spectral impedance of the medium. For K layers it is given by the formula

$$R^* = \tanh\left(n_1 h_1 + \tanh^{-1}\left(\frac{n_1}{n_1}\tanh\left(n_2 h_2 + \cdots\left(n_{K-1} h_{K-1} + \tanh^{-1}\frac{n_{K-1}}{n_K}\right)\ldots\right)\right)\right),$$

for $n_k = \sqrt{n_0^2 - \frac{i\omega\mu_0}{\rho_k}}, Re\ n_k > 0$.

In the above formula $\mu_0 = 4\pi \times 10^{-7}$ H/m the magnetic permittivity, ρ_k is the resistivity of k'th layer.

The possible approach to solving the inverse problem (that is, estimating resistivities and thicknesses of the layers) is the Kalman filter. The presence of non-linearities advocates the use of variants of Kalman approach, such as Extended and Iterated filters (Karshakov, 2020). Since these methods rely on gradient approximation, there are no easy-to-check theoretical guarantees of convergence. Hence in order to analyse real data, one often has to run the algorithm several times with different initial conditions and hyperparameters.

The formulas above are derived through explicit analysis of Maxwell equations. In the presence of environment inhomogeneous with respect to vertical coordinate only, equations can be uncoupled and reduced to second-order linear ones. Therefore, from mathematical point of view, ρ_k can be complex or even frequency dependent (as soon as we produce computations in spectral domain).

The effect of IP is usually modelled by introducing resistivity of a special form, governed by Cole-Cole equations (Cole and Cole, 1941, Pelton *et al*., 1978):

$$\rho = \rho_0\left(1 - m\left(1 - \frac{1}{1 + (i\omega\tau)^c}\right)\right),$$

where ρ_0 is DC current resistivity, m is chargeability constant, τ is a relaxation time, c is a phase constant. Equations of this form first occurred in papers devoted to slow electromagnetic processes (such as electrochemistry), but later were applied for modelling other phenomena, including AEM data processing. It should be noted that the Cole-Cole equation is not the only one used in literature (see Dias (2000) for excellent review), but other models include more parameters, which makes computation problem intractable in practice.

Another thing to notice is that the function $(i\omega\tau)^c$ has several branches, and hence we must choose among a set of possible values. Indeed, $i = \exp\left(i * \frac{\pi}{2}\right) = \exp\left(i * \left(\frac{\pi}{2} + 2\pi k\right)\right)$ for integer k. Hence after raising it to the power of c we obtain $\exp\left(i\frac{c\pi}{2}\right)$, $\exp\left(i\frac{5c\pi}{2}\right)$ ... as possible values, all distinct as soon as c and π are incommensurable. We further remark on this issue in the next section.

Theoretical considerations

As it was already mentioned, one of the main practical indicators of IP in frequency domain is the presence of negative in-phase response. We tried to obtain it in simulation by posing optimisation problem $Re\ H_z(\omega) \to min$ and solving it over ω and resistivity parameters. It turned out that in order for the problem to have negative solution one must have $Re\ \rho_k > 0, Im\ \rho_k > 0$ for resistivity of at least one of the layers. However, the vanilla Cole-Cole model with $i^c = \exp\left(i\frac{c\pi}{2}\right)$ is uncapable of producing such resistivity. Hence we have chosen another branch of the function, taking $i^c = \exp\left(i\frac{5c\pi}{2}\right)$. The results of simulating half-space model with parameters $\rho = 1000\ \Omega m, m = 0.5, \tau = 0.001\ s, c = 0.5$ are presented in figure 1. There we present three curves for each graph: quadrature (Im) and inphase (Re) components in frequency domain and off-time signal in time-domain. Index "IP0" is related to the branch number 0 with $i^c = \exp\left(i\frac{c\pi}{2}\right)$, "IP1" is related to the branch number 1 with $i^c = \exp\left(i\frac{5c\pi}{2}\right)$, "noIP" is related to $\rho = \rho_0$.

However, it is not clear why we should choose this branch of power function instead of any other. One of the possible approaches would be to introduce additional phase parameter in Cole-Cole formula and search for branch of the form $\exp(i\phi)$. But this leads to functions with singularities in the domain and is a subject of further investigation.

If the model has all resistivities determined by Cole-Cole formula, the number of parameters is high. Hence one needs an additional regularization in order for the inverse problem to be tractable. We adopted a hypothesis that chargeability is determined by relatively small number of layers (1-3). To find these layers, we fitted a model with one chargeable layer and non-chargeable others. After varying the depth in which chargeability was located, we could obtain residuals between model prediction and measured response. For some depths, the residual turned out to be several times lower (30-40 as compared to 150-200) than for others. Although it was still too high to consider any of obtained result a good fit, this procedure enabled us to make a choice as to which layers should be chargeable.

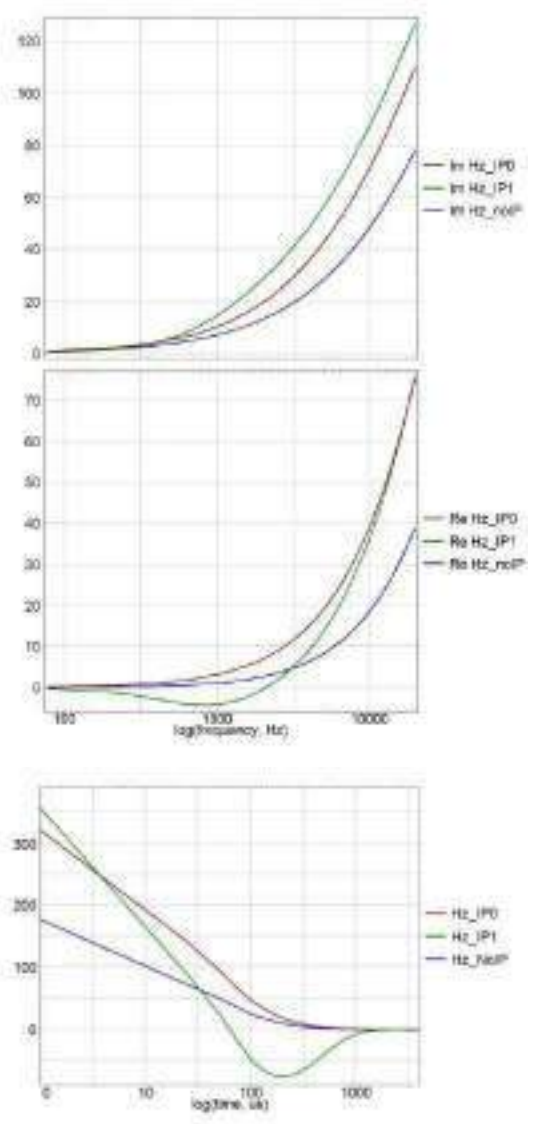

Figure 1. The response of half-space model in frequency (quadrature and inphase) and time domains

This simple algorithm is valid only for small sections of data, since the actual profile can change significantly on large scales. When the residual of final model becomes too high, one needs to repeat the procedure and determine new depths of chargeable layers.

Main results

Here we provide results of real data processing based on our approach. The data consisted of responses for 15 frequencies ranging from 77 to 15000 Hz, with in-phase and quadrature components measured for each. We used model with 25 layers with thickness of i'th layer equal to $4 * 1.1085^i$ meters. The first step of the algorithm consisted in fitting the model which had frequency dependent resistivity in one of 25 layers. An example of relative discrepancy (determined by formula

$\left(\sum_{freqs} \frac{(response_{estimated}(freq) - response_{true}(freq))^2}{\sigma^2_{noise}(freq)}\right)^{\frac{1}{2}}$) is presented in figure 2.

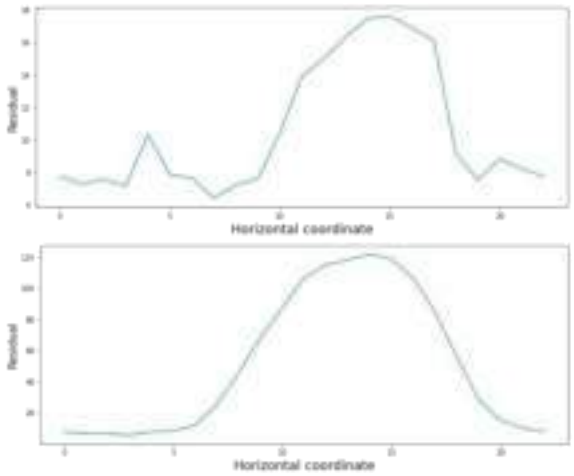

Figure 2. The residual of model with one chargeable layer (a) Chargeability in layer # 2(b) Chargeability in layer # 5 The second graph clearly exceeds the first

It is easy to see that by locating chargeability in layer #2 we decrease residual significantly compared to locating it in layer #5.

It turned out that in order to decrease the residual one must locate chargeability in layers 2, 4, 6 and 7. In order to further decrease the number of parameters we changed consecutive layers 6 and 7 to one layer with thickness equal to the sum of respective thicknesses. Hence we had to fit a model with 33 parameters. The resulting relative discrepancy is given in figure 3. It is easy to see that residual does not exceed 10, which may be considered a good fit.

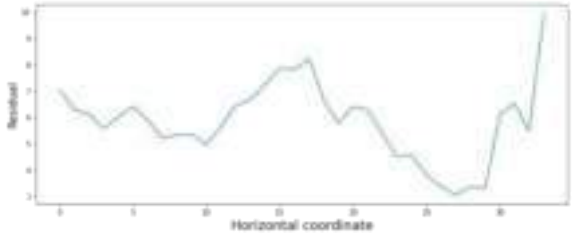

Figure 3. The residual of the final model

Figure 4 gives values of Cole-Cole parameters for each of the layers obtained by model.

Figure 5 shows the results of data inversion. The survey was carried out in Siberia, in the permafrost region. The melting zone is considered to be the main source of chargeability. We would like to point out the following features. First, after applying the chargeable model for the inversion, we see horizontally continuous layers. Second, even in the case of positive inphase responses (left part), the chargeability model provides more adequate solution according to known local geological properties: the lower conductive layer is presented along the whole flight trajectory.

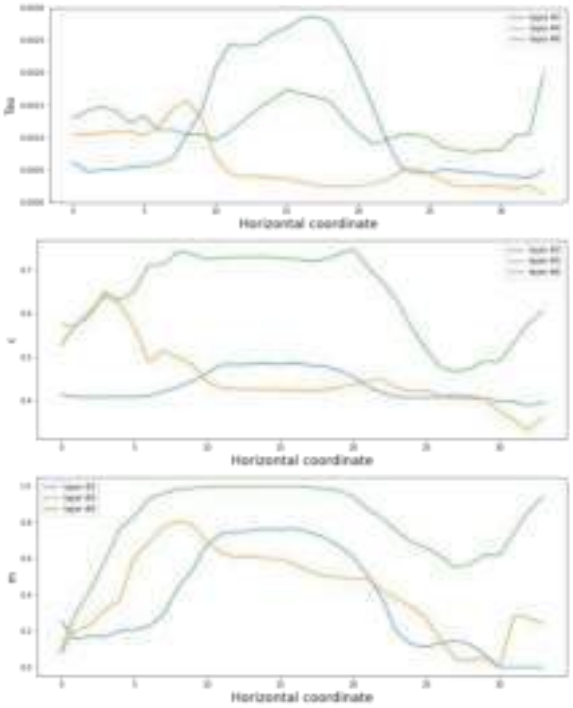

Figure 4. The Cole-Cole parameters: time constant, exponent and chargeability

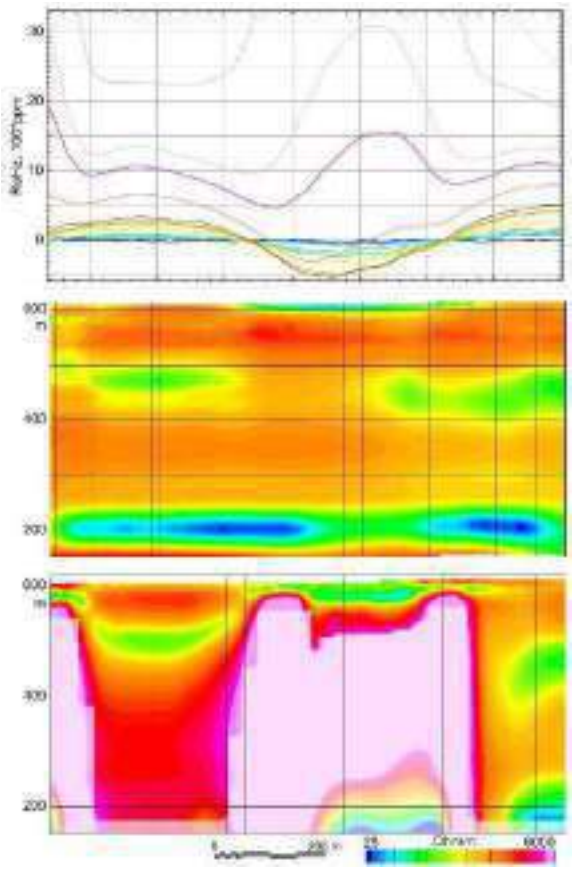

Figure 5. The inphase response curves and inversion results for the models with (top) and without (bottom) chargeability.

CONCLUSIONS

In this work we studied the problem of inverting AEM data in the presence of IP effects. We considered horizontally layered one dimensional model with frequency dependent resistivity, given by Cole-Cole formula. It has been shown that IP effects are mostly determined by local properties of environment and are concentrated in a small number of layers. Based on this, we suggested an approach to choosing the depth of chargeable layers by fitting several simpler models and analysing residuals.

For a demonstration of our approach, we analysed real data by estimating parameters of our model. We used dataset obtained by the EQUATOR AEM system. The environment demonstrates signs of IP presence, most likely connected to ice melting.

Further research directions include formalizing the procedure of chargeable layer identification. Some additional investigation should be conducted on choosing the appropriate branch of complex-valued resistivity function, discussed above.

ACKNOWLEDGMENTS

We would like to thank Dr. A. Volkovitsky for a fruitful discussion of the chargeability model, and Dr. J. Moilanen for help with result visualization.

REFERENCES

Cole, K.S., and R.H. Cole, 1941. Dispersion and absorption in dielectrics I. Alternating current characteristics. *The Journal of chemical physics* 9(4): 341-351.

Dias, C., 2000. Developments in a model to describe low-frequency electrical polarization of rocks. *Geophysics* 65(2): 437-451.

Gurin, G., Titov, K., and Y. Ilyin, 2019. Induced polarization of rocks containing metallic particles: evidence of passivation effect. *Geophysical Research Letters* 46(2): 670-677.

Kaminski, V., and A. Viezzoli, 2017. Modeling induced polarization effects in helicopter time-domain electromagnetic data: Field case studies. *Geophysics* 82(2): B49-B61.

Karshakov, E., and J. Moilanen, 2019. Overcoming Airborne IP in Frequency Domain: Hopes and Disappointments. *SAGA Biennial Conference & Exhibition*: 1-4.

Karshakov, E., 2020. Iterated extended Kalman filter for airborne electromagnetic data inversion. *Exploration Geophysics* 51(1): 66-73.

Moilanen, J., Karshakov, E., and A. Volkovitsky, 2013. Time-domain helicopter EM System "Equator": resolution, sensitivity, universality. *13th SAGA biennial and 6thInternational AEM conference AEM-2013*, Expanded Abstracts: 1-4.

Pelton, W.H., Ward, S.H., Hallof, G., Sill, W.R., and P.H. Nelson, 1978. Mineral discrimination and removal of inductive coupling with multifrequency IP. *Geophysics* 43(3): 588-609.

Zhdanov, M. S., 2009. Geophysical electromagnetic theory and methods. Elsevier.

Thoughts on layered inversions

Andrew King
CSIRO
Dick Perry Ave, Kensington WA 6152
andrew.king@csiro.au

SUMMARY

The earth is composed of layers of rock of different lithology, with sharp boundaries between them, so surely it is better to use layered AEM models than smooth models? However, this idealised cartoon model is complicated by the fact that most electrical conductance is through pore water of varying salinity rather than through the rock matrix, and by factors, such as weathering gradients, which will induce gradients in physical properties. This paper discussed experiences with trying to use layered, rather than smooth, inversions of AEM data.

Key words: Airborne electromagnetics, layered-earth model, inversion

INTRODUCTION

Most airborne electromagnetic (AEM) inversions are smooth 1D inversions, stitched into a section under the flight line. Individual decay curves are inverted for a conductivity distribution which is smooth in the depth direction (Farquharson & Oldenburg, 1993; Christensen, Reid, & Halkjær, 2009; Brodie, 2016), sometimes including lateral constraints between adjacent soundings. These conductivity sections are then interpreted, typically by choosing some conductivity threshold to represent a geological or groundwater feature of interest.

However, we know that the earth is not smooth. A glance at a geophysical borehole log will show that there is variation in physical properties at all scales. In particular, there are often sharp boundaries between different lithological units. If different units have differing porosity, then we could expect them to have different electrical conductivity, especially in the sedimentary environments conducive to modelling using 1D codes. The question is, can we use our knowledge that the earth is composed of layers to improve inversion results?

This talk looks at inversion using a layered model, where the layers are intended to represent geological units. An advantage is that the model is parameterised in terms of depths to geological layer boundaries, which are quantities that we are actually interested in, rather than having to draw lines on a coloured section. Another advantage is that, if the earth's conductivity really is layered, then we ought to get a better result.

In order to assess this approach, there are a few questions that need to be addressed:

1. What is the consequence of a model with the wrong number of layers?
2. In most earth materials, the electrical conductivity is through water in the pore spaces, rather than through the rock matrix, which means that water content and salinity strongly affect the electrical conductivity. So, to what extent do conductivity changes parallel geology, rather than possibly cross-cutting groundwater differences?
3. How does the water table affect the conductivity structure? We know that rocks remain conductive when partially saturated, and Archie's law, along with modifications to account for clays, gives us an indication of the relationship between saturation and conductivity. So, there should be a drop-off in conductivity above the water table, but what does it look like?
4. Many geological processes probably result in gradients in physical properties, rather than sharp changes between homogeneous units. Examples are chemical weathering processes in the regolith, and upward-fining or -coarsening sequences in sedimentary rocks, both of which could well result in electrical conductivity gradients. To what extend can these be detected in AEM data? And how useful is some kind of average property?

This talk is an attempt to make a start in addressing some of these questions.

MODELLING AND INVERSION

Forward modelling has been done using the freely-available AMIRA P223 code Airbeo (Raiche et al. 2007), which computes the response of a 1D layered earth. The code is capable of including induced polarisation effects as well as simple induction. For 2- and 3-D situations, an approximate forward model computes the 1D response due to the earth directly beneath each sounding point.

Inversion has been done using bespoke python algorithms, mostly built around the scipy optimization least-squares code. The inversions are 2D or 3D, and include lateral constraints in the form of distance-based prior covariances between model parameters (see, e.g. Tarantola, 1987). Generally, the covariances are between parameters of the same class, such as between thicknesses or conductivities of a given layer, with zero prior covariance between classes. I have (mostly) chosen to model conductivities using an exponential covariance,

$$C_M(m_1, m_2) = \sigma_1 \sigma_2 \exp\left(-\frac{D(\mathbf{r}_1, \mathbf{r}_2)}{L}\right).$$

Here m_1 and m_2 represent, for example, the conductivity of a given layer at two points, σ_k and $\mathbf{r}_k$ are the conductivity of and location of point k, D(. , .) is a distance, and L is the correlation scale length. Large values of L imply large correlation lengths, which would be appropriate for well-mixed sediments in a channel, for example. I have modelled thicknesses using a

Gaussian functional form (where the argument to the exponential is squared).

DO LAYERED MODELS WORK?

An example that gives some confidence to the idea of modelling AEM using geological layers is shown in Figure 3. A very dense grid of boreholes was mapped, and geology characterised as being in one of four categories: alluvium/colluvium, channel sediments, saprolite, and basement. Each of these units was assumed to have a homogeneous conductivity. Water table depth information was also available, and the water table was modelled as splitting whatever layer it passed though into wet (conductive) and dry (resistive) sub-layers. An inversion was done for the layer conductivities, with the layer thicknesses and water table depths fixed at values interpolated from borehole measurements (King and Gonzalez-Alvarez, 2018). Although this is a dramatic over-simplification – we know that the saprolite conductivity will vary internally with degree of weathering, and the water table effect is more complicated than a simple extra boundary, for example – the fit to the data is remarkably good. A second-pass inversion, this time allowing conductivities of the different layers to vary from fid to fid, produced convincing results. Figure 1 shows an example where a 3D region has been inverted, this time holding the conductivities fixed at the values determined from the line inversion, but allowing thicknesses to vary.

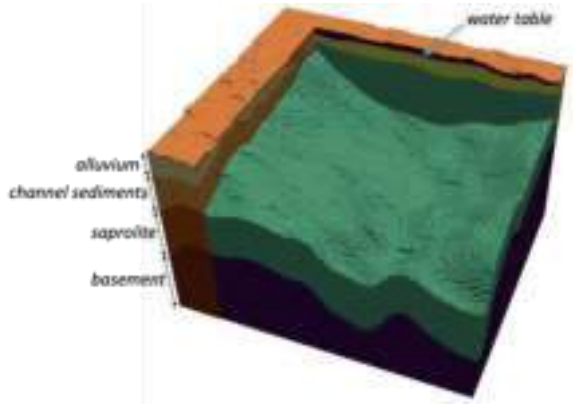

Figure 1. 3D example of homogeneous-layer inversion. Here layer conductivities were held fixed, and thicknesses were allowed to vary.

WHAT CAN WE IMAGE?

Figure 2 compares two inversions of the same decay: a smooth model, and a layered model where the depths have been fixed according to those in a nearby borehole. While the models are very different, the fit to the data is almost identical. This shows how little we can determine using AEM data alone. It makes much more sense to use AEM inversions as a kind of hypothesis test: a hypothesised geological can be parameterised in terms of its unknowns, say, the thicknesses of a fixed number of layers, and an attempt can be made to fit the data. If data cannot be fitted, then the hypothesis should be rejected.

In the context of this talk, this large ambiguity means that, if (and only if) the layers can be characterised as homogeneous, or nearly so, then a meaningful inversion for layer thicknesses can be done, and the layered model is useful. If individual geological layers have conductivities that vary internally as much as they do between layers, then the approach is doomed to failure.

An interesting point to note regarding this example, is that the layered model requires the addition of a water-table effect (splitting the shallowest layer into two) in order to fit the data. The smooth model also shows an increase in resistivity at the surface. This also illustrates that, although the water table might be more complex than a simple split into wet and dry, that simple split might be the best we can image with most AEM systems.

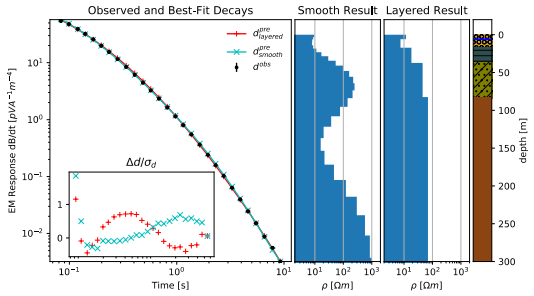

Figure 2. Comparing smooth and layered inversions. The layered-inversion boundary depths were constrained by a nearby borehole. Large model differences can nonetheless have small differences in data fit. (a) Observed and predicted data. The inset shows residuals scaled by data errors. (b) and (c) Smooth and layered model resistivities vs depth. (d) Nearby borehole log used to constrain depths.

CONCLUSIONS

In many cases that I have looked at, modelling the earth as a set of near-homogeneous layers, and including the water table as a "layer splitter", is able to successfully fit AEM data. Where layer depths are known at a single sounding, layer conductivities determined at that sounding can be used to determine thicknesses away from that point. However, the inherent ambiguity of AEM inversion means that this can only be done if the layer conductivities can be constrained to be close to homogeneous.

REFERENCES

Brodie, R. C. (2016). Holistic Inversion of Airborne Electromagnetic Data. PhD Thesis, ANU.

Christensen, N. B., Reid, J. E., & Halkjær, M. (2009). Fast, laterally smooth inversion of airborne time-domain electromagnetic data. *Near Surface Geophysics*, 599-612.

Farquharson, C. G., & Oldenburg, D. W. (1993). Inversion of time-domain electromagnetic data for a horizontally layered Earth. *Geophysical Journal International*, 114(3), 433-442.

King, A., & Gonzalez-Alvarez, I. (2018). Constraining Airborne Electromagnetic Interpretation with Regolith Stratigraphy and Landscape Evolution Processes. *ASEG Extended Abstracts, 2018*(1), 1-5.

Raiche, Art, Fred Sugeng, and Glenn Wilson. 2007. "Practical 3D EM Inversion - the P223F Software Suite." *ASEG Extended Abstracts* 2007 (1). ASEG2007ab114: 1. doi:10.1071/ASEG2007ab114.

Tarantola, A. 1987. Inverse Problem Theory: Methods for Data Fitting and Model Parameter Estimation. SIAM

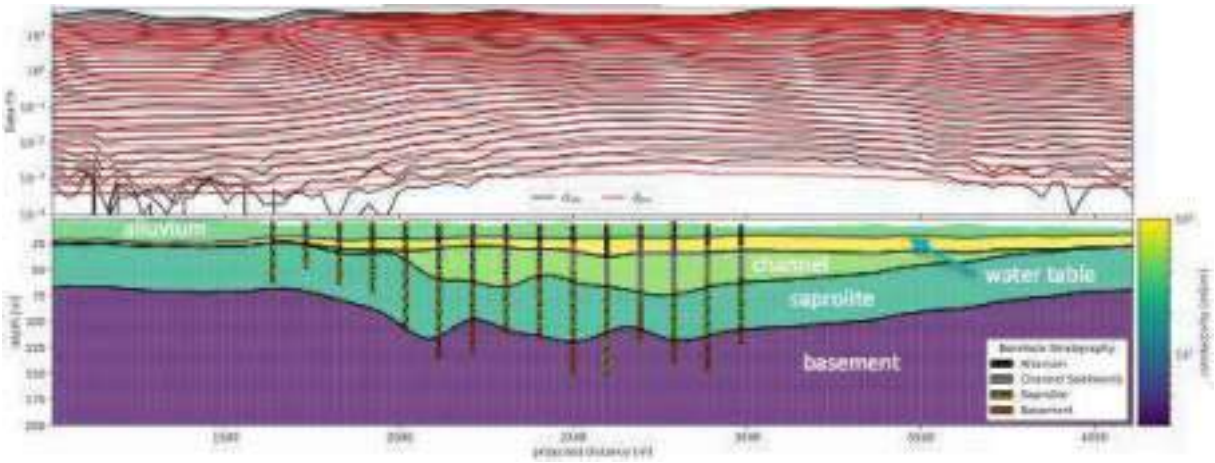

Figure 3. An inversion for homogeneous layer conductivities, where layer thicknesses are fixed at values interpolated between dense borehole measurements. The water table, whose depth is also fixed from borehole measurements, is modelled as splitting a layer into wet (conductive) and dry (resistive) sub-layers. Boreholes are oblique to the flight line. The fit is remarkably good, considering how simple the model is.

ZTEM Airborne Natural Field EM-Magnetics and Mineral Targeting Results over the Berg Porphyry Copper Project, near Houston, British Columbia.

Jean M. Legault
Geotech Ltd.
Aurora ON CAN
Jean.legault@geotechairborne.com

Karl Kwan
Geotech Ltd.
Aurora ON CAN
karl.kwan@geotechairborne.com

Shane Ebert
Surge Copper Corp.
Vancouver BC CAN
shane@surgecopper.com

SUMMARY

A ZTEM natural field helicopter EM and magnetic survey was flown over the Berg copper-molybdenum-silver project in the Huckleberry district, near Houston in central British Columbia, Canada. Mineralisation at Berg surrounds a quartz monzonite intrusion. Analyses of the airborne geophysical responses, using 2D-3D inversions, show combined well-defined ring-like resistivity low surrounding a resistive core and similar annular magnetic high and low signatures over the known and suspected porphyry deposits, similar to those previously found in ZTEM surveys over other porphyry deposits in the Western Cordillera. A mineral targeting approach is implemented that uses a semi-automated, machine-learning (ML) assisted method that includes: Structural Complexities (SC), Self-Organizing Map (SOM) classifications, and Supervised Deep Neural Network (SDNN) targeting of the geophysical data. The new targeting approach has identified both the Berg and Bergette porphyry copper occurrences, as well as two others our areas for follow-up that also host known mineral showings.

Key words: Porphyry copper, ZTEM, electromagnetics, resistivity, magnetics, 3D inversion, mineral targeting.

INTRODUCTION

In May 2021, Surge Copper Corp. announced plans for a new district wide exploration program over its Ootsa and Berg Projects in the Huckleberry district, near Houston, north central British Columbia, including a ZTEM (Z-axis Tipper Electromagnetic; Lo and Zang, 2008) geophysical survey (Surge, 2021). The Ootsa-Berg project (Figure 1) is host to 4 advanced porphyry projects, including the undeveloped Berg copper-molybdenum-silver porphyry deposit. In June-July 2021 a ZTEM helicopter natural field electromagnetic and magnetic survey was flown over Ootsa-Berg and the results that focus on the Berg porphyry copper deposit and nearby occurrences are described in this study.

The Berg and Ootsa properties are adjoined on the west side, with Berg project lying immediately northwest of Imperial Metals' Huckleberry porphyry Cu-Mo-Ag mine and mill complex, and the Ootsa property to the southeast (Figure 1). The two properties cover a total combined area of >120,000 hectares and encompass the Seel-Huckleberry-Berg porphyry trend. The Berg claims were initially prospected in the late 1920's by Cominco but the Berg porphyry system was discovered by Kennecott following trenching and drilling in 1964. Subsequent exploration drilling by operators Placer Dome, Terrane Metals, Thompson Creek Metals, Centerra Gold and now Surge Copper total over 56,000 m in 224 holes. A resource estimate in 2021 established a measured and indicated mineral resource of 610 Mt grading 0.27% Cu, 0.03% Mo and 3 g/t Ag. The Berg deposit currently remains undeveloped (Norton et al., 2021).

Figure 1: Ootsa-Berg Property location, showing nearby Huckleberry Mine and regional deposits in north central British Columbia (modified after Purich et al., 2016).

ZTEM (z-axis tipper electromagnetic; Lo and Zang, 2008; Legault et al., 2012) helicopter natural field EM has been widely used in porphyry copper exploration for >15 years in mapping resistivity contrasts that characterize porphyry copper deposit alteration systems (Hoschke, 2011). ZTEM case-study examples over porphyry deposits include Lo and Zang (2008) in Safford, Arizona; Holtham and Oldenburg, (2010) at Bingham Canyon, Utah, Izarra et al. (2011) at Copaquire, Chile, and Burge (2014) at Cobre Panama. ZTEM examples in Western Cordillera include Sattel et al. (2010) at Mt Milligan, BC, and Lee et al. (2017) at Morrison, BC, and Paré et al. (2012) at Pebble, Alaska.

The Berg ZTEM-Magnetic case study has been presented in Legault et al. (2022). This paper adds to that study by presenting a new targeting approach, described in Legault (2023ab) that

uses a semi-automated, machine-learning (ML) assisted approach that includes: Structural Complexities (SC), Self-Organizing Map (SOM) classifications, and Supervised Deep Neural Network (SDNN) approach to mineral targeting.

Geology and Mineralisation

Berg (Figure 2) is a classic calc-alkaline Cu-Mo porphyry deposit, which are typically marked by complex alteration zones that are usually centred around an intrusive complex. The Berg mineralisation forms an annulus along the contact between the 50 Ma quartz monzonite stock and the hornfelsed Hazelton Group volcanic rocks and quartz diorite which it intrudes (Norton et al., 2021).

Figure 2: Plan view of the Ootsa-Berg porphyry project, showing the four main porphyry occurrences (Berg, Bergette, Ox, Seel) and nearby Whiting Creek prospect and Huckleberry Mine (green star), with ZTEM flight lines (Berg-black & Ootsa-blue) overlaid on contoured topography (modified after www.surgecopper.com).

Hypogene mineralisation at Berg is characterised by several generations of veining. Disseminated mineralisation containing copper and molybdenum is only important in the outer anulus of the quartz monzonite stock and in the adjacent volcanic rocks and quartz diorite. Associated alteration envelopes are either potassic or sericitic. A well-developed supergene enrichment blanket is superimposed on the hypogene mineralisation, and consists mainly of chalcocite, covellite and digenite, with trace amounts of copper oxides in the overlying leached cap. The surrounding phyllic and propylic alteration zones are typically poor in Cu+/-Mo sulphides (Norton et al, 2021). Mineralisation at Berg is open to depth and outward from the Berg monzonite Stock. The deposit has been shown to have excellent vertical continuity with significant mineralisation intersected greater than 550m below surface (www.surgecopper.com).

Another known mineral occurrence of importance on the Berg property is the Bergette prospect that lies 10 km east of the Berg deposit (Figure 2-Figure 3). Bergette consists of a large gossan and mineralisation is marked by strong Cu-Mo response in soils, across a 2x5 km northeast trending zone. Limited drilling and mapping indicate that Bergette is underlain by Hazleton Group volcanic and sedimentary rocks, intruded by granodioritic Sibola stock. Sulphides occur in breccias and fractures. An AeroTEM III (Allard, 2007) helicopter TDEM survey over the Berg-Bergette area in 2010 shows that Bergette has a similar size resistivity response (Norton et al., 2021).

At the Tara/Sibola occurrence, roughly 5.5 km NE of Bergette (Figure 2 & Figure 3), low-grade porphyry-style mineralisation is hosted in a felsic stock and occurs within the central part of a broad qtz-sericite-pyrite alteration zone (S. Ebert, SCC, pers. comm., 03-2022).

METHOD AND RESULTS

Helicopter ZTEM Natural Field EM and Magnetic Survey

Helicopter-borne geophysical surveys were carried out over the Ootsa-Berg Project from June 8th to 30th, 2021, on behalf of Surge Copper Corp. Principal geophysical sensors included a Z-Axis Tipper electromagnetic (ZTEM) system (Lo and Zang, 2008), and a caesium magnetometer. Two Geotech ZTEM base station sensors measured the orthogonal, horizontal X and Y components of the natural EM field. Data from the three coils are used to obtain the Tzx and Tzy Tipper (Labson et al., 1985) in-phase and quadrature components at six frequencies in the 30 to 720 Hz band. A total of 4,224 line-kilometres were flown, including approximately 1,779 line-km at Berg, along 300m spaced, north-south oriented flight lines and 3 km spaced east-west tie lines. The nominal EM bird terrain clearance was 85 metres, and magnetic sensor clearance was 100 metres. The Berg survey block is relatively rugged, with >1,600 m of vertical relief, particularly in the Berg porphyry region (Figure 2).

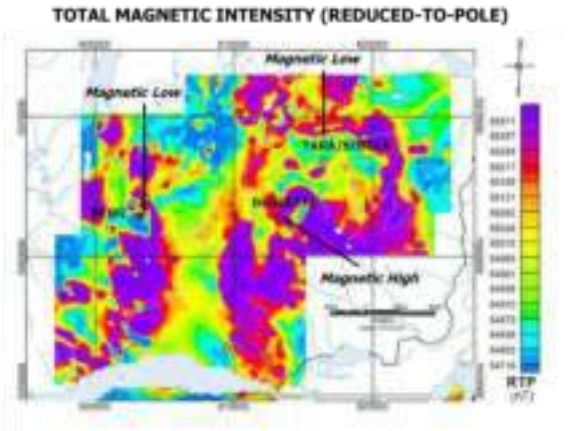

Figure 3: Total magnetic intensity (reduced to pole), showing Berg porphyry and other occurrences from Figure 2, and highlighting some features of interest.

ZTEM and Magnetic Survey Results

Figure 3 presents the reduced to pole (RTP) total magnetic intensity results, and the corresponding Berg porphyry and other mineral occurrences from Figure 2. The magnetic results highlight a prominent, large (~1.5x1.5 km), magnetic low feature centred on the Berg porphyry, which is in turn surrounded by a reverse C-shaped magnetic high. Worthwhile noting that similar ring-like magnetic patterns observed over the porphyry copper cluster at Cobre Panama are interpreted to represent demagnetized areas due to porphyry-related phyllic alteration (Burge, 2014; Legault et al., 2016). Conversely, Bergette lies within a magnetic high but is indistinct. Tara/Sibola occurs in low magnetic rocks but lies adjacent to a

small, intrusion like magnetic high feature. Other distinctive circular or ring-like magnetic high and low signatures are noted across the Berg Project.

The RTP magnetic data were then analysed for structural complexity (SC), using the Geosoft CET (Center for Exploration Targeting) grid analysis tool (Holden et al., 2012). The CET SC analysis tool outputs two parameters: i) the Contact Orientation Density (COD), and the Orientation Entropy (OE). Figure 4 presents the SC-derived COD image. As shown, the structural complexity highs are concentrated in areas with porphyry occurrences.

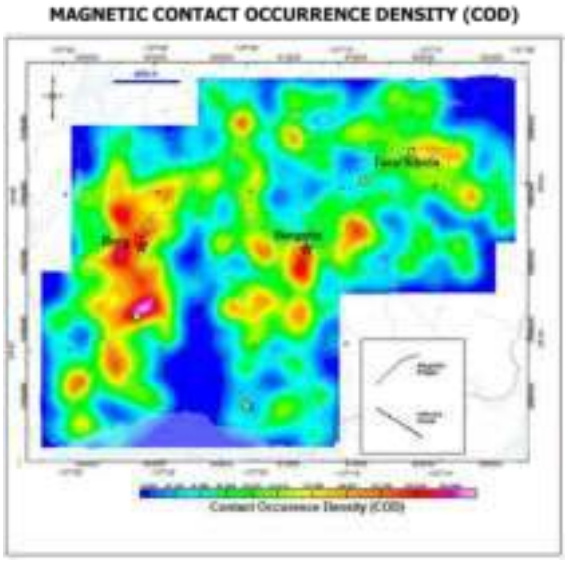

Figure 4: Structural complexity (SC) analysis of magnetic data, showing the Contact Occurrence Density (COD), over mineral occurrences and inferred faults (dashed lines), and magnetic ridges.

Figures 5ab present the ZTEM tipper data, displayed as both Total Phase Rotation and Total Divergence (DT; Lo and Zang, 2008) at the 90 Hz frequency. The TPR and DT image map resistivity variations in plan, in addition to artefacts caused by topography (Sattel and Witherly, 2012). The TPR and DT image highlights the pronounced circular or ring-like pattern anomaly over the Berg porphyry, which also agrees with the annular geology and alteration patterns that occur within the deposit. Similar ring-like patterns are observed in ZTEM data over other porphyries in Western Cordillera, such as Pebble, Morrison, and Mt Milligan, and elsewhere. Other circular/ring-like DT signatures are also defined across the Berg survey area, including at Bergette, whereas Tara/Sibola lies along strike with a linear conductive feature in the TPR and DT (Figure 4ab).

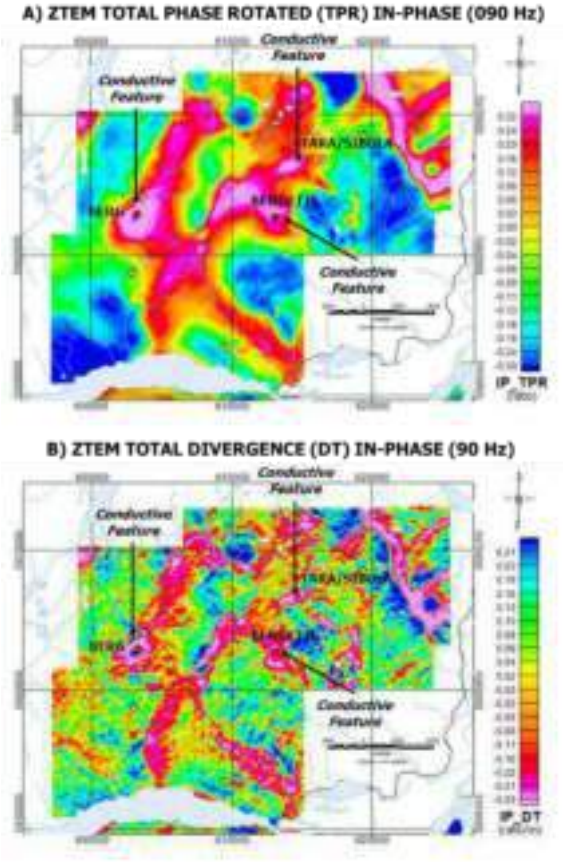

Figure 5: a) ZTEM In-phase Total Phase Rotation (TPR) at 90Hz, and b) Total Divergence (DT) at 90Hz, showing Berg porphyry and other occurrences from Figure 2, and highlighting some features of interest.

ZTEM and Magnetic Inversion Results

The ZTEM data have been converted to equivalent resistivity-depth distributions using 2D and 3D ZTEM inversions, with the Geotech Av2dtopo code (Legault et al., 2012) and UBC MT3dinv code (Holtham and Oldenburg, 2008), respectively. Both the 2D and 3D inversions account for topography and used 500 and 750 ohm-m half-space apriori start models, respectively. Figure 6a presents the 2D resistivity depth slice at -300m and Figure 6b presents the 3D inversion result at -300m depth. Both depth slices are shown with identical colour bars (~100-3k ohm-m). The images in Figure 5ab resemble each other reasonably well, including well defined conductive centre that coincides with the main Berg porphyry. However, the 3D inversion depth slice defines additional conductive anomalies not observed in 2D, particularly over Bergette.

Figure 6 presents the corresponding 3D magnetisation amplitude depth slice at -300m, obtained from the Geosoft VOXI MVI 3D inversion code (Ellis et al., 2012), which accounts for magnetic remanence. Berg is clearly marked by a ring-like magnetisation high that surrounds a low magnetic core, most likely reflecting alternating magnetite enrichment and depletion due to hydrothermal alteration. In contrast, as seen in the RTP results, Bergette and Tara/Sibola both coincide with high magnetisation amplitude signatures.

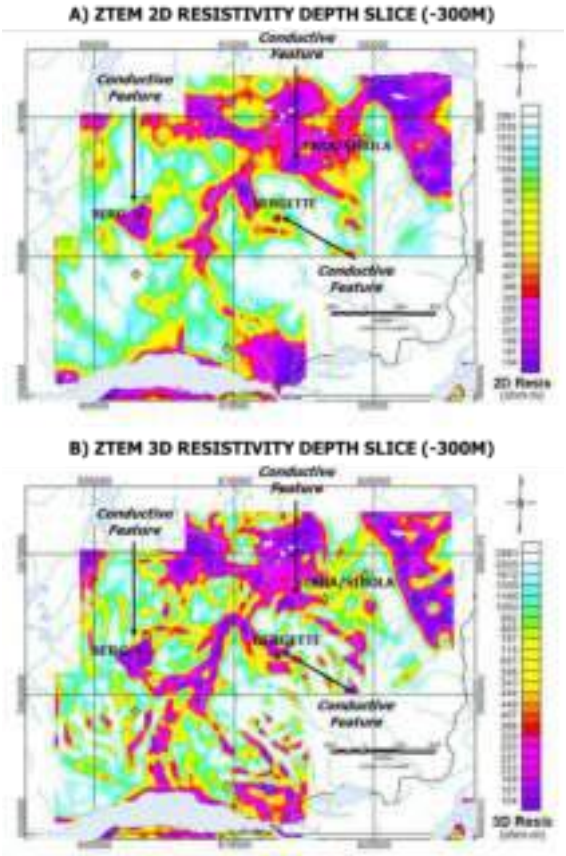

Figure 6: a) ZTEM 2D resistivity depth slice at -300m depth, and b) ZTEM 3D resistivity (red polygon) at -300m depth, highlighting some features of interest.

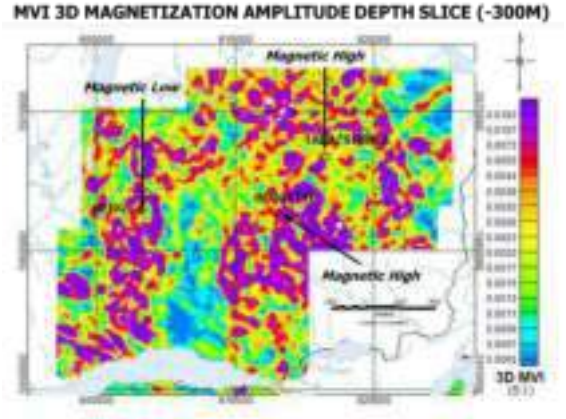

Figure 7: 3D MVI magnetisation amplitude depth slice at -300m depth, highlighting some features of interest.

Figure 8 presents the multi-parameter 2D and 3D inversion results as cross-sections along north-south line L1200 across the centre of the Berg porphyry copper deposit. Figures 7bc compare the ZTEM resistivity cross-sections obtained using 2D and 3D inversion. As shown, the ZTEM signatures from both inversions over Berg porphyry, which feature a slightly more resistive inner core that is surrounded by a more conductive outer shell, agree with the annular lithologic, mineralisation and alteration halo known to exist at Berg. The 3D inversion results further suggest that Berg's conductive phyllic halo extends to great depth as well as outward into the country rocks. Figure 7a presents the corresponding 3D MVI magnetisation amplitude section for L1200. The section shows that Berg occurs in a relative magnetic susceptibility low, likely reflecting magnetite depletion due to porphyry related hydrothermal alteration.

ZTEM 3D Synthetic Modeling

Results of 3D ZTEM synthetic modeling of the schematic Berg porphyry deposit are presented in Figure 9. The ZTEM modelling utilized an unstructured tetrahedral grid and a mimetic finite difference code based on the MT modelling program presented by Jahandari and Bihlo (2021). Figure 9c shows the calculated tipper response for 90 Hz. The ZTEM tipper values successfully indicate the presence of the porphyry deposit model, significantly overprinted by topographic effects.

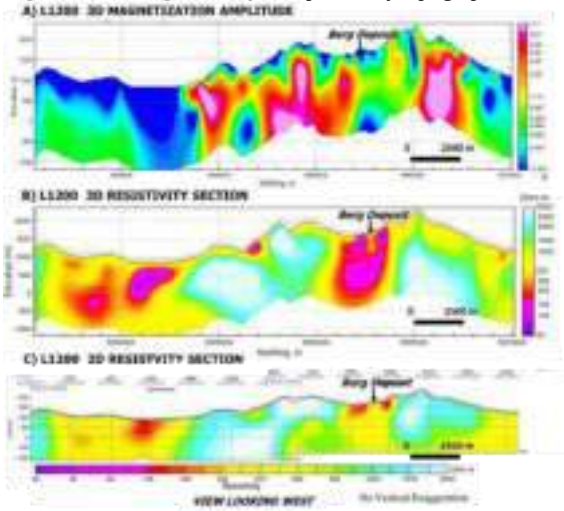

Figure 8: Multi-parameter 2D-3D inversion cross-sections along north-south L1200 across Berg porphyry deposit: a) 3D MVI magnetisation amplitude inversion; b) 3D ZTEM resistivity inversion, and c) 2D ZTEM resistivity inversion.

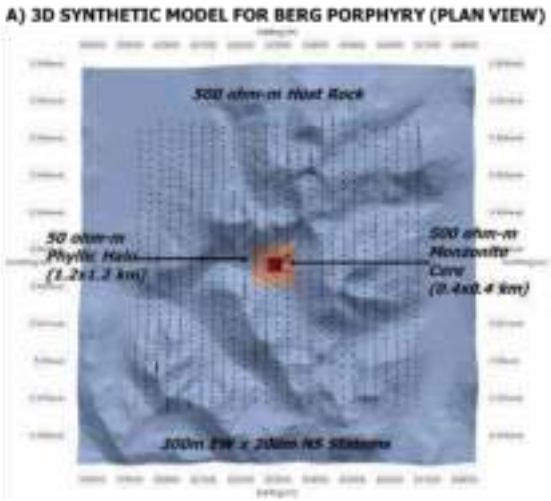

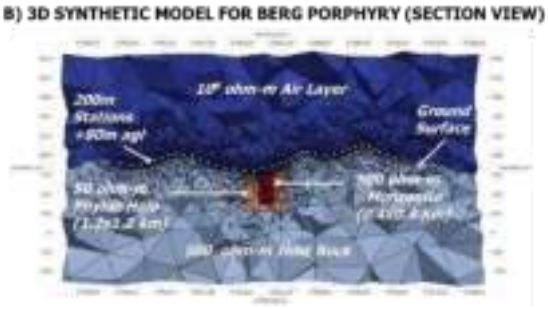

Figure 9: 3D ZTEM synthetic model for Berg porphyry deposit: a) Plan view of 3D model showing ZTEM tipper sites on topography approximated using tetrahedral grid mesh design; b) NS cross section view showing tetrahedral grid mesh design of subsurface resistivity model.

Mineral Targeting Porphyry Copper Deposits

Using recent examples of semi-automated, machine-learning assisted targeting using airborne geophysics applied to orogenic and epithermal gold-silver (Kwan and Legault, 2023; Legault et al., 2023), a similar mineral targeting approach has been tested for hidden porphyry copper deposits using the Berg ZTEM and magnetic survey results. The approach uses a semi-automated, machine-learning (ML) assisted method that includes: Structural Complexities (SC), Self-Organizing Map (SOM) classifications, and Supervised Deep Neural Network (SDNN) targeting of the geophysical data.

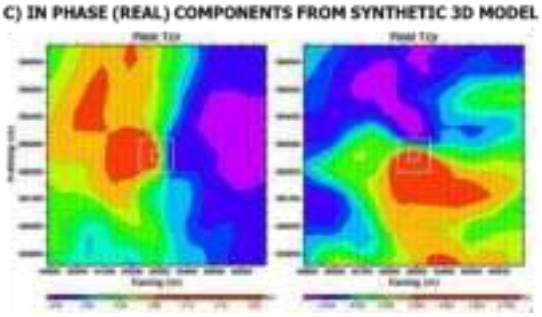

Figure 10: Calculated In-phase tippers for 3D ZTEM synthetic model of Berg porphyry deposit presented in Figure 9.

Self-Organizing Map (SOM) are useful tools in analysing and classifying multiple datasets. The magnetic SC data (COD + OE), the 3D ZTEM inversion data (-300m resistivity depth-slice), and the 3D MVI inversion data (-300m magnetisation amplitude depth-slice) were used as inputs and classified using the Geosoft SOM GX tool (https://geosoftgxdev.atlassian.net). As shown in Figure 11, the anomalous SOM classes (12 to 17) coincide with the known porphyry copper occurrences, namely Berg and Bergette, as well as lesser showings.

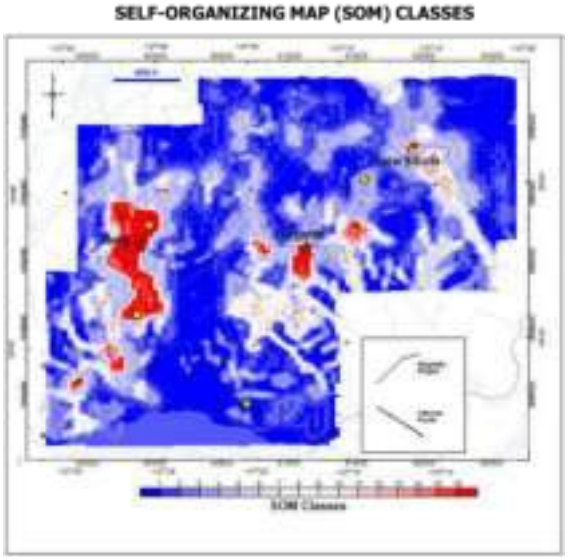

Figure 10: Self Organizing Map (SOM) results, showing anomalous SOM classes covering all the known porphyry copper occurrences, including Berg and Bergette.

The final mineral targeting step used the Supervised Deep Neural Network (SDNN) module in Google TensorFlow version TF 2.30 (https://www.tensorflow.org/). The training of the SDNN was performed on the Berg deposit area (Figure 12) using the magnetic COD and OE layers, the SOM classification results, the ZTEM 3D -300 m resistivity depth slice, and the MVI 3D -300 m magnetisation amplitude depth slice information,. The top 3.3% probability was selected for porphyry targeting (Figure 11b).

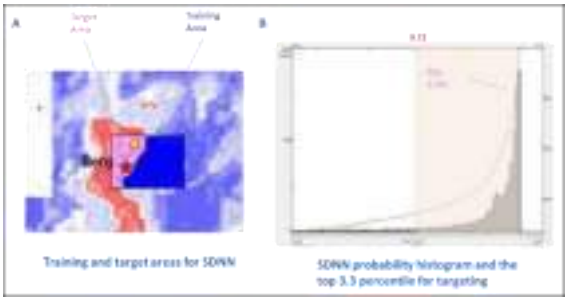

Figure 12: (A) Berg deposit training area for SDNN, (B) top 3.3% target probability cut-off for targeting.

The SDNN targeting was then applied to the entire Berg survey area, using similar multi-parameter data inputs as used in the initial SDNN training. Figure 12 presents the top 3.3% targeting probabilities over the DEM data, and the selected targets, T1-T4, which include Berg (T1) and Bergette (T2) as well as two other targets that also host known mineral showings and therefore represent potential areas for follow-up.

Figure 12: The SDNN top 3% probabilities over the DEM data and the selected potential porphyry targets (T1-T4), including Berg (T1) and Bergette (T2).

CONCLUSIONS

The ZTEM and magnetic results from the Berg Project present an excellent opportunity to study the geophysical signatures over an undeveloped yet significant porphyry copper deposit and the surrounding region. The Berg survey has led to the successful characterisation of the known porphyry deposit based on resistivity and magnetic susceptibility. The ZTEM survey results, assisted by 2D and 3D inversions, appears to map all the known porphyry deposits and occurrences at Berg, including the Bergette target. 2D-3D inversion analyses appear to confirm the bedrock source of conductivity that extend from surface to >500m depths. The magnetic and ZTEM results at Berg closely resemble those previously found in ZTEM surveys in the Western Cordillera, such as Morrison, Pebble, and Mt Milligan, including alteration-related, ring-like conductive highs that surround higher resistivities in the core and similar ring-like magnetic highs surrounding magnetic lows in the porphyry centres. The magnetic response is expected to be caused by magnetite enrichment in the outer halo and depletion in the centre. The increased conductivity within the mineralized porphyries at Berg show reasonable correlation with moderate to weak intensity phyllic alteration associated with hypogene mineralisation.

Finally, an approach for porphyry targeting has been tested, which uses a semi-automated, machine-learning (ML) assisted method that includes: Structural Complexities (SC), Self-Organizing Map (SOM) classifications, and Supervised Deep Neural Network (SDNN) targeting of the geophysical data. SC analysis of magnetic results has shown a close relationship between areas of structure intersection density and orientation diversity and the known porphyry occurrences. The SOM analysis showed the most anomalous classes coincide with the known porphyry copper occurrences, and other showings. Finally, the SDNN analysis, using Berg deposit as a training area, identified four main target areas that include both Berg and Bergette, as well as two other known mineral showings and that represent potential areas for follow-up.

ACKNOWLEDGMENTS

The authors wish to thank Surge Copper Corp. and Geotech for allowing us to present these results. We thank Hormoz Jahandari for contributing the 3D ZTEM synthetic modelling.

REFERENCES

Allard, M., 2007, On the Origin of the HTEM Species: In "Proceedings of Exploration 07: Fifth Decennial International Conference on Mineral Exploration" edited by B. Milkereit, 2007, p. 355-374.

Burge, C., 2014, A new porphyry copper deposit at Cobre Panama project: presented at PDAC Prospectors and Developers Convention, Discoveries and Developments session, Toronto, Canada.

Ellis, R.G., de Wet, B., and Macleod, I.N., 2012, Inversion of magnetic data for remanent and induced sources: 21ST ASEG Annual Conference and Exhibition, Extended Abstracts, 4 p.

Holden, E.-J., Wong, J. C., Kovesi, P., Wedge, D., Dentith, M., Bagas, L., 2012. Identifying structural complexity in aeromagnetic data: An image analysis approach to greenfields gold exploration. Ore Geology Reviews 46: 47–59.

Holtham, E., and Oldenburg, D.W., 2008, Three-dimensional forward modelling and inversion of Z-TEM data: 78TH SEG Annual International Meeting, Expanded Abstracts, 564-568.

Holtham, E., and Oldenburg, D.W., 2010, Three-dimensional inversion of ZTEM data: Geophysical Journal International, 182, 168-182.

Hoschke, T., 2011, Geophysical signatures of copper-gold porphyry and epithermal gold deposits, and implications for exploration: CODES-ARC Center of Excellence in Ore Deposits, University of Tasmania, 47 p.

Izarra, C., Legault, J.M. and Latrous, A., 2011, ZTEM airborne tipper AFMAG results over the Copaquire porphyry, northern Chile: 81ST SEG Annual International Meeting, Expanded Abstracts, 1257-1261.

Jahandari, H., and Bihlo, A., 2021, Forward modelling of geophysical electromagnetic data on unstructured grids using an adaptive mimetic finite-difference method: Computational Geosciences, 25, 1083-1104.

Kwan, K., and Legault, J.M., 2023, Gold targeting of fixed wing aeromagnetic Data using structural complexity, self-organizing map and supervised deep neural network analyses: A case study from the Red Lake camp, Superior Province, Ontario, Canada: Unpublished abstract submitted to IMAGE 2023 conference.

Labson, V. F., Becker, A., Morrison, H.F., and Conti, U. [1985] Geophysical exploration with audio frequency natural magnetic fields. Geophysics, 50, 656–664.

Lee, B.M., Unsworth, M., Hubert, J., Richards, J.P., and Legault, J.M., 2017, Geophysical Prospecting, 6, 397-421.

Legault, J.M., 2012, Ten years of passive airborne AFMAG EM development for mineral exploration: 82ND SEG Annual International Meeting, Expanded Abstracts, 5 p.

Legault, J.M., Wijns, C., Izarra, C., and Plastow, G., 2016, The Balboa ZTEM Cu-Mo-Au porphyry discovery at Cobre

Panama: 25TH ASEG-PESA-AIG Geophysical Conference and Exhibition, Extended Abstracts, 6 p.

Legault, J.M., Jahandari, H., and Ebert, S., 2022, ZTEM airborne natural field EM and magnetic case study over the Berg porphyry copper project, Huckleberry District, British Columbia: IMAGE, expanded abstracts, 5 p.

Legault, J.M., Kwan, K., Greig, J., Webster, E., and Hanki, M., 2023, Targeting epithermal Au-Ag using helicopter TDEM, magnetic, and radiometric data at Lawyers Project, North-Central BC, Canada: Unpublished expanded abstract submitted to AEM 2023 conference.

Lo, B., and Zang, M., 2008, Numerical modelling of Z-TEM (airborne AFMAG) responses to guide exploration strategies: 78th SEG Annual International Meeting, Expanded Abstracts, 1098-1101.

Norton, C., Huang, J., and Lui, D., 2021. Updated Technical Report and Mineral Resource Estimate on the Berg Project, British Columbia: Technical (NI 43-101) report to Surge Copper Corp., prepared Tetra Tech Canada Inc., 146 p.

Paré, P., Gribenko, A.V., Cox, L.H., Cuma, M., Wilson, G.A., Zhdanov, M.S, Legault, J.M., Smit, J. and Polomé, L., 2012, 3D inversion of SPECTREM and ZTEM airborne electromagnetic data from the Pebble Cu-Au-Mo porphyry deposit, Alaska: Exploration Geophysics, 43, 104-115.

Purich, E., Ray, B., Barry, J., Hayden, A., Yang, D., Schmidtt, H.R., 2016, Updated Resource Estimate and Preliminary Economic Assessment on the Ootsa Property, British Columbia, Canada: NI 43-101 Technical Report (No. 306) for Gold Reach Resources Ltd., by P & E Mining Consultants Inc. 433 p.

Sattel, D., Thomas, S. and Becken, M., 2010, An analysis of ZTEM data over the Mt Milligan porphyry copper deposit, British Columbia: 80th SEG Annual International Meeting, Expanded Abstracts, 1729–1733.

Sattel, D. and Witherly, K., 2012, Extracting information from ZTEM data with 2D inversions: 21ST ASEG Annual Conference and Exhibition, Extended Abstracts, 4 p.

Surge Copper Corp., 2021, Surge Copper Announces 2021 Exploration Plans: Press Release May 12, 2021, www.surgecopper.com.

Reconciling the previously incompatible through the continental scale AusAEM survey

Alan Yusen Ley-Cooper*, Ross C. Brodie, Anandaroop Ray and Neil Symington
Geoscience Australia,

SUMMARY

Geoscience Australia (GA) has acquired hundreds of thousands of line kilometres of airborne electromagnetic (AEM) data over the years to better understand the Australian subsurface. A more recent planned approach of acquisition has been the AusAEM programme. This systematic effort has delivered extensive detailed conductivity-depth-models over large swaths of land. This effort will deliver a continental-scale, long lasting geophysical dataset. Simultaneously, GA's in-house processing and inversion codes enable the seamless integration of conductivity models from both helicopter and fixed wing systems, compatibility of X and Z component data from the same survey, as well as the reconciliation of historical and recent datasets. Of particular note, is the reprocessing of data using the magnitude of the measured magnetic field in the plane of the inline flight direction. It deals with many transmitter-receiver geometry problems and leads to glitch-free subsurface images. GA's efforts in advancing the modelling and inversion codes have verified the presence of geological units at deeper depths in stratigraphic sequences than we were able to resolve pre-2016. The concerted development of a strategic acquisition program together with modelling and inversion codes have allowed us to stitch together a nearly continent-wide dataset.

Key words: Airborne electromagnetics, Australia, exploration; regional studies, time-domain AusAEM, Inversion, GA-LEI, HiQGA.

INTRODUCTION

Using an aircraft for mapping the electrical conductivity of subsurface materials is non-invasive and cost-effective. AEM surveying is a geophysical method that assists in understanding the composition, internal architecture and thickness of its vast sediment cover to unveil Australia's hidden geology.

Australia has a long history of AEM use. Some early acquisition trials date back to the early 1990s. Since then, AEM surveys have become an important tool for various applications, and are increasingly essential for exploring minerals, groundwater mapping, and environmental studies. To further understand the country's subsurface, Geoscience Australia has acquired hundreds of thousands of kilometres of airborne electromagnetic data over the years. The recent AusAEM programme was designed to systematically acquire AEM across much of the continent (Ley-Cooper et al. 2020). This effort has delivered extensive detailed conductivity-depth models over large swaths of land at a scale that previously seemed unlikely to be accomplished or found useful.

The effort invested in planning and acquisition as well as the modelling will lead to a new generation of active source geophysics to complement GA's continental-scale legacy passive geophysical datasets such as the magnetic (Milligan et al. 2009), gravity (Lane et al. 2019) and radiometric (Minty et al. 2009) compilations. Results of the AusAEM imaging (**Figure 1**) has already started showing rich dividends in spurring economic activity in the search for minerals, as well as the conservation of water resources in rural Australia. We are confident the AusAEM dataset will be a key component in ensuring a sustainable and prosperous future in Australia aswe transition to a green economy.

METHODS AND RESULTS

Harmonising AEM models from helicopter, fixed-wing, historic and current datasets.

Given the extent of the AusAEM programme (over 200,000 line-km and increasing), we have had to cater to the acquisition of time-domain electromagnetic data using both helicopter-borne and fixed-wing systems. The two types of AEM platforms have noticeable differences in their acquisition parameters including flying heights, transmitter dipole moments, waveforms, transmitter and receiver geometries, frame types and aerodynamic stability, speed of acquisition, and receiver gate times.

When dealing with various AEM datasets acquired at regional to continental scales, unlike for potential field data, simple levelling from surveys and different systems would yield a patchwork of channel data with a high degree of incoherence. Instead, as data are acquired, we invert them to conductivity with similar inversion parameters, while taking care that acquisition parameters such as flying height and geometry remain within a small set of humanly achievable, safe and acceptable bounds. Inversion enables the conversion from transient electromagnetic decays measured in Teslas or Volts into individual quantitative conductivity-depth models, which we stitch together as subsurface profiles suitable for geological interpretation. We use the AEM conductivity and depth models as proxies for near-surface geological architecture and natural resource (e.g., groundwater aquifers or sulphide deposits) or natural hazard (e.g., saline intrusions in drinking water) hosting materials.

Despite their dissimilar characteristics, all AEM systems should ultimately model and image broadly similar subsurface geology. Geoscience Australia has developed a suite of open-source algorithms GALEI (Brodie 2015) and HiQGA (Ray et al. 2022), which can deterministically and stochastically invert data collected by most currently operational AEM instrument systems. We have derived all the AusAEM conductivity sections from these GA open-source algorithms. As detailed next, this is done by a careful treatment of acquisition

parameters, without using processed "nominal" values for transmitter-receiver (Tx-Rx) geometries.

A crucial step in the development of GA codes and AEM system calibration is semi-quantitative subsurface validation by overflying different systems over the same geology and high-altitude flights over the Menindee test range in New South Wales. This also allows us to measure survey noise levels and understand inversion stoppage criteria.

Reconciliation of fixed-wing Bx and Bz magnetic field component data, through a vector-sum inversion.

In most fixed-wing systems, because the Tx is mounted on the aircraft, Tx height above ground and orientation (roll, pitch and yaw) are routinely measured as part of navigation. However, the imprecise knowledge of Tx-Rx relative geometries and estimating the Rx bird position in fixed-wing aircraft is particularly challenging for modelling conductivity. Inaccurate geometry information propagates into subsurface conductivity images, making inversion impossible, incorrect, or in the best-case, noisy.

When using secondary-field data processed under the assumption of a nominal orientation-geometry with imprecise primary-field removal, we routinely have found that the Bx and Bz data can often be independently inverted to different conductivity models but cannot simultaneously be inverted with the same model. As discussed previously, this problem usually stems from inaccurate decomposition of the primary and secondary fields in the initial data processing and the subsequent inaccurate estimation of the system geometry calculated from the poorly determined primary-field. To circumvent this, for GA's inversion of TEMPEST fixed-wing data, we invert the total field (primary plus secondary) Bx-and Bz component data jointly to derive a layered conductivity model regularised via a reference model and smoothness constraints. To find an acceptable data misfit, we find it is necessary to solve for three extra geometry parameters as in Figure 2. Panel (1) Rx pitch, (2) Tx-Rx vertical (Dz) separation and (3) horizontal (Dx) separation. The need to solve for these geometry parameters holds despite efforts to calibrate and record the geometry and orientation with GPS and the Rx bird inertial measurement unit (IMU) in fixed-wing systems (Brodie et al. 2019). We use these IMU values as a starting estimate, instead.

In a separate type of inversion, we have been using as data the magnitude of the vector sum of the B field in the inline flight direction. In this formulation, the resulting in-plane amplitude data is derived using equation 1.

$$B_{amp} = \sqrt{B_x^2 + B_z^2} \quad . \quad (1)$$

Dealing with B_{amp} instead of joint B_x and B_z, reduces the number of unknown parameters we need to solve for in our inversions, as the formulation in (1) is independent of Rx-pitch.

An example from our separate XZ-component joint inversion and combined XZ-vector-sum inversion (**Figure 2**) shows a line segment from the AusAEM Western Resources Corridor data acquired over the Kimberley Region in WA. The geology mapped in this area by Gellatly and Derrick (1967) and Phillips et al. (2018), established that the Kimberley Group consists of sandstone, basalt, siltstone, and carbonate rocks, occasionally intruded locally by dolerite. Zhan (2022) recently concluded that the siltstone components of the Pentecost Sandstone, and the underlying Elgee Siltstone, could be mapped in the AusAEM profiles because of the conductivity contrasts within the surrounding resistive sandstone units.

In Figure 2, panel (4) shows an overall better data fit for the modelled B_{amp} vector sum (blue) than our joint B_x and B_z (black) expressed as a single value (PhiD). The closer the value is to one, the greater the model represents the observed data. In Panel (5), we show the observed (black), and modelled (coloured) Z-component data for the joint Bx and Bz – inversion, and similarly (6) the X-component data for the same joint inversion. Alternatively, panel (7) shows the observed combined XZ vector-sum inversion input data (black) and the corresponding modelled (coloured) data. Panel (8) shows the joint inversion results and (9) the vector sum inversion results as conductivity sections.

The geology in the leftmost 40 km of the section (panels (8) and (9)), shows layers of alternating conductivity within the asymmetric synclines, which is consistent with the mapped bedrock geology by Phillips et al. (2018). Panel (9) (vector-sum inverted section) shows a deeper coherent conductive layer associated with siltstones that has not been imaged in (8). In addition, sub-horizontal conductors are resolved more discretely in (9) than in (8), at 30 km and 50 km distances from the right side of the section.

Patching the new data with the old legacy data or vice-versa

Hundreds of thousands of line-km of AEM data have been flown by the exploration industry and hydrogeologists all over Australia. The largest Australian state, WA, reports the acquisition of close to 800 individual surveys since the 1990s, of which only 35 have been acquired by the government. Similar trends of private-to-public acquisition are expected in other states. However some of these legacy datasets will have missing information and may never have been quantitatively modelled. To extract useful subsurface information from these disparate AEM datasets, we need to invert them using similar procedures to the more modern regional surveys. Previous work by Ley-Cooper et al. (2015, 2016) and more recently by Mule and Brodie (2023), have shown the value of reprocessing historic data with more modern inversion schemes.

As part of GA's work in assessing regional groundwater resources, we reinverted 36,000 line-km of high-resolution AEM data acquired originally for mineral exploration. These 11 surveys from the Musgraves region of Western and South Australia (Symington et al. 2022) were flown with the SPECTREM system. This was a set of challenging surveys in which the actual geometry of the system was not known, and the primary field had been removed during the original processing. Following the primary field reconstruction process and converting the data from ppm units to Femto Teslas as outlined by Ley-Cooper & Brodie (2013), the reprocessed data were successfully inverted using the XZ-vector-sum inversion. The new conductivity-depth structure recovered from these surveys are quite compatible with those obtained from a fixed-wing system as part of the AusAEM survey (**Figure 3)**. The integrated conductivity models from both surveys will be used to map palaeovalleys for assessing regional groundwater resources, and shows the value of legacy data.

CONCLUSIONS

To reconcile differences in AEM systems and models from different surveys through geophysical inversion, we use a consistent approach across surveys, different systems and historical datasets. This means the same mathematical algorithms and constraints are applied to the dataset – regardless of the equipment used. This ensures that the resulting models are comparable and can be used to make meaningful interpretations of the subsurface.

The in-house development of GA's codes allow for the flexibility to reprocess the data in innovative ways, e.g., using a vector sum magnitude of the measured components. This approach makes the conductivity models smoother, providing more lateral coherence at depth. It effectively deals with needing to know the Rx-pitch exactly and reconciles the measured and modelled data better.

For inversion of measured voltages and fields to conductivities, we use electromagnetic physics, and High-Performance Computing tools to estimate the geology of the subsurface. These improvements lead to better imaging, as in the case of Kimberley, where we have helped delineate a sequence of sandstones and siltstones within a known syncline. The benefits of our acquisition and technical development efforts as part of AusAEM are many, from improving our ability to map the subsurface for minerals, energy and groundwater purposes, to extending the utility of fixed-wing systems for the wider METS (Mining, engineering and technology services) sector.

ACKNOWLEDGEMENTS

The authors acknowledge Geoscience Australia's Exploring for the Future Programme (https://eftf.ga.gov.au). The valuable input of many colleagues from across Geoscience Australia, has helped throughout the different stages of the AusAEM programme. This work is published with the permission of the CEO, Geoscience Australia. Any mention of trademarks, firms, or product names is merely for descriptive or illustrative purposes and does not imply endorsement by Geoscience Australia.

REFERENCES

Brodie R.C., 2015. User Manual for Geoscience Australia's airborne electromagnetic, inversion software. Geoscience Australia. https://github.com/GeoscienceAustralia/ga-aem

Brodie R.C., Ley-Cooper, Y., Lockwood R. and Murray D. 2019 AusAEM Year 1: Some aspects of quality control and calibration. *AEGC Extended Abstracts* 2019 (1), 1-5.

Gellatly, DC and Derrick, GM 1967, Lansdowne, Western Australia:Geological Survey of Western Australia, 1:250 000 *Geological Series Explanatory Notes*, 26p.

Lane, R.J.L. ; Wynne, P.E. ; Poudjom Djomani, Y. ; Stratford, W.R. ; Barretto, J.A. ; Caratori Tontini, F. (2019): 2019 Australian National Gravity Grids: Free Air Anomaly, Complete Bouguer Anomaly, De-trended Global Isostatic Residual, 400 m cell size (includes Point Located Data). .dataset. http://pid.geoscience.gov.au/dataset/ga/133023

Ley-Cooper, A. Y., & Brodie, R. C. (2013). Inversion of SPECTREM AEM data for conductivity and system geometry. *ASEG Extended Abstracts,* 2013(1), 1-4.

Ley-Cooper AY, Munday T, Gilfedder M, Ibrahimi T, Annetts D, and Cahill K, 2015, Inversion of legacy airborne electromagnetic datasets to inform the hydrogeological understanding of the northern Eyre Peninsula, South Australia,Goyder Institute for Water Research Technical Report Series No. 15/50, Adelaide, South Australia.

Ley-Cooper AY, Munday T, Gilfedder M, Ibrahimi T, and Cahill K, 2016, Analysis and reinterpretation of historical AEM data sets: McArthur Basin, NT. *Conference: Annual Geoscience Exploration Seminar (AGES) Proceedings* ,At: Alice Springs, Northern Territory Volume: 2016

Ley-Cooper, A.Y., Brodie, R.C., and Richardson, M., 2020. AusAEM: Australia's airborne electromagnetic continental-scale acquisition program, Exploration Geophysics 51(1): 193-202, DOI: 10.1080/08123985.2019.1694393

Milligan, PR, Minty, BRS, Richardson, M and Franklin, R. 2009. The Australia-Wide Airborne Geophysical Survey - Accurate Continental Magnetic Coverage. *ASEG Extended Abstracts* 2009 (January 1, 2009): https://doi.org/10.1071/ASEG2009ab075.

Minty, B, Franklin, R, Milligan, P, Richardson, LM and Wilford, J 2009, 'The Radiometric Map of Australia', *Exploration Geophysics,* vol.40, no.4, pp. 325-333. https://doi.org/10.1071/EG09025.

Mule, S. and Brodie, R.C (2023). Leveraging the true value of historic AEM data sets with quantitative inversion. *AEGC Extended Abstracts*, 2023(1), 1-5.

Phillips, C, Maidment, DW and de Souza Kovacs, N 2018, Lansdowne, WA Sheet SE 52-5 (2nd edition*): Geological Survey of Western Australia*,1:250 000 Geological Series.

Ray A., Taylor R., Symington N., Brodie R.C. Ley-Cooper Y. and Moghaddam N. F., 2022, High Quality Geophysical Analysis software package. https://github.com/GeoscienceAustralia/HiQGA.jl Geoscience Australia eCat Id 146706

Symington, N., LeyCooper, Y., Smith, M. 2022. West Musgrave AEM conductivity models and data release. *Geoscience Australia*, Canberra. https://dx.doi.org/10.26186/146278

Zhan, Y 2022, Airborne electromagnetic survey, northern Western Australia: an integrated interpretation of selected features: *Geological Survey of Western Australia*, Report 234, 78p.

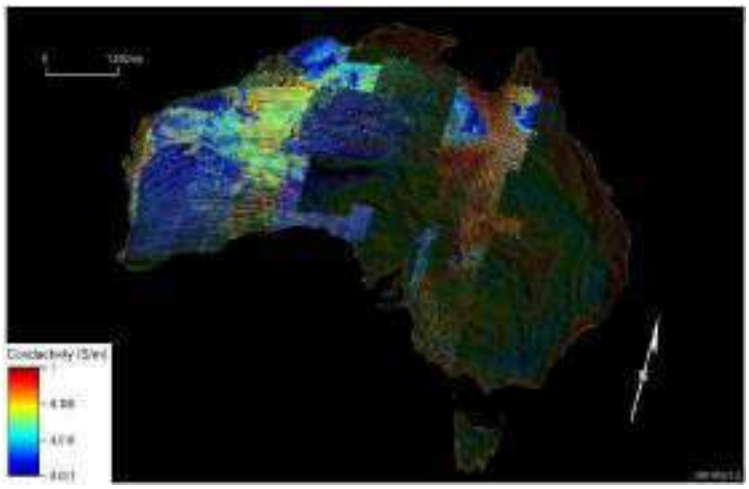

Figure 1. Current extent of the inverted AusAEM survey conductivity sections (red=conducting, blue=resistive), projected over a continental filtered Bouguer gravity map. The contiguous continental AEM coverage is what Geoscience Australia aspires to acquire in the near future.

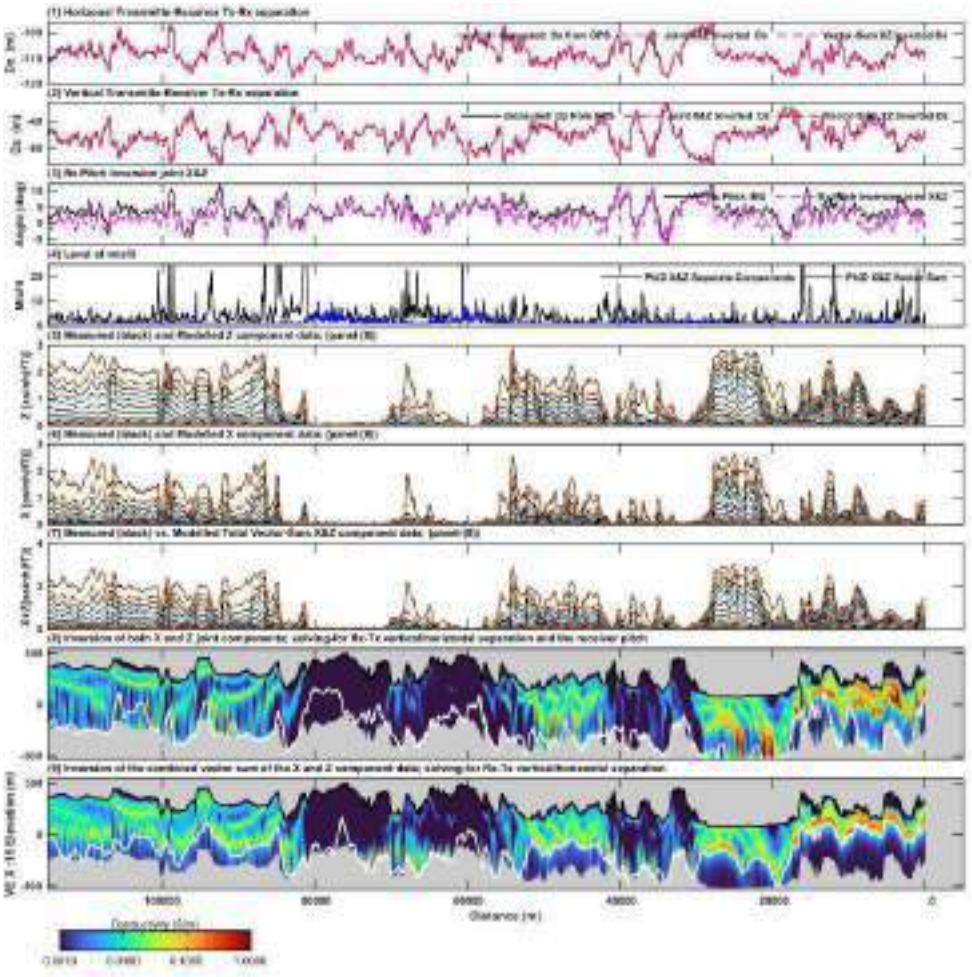

Figure 2. Representative conductivity-depth section of a ~120 km long line segment from AusAEM Western Resources Corridor Line 4130001, from the northern Kimberly in the WA, flown North-South. Details of panels are in the text. In panel (8), we show a section derived from the standard separate XZ joint inversion GALEI algorithm, and in panel (9), we illustrate a section from GALEI combined vector-sum XZ inversion. Models derived by the vector sum XZ inversion highlight improvements in the coherence at depth, have a better resolution of sub-horizontal conductors and removal of glitches between individual soundings at the base of the conductivity section.

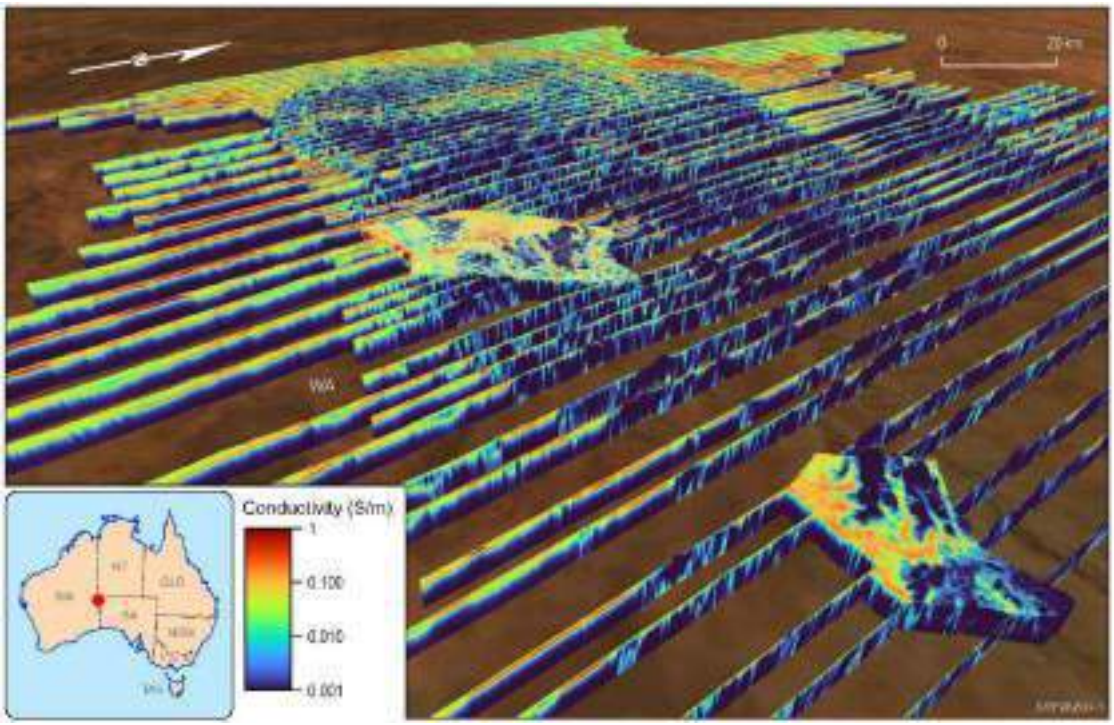

Figure 3. AusAEM Western Resource Corridor regional data acquired in 2022, integrated with legacy industry data acquired in 2009. New inversions seamlessly delineate the dendritic patterns characteristic of palaeovalleys across both surveys.

HiQGA: Open source deterministic and probabilistic AEM inversion

Anandaroop Ray*
Geoscience Australia, Symonston, ACT, Australia
anandaroop.ray@ga.gov.au

Richard Taylor
Formerly at Geoscience Australia

Ross C. Brodie
Geoscience Australia, Symonston, ACT, Australia
Ross.C.Brodie@ga.ga.gov.au

Yusen Ley-Cooper
Geoscience Australia, Symonston, ACT, Australia
Yusen.LeyCooper@ga.gov.au

Neil Symington
Geoscience Australia, Symonston, ACT, Australia
Neil.Symington@ga.gov.au

Negin F. Moghaddam
Formerly at Geoscience Australia

SUMMARY

The High Quality Geophysical Analysis (HiQGA) package is a framework for geophysical forward modelling, Bayesian inference, and deterministic imaging. A primary focus of the code is production inversion of airborne electromagnetic (AEM) data from a variety of acquisition systems. Adding custom AEM systems is simple using a modern computational idea known as multiple dispatch. For probabilistic spatial inference from geophysical data, only a misfit function needs to be supplied to the inference engine. For deterministic inversion, a linearisation of the forward operator (i.e., Jacobian) is also required. For fixed wing geometry nuisances, probabilistic inversion is carried out using Hierarchical Bayesian inference, and deterministic inversion for these nuisances is done using BFGS optimisation. The code is natively parallel, and inversions from a full day of production AEM acquisition can be inverted on thousands of CPUs within a few hours. This allows for quick assessment of the quality of the acquisition, and provides geological interpreters preliminary subsurface conductivity images and associated uncertainties. These images are used to create subsurface models for a range of applications from natural resource exploration to its management and conservation.

Keywords: Inversion, open-source, Julia, airborne, electromagnetic, Occam, Bayesian.

INTRODUCTION

Airborne electromagnetic (AEM) methods are a mainstay for geophysical imaging of the top hundreds of meters of the Earth's crust. While AEM has been in use for decades (Palacky and West, 1991), until relatively recently, it has been used largely as a "bump finding tool". To be explicit, currents are induced in the earth using a transmitted, time varying pulse from an airborne antenna, in accordance with Faraday's Law. The secondary magnetic field due to these induced currents are then picked up by an airborne receiver. For a system operating in the time domain, the induced response is often anomalous (i.e., has "bumps") in the presence of conducting heterogeneities within resistive host rock. While these bumps are useful to first order for locating anomalous ore bodies, quantitative physics modelling to match the earth response, typically through an inversion routine, provides far more useful subsurface information. By inverting closely spaced soundings acquired rapidly by low-flying aircraft travelling at speeds of over a hundred kilometres an hour, large swathes of land can be surveyed quickly. High performance inversion tools can then generate images of the earth's conductivity structure down to approximately 300 m depth. These images allow for geological interpretation of the subsurface for a variety of purposes from geotechnical investigation to natural resource exploration, management and conservation (see Brodie, 2010 for an overview).

While there exist various software packages for inverting AEM data, e.g., the Aarhus Workbench (based on Auken and Christiansen, 2004), there are few which are open source (e.g., the Python-based SIMPEG, Heagy et al., 2017), and handle most commercially available AEM systems (e.g., the C++ code GA-AEM, Brodie, 2016). Of the just-listed references, GA-AEM is fully open source, capable of inverting hundreds of thousands of soundings in parallel and can carry out both probabilistic and deterministic inversion of production AEM data. In this work, we present HiQGA, a Julia language (Bezanson et al., 2017) based code which is open source, and can invert high-density production AEM data in an HPC (High performance computing) environment. For AEM data, it is the only codebase we are aware of which can carry out both probabilistic and deterministic inversion, while taking fixed-wing geometry nuisance parameters into account.

METHODS

HiQGA is a multi-physics inference and imaging codebase, which is agnostic to the spatial dimension of the geophysical modelling and inversion being carried out. For probabilistic inversion, HiQGA uses a Gaussian process (GP) based trans-dimensional inference scheme (Ray and Myer, 2019; Ray, 2021). For deterministic inversion, it uses an Occam inversion scheme (Constable et al., 1987) with a within-bounds modification. Given the "multiple dispatch" capabilities of the Julia language, for any new geophysical method added to the framework, no HiQGA source code needs to be modified. Available functions are simply imported and extended, leading to a rich codebase suitable for both prototyping and production work. Julia is also natively parallel, obviating the use of bolt-on parallelisation after serial code has been written. The framework provides a natural testbed for joint inversions of geophysical data – from an optimisation or inference point of view, different types of geophysical observations are equivalent once a negative log likelihood (i.e., misfit function) normalised by data errors is provided.

The production AEM codes are for 1D earth models, based on the time domain codes in Blatter et al. (2018). For deterministic AEM inversion where nuisances are also inverted, this is done

in a two-stage scheme employing Occam for conductivities and a barrier enforced BFGS (Nocedal and Wright, 2006) for the nuisance parameters. Probabilistic AEM inversion for any geophysical nuisances is done through a Hierarchical Bayesian scheme (Gelman, 2006) with one reversible jump Markov chain step (Green, 1995) for conductivities followed by a Metropolis-Hastings (Metropolis et al. 1953; Hastings, 1970) step for the nuisances. This is done within an efficient parallel tempering framework to overcome local likelihood maxima (Swendsen and Wang, 1987).

The HiQGA codebase is easy to install and available within the Julia ecosystem. From within Julia, an installation is as simple as issuing the following command from the package manager: **Pkg> add HiQGA**. All that is required is a computer with internet connectivity. Under the permissive MIT license, source code is available on Geoscience Australia's (GA) GitHub repository. Detailed install instructions for both a PC (MacOS/Windows/Linux) and a supercomputer environment are available at https://github.com/GeoscienceAustralia/HiQGA.jl. A number of examples to get started can also be found in the **examples/** folder at the above URL.

RESULTS AND IMPLEMENTATION DETAILS

A demonstration of the various kinds of AEM inversion HiQGA can perform is shown at one sounding location in **Figure 1**. The AEM data in the figure are from a TEMPEST fixed-wing survey.

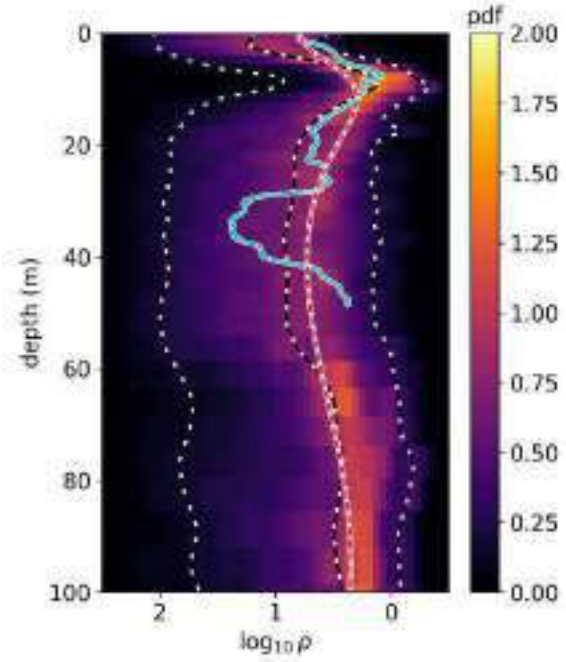

Figure 1. Deterministic and probabilistic inversion of AEM data at a sounding close to a logged borehole. Induction log values are shown with a blue line, and deterministic inversion results taking geometry nuisances into account are shown with a dashed red and white line. Higher probability resistivities are shown with hotter shades, and the 5th, 50th and 95th posterior percentiles of resistivity are shown with dashed black and white lines.

Deterministic inversion of a single sounding is quick and completes within tens of seconds on one CPU. Probabilistic sampling of one sounding requires 6-8 CPUs in parallel and convergence to the Bayesian posterior conductivities requires between 2 to 4 hours, depending on the AEM system. However, the confidence with which we can make geological interpretations is far greater when using a probabilistic inversion. This is evident from an inversion of data from a SkyTEM 312 helicopter AEM system over the Upper Darling floodplain, as shown in **Figure 2** (deterministic) when compared with **Figure 3** (probabilistic). When studying variation in the percentiles of conductivity across all soundings in a line, far more interpretive detail can be gleaned when contrasted with examining a single deterministic estimate of conductivity across the line. This holds true for fixed-wing systems as well, as shown in **Figure 4** (deterministic) when compared with **Figure 5** (probabilistic) for the TEMPEST system flown over the Menindee test line in New South Wales, Australia. The location marked with a dashed vertical line between 10 and 11 km line distance was previously examined in detail in **Figure 1**. Irrespective of whether the reference model for a deterministic inversion is resistive or conductive, the probabilistic inversion posterior conductivity percentiles and their variation with depth give a clearer indication of how conductivities behave at depth. This is especially critical when we lose sensitivity to structure with depth.

Finally, since all soundings are inverted in parallel, both in the deterministic and probabilistic case, an entire day's production with over 100,000 soundings can be quality checked rapidly. All soundings can be inverted deterministically within a few hours, and a few subset lines or soundings of interest can also be probabilistically inverted within hours, given that the time for one sounding is the time for all soundings if enough CPUs are available. If the number of CPUs is less than what is required to invert a set of soundings in one go, soundings are inverted in batches till all soundings in the set are exhausted.

CONCLUSIONS

We have presented the open-source Julia package HiQGA.jl, which can carry out both probabilistic and deterministic inversion of AEM data inclusive of geometry nuisances. Algorithms available for this are trans-dimensional GP + Hierarchical Bayes and Occam's inversion + BFGS. The usability barrier is low, as installation on a desktop computer (Windows, MacOS or Linux) only requires installation from within the Julia ecosystem. Examples can be run and plots generated in notebook fashion, to provide quick intuition on AEM system responses and sensitivity to subsurface structure. The code is HPC ready, making it suitable for inverting large datasets which now cover much of Australia at 20 km between-line resolution (Ley-Cooper et al., 2020).

ACKNOWLEDGMENTS

All computation was carried out at the National Computational Infrastructure's *Gadi* supercomputer. The HiQGA project is part of the Australian Government's Exploring for the Future program (https://eftf.ga.gov.au). All code is freely available at: https://github.com/GeoscienceAustralia/HiQGA.jl

This abstract is published with the permission of the CEO, Geoscience Australia.

REFERENCES

Auken, Esben, and Anders Vest Christiansen. "Layered and laterally constrained 2D inversion of resistivity data." Geophysics 69, no. 3 (2004): 752-761.

Brodie, Ross C. "Holistic inversion of airborne electromagnetic data." (2010). PhD Thesis, Australian National University

Brodie, Ross C. GA-AEM Source code repository: https://github.com/GeoscienceAustralia/ga-aem/releases/tag/Release-20160606 (2016)

Bezanson, Jeff, Alan Edelman, Stefan Karpinski, and Viral B. Shah. "Julia: A fresh approach to numerical computing." SIAM review 59, no. 1 (2017): 65-98.

Constable, Steven C., Robert L. Parker, and Catherine G. Constable. "Occam's inversion: A practical algorithm for generating smooth models from electromagnetic sounding data." Geophysics 52, no. 3 (1987): 289-300.

Hastings, W. Keith. "Monte Carlo sampling methods using Markov chains and their applications." (1970): 97-109.

Heagy, Lindsey J., Rowan Cockett, Seogi Kang, Gudni K. Rosenkjaer, and Douglas W. Oldenburg. "A framework for simulation and inversion in electromagnetics." Computers and Geosciences 107 (2017): 1-19.

Metropolis, Nicholas, Arianna W. Rosenbluth, Marshall N. Rosenbluth, Augusta H. Teller, and Edward Teller. "Equation of state calculations by fast computing machines." The journal of chemical physics 21, no. 6 (1953): 1087-1092.

Jorge Nocedal and Wright, Stephen. "Numerical optimization." Springer Science 35, no. 67-68 (2006): 7.

Ley-Cooper, Alan Yusen, Ross C. Brodie, and Murray Richardson. "AusAEM: Australia's airborne electromagnetic continental-scale acquisition program." Exploration geophysics 51, no. 1 (2020): 193-202.

Palacky, G. J., and G. F. West. "Airborne electromagnetic methods." (1991). Electromagnetic Methods in Applied Geophysics: Volume 2, Application, Parts A and B. January 1991, 811-880

Ray, Anandaroop. "Bayesian inversion using nested trans-dimensional Gaussian processes." Geophysical Journal International 226, no. 1 (2021): 302-326.

Ray, Anandaroop, and David Myer. "Bayesian geophysical inversion with trans-dimensional Gaussian process machine learning." Geophysical Journal International 217, no. 3 (2019): 1706-1726.

Swendsen, Robert H., and Jian-Sheng Wang. "Nonuniversal critical dynamics in Monte Carlo simulations." Physical review letters 58, no. 2 (1987): 86.

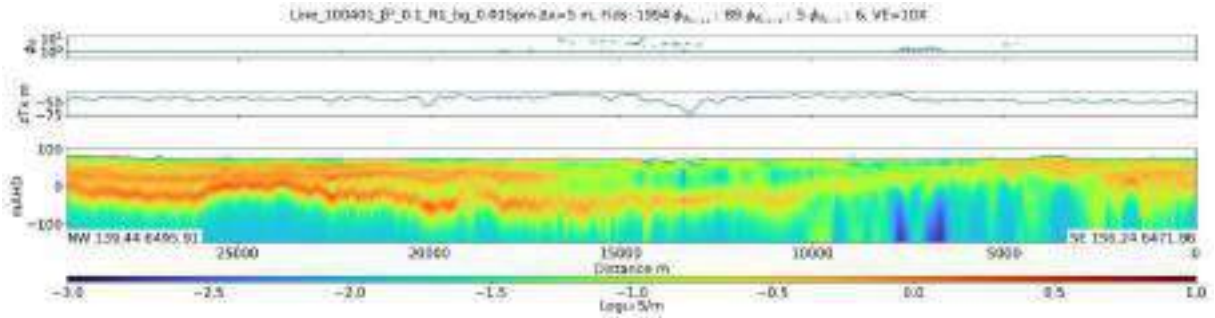

Figure 2. Deterministic inversion of SkyTEM 312 helicopter EM data from the Upper Darling floodplain. The top row indicates data fit, with 1 indicating a fit to within noise. The second row shows the height of the transmitter frame. The bottom row displays subsurface conductivity at metres above Australian height datum (mAHD). Note the fine conductive near surface layering, as well as ambiguity in this layering between 17 km and 7.5 km line distance.

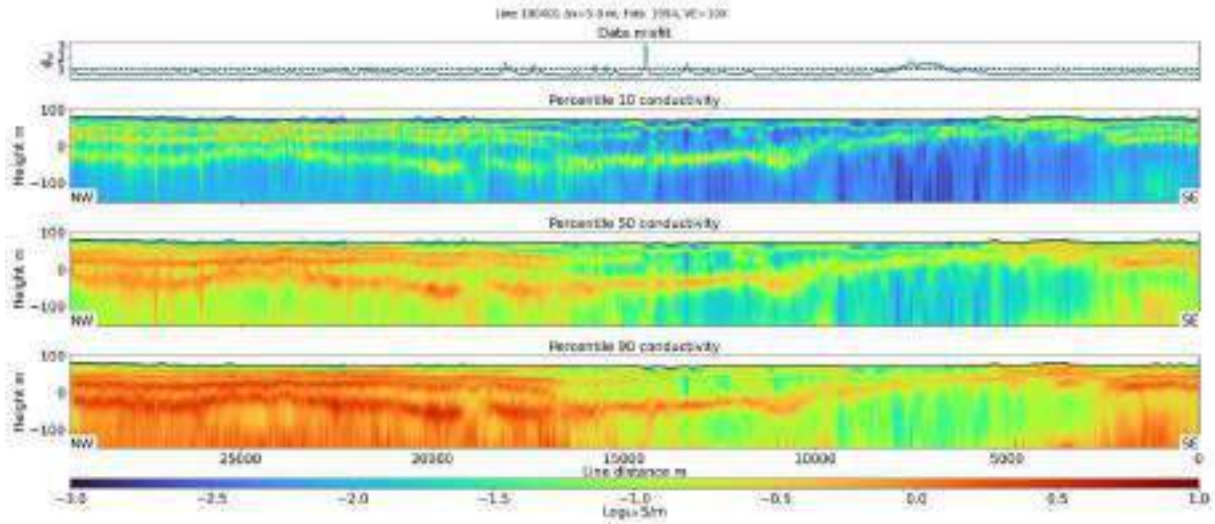

Figure 3. Probabilistic inversion of the same AEM data used in Figure 2. Different percentiles of conductivity change similarly for more certain features. Near surface structure between 17 km and 7.5 is now clearly interpretable, compared to Figure 2.

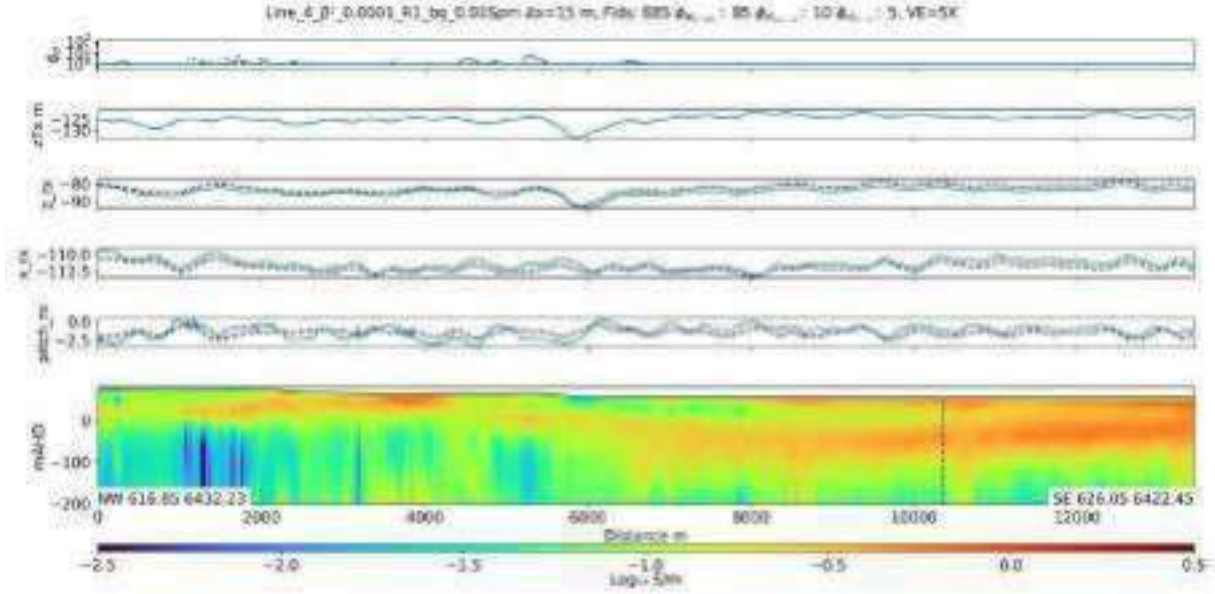

Figure 4 Deterministic inversion of fixed-wing data from the TEMPEST system. As before, the first row from the top indicates fit to the data and the second row shows transmitter loop height. The next few rows show the receiver height (z_rx), receiver inline distance to transmitter (x_rx), and the receiver pitch (pitch_rx) – with measured and inverted values given by dashed and blue lines respectively. The bottom row shows the inverted conductivity section. A lens shaped resistive structure is clearly visible within Menindee Lake at line distances from 6 km – 14 km.

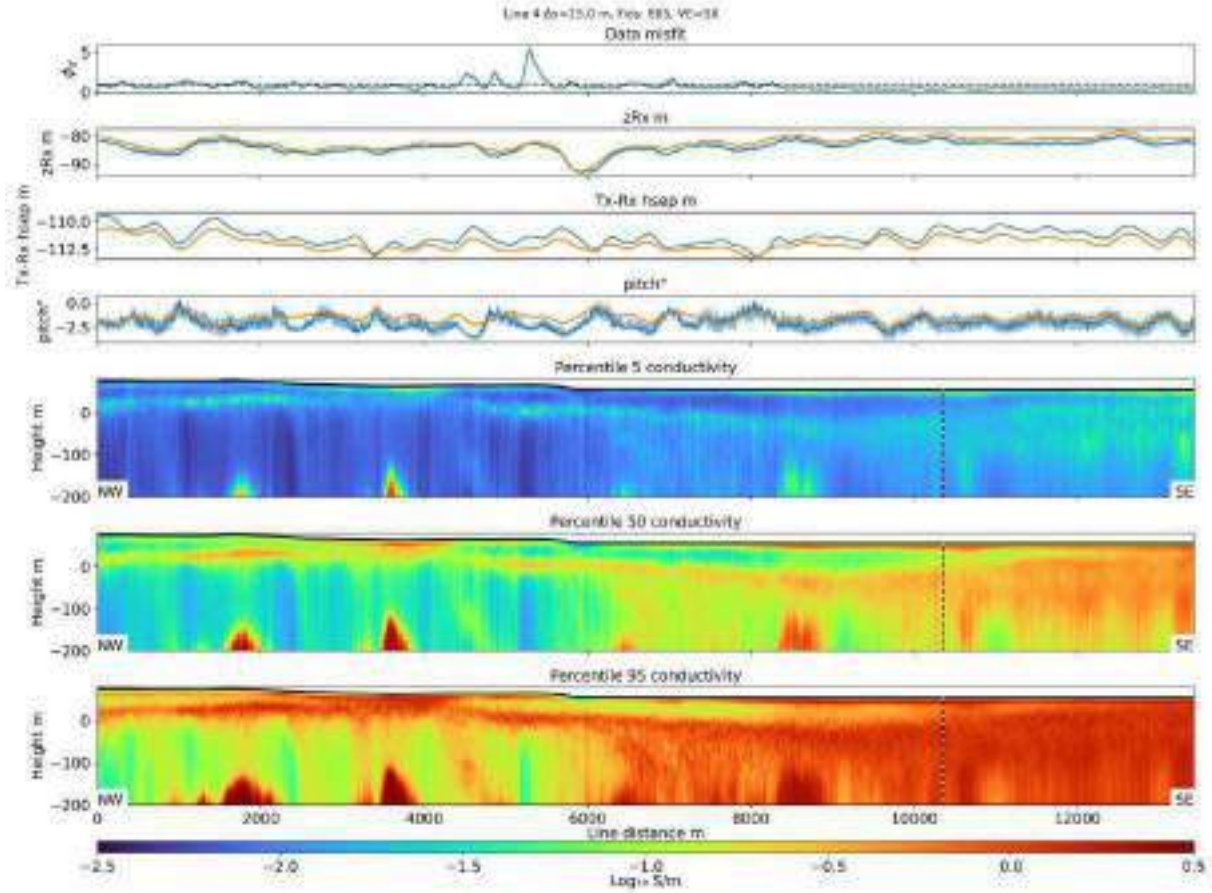

Figure 5. Probabilistic inversion of the same AEM data used in Figure 4. Again, similar features in all percentiles can be interpreted with confidence. It is quite certain that the subsurface at datum height below 0 m is resistive in the north-western half of the line, when compared to the south-eastern half. Such a determination is hard to make from Figure 4 alone.

Design of BIPTEM: an airborne B field IP and TEM system

James Macnae*
CD3D
Melbourne
jcm@c3dmap.com

Terry Kratzer
CD3D / Biptem
Melbourne
terry@biptem.com

Duncan Massie
Monex Geoscope
duncan.massie@
monexgeoscope.com.au

Paul Rogerson
Thomson Airborne
Griffith, NSW
paul@thomsonair.com

SUMMARY

The BIPTEM project was funded by several companies and developed a 1 MAm^2 transmitter which was tested with a concentric loop B field inductive magnetometer in 2017. A report on the system was presented at AEM18. With the rotation sensing and inertial navigation technology available at that time, motion noise corrections to the collected data did not perform well enough to justify further substantial investment and the project was mothballed. Following improvements in fibre-optic technology, and the announced future commercial availability of breakthrough quantum rotation sensors, Newmont funded research to improve the BIPTEM system and test its ability to map IP targets.

Many experiments and flight tests were conducted, and extensive software developments were undertaken to bring the system to full operation. Parallel modelling and ground experiments showed that the optimum system for IP effect detection has a large Tx and a horizontal component Rx (separated by about 300m in the Slingram geometry.

Key words: B field TEM Airborne IP Slingram

INTRODUCTION

Initial developments towards an airborne IP system were conducted from 2011-2016 in AMIRA Projects P1036 and P1036a. The AMIRA project developed and tested airborne electric field sensors and the 3-component RMIT University ARMIT B field sensor, but the RMIT proposal to continue development in P1036b was not funded. Independently, Source Geophysics, Monex Geoscope and Thomson Aviation developed the hardware for an AEM/AIP transmitter and receiver to house the ARMIT B field sensors.

Post the AMIRA projects, tests using a different (BIPTEM) inductive magnetometer with concentric loop geometry followed in 2017, but the available Russian molecular electronic technology (MET) rotation sensors proved inadequate to measure rotations accurately enough for the required corrections to motion-noise affected B field data. The project was then mothballed, with a watching brief focussed on rotation measurement technology.

In 2021, new inertial navigation sensors (INS) came on the market, and inexpensive sensors were announced for future (2023) commercialisation at an order of magnitude or more increased sensitivity; with a fraction of the cost, size and weight of other technologies With technology becoming available to address the shortcomings of the 2017 BIPTEM experiments, Newmont Inc, CD3D, Thomson Airborne and Monex Geoscope agreed to fund further development and field testing of the BIPTEM system.

SYSTEM DESIGN

Choice of Sensor

There are several choices to be made in an airborne EM system that is designed to measure IP effects. There are potentially 3 possible sensor choices to measure EM fields containing IP information. These and the relevant considerations are
Electric E field sensors (1). Theoretically the electric field is much more sensitive to IP effects than the magnetic field which requires significant current flow to be detectable. One implementation of such sensors were investigated over a decade ago in AMIRA Project P1036, and while the sensors had sufficient sensitivity, atmospheric signals (coupling to rapidly varying earth-ionosphere electric field, wind carried charge on dust particles) dominated observed responses
Coil dB/dt sensors (2) almost universally used in airborne EM systems. These sensors have a response that falls off as 1/f towards low frequencies, and hence have reduced sensitivity to the slow decays characteristic of IP effects.
Magnetometers (3) measuring B fields which are much more sensitive to IP effects that dB/dt sensor (Figure 1)

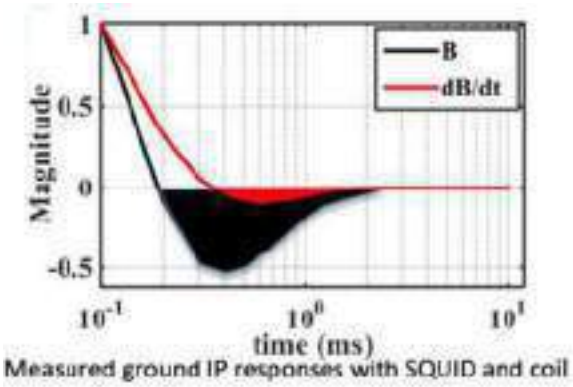

Figure 1: Comparison over polarizable ground of measured decays between coil and SQUID sensors using the same transmitter and receiver locations.

There are 3 B field vector sensor types commercially used in electromagnetic geophysics: Fluxgates (which are too noisy), SQUIDS (logistically inconvenient, Foley et al, 1999, Stolz et al, 2022) and Inductive Magnetometers. (commonly used in MT and AMT systems). There are also two types of inductive magnetometers: feedback (e.g. Zonge) or current sensing (e.g. ARMIT, Macnae and Kratzer, 2013). Inductive magnetometers have internal noise level substantially less than ambient (sferic) and rotation noise, so were chosen for BIPTEM.

Motion Noise

Having settled on an inductive B field sensor, we chose a cube geometry based on an expired/abandoned UNB patent (duPuis et al, 2008) which ensured orthogonality between inductive magnetometers (Figure 2). Figure 3 shows a suspended test jig of the sensor layout on a plywood cube with attached GPS and inertial navigation IMU sensors.

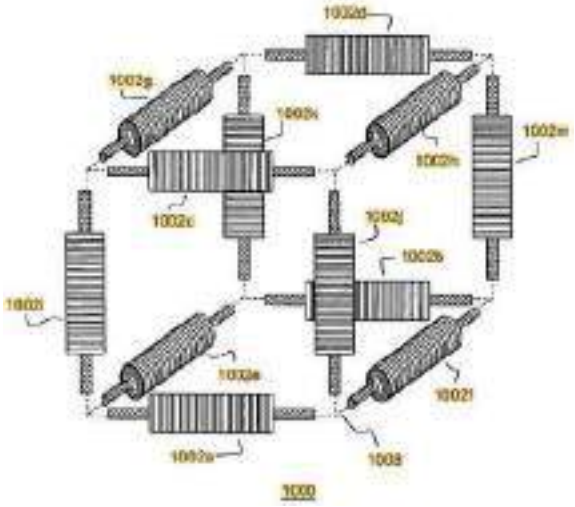

Figure 2: Patent US7375529B2 Figure 10 depicting a good layout for inductive magnetometer sensors with a high moment of inertia (resistance to rotation)

The reason motion (strictly rotation) noise is important is that magnetometers couple to the earth's magnetic field B_E, nominally say 50,000 nT in amplitude. BIPTEM inductive magnetometers have a sensitivity better than 0.5 pT, which is more than 100 million times smaller than B_E. Figure 4 illustrates that only rotations about the x and y axes affect the magnitude of the z component measurement Bz due to the earth's field.

It is of note that inductive magnetometers do not have "DC" magnetic field sensitivity, and as such do not detect B_E directly, but rather measure any changes due to coupling in the bandwidth of the sensor/system from say 0.1 Hz to 50 kHz.

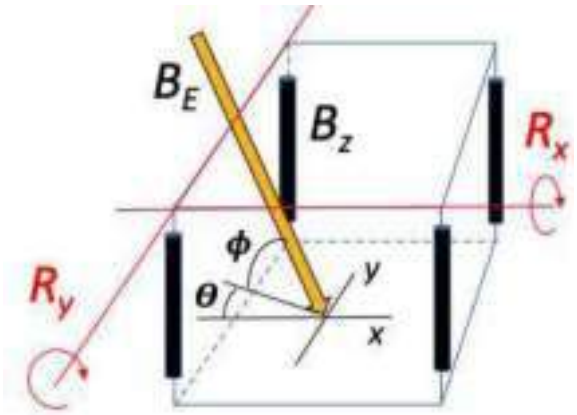

Figure 4: B_z sensor coupling to the Earth's magnetic field B_E changes with rotations R about the x and y axes, and can be expressed as trigonometrical functions of the rotations R_x, R_y and coupling angles θ, ϕ .

Figure 3: Test jig with 3 (x,y,z) component B field sensors with rotation measuring hardware.

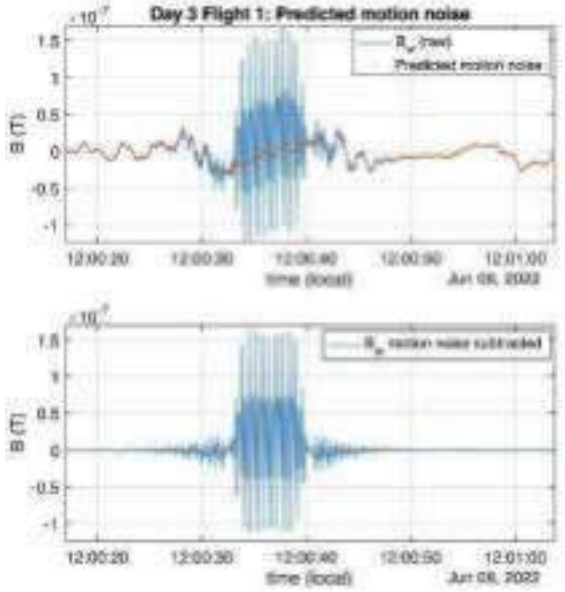

Figure 5: Effect of rotation corrections (motion noise) on measured B field during overflight of a transmitter

Figure 5 shows the result of motion noise corrections using about 50 seconds of streamed data with measured rotations and an assumed background magnetic field. Quite clear is that away from the transmitter, the predicted response matches the observed data, and that corrections reduce the variations seen in the measured data

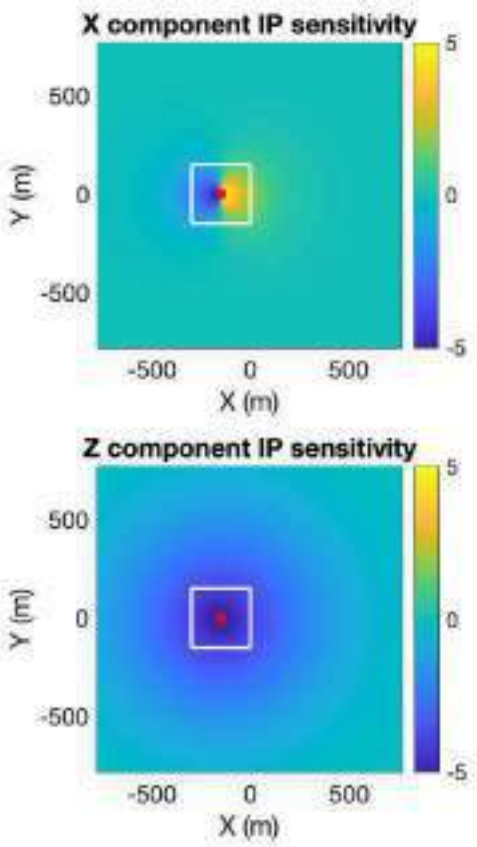

Figure 6: A central x directed horizontal sensor has equal and opposite sensitivity to the circulating EM induced current and reverse polarization currents either side of it. If the surficial polarizable conductor is uniform, then there is no net response in the X (or Y) components at the central position. A vertical Z component sensor responds to circulating reversed IP currents from a large region within and just outside the transmitter loop.

System Geometry Considerations

Most published studies of IP effects as seen from inductive EM sources have used coil sensors measuring the rate of change of the magnetic field dB/dt. Most IP effects seen in ground EM have been attributed to clays. Smith and West (1988) outline the three requirements for IP effects to significantly exceed the responses from EM induction. They can be simplified in time domain to:

1) The transmitter must couple well to a regional or local conductor so that induced polarizing currents are large at early delay times
2) The induced EM current must decay close to zero within the measured time window
3) The polarization current must be well coupled to the receiver

The most common case where these 3 conditions are met has been the Z component of coincident or concentric loop geometry used on the ground or in helicopter TEM surveys (Macnae, 2016) with sensitivity illustrated in Figure 6.

In the case of Slingram geometry (moving Tx with separated Rx) we will see that a large loop transmitter and a horizontal X component receiver satisfy these 3 conditions. This geometry was also recommended in the duPuis et al (2004) patent application as illustrated in Figure 7.

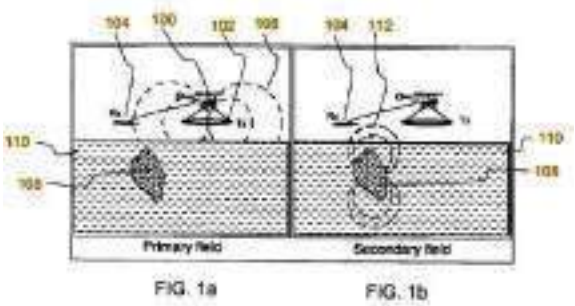

Figure 7. Suggested survey geometry from Patent US7375529B2 to minimise primary and maximise secondary field.

Figure 8 shows the sensitivity to IP effects of a magnetic field sensor located 300 m from a transmitter loop. This calculation shows that the x component has simple coupling to any IP reversed currents in the near surface.

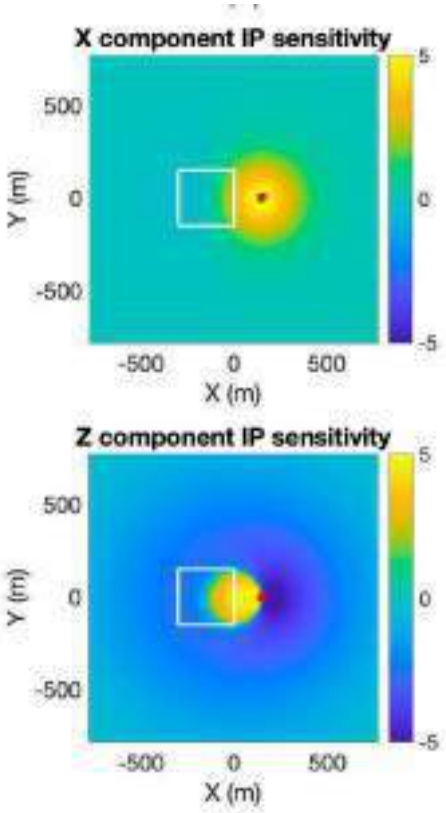

Figure 8: Slingram geometry X and Z component sensitivity to a 40 m deep polarizable sheet conductor. This incidentally would be the sensitivity of an airborne Slingram system flying at a height of 40 m over a surficial polarizable conductor. The x component is simply coupled to the smoke ring current, whereas the Z component has both positive and negative contributions.

Figure 9 presents a Bz vertical component profile flown over a transmitter loop operating with a 50% duty-cycle and 12.5 Hz repetition rate. The typical pattern of crossovers migrating away from the transmitter on either side is inductive of the conductive regolith in this location. The negatives located directly under the transmitter at late delay times (yellow profiles) indicate the presence on polarizable near-surface material.

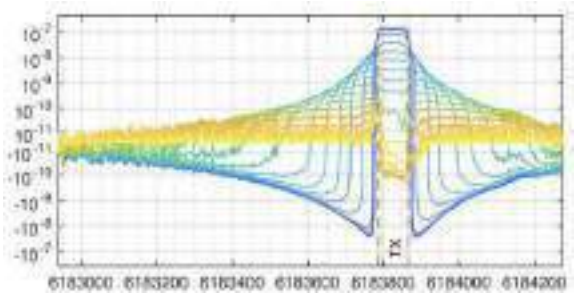

Figure 9. 12.5 Hz Z component data from a profile flown directly over a ground Tx has late time negative indicative of polarizable clays in the regolith with τ_{IP} = 15 ms

Figures 10 and 11 show vertical Bx and horizontal Bh component decays measured in a ground survey with a B field sensor and Slingram geometry. Consistent with sensitivity analysis that Bz IP anomalies may have either sign or be zero. The Bz component has a far smaller time window where negative IP effects dominate the EM decay.

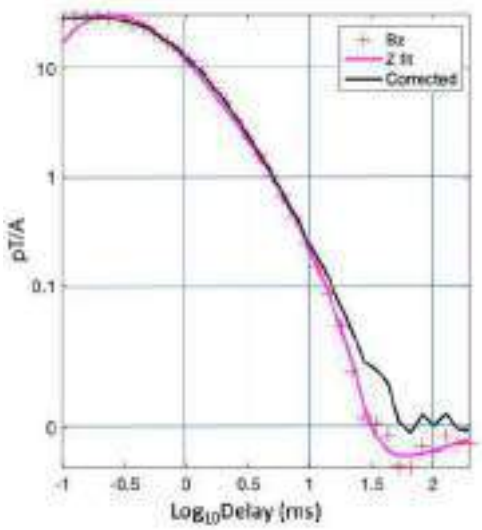

Figure 10: Bz decay 300 m from Tx loop. There is a small IP response visible at late delays. The black profile shows a corrected EM decay. Both measured and corrected data appear noisy at late delays on the logarithmic vertical scale.

FIELD TEST

A field test of the BIPTEM system in Slingram mode is to be conducted on April 19th, just after the deadline for abstract submission. Field testing requires an airborne transmitter as well as separated receiver, and we have designed and tested a 1

MAm^2 rigid transmitter to provide sufficient dipole Moment for effective data collection (Figure 12). Because the induced current "smoke ring" moves downwards and outwards, and it is necessary to have a receiver well-coupled to the reversed IP currents, we will use two helicopters to carry the transmitter and receiver (Figure 13)

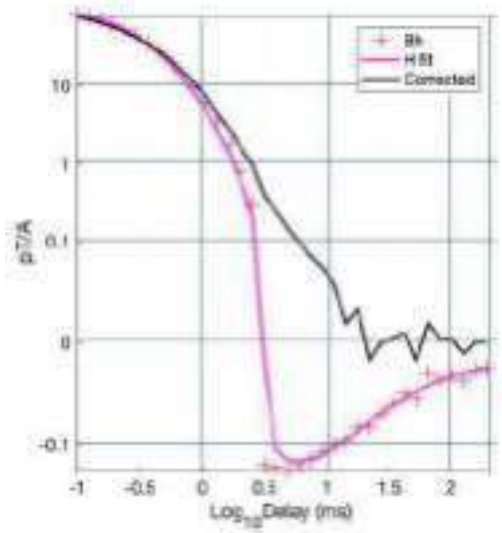

Figure 11: Corresponding Bx decay 300 m from Tx loop. There is a much larger IP response visible from medium to late delays. Again, noise is evident at late delays in the original and corrected data.

Figure 12: The transmitter in flight, with a 3 component BIPTEM sensor in the centre

CONCLUSIONS

Measuring airborne B fields to detect IP effects (and excellent conductors) presented a large number of challenges. These included design of a transmitter loop and sensor suspension systems that do not conflict with patents in the field. The biggest challenge however is measurement of rotations and the Earth's field to sufficient accuracy to permit rotation noise corrections.

Many experiments and flight tests have been conducted with prototype, and extensive software developments were undertaken to bring the system to full operation. Parallel modelling and ground experiments showed that the optimum system for IP effect detection has a large Tx and a horizontal component Rx (separated by about 300 m in the Slingram geometry.

ACKNOWLEDGMENTS

We thank Greg Walker for his confidence in our proposed technology and Newmont for funding this research.

REFERENCES

Du, S., Y. Zhang, Y. Pei, K. Jiang, L. Rong, C. Yin, Y. Ji , and X. Xie. (2018), Study of transient electromagnetic method measurements using a superconducting quantum interference device as B sensor receiver in polarizable survey area, GEOPHYSIC 83, https://doi.org/10.1190/geo2017-0197.1

Foley, C., K. Leslie, R. Binks, C. Lewis, W. Murray, G. Sloggett, S. Lam, B. Sankrithyan, N. Savvides, A. Katzaros, K. Muller, E. Mitchell, J. Pollock, J. Lee, D. Dart, R. Barrow, M. Asten, A. Maddever, G. Panjkovic, M. Downey, C. Hoffman, R. Turner. "Field trials using HTS SQUID magnetometers for ground-based and airborne geophysical applications," in IEEE Transactions on Applied Superconductivity, vol. 9, no. 2, pp. 3786-3792, June 1999, doi: 10.1109/77.783852.

Macnae J., and T. Kratzer, 2013, Joint sensing of B and dB/dt responses, ASEG2013 - 23rd Geophysical Conference

Macnae, J., 2016, Quantifying airborne Induced Polarization effects in helicopter time domain electromagnetics, Journal of Applied Geophysics 135, 495-502

R.S. Smith and G.F. West (1988) An explanation of abnormal TEM responses: coincident-loop negatives, and the loop effect. Exploration Geophysics 19(3) 435 - 446

Stolz, R, M Schifer, M. Becken, A. Thiede, M. Schneider G. Chubak P. Marsden A. Braña Bergshjorth M. Schaefer, O. Terblanche, 2022, SQUIDs for magnetic and electromagnetic methods in mineral exploration; Mineral Economics https://doi.org/10.1007/s13563-022-00333-3

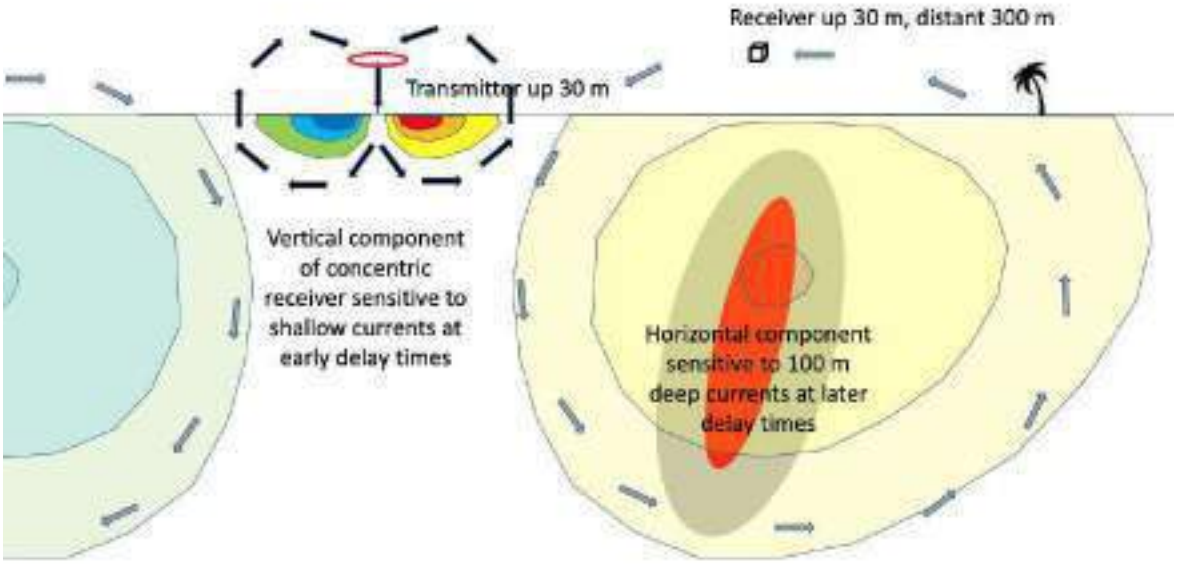

Figure 13. Currents induced in a background half-space below the transmitter location are shallow. The induced currents spread down and out, and having a receiver 300m behing the transmitter is optimum to detect induced currents (and thus reversed IP currents due to e.g. sulphides) at depths of 100 m or more

System-scale airborne electromagnetic surveys in the lower Mississippi River Valley support multidisciplinary applications

Burke J Minsley*
U.S. Geological Survey
Denver, Colorado, USA
bminsley@usgs.gov

Ryan F Adams
U.S. Geological Survey
Nashville, Tennessee, USA
rfadams@usgs.gov

William Asquith
U.S. Geological Survey
Lubbock, Texas, USA
wasquith@usgs.gov

Bethany L Burton
U.S. Geological Survey
Denver, Colorado, USA
blburton@usgs.gov

Bennett E Hoogenboom
U.S. Geological Survey
Denver, Colorado, USA
bhoogenboom@usgs.gov

Stephanie R James
U.S. Geological Survey
Denver, Colorado, USA
sjames@usgs.gov

Courtney Killian
U.S. Geological Survey
Bridgeville, Pennsylvania, USA
ckillian@usgs.gov

Katherine J Knierim
U.S. Geological Survey
Little Rock, Arkansas, USA
kknierim@usgs.gov

Wade H Kress
U.S. Geological Survey
Nashville, Tennessee, USA
wkress@usgs.gov

Max Lindaman
U.S. Geological Survey
Baton Rouge, Louisiana, USA
mlindaman@usgs.gov

Andy Leaf
U.S. Geological Survey
Madison, Wisconsin, USA
aleaf@usgs.gov

J.R. Rigby
U.S. Geological Survey
Oxford, Mississippi, USA
jrigby@usgs.gov

JP Traylor
U.S. Geological Survey
Lincoln, Nebraska, USA
jtraylor@usgs.gov

SUMMARY

The lower Mississippi River Valley spans over 200,000 square kilometres in parts of seven states, encompassing areas of critical groundwater supplies, natural hazards, infrastructure, and low-lying coastal regions. From 2018 – 2022, the U.S. Geological Survey acquired over 82,000 line-kilometres of airborne electromagnetic, radiometric, and magnetic data over this region to provide comprehensive and systematic information about subsurface geologic and hydrologic properties that support multiple scientific and societal interests. Most of the data were acquired on a regional grid of west-east flight lines separated by 3 – 6 kilometres; however, several high-resolution inset grids with line spacing as close as 200 m were acquired in targeted areas of interest. Approximately 8,000 line-kilometres were acquired along streams and rivers to characterise the potential for surface water-groundwater connection, and another 6,000 line-kilometres were acquired along the Mississippi and Arkansas River levees to characterise this critical infrastructure. Here, we present a summary of the data along with several examples of how they are being used to inform regional groundwater model development, inferences of groundwater salinity, identification of faults in the New Madrid seismic zone, and levee infrastructure.

Key words: airborne electromagnetic, lower Mississippi River Valley, groundwater, hazards, levee infrastructure

INTRODUCTION

The Mississippi Alluvial Plain (MAP) hosts one of the most prolific shallow aquifer systems in the United States but is experiencing chronic groundwater decline over much of its spatial extent. The Mississippi River Valley alluvial aquifer (MRVA), the surficial aquifer within the MAP region, was among the most heavily withdrawn aquifers for irrigation in the United States in 2015 (Lovelace et al. 2020). Furthermore, the Reelfoot rift and New Madrid seismic zone underlie the region and represent an important and poorly understood seismic hazard (Frankel et al. 2009). Despite its societal and economic importance, the shallow subsurface architecture has not been mapped with the spatial resolution needed for detailed scientific studies and prudent resource management.

Here, we present airborne electromagnetic (AEM), magnetic, and radiometric observations, measured over 82,000 flight-line-kilometres, which collectively provide a system-scale snapshot of the entire region of more than 270,000 square kilometres (Figure 1). This work nearly doubles the extent of regional airborne geophysical coverage originally completed in 2019 (Minsley et al. 2021), extending coverage south to the gulf coast of Louisiana as well as expanding laterally to cover recharge areas of the Mississippi Embayment and the Chicot aquifer system. Additional cooperator funding was leveraged to investigate the confining unit in Shelby County, Tennessee as well as improve coverage of the entire Mississippi River and Arkansas River levees within the study area.

We developed detailed maps of aquifer connectivity and shallow geologic structure, inferred relations between structure and groundwater age, identified previously unseen palaeochannels and shallow fault structures, and characterised variability in the surficial fine-grained deposit on which the levee system is built. This work demonstrates how regional-scale airborne geophysics can close a scale gap in Earth observation by providing observational data at suitable scales and resolutions to improve our understanding of subsurface structures. In addition to supporting a range of applications today, comprehensive and foundational data collection efforts support a large 'decision-space' that will contribute to future

studies with emergent sets of questions benefiting from expanded knowledge of regional geologic and hydrologic properties.

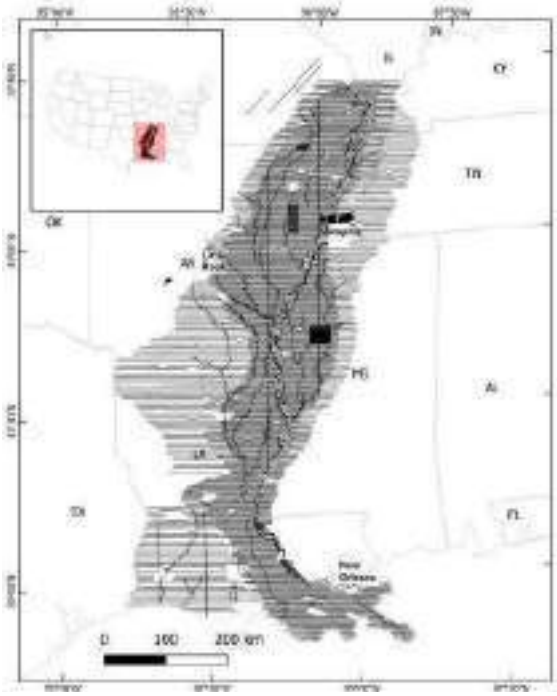

Figure 1. Airborne geophysical flight lines collected from 2018 - 2022.

METHOD AND RESULTS

Data acquisition and processing

Airborne geophysical data were collected over multiple phases from 2018–2022. Data were collected with both the helicopter frequency-domain Resolve AEM instrument and the fixed-wing Tempest time-domain system. One-dimensional electrical resistivity models were recovered for the Resolve data using Aarhus Workbench (Auken et al. 2015) and for the Tempest data using GALEI (Brodie 2017). Both radiometric and magnetic data were acquired together with the AEM surveys (Figure 2A,C).

Native-resolution models (~30 m spacing for Resolve and ~150 m spacing for Tempest) are investigated along flight lines in specific areas of interest. However, given the widely spaced (3–6 km) flight lines and regional nature of the investigation covering a large area, we also produced a coarse three-dimensional gridded resistivity grid that combines data from both sensors (Figure 2B, Figure 3). Resistivity models from each AEM instrument were kriged separately onto a common 1 km by 1 km grid with 5 m vertical intervals. The two grids were then combined using a depth-weighting function that favours the Resolve models at shallow depths, transitioning to Tempest models towards the maximum depth of investigation for Resolve (Minsley et al. 2021).

Hydrogeology

Regional-scale resistivity models agree with known hydrogeologic structures and areas of high groundwater salinity (Figure 2B, Figure 3), and provide additional detail needed to refine the geometry of hydrologic structures and variability within units. Binned resistivity classes were the basis for several interpretive products derived from the AEM data; these include thickness and extent of shallow confining materials, connectivity between the surficial aquifer and deeper geologic units, and connectivity between the aquifer and streams and rivers (Minsley et al. 2021).

The configuration of different resistivity classes, inferred to have different hydrologic properties, were used to inform both regional and inset groundwater models in the study area. Resistivity classes were used to inform layering of the groundwater models during model construction, then to assign initial values to the aquifer properties, streambed conductance, and recharge zonation in the calibration process.

Resistivity models and their derived interpretive products, together with the radiometric data and in situ measurements of groundwater chemistry and water quality have been incorporated into machine learning algorithms to predict distributions of manganese and arsenic (Knierim et al. 2022) and groundwater salinity in the surficial aquifer. A separate multi-method machine learning model incorporates geophysical information along with hydrologic and climatological variables to predict monthly groundwater levels with uncertainty bounds for the MRVA from 1980 through 2020 (Asquith and Killian 2022).

Hazards

In northeast Arkansas and southeast Missouri, west of the New Madrid Seismic zone, a previously undocumented fault was identified along multiple AEM profiles spanning an along-strike distance of more than 100 km. Fault offset of about 50–75 m is observed, clearly extending at least to the base of the shallow surficial aquifer (Minsley et al. 2021). Several shallow features attributed to sand boils caused during past earthquake liquefaction events are identified along several higher-resolution Resolve flight paths.

Infrastructure

Resistivity models from flight lines acquired along the Mississippi River and Arkansas River levees were classified into 10 groups using a k-means clustering algorithm. Individual clusters identify resistivity models that share similar layering structure and lithologic characteristics. Cluster numbers were mapped back to positions along the levees in order to identify regions of interest for follow-up investigation with drilling or other ground-based methods.

Outreach

We have focused on raising community awareness about airborne geophysical surveys and the value provided by these data throughout the project. Outreach efforts have included: multiple stakeholder and public events held during survey operations, presentation of data interpretations, and publication of online geonarratives that describe the results of the geophysical surveys for the general public. We developed a 3d-printed physical model interpreted from a subset of our AEM

data for use as a communication tool and handout for cooperators and other officials (Figure 4).

CONCLUSIONS

Airborne geophysical data extend our view into the subsurface, transforming our ability to inform three-dimensional mapping from catchment to basin scales in a cost-effective and systematic approach. Here, we demonstrated that system-scale airborne geophysical data of the lower Mississippi River Valley provide a robust platform from which to address a host of subsurface questions with important scientific and societal applications.

ACKNOWLEDGMENTS

This study was primarily funded by the U.S. Geological Survey (USGS) MAP project, as a federal appropriation to the USGS Water Availability and Use Science Program. Partial funding for airborne geophysical survey data came from the U.S. Army Corps of Engineers and the University of Memphis. Airborne geophysical data were acquired by Xcalibur Multiphysics and CGG Airborne through a competitive open solicitation. Anyuse of trade, firm, or product names is for descriptive purposes only and does not imply endorsement by the U.S. government. Data acquired in this study are available online: https://www.sciencebase.gov/catalog/item/58a5d9c5e4b057081a24f3fd.

REFERENCES

Asquith, W. H., and C. D. Killian. 2022. "CovMRVAgen1—Source Code for Construction of Covariates Bound to Monthly Groundwater Levels for Purposes of Statistical Modeling of Water Levels in the Mississippi River Valley Alluvial Aquifer." *U.S. Geological Survey Software Release*. https://doi.org/10.5066/P9TPGI0O.

Auken, E., A. V. Christiansen, C. Kirkegaard, G. Fiandaca, C. Schamper, A. A. Behroozmand, A. Binley, et al. 2015. "An Overview of a Highly Versatile Forward and Stable Inverse Algorithm for Airborne, Ground-Based and Borehole Electromagnetic and Electric Data." *Exploration Geophysics* 46 (3): 223–35. https://doi.org/10.1071/EG13097.

Brodie, R. 2017. "Ga-Aem: Modelling and Inversion of Airborne Electromagnetic (AEM) Data in 1D." C++. Geoscience Australia. https://github.com/GeoscienceAustralia/ga-aem.

Frankel, A. D., D. Applegate, M. P. Tuttle, and R. A. Williams. 2009. "Earthquake Hazard in the New Madrid Seismic Zone Remains a Concern." *U.S. Geological Survey Fact Sheet 2009-3071*.

Hart, R. M., B. R. Clark, and S. E Bolyard. 2008. "Digital Surfaces and Thicknesses of Selected Hydrogeologic Units within the Mississippi Embayment Regional Aquifer Study (MERAS)." *U.S. Geological Survey Scientific Investigations Report 2008-5098*, Scientific Investigations Report, . https://doi.org/10.3133/sir20085098.

Knierim, K. J., J. A. Kingsbury, K. Belitz, P. E. Stackelberg, B. J. Minsley, and J.R. Rigby. 2022. "Mapped Predictions of Manganese and Arsenic in an Alluvial Aquifer Using Boosted Regression Trees." *Groundwater* 60 (3): 362–76. https://doi.org/10.1111/gwat.13164.

Lovelace, J. K., M. G. Nielsen, A. L. Read, C. J. Murphy, and M. A. Maupin. 2020. "Estimated Groundwater Withdrawals from Principal Aquifers in the United States, 2015." *U.S. Geological Survey Circular 1464*, Circular, , 82. https://doi.org/10.3133/cir1464.

Minsley, B. J., J. R. Rigby, S. J. James, B. L. Burton, K. J. Knierim, M. D. M. Pace, P. A. Bedrosian, and W. H. Kress. 2021. "Airborne Geophysical Surveys of the Lower Mississippi Valley Demonstrate System-Scale Mapping of Subsurface Architecture." *Communications Earth & Environment* 2 (1): 131. https://doi.org/10.1038/s43247-021-00200-z.

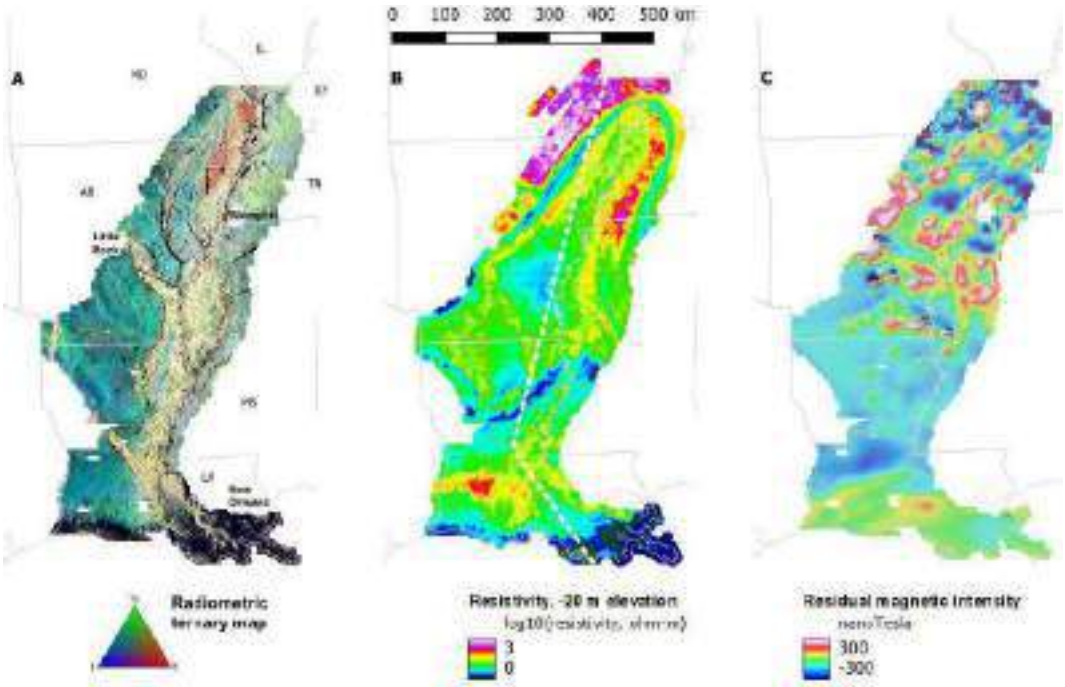

Figure 2. Gridded airborne geophysical results. (A) Ternary radiometric map showing relative abundance of Potassium (K), Thorium (Th), and Uranium (U). (B) Electrical resistivity at a constant elevation of 20 m below sea level. (C) Residual magnetic intensity.

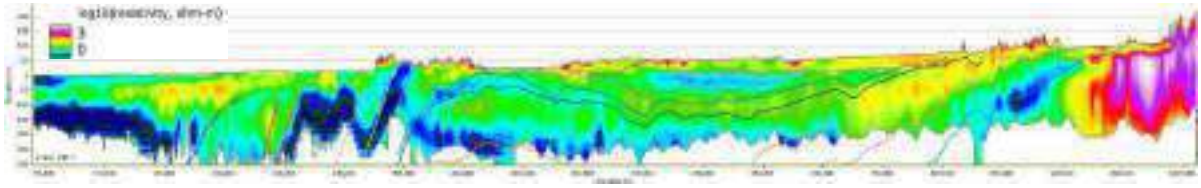

Figure 3. South-north resistivity cross-section. Gridded resistivity models are shown along a ~1,100 km cross-section from the Louisiana gulf coast on the left, where elevated groundwater salinity can be seen as a low-resistivity lens in the near surface, to the upland area outside the alluvial plain in southeast Missouri (white dotted line, Figure 2b). The subsurface resistivity architecture closely corresponds with the top surfaces of hydrogeologic units (colored lines, Mississippi Embayment Regional Aquifer Study (MERAS) model (Hart, Clark, and Bolyard 2008)).

Figure 4. Outreach and communication examples. (top-right) Open-house events were held during survey operations to provide opportunities for media and the public to view the AEM survey equipment and learn about the project. Follow-on meeting sessions were held with cooperators to review datasets and discuss interpretations. Photo credits: Roland Tollett (USGS) and Randy Hunt (USGS). (top-left) A physical 3d-printed model of three layers interpreted from the AEM data collected over one of the high-resolution survey blocks in Mississippi is a useful communications tool and handout for cooperators. Photo credit: Department of the Interior. (bottom) Online geonarratives were created to present both regional and high-resolution inset AEM datasets in a simplified format to showcase the survey results to public audiences. The geonarratives can be found at:
https://www2.usgs.gov/water/lowermississippigulf/map/regional_SM.html
https://www2.usgs.gov/water/lowermississippigulf/map/shellmound_SM.html

AEM survey of the Neretva Delta (Croatia): a case study for hydrogeology

John Moilanen*
LLC Geotechnologies,
21, Yubileynaya st.
141540, Povarovo, Russia
info@geotechnologies.ru

Pietro Teatini
University of Padua
via Marzolo 9
35122 Padova
pietro.teatini@unipd.it

Giulio Vignoli
University of Cagliari
Via Marengo 2,
09124 Cagliari, Italy
gvignoli@unica.it

Veljko Srzić
University of Split
Matice hrvatske 15,
21000 Split, Croatia
veljko.srjic@gradst.hr

SUMMARY

Groundwater salinisation is a serious problem affecting numerous areas of the world, and Neretva's delta in Croatia is one of them. Airborne electromagnetics is already widely used to feed data-driven decision and management processes with accurate (hydro)geomodels and, by doing so, to mitigate the detrimental effects of salinisation.

In this perspective, in 2021, an airborne electromagnetic survey was flown over about 100 km^2. The overall goal of the survey was to better understand the hydrogeology of the plain leading to a more quantitative assessment of the saltwater intrusion and possible preferential paths.
Here, we present the results of data processing and inversion. We built a (pseudo-)3D resistivity model based on 1D forward approximation. And we compare it against ground-based electrical measurements. According to the available boreholes, freshwater is related to a relatively resistive unit.

Key words: inversion, saltwater intrusion, airborne electromagnetics, frequency-domain, time-domain.

INTRODUCTION

Over the past years, airborne electromagnetics (AEM) has become a key tool to tackle hydrogeological problems (Christiansen et al., 2006; Viezzoli et al., 2010; Ageev et al., 2022; Knight 2022). Specifically, numerous works have been devoted to investigating groundwater salinisation problems (Palamara et al., 2010; Ball et al. 2020; Tosi et al., 2022; Billy et al., 2022). Generally, during coastal surveys, it is reasonable to expect quite low resistivity values: in the order of 0.2-0.3 Ω·m for the seawater, and about 0.3-0.8 Ω·m for the seafloor. In our case, the task was to detect and characterise a relatively resistive layer supposedly at around 100-m depth. The target was quite challenging because of such a conductive overburden. The area under investigation was the Neretva Delta in Croatia (Figure 1). Originally, there were swamps, but now, the area is actively used for agricultural purposes. While the river itself is significantly affected by seawater encroachment, aquifers are less impacted by saltwater.

In terms of AEM measurements, in addition to the problems connected with the reduced signal penetration due to the electrically conductive environment, issues are due to the presence of sources of anthropic noise. In fact, together with several power lines crossing the investigated area, the northern portion of the survey is characterised by the presence of a DC-powered railway.

The AEM system used to perform the survey is EQUATOR (Figure 2). EQUATOR has been developed by Geotechnologies LLC as a tool providing EM data both in frequency and time domains (Moilanen et al., 2013; Karshakov et al. 2017; Moilanen 2022). Such a system was necessary to meet the goals of the project: high productivity (it can fly at 150 km/h), high vertical and lateral resolution (due to the capability to measure on-time and its 77 Hz base frequency) to infer the presence and characteristics of thin/shallow sand and clay lenses. On the other hand, to cope with the anthropic noise, instead of the commonly used spatial filtering (Kang et al. 2022), we managed to effectively remove the industrial noise in the frequency-domain by suppressing uniquely the disturbed frequencies. At the same time, the combination of the high base frequency and the conductive environment could have prevented reaching investigation depths of 100-150 m but, as shown in the following, this did not happen.

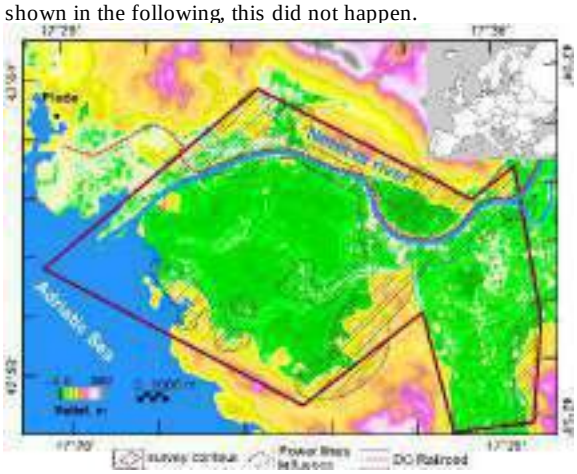

Figure 1. Overview of the survey area in Croatia.

DATA PROCESSING AND NOISE REMOVAL

Sometimes, industrial noise contaminates specific frequencies, close to harmonics of 50 Hz. In the Neretva survey, the most significant interference was found in the channels: 848 Hz (near the 17th harmonic of 50 Hz) and 540 Hz (near the 11th harmonic). In case of considerable amplitude of the industrial noise, also other harmonics were distorted. Clearly, from a time-domain perspective, noise components with low amplitude can impact merely the (low amplitude) late-time channels, whereas noise components with larger amplitudes might be able to significantly distort also earlier time gates (Figure 3). As an indicator of the presence of significant electromagnetic coupling, the 2nd-order variation of the un-

normalized adjacent Im(B_z(f)) values (at 848 Hz) has been used: when such a variation was larger than a predefined threshold, distortions were expected in all time-domain channels. The hatching area in Figure 1 shows where the noise level is higher than the selected threshold; hence it is clear that almost half of the entire survey area is potentially heavily affected by anthropic noise and, without the proper data conditioning, the inversion of the measurements would lead to artifacts and possible misinterpretations.

Figure 2. The AEM system EQUATOR during the Neretva survey in Croatia.

METHOD AND RESULTS

Generally, AEM data are inverted via 1D forward modelling approximations assuming that the subsurface can be reasonably represented locally by a 1D resistivity parametrisation (Guillemoteau et al, 2011). In this framework, in order to enforce spatial coherence to the results and provide (quasi-)3D resistivity reconstruction of the investigated volume, several schemes have been implemented (e.g.: Viezzoli et al., 2009; Bai et al., 2021; Klose et al., 2022). An alternative, and extremely efficient, approach to ensure both vertical and lateral spatial consistency of the retrieved resistivity model (while, clearly, fitting the data equally well) is based on the iterated extended Kalman filter (Karshakov, 2020). Indeed, this is the approach used for the inversion of Neretva's dataset. In particular, the used parametrisation consisted of 20 layers, and we inverted the observed data uniquely to retrieve the layers' resistivity. The initial model was a homogeneous half-space with resistivity equivalent to apparent resistivity at 77 Hz. One additional advantage of the approach based on the Kalman filter is that it naturally provides the variances of the estimation error, which can be used for the calculation of the stochastic estimability of each layer (Golovan and Parusnikov, 1998). In this way, each layer can be also characterised in terms of estimation quality and, consequently, the local penetration depth for each measurement location across the survey area can be effectively assessed.

In the case of the Neretva Delta, saltwater intrusion is occurring due to several factors, including climate change and human activities: rising sea levels are causing seawater to encroach in the river and the surrounding aquifers (Lovrinović et al., 2021; Lovrinović et al., 2022). This is exacerbated by the overuse of groundwater for irrigation, which leads to a depletion of freshwater resources and an increase in the amount of saltwater entering the aquifers. In addition, the possible wrong siting of wells might endanger the quality of different aquifers by inadvertently connecting them. In this respect, it is worth noticing how the ground-based geophysical investigation - in particular, the performed electrical surveys - could not detect the deep conductor. On this matter, Figure 4 shows an example of electrical tomography not capable to properly reconstruct the deep low resistive anomaly.

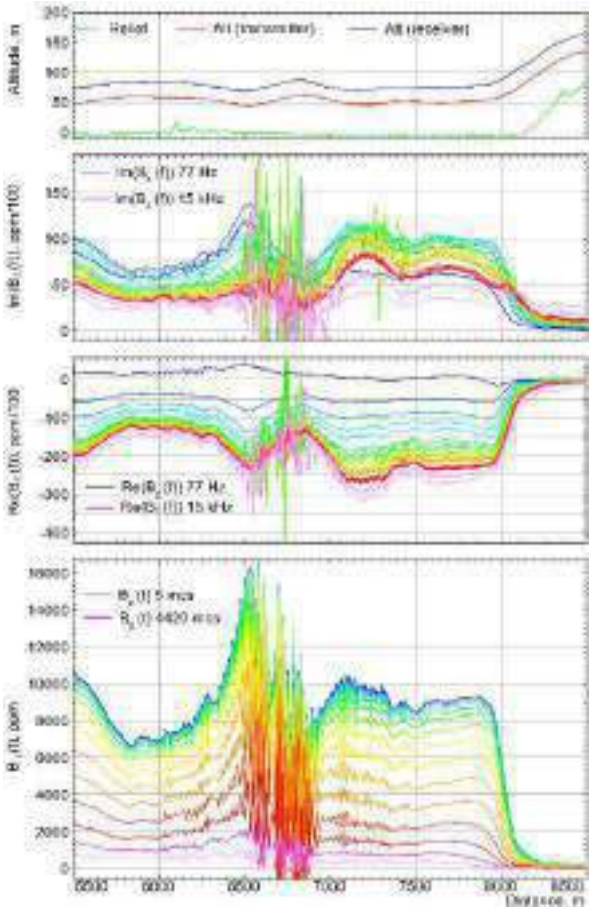

Figure 3. Industrial noise distortion on AEM data. Upper chart – the geometry of the system; central charts – imaginary and in-phase components of frequency domain data; bottom chart – time-domain data.

Similarly, in Figure 5, the bottom layer, as retrieved from the AEM data inversion, is characterised by a resistivity of 0.5. Ω·m and unknown thickness. In this context, such a low resistivity is a clear indication of saltwater presence, and in these cases, particular care should be put in siting the wells. In this respect, drilling should avoid areas in which the saltwater level could be particularly shallow (e.g.: the left side on Figure 5) and/or depths for which the pumping well could intersect unit saturated with saltwater (e.g.: the right part on Figure 5, in which the Drillhole 1 stops at the top of the last resistive unit). In Figure 6, we compare the stratigraphy deduced from Drillhole 1 against the electrical resistivity profile retrieved from the AEM data. To verify the survey proposals several drillholes were drilled (Figure 7). No freshwater has been found beneath the clay confining unit.

CONCLUSIONS

Groundwater resources need to be investigated and characterised to allow their most effective protection and

management. This is particularly true in case of coastal aquifers endangered by climate changes, subsidence, sea level rising, or, more often, overexploitation concurrently causing saltwater intrusion.

In our specific case, we make use of the large coverage and dense sampling typical of AEM data to retrieve a (quasi-) 3D reconstruction of the subsurface resistivity distribution and, in turn, of the complex geology of the Neretva Delta in Croatia.

In particular, the characteristics of the AEM system EQUATOR allowed us to meet the requirements of high spatial resolution and to naturally perform an anthropic noise removal in the frequency domain (preserving almost all the collected soundings). Despite the conductive environment, the investigation depth could reach the remarkable depth of 225 m.

The AEM results have been corroborated by the numerous ground-based measurements and the information from boreholes. In the near future, the hydrogeological model based on the geological interpretation of the AEM results will be used for scenario analyses and to undertake the most effective initiatives to counteract the salinisation of the area.

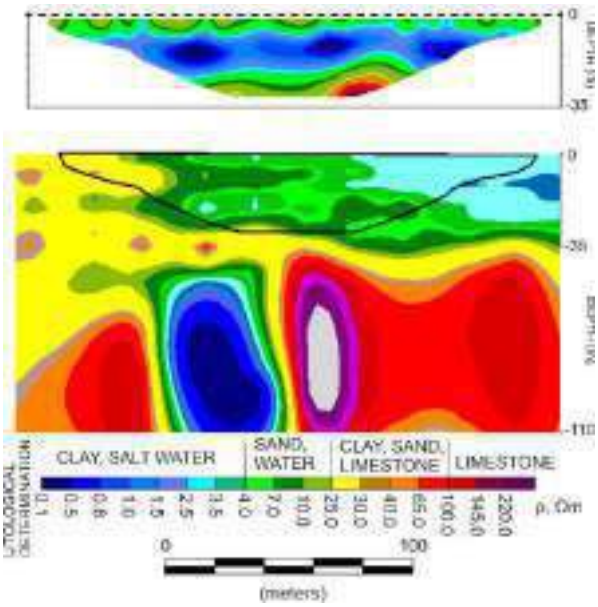

Figure 4. A geoelectrical cross-section retrieved by ground-based measurements (upper chart) compared with the AEM result.

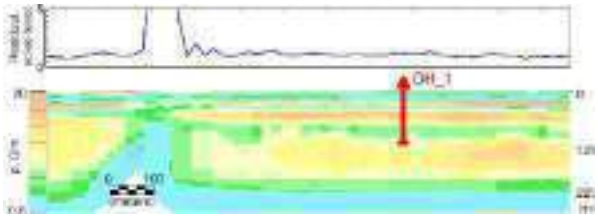

Figure 5. Resistivity section as retrieved by the AEM data (lower chart) with the corresponding data misfit (upper chart) and the location of Drillhole 1 (in red; See Figure 6).

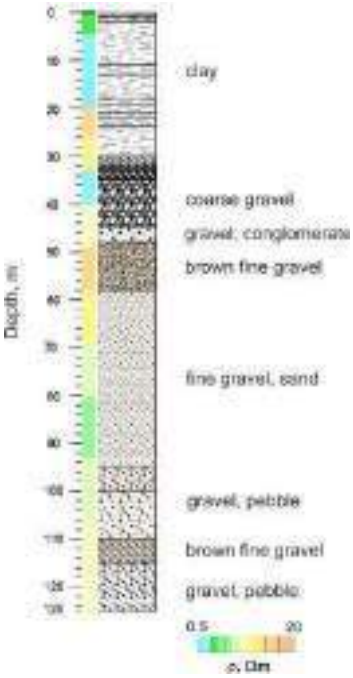

Figure 6. Stratigraphy of Drillhole 1 compared against the corresponding resistivity vertical profile as inferred from the inversion of the AEM data.

Figure 7. Drillhole B2 performed in February 2022.

ACKNOWLEDGMENTS

The AEM survey was funded by the Interreg Italy–Croatia Cross Border Collaboration (CBC) Programme 2014–2020 (Priority Axes: Safety and Resilience) through the European Regional Development Fund as a part of the projects "Monitoring sea-water intrusion in coastal aquifers and testing pilot projects for its mitigation" (MoST) (AID: 10047742) and "Saltwater intrusion and climate change: monitoring, countermeasures and informed governance" (SeCure, AID: 10419304).
We are also thankful to Andrea Viezzoli and Francesco Dauti for their company and always useful discussions.

REFERENCES

Ageev, V.V., Karshakov, E.V., and J. Moilanen, 2022. Using airborne electromagnetic survey to solve hydrogeological problems. *Izvestiya, Physics of the Solid Earth* 58 (5): 765-771.

Bai, P., Vignoli, G., and Hansen, T. M., 2021. 1D stochastic inversion of airborne time-domain electromagnetic data with realistic prior and accounting for the forward modeling error. *Remote Sensing*, 13(19), 3881.

Ball, L. B., Davis, T. A., Minsley, B. J., Gillespie, J. M., & Landon, M. K. (2020). Probabilistic categorical groundwater salinity mapping from airborne electromagnetic data adjacent to California's Lost Hills and Belridge oil fields. *Water Resources Research*, 56(6), e2019WR026273.

Billy, J., Reninger, P.-A., Raingeard, A., Chaumillon, E., and C. Bouvier, 2022. Airborne electromagnetics as a tool to image the land-to-sea sedimentary continuum: A complementary geophysical approach to improve coastal characterization. *Marine geology* 454: 106945.

Christiansen, A.V., Auken, E., and K. Sørensen, 2006. The transient electromagnetic method. In *Groundwater Geophysics. A tool for hydrogeology*: 179-225.

Golovan, A.A., and N.A. Parusnikov. 1998. A relationship between the stochastic estimability measure and singular matrix expansions. *Automation and Remote Control* 59 (2): 190-193.

Guillemoteau, J., Saihac, P. and M. Behaegel, 2011. Regularization strategy for the layered inversion of airborne TEM Data: application to VTEM data acquired over the basin of Franceville (Gabon). *Geophysical Prospecting* 59 (6): 1132-1143.

Kang, S., Knight, R., and Goebel, M., 2022. Improved Imaging of the Large-Scale Structure of a Groundwater System With Airborne Electromagnetic Data. *Water Resources Research*, 58(4), e2021WR031439.

Klose, T., Guillemoteau, J., Vignoli, G., and Tronicke, J., 2022. Laterally constrained inversion (LCI) of multi-configuration EMI data with tunable sharpness. *Journal of Applied Geophysics*, 196, 104519.

Karshakov, E. V., Podmogov, Y. G., Kertsman, V. M., and Moilanen, J., 2017. Combined Frequency Domain and Time Domain Airborne Data for Environmental and Engineering Challenges. *Journal of Environmental and Engineering Geophysics*, 22(1), 1-11.

Karshakov, E., 2020. Iterated extended Kalman filter for airborne electromagnetic data inversion. *Exploration Geophysics* 51(1): 66-73.

Knight, R., Steklova, K., Miltenberger, A., Kang, S., Goebel, M., and Fogg, G., 2022. Airborne geophysical method images fast paths for managed recharge of California's groundwater. *Environmental Research Letters*, 17(12), 124021.

Lovrinović, I., Bergamasco, A., Srzić, V., Cavallina, C., Holjević, D., Donnici, S., Erceg, J., Zaggia, L. and Tosi, L., 2021. Groundwater monitoring systems to understand sea water intrusion dynamics in the Mediterranean: The Neretva valley and the southern Venice coastal aquifers case studies. *Water*, 13(4), 561.

Lovrinović, I., Srzić, V., Matić, I., and Brkić, M., 2022. Combined Multilevel Monitoring and Wavelet Transform Analysis Approach for the Inspection of Ground and Surface Water Dynamics in Shallow Coastal Aquifer. *Water*, 14(4), 656.

Moilanen, J., Karshakov, E., and A. Volkovitsky, 2013. Time-domain helicopter EM System "Equator": resolution, sensitivity, universality. 13th SAGA biennial and 6thInternational AEM conference AEM-2013, Mpumalanga, South Africa, Expanded Abstracts: 1-4.

Moilanen, J., 2022. Modern Methods of Airborne Electromagnetic Survey. *Izvestiya, Physics of the Solid Earth*, 58(5), 755-764.

Palamara, D.R., Rodriguez, V.B., Kellett, J., and S. Macaulay, 2010. Salt mapping in the Lower Macquarie area, Australia, using airborne electromagnetic data. *Environmental Earth Sciences* 61: 613-623.

Tosi, L., Da Lio, C., Bergamasco, A., Cosma, M., Cavallina, C., Fasson, A., Viezzioli, A., Zaggia, L., and S. Donnici, 2022. Sensitivity, hazard, and vulnerability of farmlands to saltwater intrusion in low-lying coastal areas of Venice, Italy. *Water* 14 (64): 1-23.

Viezzoli, A., Auken, E., and Munday, T., 2009. Spatially constrained inversion for quasi 3D modelling of airborne electromagnetic data–an application for environmental assessment in the Lower Murray Region of South Australia. *Exploration Geophysics*, 40(2), 173-183.

Viezzoli, A., Tosi, L., Teatini, P., and Silvestri, S., 2010. Surface water–groundwater exchange in transitional coastal environments by airborne electromagnetics: The Venice Lagoon example. *Geophysical Research Letters*, 37(1).

The Valen Prospect: It's SPM,… No it's not,…Yes it is!.. No wait….

Tim Munday*
CSIRO DEI
Perth, WA, Australia
tim.munday@csiro.au

Mike McMillan
Computational Geosciences Inc
Vancouver, B.C, Canada
mike@compgeoinc.com

Rod Paterson
Intrepid Geophysics,
Brighton, VIC, Australia
rod@intrepid-geophysics.com

Daniel Sattel
Golden, CO, USA
dsattel@comcast.net

Camilla Sørensen
Aarhus Geosoftware,
Aarhus C, Denmark
camilla.soerensen@seequent.com

Noelene Dorn
ElectroMagnetic Imaging Technology Pty Ltd
Perth, WA, Australia
ndorn@electromag.com.au

SUMMARY

The choice of systems and interpretation approaches for the exploration for critical mineral systems under a complex and varying regolith cover using airborne electromagnetics, can be informed by forward modelling methods. However, the direct assessment of systems and modelling algorithms using data acquired under real survey conditions can be equally informative. For example, it provides an opportunity to assess the effects of real geological variability and noise, arising in a true survey configuration for different systems, and the artefacts that may result from the use of different inversion codes. Here we discuss the application of 1, 2 and 3D inversion approaches to resolving the geometry and complexity of the geology in an area on the South Australian side of the Musgrave province and consider modelled responses from coincident lines of fixed wing (SPECTREM-Plus and TEMPEST – High Moment), and heliborne (VTEM and SkyTEM) time domain EM systems over a known (from ground EM and drilling) deep, steeply dipping, conductor - the Valen Prospect.

All inversion methods and AEM systems contributed to our understanding of geological variability and structural complexity, although all generate smoothed versions of geological reality. Results from the 1D inversions appear to map geological variability and complexity in the near surface (regolith character?) in greater detail compared to those from the 2 and 3D inversions, even though the geology is recognisably 3D in character. The Valen Prospect characterised as a distinct, small, and narrow late time anomaly, is modelled in 1D, albeit deeper than drilling and ground EM suggests. While the 2 and 3D models have good global data fits, in some instances they failed to fit measured data at late time, consequently overlooking Valen. It was suggested that problems with fitting the anomaly at late times may be the result of regolith-related superparamagnetism (SPM) in the near surface which often beset AEM data sets in Australian settings. However, decay-rate analysis of the Valen anomaly suggests a deep conductor response for the SkyTEM, SPECTREM and TEMPEST systems. The decay rate of the corresponding VTEM anomaly suggests an SPM response. However, the shape of the VTEM decay also suggests the presence of deeper conductive material.

Key words: SPM, Critical Minerals, 1, 2 and 3D inversion, Fixed-wing and Helicopter time-domain AEM systems, Regolith

INTRODUCTION

The presence of a thick and complex transported regolith cover in many parts of Australia, represents a significant impediment to critical minerals exploration. The Musgrave Province, located in the far north-west of South Australia (Figure 1), highly prospective with magmatic Ni-Cu-PGE's among key mineral systems being targeted (Woodhouse and Gum 2003), is characterised by such cover. In this region, transported cover can exceed 100m thick, particularly where palaeovalley systems eroded into the Meso-Proterozoic crystalline basement, have been filled with Pliocene to Pleistocene clastic sediments and which have then been covered with Quaternary sand dunes (Figure 1).

Airborne electromagnetics (AEM) is used as a key exploration technology, being employed in the exploration for mafic to ultramafic layered intrusions which are the primary focus for Ni-Cu mineralisation. These intrusions (e.g., of Giles Complex – Figure 1- inset map) which commonly occur as a series of vertically stacked dykes which may act as potential traps for Ni-Cu sulphides.

The motivation for conducting this research was an interest in the application of 1, 2 and 3D inversions on AEM data with non-dispersive, conventional conductivity or resistivity modelling codes, applied to the targeting of conductive 'critical mineral system' targets at depth in complex weathered settings. Their ability to resolve other relevant geological characteristics, such as regolith thickness and spatial variability (also aspects of the "mineral system") was also of concern. Some may argue that the choice of survey technologies and interpretation method can, in large measure, be informed by forward modelling approaches. We accept this has merit, but also believe that more direct assessments with data acquired under survey conditions can be equally informative. In this study we consider the modelling of data from coincident lines of VTEM and SkyTEM helicopter, and SPECTREM and TEMPEST fixed-wing EM systems. System characteristics are discussed in Munday et al. (2023).

This work builds on earlier geophysical studies undertaken in the area (see, for example, Ley-Cooper et al., 2015, Macnae et al. 2020, and Munday et al. 2020). Arising from this assessment was an awareness that in this region, the deployment of high-powered AEM systems for targeting can be challenged by the occurrence of superparamagnetism (SPM) – seen as small late time responses following a noisy 1/t decay, and/or induced polarisation (AIP) effects in the resulting data - seen as rapid decays or negative responses at late time. For SPM-induced effects, these small late-time responses can be confused with

potential mineralised targets (Mutton, 2012; Kratzer et al. 2013; Sattel and Mutton, 2015). One such example, examined here, is that associated with the Valen Prospect, a late time "conductor", originally identified as part of an exploration program undertaken by Musgrave Minerals using the VTEM heli-borne EM system and discussed by Macnae (2017).

METHOD AND RESULTS

Several inversion approaches were examined, including 1, 2 and 3D methods. In all cases, the inversions were undertaken with an induction only AEM inversion code, that is no account was taken of IP/SPM effects that are known to be present in the area. In addition, information from the ground TEM and drillhole DHEM and the presence of an inductive target was known prior to modelling using the different codes.

The 1D inversion scheme AarhusInv (Auken et al., 2015), was employed through the Aarhus Workbench to process and invert all four AEM data set. The data were inverted with a smooth 30-layer model. A 2D (or 2.5D) inversion of the four airborne data sets was undertaken using the Moksha-EM 2.5D code (Paterson et al., 2016, and Silic et al., 2015). Modelled responses are shown in Figure 2 for a subset of the data over the Valen Prospect. A 3D inversion of the AEM data sets was also undertaken using an adaptive OcTree mesh refinement, where the mesh spans the full computational domain but uses smaller mesh cells around the selected transmitters and receivers. This mesh refinement methodology results in a forward modelling mesh that has far fewer cells than the full inversion mesh. The approach is discussed Haber et al., (2012), Oldenburg et al (2013), Schwarzbach et al., 2013, and Yang et al., (2014). The 3D inversions for the individual lines were run in "2D-mode", meaning there was additional regularization applied in the crossline direction, while still modelling the full 3D physics. 3D inversions were run with data sets where there were three adjacent lines (in the case of SPECTREM, SkyTEM and VTEM). The lines were inverted as one combined 3D model for each input dataset. Model results are presented in Figure 3.

In the 1D results a deep conductive response is modelled where the Valen conductor had been defined from ground TDEM (fixed and moving loop EM) and from downhole EM in two drillholes. However, the 1D models suggest a much deeper body than was indicated in the ground data. Modelling of the ground data suggested a finite conductor at approximately 100m below the surface, dipping at approximately 60 degrees to the north. The 1D AEM results put the conductor much deeper for all four airborne systems. Drilling intersected minor accumulations of sulphide mineralisation but did not encounter any conductive source at the modelled depth of 65m. However, it intersected a 30cm zone of massive graphite at about 89.5m, which is attributed to the source of the TEM anomalism.

The 2D results from the Moksha (Intrepid) and Computational Geoscience/UBC algorithms show a varied set of results. Valen is not defined in modelling results from any system, except for a suggested presence in the SkyTEM data set inverted using the latter codes. Analysis of the data fits indicate that small amplitude late-time responses for all systems are poorly fitted, even though global data fits appear generally good. Analysis of the 3D models, for data sets where line density permitted the approach (with VTEM, SkyTEM and SPECTREM data sets), three adjacent lines were inverted as one combined 3D model. With relatively small targets it was suggested the 200m spaced lines were too far apart for the "all-at-once" 3D inversion to be better than the individual 2D line inversions. The individual 2D inversions consistently had the best data fits and overall models. If the data had been acquired with 100-150m line spacing, where there is a greater overlap of sensitivities between lines, or if more complex 3D geologic features were encountered, then the all-at-once approach may resolve greater detail.

It was suggested that the difficulty in fitting the Valen late time "anomaly" in the higher order inversion codes might be attributed to it being a superparamagnetic (SPM) response in the regolith, near surface. The decay rate of the Valen feature in VTEM indicates an SPM response. However, detailed analysis of VTEM and SkyTEM dB/dt responses suggests powerlaw decay rates similar to and different from SPM, respectively. However, even the VTEM decay does not show a constant powerlaw decay, suggesting the presence of conductive material at depth. The absence of a correlation between low system elevation and anomaly location further supports the absence of SPM, as SPM effects drop off strongly with the AEM system ground clearance. Decay-rate analysis of a late-time anomaly recorded in the Musgrave Province by AEM systems also suggests a deep conductor response for the SkyTEM, SPECTREM and TEMPEST systems.

CONCLUSIONS

This study suggests that, at a coarse scale, comparable results can be obtained for different systems, regardless of the modelling approach used. However, at a finer scale significant differences are apparent, and higher order inversion methods may struggle to fit small, late-time conductors such as Valen. Their absence in inversion products may erroneously be attributed to, for example, SPM effects, to explain poor data fits at late times. In the case of the Valen Prospect, a decay-rate analysis of the late-time anomaly for the systems tested suggests a deep conductor response rather than one attributable to SPM, which supports interpretations of the ground geophysical data The choice of exploration technologies and their incorporation in an exploration workflow will naturally vary with the experience and preferences of those involved, but in a geological setting such as found in the Musgrave Province, the application of AEM in the search for Ni-massive sulphides or other critical minerals will almost always be a case of "bump-finding", including some fast modelling (i.e. 1D LEI) and the ground follow-up.

ACKNOWLEDGMENTS

We acknowledge the support of CSIRO's Deep Earth Imaging Future Science Platform in facilitating the conduct of this work and thank the participating companies/individuals involved.

REFERENCES

Auken, E, Christiansen, A, Kirkegaard, C, Fiandaca, G, Schamper, C, Behroozmand, A, Binley, A, Nielsen, E, Effersø, F, Christensen, N, Sørensen, K, Foged, N, and Vignoli, G, 2015, An overview of a highly versatile forward and stable inverse algorithm for airborne, ground-based and borehole electromagnetic and electric data: Exploration Geophysics, 46:3, 223-235.

Haber, E. Holtham, E., Granek, J., Marchant, D., Oldenburg, D., Schwarzbach, C. and Shekhtman, R., 2012., An adaptive mesh method for electromagnetic inverse problems. SEG Technical Program Expanded Abstracts 2012: pp. 1-6.

Kratzer, T., Macnae, J. and Mutton, P., 2013., Detection and correction of SPM effects in airborne EM surveys, Exploration Geophysics, 44:1, 6-15,

Ley-Cooper, A. Y., Viezzoli, A., Guillemoteau, J., Vignoli, G. Macnae, J., Cox, L. and Munday, T., (2015). Airborne electromagnetic modelling options and their consequences in target definition: Exploration Geophysics, 46,74–84,

Macnae, J., Munday, T.J, and Soerensen, C., 2020, Estimation and geologic interpretation of regolith chargeability and superparamagnetic susceptibility in airborne electromagnetic data, Geophysics 85: E153-E162.

Macnae J., 2017., Definitive superparamagnetic source identification through spatial, temporal, and amplitude analysis of airborne electromagnetic data. Geophysical Prospecting 65, 1071-1084.

Munday, T., Macnae, J., and Viezzoli, A., 2020., Consequences for the Geological Interpretation of AEM data when Inverted for, and Stripped of, Airborne IP and Superparamagnetism Effects. KEGS Symposium 2020 "Exploration for Strategic Minerals" Toronto, Canada, February 28th.

Munday, T., McMillan, M., Paterson, R., Soerensen, C., and Dorn, N., 2023., AEM modelling and system options in the search for critical mineral systems in a regolith dominated environment – the Musgrave Province, Central Australia." KEGS Symposium 2023 Toronto, Canada, March 4th, 2023.

Mutton, P., 2012., Superparamagnetic effects in EM surveys for Mineral Exploration, ASEG Extended Abstracts, 2012:1, 1-6,

Oldenburg, D. W., E. Haber, and R. Shekhtman, (2013), Three dimensional inversion of multisource time domain electromagnetic data: Geophysics, 78, no. 1, E47–E57.

Sattel D. and Mutton P. 2015., Modelling the superparamagnetic response of AEM data. Exploration Geophysics 46, 118–129.

Schwarzbach, C., Holtham, E. and Haber, E., 2013. 3D inversion of time domain electromagnetic data. ASEG Extended Abstracts 2013, 1-4.

Silic, J., Paterson, R., FitzGerald. D. and Archer, T., 2015., Comparing 1D and 2.5D AEM inversions in 3D geological mapping using a new inversion solver. 14th International, Congress of the Brazilian Geophysical Society, Extended Abstracts

Woodhouse AJ and Gum JC (2003) Musgrave Province — geological summary and exploration history, Report Book 2003/00021. Department of Primary Industries and Resources South Australia, Adelaide.

Yang, D., Oldenburg, D. and Haber, E., 2014, 3-D inversion of airborne electromagnetic data parallelized and accelerated by local mesh and adaptive soundings, Geophys. J. Int., 196 (3), 1492-1507

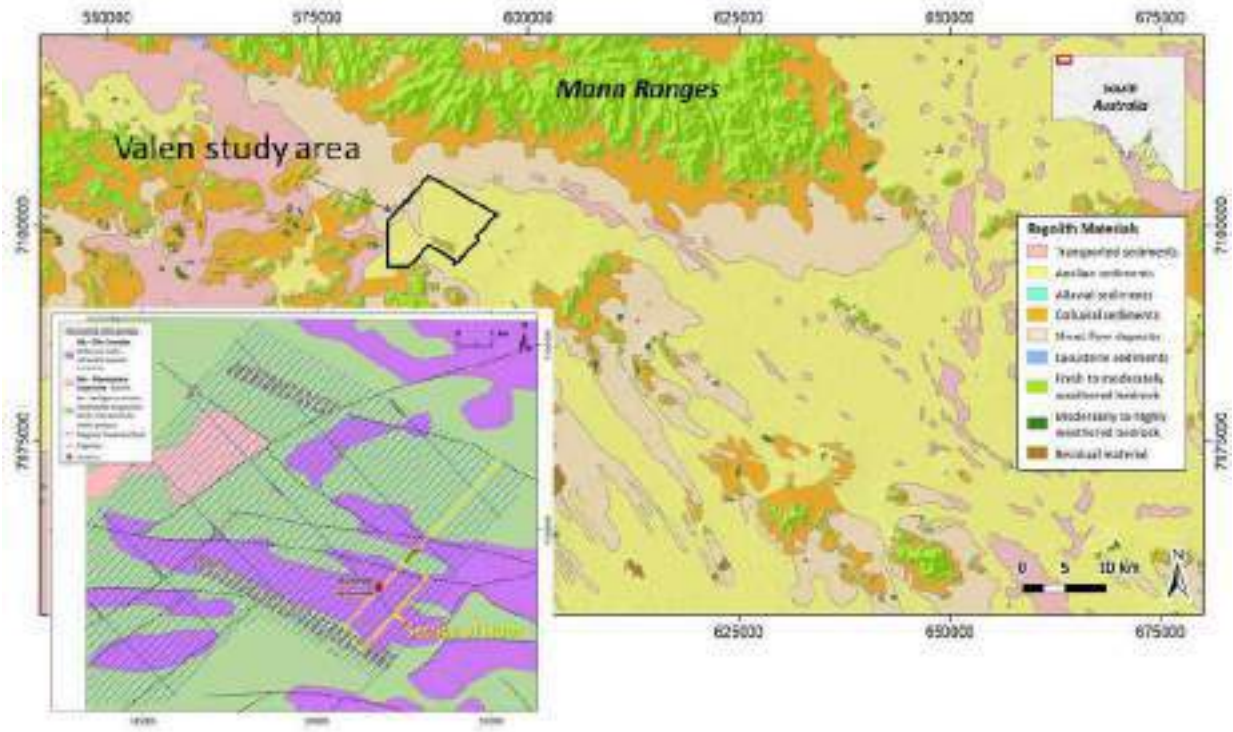

Figure 1: Regolith geology of Valen Prospect area with inset map showing flight lines form VTEM survey and sub-set of the line investigated here. The drillholes marked by the red circles are coincident with the Valen late-time anomaly observed in the AEM data sets.

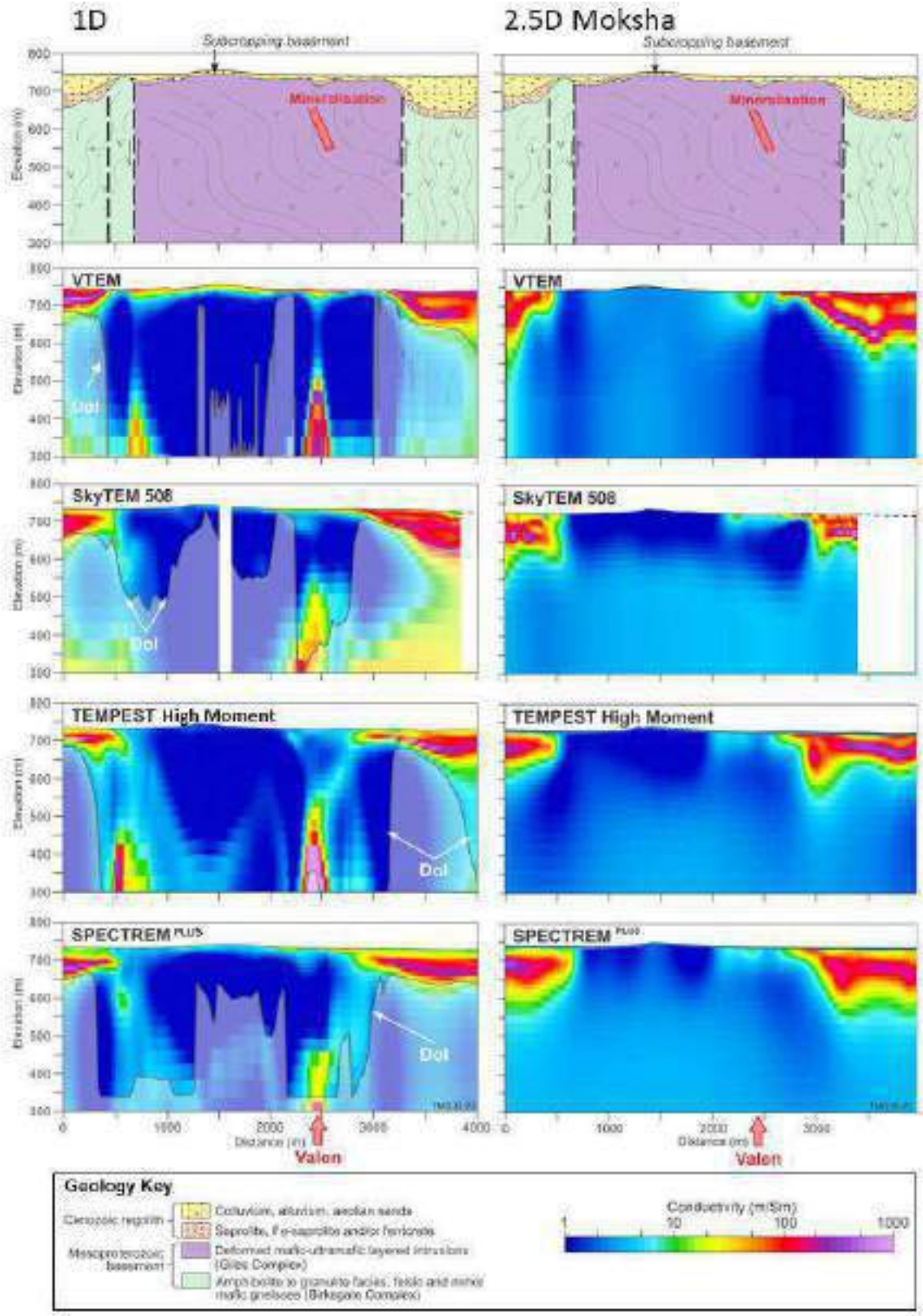

Figure 2: 1D smooth model (AarhusInv) inversion results (Left column)- presented as conductivity-depth sections for data acquired from a sub-set of coincident lines from different AEM systems across the Valen prospect. The right column shows inversion results from inversion using the 2.5D Moksha code for the systems considered. The location of the Valen conductor along the section is indicated at the bottom of the stitched sections.

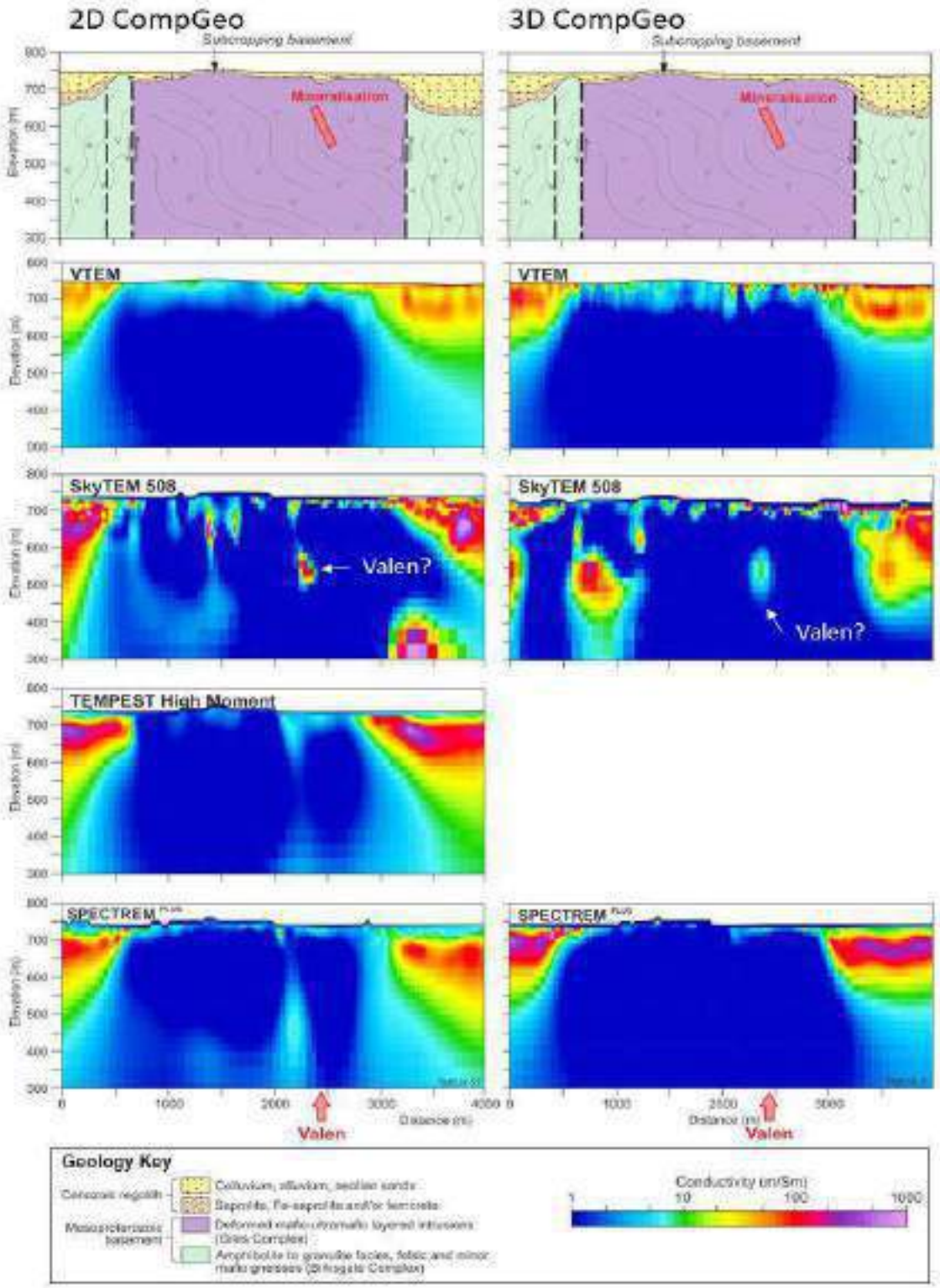

Figure 3: 2D smooth model inversion results for different AEM systems (Left column) generated form the application of the CompGeo/UBC codes, where individual lines were run in "2D-mode" where additional regularization was applied in the cross-line direction, while still modelling the full 3D physics. The right column shows model results from inversion using an "all at once" (where three adjacent lines were modelled with 3D physics. The location of the Valen conductor along the section is indicated at the bottom of the stitched sections. Suggested location of the Valen conductor is indicated in the SkyTEM data for both inversion approaches. TEMPEST High Moment data were not modelled in 3D as only a single line was acquired.

Developing a fully airborne drone TEM system

Nicklas Skovgaard Nyboe
SkyTEM Surveys ApS
Dyssen 2,
8200 Aarhus N, Denmark
nsn@skytem.com

Kristoffer Skovgaard Mohr
SkyTEM Surveys ApS
Dyssen 2,
8200 Aarhus N, Denmark
krm@skytem.com

SUMMARY

Aiming at improving the efficiency and versatility of the time-domain electromagnetic method for geotechnical and environmental applications, we are developing a fully airborne small-scale drone TEM system. In this paper we will outline the main reasonings and design choices leading to the present system implementation. The development of the complete airborne drone TEM system has involved the development of numerous system parts, which all present their own challenges and optimisations both as individual elements and when working together. In fact, our development of the airborne drone TEM system has essentially progressed in two parallel branches, where one branch has constituted drone and frame developments, while the other has constituted transmitter and receiver developments. Practical field tests of the various transmitter and receiver prototypes have typically been performed as minor surveys at various test locations using a scaled-down SkyTEM frame towed by a helicopter. We will present former and present capabilities of the system, primarily exemplified through descriptions of these prototype test surveys.

Key words: Time-domain electromagnetic, airborne, drone, UAV, near surface.

INTRODUCTION

Airborne variants of the time-domain electromagnetic (TEM) method have proven to be highly efficient for characterization of the subsurface electrical conductivity distribution on a large scale. Projects with geotechnical or environmental focus, however, often involve subsurface investigations on a smaller scale with higher demands to near surface resolution of conductivity in both the vertical and lateral dimensions. Such types of investigations are typically performed using ground based geophysical instruments, such as electrical resistivity tomography, towed frequency domain EM or, indeed, towed time-domain EM systems. Still, ground based geophysical instruments can be challenging to operate when facing issues with the practical accessibility of a target area and may prove inefficient. Furthermore, existing airborne TEM systems have high mobilisation costs, making them unfeasible for small scale investigations also from an economic perspective.

The appearance of low-cost drones capable of lifting geophysical sensors into the air have led to the development of semi-airborne TEM systems at various scales, e.g., Stoll J.B. (2022) and Liu *et al* (2022). Common to these are that the transmitter element is positioned on the ground, as it is too heavy to lift with a drone. Transporting the associated receiver coil(s) under a drone has the potential to increase efficiency, however, the need to position and reposition the transmitter means that the practical accessibility of the target area is still a significant concern.

Aiming at further improving the usability of the TEM method, we are developing a fully airborne drone TEM system. The immediate advantages of such a system derive from to its ability to fly low and slow at significantly reduced cost compared to traditional airborne TEM systems. Building upon existing SkyTEM system technology (Sørensen and Auken, 2004), we are developing a lightweight transmitter frame platform as well as specially customised transmitter and receiver electronics. We are collaborating with several project partners focusing on related aspects, such as, legislation and test flight permissions, heavy lift drone manufacturing and operation, and identification of suitable test locations and evaluation of test data.

We will outline the design choices made, and describe some of the main test surveys performed, as part of developing the new fully airborne drone TEM system. We will illustrate the present capabilities of the system as well as discuss future test- and development plans.

Figure 1. Carrier drone and drone TEM frame at Swedish airstrip.

METHOD AND RESULTS

Developing a fully airborne drone TEM system involves the development of numerous system parts, which all present their own challenges and optimisations both as individual elements and when working together.

The heavy lift drone we are using to carry the drone TEM system, shown in Figure 1, is designed, manufactured, and operated by a separate company. An advantage of the selected drone is that it is powered by an internal combustion engine and that its rotors are mechanically driven. This means that we do not need to worry about EM noise from electric motors driving the rotors.

The frame design is optimised for low weight and high stiffness. Besides providing a stable transmitter geometry for accurate system modelling, the stiffness is also important for achieving a significant reduction in primary field influence in the recorded data. We achieve this through careful receiver coil positioning to minimise flux coupling between the transmitter loop and the receiver coil. We have performed multiple test flights at Drone Center Sweden to verify operability and aerodynamic performance of the frame when carried by the drone, showing promising results (see Figure 2).

Figure 2. Airborne drone TEM system at Swedish airstrip.

Parallel to the development of the frame and drone designs, much effort has gone into adapting and improving the transmitter and receiver electronics. These ongoing developments have resulted in a number of prototype systems, which have been tested at different survey locations. Common to the prototype system tests are that they have all been flown using a scaled-down version of the traditional SkyTEM frame. The scaled down frame has an area of around 20 m^2 and is towed by a helicopter (see Figure 3).

Figure 3. Scaled-down frame used for testing the drone TEM transmitter and receiver electronics.

In the following we will show examples of how the transmitter and receiver electronics have improved between two prototype test surveys flown in 2021 and 2023 respectively.

The survey flown in 2021 was conducted at a location called Åsen near Trondheim in central Norway. Pre-existing airborne EM data were available for the survey area, and the focus of the investigation was delineation of clay deposits on top of bedrock. The prototype TEM system was flown at an average transmitter altitude of 20 m at reduced speed to simulate a drone operation.

The survey flown in 2023 was conducted at a location called Øbakker near Viborg in Denmark. The specific survey site is one of several test areas adopted for investigating the properties of Danish peatlands. Furthermore, it is a pilot site for testing rewetting efforts aiming at reducing CO_2 emissions from low-lying farmlands. The focus for the investigation was delineation of the peat extent and its varying thickness in the area. The updated prototype TEM system was flown across the test field twice at two distinct heights above ground, averaging approximately 8 m and 15 m, to further investigate the practical influence of system height on near surface resolution. Figure 4 shows the scaled-down frame towed along the Øbakker peatlands close to the ground, simulating a drone operation.

Figure 4. Low flying test frame at Øbakker, 2023.

The receiver system bandwidth has been kept at nearly 1 MHz for both prototype systems, limited primarily by the bandwidth of the receiver coil. Sampling is performed at 5 MHz, and the subsequent real-time data reduction follows the methodology presented in Nyboe and Mai (2017). However, updates to the sampling and gating hardware have significantly increased the possible data throughput of the receiver system between the two surveys. This allows us to store more and narrower gates for each transient sounding, as well as to support an increase in the transmitted current pulse rate.

The drone TEM system transmitter electronics are solely battery powered, which constitutes a major development away from the traditional electric generator power source used in larger SkyTEM systems. The transmitter used in the survey flown in 2021 had a peak current capacity of 160 A and a turnoff time around 14 µs. It was also limited to being able to transmit current pulses at a maximum rate of 150 Hz, corresponding to a signal base frequency of 75 Hz. Subsequent developments implemented in the transmitter used for the survey flown in 2023 have increased the peak current capacity to 250 A, while slightly shortening the total turnoff time of the system, as seen in Figure 5b. The transmitter capabilities related to current pulse transmission rate have also improved significantly between the two surveys. This means that we were able to optimize the pulse rate to better reject local VLF noise signals for the 2023 survey, where we settled on pulse rate of 650 Hz, corresponding to a signal base frequency of 325 Hz. Naturally, the larger number of transient decays recorded pr second allows for more signal averaging to reduce uncorrelated nose, while the higher signal base frequency inherently helps in better suppressing motion induced noise. A comparison of the transmitted current pulses from the 2021 and the 2023 surveys is shown in Figure 5a.

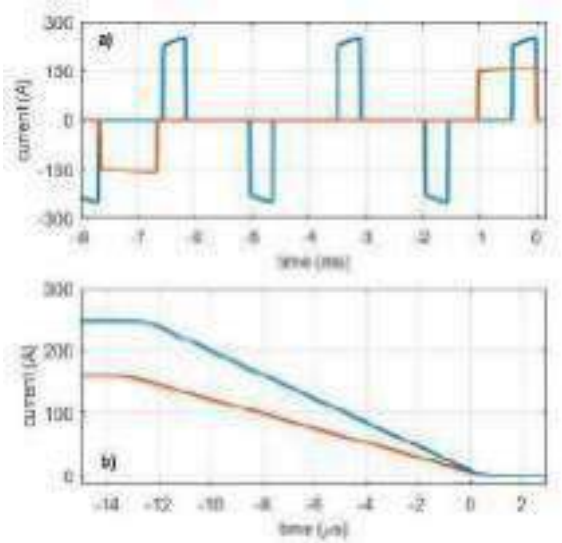

Figure 5. a) Plot of the current waveform transmitted in the 2021 survey in Norway (orange) together with the current waveform transmitted in the 2023 survey in Denmark (blue). b) Zoomed-in view of the current turn-off shape and duration for the waveforms in panel a. Notice the change in time units between the two panels.

When designing our drone TEM frame we faced a fundamental trade-off between size, weight, and stiffness of the frame, where the weight must remain low enough to allow airborne transportation by drone, while the quality of the data must remain acceptable. Reducing the area of the transmitter loop results in a smaller magnetic dipole moment of the primary magnetic field, which translates into an overall smaller ground response. Also, the smaller distance between the power electronics and the receiver coil means that the bias responses emanating from eddy currents within the power electronics and nearby conductive elements are expected to be more pronounced in the recorded data. On the positive side, moving the system closer to the ground has a major effect on the magnitude of the early time response from the ground, which is the part of the response we are typically most interested in. Also, the smaller Tx loop size and the application of only a single loop turn results in faster transient properties of the transmitted current. This further increases the early time ground response especially from relatively poor conductors (Sørensen and Nyboe, 2012). The relatively small and stiff frame we have settled upon allows us to achieve good aerodynamic manoeuvrability close to the ground and the stiff construction helps significantly in robust subtraction of unwanted bias responses.

Figure 6 shows two representative transient decay curves recorded during the 2023 survey in Denmark. As mentioned previously for the 2023 survey, the prototype TEM system was flown across the test field twice at two distinct heights above ground. The decay curves shown represent one curve from each of the two flights selected from approximately the same location in the field. The survey data have proven to contain usable gated transient decay values over the entire off-time span from before 1 µs up till about 1 ms depending on signal and noise conditions. The expected increase in signal level for early times when moving to a lower flying height has also been demonstrated by the recorded data. Focusing on the early time

behaviour of the transient decays, it should be noted that the zero-reference for the logarithmic time axis in figure 6 is the same as is used in figure 5b. The positive signal slope before around 0.6 µs is therefore due to the signal being recorded across the waveform end-of-ramp, showing part of the signal build-up before it subsequently decays.

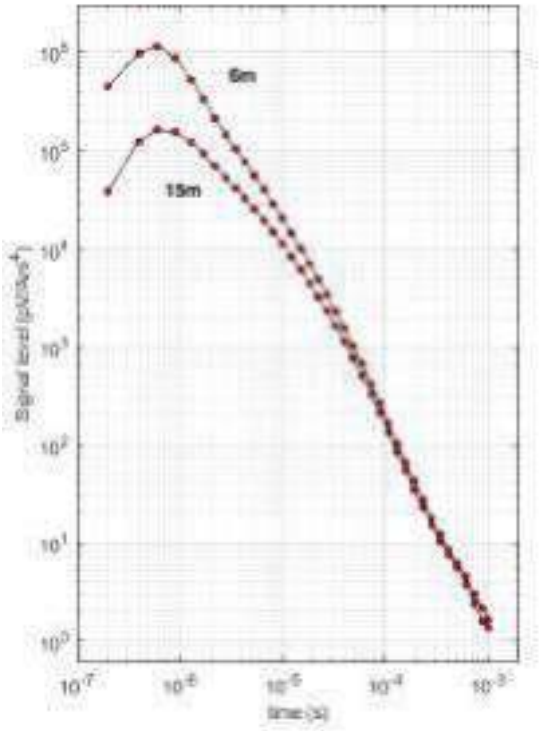

Figure 6. Transient decay curves recorded at Øbakker in 2023 for two different frame heights at approximately the same location. The data shown have been subjected to standard data processing procedures including constant bias level subtraction.

Regarding our future plans, we expect to perform an additional test survey in Denmark during 2023 using the scaled-down frame and prototype TEM system to further investigate the near surface resolution properties and robustness of these very early time data. Furthermore, the heavy-lift carrier drone is also scheduled to arrive in Denmark this summer, and we plan to perform the first actual airborne drone TEM test survey using the complete drone TEM system in 2023 as well.

CONCLUSIONS

Developing an optimized and fully airborne drone TEM system has proven to be a major challenge, and reaching the stage we are presently at with our system has taken several years of work to accomplish. At this stage we have successfully demonstrated that a small-scale airborne TEM system can indeed deliver high quality data for near surface characterisation. Going low and slow largely compensates the early- and intermediate time response for the loss of signal caused by the reduced transmitter magnetic moment, while the lateral footprint is substantially reduced. The large bandwidth of the receiver system in combination with the high degree of stability and fast transient properties of the transmitted current allows us to obtain usable data at extremely early delay times. The enhanced data throughput of the receiver system means that we can store gates up to the full 5MHz sample rate over time intervals covering the earliest and most rapidly varying parts of the ground response. Boosting the transmitter current pulse rate capability has resulted in improvements of both the noise rejection properties of the system as well as an overall better match between the off-time duration and the typical time we observe a ground signal above the noise level. So far, we have only been able to perform prototype TEM system tests at survey sites using a scaled-down SkyTEM frame carried by a helicopter. However, the actual drone frame has been successfully tested in airborne operation while towed by a heavy-lift drone. Looking ahead, we expect to be able to fly the first actual airborne drone TEM test survey using a heavy-lift drone as carrier during the summer of 2023.

ACKNOWLEDGMENTS

We would like to thank Eureka/Eurostars for the financial support of the research and development project (nr. E114169). The valuable contributions from our project partners at EMerald, the Norwegian Geotechnical Institute (NGI), and the Drone Center at the University of Southern Denmark (SDU UAS Center) are likewise most appreciated.

We are grateful that ACC Innovation and Drone Center Sweden have enabled us to perform actual drone-borne tests of our drone frame and TEM system in the air.

The Department of Agroecology at Aarhus University kindly aided with arranging access to the test site at Øbakker.

Final praise goes to the development and manufacturing teams at SkyTEM Surveys, who have been innovative, flexible, and persistent in their efforts to make the fully airborne drone system a reality.

REFERENCES

Liu W., Xu Z., Liao X., Fu Z., 2022, Rapid Investigation of Anomalies in Water by UAV Transient Electromagnetic Technology, *Summit on Drone Geophysics 2022*, SEG, virtual, Program Booklet: 25-26.

Nyboe N.S. and Mai S.S., 2017, Recent advances in SkyTEM receiver system technologies, *Second European Airborne Electromagnetics Conference*, Vol. 2017, No. 1, p. 1-5, European Association of Geoscientists & Engineers .

Stoll J.B., 2022, Drones in Geophysical Exploration – A New Era of Automation is Coming, *Summit on Drone Geophysics 2022*, SEG, virtual, Program Booklet: 9-11.

Sørensen K.I., and Nyboe, N.S., 2012, Near Surface Resolution and Turnoff Times in Airborne TEM Investigations, *Symposium on the Application of Geophysics to Engineering and Environmental Problems*, Proceedings: 104-108.

Sørensen K., and Auken E., 2004, SkyTEM - a new high-resolution helicopter transient electromagnetic system, *Exploration Geophysics* 35: 191-199.

Geotechnical ground investigations with a small airborne TEM prototype system

Martin Panzner
EMerald Geomodelling
Gaustadalléen 21,
0349 Oslo, Norway
mp@emrld.no

Andi A. Pfaffhuber
EMerald Geomodelling
Gaustadalléen 21,
0349 Oslo, Norway
aap@emrld.no

Nicklas Skovgaard Nyboe
SkyTEM Surveys ApS
Dyssen 2
DK-8200 Aarhus N, Denmark
nsn@skytem.com

SUMMARY

In this paper we show how time domain electromagnetic data from a small airborne prototype system was successfully used for geotechnical ground investigations at a road construction site in Central Norway. The measured data were processed and inverted with time efficient semi-automatic processing tools. Subsequently, the resistivity models recovered by AEM data inversion were automatically interpreted with machine learning based algorithms that were trained with geotechnical drilling data. Both the thickness of a sediment layer overlaying bedrock and the type of sediment was estimated. The measured data and the inverted resistivity models are compared to those from a regular SkyTEM304 system, which was utilized earlier at the same site. Also, the sediment depth and sediment type estimated from the two AEM datasets were compared, proving the feasibility of such a small airborne TEM system for geotechnical ground of the shallow subsurface.

Key words: Time-domain electromagnetics, geotechnics, drone, geomodelling, machine learning,

INTRODUCTION

Ground investigations prior to large infrastructure projects are predominantly based on geotechnical drillings. Ground-based geophysical investigations are rarely used because they are often tedious and expensive. On the other hand, the investigation sites are often too small for time efficient airborne geophysical investigations. Drone based geophysical measurements could fill this gap, providing fast and efficient scanning of construction sites, allowing for low flight altitudes and high spatial sampling. Furthermore, the required depth of investigation for geotechnical applications is often limited to a few tens of meters, favouring small low power systems.

In this paper we describe the results from geophysical ground investigations conducted with a prototype for a new small airborne time-domain electromagnetic (A-TEM) system. This development is the first step towards a small TEM system that could potentially be carried by a drone. The system was field-tested in at a road construction site called Åsen in Trøndelag, Central Norway in fall 2021. The purpose of the field test was to investigate whether such a significantly smaller system can have a sufficiently high dipole moment and sensitivity to conduct meaningful ground investigations. At the same site, A-TEM data with the much bigger SkyTEM304 (Sørensen, 2004) was acquired in 2019, which is used for comparison and benchmarking.

Figure 1: Picture of a miniature airborne TEM system called SkyTEM21HR used in this geotechnical ground investigation study.

METHOD AND RESULTS

A downsized TEM protype system, called SkyTEM21HR, was used to test the performance and verify the benefits of small A-TEM system. The transmitter area is reduced to 21.74 m2 and the maximum transmitter current is 160 A, which results in a maximum dipole moment of 3'480 Am2. The transmitter base frequency is 75 Hz, transmitting a square pulse of 1 ms duration for each 6.6666 ms interval with sign-alternating repetitions. The turn-off time is approximately 14 µs. The smaller physical dimensions of the transmitter loop allow for shorter timescales with regards to the properties of the transmitted waveform. This requires a larger bandwidth in the receiver system to preserve the detailed ground response information in the recorded data. A vibration damped 5 m^2 receiver coil is mounted in zero-position to minimize the primary field. The complete system has a total weight of 150 kg and a power consumption of 300 W.

The analogue system bandwidth is approximately 900 kHz, and the TEM signal is initially digitized at 5 MHz sample rate. Subsequently, the raw sampled data are subjected to a real-time data reduction process in which the large number of samples in each predefined gate interval are converted to a few polynomial coefficients. This allows for flexibility in the final gate

formation while maintaining reasonable data file sizes (Nyboe and Mai, 2017).

Data acquisition and processing

Airborne TEM data had been acquired with a SkyTEM304 system at a location called Åsen, North-East of Trondheim in Central Norway (Figure 2) in conjunction with geotechnical ground investigations prior to a large road-tunnel construction project. At the same site, we have subsequently acquired A-TEM with the much smaller SkyTEM21HR system at coincident flightlines.

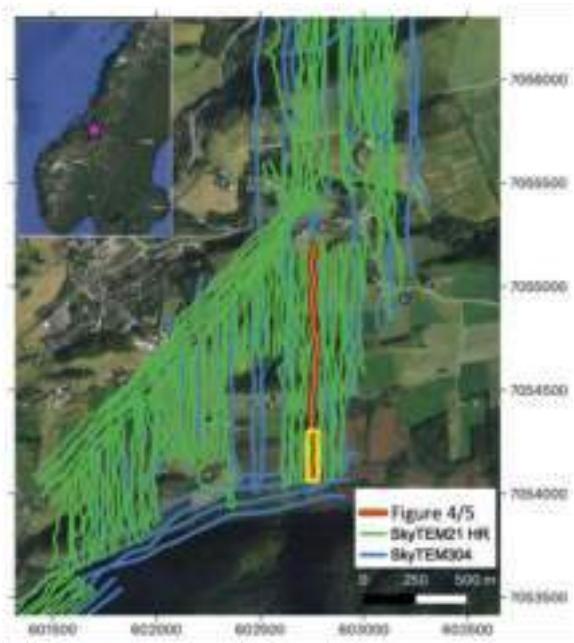

Figure 2: Map of the survey area in Åsen, Central Norway. The yellow box is indicating location of sounding data in Figure 3 and the red line shows the location of the profile in Figure 4. (background map source: maps.google.com)

As part of the initial processing, the gated transients are averaged using a moving average approach with non-uniform weighing, equivalent to simple linear convolution filtering, as well as being subjected to a non-linear despiking process to remove impulsive noise. Due to the relative proximity of the transmitter electronics and the receiver coil on the smaller platform, the signal contribution from eddy-currents in the transmitter electronics will appear as a noticeable bias. We subtract the bias response from the recorded signal as a separate post-processing step involving high-altitude data. We experienced that the rigid mechanical platform and the very stable transmitter waveform resulted in a bias response that was nearly constant, and the subtraction process worked well.

The data preconditioning and processing was done using inhouse processing software, automatically removing data that showed interference with infrastructure (couplings) or poor signal to noise levels. To allow for a fair comparison of the data from the SkyTEM21HR and the SkyTEM304 system, we tried to keep the processing as similar as possible. However, the two systems are fundamentally different. The much smaller and lighter SkyTEM21HR can only transmit one dipole moment but thanks to the updated digital data recording and electronics, the system is able to provide useful TEM data, densely sampled with 50 time-gates, in the time interval [10^{-6} s to 8×10^{-4} s] (Figure 3a) at an average transmitter-receiver altitude of 20m. In comparison the SkyTEM304 system can measure good quality data with 15 time-gates in the interval [8×10^{-6} s to 2×10^{-4} s] with a low-dipole moment and 16 time-gates in the interval [5×10^{-5} s to 10^{-3} s] with a high dipole moment (Figure 3b) at an average transmitter-receiver altitude of 40 m.

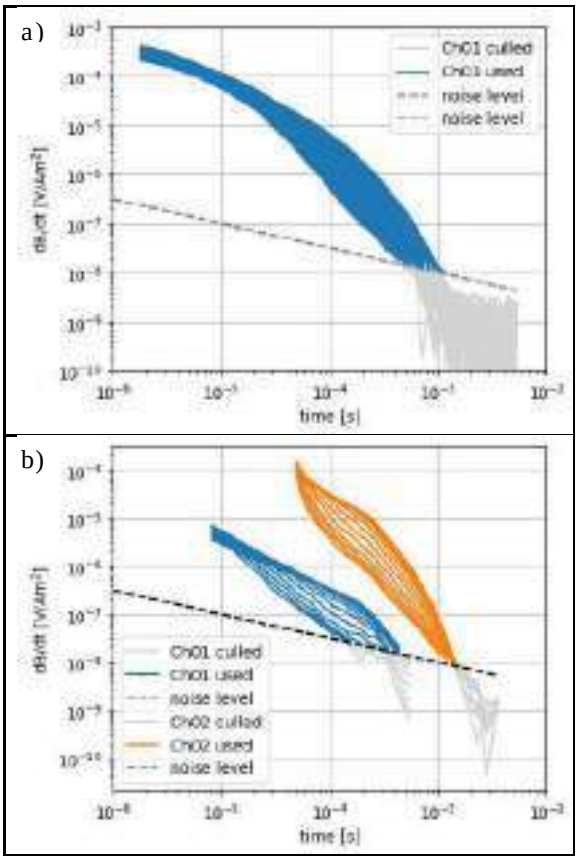

Figure 3: Examples of measured data from the SkyTEM21HR system (a) and the SkyTEM304 system (b), acquired at the same geographical location (yellow box in Figure 2). Datapoints that are greyed out were omitted in the inversion.

For further comparison, both the SkyTEM21HR and the SkyTEM304 data were inverted with the same inversion software (Auken et al. 2015), using the same vertical discretization of the inversion parameters and the same spatial smoothness constraints and regularization weights. The inversion results from both datasets show strong similarities in the depth interval were both systems have high sensitivity (Figure 4). Both results explain the measured data well with an RMS=1.6 for SkyTEM21HR data inversion and RMS=1.3 for the SkyTEM304 data inversion. However, the SkyTEM21HR system is significantly smaller and lighter than the SkyTEM304 system and can thus be flown lower to the ground. That results in a significantly smaller sensitivity footprint, which allows for a higher lateral sampling frequency and provides a significantly higher lateral subsurface resolution. Also, the vertical resolution of the very shallow subsurface is significantly improved with the SkyTEM21HR system, due to the

availability of very early time gates, facilitated by the fast ramp-down. Nevertheless, in some locations, where the subsurface is known to be very resistive and/or the flight altitude was high only a few early time gates with sufficient signal to noise ratio could be registered, due to the small dipole moment of the SkyTEM21HR system., resulting in a significantly reduced depth of investigation (DOI) (Vest & Auken, 2012.

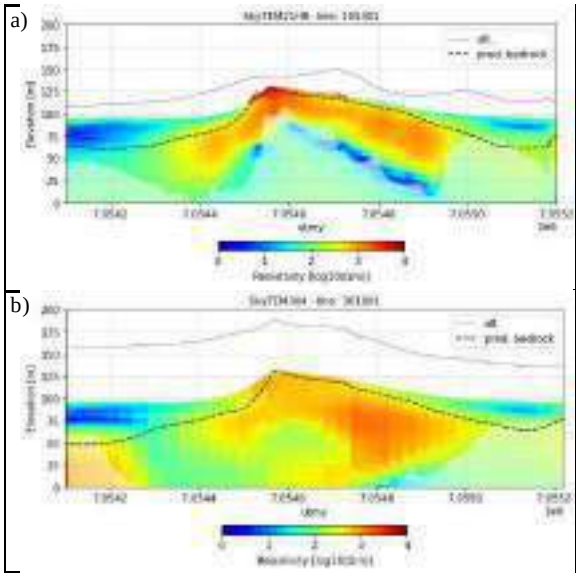

Figure 4: Comparison of resistivity sections reconstructed by inversion of the SkyTEM21HR data (a) and the SkyTEM304 data (b) along co-located profiles (red line in Figure 2). The flight altitude and the predicted bedrock depth marked by blue and black dashed lines.

Machine Learning based interpretation

We have applied machine learning (ML) based data interpretation workflows that can integrate available geotechnical data and geophysical parameter models to estimate bedrock depth and predict the probability for the presence of various soil types (e.g., brittle clay vs marine clay). These ML based algorithms allow for much faster and more subjective interpretation of large geophysical datasets.

The bedrock interpretation algorithm is based on an artificial neuronal network (ANN) that is trained with outcrop locations and geotechnical drilling data, which provide a depth to bedrock or a minimum sediment depth at discrete drilling locations. Strongly simplified, the ANN is "learning" the resistivity patterns associated with certain bedrock depths at discrete drilling locations. These "learned" patterns are then used to automatically interpret the entire resistivity model from AEM data inversion. A detailed description of the ANN based bedrock interpretation algorithm is given in Lysdahl et al. (2022). The predicted bedrock depths for the two resistivity models are shown in Figure 4.

The machine learning (ML) based volume classification algorithm is designed to predict the geological/geotechnical material type based on a few existing training data points for a large 3D resistivity volume from AEM data inversion. In this study, we limit ourselves to a classification brittle/non-brittle clay. The algorithm uses a two-step approach. Firstly, the soil-type is predicted for several geotechnical boreholes, in which feed-force data were measured. The training data are sparsely sampled material labels, either from human analysis of drilling samples, outcrops, or geologic/geotechnical rules (e.g., hammering and flushing means non-brittle bedrock encountered). These training data are used to train a ML model-1 to predict the probability for material types in all the geotechnical boreholes with feed-force data, providing vertical profiles of the material types present at all drilling locations. Secondly, another ML model-2 is trained, using the previously predicted material types in all the boreholes to predict the material type for the entire 3D resistivity volume. A direct comparison of the predicted material types is given in Figure 5, for the two resistivity models recovered from the two A-TEM systems. A more detailed description of the volume classification algorithm is given in Christensen et al. (2021).

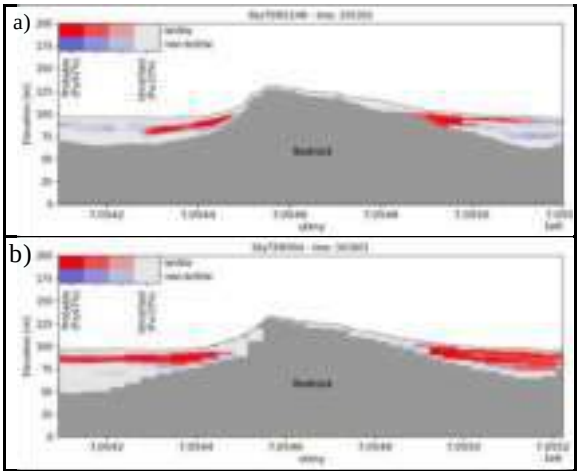

Figure 5: Comparison of predicted probabilities for the presence of brittle clay based on the inverted resistivity models from the SkyTEM21HR (a) and the SkyTEM304 (b) systems. The location of the profiles is indicated with a red line in Figure 2.

CONCLUSIONS

We have shown that a significantly smaller and lighter airborne TEM system than currently available commercial TEM systems, can produce useful geophysical data. The data can be interpreted and provide inside into subsurface resistivity structures and geology. In the case of geotechnical applications, where the focus is on the shallow subsurface, such a smaller system has in fact some significant advantages. The system operates with a much smaller magnetic dipole moment and state of the art transmitter and receiver electronics combined with digital data recording provide high quality early time data. Lower flight altitudes and higher spatial sampling along the flightlines further improve the sensitivity to the shallow subsurface. Resistivity models recovered by TEM data inversion show strong similarities between the small SkyTEM21HR system and the much bigger SkyTEM304 system in the parts of the subsurface where both systems have good sensitivity. However, the resistivity models recovered from the SkyTEM21HR data provide a more detailed definition of the shallow resistivity structures, even though the depth of investigation is somewhat reduced.

Higher spatial and temporal data sampling requires more automation in the data processing and interpretation. With the results presented in this study we show that automated data

processing and machine learning based data interpretation algorithms can be used to efficiently process and interpret this type of high resolution AEM data. We have successfully performed an automated bedrock topography interpretation using an artificial neuronal network. We also conducted an automated volume material classification based on random forest classifiers. Generally, the interpretation results for high resolution SkyTEM21HR data show strong similarities to the interpretation results for the SkyTEM304 data. However, there are some significant differences, especially in the shallow subsurface that can be linked to the higher resolution of the SkyTEM21HR data.

ACKNOWLEDGMENTS

We would like to thank Eureka/Eurostars for the financial support of this research and development project (nr. E114169). We would also like to thank the collaboration partners within this project, the Norwegian Geotechnical Institute (NGI) and the Drone Centre at the University of Southern Denmark (SDU) for fruitful discussions and valuable contributions to this project. We further want to acknowledge Nye Veier, the project owner of the construction site presented here.

REFERENCES

Auken E., Christiansen A. V., Kirkegaard C., Fiandac G., Schamper, C., Behroozmand A. A., Binley A., Nielsen E., Effersø F., Christensen N. B. and others, 2015, An overview of a highly versatile forward and stable inverse algorithm for airborne, ground-based and borehole electromagnetic and electric data, *Exploration Geophysics*, Vol. 46, No. 3, p. 223-235.

Christensen, C. E., Harrison E. J., Pfaffhuber A. A., Lund A. K., 2021, A machine learning--based approach to regional-scale mapping of sensitive glaciomarine clay combining airborne electromagnetics and geotechnical data, *Near Surface Geophysics* , Vol. 19, No. 5, European Association of Geoscientists & Engineers, p. 523-539

Lysdahl A. K., Christensen C. W., Pfaffhuber A. A., Vöge M., Andresen L., Skurdal G. H., Panzner M., 2022, Integrated bedrock model combining airborne geophysics and sparse drillings based on an artificial neural network, *Engineering Geology* , Vol. 297 , Elsevier, p. 106484

Nyboe N. S. and Mai S. S., 2017, Recent advances in Skytem receiver system technologies, *Second European Airborne Electromagnetics Conference*, Vol. 2017, No. 1, p. 1-5, European Association of Geoscientists & Engineers

Sørensen K. I. and Auken E., 2004, SkyTEM – A new high-resolution helicopter transient electromagnetic system, *Exploration Geophysics*, Vol. 35, No. 3

Vest C. A. and Auken E., 2012, A global measure for depth of investigation, *Geophysics*, Vol. 77, No. 4, p. WB171-WB177

A Forward Model Study to Investigate 25, 12.5 and 6.25Hz AEM System responses to IP and SPM Effects in the Regolith

Rod Paterson
Intrepid Geophysics Contractor
rod@intrepid-geophysics.com

Jovan Silic
Jovan Silic & Associates
jsilic@bigpond.com

SUMMARY

2.5D forward modelling has been completed on a series of synthetic electrical property models to evaluate and compare the responses of the 25Hz Tempest, 25Hz VTEM^{plus} and 12.5 and 6.25Hz HeliTEM^{2} systems to a large tabular conductor buried between 30 and 430m below 30m of conductive cover with and without chargeable IP properties. The response to a surface SPM layer above the conductive cover or at surface in the resistive host is also modelled and compared.

The properties chosen to populate the model are representative of environments encountered in recently inverted surveys for these systems.

The model results show that as the waveform turnoff sharpens and the system frequency decreases the sensitivity to shallow near surface IP effects increases dramatically and suggests that in this environment common in Australia and other deeply weathered regions in Africa, the benefits of using these systems to detect deeper and more subtle conductors are not being realised.

A selection of the model results were inverted using the Moksha 2.5D inductive only and the joint inductive and IP inversion methods to determine if these complex models are accurately recovered.

The results indicate that it is very difficult or nearly impossible to recover the original geoelectric section when IP dominates the inductive signal in this way.

Key words: Forward Models, AEM 2.5D Inversion, IP effects, Electrical properties, Conductive cover, Superparamagnetic

INTRODUCTION

We have built three 2D geology models to simulate a moderately conductive 200m wide, 500m high, vertical tabular body buried 30, 230 and 430m beneath a 2800 long, 30m thick, horizontal weathered regolith layer within a 4800m wide resistive host. The vertical bodies are surrounded on both sides by a 50m wide alteration halo. Two 200m wide, 5m thick horizontal zones with superparamagnetic properties sit at surface above the conductive regolith and above the resistive host respectively, Figure 1. Table 1 summarises the formation properties assigned in the forward models. The system specifications of the four systems appear in Table 2. The forward models run for each system are listed in Table 3. The Cover IP properties are

Table 1. Forward Model Properties

Formation	Dx Cellsize	Res ohm-m	Cha (0-1	Ctau (0- 1)	Cfreq	Susc (SI)
Host	25	1000	0	0	0	0
Dyke_Halo	5	400	0.7	0.3	0.3	0
Dyke_Vert	5	20	0.01	0.001	0.3	0
Cover	25	20	0	0	0	0
Cover with IP	25	20	0.1	0.03	0.7	0
SPM1 in Cover	25	20	0	0	0	0.075
SPM2 in Host	25	1000	0	0	0	0.075
AboveTopo	25	10000 0	0	0	0	

Table 2. AEM System Specs for Modelling

AEM System Specifications for Modelling						
System	Freq	Field	Units	Waveform	Type	Sensor
TEMPEST	25Hz	Bfield	fT	Step	Fixed Wing	Towed Bird
VTEMplus	25Hz	dB/dt	pT/s	Stepped	Heli	Susp. Loop
HeliTEM2	12.5Hz	dB/dt	nT/s	~Square	Heli	Susp. Loop
HeliTEM2	6.25Hz	dB/dt	nT/s	~Square	Heli	Susp. Loop

Modelled System Geometry						
System	TxAlt	RxAlt	Pitch	TxRx Zsep	TxRx Xsep	Comps
TEMPEST	120	73	2.7	47	111	X/Z
VTEMplus	30	30	0	0	0	X/Z
HeliTEM2	30	30	0	0	0	X/Z
HeliTEM2	30	30	0	0	0	X/Z

AEM System Tx/Rx Electronic Summary						
System	Freq (Hz)	Peak NIA	OnTime (ms)	OffTime (ms)	LastGate (ms)	Gates
TEMPEST	25	86240	10	0.0000	7.878	15
VTEMplus	25	407753	7.47	12.5300	18.137	45
HeliTEM2	12.5	571813	20.01	19.9000	38.140	28
HeliTEM2	6.25	566000	39.873	40.1270	80.000	25

Table 3. Forward Models Completed

Model 6002010 Shallow	Model 6004050 Middle	Model 6006100 Deep
Cover (No IP, with SPM)	Cover (No IP)	Cover (No IP)
Cover (with IP and SPM)	Cover (With IP)	Cover (With IP)
4 Systems	4 Systems	3 Systems (not TEMPEST)

METHOD

The AEM forward modelling was completed using the 2.5D Moksha software. Both X and Z components were modelled. GeoModeller provides the interface to the 3D model building tools and assigns physical properties to the mesh. The 2D finite element mesh is adapted to the model so that mesh resolution is higher where greater accuracy is required. The forward code includes the ability to model IP and SPM effects.
Selected forward model results were inverted to gauge the impact of IP and SPM effects in the Cover layer and to determine if the model could be recovered with a standard

Moksha 2.5D inversion or a joint inductive and IP 2.5D inversion procedure.

RESULTS

The forward model and inversion figures display channel profiles for each measurement time with early, mid and late times grouped together in 3 panels ordered from top to bottom. The inverted profiles are displayed in black and the observed profiles in cycled colours. Below the profiles we show a single panel illustrating the impact of noise thresholding on the X and Z components. The base panels show the 2.5D inversion log conductivity section, chargeability section (joint IP only) and the original forward model.
Noise estimates are not included in the forward models but they are included when inverting. These noise estimates are based on experience with these systems and are derived from survey data rather than contractors estimates or high-level flight measurements.

The four systems were first tested on selected models free of IP and SPM effects to assess the impact of conductive cover and depth to top for the three base models. The forward X and Z component models were inverted jointly using the Moksha 2.5D inversion code to make this assessment. With the exception of TEMPEST all systems were able to detect/resolve the deeper targets.

This was followed by repeating the modelling with IP effects in the cover sequence, Table 1. The forward modelled results for the VTEM and HeliTEM systems are summarised side by side with increasing depth in Figure 3. It is clear that the impact of IP increases as the frequency decreases and the pulse width increases.

The 2.D inversion of Tempest and VTEMplus system forward models was able to recover the shallow IP contaminated models to a moderate degree. The most significant outcome from this work was that 2.5D inversion of the 12.5Hz and 6.25Hz HeliTEM models was unable to recover the 6004050 middle and 6006100 deeper IP contaminated models Figures 8 to 13 and even the shallow models were not fully recovered. Surprisingly the inversion of VTEM^{plus} recovered the 6006100 deeper IP contaminated model but not the 6004050 middle depth model, Figures 7. The partial fits in the presence of IP show thin responses at the top of the conductor (12.5Hz) or may be pushed down below the conductor (6.25Hz), Figures 8 to 10.

Other forward and inverse model pairs investigated were VTEM^{plus} with SPM embedded in Cover and Host (no IP or SPM inversion), Figures 16 and 17. Results highlight the independence of SPM response to host resistivity. The two SPM occurrences are in Cover and Host respectively. In this case the use of joint X and Z in the inversion has caused the SPM effect to be partly fitted. This creates havoc with the inversion geometry. Normally when inverting Z only we find that the 2.5D inversion will not fit an SPM anomaly.

The joint inversion of the X and Z components from the forward modelling outputs appears to help with the inversion in the presence of IP as the assumed near horizontal IP layer is not as well coupled with X. However, in practice we are not able to jointly invert the X and Z components as the X is usually incompatible with the Z component due to the effects of motion or other related noise.

In the case of the VTEM^{plus} forward modelled deep target 6006100 with IP in Cover the X component assists the inversion even though the late time Z component is not fitted. The inversion is standard and not a joint IP inversion in this case, Figures 11 and 12.

CONCLUSIONS

Once the relatively modest IP properties are included in the low-density cover, the 2D inversion struggles to fit the vertical targets. The impact of IP increases significantly for the lower frequency, longer pulse HeliTEM^2 systems with their near square wave and sharper turn off, Figure 2. VTEM^{plus} appears to be less impacted because earlier and slower turnoff results in a reduction in IP signal although it may still be decaying into the next duty cycle. The presence of IP in the halo around the conductor does not have a major impact on the inversion.

The TEMPEST towed bird system is less impacted by IP effects although they are still recognisable in the forward models. The deeper targets were not detected. The lower power and increased height of the sensor above the ground will contribute although the SPM effects are still strongly represented in the forward models.

The move towards lower transmitter frequencies and longer pulse lengths in AEM systems results in greater exposure to IP effects when they are present near the surface. 25Hz moderately powered systems may be better suited in areas with strong surface IP responses.

Apart from improving the joint IP inversion approach there is very little that can be done practically to manage the problem except to map the extent and strength of the IP effects and advise the client of the limitations in this environment.

Use of the X component in a joint inversion shows some promise but so far resolving the issues in this area do not seem to be a high priority amongst contractors.

Further work is planned to evaluate these models with other inversion methods (1D/CDI) and investigate narrower dipping targets and more IP properties variations.

ACKNOWLEDGMENTS

I would like to acknowledge the contribution of Jovan Silic in rewriting Arjuna. He invested a lot of his own time to make this possible using his detailed knowledge of electromagnetics and his many years of experience working in this domain.

REFERENCES

Rod Paterson (2020) 2.5D Airborne Electromagnetic inversion: A review of the benefits of moving to a higher dimension, Preview, 2020:207, 33-47,
DOI: 10.1080/14432471.2020.1801314

Paterson, R., Silic, J., FitzGerald, D. and Jakica, S., 2017. High Accuracy 2.5D AEM Inversion Method for Banded Iron-Formation (BIF) and Other Geological Settings, AusIMM Iron Ore 2017, Paper Number: 85

Raiche A., Sugeng F., and others, 2008. Developing the Modelling & Inversion Environment, Electromagnetic

Modelling Group, CSIRO Exploration & Mining, AMIRA Project 223, Report.

Silic, J., Paterson, R., FitzGerald, D. and Archer, T., 2015. Comparing 1D and 2.5D AEM inversions in 3D geological mapping using a new adaptive inversion solver, 14th International Congress of the Brazilian Geophysical Society, Brazil.

Silic, J., Paterson, R., and FitzGerald, D., 2016. Improved Structural Mapping and Conductive Targeting Delivered by a new 2.5D AEM Inversion Solver, ASEG-PESA-AIG 25th Geophysical Conference and Exhibition Abstracts.

Wilson, G.A., Raiche, A.P. and Sugeng, F., 2006. 2.5D inversion of airborne electromagnetic data. Exploration Geophysics, 37, 363–371.

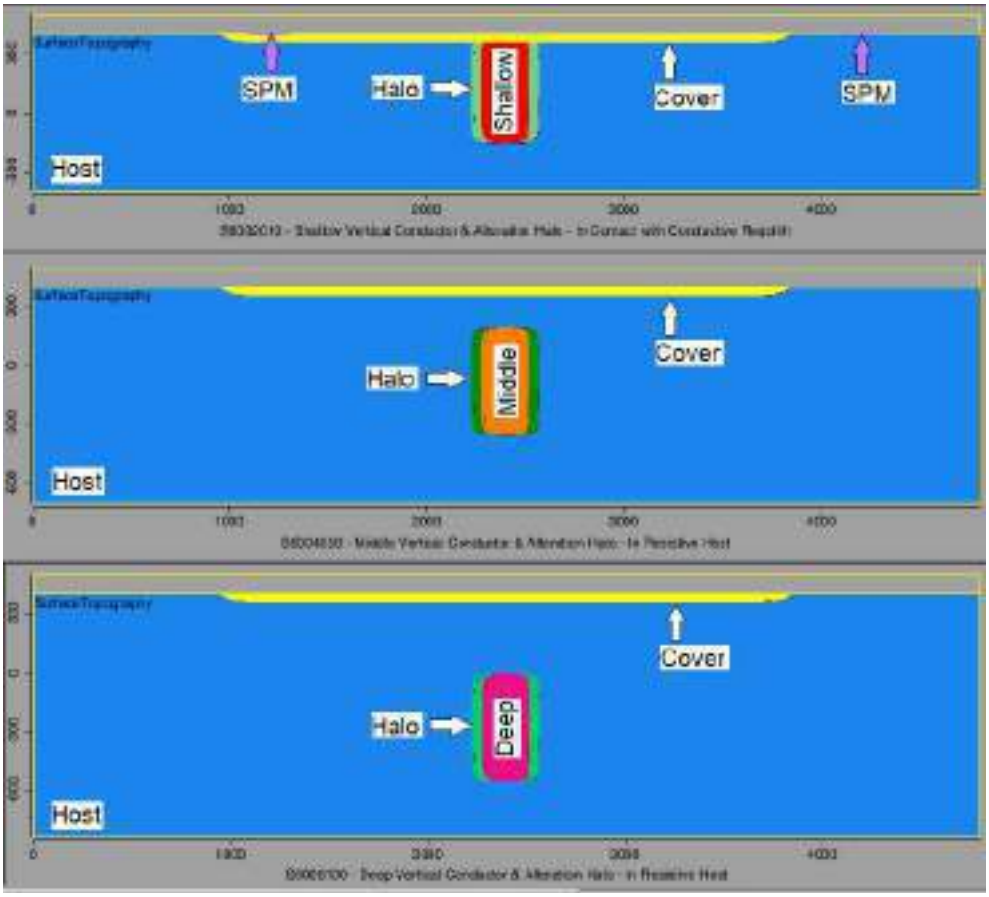

Figure 1. Forward Model Geology (Assigned Properties are shown in Table 1).

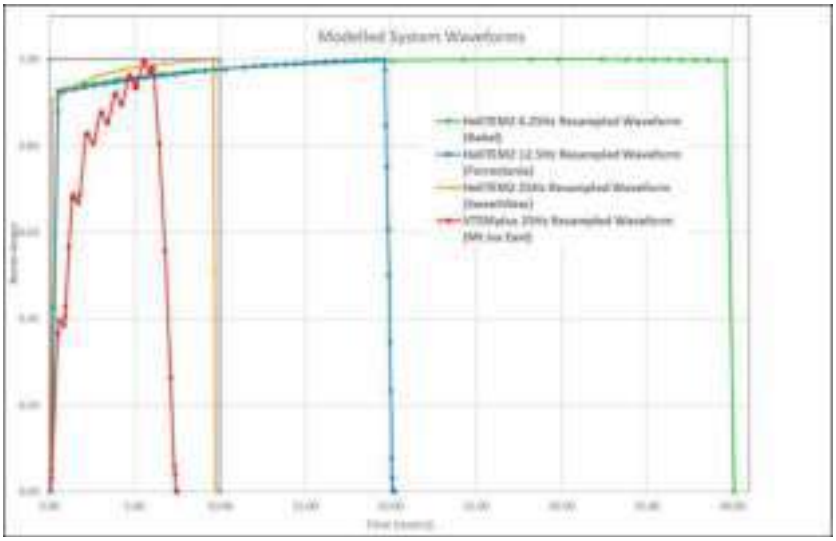

Figure 2. Modelled System Waveforms

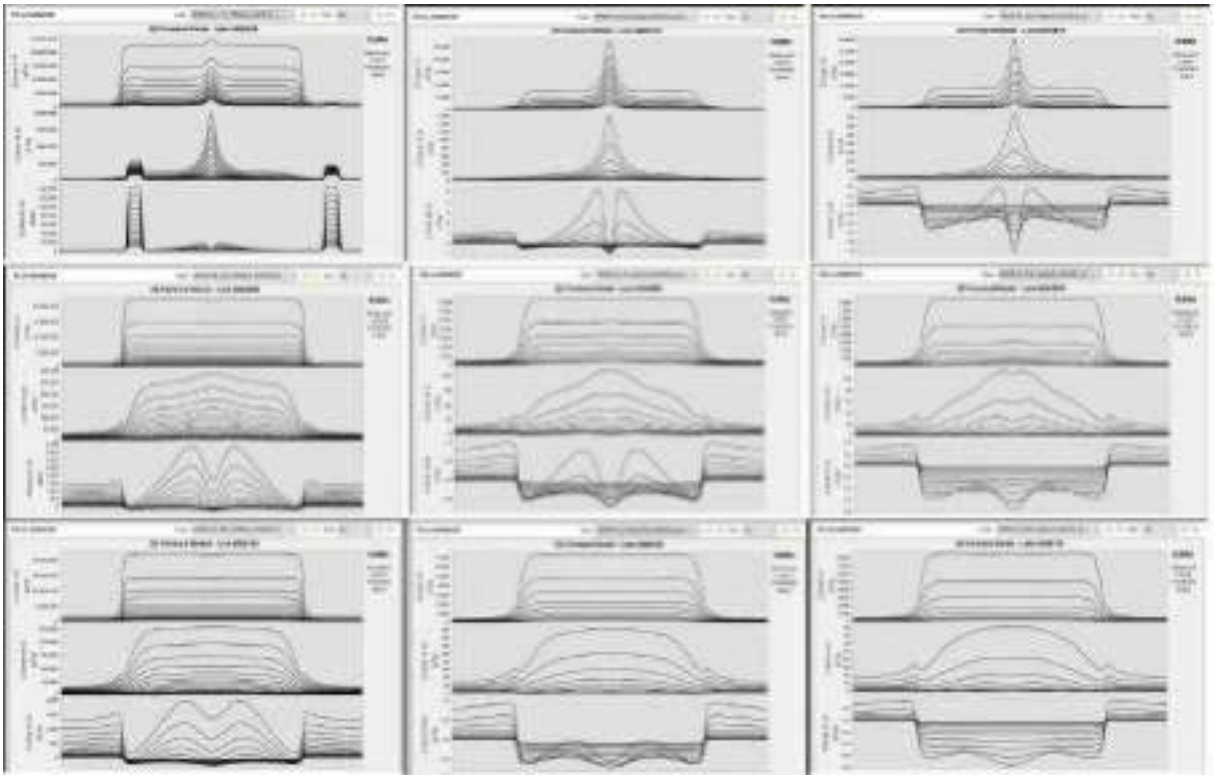

Figure 3. Fwd Model Comparisons for VTEMplus25Hz, HeliTEM212.5Hz and HeliTEM2 6.25Hz with increasing target depth below Cover with IP.

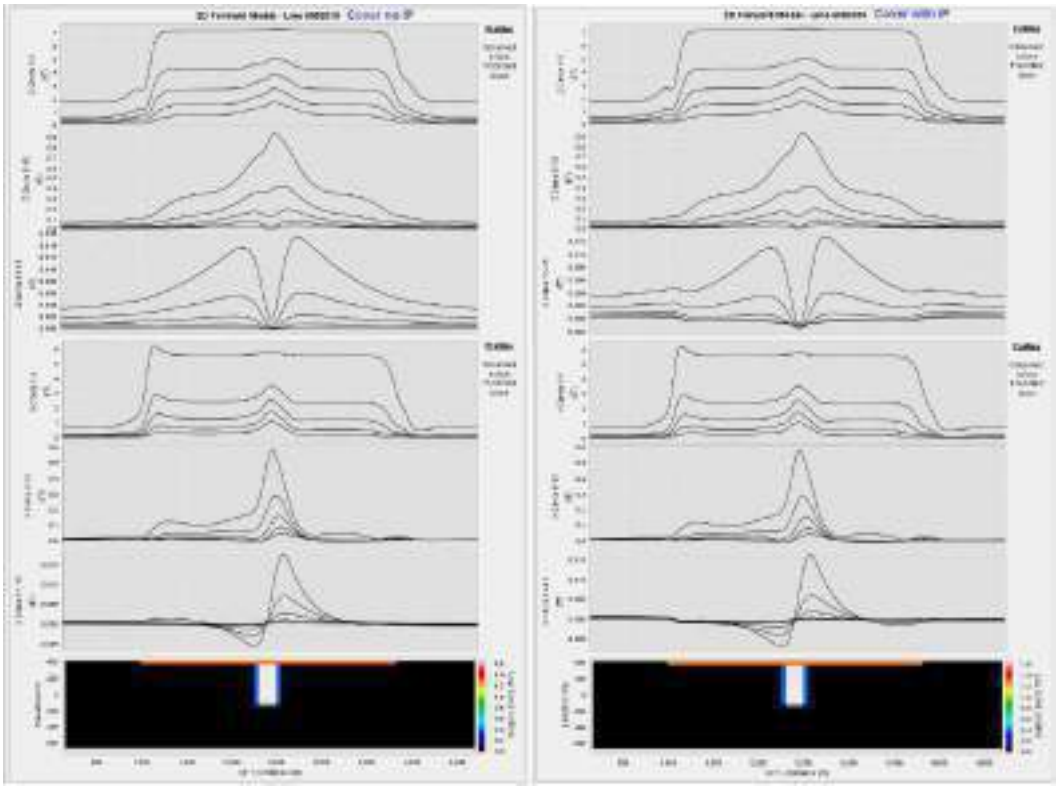

Figure 4. TEMPEST Forward Model 6002010 (shallow) – Cover with IP (right) and without IP (left) - (X/Z Components)

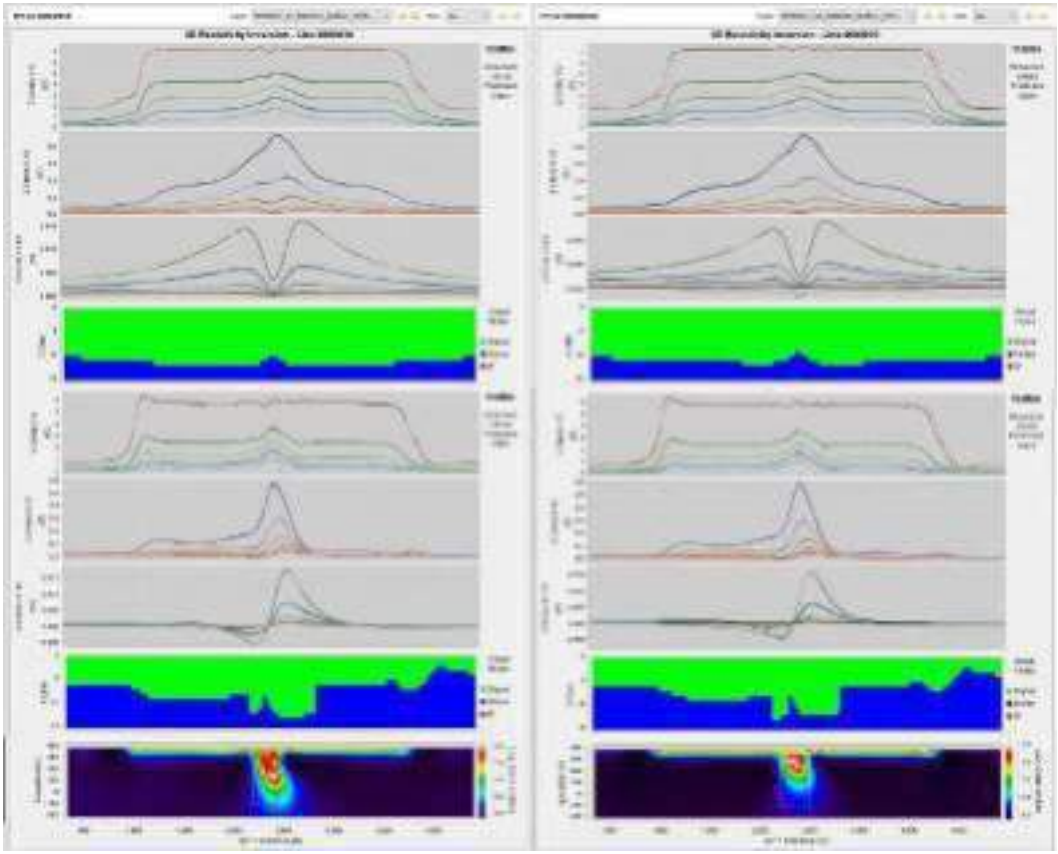

Figure 5. TEMPEST EM2.5D Inversion 6002010 (shallow) – Cover with IP (right) and without IP (left) - (X/Z Components)

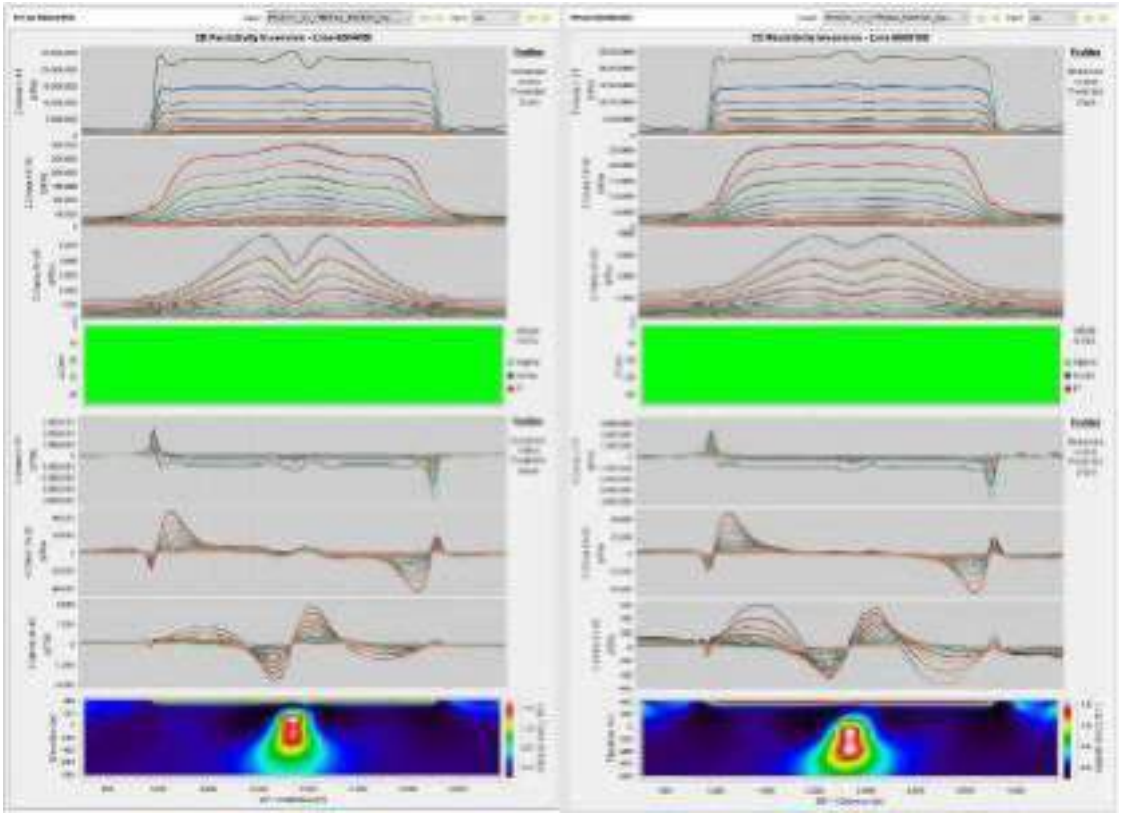

Figure 6. VTEMplus EM2DInv 6004050 middle and 6006100 deep - no IP in Cover

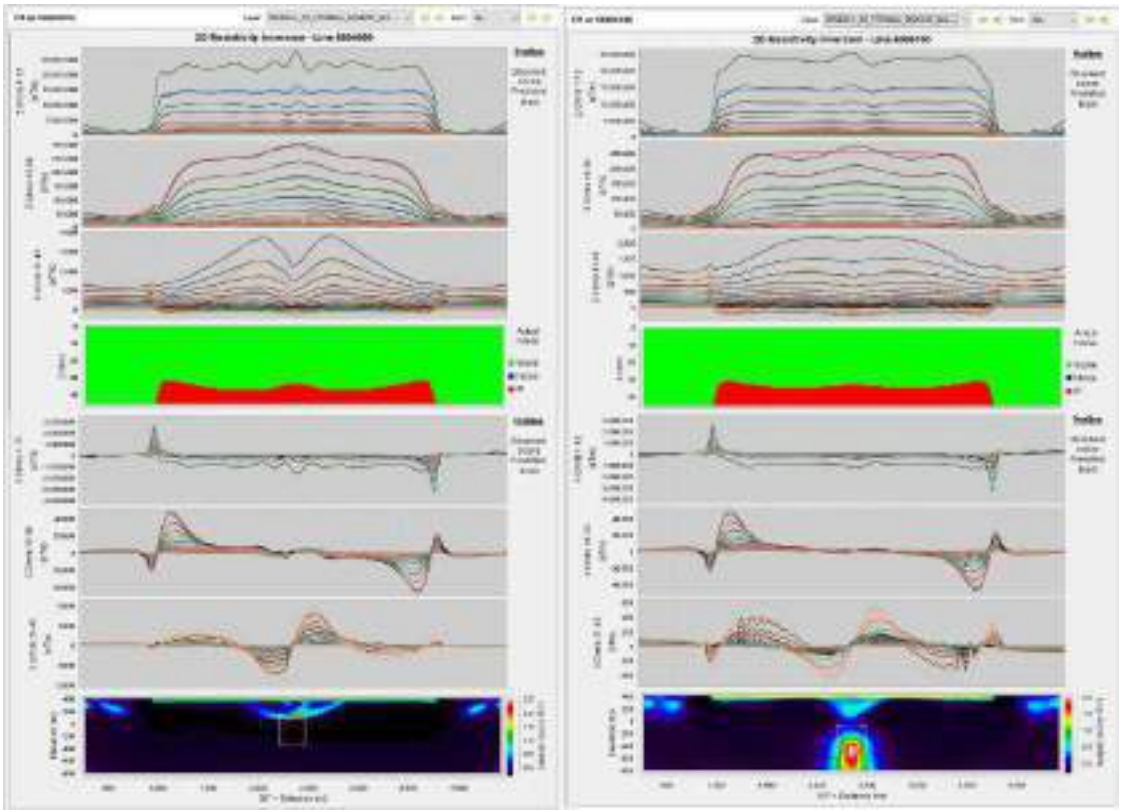

Figure 7. VTEMplus EM2DInv 6004050 middle and 6006100 deep - with IP in Cover

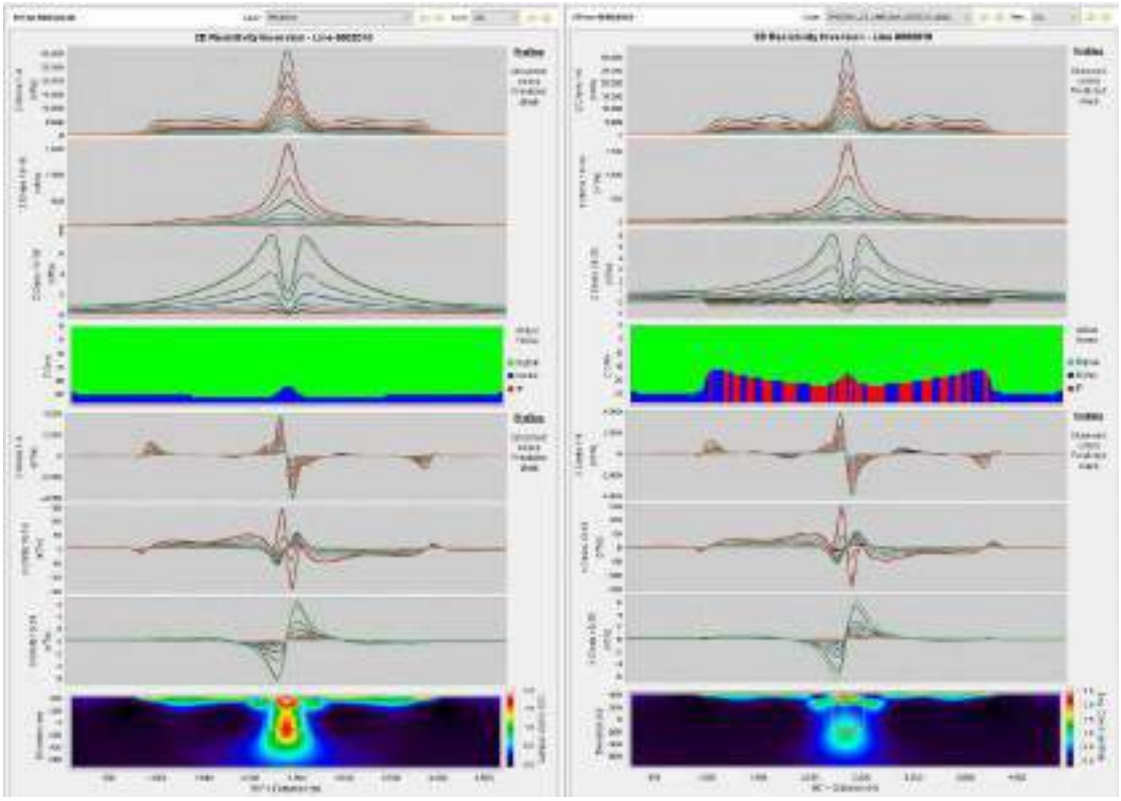

Figure 8. HeliTEM^2 12.5Hz EM2DInv 6002010 shallow - without IP (left) and with IP in Cover (right)

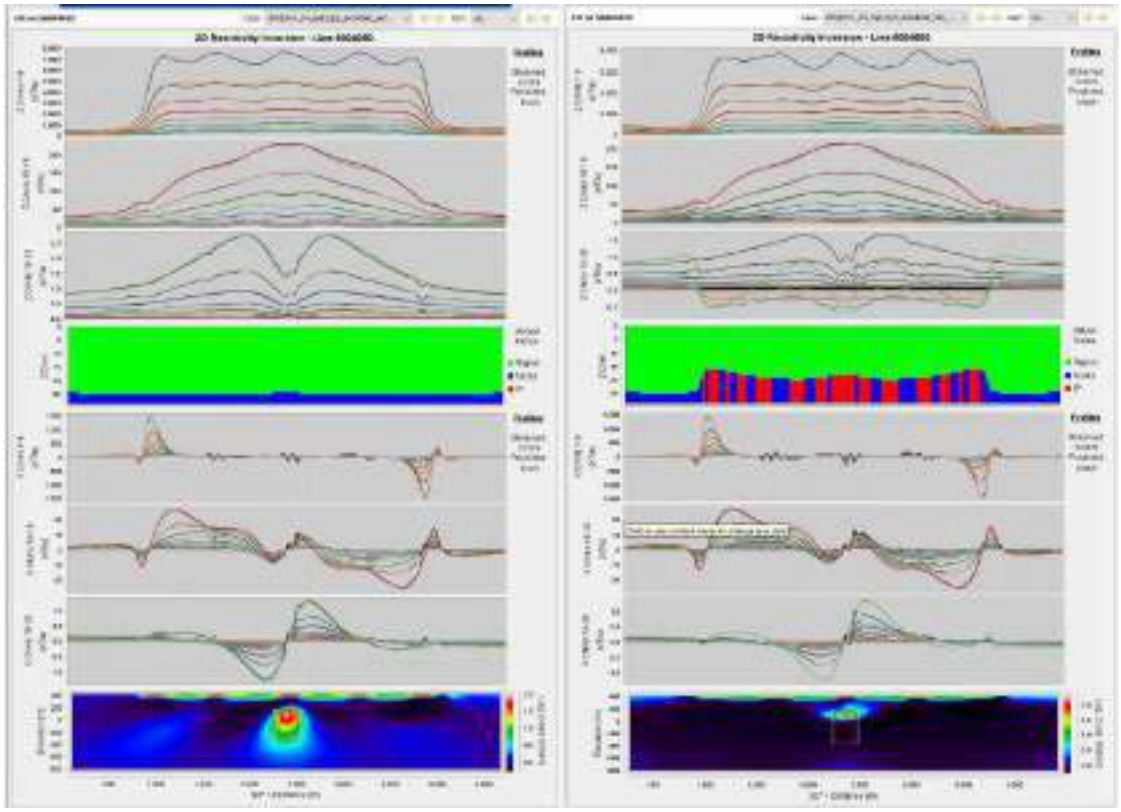

Figure 9. HeliTEM^2 12.5Hz EM2DInv 6004050 deep - without IP (left) and with IP in Cover (right)

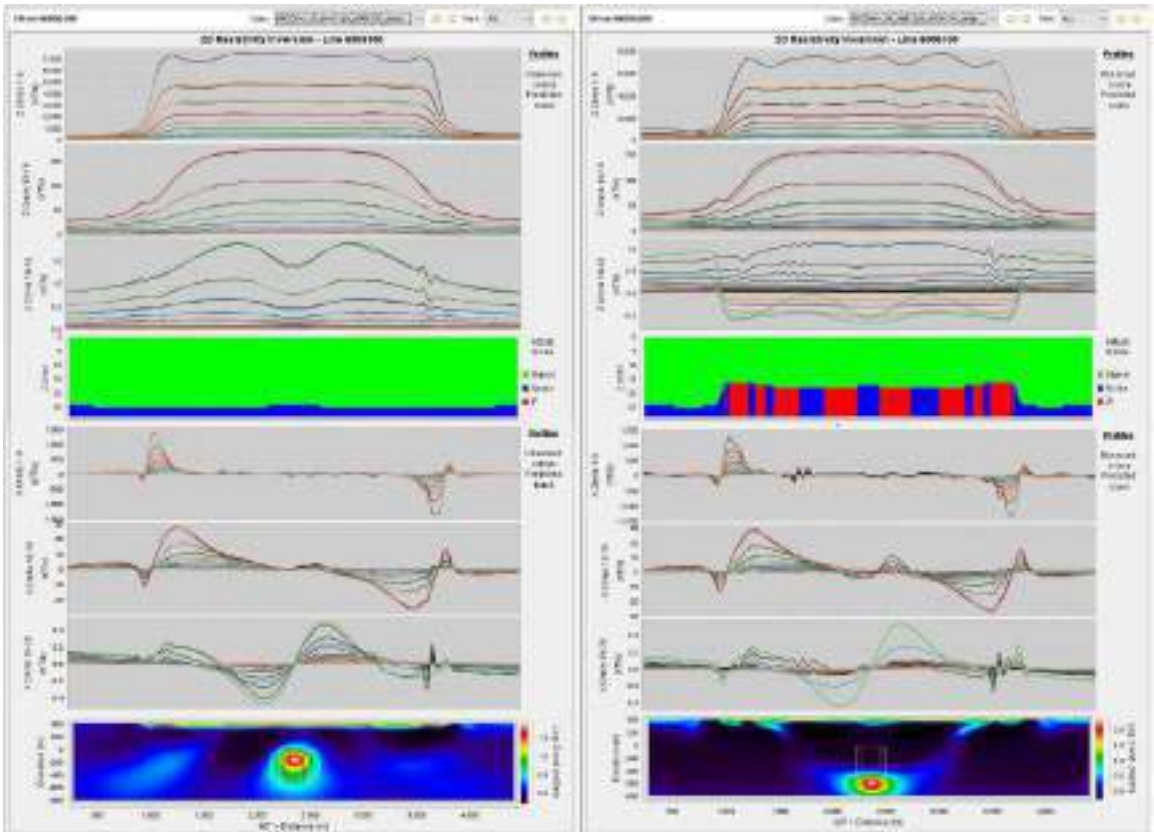

Figure 10. HeliTEM^2 12.5Hz EM2DInv 6006100 deep - without IP (left) and with IP in Cover (right)

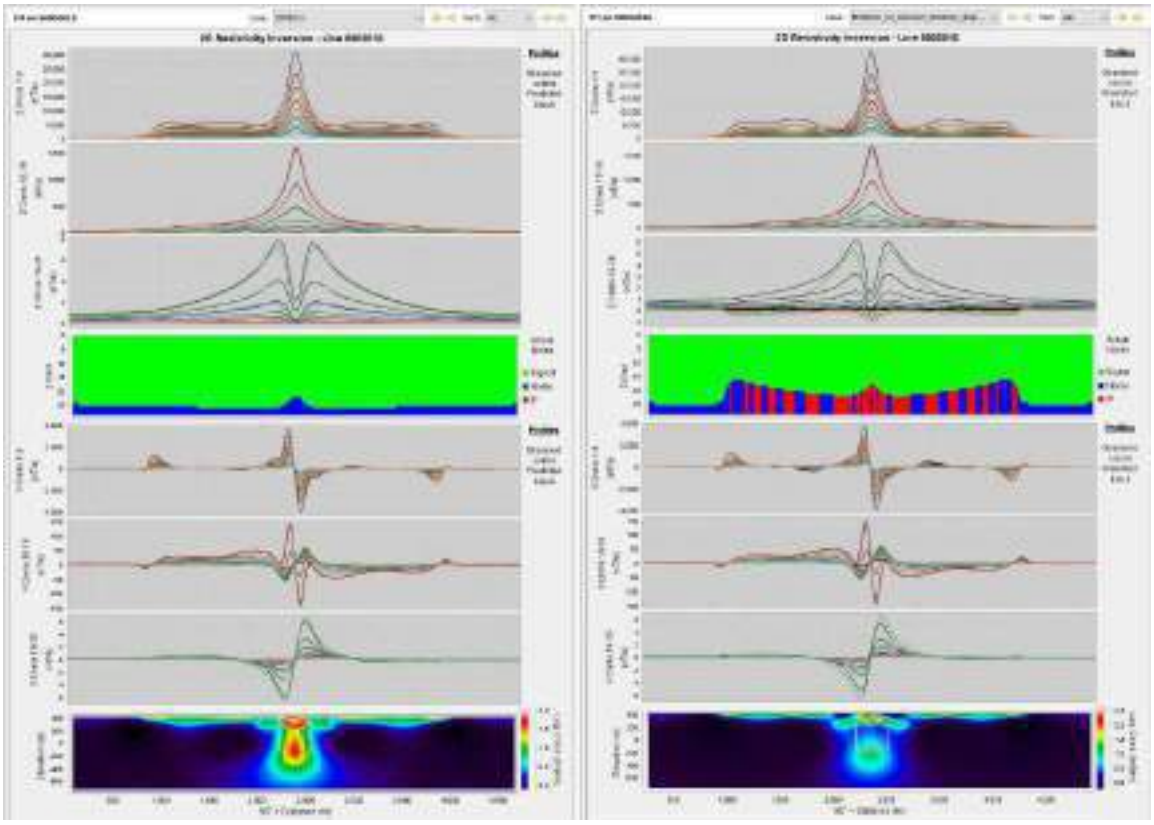

Figure 11. HeliTEM^2 6.25Hz EM2DInv 6002010 shallow - without IP (left) and with IP in Cover (right)

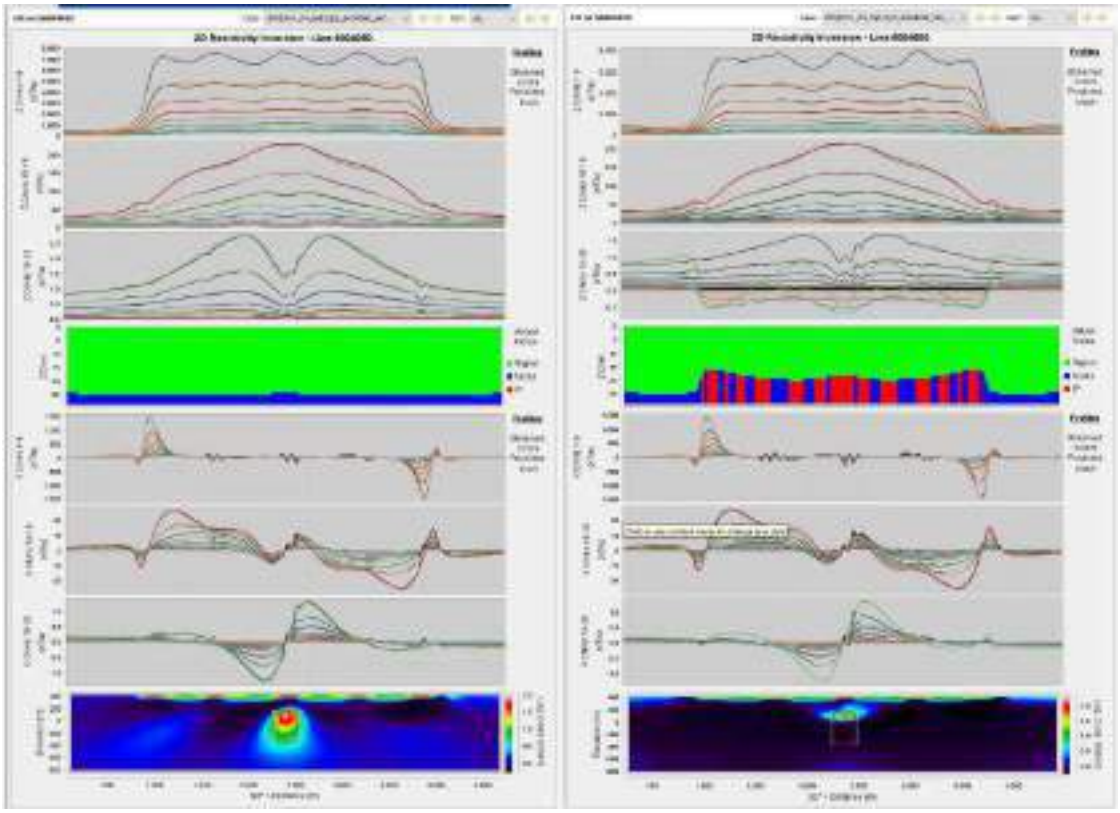

Figure 12. HeliTEM^2 6.25Hz EM2DInv 6004050 middle - without IP (left) and with IP in Cover (right)

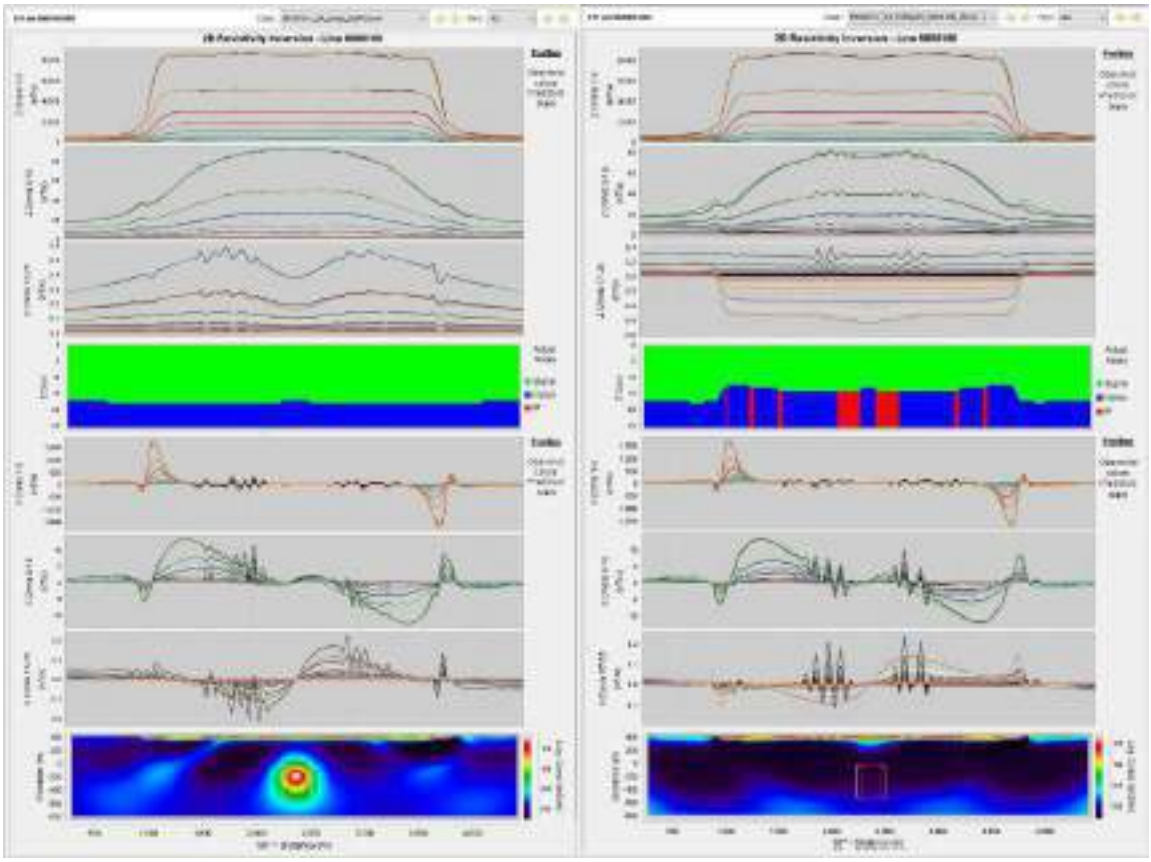

Figure 13. HeliTEM^2 6.25Hz EM2DInv 6006100 deep - without IP (left) and with IP in Cover (right)

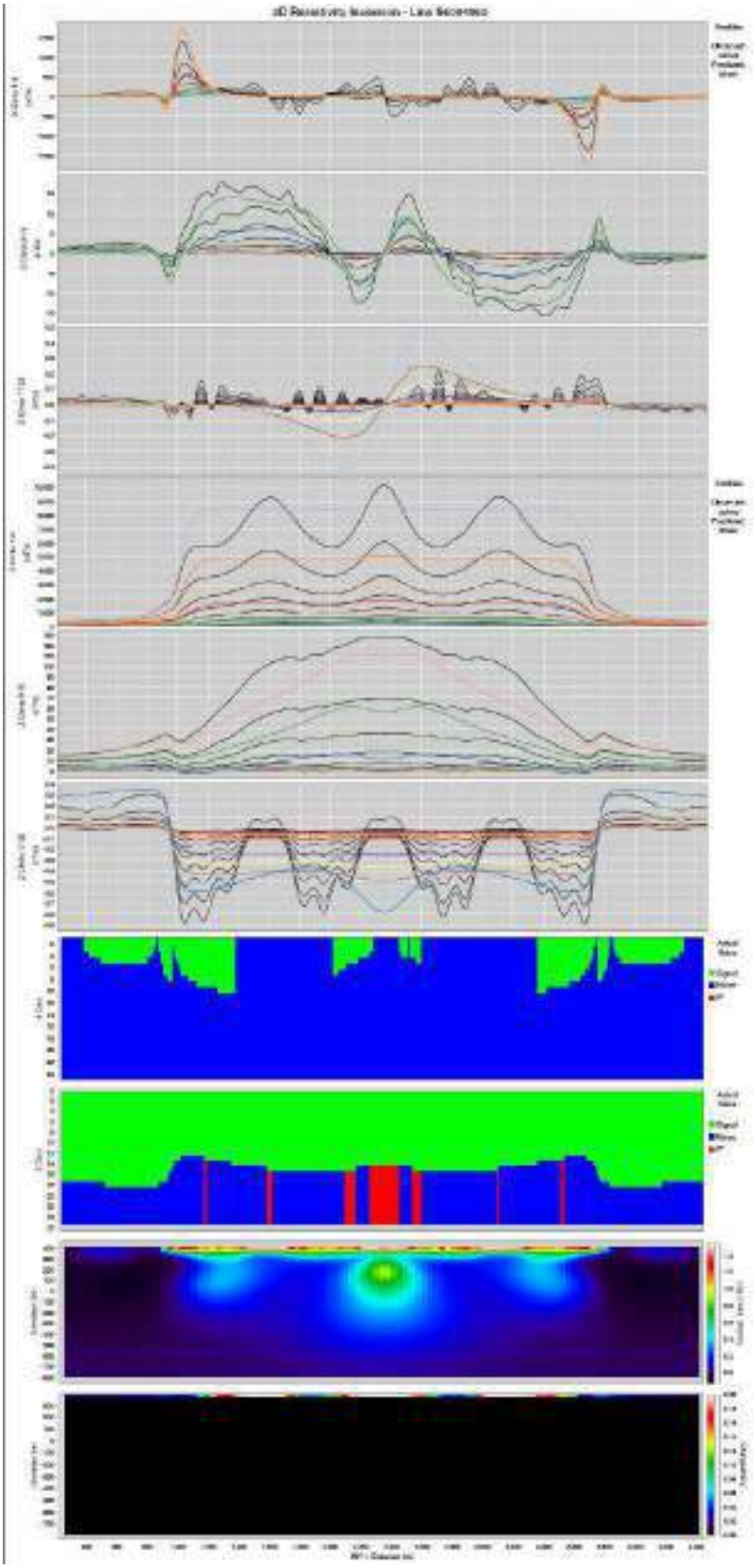

Figure 14. HeliTEM2 6.25Hz EM2DInv 6004050 Joint IP Inversion (X/Z Components)

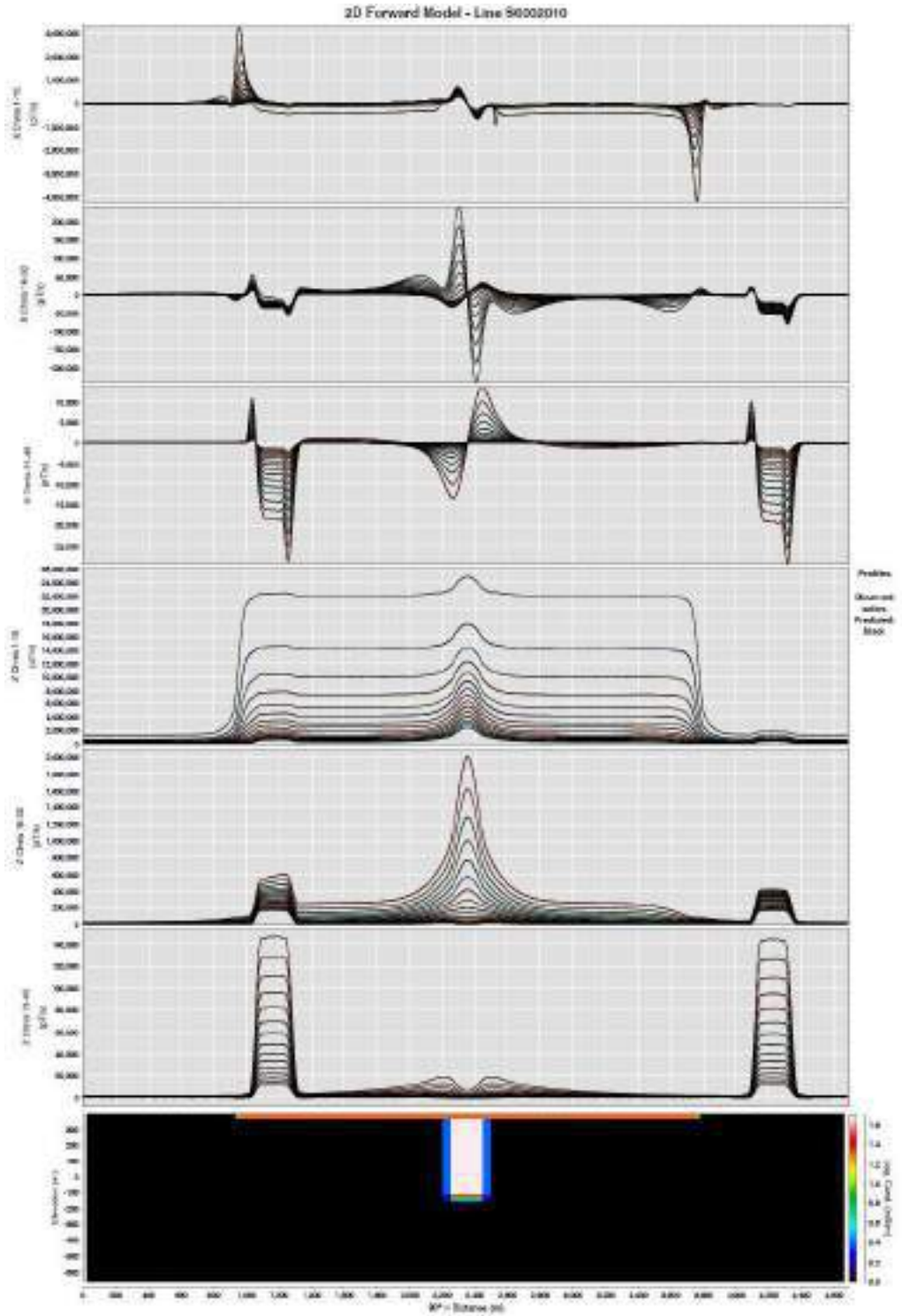

Figure 15. VTEM^{plus} Forward Model 6002010 with SPM (X/Z Components)

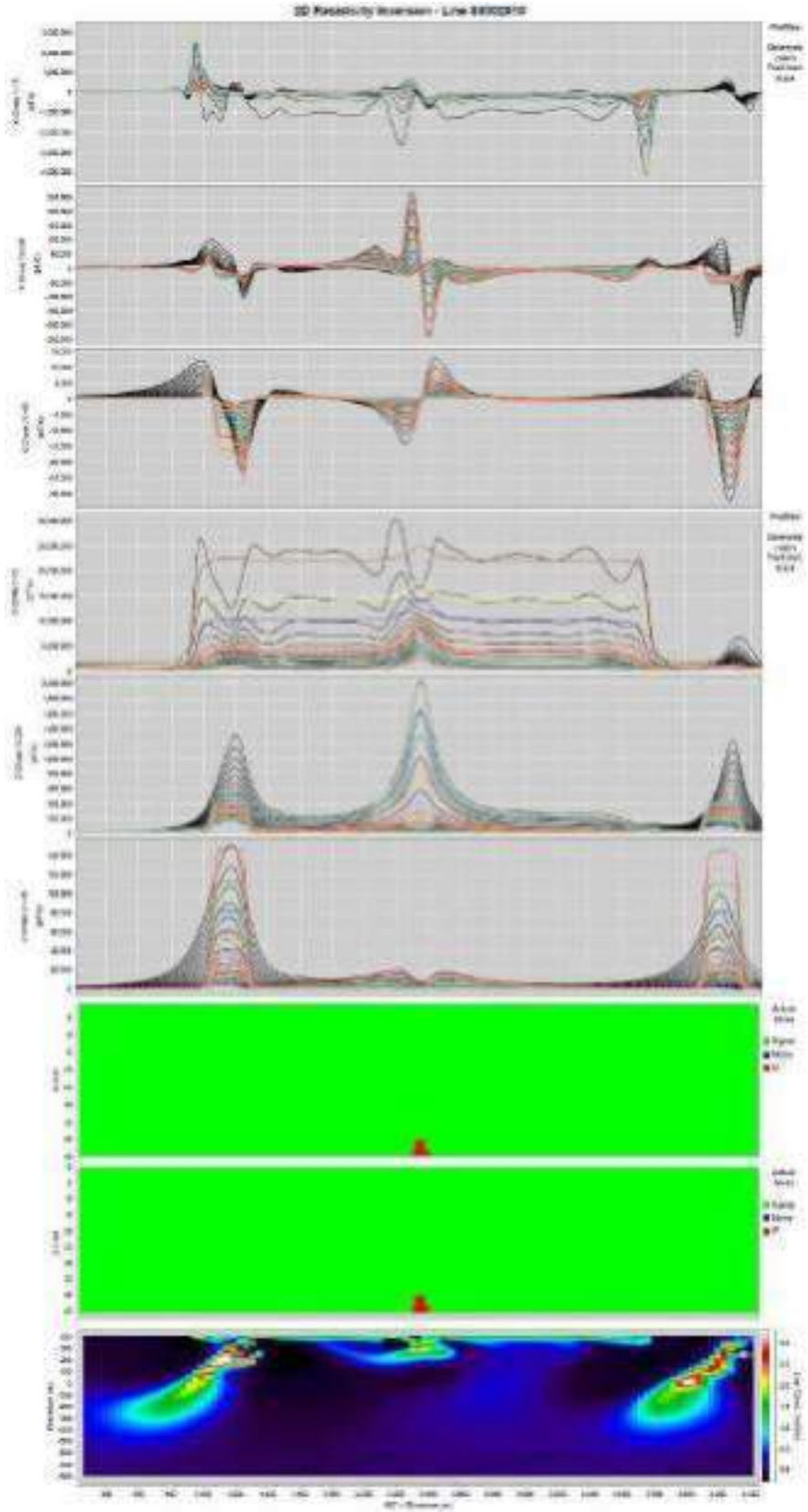

Figure 16. VTEM^{plus} EM2.5D Inversion 6002010 with SPM (X/Z Components)

Passive and active airborne electromagnetics – separate and combined technical solutions and applicability

Alexander Prikhodko
Expert Geophysics Limited
Units 3 & 4, 16 Mary St.,
Aurora, ON, L4G1G2, Canada
alexander@expertgeophysics.com

Andrei Bagrianski
Expert Geophysics Limited
Units 3 & 4, 16 Mary St.,
Aurora, ON, L4G1G2, Canada
anrei@expertgeophysics.com

Petr Kuzmin
Expert Geophysics Limited
Units 3 & 4, 16 Mary St.,
Aurora, ON, L4G1G2, Canada
petr@expertgeophysics.com

Andrew Carpenter
Expert Geophysics Pty Ltd
12/110 Inspiration Drive,
Wangara, WA 6065, Australia
andrew@expertgeophysics.com

SUMMARY

Airborne electromagnetic methods are divided, by primary field sources, into 'active' (with controlled primary field sources) and 'passive' (without the ability to control the primary field). Each has pros and cons related to the depth of investigation, bandwidths, sensitivity, resolution, terrain clearance requirements, and parasitic effects. Expert Geophysics Limited has developed AEM systems utilizing active and passive principles, separate and combined. The MobileMT system is an entirely passive system using a remote reference technique. The system provides low-noise broadband data extracted from natural field audio frequency (AFMAG) and a very-low-frequency (VLF) power spectra. In addition to the passive field data, but with limited broadband, the TargetEM system measures time-domain data with an active and focused source of the primary transmitting field. The combined (active and passive) airborne electromagnetic system records broadband streaming data used to extract AFMAG, VLF, and time-domain components. The natural field data, even in a limited frequency range, is valuable in filling the gaps when the time-domain method is limited – at mapping highly resistive geological terrains, in detecting superconductors, during surveys in rugged relief conditions, and at parasitic effects appearance. In this paper, we present the combined "active-passive" system.

Keywords: Electromagnetics, AFMAG, VLF, time-domain.

INTRODUCTION

Using airborne electromagnetic time-domain systems (ATDEM) is applicable across various exploration purposes. High spatial resolution, focused transmitting field, depth of investigation exceeding the frequency-domain method several times, and well-developed interpretation theory and tools make the airborne EM method popular in exploration programs. Regardless of their popularity, the ATDEM systems have several limitations in data acquisition. ATDEM capabilities in mapping resistivity are limited in the range higher than 1000 ohm-m (Annan et al., 1996). However, depending on a system's noise level, they can vary in some limits. Conductive target detection seems the best application for ATDEM, but most common off-time systems "fail to detect or adequately discriminate targets of high conductance" (Witherly, 2007). As for any controlled field source method, ATDEM data quality and informativeness are highly dependent on terrain clearance which is especially critical in areas with rugged relief (Allard, 2007). Induced polarisation (IP) and superparamagnetic (SPM) effects are not exotic in ATDEM data (Kratzer & Macnae, 2012; Mutton, 2012) and are often considered parasitic and destroy the induction response (IP effect) or create false "late-time" anomalies (SPM effect). The depth of investigation (DOI) of time-domain systems is not always capable of reaching exploration goals and is very limited in conductive conditions (Allard, 2007).

MobileMT, the latest development in airborne passive field methods, overcomes all the limitations inherent to ATDEM (Prikhodko et al., 2022). The technology has comparable detection capabilities with three other airborne EM principles, including VLF, time-domain, and a predecessor in the natural field domain, but covering the entire depth range beginning from the near-surface (Moul & Witherly, 2020).

Figure 1 demonstrates the limitations of a time-domain system (400k NIA, trapezoidal waveform, 30 Hz base frequency) over a resistive geological terrain. The ATDEM detected only near-surface moderately conductive alluvium sediments, whereas MobileMT recovered resistivity differentiations in the range of thousands ohm-m with a greater depth of investigation. Another example in Figure 2 shows combined ATDEM and MobileMT data along a line crossing a known KL-22 kimberlite pipe in northeastern Ontario (McClenaghan et al., 2008). The off-time dB/dt ATDEM data is heavily impacted by the IP effect excited, most likely by the documented surficial till layer. A complete resistivity picture is recovered from MobileMT data since the IP effect does not destroy it, and MobileMT is sensitive to a broader range of resistivity differentiations.

These examples demonstrate that natural field data can be a very supportive addition to time-domain data. Combining multiple techniques in one system is an attractive solution for applications in a wide range of conditions. The technique of extracting multiple electromagnetic components from recorded, streaming data in the presence of a controlled current pulse source has been under discussion and development since 1997 (Lane et al., 1998). The latest investigations (Sattel and Battig, 2018, 2018a, 2021) achieved decent results in extracting and modelling passive EM tipper responses from accessible streamed time-domain data but with noted inadequate S/N levels and poor quality of extracted AFMAG data.

Expert Geophysics Limited introduced a system that measures natural-field and VLF EM data, acquiring three-component airborne magnetic-field data while monitoring the horizontal electric field at a base station used as a field variations reference. (Sattel et al., 2019). The same technology can be combined with active source time-domain measurements.

Passive MobileMT technology and its combination with the active TargetEM system

MobileMT passive airborne EM technology utilises natural audio frequency electromagnetic fields to measure simultaneously: 1) variations of the magnetic field along three orthogonal axes (airborne receiver) over survey areas (Figure 3) 2) variations of the electric field associated with telluric currents using two grounded horizontal orthogonal dipoles (Figure 4). All seven data streams are synchronised and recorded in the same frequency band at a 73,728 Hz sampling rate. The ground electric sensor system calibrates the airborne sensor system and extracts denoised and unbiased data. The electrical admittance of the subsurface for each frequency window is calculated by processing the airborne inductive receiver XYZ data and the ground electric field sensor system XY data using the calibration data. In general, differences between calibration parameters and the ratio between the magnetic field strength and the electric field strength at different positions on the survey lines indicate geoelectric differentiations along the lines. The calibration coefficients are calculated as the ratios but in the vicinity of the magnetic and electric components. Previous developments in airborne AFMAG lack the advantages of a remote reference technique (Ward, 1959; Barringer, 2002; Morrison & Kuzmin, 2005; Kuzmin et al., 2012).

Figure 3. MobileMT magnetic field variations receiver with auxiliary sensors under a helicopter

Figure 4. MobileMT electric field variations remote base station

The TargetEM system (Figure 5) is a time-domain system that when synchronized with the electric field base station (Figure 4); in addition to time-domain EM data, also provides natural field apparent conductivities (AFMAG) and VLF data.

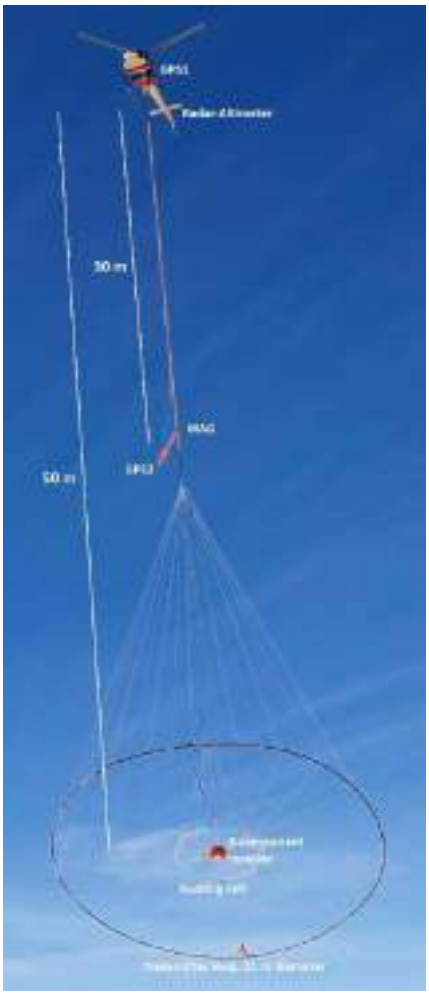

Figure 5. TargetEM broadband passive and time-domain active system with auxiliary sensors under a helicopter

Specifications of the TargetEM system:

- Transmitter loop diameter – 21 – 26 m
- Number of turns – 4 - 6
- Peak transmitter current – 230 A
- Dipole moment – 320,000 – 700,000 NIA
- Transmitter bipolar pulse shape – rectangular
- Transmitter pulse width – selectable, typical 6 ms
- Turn-off time – typical 1 ms
- Base frequency – 25/30 Hz
- Receiver – 3 orthogonal inductive coils (X, Y, and Z)
- Number of turns – 120
- Z coil diameter – 1 m
- Full waveform recording at a digitising rate of 73,728 Hz
- Very high signal-to-noise ratio
- Two time-domain EM data output formats: raw streaming data; stacked and processed time-domain data.

Synchronized electric and magnetic variations time series recordings (streamed data) include eight channels: 3 orthogonal magnetic variations components, two pairs of horizontal electric components, and transmitter current. The time-domain active source EM data is derived by thresholding, stacking, windowing, and filtering standard procedures on the raw streaming data. The VLF radio-field signals (15-30 kHz) are identified and extracted based on comparison with the electrical base station data. The extraction and processing of natural field AFMAG data correspond to the MobileMT data processing scheme (Prikhodko et al., 2022). In the case of TargetEM, the natural field frequency range with informative data depends on the controlled primary field source base frequency and the current waveform duty cycle. For this reason, apparent conductivities derived from TargetEM data cannot be equal to MobileMT due to a limitation in the frequency range.

The single platform combination of time-domain active source, natural field AFMAG, and VLF radio-field data processing and extraction has been successfully tested over conductive structures in northern Ontario.

CONCLUSIONS

The airborne time-domain active field source method has several limitations under certain circumstances, regardless of its progressive improvements and inherent advantages. The limitations are associated with a narrow range of resistivity sensitivity, strict requirements for terrain clearance, depth of investigation, particularly in a conducive environment, and susceptibility to parasitic IP and SPM effects. Natural field AFMAG and complimentary VLF radio-field data can be a valuable addition to the active source EM data, especially with simultaneous recording. Combining streamed time series recordings over survey lines and recordings from a synchronized reference base station provides high-quality natural and radio fields electromagnetic data. The jointly acquired data recordings and processing (active-source EM, natural field AFMAG, and VLF frequencies), combined with a remote reference technique for providing high-quality data, are realized in the TargetEM system.

REFERENCES

Allard, M., (2007). On the Origin of the HTEM Species, In "Proceedings of Exploration 07: Fifth Decennial International Conference on Mineral Exploration" edited by B. Milkereit, 355–374.

Annan, P., Smith, R., Lemieux, J., O'Connell, M., and Pedersen, R., (1996). Resistive-limit, time-domain AEM apparent conductivity, GEOPHYSICS, VOL. 61, NO. 1, 93–99.

Barringer, A.R., 2002. Magnetotelluric geophysical survey system using an airborne survey bird. US Patent No. 6,765,383.

Kuzmin, P.V., Borel, G., Morrison, E., Dodds, J., (2012). Geophysical Prospecting Using Rotationally Invariant Parameters of Natural Electromagnetic Fields. US Patent No. 8,289,023.

Lane, R., C. Plunkett, A. Price, A. Green, & Y. Hu. (1998). Streamed data – a source of insight and improvement for time domain airborne EM. Exploration Geophysics 29:16–23.

McClenaghan, M.B., Kjarsgaard, I.M. and Kjarsgaard, B.A., 2008. Indicator mineralogy of the KL-01 and KL-22 kimberlites, Lake Timiskaming kimberlite field, Ontario. Geological Survey of Canada, open file 5800, 47 p.

Morrison, E.B.; Kuzmin, PV, 2005. System, Method, and Computer Product Geological Surveying Utilizing Natural Electromagnetic Fields. US Patent No. 6,876,202.

Moul, F., Witherly, K., (2020). A comparison of MobileMT with ZTEM and HELITEM over isolated conductors in the Athabasca Basin, Saskatchewan, Canada. 90th annual meeting, SEG, Expanded Abstracts, 1389–1393.

Mutton, P., Superparamagnetic effects in EM surveys for Mineral Exploration, 2012. ASEG extended abstracts, 1–4.

Prikhodko, A., Bagrianski, A., Kuzmin, P., Sirohey, A., (2022). Natural field airborne electromagnetics – history of development and current exploration capabilities. Minerals, 12, 583, 1-16.

Sattel, D., and Battig, E., 2018. Modeling sferic signals extracted from active-source AEM data. 88th annual meeting, SEG, Expanded Abstracts, 1883-1887.

Sattel, D., and Battig, E., 2018a. Passive EM Processing of MEGATEM and HELITEM Data, ASEG Extended Abstracts, 1-8.

Sattel, D., and Battig, E., 2021. Processing of passive EM fields acquired during active-source airborne EM surveys, Exploration Geophysics, 52:6, 680-693.

Sattel, D.; Witherly, K.; Kaminski, V., 2019, A Brief Analysis of MobileMT Data: 82nd Society of Exploration Geophysicists International Exposition and Annual Meeting, SEG, Proceedings, 2138–2142.

Kratzer, T. and Macnae, J.C., 2012. Induced polarization in airborne EM, Geophysics, 77, E317-327.

Ward, S.H., (1959). AFMAG—Airborne and Ground. Geophysics, pp. 24, 761–787

Witherly, K., 2007. Mapping targets of high conductance with the VTEM airborne EM system, ASEG Extended Abstracts, pp. 1-4

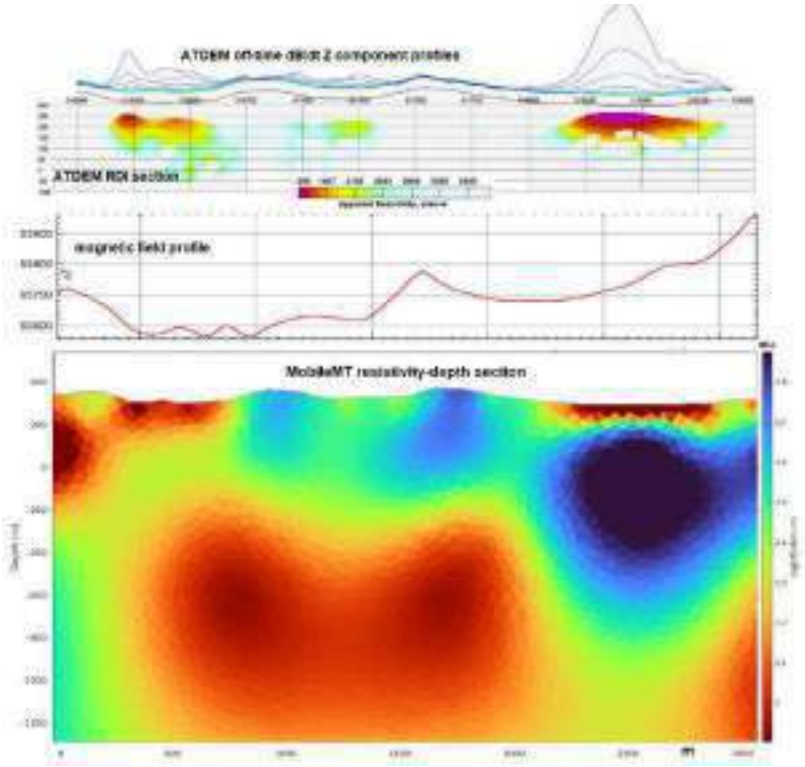

Figure 1. A MobileMT and ATDEM survey line in a resistive environment (Northern Ontario). From top to bottom: dB/dT time-domain off-time Z component profiles; ATDEM Resistivity-Depth image; magnetic field profile; MobileMT resistivity section (2D inversion).

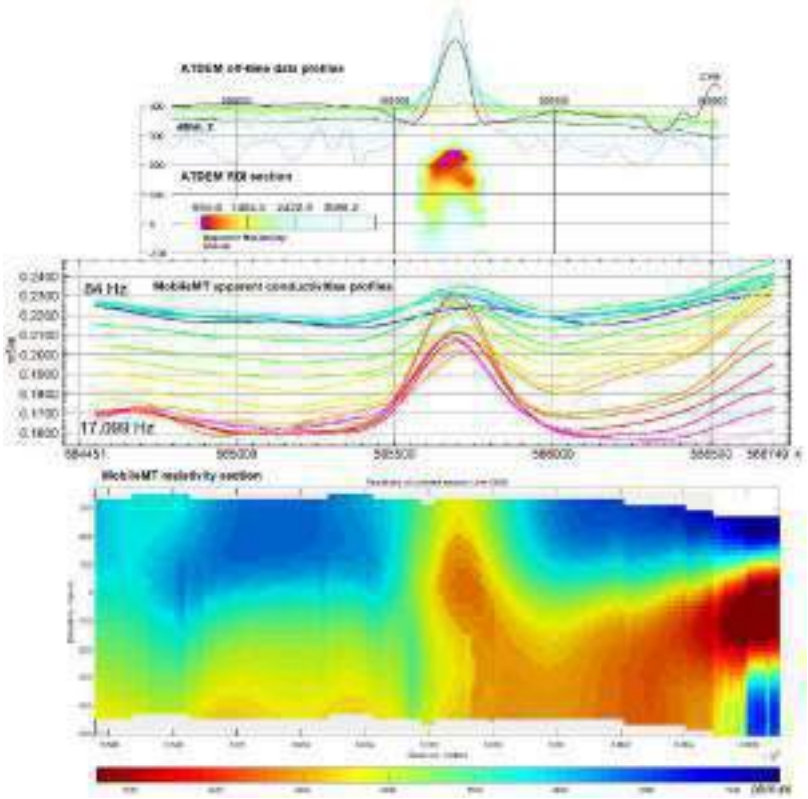

Figure 2. A MobileMT and ATDEM survey line over a known kimberlite pipe KL-22 (Northern Ontario). From top to bottom: dB/dT time-domain off-time Z component profiles; ATDEM Resistivity-Depth image; MobileMT apparent conductivity profiles; MobileMT resistivity section (1D inversion).

AEM imagery down to one kilometer depth: New constraints for geological and hydrogeological modeling in volcanic contexts

Anne Raingeard
BRGM
Orléans, France
a.raingeard@brgm.fr

Pierre-Alexandre Reninger
BRGM
Orléans, France
pa.reninger@brgm.fr

Aurélie Peyrefitte
BRGM
Orléans, France
a.peyrefitte@brgm.fr

Guillaume Martelet
BRGM
Orléans, France
g.martelet@brgm.fr

Bertrand Aunay
BRGM
St Denis, La Réunion, France
b.aunay@brgm.fr

Arnauld Malard
ISSKA
La Chaux-de-Fonds, Suisse
arnauld.malard@isska.ch

SUMMARY

We present the integration of airborne magnetic data and five different airborne electromagnetics data sets spaning from 3 000 NIA up to 1 000 000 NIA magnetic moments (three different AEM systems were used) in La Réunion volcanic island. Subsequently, a 3D geological model of the first kilometer beneath the Plaine des Fougères was built, in order to constrain 3D hydrogeological modeling.

This approach allowed for the correlation of different datasets, providing a comprehensive image of the subsurface and enabling a greater hydrogeological understanding. It was used to position the route of a deep water drainage gallery and has great potential for applications in other areas.

Key words: Airborne electromagnetics, Time Domain ElectroMagnetics, aeromagnetic, volcanic island, geological modelling, hydrogeological modelling

INTRODUCTION

In order to bring fresh water to the northern part of La Réunion volcanic island (Indian Ocean), the County Council of La Réunion (CD974) requested an assessment of the geological and hydrogeological risks related to the drilling of a new water drainage gallery at great depths (300 to 1000 m) below the Plaine des Fougères. This new "GANOR" gallery will be connected to the existing deep GSAM gallery, which is covered by up to 1000 meters of volcanic materials. To assess the risks, BRGM has established a 3D geological model. This model then supported a 3D hydrogeological model in order to identify potential hydrogeological risks of drilling in the surrounding of highly permeable aquifers under high pressure. Peyrefitte et al (2022) present this work in a technical report.
The local geological map exhibits very monotonous surface information, mainly with lava flows and tuffs PN3 and PN4 (Figure 1). The few existing soundings in the area never go deeper than a few dozen of meters.

DATA ACQUISITION

In 2014, an airborne electromagnetics (AEM) survey was conducted using the SkyTEM 304 system over the entire La Réunion island. This survey gave an image of the first 300 meters (line path in Figure 1).

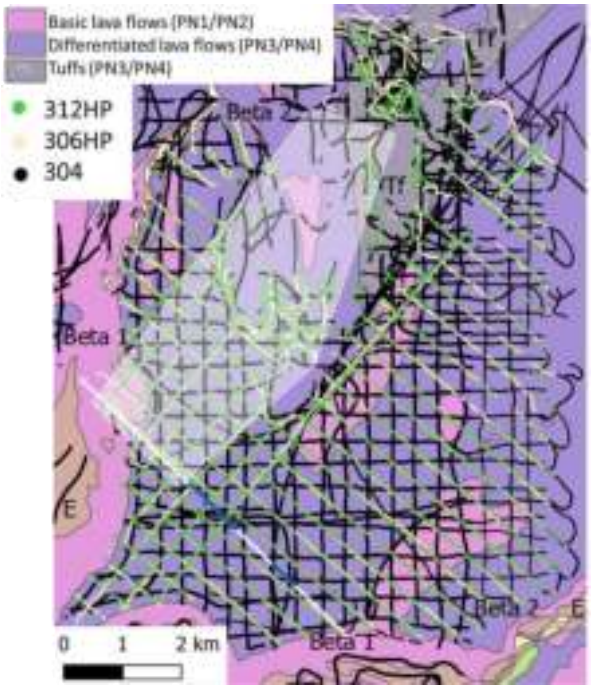

Figure 1: Geological map over the Plaine des Fougères. GSAM gallery is represented with a white line, the possible area of the future gallery in a white polygon and in blue, the aquifers crossed during the GSAM drilling. Airborne acquisitions are represented in black (304 system), light orange (306 HP system) and green (312 HP system).

A first study creating a 3D geological model combining this AEM dataset with magnetic modelling was performed. To allow a preliminary geological/ hydrogeological interpretation, the lack of resistivity information at great depths, but also the lack of rock magnetization data, resulted in a preliminary understanding of the deep hydrogeology. This result was promising, but still highly hill-constrained.

Two surveys were then flown in 2021 over the Plaine des Fougères area, using SkyTEM 306HP and SkyTEM 312HP systems in order to extend the imagery, down to 1 000 m depth. These two new AEM datasets and the previous one are presented in Table 1. Figure 4 is an example of South-North resistivity profiles, illustrating the increase of investigation depth: SkyTEM 304 images resistivity up to 200-400 m depth,

whereas SkyTEM 306 HP and 312 HP system reach 800-1000 m depth in this area, down to a maximum of 1200 m. Combining the three AEM datasets, a high-resolution / deep penetration 3D resistivity block of the Plaine des Fougères was generated from the surface down to 1000 m depth.
The careful preprocessing of each dataset, their inversion and their combination into a single resistivity model is explained below.

DATA PROCESSING

BRGM processing methodology of AEM data is presented in Reninger et al (2020), it includes the use of the singular value decomposition (Reninger et al., 2011). Also, to increase the signal/noise ratio, this processing includes an adaptative stack that changes its span according to the noise level, optimising resolution and depth of investigation. A manual editing of the residual noise was also achieved to complete the processing of each EM dataset. Such a processing strategy has proven to be essential for imaging resistivity contrasts up to one kilometer.

A joint smooth SCI inversion (Viezzoli et al, 2007) was run considering all AEM datasets. This inversion resulted at the location of each AEM data in a 1D-resistivity model, made of 40 layers, having a fixed thickness and variable resistivity with depth.

A 3D resistivity model was then generated by the interpolation of the 304 and 306HP 1D resistivity models for the near surface (the first 200 m) and the interpolation of 306HP and 312HP 1D resistivity models for greater depths (from 200 to 1000 meters); the estimated depth of investigation was taken into account for interpolating data. The resulting 3D resistivity model takes full advantage of the resolution of the 304 and 306 HP systems for the 200 upper meters and of the depth of investigation of the 306HP and 312HP systems for mapping deeper geological bodies, allowing for greater modelling of the geological structure and understanding of the hydrogeology of the Plaine des Fougères.

During the AEM surveys, airborne magnetic data were also acquired. They were all combined to obtain a high-resolution magnetic map. Given that the surveys were conducted with the same magnetic instrumentation and parameters (acquisition height, diurnal removal, the assembly was quite simple: data points measured along flight lines of the surveys were checked for consistency and subsequently gathered in a common database. A high resolution 100 m magnetic anomaly grid was derived using a simple interpolation of this new combined dataset (Figure 2).

Oriented rock sampling was made by geologists over the area from May to June 2021. A sample magnetisation library was compiled, combining laboratory measurements (performed on oriented samples with a JR5-A magnetometer) and field magnetic susceptibility (with a kappameter). This library provides rock magnetization constraints for deposits of each activity period of the Piton des Neiges (the volcano on which is located the study area). A total of 75 rock samples were used as reference for further magnetic modelling.

Taking into account the volcanic history, 2D magnetic modeling was conducted, using the geological map, the AEM resistivity model as background preliminary geometry and rock sample magnetic measurements to constrain the geological magnetic responses. The obtained modelling generated geologically realistic cross-sections (example in Figure 5).

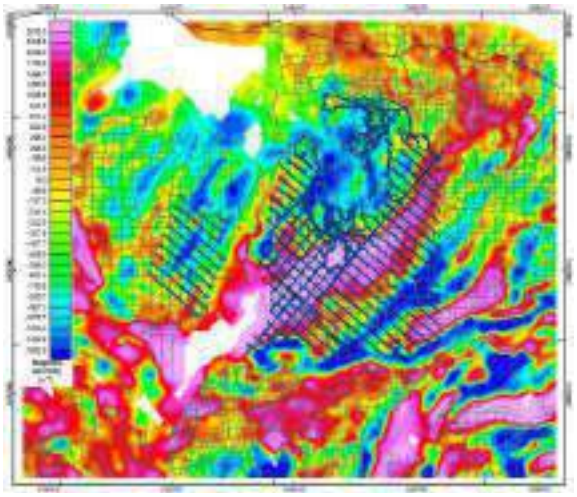

Figure 2: Magnetic anomaly map made with the fusion of 2014 and 2021 surveys (green lines show 2021 flight path).

The resistivity model provided the overall geometry of the volcanic layers and their degree of alteration. The magnetic data refined the geological model in depth, thereby highlighting distinct geological units within relatively homogenous resistivity layers.

The integration of the different datasets had the added benefit of providing a more detailed geological understanding of the area and allowing for more accurate interpretations of the hydrogeology.

RESULTS

Combining all the available geological information with series of 2D geophysically constrained cross-sections, a 3D geological model was derived all over the Plaine des Fougères on a depth range of -1000 m below the topography (1500 meters above sea level). We used GeoModeller® software which previously proved to allow the successful integration of geophysics in complex 3-D geological models (e.g. Martelet et al. 2004; Calcagno et al. 2008). Figure 3 displays the resulting 3D geological model, built up upon geological units classified by their increasing age, ranging from PN0 to PN4. Based on the interpretation of resistivity signatures, some of the modelled units are differentiated based on their alteration or water saturation.

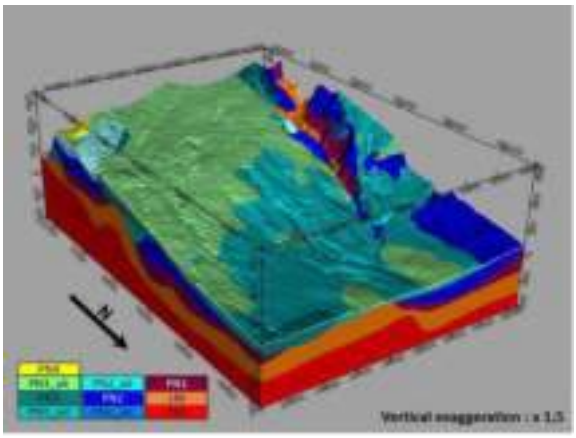

Figure 3: 3D geological model of Plaine des Fougères.

The 3D geological model was developed to assess the hydrogeological risk of different scenarios of gallery route. The 3D model was therefore implemented in a hydrogeological model performed in Visual KARSYS, a free software designed for assessing hydrogeological risk (Malard et al, 2018). The 3D geological geometries were used as input (as well as springs, geological sounding…) to simulate the hydrogeological conditions within the 3D model. The analysis of this hydrogeological model was focused along several possible gallery routes. Taking into account the expected lithological and hydrological characteristics of the modelled geological layers the hydrogeological risk was assessed, along the different gallery routes, depending on the proximity of overlying aquifers and hydraulic head.

CONCLUSIONS

Combining high-resolution near surface and deep AEM surveys with aeromagnetic data, geological knowledge and rock sample measurements, it was possible to generate a comprehensive 3D geological model down to a depth of 1000 meters below the Plaine des Fougères. The deep AEM investigation was possible with the combination of a high power emission and a resistive underground (mainly above 300 Ohm.m in the first 400 meters). The generated 3D geological model allowed for the characterisation of the subsurface materials, as well as a better understanding of the geological structure and hydrogeological system of the area. This made it possible to map geometry of hydrogeological bodies within the first kilometer below the surface, and thus reduce the risk associated with the drilling of a deep gallery. Since, previous deep tunnelling in the area faced enormous difficulties (and loss of money), anticipating the geological and hydrogeological environment of tunnelling is of utmost importance to mitigate the geological risks prior committing heavy construction operations.

ACKNOWLEDGMENTS

This project is funded by the County Council of Réunion (CD974) and the Water Office of La Réunion. We thank the University of La Réunion for cooperation in sampling volcanic rocks.

REFERENCES

Calcagno, P., Chilès, J.P., Courrioux, G. and Guillen, A., 2008, Geological modelling from field data and geological knowledge: Part I. Modelling method coupling 3D potential-field interpolation and geological rules. Phys. Earth Planet. Inter., 171, 147–157.

Malard, A., Randles, S., Hausmann, P., Bucev, M., Lopez, S., Courrioux, G., Jeannin, P.Y., Vogel, M., 2018. Visual KARSYS, a web-platform for the documentation of karst aquifers including online geological modelling, in: Delivering Subsurface Models for Societal Challenges - *4th Meeting of the European 3D Geomodelling Community*, 21st to 23rd February 2018, Orléans, France. p. 39

Martelet, G., Calcagno, P., Gumiaux, C., Truffert, C., Bitri, A., Gapais, D. and Brun, J.P., 2004, Integrated 3D geophysical and geological modelling of the Hercynian Suture Zone in the Champtoceaux area (South Brittany, France). Tectonophysics, 382, 117–128.

Peyrefitte A, Reninger PA, Malard A, Raingeard A, Aunay B (2022) BRGM-RP-71628-28: Aide à l'implantation d'une gallerie souterraine (GANOR): acquisition et valorisation de données géophysiques héliportées pour la caractérisation profonde géologique et hydrogéologique de la Plaine des Fougères. Tech. rep., BRGM, URL http://infoterre.brgm.fr/

Reninger PA, Martelet G, Deparis J, Perrin J, and Chen Y (2011) Singular value decomposition as a denoising tool for airborne time domain electromagnetic data. *Journal of Applied Geophysics* 75: 264–76.

Reninger PA, Martelet G, Perrin J, Dumont M (2020) Processing methodology for regional AEM surveys and local implications. *Exploration Geophysics* 51(1):143–154

Viezzoli A, Christiansen AV, Auken E, Sørensen K (2007) Spatially constrained inversion for quasi 3D modelling of aem data. *ASEG Extended Abstracts* 2007(1):1–4

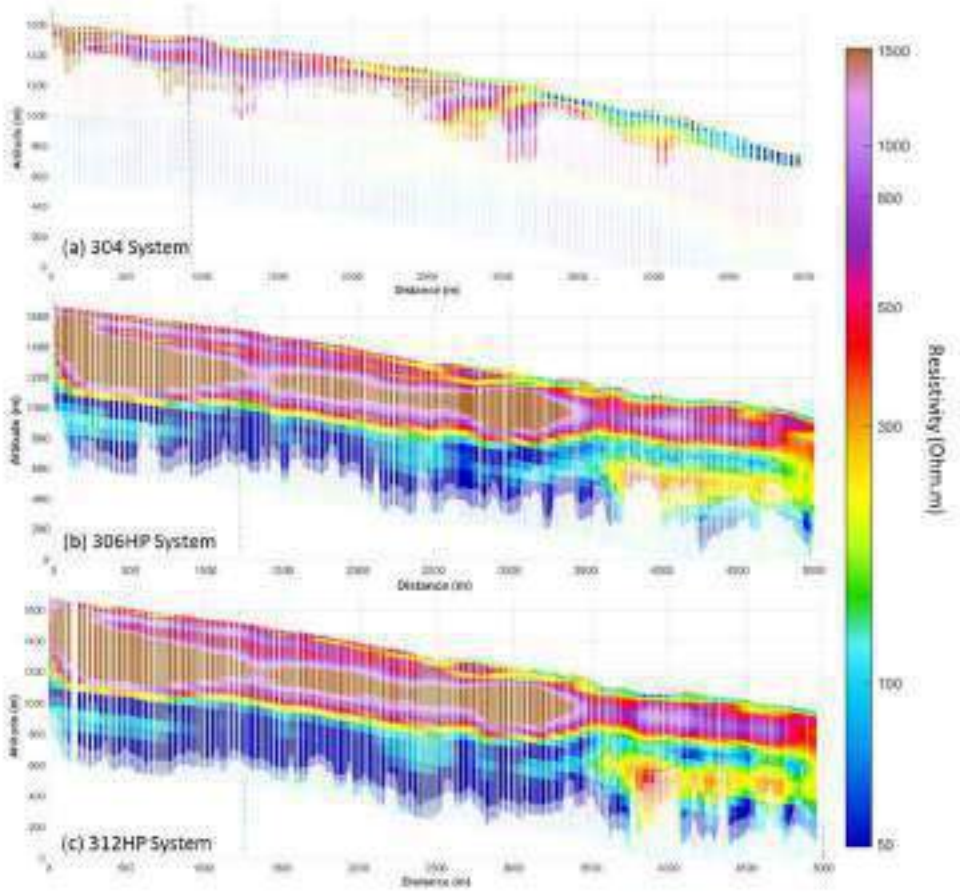

Figure 4: South-North resistivity profiles acquired with 304 (a), 306HP (b) or 312HP (c) systems in the Plaine des Fougères area. (a) is oriented S/N, (b) and (c) are overlapping, SW/NE. Dotted blue line shows a point where lines are intersecting.

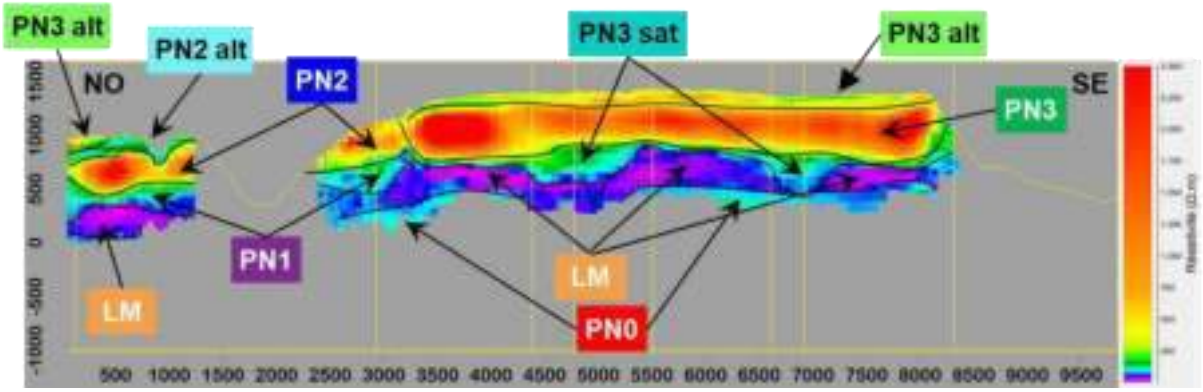

Figure 5: Example of an interpolated resistivity profile along the existing underground Salazie amont gallery, with geological interpretation. PN0 to PN4 represent old to recent volcanic formations.

Parameters	304 (2014)		306 HP (2021)		312 HP (2021)
	LM	HM	LM	HM	HM
Used time gates	6.8 µs to 5.53 e -4 s	60.42 µs to 8.9 ms	6.6 µs to 4.8e-4 s	351 µs to 1.02e-2 s	1.06 to 13.79 ms
On Time	800 µs	10 ms	1 ms	5 ms	5 ms
Off Time	738 µs	10 ms	0.5 ms	15 ms	15 ms
Number of gates used	20	28	41	26	27
Number of turns	1	4	1	6	12
Loop surface	340.82 m²	340.82 m²	342 m²	342 m²	342 m²
Repetition frequency	325 Hz	25 Hz	333.33 Hz	25 Hz	25 Hz
Flight line spacing	400 m	400 m	400 m	400 m	400 m
Kilometers of data	489 km used in this project	489 km used in this project	232 km	232 km	226.5 km
Average height	82.8 m	82.8 m	51.1 m	51.1 m	54.2 m
Average current	9.2 A	117 A	8.72 A	240.9 A	229.7 A
Cut-off duration	3.34 µs	50 µs	6 µs	272 µs	985 µs
~ Magnetic moment	3 000 NIA	160 000 NIA	3 000 NIA	500 000 NIA	950 000 NIA

Table 1: Comparison of acquisition parameters during the 3 AEM surveys used in this study.

Supervised stacking to improve the signal-to-noise ratio of AEM data

Pierre-Alexandre Reninger
BRGM
3, avenue Claude Guillemin
45060 Orléans, France
pa.reninger@brgm.fr

SUMMARY

AEM method has proven to provide useful information on the subsurface for many applications. However, measured decays are affected by many noises, limiting its effectiveness and which may prevent to acquire usable data, especially in resistive environments. Stacking techniques are applied in an attempt to improve the signal-to-noise ratio. However, stacking all decays falling within a stack interval can be ineffective, given the nature of noises that can affect the data from decay to decay. To a lesser extent, arbitrarily increasing the stack size may also be ineffective, especially in an anthropized environment. Stacking is generally done without any real control on the data taken into account.

This paper introduces a supervised stacking method that stacks decays falling within a stack interval considering different combinations and estimates the signal-to-noise ratio of the resulting decays. The estimation of the signal-to-noise ratio is performed using the singular value decomposition filtering which has proven to be effective in identifying and removing noise affecting an AEM dataset.

The supervised stacking method is applied on the raw data. It has been tested on two AEM datasets, acquired in Reunion and Auvergne (France), where EM noise is high and resistivity can easily exceed 1000 ohm.m in some places. The results show that the presented method improves the signal-to-noise ratio and can reduce sferics and certain noises from man-made installations. It provides less noisy decays for post-processing and offers new possibilities for processing AEM data.

Key words: AEM, processing, electromagnetics, time domain, airborne.

INTRODUCTION

Socio-environmental issues are at the origin of more and more projects involving Airborne ElectroMagnetics (AEM). Indeed, the surfaces to be covered and the needed coverage are generally too important for ground investigations. Moreover, AEM method has proven to provide useful information on the subsurface for many applications. Thus, AEM is increasingly used to support water resource management, risk assessments etc… This represents a challenge for the method, for example in terms of imaging, resolution, both lateral and vertical, and depth of investigation, and therefore motivates many developments in modelling and inversion and on AEM systems themselves. However, socio-environmental issues are usually focused in anthropized areas where AEM data can be affected by many noise sources, decreasing ability of AEM to image the subsurface and possibly preventing the acquisition of usable data. Therefore, development of methods to improve the signal-to-noise ratio (SNR), before rejecting the noise, is also crucial.

In order to improve the SNR, the measured decays are stacked during a pre-processing step. It is generally assumed that the larger the stack size, the more the SNR is improved (Spies, 1988). Some work has suggested improvements to stacking. The most common techniques apply thresholds when stacking the data (Macnae *et al.*, 1984 ; McCracken *et al.*, 1984) in order to limit the effect of some important noises, in particular the sferics. Stack size can also be set based on SNR.

However, the stacking is generally done without any real control on the decays taken into account. Indeed, stacking all the decays falling within a stack interval can be ineffective, given the nature of noises that can affect the AEM data from decay to decay. To a lesser extent, arbitrarily increasing the stack size may also be ineffective, especially in an anthropized environment.

This paper introduces a method that shuffles AEM decays into combinations when stacking. This method aims to identify the combinations of decays which seem to lead, after stacking, to the least noisy data and therefore to improve the SNR. The method is first exposed and the approach is then tested on two AEM datasets, acquired in Reunion and north of the Chaîne des Puys (Auvergne, France). The method appears effective in improving the SNR, providing less noisy data for post-processing.

METHOD

During an acquisition, decays are measured by repeating a sequence defined by an emission and the recording of the ground response. In order to improve the SNR, the acquired decays are then usually stacked considering a user-defined stack size.

Instead of stacking all decays falling within a stack interval, the presented methodology proposes to shuffle these decays into combinations of n decays; n ranges from 1 to the defined stack size. Depending on the stack size and the amount of acquired data, it may be too time-consuming to test all possible combinations. Thus, combinations characterised by few or many decays can all be tested. In between, combinations are randomly generated, since the number of possibilities can be very important. The notions of few, many are defined by the user and configured according to the user's computer, the size of the dataset and the desired computation time.

For each combination, the decays are stacked and the SNR of the resulting decay is evaluated to identify the combinations resulting in decays with the highest SNR. These combinations can then be statistically analysed to obtain, for each stack interval, the least noisy decay, which will be post-processed.

It is possible to use different methods to evaluate the SNR associated with the different combinations. For example, machine learning based methods seem well suited to evaluate the SNR. However, the singular value decomposition (SVD) filtering was preferred; filtering based on wavelet decomposition or principal component analysis could also have been used.

The SVD filtering is a statistical procedure that has proven effective in de-noising AEM datasets (Reninger *et al.*, 2011). This filtering has proven its effectiveness in identifying and rejecting different types of noise affecting the data, whether natural (background noise, sferics) or man-made (capacitive couplings). The SVD filtering is statistically adapted to the entire dataset. It was trained on the standard stacked dataset and then the SVD components were used to evaluate the SNR associated with each combination.

RESULTS

The Supervised Stacking Method (SSM) presented above was tested on two surveys carried out by the French geological survey (BRGM). The first was conducted in 2014 in Reunion and the second was conducted in 2020 north of the Chaîne des Puys (Auvergne, France). These two areas are anthropized and many high amplitude noises affect the EM datasets. Moreover, the resistivity can easily exceed 1000 Ω.m in some places resulting in a low SNR. Only the results obtained on the Chaîne des Puys are presented in this extended abstract; similar results were obtained on the data acquired in Reunion.

The SkyTEM 304 system (Sørensen and Auken, 2004) was used during these two surveys. SkyTEM systems have the particularity of emitting two different magnetic moments, a low moment and a high moment, in order to provide near-surface and deep information respectively. Only the results obtained on the high moment are discussed here but the same observations were made on the low moment.

The high moment has a magnetic moment of approximately 145,000 A.m². The on-time has a duration of 2.5 ms and the off-time lasts 4.167 ms; given the very high resistivity expected for the volcanic cover, the duration of the sequence was reduced and the stack size was increased. The decays are defined by 22 time gates, from 70 µs to 3.2 ms, and the defined stack size is 162. The decays falling within each stack interval were stacked 6 by 6, leading to a stack size of 27 for the tests performed.

Figure 1 shows, for a stack size of 27, the number of possible combinations as a function of the number of decays (i.e. the size of the combinations). The number of possible combinations is relatively small for combinations composed of few or most decays. For combinations of intermediate size, the number of possible combinations starts to become important. Given the amount of data acquired during the AEM survey, this can involve significant computation time. Therefore, in this case, only a limited number of combinations was randomly evaluated. Thus, to test the SSM, between a combination size of 7 and 20 (blue lines in Figure 1) only 100,000 random combinations were evaluated for each combination size.

Figure 2 compares, at two different locations, the stacked decays obtained (1) by stacking all the decays falling within the stack interval and (2) by considering the combinations giving the decays with the highest SNR. The decays obtained using the SSM (blue curves) seem to have a better SNR than those obtained in a more standard way (red curves). Figure 2b also gives a glimpse of the ability of the SSM to reduce certain local noises due to the presence of man-made installations in the surveyed area. Indeed, the noise affecting the red curve between gates 5 and 10 has been significantly reduced on the blue curve, thus making it possible to reliably invert the early times.

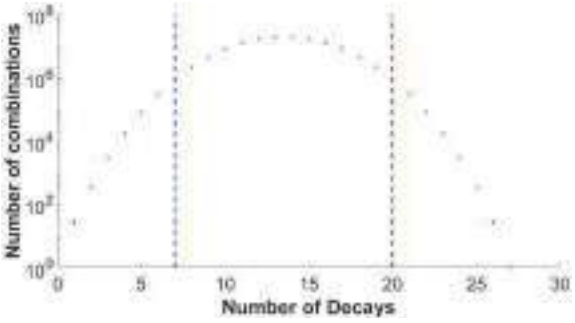

Figure 1. Number of possible combinations as a function of the number of decays, for a total of 27 decays. The blue dashed lines highlight the interval in which the combinations are randomly generated. Outside, all the combinations are evaluated.

Figure 3 compares, on the same portion of flight line, the decays obtained with a standard stacking and with the SSM. The noise on profile b is visibly lower. Decays obtained with the SSM are consistent with each other and up to 7 additional gates can be used at late times (Figures 2 and 3). This shows the ability of the SSM to improve the SNR, without arbitrarily increasing stack size or setting subjective thresholds. Thus, the SSM allows reducing the background noise, which affects the entire dataset. This is imperative in order to improve the depth of investigation of the AEM method. Moreover, certain local noises due to the presence of man-made installations tend to be significantly reduced, for example on decays 4 to 11 and on decays 33 to 57 (Figure 3), thus providing less noisy input data for post-processing to improve imaging of subsurface resistivity contrasts.

These results are promising, in particular for improving the imaging of resistivity contrasts in anthropized areas, where socio-environmental issues are numerous. In some cases, the gain appears to be significant; it should be noted that the decays obtained using the SSM cannot have a lower SNR than those obtained with standard stacking, since this combination is also evaluated.

CONCLUSIONS

It is generally assumed that the larger the stack size, the more the SNR is improved. This study shows that it is possible, as a first step, to noticeably improve the SNR by choosing the right combination of decays before having to arbitrarily increase the stack size. Moreover, the SSM turned out to be effective in

reducing certain cultural noises and sferics, which is rarely possible by playing on stack size. Thus, the SSM provides less noisy decays for post-processing.

The SSM tends to improve the depth of investigation and the coverage, while preserving lateral and vertical resolution. These improvements could allow a better characterisation of anthropized areas, where most of the socio-environmental issues are concentrated.

The SSM gave promising results by testing only a limited number of combinations compared to the number of possible combinations. The SSM must still be optimised, especially on the computation time and the number of combinations to be considered. It should be noted that the code is perfectly parallelizable, since each stack interval can be processed independently. However, it may not be possible to consider all combinations without significantly increasing the computation time. The first results would show that the decays with the highest SNR can be obtained from combinations composed of only a few decays. This would then represent an important result for the reduction of the computation time. Tests on the number of combinations to consider are still to be carried out.

The SSM offers new possibilities for improving the SNR, which is essential in the exploitation of AEM data. The SSM is also perfectly complementary to the other existing processing strategies and can be easily implemented in a processing chain.

ACKNOWLEDGMENTS

The survey in Reunion was co-funded by Région Réunion, FEDER Réunion, the Water Office of Reunion and the BRGM.

The survey carried out north of the Chaînes des Puys was co-funded by FEDER Auvergne and the BRGM.

REFERENCES

Macnae, J.C., Lamontagne, Y., and G.F. West, 1984. Noise processing techniques for time-domain EM systems? *Geophysics* 49: 934-948.

McCracken, K.G., Pik, J.P., and R.W. Harris, 1984. Noise in EM exploration systems. *Exploration Geophysics* 15: 169-174.

Reninger, P.A., Martelet, G., Deparis, J., Perrin, J., and Y. Chen, 2011. Singular Value Decomposition as a denoising tool for airborne time domain electromagnetic data. *Journal of Applied Geophysics* 75: 264-276.

Sørensen, K.I. and E. Auken, 2004. SkyTEM – a new high-resolution helicopter transient electromagnetic system. *Exploration Geophysics* 35: 191-199.

Spies, B.R., 1988. Local noise prediction filtering for central induction transient electromagnetic sounding. *Geophysics* 53: 1068-1079.

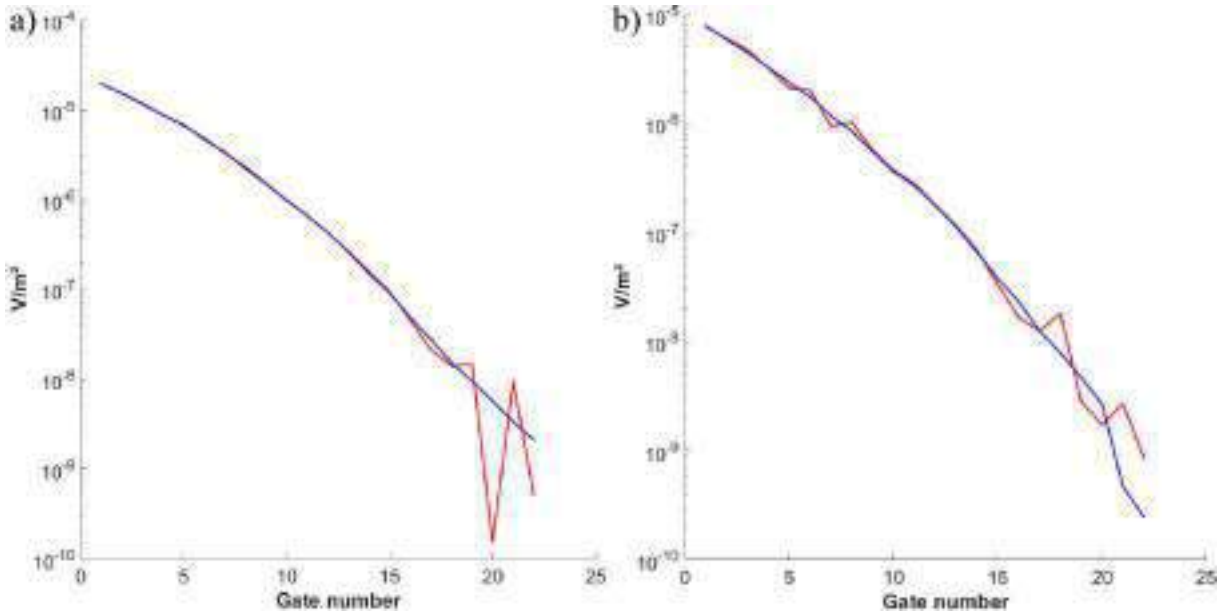

Figure 2. Stacked decays as a function of gate number considering all decays falling within the stack interval (in red) and combinations giving the highest SNR (in blue).

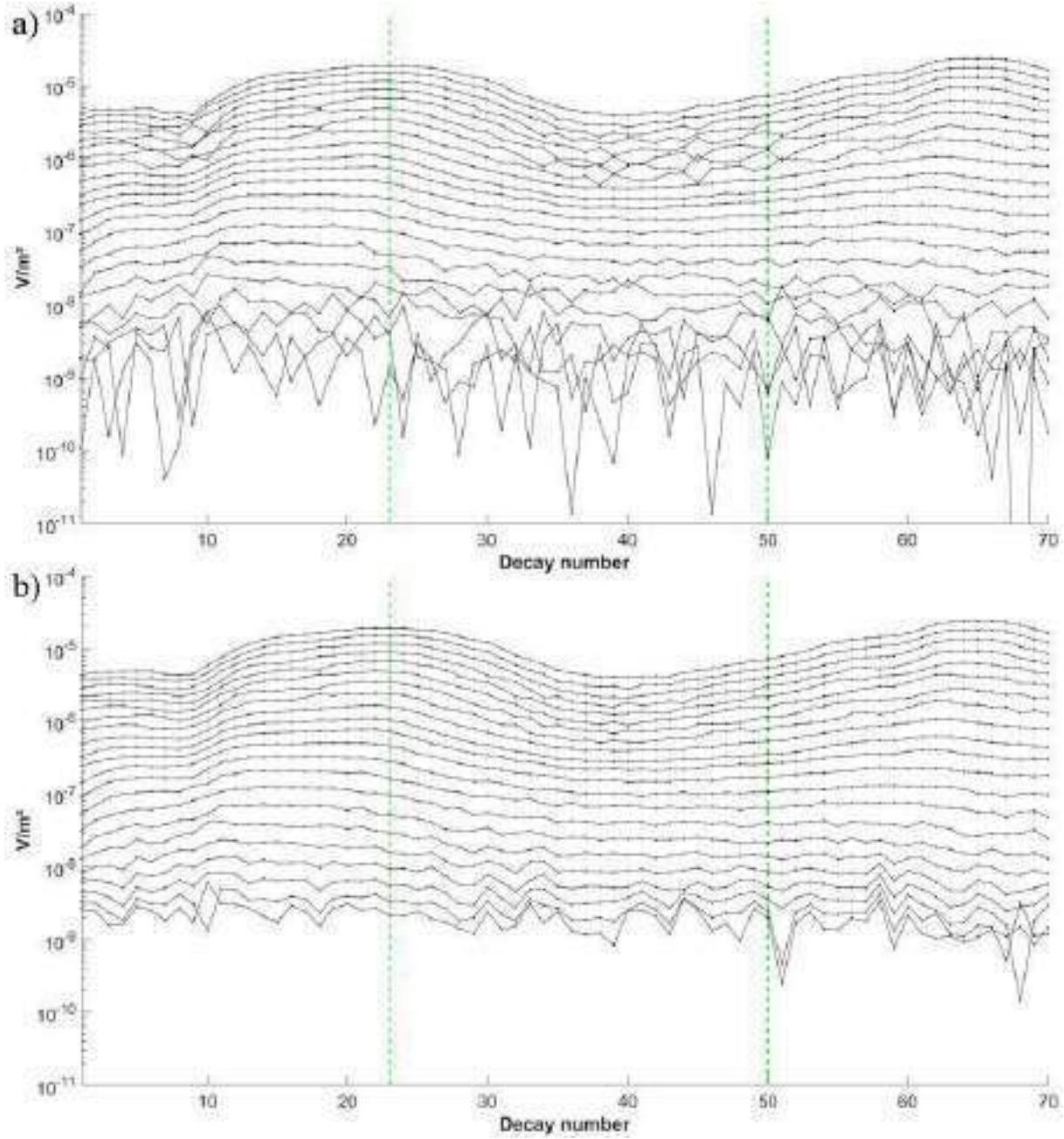

Figure 3. Decays along the same portion of flight line after applying standard stacking (a) and the SSM (b). Green dashed lines highlight the decays shown in Figure 2.

Airborne magnetics as structural guide in the 3D inversion of Airborne EM data

Carsten Scholl
CGG
Address
Carsten.Scholl@CGG.com

Stephen Hallinan
CGG
Address
Stephen.Hallinan@CGG.com

Marianne Parsons
CGG
Address
Marianne.Parsons@CGG.com

Tom Kimura
CGG
Address
Tom.Kimura@CGG.com

SUMMARY

Airborne Magnetics and Electromagnetics surveys are widely used in mineral resource exploration. Beyond the sensitivity of both to certain mineral deposits, magnetics serves as a useful proxy for geological structure.

We extend our previous work on cross-gradient, structurally-guided 3D EM inversions to use two-dimensional gradients derived from pre-processed magnetic grids as a structural guide in inversions of AEM data sets

We compare 3D resistivity inversion results obtained with this structural guiding approach to those without, for AEM data recorded in a survey in New Brunswick, Canada.

This structurally-guided 3D inversion method using magnetics data is generic and can be applied to inversion of other geophysics data such as ground electromagnetics, etc.

Key words: 3D inversion, joint inversion, AEM, magnetics, structural constraint.

INTRODUCTION

The Airborne Electromagnetic (AEM) method has been widely adapted in the mining industry to detect large mineral deposits with conductive material. The data is either interpreted either using maps of simple conductivity transforms (Huang and Fraser, 1996) or resistivity models obtained by using 1D (Farquharson et al., 2003; Vallée and Smith, 2007) or – more recently – multidimensional inversion algorithms (Cox and Zhdanov, 2008; Haber and Schwarzbach, 2014, Scholl and Miorelli, 2019).

In addition to standalone magnetics surveys at regional and prospect scale surveys – a useful proxy for geological trends as well as deposit detection – magnetics data are frequently measured simultaneously with AEM surveys. Combined interpretations are usually qualitative, however.

In this paper, we present a quantitative approach to use the magnetic data directly during the AEM inversion, but as a structural guide to the 3D resistivity inversion rather than a joint inversion of the resistivity and magnetic susceptibility volumes. The goal is to derive, out of the models that sufficiently explain the data, a resistivity volume that more closely resembles structures that are visible in the magnetic anomaly maps.

For this, we employ the cross-gradient approach (Gallardo and Meju, 2003), originally intended to structurally link two properties in a joint inversion of different parameters, since extended to support certain geological structures in the inversion of a single method. This application of the method relates the gradients of the model that are inverted with the gradients defined by some structural reference. Previous examples used a known regional strike (Scholl et al., 2015), near surface dip measurements or seismic volumes (Scholl et. al., 2017) or complex geological models (Mackie et al., 2020) to define these reference gradients.

In all of the 3D examples, the gradients were also 3D vectors. However, if we want to use a 2D structural map of the area in a 3D inversion, the algorithm needs some small but important changes to get to useful results. In this paper, we show the required modifications to the algorithm and demonstrate its use on a real data set.

METHOD

A linearized inversion is typically formulated in terms of a quadratic cost function that needs to be minimized. Often, the cost function contains a part that relates to the data misfit and one that relates to the roughness of a model (e.g. Constable et al., 1987):

$$\Phi(\mathbf{m}) = \|\mathbf{d} - \mathbf{f}(\mathbf{m})\|^2 + \beta \int_V \|\nabla\mathbf{m}\|^2 dV,$$

Here, Φ is the cost function, $\mathbf{m}$ is the model vector, $\mathbf{d}$ and $\mathbf{f}$ are the measured data and model response, respectively, and β is the trade-off parameter that weights the data misfit (the first term) against the model roughness (the second term). The roughness here is defined using the integral of the model gradient $\nabla\mathbf{m}$ as model regularization. All values in the equation above are assumed to be dimensionless.

The cross-gradient approach as published in previous papers adds an additional regularization term

$$\Phi(\mathbf{m}) = \|\mathbf{d} - \mathbf{f}(\mathbf{m})\|^2 + \beta \int_V \|\nabla\mathbf{m}\|^2 dV + \gamma \int_V \|\nabla\mathbf{m} \times \nabla\mathbf{s}\|^2 dV,$$

where in the general case $\nabla\mathbf{s}$ is a 3D gradient of the structural model and γ is a different trade-off parameter that balances the cross-gradient term with the other two terms. The contribution of the cross-gradient term is zero when the cross product of the two gradients $\nabla\mathbf{m}$ and $\nabla\mathbf{s}$ is zero, which is the case when either the gradients are parallel or antiparallel, or when either of them is zero. Note that the amplitude of the gradient $\nabla\mathbf{s}$ only defines how strong the regularization is at a given cell.

The integral is numerically evaluated in a discrete form where the norm of the cross product is evaluated for each cell *i* of model. In components this yields

$$\|\nabla m_i \times \nabla s_i\|^2 = \left\| \begin{pmatrix} \partial_y m_i \partial_z s_i - \partial_z m_i \partial_y s_i \\ \partial_z m_i \partial_x s_i - \partial_x m_i \partial_z s_i \\ \partial_x m_i \partial_y s_i - \partial_y m_i \partial_x s_i \end{pmatrix} \right\|^2$$

$$= \left(\partial_y m_i \partial_z s_i - \partial_z m_i \partial_y s_i\right)^2 + \left(\partial_z m_i \partial_x s_i - \partial_x m_i \partial_z s_i\right)^2 + \left(\partial_x m_i \partial_y s_i - \partial_y m_i \partial_x s_i\right)^2,$$

where ∂_x, ∂_y and ∂_z denote partial derivative operators in x, y and z direction, respectively.

In this paper, we want to use a 2D map as a structural guide. This means that $\partial_z s_i$ is not defined. Furthermore, we want to apply the structure not only to the uppermost layer, but to all depths. For simplicity, we therefore assign the map to each grid level of our model. This means that $\partial_z s_i$ now is defined, but is $\equiv 0$ everywhere. With this, the expression above becomes

$$\left(\partial_z m_i \partial_y s_i\right)^2 + \left(\partial_z m_i \partial_x s_i\right)^2 + \left(\partial_x m_i \partial_y s_i - \partial_y m_i \partial_x s_i\right)^2.$$

To minimize this term for an arbitrary s_i, $\partial_z m_i$ needs to be $\equiv 0$ as well, so the regularization will suppress any vertical changes in the inverted model, which is not desirable. The solution is to only use the z-component of the cross product $\left(\partial_x m_i \partial_y s_i - \partial_y m_i \partial_x s_i\right)^2$ as the regularization, which means that the cross-gradient term provides no regularization to the vertical gradient of the model.

Using structural regularization in inversions

Inversions of geophysical data are inherently non-unique, either due to the physics involved or the presence of data uncertainties. The commonly applied "smooth model" inversion approach seeks to find the "simplest" possible solution to out of all the potential solutions that would yield a similar misfit (Constable et al., 1987).

The main reason for adding an additional structural regularization to the inversion is to bias the ambiguous parts of the solution closer to what the interpreter considers a geologically more plausible model that agrees better with some auxiliary structure. This can help to find a unified model across multiple methods or for hypothesis testing.

The inversion, however, is still supposed to fit the data, which means that the structural constraint can only have a noticeable effect in parts of the model that are less well resolved by the data. This means that the auxiliary texture should at least to some extend fit the structures required by the data. Otherwise, the inversion might converge at high misfits, or the trade-off parameter for the cross-gradient term γ has to be set to a value so small that the term has no effect on the inversion.
EM data by itself will overall provide a reasonable horizontal resolution of the resistivities in the near surface. So, adding an additional regularization of the horizontal structure is likely only going to work well in cases where the overall patterns that can be inferred from the EM data is to some extend similar to the auxiliary structure.

FIELD DATA EXAMPLE

The data set used in this paper is a subset of data recorded near Kedgwick, New Brunswick, available from the geoscience data repository of Natural Resources Canada (Kiss et al, 2000, see Figure 1). The data itself were recorded with a DIGHEMV system (Fraser, 1972; Bouvier et al., 1999). We used CGG's proprietary multidimensional inversion code Otze (Scholl and Miorelli, 2019) for the inversions.

In all cases we inverted the three co-planar channels at frequencies 867 Hz, 7,193 Hz, and 56,550 Hz. We assumed standard deviations of 5% plus 2, 5, and 10 PPM, respectively. As indicated in Figure 1, we inverted only a smaller subset of the data. All inversions started from a homogeneous half-space including the real topography of the area.

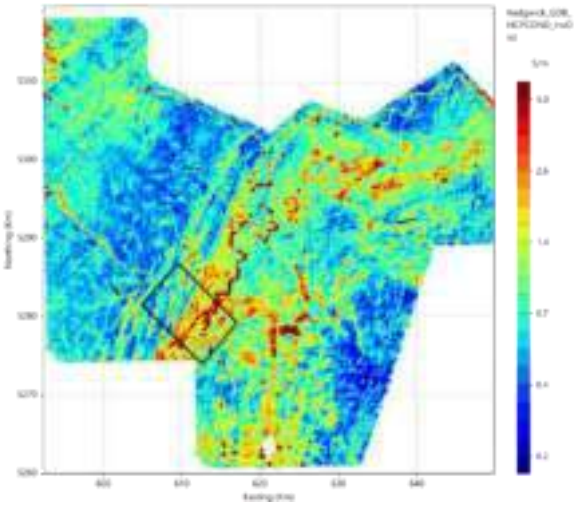

Figure 1. Map of the conductivity transform for the high frequency (56 kHz), coplanar channel of the system over the complete Kedgwick area; the black shape denotes the data mask for the inversions. Coordinates are in NAD83/UTM zone 19N.

Regular inversion of the EM data

The regular 3D smooth model inversion of the EM data reached the target misfit of a normalized root-mean-square (RMS) of 1.0 after 9 iterations. Figure 2 shows the result of the inversion at a depth of 100 m below ground level (bgl).

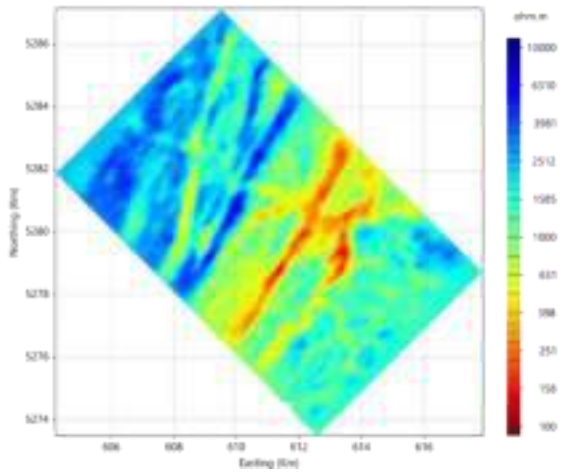

Figure 2. Inversion result for the EM data at a depth of 100 m bgl.

Magnetic data as structural constraint

Figure 3 shows the magnetic data recorded during the survey. The left subfigure shows the residual magnetic signal, that is, the measured signal minus the international geomagnetic reference field (IGRF, see Kiss, 2000). The dominant features have a relatively long wavelength. For a structural constraint, we are interested mostly in smaller scale, near surface structures. Therefore, we applied a 140m match filter to the magnetic data (Spector and Grant, 1970). The result of this filter operation is shown in the right panel of Figure 3.

For the inversion with a structural constraint, the match filtered magnetic data is mapped onto all depth levels of the 3D model domain. During the mapping, the maxima were limited to a value of 10 nT. Afterwards, the structural map was smoothed horizontally. The final structure mapped onto the model is shown in Figure 4 (left).

The inversion was started again from a homogenous half-space, including the additional regularization term for the modified cross-gradient link to the structural model. Also this inversion reached the target misft, but it required 13 iterations. Figure 4 (right) shows the result of the inversion with the structural constraint at a depth of 100 m bgl.

For better comparison, Figure 5 shows the results of the regular inversion without structural constraint (left) and the one with the structural constraint (right). On both plots, the original, match filtered magnetic data (Figure 3, right) is superimposed with contour lines.

The inversion result with the structural constraint matches the contour lines nearly perfectly. Fundamentally, the resistivity patterns obtained from the two inversions are similar. But there are several details in which the results differ. The eastern part (red ellipse) appears less noisy on the right. Also, the hook like feature in the white ellipse is different. Without the structural constraint, the southern tip of the hook seems more connected to a linear feature that extends to the SE. The two linear features that are crossing the strike direction in the centre (black ellipse) are suppressed in the result with structural constraint.

Just because the inversion result is closer to the magnetics does not necessarily mean that it is more correct. The anomalies in the blue ellipse are changed from a curved, linear feature (left) to individual blobs (right) as indicated in the magnetic data. It seems likely that these blobs are imprints of culture and not of geological origin.

Likewise, several of the mostly linear features (e.g. the blue one in the purple ellipse) appear with more beads along its length, because the original magnetic data exhibits these. Again, they are more likely to be artefacts of the line spacing and gridding than geologically relevant.

In order to reduce these probably artificial features we modified the filtered magnetics further manually. The figure with the filtered grid in grayscale was saved to a TIF file. It was then loaded into a picture editing tool for manual editing, using a cloning tool to remove most of the pockmarks and a smudging tool in the direction of the linear features to smooth out the beads related to the line spacing and higher frequency noise. Figure 6 shows the result of that operation on the left. The resulting TIF was then in turn mapped back onto the model (Figure 6, right).

With this structural constraint, the inversion reached the target misfit after 15 iterations, shown in Figure 7. The artificial blobs now disappeared, and the overall appearance is much smoother than both previous results while adhering well with the magnetics structural map.

Figure 8 shows a map view at 50 m bgl through the three inversion results as well as a cross section with a vertical exaggeration of three for each. “w/o structure” refers to the model that was obtained by the standard smooth model inversion, while “w/ structure” and “w/ edited structure” refer to the model with structural constraint as shown in Figure 4 and Figure 6, respectively.

The three results are overall similar, but the two that included the magnetics information look cleaner and more structurally consistent, depending of course on how geologically relevant the structural information in the magnetics is.

DISCUSSION

We derived a formulation for a cross-gradient structural constraint that is suitable for using a 2D map as structural guide in a 3D inversion. The approach was demonstrated for a field data example. The inversion result was closer to the texture of the magnetic data when the latter was used as a structural constraint, meaningful to the extent that the magnetics are a reliable guide to the geological structure.

In the first inversion example, we used magnetic data as structural constraint, and in the second case we used a manually modified “enhanced” image of the grid. At this point, the structural guide is merely generated from a georeferenced figure, so it is clear that the approach works as well with any arbitrary figure, as long as the texture is in some agreement with the measured data. For example, the user might use a geological map or a structural interpretation as the basis.

The caveat with arbitrary figures might be that those might contain structures that are finer than the cell spacing of the model, so a simple mapping as used in this paper is likely not the best approach. Instead, it would be beneficial to compute the gradients directly on the figure, use a structural tensor approach for the upscaling (Zhou et al. 2014, Scholl et al., 2017;

Kim et al., 2019) and then use these as structural constraint as shown in this paper.

ACKNOWLEDGMENTS

We thank Natural Resources Canada providing the Kesdgwick data used in this study.

REFERENCES

Bouvier, A., Elkaim, P., Hodges, G., 1999, Heliborne Electromagnetic & Magnetic Surveying Applied to a Pipeline Construction Project in Canada, EEGS Annual Meeting, Budapest.

Constable, S.C., Parker, R.L., Constable C.G., 1987, Occam's inversion: A practical algorithm for generating smooth models from electromagnetic sounding data, Geophysics, 52, 289-300.

Cox, L.H., and Zhdanov, M.S., 2008, Advanced computational methods for rapid and rigorous 3D inversion of airborne electromagnetic data: Communications in Computational Physics, 3, 160–179.

Farquharson, C.G, Oldenburg, D.W., and Routh P.S., 2003, Simultaneous 1-D inversion of loop-loop electromagnetic data for magnetic susceptiblility and eletrical conductivity, Geoph ysics, 68, no. 6, 1857-1869.

Fraser, D.C., 1972, A new multicoil aerial electromagnetic prospecting system. Geophysics, 37, 518-537.

Gallardo, L.A., and Meju, M.A., 2003, Characterization of heterogeneous near-surface materials by joint 2D inversion of dc resistivity and seismic data. Geophys. Res. Lett., 30, 1658.

Haber, E. and Schwarzbach, C., 2014, Parallel inversion of large-scale airborne time-domain electromagnetic data with multiple OcTree meshes, Inverse Problems, 30, no. 5.

Huang, H., and Fraser, C.D., 1996, The differential parameter mapping for multifrequency airborne resisitivty mapping, Geophysics, 61, no.1, 100-109.

Kim, B., Seol, S.J., Byun, J., and Cho., S., A structure-tensor-constraint cooperative inversion using an extracted physical property distribution, Geophysical Journal International, Volume 217, Issue 2, May 2019, Pages 1334–1352, https://doi.org/10.1093/gji/ggz082.

Kiss, F., Carson, J., McCutcheon, S.R., Oneschuk, D., and Holman, P., 2000, Detailed multiparameter airborne geophysical survey data release, Kedgwick area, New Brunswick / Diffusion des données d'un levé géophysique aérien à paramètres multiples (levé détaillé), région de Kedgwick, Nouveau-Brunswick: Geological Survey of Canada, Open File 3784, 2000, 54 sheets, https://doi.org/10.4095/211491; https://open.canada.ca/en/open-government-licence-canada.

Mackie, R.L., Meju, M.A., Miorelli, F., Miller, R.V., Scholl, C., and Saleh, A.S., 2020, Seismic image-guided 3D inversion of marine CSEM and MT data. Interpretation, 8 (4) 1-13, http://dx.doi.org/10.1190/INT-2019-0266.1.

Scholl, C., Neumann J., and Watts, M.D., 2015, Geosteered 3D Inversion of Airborne EM Data in Rugged Terrain. EAGE Near Surface Geoscience (Turin) AEM Workshop Abstracts.

Scholl, C., Hallinan, S., Watts, M.D., and Mirorelli, F., 2017, Geological consistency from inversions of geophysical data: 79th EAGE Annual Meeting, Abstracts, doi: 10.3997/2214-4609.201700849.

Scholl, C., and Miorelli, F., 2019, Airborne EM inversion on vertically unstructured model grids. Exploration Geophysics, doi: 10.1080/08123985.2019.1668239.

Spector, A., and Grant, F. S., 1970, Statistical models for interpreting aeromagnetic data. Geophysics, 35, no. 2, 293-302.

Vallée, M., and Smith, R., 2007, Comparison of fixed-wing airborne electromagnetic 1D inversion methods. Proceedings of Exploration 07: 5th Decennial International Conference on Mineral Exploration, 1067–1072.

Zhou, J., Revil, A., Karaoulis, M., Hale, D., Doetsch, J., and Cuttler, S., 2014. Image-guided inversion of electrical resistivity data, Geophys. J. Int., 197, 292–309, 10.1093/gji/ggu00.

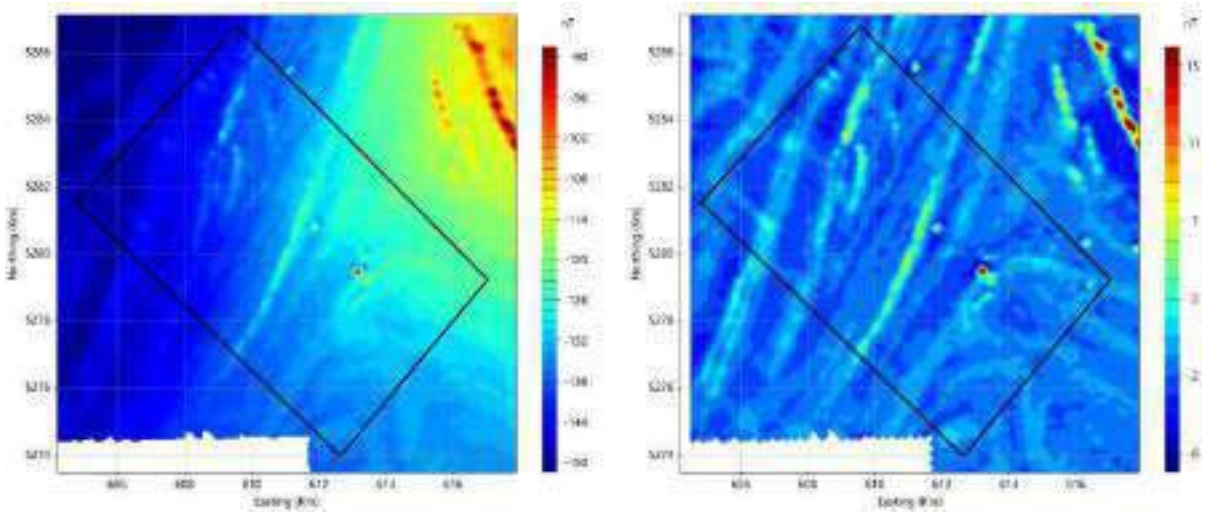

Figure 3. Magnetic data recorded in the survey; the left panel shows the total residual magnetics, the panel on the right hand the match-filtered residual used as the structural constraint in the EM inversions.

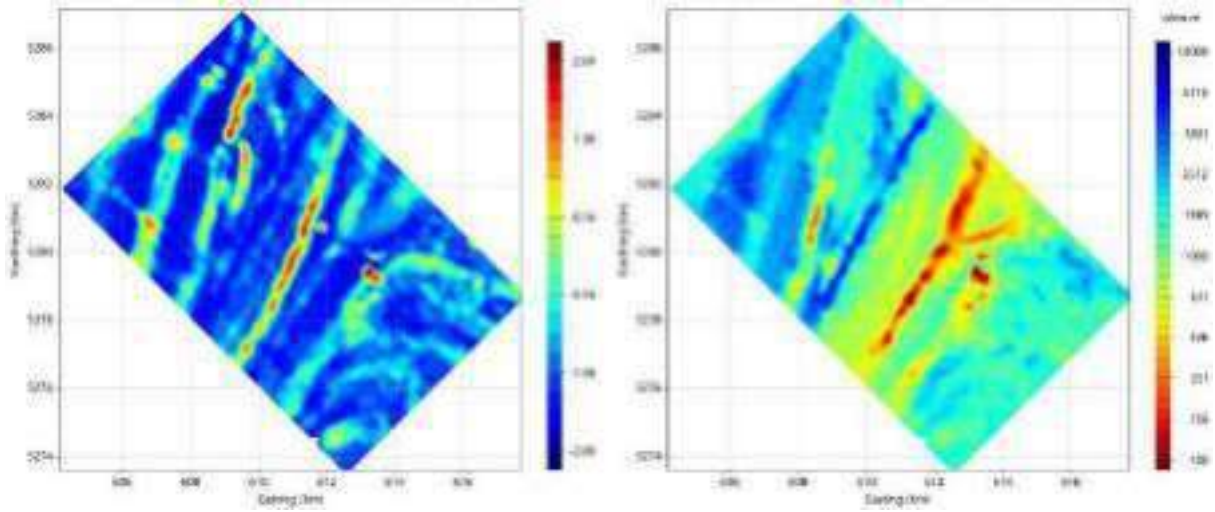

Figure 4. Filtered magnetics mapped onto the grid (left) and result of the EM inversion with structural constraint from the magnetics at a depth of 100 m bgl.

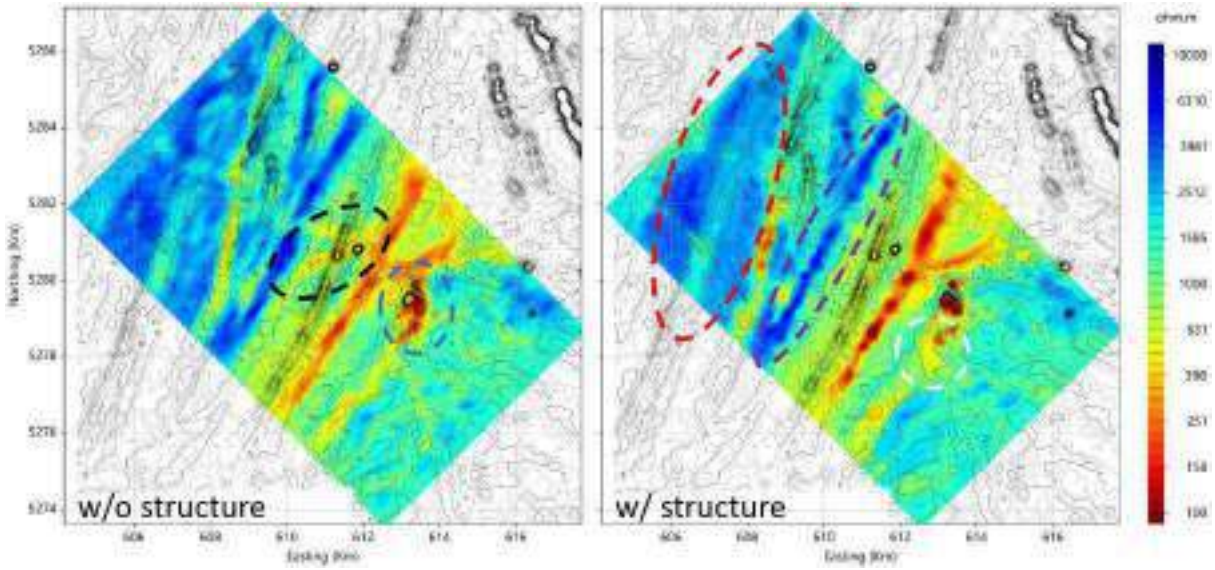

Figure 5. Results w/o (left) and w/ (right) structural constraint at 100 m bgl; superimposed contour lines are the filtered magnetic data. The dashed ellipses mark areas discussed in the text.

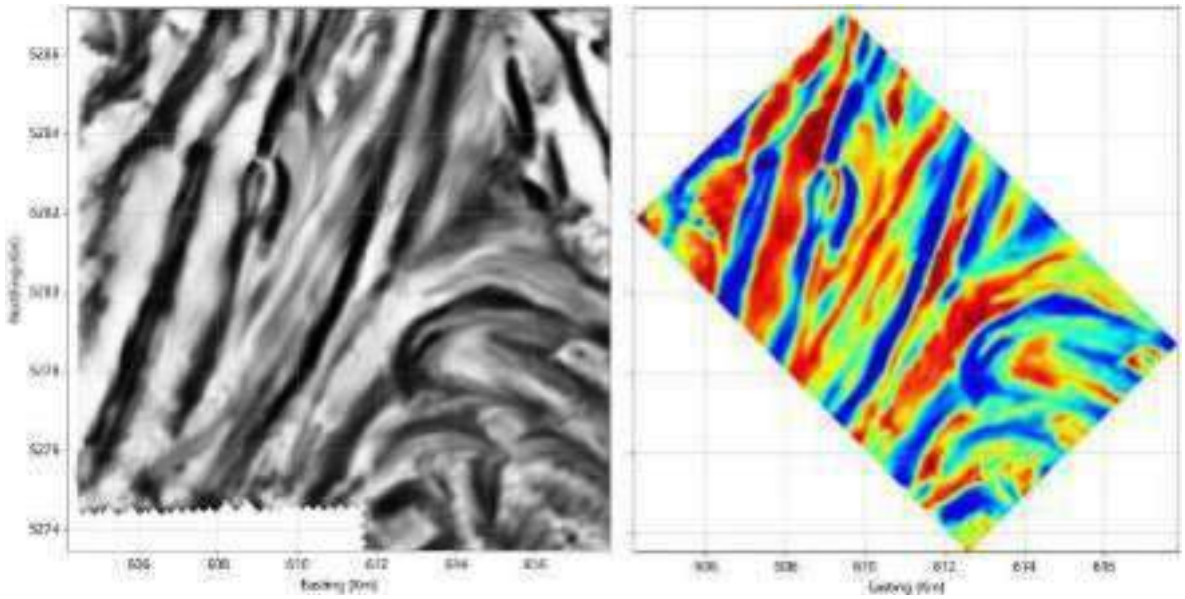

Figure 6. Modified version of the original filtered magnetics data (left) and its mapping onto the model (right).

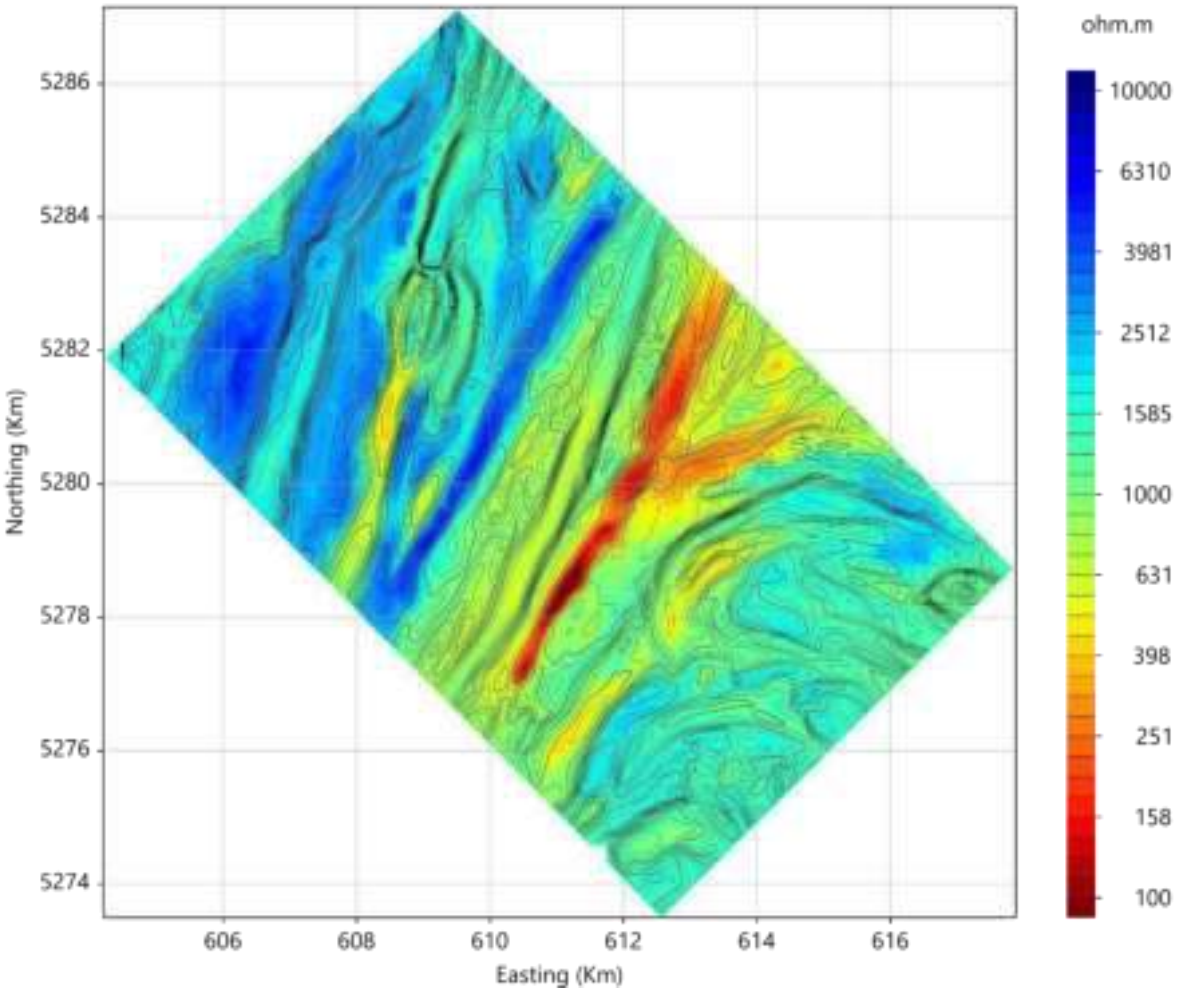

Figure 7. Inversion result using the edited structural map from Figure 6 as structural constraint (contour lines) at a depth of 100 m bgl.

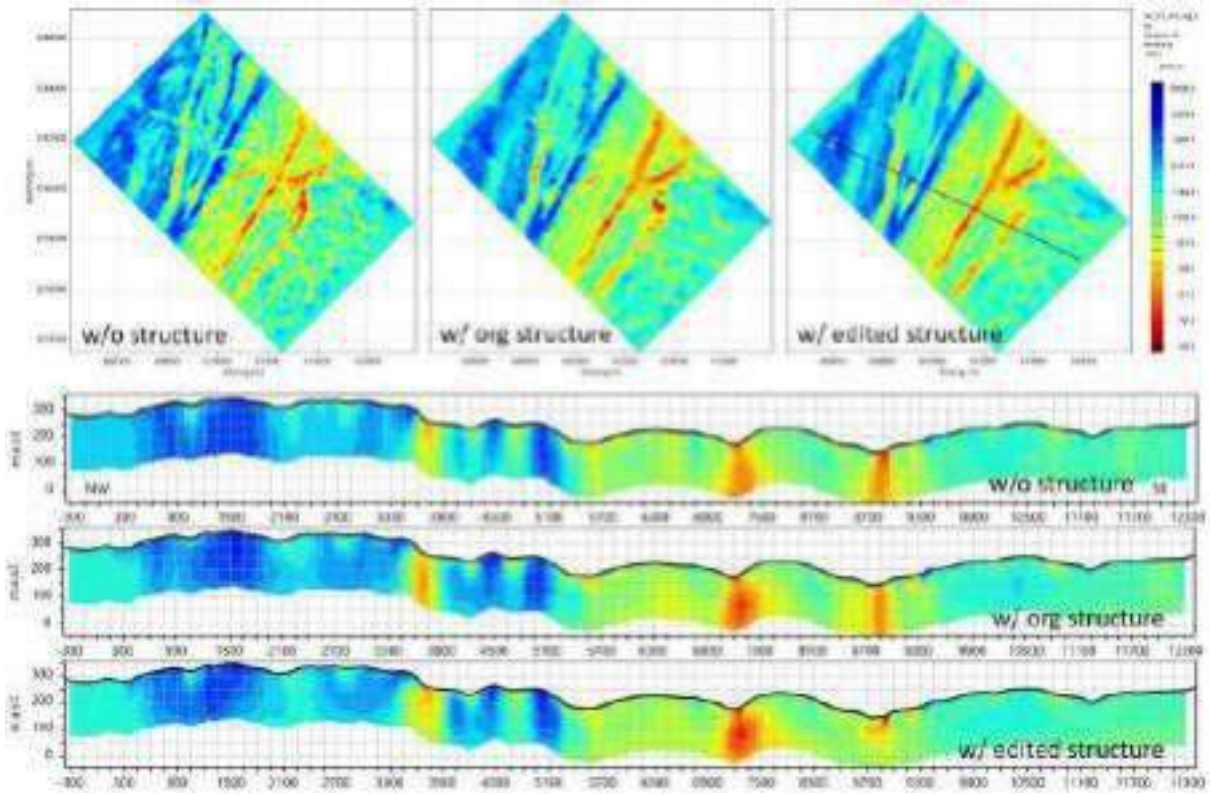

Figure 8. Comparison between the three inversion results; the top row shows the three models at a depth of 50 m bgl. The sections below are along the profile marked in the upper right map view.

BGR helicopter-borne frequency-domain EM – past, present, future

Bernhard Siemon
Federal Institute for Geosciences and Natural Resources (BGR)
Stilleweg 2, D-30655 Hannover
bernhard.siemon@bgr.de

SUMMARY

The German Federal Institute for Geosciences and Natural Resources (BGR) has been conducting airborne geophysical surveys worldwide for more than four decades. Most of these airborne surveys applied frequency-domain helicopter-borne electromagnetics (HEM) in combination with magnetic and radiometric measurements.

HEM surveys served and still serve as acquisition of baseline data for a number of applications in mineral, groundwater and soil exploration. After starting with anomaly detection in mineral exploration surveys, the focus was set to groundwater surveys during the following decades. Spatial mapping of freshwater resources, seawater intrusion, submarine fresh-water outflows, and buried valleys are some typical applications. Recently, environmental issues gain more and more importance. Therefore, BGR conducted most of the current surveys in Germany. These provided not only resistivity distributions, but also estimated parameters such as groundwater chloride content in coastal and salt dome areas, groundwater iron content in former lignite mining areas, and peat volumes of mires. These applications combined local data (e.g boreholes) or external models as well as airborne geophysical data to derive spatial estimates, which then served as baseline date for advanced (hydro-) geological modelling.

Key words: Helicopter-borne electromagnetics, BGR, mineral exploration, groundwater and soil investigations.

INTRODUCTION

Airborne geophysics has a long tradition at the German Federal Institute for Geosciences and Natural Resources (BGR). For more than four decades, BGR has conducted airborne surveys worldwide applying a variety of geophysical methods. Most often, the BGR helicopter carried a combination of electromagnetic, magnetic and radiometric systems. BGR started airborne geophysics for mineral exploration in the mid-1970s. The first groundwater survey over the German East Frisian island of Spiekeroog took place in 1978 (Sengpiel and Meiser, 1981). Since then, BGR has focused on groundwater surveys (Siemon et al., 2009b), but other surveys were also conducted.

SYSTEMS

BGR's current standard helicopter-borne geophysical system consists of a Sikorsky S-76B helicopter, three geophysical systems (electromagnetics, magnetics, and gamma-ray spectrometry), navigation and positioning (incl. inertial measurement unit) systems, a data acquisition system, and a base station recording diurnal variations. The first helicopter-borne electromagnetic (HEM) system BGR used was a Dighem II, which operated at about 900 Hz in horizontal-coplanar (HCP) and vertical coaxial (VCX) coil configuration (Fraser, 1979). Later, two-, three- and five-frequency systems followed. Both of the current HEM systems (Resolve) operate at six frequencies ranging from 380 Hz to 130 kHz and have on-board calibration facilities. Transmitter and receiver coils are oriented in a horizontal-coplanar (5 × HCP) or vertical-coaxial (1 × VCX) position (Siemon et al., 2009b). The maximum investigation depth is limited to 50-150 m, depending on the conductivity of the subsurface. The high frequency range and phase angle measurements make HEM systems optimal for mapping wide-ranging resistivity (0.1-50,000 Ωm) with high near-surface layer resolution (Hodges, 2013).

METHODS

Thoroughly processed HEM data is the basis for any quantitative analysis. In-house and commercial software is applied to correct the data for calibration errors, thermal drifts, and baseline shifts as well as for the reduction of cultural noise (Siemon *et al.*, 2011). Homogeneous half-space (single-frequency inversion) and layered half-space models (multi-layer inversion) are used to derive spatial resistivity distributions. The multi-layer (1D) inversion applies a Levenberg-Marquardt procedure in combination with general matrix inversion that is able to use both few and many layers (Sengpiel and Siemon, 2000; Siemon *et al.*, 2009b). Additionally, lateral constraints can be applied (Siemon *et al.*, 2009a). Time-consuming 3D modelling and inversion is only applied where 1D inversion fails to produce plausible results (Ullmann *et al.*, 2016).

RESULTS

Past – a brief review

Airborne geophysics at BGR started with mineral and groundwater exploration surveys as part of development aid projects in South America, Asia, and Africa (e.g. Eberle, 1995, Sengpiel and Fluche, 1992). After the 2004 tsunami, BGR helped to assess freshwater resources in the coastal areas of Aceh, Sumatra (Siemon *et al.*, 2007). Nowadays, research and development projects in Europe dominate. The variety of applications comprises besides groundwater and geological mapping (Jordan and Siemon, 2002), the investigation of buried valleys (Eberle and Siemon, 2006), abandoned salt mines (Siemon *et al.*, 2012) or military (Siemon *et al.*, 2002) and civil (Sengpiel and Siemon, 2005) waste sites. Recently, BGR restarted mineral exploration

surveys applying both the standard BGR helicopter-borne geophysical system (Siemon *et al.*, 2016) and a novel semi-airborne electromagnetic system (Steuer *et al.*, 2020). The value of the HEM results increased from simple mapping or anomaly detection surveys to being a fundamental part of numerical geological and groundwater modelling (e.g. Rumpel *et al.*, 2009, Steinmetz *et al.*, 2015, Delsman *et al.*, 2019, Siemon *et al.*, 2020b).

Present – two case histories

The before mentioned applications are still up-to-date. Thus, only two further applications concerning climate change issues are described in the following.

I – Investigation of former opencast lignite mining areas

The region near the towns of Cottbus and Senftenberg in Lusatia, Eastern Germany, was one of the largest mining areas in Germany. Most of opencast lignite mines have been closed during the last three decades and a post-mining recultivation is ongoing. For this, extensive information on aquifers is required, in particular on their mineralization, depth and thickness. One problem is the contamination of the groundwater and lakes with acids and dissolved iron.

In July 2021, BGR conducted a one-week airborne survey over an area (200 km², 1680 line-km) between Finsterwalde and Lauchhammer (Figure 1). The apparent resistivity at the highest frequency (128 kHz) fits very well with the water resistivity sampled in lakes, as long as the width of the lakes exceeds 200 m so that the distance to the lakeshores outreaches the system's footprint (Figure 2). This demonstrates that the transformation of the HEM data based on homogeneous half-space models is sufficient to reveal water resistivity as a proxy for water quality, at least for larger lakes. For smaller or shallow lakes, however, 3D or full 1D inversion, respectively, is mandatory to achieve accurate water quality parameters.

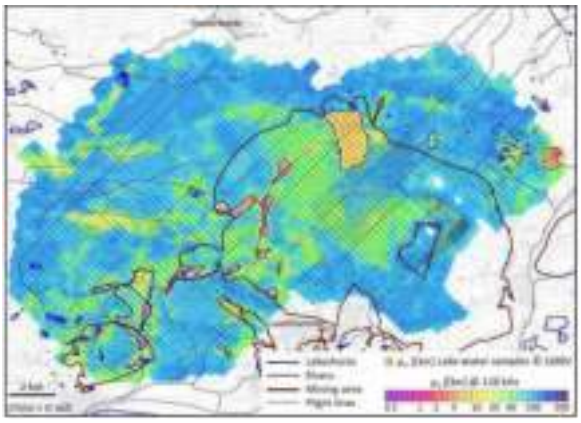

Figure 1. Apparent resistivity ρ_a @ 128 kHz (grid) vs. resistivity ρ_w of water samples in lakes (dots). Marked are lakeshores, rivers, mining area, and flight lines.

While the contamination of surface water can be easily sampled in-situ, groundwater sampling requires observation wells. As these are often sparsely distributed in a survey area, the question is, whether HEM results can help to close the gaps. Figure 3 shows the resistivity distribution at 90 m asl, derived from 1D inversion models with 20 layers. Most of the filters in the observation wells are located in a sandy aquifer at this elevation. The coloured dots plotted on Figure 3 representing the bulk resistivity (using a formation factor of 4) at the observation wells generally agree with the HEM derived resistivities. Deviations occur where filters are deeper/shallower or lithology (clay or silt layers close to filter sections) affects the HEM data.

The analysis of 26 groundwater samples shows (Figure 4, left) that groundwater EC seems to correlate with dissolved iron (Fe^{2+}) content based on a square-root relation. Transferring this

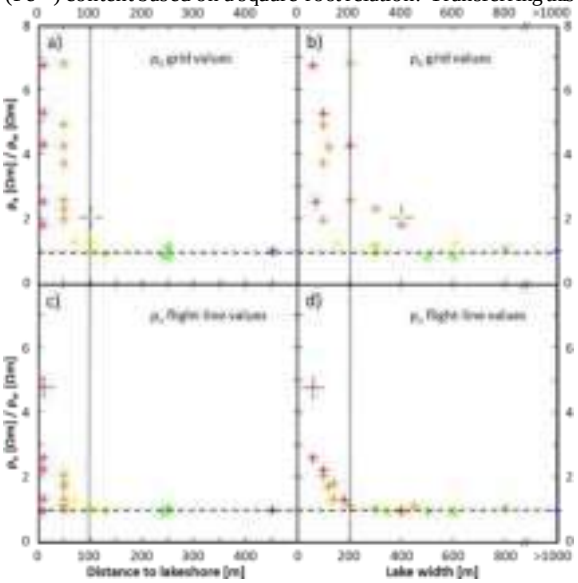

Figure 2. Ratios of apparent resistivities @ 128 kHz and resistivities of lake water. a) & b): values picked from grids, c) & d): values picked on closest flight lines. Colours refer to distance to lakeshore. Dashed lines indicate the 1:1 line; dotted lines indicate 100 m distance to lakeshore and 200 m lake width.

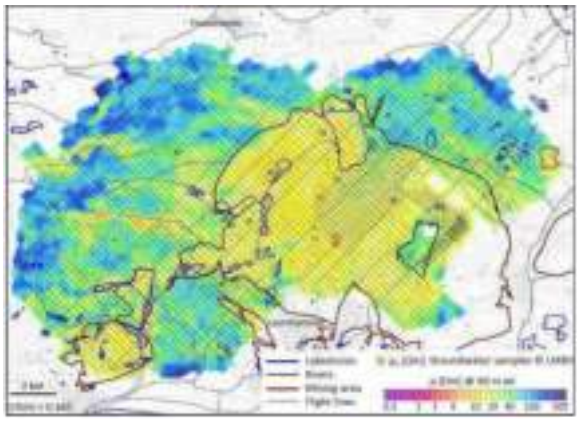

Figure 3. Resistivity ρ @ 90 m asl (grid) vs. bulk resistivity ρ_b derived from groundwater samples (dots). Marked are lakeshores, rivers, mining area, and flight lines.

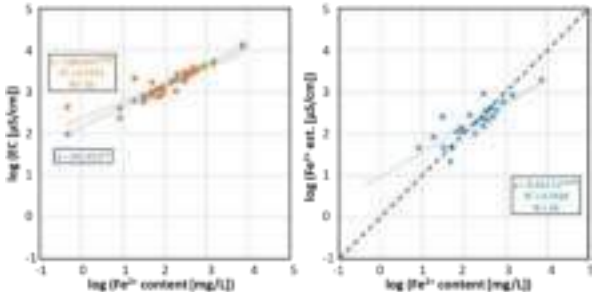

Figure 4. Left: groundwater EC vs. Fe^{2+} content with calculated (orange) and estimated (blue) trend line, right: estimated Fe^{2+} content derived from resistivities @ 90 m asl vs. Fe^{2+} content in groundwater. Dotted line indicates the calculated trend line; dashed line indicates the 1:1 line.

approach to HEM resistivity data leads to estimated Fe-content: Fe^{2+}est. = $10000/2 \cdot (F/\rho)^2$ with formation factor F = 4 and ρ = resistivity @ 90 m asl. Although the corresponding trend line (Figure 4, right) deviates from the 1:1-line, this result is promising for an estimation of the Fe-content in groundwater derived from spatial HEM results.

II- Peat volume estimation of peatlands

Peatlands release greenhouse gases to the atmosphere, particularly if anthropogenic drainage and land use for agricultural, silvicultural or horticultural purposes take place. In Germany, 2.8% (7.8 Mio. T CO_2-C-equivalents) of the total national greenhouse budget of 2006 came from peatlands used (Höper, 2007). Knowledge on peat volumes of peatlands is essential to estimate carbon stocks accurately and to facilitate appropriate peatland management (Gatis et al., 2019). Commonly used direct soil probing of peatlands as well as geophysical methods applied on ground are labour intensive and unfeasible to capture spatial information at landscape extents. Remote sensing and airborne geophysical methods may help to overcome this challenge (Siemon *et al.*, 2020a).

An airborne geophysical survey (173 km², 887 line-km) conducted in May 2022 within 4 days covered the northern half of the "Teufelsmoor" which is one of the largest contiguous areas of bog in northwest Germany. The lateral extend of the peatland was estimated from a combination of radiometric (exposure rate E) and HEM (apparent depth d_a @ 133 kHz) data. In order to balance both parameters, each one was scaled with respect to drilled peat thicknesses providing a parameter (peat index PI) that represents a thickness: for $d_a < 0.5$ m, $E < 1.25$ µR/h, PI > 0: $PI = -(1.5 \cdot d_a + 2.8 \cdot \ln(E))/2$, else: PI = 0. Figure 5 (left) shows the PI contour in comparison with mapped mires (size of fen and bogley areas could be diminished today).

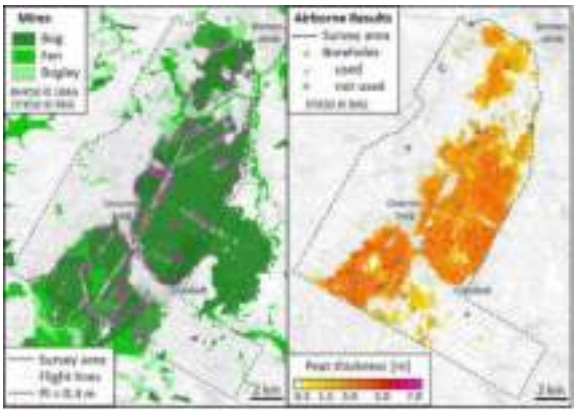

Figure 5. Left: mapped mires vs. peat index PI (airborne), right: peat thickness estimated from airborne data (grid) vs. borehole data (dots).

HEM inversion models are used to estimate peat thicknesses. While few-layer models normally contain the information on peat in the first layer (ρ_1, d_1), multi-layer models require more analysis. Siemon et al. (2020a) showed that the steepest positive log(ρ)-log(z) gradients (SG) derived from spline interpolated HEM models helped to estimate resistivity ρ_p and thickness t_p of peat. The few- and multi-layer results, however, differ somewhat from each other and show resistivity dependent deviations from drilled peat thicknesses t_d. The deviations of the corrected estimates could be reduced using constant scaling factors: ρ_c: $t_{pk} = d_m \cdot \rho_c / \rho_m$, where $d_m = d_1$, $\rho_m = \rho_1$, $\rho_c = 50$ Ωm for few-layer models and $d_m = t_p$, $\rho_m = \rho_p$, $\rho_c = 40$ Ωm for multi-layer models. The final estimate for peat thickness combines (average) PI and t_{pk} values (Figure 5, right). Figure 6 compares estimated (h_a) and drilled (h_p) peat base elevations (difference of surface and peat thickness values).

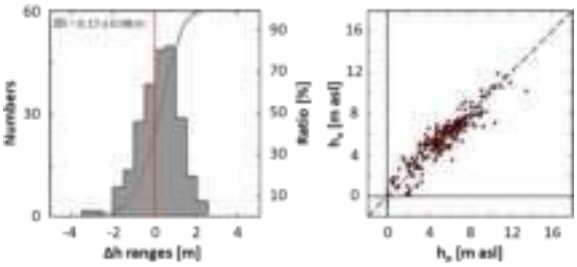

Figure 6. Comparison of drilled peat base elevations (h_p) with airborne derived estimates (h_a). Left: histogram of differences $\Delta h = h_a - h_p$, right: scatter plot h_a vs. h_p.

Future – an outlook

Although the number of HEM systems has decreased over the last decades due to an increase of time-domain systems, they are still useful and have some advantages. The rigid-beam birds are easy to fly, even with higher speed/stronger winds. The low drag (close terrain following) and short stack time enables high lateral resolution for both discrete conductors and changing layer resistivity (Hodges, 2013). Independent coil systems per frequencies enable selective corrections with respect to cultural noise. The high-frequency data is at all less sensitive to that noise and low frequency quadrature data is sensitive to conductors in resistive host as well as to magnetic susceptibility.

Due to the effects climate change, airborne EM surveys may be increasingly demanded for soil mapping and near-surface groundwater observations. Particularly for these shallow investigations, HEM can provide large-scale baseline data. Integrated modelling, combining HEM with other types of data, and using data uncertainties are only a few examples for future trends.

CONCLUSIONS

Several case histories cited or presented here demonstrate the variety of applications that are feasible with HEM. Besides a number of studies, which qualitatively interpreted HEM results, recent studies focussed on the integration of HEM models into 3D geological and groundwater modelling. The frequency-domain HEM method is suitable for surveys, which require limited exploration depth (in the order of a hundred metres). If greater exploration depth is required, time-domain or semi-airborne electromagnetic systems have to be used. Thus, the focus of HEM surveys should primarily be set on shallow large-scale investigations, particularly where target conductance is low, host resistivity is high, near-surface layer resolution is critical, targets are small, and where terrain is difficult.

ACKNOWLEDGMENTS

Thanks to the Lusatian and Central German Mining Administration Company (LMBV) and to the Lower Saxony State Office for Mining, Energy and Geology (LBEG) for providing borehole and other geoscientific data.

REFERENCES

Delsman, J.R., van Baaren, E.S., Siemon, B., Dabekaussen, W., Karaoulis, M., Pauw, P., Vermass, T., Bootsma, H., de Louw, P.G.B., Gunnink, J.L., Dubelaar, W., Menkovic, A., Steuer, A., Meyer, U., Revil, A., and G.H.P. Oude Essink, 2018. Large-scale, probabilistic salinity mapping using airborne electromagnetics for groundwater management in Zeeland, the Netherlands. *Environmental Research Letters* 13(8): 1-12.

Eberle, D., 1995. Geophysical mapping in Archean greenstone beits of Tanzania as an aid for gold prospecting. *First Break* 13(9): 357-367.

Eberle, D.G., and B. Siemon, 2006. Identification of buried valley using the BGR helicopter-borne geophysical system. *Near Surface Geophysics* 4(2): 125-133.

Fraser, D.C., 1972. A new multicoil aerial electromagnetic prospecting system. *Geophysics* 37: 518-537.

Gatis, N., Luscombe, D.J., Carless, D., Parry, L.E., Fyfe, R.M., Harrod, T.R., Brazier, R.E., and K. Anderson, 2019. Mapping upland peat depth using airborne radiometric and lidar survey data. *Geoderma* 335: 78–87

Hodges, G., 2013. The Power of Frequency Domain: When you should be using it. 6th AEM Conference, Skukuza Rest Camp, Kruger National Park, South Africa, AEM2013 Handbook: 63.

Höper, H., 2007. Freisetzung von Treibhausgasen aus deutschen Mooren (Emission of greenhouse gases from German peatlands). *TELMA* 37: 85–116.

Jordan, H., and B. Siemon, 2002. Die Tektonik des nordwestlichen Harzrandes - Ergebnisse der Hubschrauber-Elektromagnetik. *Zeitschrift der Deutschen Geologischen Gesellschaft* 153(1): 31-50.

Rumpel, H.-M., Binot, F., Gabriel, G., Siemon, B., Steuer, A., and H. Wiederhold, H., 2009. Benefit of geophysical data for hydrogeological 3D modelling - An example of the Cuxhaven buried valley. *Zeitschrift der Deutschen Geologischen Gesellschaft* 160(3): 259-269.

Sengpiel, K.P., and P. Meiser, 1981. Locating the freshwater/salt water interface on the island of Spiekeroog by airborne EM resistivity/depth mapping. *Geologisches Jahrbuch* C29: 255-271.

Sengpiel, K.-P., and B. Fluche, 1992. Application of Airborne Electromagnetics to Groundwater Exploration in Pakistan. *Zeitschrift der Deutschen Geologischen Gesellschaft* 143(2): 254-261.

Sengpiel, K.-P., and B. Siemon, 2000. Advanced inversion methods for airborne electromagnetic exploration. *Geophysics* 65: 1983-1992.

Sengpiel, K.-P., and B. Siemon, 2005. Aerogeophysik. In *Handbuch zur Erkundung des Untergrundes von Deponien und Altlasten, Band 3: Geophysik*: Springer-Verlag, Berlin, Heidelberg, 771-810.

Siemon, B., Auken, E., and A.V. Christiansen, 2009a. Laterally constrained inversion of frequency-domain helicopter-borne electromagnetic data. *Journal of Applied Geophysics* 67(3): 259-268.

Siemon, B., Christiansen, A.V., and E. Auken, 2009b. A review of helicopter-borne electromagnetic methods for groundwater exploration. *Near Surface Geophysics* 7: 629-646.

Siemon, B., Ibs-von Seht, M., and S. Frank, S., 2020a. Airborne electromagnetic and radiometric peat thickness mapping of a bog in Northwest Germany (Ahlen-Falkenberger Moor). *Remote Sensing* 12(2), 203.

Siemon, B., Ibs-von Seht, M., Steuer, A., Deus, N., and H. Wiederhold., 2020b. Airborne electromagnetic, magnetic, and radiometric surveys at the German North Sea coast applied to groundwater and soil investigations. *Remote Sensing* 12(10), 1629.

Siemon, B., Ibs-von Seht, M., Steuer, A., Pielawa, J., and U. Meyer, 2016, Aerogeophysikalische Erkundung von metallischen Rohstoffen im Geyerschen Wald / Erzgebirge: 76. Jahrestagung der Deutschen Geophysikalischen Gesellschaft, Münster, Expanded Abstracts.

Siemon, B., Kerner, T., Krause, Y., and U. Noell, 2012. Airborne and ground geophysical investigation of the environment of abandoned salt mines along the Staßfurt-Egeln anticline, Germany. *First Break* 30(2): 43-53.

Siemon, B., Steuer, A., Meyer, U., and H.-J. Rehli, 2007. HELP ACEH – A post-tsunami helicopter-borne groundwater project

along the coasts of Aceh, northern Sumatra. *Near Surface Geophysics* 5(4): 231-240.

Siemon, B., Steuer, A., Ullmann, A., Vasterling, M., and W. Voß, 2011. Application of frequency-domain helicopter-borne electromagnetics for groundwater exploration in urban areas. *Physics and Chemistry of the Earth* 36(16): 1373–1385.

Siemon, B., Stuntebeck, C., Sengpiel, K.-P., Röttger, B., Rehli, H.-J., and D.G. Eberle, 2002. Investigation of hazardous waste sites and their environment using the BGR helicopter-borne geophysical system. *Journal of Environmental & Engineering Geophysics* 7(4): 169-181.

Steinmetz, D., Winsemann, J., Brandes, C., Siemon, B., Ullmann, A., Wiederhold, H., and U. Meyer, 2015. Towards an improved geological interpretation of airborne electromagnetic data: a case study from the Cuxhaven tunnel valley and its Neogene host sediments (northwest Germany). *Netherlands Journal of Geosciences* 94(2): 201-227.

Steuer, A., Smirnova, M., Becken, M., Schiffler, M., Günther, T., Rochlitz, R., Yogeshwar, P., Mörbe, W., Siemon, B., Costabel, S., Preugschat, B., Ibs-von Seht, M., Zampa, L.S., and F. Müller, 2020. Comparison of novel semi-airborne electromagnetic data with multi-scale geophysical, petrophysical and geological data from Schleiz, Germany. *Journal of Applied Geophysics* 182, 104172: 1-19.

Ullmann, A., Scheunert, M., Afanasjew, M., Börner, R.-U., Siemon, B., and K. Spitzer, 2016. A cut-&-paste strategy for the 3-D inversion of helicopter-borne electromagnetic data – II. Combining regional 1-D and local 3-D inversion. *Journal of Applied Geophysics* 130: 131-144.

The HydroGeosITe for AEM mapping: characterization through joint inversion of AEM, ground EM and DCIP data

Alessandro Signora
The EEM Team for Hydro & eXploration,
Dep. of Earth Sciences A. Desio,
Università degli Studi di Milano,
Via Botticelli 23, Milano (Italy)
alessandro.signora@unimi.it

Stefano Galli
The EEM Team for Hydro & eXploration
Dep. of Earth Sciences A. Desio
Università degli Studi di Milano,
Via Botticelli 23, Milano (Italy)
stefano.galli2@unimi.it

Matteo Gisolo
A2A Ciclo Idrico S.p.a.

Via Lamarmora 230, Brescia (Italy)
matteo.gisolo@a2a.eu

Gianluca Fiandaca
The EEM Team for Hydro & eXploration
Dep. of Earth Sciences A. Desio,
Università degli Studi di Milano,
Via Botticelli 23, Milano (Italy)
gianluca.fiandaca@unimi.it

SUMMARY

The HydroGeosITe project aims at the establishment of the first Italian calibration and reference site for airborne electromagnetic (AEM), ground EM and electric geophysical methods within the largest AEM campaign carried out in Italy for groundwater mapping and management.

The geophysical characterization of the HydroGeosITe combines AEM, ground EM and galvanic direct current and induced polarization (DCIP) surveys, for the retrieval of a unique 3D distribution of conduction and polarization electrical properties, able to describe all geophysical data. This is achieved through a joint inversion of all inductive and galvanic data in terms of dispersive resistivity, with data misfit comparable to the independent inversions and significantly improved resolution.

The HydroGeosITe will serve as calibration site for future AEM campaigns, as well as for ground-based EM and galvanic surveys. Furthermore, borehole drillings down to several hundreds of meters are being carried out, with lithological description and geophysical logging, for establishing a reference in the interpretations of the resistivity models retrieved by the AEM campaign.

Key words: Calibration, Reference, Joint inversion

INTRODUCTION

In the spring of 2021 over 2000 line-km of airborne electromagnetic (AEM) data have been acquired for mapping and managing groundwater resources in the Brescia province, West of Garda Lake, and another 20000 line-km survey is currently ongoing to cover the entire plain of Brescia province and a mountainous sector within summer 2023, over an area of approximately 1800 km^2 (Figure 1).

Within this AEM campaign, the largest ever carried out in Italy for groundwater mapping and management, the water management company A2A Ciclo Idrico S.p.A. financed the HydroGeosITe project, which aims at establishing the first calibration and reference site for AEM, ground EM and galvanic geophysical methods for hydrogeological purposes.

The need for calibration sites of EM systems derives by the sensitivity of EM data to system characteristics, such as receiver transfer function, transmitter current waveform, and transmitter-receiver synchronization and geometry, which if neglected lead to significant bias in the retrieval of the electrical properties (Christiansen et al., 2011). For instance, the Lyngby Danish reference site has been established for ensuring the calibration of both airborne and ground-based EM systems (Foged et al., 2013), while the Menindee Australian test range (Brodie and Cooper, 2018) focuses only on airborne systems, but covers a much longer stretch (more than 35 km). In both cases, calibrated systems are expected to retrieve satisfactory resistivity models, the eventual calibration consisting in adjusting the system characteristics until the inversion model compares well enough with the reference model.

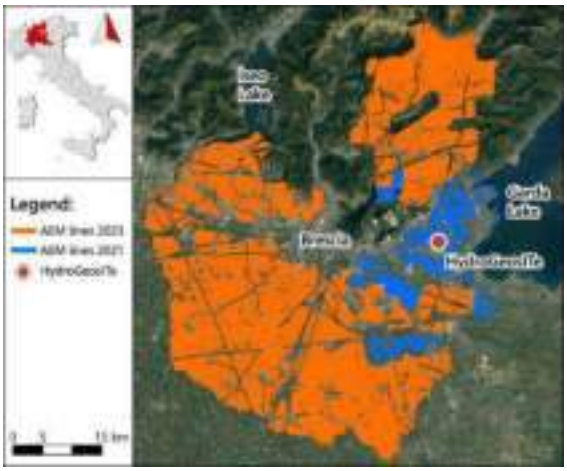

Figure 1: Flight lines of 2021 and 2023 AEM campaigns in Brescia province. Blue lines represent the 2000 line-km of data flown in 2021; orange lines represent the 20000 line-km of the 2023 survey. The red dot shows the position of the HydroGeosITe.

With the HydroGeosITe we want to raise the bar even higher: we aim at characterizing the electrical properties at the site, both in terms of conduction and polarization, for modelling jointly inductive and galvanic direct current and induced polarization (DCIP) data. Furthermore, borehole drillings down to several hundreds of meters will be completed within

summer 2023, and the lithological description and geophysical logging will allow to use the HydroGeosITe as a reference in the interpretation of the AEM campaign. In the following, the details about the geophysical characterization of the HydroGeosITe are presented, as well as the inversion procedure for the joint interpretation of inductive and galvanic data and the modelling results.

SITE CHARACTERIZATION

The HydroGeosITe is located in northern Italy, close to the southern margin of the Italian Alpine chain (Fig. 1), within a fluvioglacial and glacial depositional environment which lays on bedrock, supposedly Pliocene marine bedrock. Therefore, the near surface deposits expect the complex superimposition and interdigitation of morain and fluvial deposits due to the repeated advance and retreat of the glacial system (Plesitocene) followed by the quaternary alluvial deposit of Chiese river's alluvial plain (Conti et al., 2009).

AEM acquisitions.

The geophysical characterization has been carried out through AEM acquisition, ground EM surveying with four different systems and galvanic acquisition of DCIP data (Figure 2).

In particular, SkyTEM AEM data (Fig. 2, bottom left map) have been acquired in 2021 through the SkyTEM 312 system, and the AEM characterization is going to be repeated with the new SkyTEM 306HP within summer 2023, to overlap the geophysical ground measurements with three different flight heights to ensure the absence of system bias.

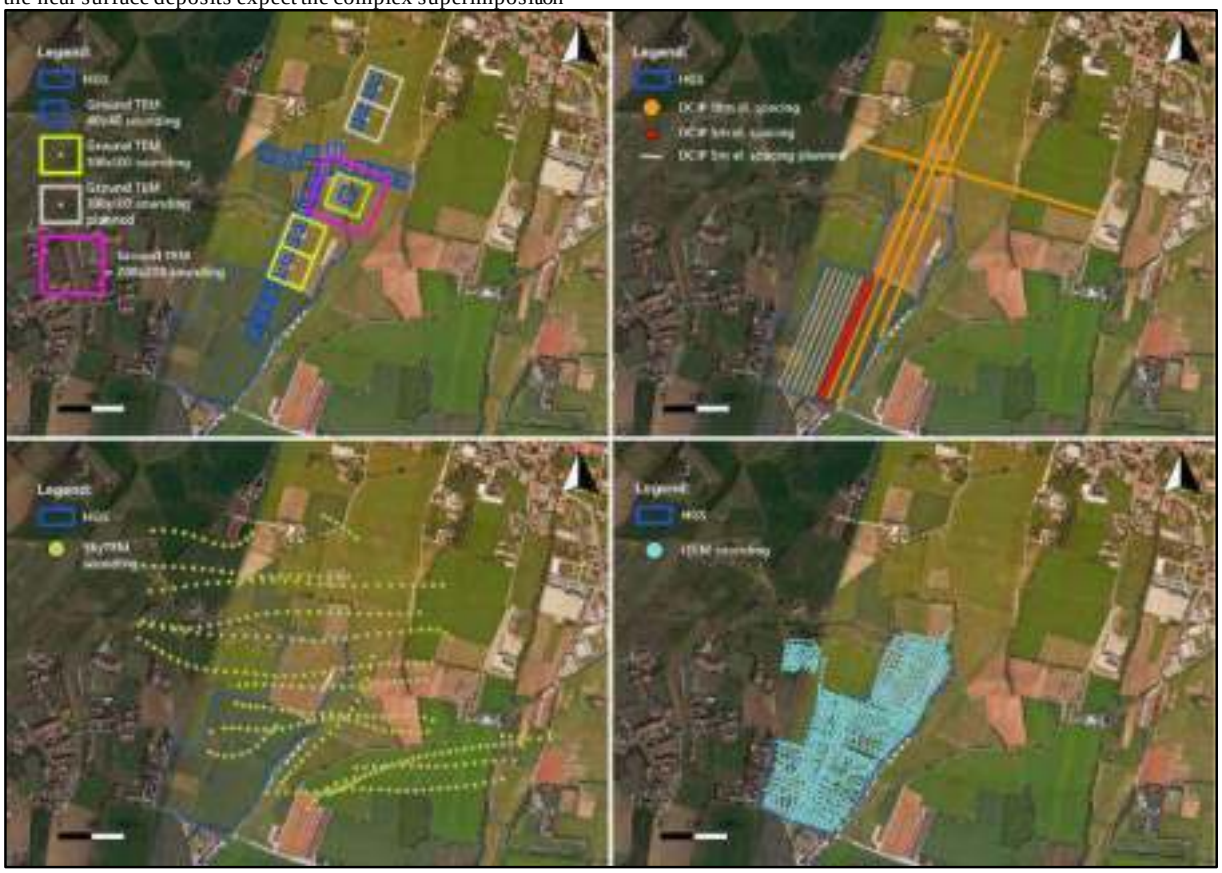

Figure 2: Maps of the geophysical surveys carried out (coloured lines/symbols) and planned (grey lines/symbols) at the HydroGeosITe, with the perimeter of the area always accessible indicated in blue (HGS in the legend). Top left – Ground TEM soundings with 40x40 m^2 (blue squares) 100x100 m^2 (yellow/grey squares) and 200x200 m^2 (magenta square) loop sizes. Top right – DCIP profiles with 10 m spacing (dotted orange lines, ≈ 4 km) and 5 m spacing (dotted red/grey lines, ≈ 4 km) Bottom left – SkyTEM 312 2021 soundings; further AEM data will be acquired by SkyTEM 306HP system in 2023 at 3 different flight heights along NS/EW profiles. Bottom right – tTEM soundings; the same area has been covered with the Loupe system.

Ground TEM acquisitions

Several ground transient electromagnetic (TEM) soundings have been measured with the ABEM WalkTEM 2 instrument in central-loop configuration, with two different transmitter units (TX-20 and TX-60, with 20 ampere and 60 ampere peak-to-peak maximum current, respectively) and three transmitter sizes (Fig. 2, top right map):

- thirty 40x40 m^2 Tx-20 soundings, with 30 minutes of stacking time and 10 ms of acquisition time;
- five 100x100 m^2 Tx-60 soundings, with 60 minutes of stacking time and 30 ms of acquisition time;
- one 200x200 m^2 Tx-60 sounding, with 100 minutes of stacking time and 30 ms of acquisition time.

All soundings were measured with two different receivers, RC5 and RC200, with 5 m^2 and 200 m^2 effective area, respectively.

The 40x40 m^2 soundings reached approximately 300 m of depth of investigation (Christiansen and Auken, 2012), while the 100x100 m^2 went down to ≈ 400 m and the 200x200 m^2 down to ≈ 700 m.

tTEM and Loupe acquisitions
The tTEM system (Auken et al., 2019) has been employed to acquire more than 30 km of data (Fig. 2, bottom right) through a 3x3 m^2 transmitter with receiver in offset configuration (-9.5 m from the transmitter). This system allows to carry out continuous TEM measurements when pulled by an ATV vehicle at the max speed of 20 km/h, to retrieve subsoil models up to ≈ 100 meters of depth. The same area has been surveyed with the Loupe portable system (Street & Duncan 2018) over 20 km of lines.

DCIP acquisitions
The DCIP data have been measured with the ABEM Terrameter LS2 system in 100% duty cycle (Olsson et al., 2015) with full waveform acquisition, and gated after harmonic denoising and drift removal following Olsson et al. (2016). As shown in Fig. 2, top right panel, approximately 4 km of data have been measured with 10 m electrode spacing, and another 4 km with 5 m electrode spacing (0.8 km have been already acquired and the acquisition of another 3.2 km is planned for late April). The gradient protocol has been used for acquisition, with 12 seconds of acquisition time and two stacks per quadrupole, with mean injected current of approximately 0.5 Amperes. The number of quadrupoles acquired among the different profiles ranges between 1400 and 2700 ca., depending on the profile length and the electrode spacing.

Drillings
Three drillings down to a few hundreds of meters (100 m, 190 m, 350 m) are going to be executed within summer 2023, with lithological description and resistivity logs.

DATA MODELLING AND JOINT INVERSION SCHEME

Inductive and galvanic data give usually significantly different inversion models, due to their different sensitivity to the resistivity distribution. Often resistivity anisotropy is used to justify the lack of accordance between the two methods (e.g. Christiansen et al., 2007), even if recent publications have shown compatibility between AEM and galvanic data (Christensen, 2022), but without considering the induced polarization effect. However, Fiandaca et al. (2022) have shown that the IP phenomenon has a strong effect on inductive data also in environmental applications, with significant dependence of the effect on the system characteristics.

Following these findings, we propose a joint inversion scheme that models both galvanic and inductive data taking into induced polarization. In particular, the inversion is carried out following Fiandaca et al. (2023) with EEMverter, a software specifically designed for modelling IP in joint inductive/galvanic inversions.

EM data are modelled in 1D, while the galvanic DC and full-decay IP data are modelled in 2D (Fiandaca et al., 2013) in terms of the maximum phase angle (MPA) Cole-Cole re-parameterization (Fiandaca et al., 2018). The objective function of the inversion is defined as:

$$Q = \left[\frac{1}{N_d+N_r}\left(\sum_{i=1}^{N_d}\frac{(d_{obs}-d_{forward})^2}{\sigma_{d_i}^2} + \right.\right.$$
$$\left.\left. + \sum_{i,j}\frac{(m_i-m_j)^2}{\sigma_{r_{i,j}}^2}\right)\right]^{\frac{1}{2}} \quad (1)$$

Where N_d and N_r are the numbers of data d_{obs} (both inductive and galvanic) and roughness constraints (on the unique joint model $\boldsymbol{m}$), respectively, and the balance between inductive and galvanic data is achieved through their standard deviation σ_d. The independent inversions have been carried out with the same forward schemes of the joint inversion, but using only one data type at once. All data have been processed in EEMstudio (Sullivan et al., 2023) for culling outliers out before inversion.

RESULTS

The resistivity sections of the joint MPA inversion models of two crossing profiles, oriented North-South and West-East, are presented in Figure 3, together with the inversion models of inductive-only data and galvanic-only DCIP data, while Table 1 shows the data misfits of all the inversions, divided by data type and profile.

Table 1: Final misfit of all the different datasets employed within independent and joint inversions.

			Data misfit			Data num.
			Inductive Inversion	Galvanic Inversion	Joint Inversion	
P1 N S	SkyTEM		1.3	/	1.6	296
	Walk TEM	RC5	1.0	/	1.5	532
		RC200	1.05	/	1.8	624
	tTEM		/	/	1.5	1686
	DCIP	DC	/	1.1	1.1	2773
		IP	/	1.7	1.6	67791
P2 W E	SkyTEM		1.3	/	1.4	667
	Walk TEM	RC5	1.9	/	1.9	274
		RC200	2.0	/	2.0	373
	tTEM		/	/	/	1686
	DCIP	DC	/	1.1	1.0	1180
		IP	/	1.3	1.2	29631

In particular, SkyTEM data, 40x40 m^2 ground EM data, tTEM data and DCIP data are jointly inverted along the 1.2 km long North-South profile, while SkyTEM data, 40x40 m^2 ground EM data and DCIP data are inverted along the 0.8 km long West-East profile (with 10 m electrode spacing in both DCIP profiles).

The misfit analysis shows that the joint inversion is able to fit the data reasonably well compared to the galvanic and inductive independent inversions. However, the joint inversion takes fully into account the IP phenomenon also in the inductive data, and shows much more definition in the reconstruction of the resistivity model. This is in accordance with the synthetic tests presented in Fiandaca et al. (2023), which show how inductive and galvanic data complement each other in retrieving accurate values for both conductive and resistive anomalies the joint inversion, contrary to the independent inversions.

These findings are in agreement also with the borehole information available at this time, i.e. the lithological

description of a borehole on the North-East of the profiles. Indeed, the thin resistive layer evident in the joint inversions at depth around 60 meters is in accordance with a conglomerate layer found in the borehole.

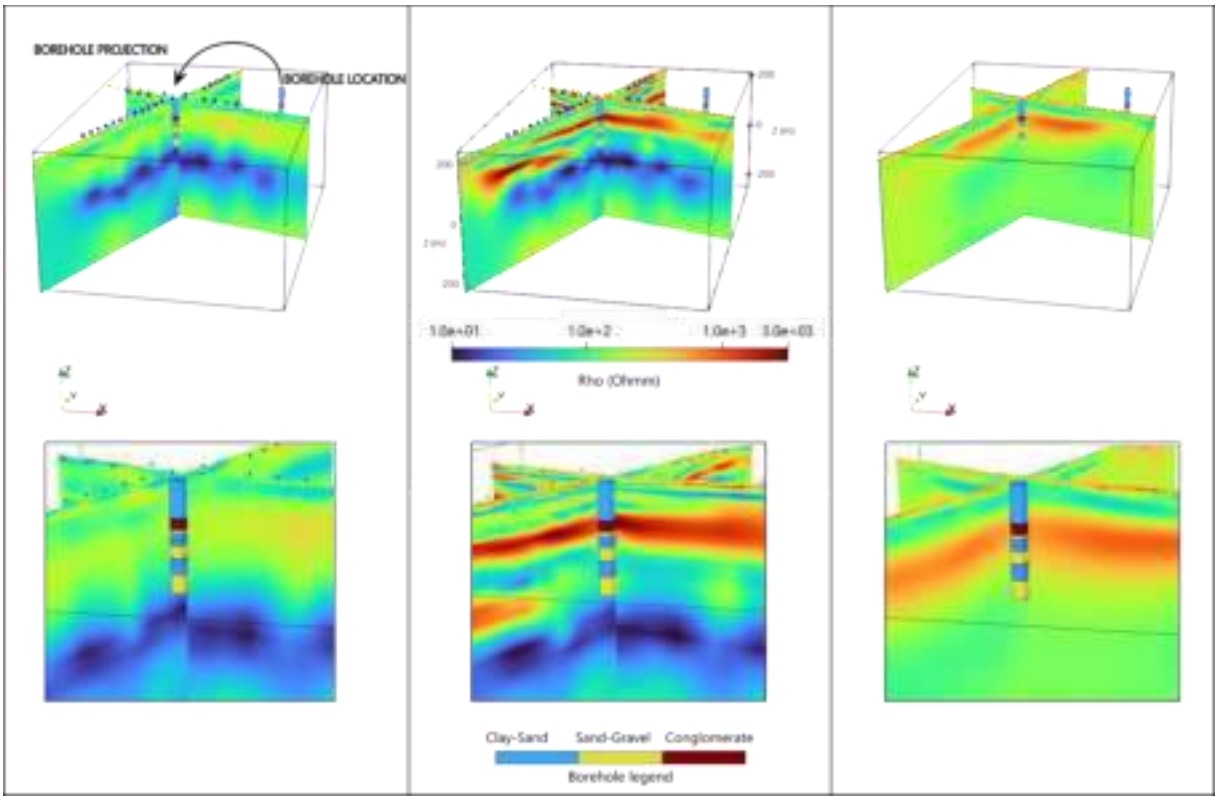

Figure 3: Inversion models of the crossing North-South and West-East profiles obtained through inductive-only AEM and ground TEM data (left), joint AEM-Ground EM-tTEM-DCIP data (center) and galvanic-only DCIP data (right), with full profile view in the top panels and zoom-in close to the crossing point in the bottom panels. The lithological description of a borehole near to the profiles is shown in color bars; for helping the comparison between borehole information and inversions, the borehole has been projected from its true position to the crossing point of the profiles. Ground EM, SkyTEM, tTEM sounding positions and electrodes are indicated with the same color coding of Figure 2.

Furthermore, the joint model shows higher resolution in the shallow subsoil (<50 meters from the surface), depicting some conductive bodies not shown even in the EM independent inversion. The Loupe data have not been used in this joint inversion yet, because the Loupe system is very sensible to the acquisition geometry, which presents pitch, roll and yaw in both transmitter and receiver. We are currently working on a new inversion scheme for loupe data, able to model the transmitter/receiver geometry thanks to the on-time measurement of the primary field. Further improvements are also pursued for the WalkTEM data fits, allowing for small deviation of the receiver area from the nominal value.

CONCLUSIONS

This study presents the geophysical characterization of the HydroGeosITe, the calibration and reference site for the largest AEM campaign ever carried out in Italy for groundwater mapping and management. AEM data have been acquired at the site, together with ground-based TEM data with 40x40 m^2, 100x100 m^2 and 200x200 m^2 transmitter area and full-decay DCIP galvanic data; furthermore, ground-based TEM data in continuous acquisition, measured with the tTEM and Loupe systems, have been measured.

The inductive and galvanic data have been successfully inverted in a joint scheme that takes into account induced polarization, with data misfit comparable with independent inversions. However, the joint inversion shows significantly improved resolution, in accordance with the available borehole information and synthetic tests. Further validation of these inversion results will be provided shortly, through the analysis of the borehole drillings that are going to be completed within the 2023 summer. The lithological and resistivity logs that are going to be retrieved in the new drillings will help in the interpretation of the results of the AEM ongoing campaign. We believe that all this information will make the HydroGeosITe a significant calibration and reference site not only within the ongoing Italian AEM campaign, but also for the entire AEM community.

ACKNOWLEDGMENTS

The HydroGeosITe project is funded by A2A Ciclo Idrico S.p.A. We acknowledge Emergo S.r.l for the support with AEM data.

REFERENCES

Auken E., Foged N., Larsen J.J., Trøllund Lassen K.V., Maurya P.K., Dath S.M., Eiskjær T.T (2019). tTEM — A

towed transient electromagnetic system for detailed 3D imaging of the top 70 m of the subsurface. *Geophysics, 84 (1), E13-E22*.

Brodie R. C., Cooper, Y., (2018). Spatially and conductivity Log constrained AEM inversion. *AEGC2018 – 1st Australian Exploration Geoscience Conference, 18-21 February 2018, Sydney, Australia*.

Christensen, N. B. (2022). Joint inversion of airborne TEM data and surface geoelectrical data. The Egebjerg case. *Journal of Applied Geophysics*, *196*, 104511.

Christiansen, A. V., Auken, E., Foged, N., & Sørensen, K. I. (2007). Mutually and laterally constrained inversion of CVES and TEM data: a case study. *Near Surface Geophysics*, *5*(2), 115-123

Christiansen, A. V., Auken, E., & Viezzoli, A. (2011). Quantification of modeling errors in airborne TEM caused by inaccurate system description. *Geophysics*, *76*(1), F43-F52.

Christiansen, A.V. & Auken, E. (2012). A global measure for depth of investigation. *Geophysics*, *77*(4), WB171-WB177. Conti M. and Conti A., Tech. Rep. Comune di Bedizzole, Comune di Bedizzole (2009)

Fiandaca, G., Ramm, J., Binley, A., Gazoty, A., Christiansen, A. V., & Auken, E. (2013). Resolving spectral information from time domain induced polarization data through 2-D inversion. *Geophysical Journal International*, *192*(2), 631–646.

Fiandaca, G., Madsen, L. M., & Maurya, P. K. (2018). Re-parameterisations of the Cole–Cole model for improved spectral inversion of induced polarization data. *Near Surface Geophysics*, *16*(4), 385-399.

Fiandaca, G. Dauti, F., Signora A., (2022). Effect of induced plarization on galvanic and inductive data: where is it stronger? *Near Surface Geoscience Conference, 18-22 September 2022, Belgrade, Serbia*

Fiandaca, G., Zhang, B., Chen, J., Signora, A., Dauti, F., Galli, S., Sullivan, N.A.L., Viezzoli, A. (2023). Closing the gap between galvanic and inductive methods: EEMverter, a new 1D/2D/3D inversion tool for Electric and Electromagnetic data with focus on Induced Polarization *AEM2023 - 8th International Airborne Electromagnetics Workshop, 3-7 September 2023, Fitzroy Island, QLD, Australia*.

Foged, N., Auken, E., Christiansen, A. V., & Sørensen, K. I. (2013). Test-site calibration and validation of airborne and ground-based TEM systems. *Geophysics*, *78*(2), E95-E106.

Olsson, P. I., Dahlin, T., Fiandaca, G., & Auken, E. (2015). Measuring time-domain spectral induced polarization in the on-time: decreasing acquisition time and increasing signal-to-noise ratio. *Journal of Applied Geophysics*, *123*, 316-321.

Olsson, P. I., Fiandaca, G., Larsen, J. J., Dahlin, T., & Auken, E. (2016). Doubling the spectrum of time-domain induced polarization by harmonic de-noising, drift correction, spike removal, tapered gating and data uncertainty estimation. *Geophysical Journal International*, *207*(2), 774–784.

Street, G., Duncan, A., Fullagar, P., & Tresidder, R. (2018). Loupe-a portable EM profiling system. *ASEG Extended Abstracts*, *2018*(1), 1-3.

Sullivan N. A. L., Viezzoli. A., Fiandaca, G.,(2023). EEMstudio: an open-source freeware QGIS plugin for processing, modelling and inversion of electric and electromagnetic data. *AEM2023 - 8th International Airborne Electromagnetics Workshop, 3-7 September 2023, Fitzroy Island, QLD, Australia*.

Going the extra mile – Julimar, a case study from Western Australia

Camilla Soerensen
Seequent
Skolegade 21, 8000 Aarhus C
Denmark
Camilla.soerensen@seequent.com

Tim Munday
CSIRO
26 Dick Perry Avenue, Kensington
Australia
Tim.munday@csiro.au

Toke Højbjerg Søltoft
Seequent
Skolegade 21, 8000 Aarhus C
Denmark
toke.soeltoft@seequent.com

SUMMARY

The Julimar Complex, which is located in Western Australia, hosts the recently discovered Gonneville deposit which contains massive sulphide mineralisation (Pd, Pt, Ni, Cu and Co). The deposit was discovered by using a moving loop EM survey and follow up geophysics including AEM confirmed the find.

In this study we use a SkyTEM AEM line which was acquired as part of the AUS-AEM initiative, which cross the Gonneville deposit. The objective is to extract as much information from that data as possible to demonstrate that AEM can be used for general geological mapping in addition to anomaly detection. By using several inversion methods and analysing the results we get an understanding of the most believable model.

In addition to a deterministic full non-linear inversion of the data, we also use a stochastic reverse jump Monte carlo Markov Chain inversion on the SkyTEM data.

The results from both algorithms are comparable and correlate well with the known geological information published by Chalice mining, based on drill holes and other geophysical surveys.

Using Airborne EM for exploring for minerals under cover could provide a lot more information about the subsurface than just mapping highly conductivity sulphide mineralisation zones.

Key words: Julimar, SkyTEM, AUS-AEM, RJ-McMC, Stochastic inversion

INTRODUCTION

The demand for critical minerals including Ni, Cu, and PGE's is projected to increase by over 30% annually to beyond 2050 (Gasson et al. 2021). Consequently, the exploration for these mineral systems has become a priority among juniors and majors alike. Careful planning, the analysis of large amounts of pre-competitive data, experienced geoscientists and a little bit of luck are some of the key ingredients to being successful. One such discovery was made in 2020 – when Chalice Mining went hunting for base metals within the Julimar Complex just 70km northeast of Perth, Western Australia. Chalice Mining first staked this greenfield project located within the emerging Western Yilgarn Ni-Cu-PGE province in 2018, based on a 26km long mafic-ultramafic intrusive complex interpreted from open file aeromagnetic surveys (Paggi et al. 2021).

The Gonneville deposit itself was then discovered following a moving loop EM survey – which showed multiple EM conductors (Paggi et al. 2021). Follow up RC drilling defined massive sulphide mineralisation containing Pd, Pt, Ni, Cu and Co from 48m downhole. Additional gravity, magnetics, downhole and airborne electromagnetic data were subsequently acquired over the Julimar Complex and has assisted in identifying new anomalies as well as improving the understanding of the geology and structure of the intrusion that is a key part of the mineral system present.

Airborne electromagnetic (AEM) methods can be a great tool for discovering anomalies – i.e., highly conductive bodies within a resistive host – in this case massive sulphide sources/zones and are as such commonly used for defining targets for follow up ground geophysics and drilling. They can however also be used for general geological mapping and therefore assisting in gaining an understanding of the geology surrounding the anomaly. Understanding the broader capability of an AEM system in mapping elements of a mineral system is relevant in exploration as these may vary in relative importance depending on the setting of interest.

The motivation for this study was to examine whether AEM data could be employed for more than simply identifying conductive targets. Through a detailed analysis of AEM data across the Gonneville deposit, we consider how these data can contribute to a broader understanding of the mineral system, by mapping elements of the host sequence in addition to mapping the highly conductive sulphide mineralisation zones. We also give consideration to the careful processing and alternative inversion approaches in the analysis of AEM data to maximise the information content they contain.

METHOD AND RESULTS

AEM system

As part of the AUS-AEM (https://www.eftf.ga.gov.au/ausaem) initiative airborne electromagnetic data were acquired over the Julimar complex in WA, in 2020 using the SkyTEM system. In this study we look at one line of data that pass through the Gonneville deposit (see Figure 1 for location) with the aim of trying to gain an understanding of the geology of the prospect based on the AEM inversion results.

For the part of the AUS-AEM survey that we look at, a SkyTEM^{312} FAST system was used. The SkyTEM system is a helicopter time domain electromagnetic system, which carries the transmitter and receiver as a sling load beneath the helicopter. It uses interleaved low and high moments, which provides information of both the near surface and deeper parts of the subsurface depending in the conductivity of the ground. The low and high moments have a base frequency of 275 Hz and 25 Hz respectively and nominal peak currents of 5.9 A and 109A. The low moment has 2 transmitter turns whereas the

high has 12, giving peak moments of 4036 Am^2 and 447336 Am^2 respectively.

Inversion algorithms

One of the key interests when exploring under cover, is to be able to define the depth of the mineralised zones, and the host units in which they sit. One way to achieve that might be to favour a few layer inversion model over a smooth one, as the former allows the layer boundaries to move, whereas the layer boundaries are fixed in a smooth layer model. Another option is to run a stochastic inversion where the output is a model as well as uncertainties related to that model. We examine the results of two inversion methods; a deterministic full non-linear 1D inversion (Auken et al., 2015, Auken and Christiansen, 2004), and a stochastic reverse jump Markov chain Monte Carlo inversion (Brodie and Sambridge, 2012, Brodie and Reid, 2013) and discuss the differences and commonalities between the results from the different methods and look at how they define elements of the mineral system at Gonneville.

The deterministic inversion approach finds one earth model that fits the data within the given noise level, often judged to be the best solution. The deterministic approach will usually be concerned with finding the global minimum, this process is also called an optimisation approach. In contrast the probabilistic method aims to not just settle for one model, but to collect statistics about all the models that are feasible after consideration of both data fit and prior information. The output from the probabilistic inversion is therefore an ensemble of models in the vicinity of the global extrema or possibly several local extremas.

The 1D full non-linear inversion was run using the Aarhus Workbench processing and inversion software. The data were processed in a standard way where late time noise was removed from the data before the inversion was run. Both a smooth layered inversion consisting of 30 layers and a few layer model were run. The results presented as a conductivity depth sections are shown in Figures 2A and 2B).

Results from a stochastic inversion using a reversible jump Markov chain Monte Carlo (rj-McMC) 1D inversion algorithm for the same data are presented in Figures 2C and 2D). In a stochastic inversion a suite of tens to hundreds of thousands of models are generated – which all fit the data within the specified noise levels. The reversible jump part of the algorithm means, that the number of layers for the model does not need to be specified beforehand, as the inversion explores a range of models with different number of layers but favours the models with the fewest number of layers.

Geology

The Gonneville deposit is hosted in a 1.6 x 0.8 km ultramafic-mafic intrusion within the Julimar Complex which has a >26km strike length and is up to 3km wide (Paggi et al. 2021). The Gonneville intrusion strikes NNE and covers an area of approximately 1.9 x 0.9km and is interpreted as an ultramafic-mafic sill with a maximum thickness of app 650m, with an approximate 45degree WNW dip and gentle northerly plunge. The intrusion is predominantly composed of serpentinised olivine peridotite/harzburgite with lesser intervals of pyroxenite, gabbro and leucogabbro. PGE-Ni_Cu_Co-Au sulphide mineralisation is widespread throughout these mafic and ultramafic units The main intrusion is cut by a later granite body that is parallel to the dip and strike of the mafic-ultramafic package. The intrusive complex is crosscut by a series of sub vertical NE to NW striking dolerite dykes, these contain no Ni-Cu-PGE mineralisation. The Gonneville intrusion is surrounded by a package of meta-sedimentary rocks. The regolith profile in the area extends to a depth of 30-40m below the surface with well-developed laterite and saprolite.

Primary Ni-Cu-PGE sulphide mineralisation within the Gonneville deposit is mostly found in the ultramafic harzburgite and pyroxenite domains. The mineralisation occurs as sub-parallel zones which are typically 5-40m thick and found within broader 100-150m zones of weakly disseminated sulphides. The sulphide content correlates well with the metal grade, with higher sulphide concentrations corresponding to higher metal contents (Chalice mining ASX release November 2021). PGE's are also hosted in the regolith from near surface to 25m depth (see Figure 4). In addition to the Gonneville mineralisation, further prospects to the north have been identified from an Airborne Electromagnetic survey conducted by Chalice Mining using the HeliTEM electromagnetic system (Figure 1). These are the Hartog prospect immediately to the NNE of Gonneville and extending over 6.5km, Baudin which is located 3.5km NE of the northern tip of Hartog and Jansz a further 6km NE of Baudin. While considerable knowledge has been gained on the geometry of the Julimar complex, much remains to be learned about the specific geometry of mafic intrusions, and how they vary through the region. Potentially AEM data can contribute to this understanding.

Results

The deterministic and the probabilistic inversions map a highly conductive zone that is associated with the Pyroxenite unit on the eastern side of the Gonneville intrusion. (Figure 3). The results from the different inversion approaches (see Figure 2) shows that the inverted models all map a conductive regolith profile (from surface to 30-40m). The mean model from the rj-McMC inversion (Figure 2C) suggest the regolith has a relatively uniform thickness particularly on the western side of the intrusion, conforming with the interpretation from drilling (Figure 4) A comparison between the model sections and the geological section (Figure 4) shows that the mafic-ultramafic units dip westwards corresponding well with the observed 45-degree WNW dip in the geological section. Zones of mineralisation a defined in drilling by Chalice Mining corresponds well with the zones of higher conductivity, but the AEM data does not appear to define specific high-grade zones associated with mineralisation, rather the models suggest the AEM defines an amalgamated response from sub-parallel zones.

The main benefit of using a rj-McMC inversion is the possibility to explore the uncertainties related to the obtained models, and therefore also be able to establish both layer boundaries and conductivities with greater certainty. One of the many outputs of the rj-McMC inversion is the possibility to identify and visualise changepoints. These indicate the depth at which interfaces were most likely to occur in the models that were accepted into the Markov chains (Figure 2E). Although being a "busy" figure, it does provide some confidence in which layer boundaries are likely to be present, but also what areas of the model that layers are expected to be homogeneous and continuous.

DISCUSSION AND CONCLUSIONS

Both the deterministic and stochastic inversions can map the highly conductive zones associated with the Gonneville Intrusion. However, when comparing results from different inversion algorithms consideration needs to be given to whether the algorithms account for noise in a similar way, (see discussion by Mulé et al. 2019). Currently the GA-AEM code used for the rj-McMC inversion does not allow for a different number of gates to enter the inversion – i.e., removing late-time noise for individual soundings is not an option. This is an option in in AarhusInvn (the inversion algorithm used by Aarhus Workbench).

Another thing to keep in mind is that these data may benefit from running an inversion that accounts for IP effects, as they appear to be present in the data, particularly for the more resistive areas surrounding the Gonneville Deposit.

We conclude that by carefully processing and inverting the AEM data, it is possible to map a broader range of geological elements that characterise the Gonneville mineral system,rather than just sulphide mineralisation. Although the deterministic inversion provides a model, that corresponds well to the geological information – it may be beneficial to look at the deterministic and stochastic inversion in conjunction, to better establish layer boundaries and broader characteristics of the intrusion.

REFERENCES

Auken, E., and A.V. Christiansen. 2004. Layered and laterally constrained 2D inversion of resistivity data. Geophysics 69: 752–61.

Auken, E., A.V. Christiansen, G. Fiandaca, C. Schamper, A.A. Behroozmand, A. Binley, E. Nielsen, et al. 2015. An overview of a highly versatile forward and stable inverse algorithm for airborne, ground-based and borehole electromagnetic and electric data. Exploration Geophysics 46: 223–35.

Brodie, R., and Sambridge, M., 2012, Transdimensional Monte Carlo Inversion of AEM Data: 22nd International Geophysical Conference and Exhibition, Australian Society of Exploration Geophysicists, Extended Abstracts.

Brodie, R. and Reid, J., 2013, Monte Carlo Inversion of SkyTEM^{TM} AEM data from Lake Thetis, Western Australia. 23rd International Geophysical Conference and Exhibition, ASEG, Extended Abstracts.

Chalice mining, https://chalicemining.com/ ASX release November 2021, accessed April 2023.

Gasson, B Lewis C and Martin, K, 2022 Outlook for Selected Critical Minerals 2021, Department of Industry, Science, Energy and Resources (DISER), Australian Government, 2021, p 4.

Mulé, S., Soerensen, C. and Munday, T., 2019, Handling noise in AEM inversion – implications for subsurface characterisation. ASEG Extended Abstracts.

Paggi, J., Frost, K. and Kendall, B., 2021, The Role of Geophysics in the Discovery of the Gonneville PGE-Ni-Cu-Co-Au Deposit, Julimar, Western Australia. MAG21 Symposium, ASEG.

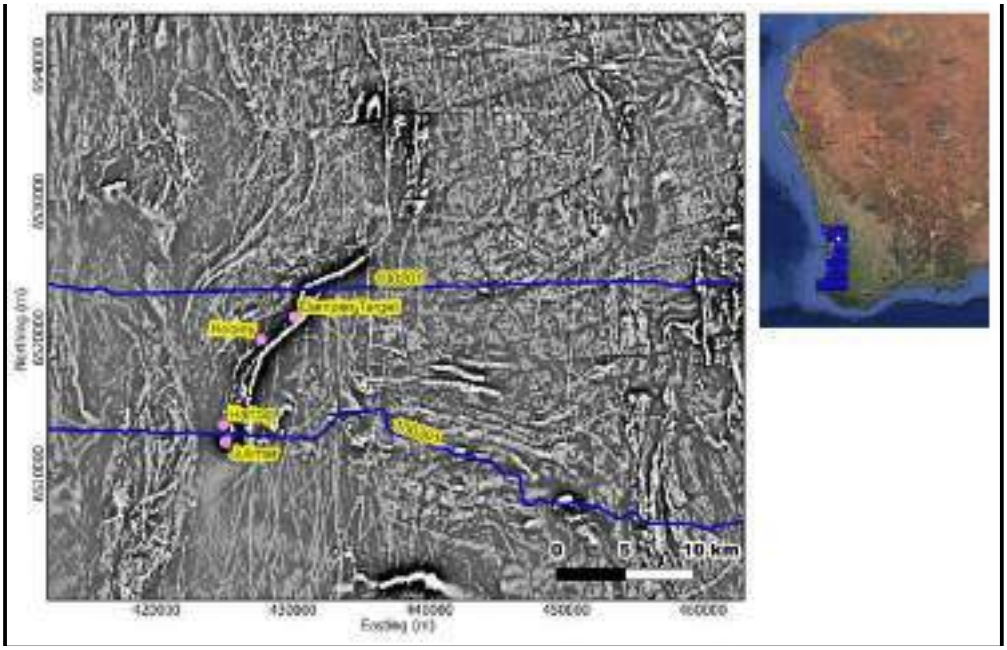

Figure 1. The location of the two AUS-AEM lines (100201 and 100301) closest to the Julimar complex, and the main targets overlaid on the TMI RTP1VD magnetic image.

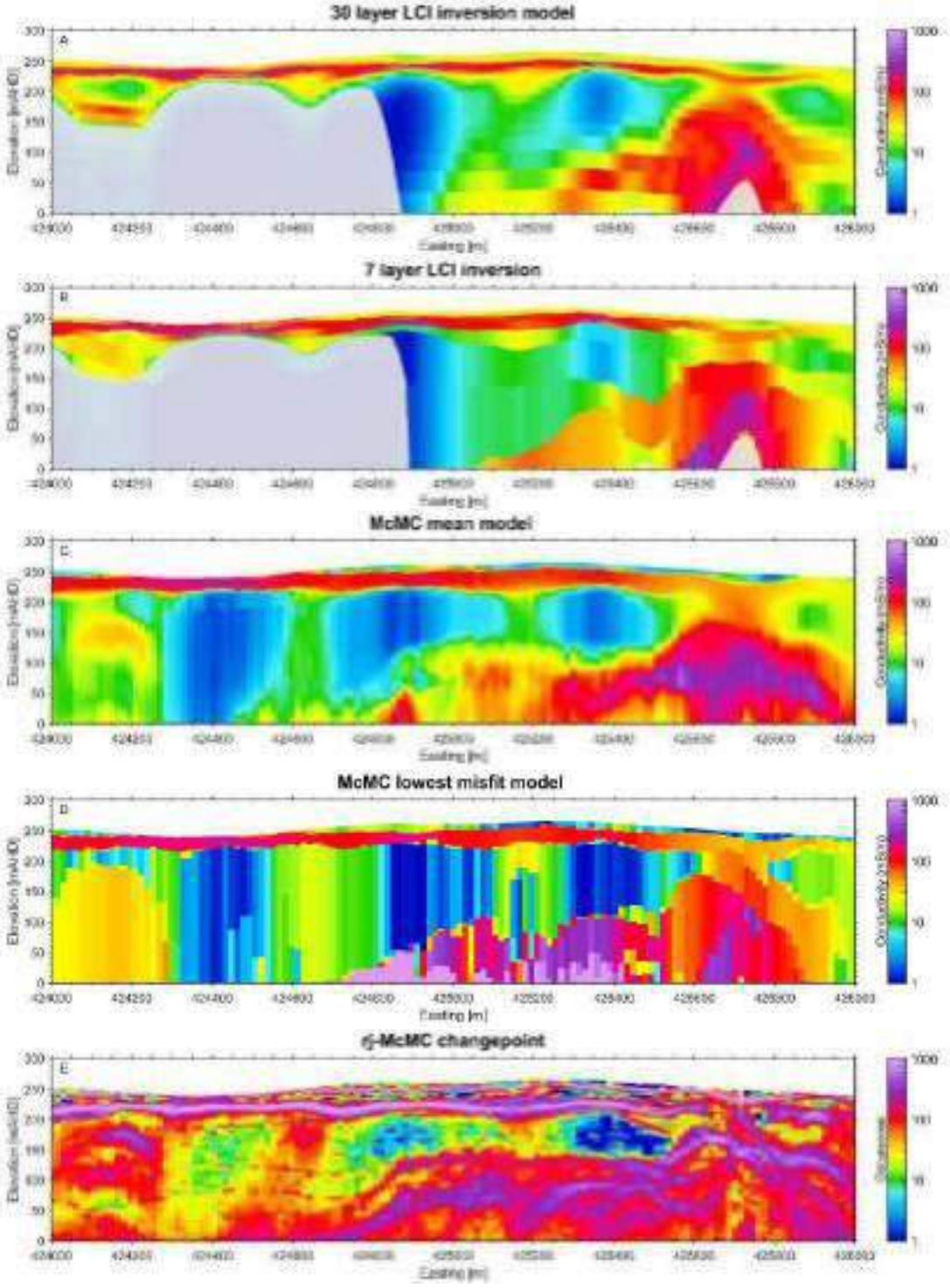

Figure 2. The results of the different inversions of line 100301 over the Gonneville prospect. A-B show the inversion result from using a 30 and 7 layer model discretization following a full processing of the data before inverting them using Aarhus Workbench. Panel C and D show the mean and lowest misfit models obtained by running a stochastic rj-McMC inversion.

Panel E shows a plot of the "changepoints" which indicate the depth at which interfaces were most likely to occur in the models that were accepted into the Markov chains.

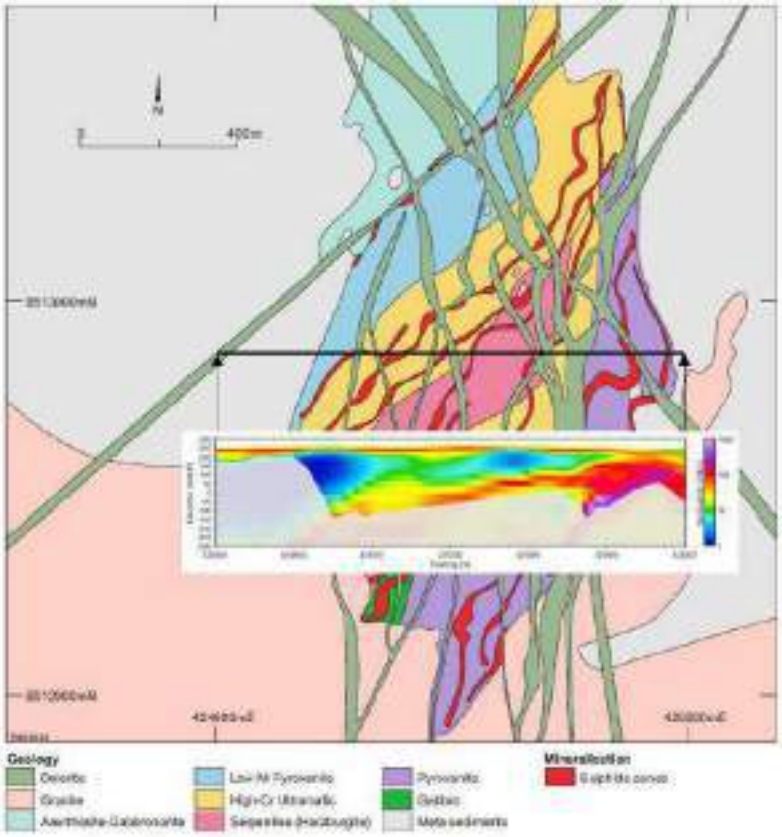

Figure 3. (Adapted from Chalice) shows the Gonneville intrusion plan view along with the location of the AUS-AEM SkyTEM line (shown by black line) and the inverted model section.

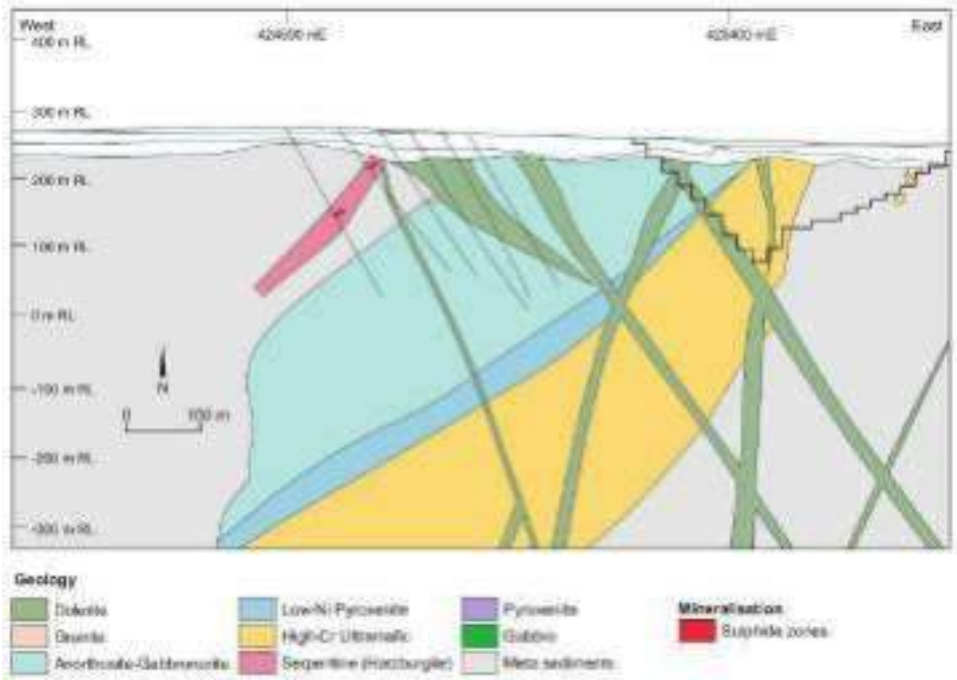

Figure 4. Geological cross section (adapted from Chalice), showing the resource pit, the mineralisation zones as well as the geology.

TEMPEST electromagnetic transmitters with multiple loops and multistep waveforms

Andrew Sunderland
University of Western Australia
35 Stirling Highway Crawley WA Australia
andrew.sunderland@uwa.edu.au

Eric Steele
Xcalibur Multiphysics
10 Compass Road Jandakot WA Australia
eric.steele@xcaliburmp.com

SUMMARY

The vertical resolution of airborne electromagnetic systems is limited by the earliest time window and how fast the transmitter current can transition. Presented is how transmitter loop geometry and different transmitter waveforms could decrease the transmitter ramp time by up to a factor of 8.

Key words: transmitter, electromagnetic, resolution, waveforms.

INTRODUCTION

Good vertical resolution is needed for electromagnetic surveys trying to delineate structural boundaries between layers such as mapping saltwater/freshwater interfaces (Viezzoli et al, 2012). Good vertical resolution comes from early delay time measurements taken immediately after the transmitter current is switched off (Skurdal et al, 2020). However, the earth response immediately following a linear turn-off ramp is smeared out over a time scale proportional to the duration of the ramp. The vertical resolution is (Spies, 1989):

$$\text{vertical resolution in meters} = 0.55\sqrt{\frac{2\rho\Delta t}{\mu}} \qquad (1)$$

where Δt is ramp time, ρ is the resistivity of the ground, and μ is magnetic permeability.

Inductance and voltage set how fast the transmitter current can be ramped down $\Delta t = L \cdot \Delta I/V$. Excessive voltages V can overload the semiconductor switches or cause electrical arcing. Previous efforts by the industry to achieve a quick turn off time have come at a cost of lower transmitter current I and consequently reduced depth penetration. This paper presents a transmitter loop with lower inductance L and demonstrates how to replace a large current step ΔI with several smaller current steps.

MULTILOOP

Figure 1 compares a single loop transmitter with a multiloop transmitter layout using 2 parallel half loops with the same overall area. Let I_0 be defined as the current in a loop and L_0 as the inductance of a single loop. Baum (2005) showed that for a subdivided loop:

$$\text{current provided by electronics, } I = N_p I_o \qquad (2)$$

$$\text{inductance presented to electronics, } L = L_0/N_p^2 \qquad (3)$$

$$\text{ramp time, } \Delta t = LI/V = L_o I_o/(N_p V) \qquad (4)$$

The ramp time Δt is thus inversely proportional to the number of subdivided loops in parallel N_p.

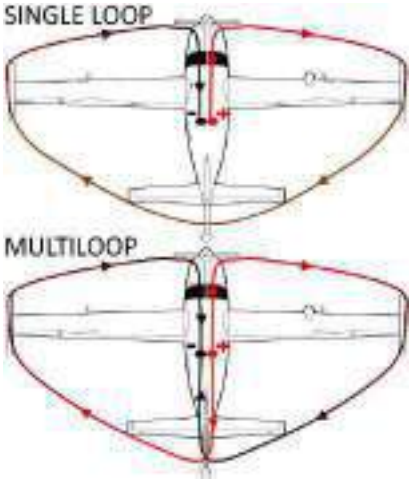

Figure 1. Single and multi-loop transmitter layouts. Current flows from + to -.

Transmitters with parallel sub-loops have previously been used in ground geophysics (Guo et al 2010), but not in airborne exploration.

MULTISTEP

Figure 2 shows multistep transmitter waveforms which have the same transmitter moment $\mathrm{m} = NI_{rms}A$ as a square wave. Large current steps have been replaced with smaller but more frequent current steps ΔI and shorter ramp times Δt. The ramp time of a multistep waveform is:

$$\Delta t = \frac{L \cdot \Delta I}{V} = \frac{2LI_{rms}}{V\sqrt{s}} \qquad (5)$$

where s is the number of current steps per half cycle.

Fourier transforms of the multistep waveforms are presented in Figure 3. Billions of multistep waveforms were examined with a computer program and only a small number of waveforms were found to have spectra matching a square wave. The multistep waveforms shown here have amplitudes that are identical to that of a square wave and only the phases of the spectrum need to be adjusted to align with that of the perfect square wave, and whereby no noise is added.

For a system using a multistep waveform, the ground response signal can be de-convolved into to a 100% duty cycle square wave, by using this formula or similar (Legault et al, 2012):

$$V_{sq}(f) = \frac{I_{sq}(f) \cdot V(f)}{I(f)} \qquad (6)$$

where $V(f)$ is the Fourier transform of the receiver voltage, $I(f)$ is the Fourier transform of the transmitter current, $I_{sq}(f)$ is the Fourier transform of an ideal square wave transmitter current, and f is frequency. This transformation allows a single transient decay to be presented which is easy to interpret (Lane et al, 2000). A multistep waveform with 2 steps per half cycle is currently used in TEMPEST (Lane et al, 2000).

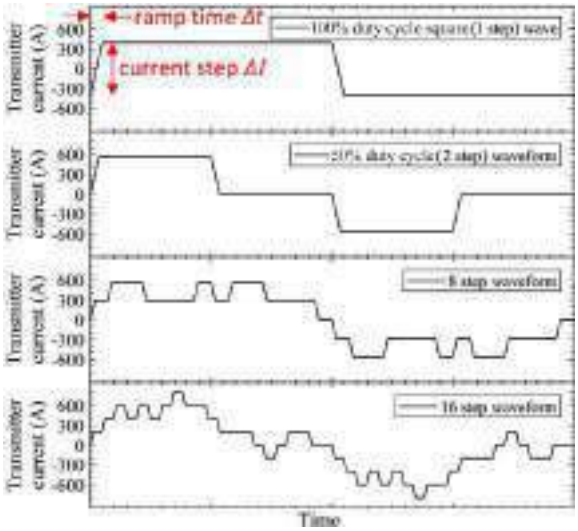

Figure 2. Multistep transmitter waveforms with identical rms currents I_{rms} and ramp rates $\partial I/\partial t$. The higher order waveforms have more steps per half period, smaller current steps ΔI, and smaller ramp times Δt.

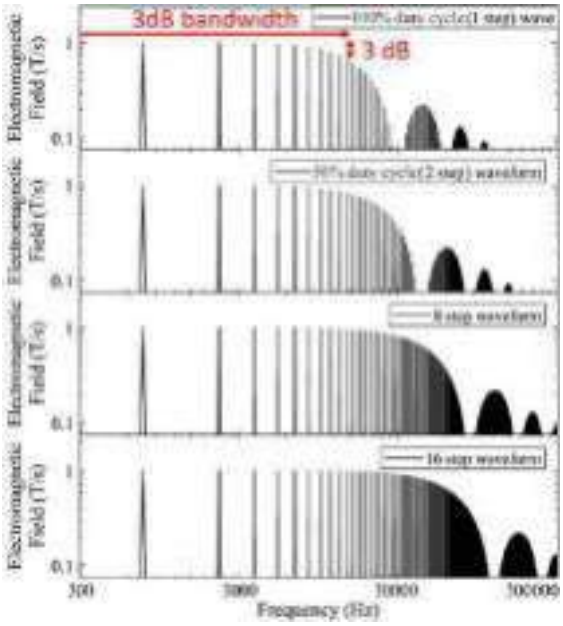

Figure 3. Fourier transforms of the waveforms shown in figure 2. The waveforms shown here are comprised of only odd harmonics of equal amplitude, up to a bandwidth of the transmitter. The higher order waveforms have a wider 3dB bandwidth due to shorter ramp times.

IMPROVED MAPPING

Combining multistep $s = 16$ current steps (Equation 5) with multiloop $N_p = 2$ (Equation 4) could decrease the ramp time by a factor of 8:

$$\Delta t \propto \frac{1}{N_p\sqrt{s}} \tag{9}$$

Electromagnetic waves diffuse downward as per the square root of time, depth $d = \sqrt{(2t\rho/\mu)}$. Figure 4 shows the mapping capability of an electromagnetic system which is limited by its earliest and latest time t windows. A system with 8 times lower ramp time will have √8 better vertical resolution (Spies, 1989).

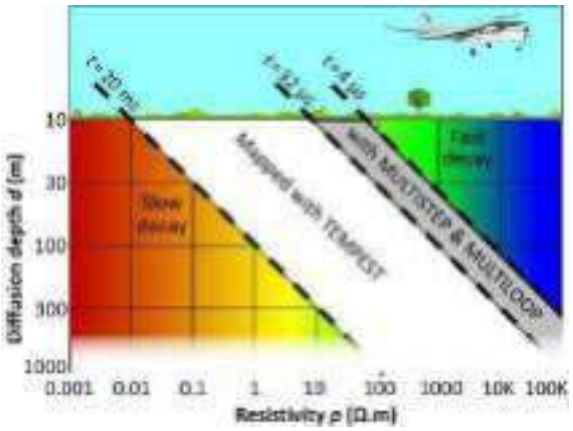

Figure 4. The minimum depth (vertical resolution) and maximum depth of a typical airborne electromagnetic system depends on the earliest and latest time windows and varies with the resistivity of the ground. The grey parallelogram shows the additional shallow and resistive geology that might be mapped with multistep and multiloop.

CONCLUSIONS

Multiloop geometry and multistep waveforms could potentially decrease the transmitter ramp time by a factor of 8. However, to make meaningful measurements of the earth response at early delay times may also require compensating the large primary field and snubbing any high frequency ringing in the transmitter electronics. An electromagnetic system with these improvements could have up to √8 better vertical resolution.

Combining a high transmitter moment and a quick transmitter ramp in a single waveform, could also give better vertical resolution at depth.

ACKNOWLEDGMENTS

The authors thank Teo Hage, Li Ju, Peter Wolfgram, and Aidan Loasby for their valuable help and suggestions.

REFERENCES

Viezzoli A., Munday T., and Ley-Cooper A.Y., 2012. Airborne electromagnetics for groundwater salinity mapping: Case studies of coastal and inland salinisation from around the world. *Bollettino di Geofisica Teorica ed Applicata* 53: p581-599 (2012).

Skurdal, G.H., Pfaffhubera, A.A., Davis, and A., Bazina, S., 2020. Improved near-surface resolution in geotechnical

applications using very early AEM time gates. *Exploration Geophysics* 51: 184–192

Spies, B.R., 1989. Depth of investigation in electromagnetic sounding methods. *Geophysics* 54: p872-888.

Baum, C.E., 2005. Compact low-impedance magnetic antennas. International Conference on Electromagnetics in Advanced Applications, http://ece-research.unm.edu/summa/notes/SSN/Note470.pdf

Guo, W.B., Xue, G.Q., Li, X., Quan, H.J., and Zhou, N.N., 2010. Study and Application of the Multiple Small-aperture TEM System. *Preview* 17: 17-22.

Legault J.M., Prikhodko A., Dodds D.J., Macnae J.C., and Oldenborger, G.A., 2012. Results of Recent VTEM Helicopter System Development Testing over the Spiritwood Valley Aquifer, Manitoba. *Symposium on the Application of Geophysics to Engineering and Environmental Problems Proceedings*: 114-130.

Lane, R., Green, A., Golding, C., Owers, M., Pik, P., Plunkett, C., Sattel, D., and Thorn, B., 2000. An example of 3D conductivity mapping using the TEMPEST airborne electromagnetic system. *Exploration Geophysics* 31: 162-172.

Using regional airborne electromagnetic conductivity data to characterise surface water groundwater interaction in the Cooper Creek floodplain in arid central eastern Australia

Neil Symington*
Geoscience Australia
Symonston
neil.symington@ga.gov.au

Tim Evans
Geoscience Australia
Symonston
tim.evans@ga.gov.au

Nadege Rollet
Geoscience Australia
Symonston
nadege.rollet@ga.gov.au

Larysa Halas
Geoscience Australia
Symonston
larya.halas@ga.gov.au

John Vizy
Geoscience Australia
Symonston
john.vizy@ga.gov.au

Sarah Buckerfield
Geoscience Australia
Symonston
sarah.buckerfield@ga.gov.au

Anandaroop Ray
Geoscience Australia
Symonston
anadaroop.rayr@ga.gov.au

Yusen Ley-Cooper
Geoscience Australia
Symonston
yusen.leycooper@ga.gov.au

Ross C. Brodie
Geoscience Australia
Symonston
Ross.Brodie@ga.gov.au

SUMMARY

Airborne electromagnetic (AEM) data has been acquired at 20 km flight line spacing across much of the Australian continent and electrical conductivity models generated by inverting these data are freely available. Despite the wide line spacing of these data, they are suitable for imaging the shallow subsurface and can greatly assist in understanding groundwater systems.

AEM data acquired using a fixed-wing towed system over the Cooper Creek floodplain, an ephemeral, anabranching river system in arid eastern central Australia, were inverted using deterministic and probabilistic methods. We integrate the AEM conductivity data with a range of surface and subsurface data to characterise the hydrogeology of the region and infer groundwater salinity from the shallow alluvial aquifer across an area of more than 14,000 km^2. The conductivity data reveal several examples of focused recharge through a river channel forming a freshwater lens within the more regional shallow saline groundwater system.

This work demonstrates that regional scale AEM conductivity data can be a valuable tool for understanding groundwater processes at various scales, with implications for water resource management. This work is particularly important in the Australian context, where high quality borehole data is typically sparse, but high quality geophysical and satellite data are often available.

Key words: AusAEM, groundwater, recharge, salinity

INTRODUCTION

Groundwater is a critical resource supporting communities, industry and the environment in many arid landscapes. High evapotranspiration rates and low rainfall in such settings often mean that groundwater recharge rates are very low with implications for water quality and responsible groundwater management. In such environments, focussed recharge through ephemeral streams during periods of high surface water flow is essential for replenishing near-surface aquifers. However, understanding recharge is challenging as borehole data is typically sparse and recharge processes may vary greatly in space and time. In this study we aim to improve understanding of surface water-groundwater interactions within the Cooper Creek floodplain, an ephemeral, anabranching river system located within the Lake Eyre Basin in arid eastern central Australia, by characterising the hydrogeological system using a range of geoscientific data including airborne electromagnetics (AEM).

The use of AEM in assessing shallow groundwater systems is becoming increasingly common, particularly in arid and semi-arid Australian landscapes (e.g., Costar et al., 2019; Mullen and Kellett, 2007). As part of the Exploring for the Future AusAEM program AEM data has been acquired at 20 km flight line spacing across large swathes of the Australian continent, providing valuable information about the conductivity structure of the upper few hundred metres of the subsurface. To characterise surface water-groundwater interactions within the Cooper Creek floodplain, we integrate AEM-derived conductivity data with a range of remotely sensed surface datasets, including satellite-derived flood inundation maps and a digital terrain model, and subsurface datasets including drillhole information water levels and seismic reflection data. By integrating these data, we are able to interpret the AEM conductivity sections to characterise the architecture of the local groundwater system, infer the distribution of groundwater salinity for the near-surface aquifer and improve our conceptual model of surface water-groundwater interaction.

The focus of this investigation is the alluvial groundwater system beneath the Cooper Creek floodplain in south-west Queensland. The floodplain represents the uppermost part of the sediments within the Cooper Creek palaeovalley, which

is infilled with a sequence of Cenozoic fluvial sands and minor clay that is up to 150 m thick (Figure 1). The predominantly Pleistocene aquifer sands were deposited in a fluvial environment, at a time when stream power was greater due to a wetter climate and steeper valley gradients (Maroulis, 2000). Quaternary aridity and decreasing valley gradients related to tectonically controlled base-level rise have modified the character of the river system to its present form (Jansen et al., 2013). Consequently, the floodplain is now almost entirely covered with several metres of cracking clay soil, which rapidly seals when saturated and is thought to minimise much of the surface water infiltration deep into the profile (Cendón et al., 2010). The valley fill sediments are underlain by the Cretaceous Winton Formation, which represents the uppermost sedimentary sequence of the Eromanga Basin.

Neotectonic deformation has contributed to uplift of the Innamincka Dome, which has created a shallow subsurface barrier to downstream flow within the Cooper Creek fluvial system. This shallow bedrock high effectively isolates the Cooper Creek groundwater system from alluvial aquifer systems further downstream (Jansen et al., 2013) (Figure 1). Deformation has also produced a series of domes and basins that influence the geometry of the floodplain (Jansen et al., 2013). The floodplain is up to 60 km wide but narrows to 15 km wide where the floodplain is deflected westwards between two north-south trending anticlines (Figure 2).

METHOD AND RESULTS

AusAEM data were acquired using the fixed-wing TEMPEST® system as part of the Exploring for the Future AusAEM Eastern Resources Corridor survey (Ley-Cooper, 2021). Flight lines were oriented east-west and spaced 20 km apart (Figure 1). The AEM bulk conductivity models were derived using the deterministic Geoscience Australia Layered Earth Inversion (GALEISBSTDEM; Brodie, 2023) by inverting for the vector sum (i.e., amplitude of the X- and Z-components) of the AEM data. In areas of potential freshwater recharge, we inverted the AEM data using the probabilistic HiQGA inversion code (Ray et al., 2022) to estimate an ensemble of models from which we calculate the posterior probability density function for conductivity down to 400 metres depth. Although these models were run only in selected areas, they provided a better understanding of AEM model uncertainty and influenced the confidence with which we could interpret the conductivity structures from the deterministic inversion.

AEM bulk conductivity models and other geoscientific data were imported into a 3D environment for interpretation. Using the AEM models, we were able to interpret a number of gentle anticlines and synclines within the top 100 metres of the subsurface below the floodplain (Figure 2). These structures are approximately coincident with structures evident in the underlying Eromanga and Cooper Basins as mapped from seismic and petroleum exploration wells (Vizy and Rollet, 2022). While the floodplain surface is relatively flat, variations in fluvial geomorphology associated with these structures are indicative of river response to deformation (e.g., Ouchi, 1985). This manifests as sediment deposition within structural depressions and incision through uplifted areas. River morphology has implications for groundwater recharge as high river flow velocities are needed to scour the ubiquitous cracking clays to permit more direct connection between surface water and shallow groundwater (Cendón et al., 2010). Moreover, some depressions in the floodplain form terminal wetlands that could provide preferential pathways for surface water infiltration through the unsaturated zone. This process may be significant in groundwater salinisation as infiltrating water can mobilise evaporatively concentrated salts within the unsaturated zone, from where they percolate down to the water table.

AEM-derived conductivity sections and pre-existing drillhole data suggest that the near-surface, Pleistocene sandy aquifer occurs across almost the entire floodplain at an approximate thickness of 20-30 metres (Figure 3). This aquifer comprises mostly fluvial sand (Maroulis, 2000), which is typically a resistive material, and we therefore assume that the high conductivity response (seen as the red response in the AEM in Figure 2) results from the presence of dissolved salts within the aquifer. The general distribution of AEM-derived bulk conductivity in the near-surface is consistent with the limited groundwater salinity measurements from boreholes (Evans, 2020), supporting the assumption of a linear relationship between bulk conductivity and groundwater salinity for this aquifer. These circumstances make AEM the ideal tool for regional scale inference of groundwater salinity.

At the floodplain scale, the distribution of bulk conductivity suggests that groundwater salinity generally increases with distance downstream (Figure 3). Bulk conductivity is generally lower (<0.1 S/m) in the upper reaches of the floodplain where the braided surface channels are indicative of higher surface water flows, as well as along the infrequently inundated eastern margins of the floodplain. Conductivity is highest (>1 S/m) in the narrow, north-south oriented section of the floodplain, and in the far south-west.

At the local scale, resistive lenses within the conductive near-surface in the AEM conductivity sections are coincident with deeply incised channels within the alluvium. These features are observed in at least 15 locations across the floodplain. Probabilistic inference across one such resistive lens (Figure 4; see Figure 1 for location) infers a maximum thickness of at least 10 m and a width of ~400 m within the east-west plane. The presence of this resistive zone in at least 90% of all models from the ensemble provides a very high degree of confidence that the feature exists in the subsurface (Figure 4). The geometry and associated morphology of these features are consistent with hundred-metre scale freshwater lenses identified during a high-resolution drilling and hydrochemical study from the Cooper Creek flood plain (Cendón et al., 2010). The results from the present study suggest that these recharge processes occur more widely than has previously been identified. This has implications for calculating floodplain water budget and identification of potential groundwater-dependent ecosystems along river channels (e.g., Crosbie et al., 2022).

CONCLUSIONS

The results of this work demonstrate that 20 km flight line spaced AEM conductivity data from a fixed-wing system can be used to infer near-surface processes in some alluvial systems. By integrating a range of geoscientific data, we are able to establish an interpretation methodology for

characterising the basic architecture of the groundwater system and make inferences regarding groundwater salinity. This allows us to refine our conceptual model of how groundwater interacts with the river. Although groundwater level time-series data and additional hydrochemical data are needed to test the conceptual models, the AEM-derived conductivity has proven valuable at informing a regional understanding by melding local observations. This work reinforces the value of acquiring pre-competitive AEM data for a variety of applications.

ACKNOWLEDGMENTS

The Exploring for the Future (https://www.ga.gov.au/eftf) National Groundwater System project is funded by the Australian Government through Geoscience Australia.

REFERENCES

Brodie, R.C. (2023). *GA-AEM Source Code Repository*. Geoscience Australia. https://github.com/GeoscienceAustralia/ga-aem

Cendón, D.I., Larsen, J.R., Jones, B.G., Nanson, G.C., Rickleman, D., Hankin, S.I., Pueyo, J.J. and Maroulis, J. (2010). Freshwater recharge into a shallow saline groundwater system, Cooper Creek floodplain, Queensland, Australia. *Journal of Hydrology* 392(3-4), 150-163. https://doi.org/10.1016/j.jhydrol.2010.08.003

Costar, A., Love, A., Krapf, C., Keppel, M., Munday, T., Inverarity, K., Wallis, I. and Soerensen, C. (2019). Hidden water in remote areas—Using innovative exploration to uncover the past in the Anangu Pitjantjatjara Yankunytjatjara Lands. *Mesa Journal 90*, 23-35. https://sarigbasis.pir.sa.gov.au/WebtopEw/ws/samref/sarig1/image/DDD/MESAJ090023-035.pdf

Crosbie, R.S., Holland, K.L. and McVicar, T.R. (2023) Regional□scale partitioning of transmission losses and groundwater recharge using satellite estimates of actual evapotranspiration in an arid environment. *Ecohydrology* 16(1) https://doi.org/10.1002/eco.2490

Evans, T. J., Martinez, J., Lai, E., Raiber, M., Radke, B. M., Sundaram, B., Ransley, T., Dehelean, A., Skeers, N., Woods, M., Evenden, C., and Dunn, B. (2020). *Hydrogeology of the Cooper GBA region. Technical appendix for the Geological and Bioregional Assessment Program: Stage 2*. Department of the Environment and Energy, Bureau of Meteorology, CSIRO and Geoscience Australia. https://www.bioregionalassessments.gov.au/sites/default/files/gba-coo-stage2-appendix_hydrogeology_final_0.pdf

Jansen, J.D., Nanson, G.C., Cohen, T.J., Fujioka, T., Fabel, D., Larsen, J.R., Codilean, A.T., Price, D.M., Bowman, H.H., May, J.H. and Gliganic, L.A. (2013). Lowland river responses to intraplate tectonism and climate forcing quantified with luminescence and cosmogenic ^{10}Be. *Earth and Planetary Science Letters 366*, 49-58. https://doi.org/10.1016/j.epsl.2013.02.007

Ley-Cooper, Y. (2021). *Exploring for the Future AusAEM Eastern Resources Corridor: 2021 Airborne Electromagnetic Survey TEMPEST® airborne electromagnetic data and GALEI inversion conductivity estimates*. Geoscience Australia, Canberra. https://dx.doi.org/10.26186/145744

Maroulis, J. (2000). *Stratigraphy and mid-to-late quaternary chronology of the Cooper Creek floodplain, Southwest Queensland, Australia*. PhD Thesis, University of Wollongong. https://ro.uow.edu.au/theses/1982

Mullen, I., and Kellett, J. (2007). Groundwater salinity mapping using airborne electromagnetics and borehole data within the lower Balonne catchment, Queensland, Australia. *International Journal of Applied Earth Observation and Geoinformation 9*(2), 116-123. https://doi.org/10.1016/j.jag.2006.07.004

Ouchi, S. (1985). Response of alluvial rivers to slow active tectonic movement. *Geological Society of America Bulletin 96*(4), 504-515. https://doi.org/10.1130/0016-7606(1985)96%3C504:ROARTS%3E2.0.CO;2

Ray, A., Taylor, R., and Moghaddam, N. (2022). *HiQGA.jl*. https://github.com/GeoscienceAustralia/HiQGA.jl

Vizy, J., Rollet, N. (2022). *Great Artesian Basin geological and hydrogeological surfaces update: report and data package*. Record 2022/019. Geoscience Australia, Canberra. http://dx.doi.org/10.11636/Record.2022.019

Figure 1. a) True colour visible satellite image of the Cooper Creek floodplain overlain with AusAEM survey flight lines. b) Inset showing segment of AEM flight line 10190001 crossing the Cooper Creek main channel. This line segment was inverted using probabilistic methods – results shown in Figure 4.

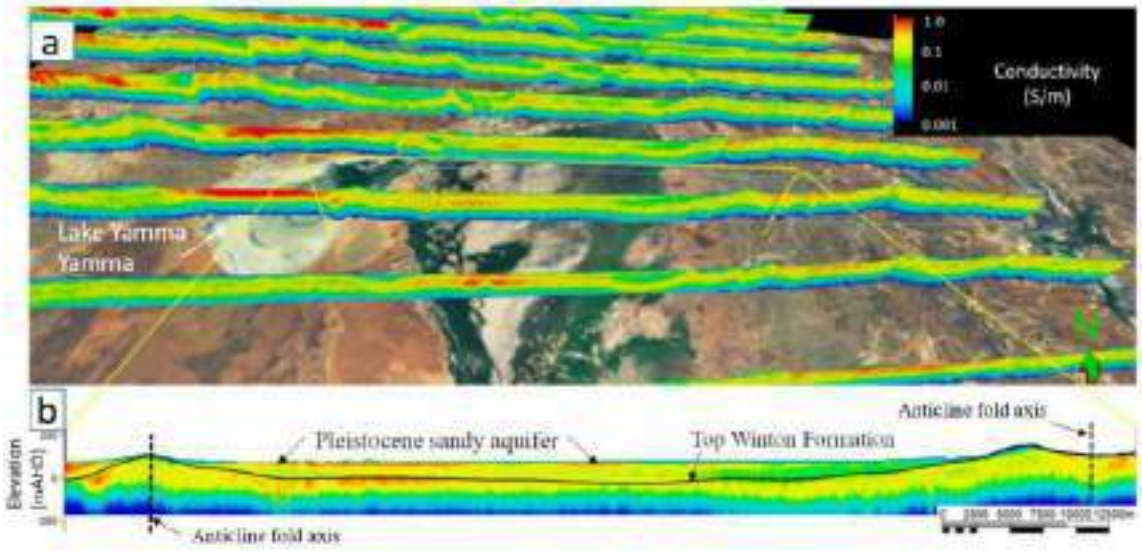

Figure 2. a) Oblique view of of AEM conductivity sections across the central Cooper Creek floodplain east of Lake Yamma Yamma, overlain on true colour visible satellite imagery. b) AEM section 1014001 showing both the flat-lying, conductive Pleistocene sandy aquifer sediments and the gently folded Winton Formation. The floodplain, which contains up to 150 m of Cenozoic sediment, lies within a broad syncline between two anticlinal folds.

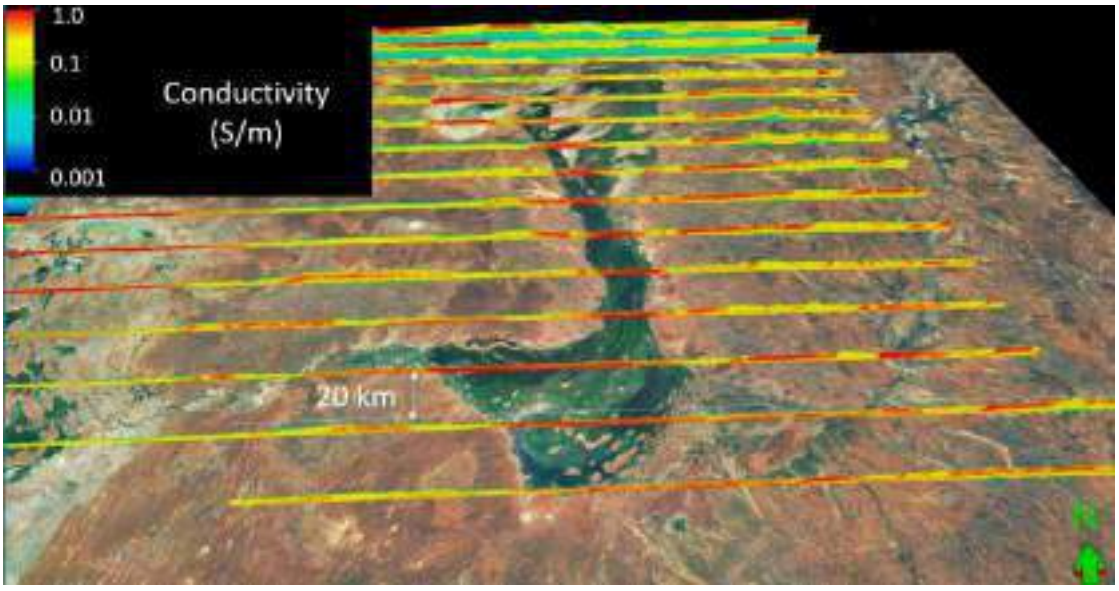

Figure 3. AEM conductivity sections across the Cooper Creek floodplain imaging to depths of ~300 m overlain on true colour visible satellite imagery. The electrical conductivity beneath the floodplain increases where the floodplain narrows in the north, and remains relatively high, peaking again immediately upstream of the Innamincka Dome constriction in the south.

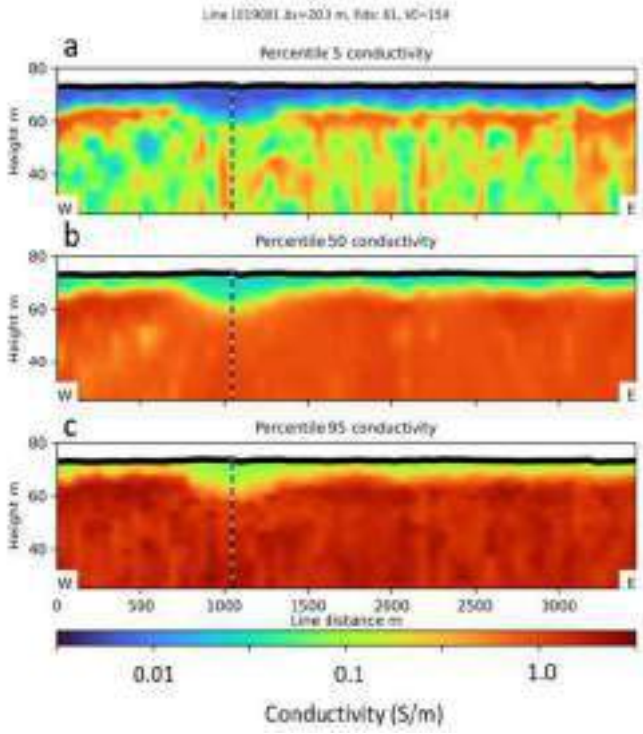

Figure 4. Results from probabilistic modelling of 61 fiducials from AEM flight line 1019001, with conductivity depth sections for a) 5th, b) 50th and c) 95th percentiles. The presence of an approximately 10 metre thick and 400 m wide resistive lens in all sections indicates that this feature persists throughout the model ensemble, giving high confidence in the presence of a real subsurface feature. The persistent resistive feature is interpreted as a freshwater lens perched on the saline groundwater table, indicating focussed recharge of freshwater through the river channel at this location.

New helicopter-borne TEM system HoriZOND for effective exploration

Alexey Trusov
Aerogeophysica
Moscow, Russia
trusov@aerogeo.me

Oleg Kontarovich
Aerogeophysica
Moscow, Russia

SUMMARY

Airborne electromagnetic (AEM) methods have been widely used for mineral exploration and environmental and geotechnical applications because of their efficiency in covering vast survey areas without ground access. Over a few decades, various airborne EM systems have been developed.
As a result of many years of R&D, a newest time-domain EM helicopter system named HoriZOND was developed. The first tests were conducted in 2019.

Key words: time-domain system, development, processing.

INTRODUCTION

HoriZOND combines the latest advances in electronics, signal processing and data processing to provide reliable, high resolution geoelectrical data of the highest quality. HoriZOND system helicopter airborne electromagnetic system provides high-resolution, broad-bandwidth conductivity data for both mapping and discrete targeting applications.

The system can be easily reconfigured to suit different geological environments. The first commercial survey with the HoriZOND system was completed in 2021.

METHOD AND RESULTS

The system is comprised of a transmitter loop with a diameter of 20 meters, four turns of wires (standard configuration) with a soft frame structure; a three-component balanced receiver located in the middle of the transmitter loop. The system is towed by helicopter with the total field magnetometer located 20 meters above the transmitter loop that is suspended 50 meters below the helicopter.

In addition, to evaluate and correct the observation errors caused by flight attitude in the later stage, the system is equipped with many auxiliary sensors such as three-component attitude sensor, post-differential GPS, radar, and laser altimeter. An inertial system is also placed on the loop. It allows full tracking of the transmitter orientation to track the loop's deviations from the horizontal and take this information into account during data inversion.

Receiver coils fully integrated into a single housing with a custom-designed vibration-dampening suspension system. Receiver with lower noise levels caused by sensor movement as well as improved low-noise electronics and engineering structure allowed to achieve a high signal-to-noise ratio.

Special efforts have been made to increased receiver bandwidth and shorter transmitter current waveform turn-off. Each of these improvements contributes to an overall increase in the system's sensitivity to changes in the near surface geology.

To increase the receiver's dynamic range, a double-gain channel strategy is adopted, which means inputting a signal into two channels with different amplification gains, and then synthesizing them into one signal after amplification.

Base frequency: 25Hz or 75Hz (in a 50 Hz environment) / 30Hz or 90Hz (in a 60Hz environment). The trapezoid-like waves are used as transmitting current waveform.

The system uses programmable transmitters which permit adjustable transmitter waveform pulse width, shape, turn-off, and dipole moment. With a base frequency of 25 Hz there is a possibility to use two pulses with different amplitude. The high power pulse ensures good depth of exploration and the low power pulse allows a fast transmitter current turn off and earlier off-time measurement thus providing higher frequency signals, which allows higher near-surface resolution and better sensitivity to weak conductors.

Since a waveform with fast turn off contains higher frequency signals than one with a slow turn-off, dual waveforms consisting of repeated high moment pulses followed by low moment pulses are used to increase the overall bandwidth.

The HoriZOND is a stand-alone system - operation of the equipment requires no personnel on board the helicopter other than the pilot.

EM full waveform streamed data is acquired with high-speed data acquisitions system (DAS) together with auxiliary data required for navigation and positioning accuracy (GPS, laser altimetry), and for correction of geophysical data (INS, outside air temperature and pressure, generator current). DAS also allows to connect a magnetometer, gamma-ray spectrometer and LiDAR to perform multi geophysical airborne surveys.

Figure 1. HoriZOND AEM system.

Recording the full waveform allows a better understanding of the system response that needs to be removed from the total measured field in order to isolate the earth response. The flexibility of recording streamed data allows any extraction scheme for time gates to be implemented in post-processing if required.

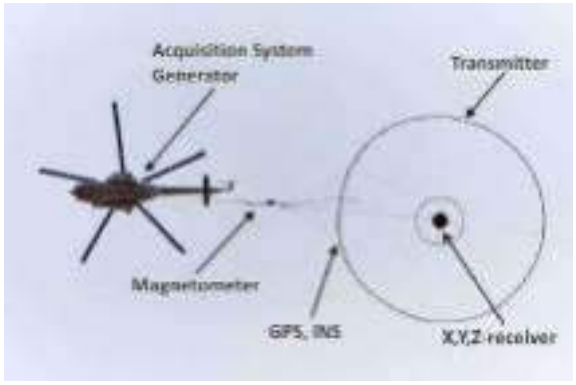

Figure 2. HoriZOND system configuration.

Raw data processing includes following steps: removal of low frequency and DC offset signals; removal of system response (remnant primary field in early channels and drift) as measured at high altitude; optional stacking, non-linear and low-pass filters. Advanced processing improves the accuracy of conductivity models.

In 2022, a hydrogeological survey was carried out using HoriZOND. The main geological structures and aquifers were mapped.

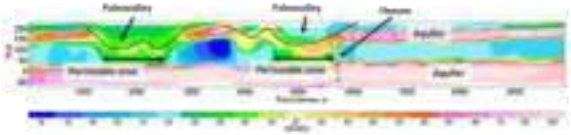

Figure 3. Spatially-constrained inversion of the conducted data with interpretation.

CONCLUSIONS

HoriZOND system provides high resolution and great depth of exploration.

As shown, the HoriZOND's technical design, advanced processing algorithms and value-added interpretation have proven to be an effective solution for geological mapping and mineral targeting in a variety of geological environments.

Lessons learned from a decade of AIP modelling

Andrea Viezzoli
Emergo s.r.l.
Pisa (IT)
andrea.viezzoli@em-ergo.it

SUMMARY

Work carried out from AEM 13 till now shows that IP effects in AEM data need to be modelled. Doings so augments the overall impact of an AEM survey on a variety of levels, whether the physical proxy for the mapping is conductivity or chargeability. Modelling IP effects in AEM data will soon become the industry standard.

Key words: airborne EM, IP, AIP, exploration, modelling, inversion.

INTRODUCTION

At AEM 2013, Viezzoli et al. (2013) discussed on the possibility of modelling IP effects in AEM data, extending beyond the seminal research of the late eighties (Smith and West, 1988). Although based on reasonable theoretical background, the AEM 2013 work was at its very early stages, and lacked significant statistics in real life applications. The last 10 years saw a continuous growth in AIP research and applications by several groups (e.g., Oldenburg and Kang, 2015, Macnae, 2016). I now summarize herein the main take home messages from the work that I, together with several colleagues, have been personally involved in during the past decade.

METHOD

The fundamental concept around AIP is that AEM too captures the dispersive nature of resistivity, a phenomenon not limited to galvanic methods. Is it only using a dispersive resistivity model that negatives in concentric loops can be explained.
The vast majority of the work we carried out is based on what is perhaps the most common of the induce polarization models, the one by Cole and Cole, in the notation given by Pelton et al. (1978). Ever present in galvanic methods, it was found to be suitable also for inductive methods.
Alternative models tested include the MPA (Fiandaca et al., 2018). These were the basis for forward models. As for inversions, the workhorse was the Spatially Constrained Inversion. Variations on the SCI included hybrid, multimesh approaches (Fiandaca) that explored more thoroughly the balance of information across the model parameters. The added value of joint inversions of ground galvanic and ground/airborne inductive data was also assessed.
Starting from the easier concentric loop AEM systems, where the presence of negatives is unmistakably associated with IP effects, we moved onto offset systems, B field (including *squids*) receivers. All the modelling, both synthetic and on real data, was carried out using Aarhus Inv (Auken et al., 2015) and, more recently, EEMverter (Fiandaca et al., 2023).

RESULTS

This sections recaps a list of the main findings of hundreds of case AIP studies, numerical experiments, discussions with clients and colleagues. Most of the work is ongoing. Space limitations allow including herein supporting evidence only for a few of them. Some were already included in the different publications on this topic (cfr Viezzoli et al., 2017; Kaminski and Viezzoli, 2017; Viezzoli and Manca, 2020; Viezzoli, et al 2020, Viezzoli and Manca, 2020; Viezzoli et al., 2021a; Viezzoli et al., 2021b; Fiandaca and Viezzoli, 2021)

1. **How does AIP manifest itself**: there is more than negatives to AIP; they usually affect entire transients, from early to late times (cfr Figure 1). The interplay between standard EM eddy currents and IP currents can alter significantly the *time/depth* relationship in TEM soundings.
2. **Relevance towards recovering correct resistivities**: Failing to model IP effects, when present in the EM data, results in erroneous resistivity models. Typical artefacts are overestimation of bedrock resistivity, underestimation of cover thickness and resistivity, geological conductors appearing as isolated bedrock conductors, but also legit bedrock conductors disappearing. On the other hand, modelling IP can (it does not always) return the correct resistivity, at all depths.
3. **How much sensitivity does AEM have on IP**: AEM's sensitivity to chargeability is limited by a number of factors (base frequency, S/N, the fact that pure induction currents and IP currents are present at once). As a consequence, the most common source of measurable AIP effects originates from shallow chargeable layers over resistive basement. It is possible to track chargeable layers to depths of hundreds of m, if buried below resistive cover. Customized regularization and model updates of the different parameters is crucial to obtain more robust results.
4. **How does AIP compare with galvanic IP**: Direct comparison on real data is hindered by the fact that they usually use different frequencies (lower for ground IP, which charges up bigger particles), and are inverted with different models (e.g., solving for *m* versus *M*). In these cases the comparison shows positive correlations only at times, and over certain subdomains. Using more similar approaches increases the correlation (cfr Figure 2). AIP will/should not replace ground IP, but rather complement it. There is room to increase further the interaction, with associated mutual benefits, between AIP and ground IP. Joint inversion of inductive and galvanic IP data is possible and can improve mapping capabilities.
5. **What does AIP-derived chargeability tell us**: This is one of the points that calls for much more work. To date, evidence has shown that chargeability recovered from standard AEM systems is more frequently associated to fine grained material such as regolith, certain types of

alterations, permafrost, lake sediments, etc. In fewer occurrences it was due to disseminated mineralization.

6. **Are fixed wing EM systems affected by IP:** there is no fundamental reason they should not. On the other hand, spotting AIP in them is harder due to a number of factors. Beside the most obvious (negatives can have a geometrical reason), these factors include the extra degrees of freedom introduced by the poorly monitored varying Tx-Rx distance and varying Rx attitude, the relatively heavy postprocessing carried often out by some of the contractors that introduce other unknowns.
7. **How pervasive/frequent are AIP effects:** experience shows that measurable IP effects can be/are present in all the instances there is both a chargeable cover and the cover itself has a conductance < 100 S. Such scenarios are very common across all latitudes. This finding agrees with theoretical results shown in Figure 3. The latter displays the measurable (i.e., above noise) distortions due to extremely strong chargeability over each one (j) of the gates of a nominal HTEM system, calculated as below: Only transients associated with conductance above 100 S can be considered safely free from measurable IP artefacts also in presence of the strongest chargeabilties. For example, a sequence of alluvium layers, with thick (> 200m), fine grained strata provide a typical examples of scenario where IP will never affect AEM data (down to frequencies presently considered realistic for these systems; ground EM can be affected further). This is because the EM currents in such layer are strong and take a long time to pass through it, therefore masking the contribution of the IP currents.

$$Distortion_j = log10\left|100\,\frac{f_{WT_{NOIP,j}} - f_{WT_{IP,j}}}{f_{WT_{NOIP,j}}}\right|$$

8. **AIP relevance towards mapping:** the goal of an AEM campaign is to investigate the electrical properties of subsurface; unattended AIP will result, in many instances, in artefacts in the recovered properties. This applies both to mineral exploration and (hydro)geological mapping.
9. **AIP in old and new data:** Virtually all "modern" data, that is acquired past 2000, can be re-modelled taking IP into account. This may unlock new value from these datasets. As for new data, the ever-increasing dipole moment, the lowering base frequencies and the greater attention contractors are devoting to IP effects, they all concur towards affirming AIP modelling as the new norm in AEM.

CONCLUSIONS

Modelling IP effects in AEM data has proven its relevance and worth over a variety of cases and applications, and is bound to become the industry standard.

AKNOWLEDGMENTS

I would like to acknowledge all the colleagues and co-authors that worked with me on this topic, together with clients that shared their feedback and allowed publishing results. They are too many to mention each of them. I do however owe a mention to Yusen Ley Cooper, Gianluca Fiandaca, Francesco Dauti, Antonio Menghini, Regis Neroni, Chris Wijns, Tim Munday, Vlad Kaminski. Part of this work was funded by the H2020 European projects "Semacret" and "Infact".

REFERENCES

Auken, E., A. V. Christiansen, G. Fiandaca, C. Schamper, A. A. Behroozmand, A. Binley, E. Nielsen, F. Effersø, N. B. Christensen, K. I. Sørensen, N. Foged, and G. Vignoli, 2015, An overview of a highly versatile forward and stable inverse algorithm for airborne, ground-based and borehole electromagnetic and electric data: Exploration Geophysics, 2015, 223-235.

Fiandaca, G., Viezzoli, A. (2021) Inversion of Airborne IP data with a multi-mesh approach for parameter definition. AEGC expanded abstracts.

Fiandaca, G., Zhang, B., Chen, J., Signora, A., Dauti, F., Galli, S., Sullivan, N.A.L., Viezzoli, A. (2023). Closing the gap between galvanic and inductive methods: EEMverter, a new 1D/2D/3D inversion tool for Electric and Electromagnetic data with focus on Induced Polarization AEM2023 - 8th International Airborne Electromagnetics Workshop, 3-7 September 2023, Fitzroy Island, QLD, Australia.

Fiandaca, G., Madsen, L.M. and Maurya, P.K. (2018), Re-parameterisations of the Cole–Cole model for improved spectral inversion of induced polarization data. Near Surface Geophysics, 16: 385-399.

Kaminski V., and Viezzoli A., 2017. Modeling induced polarization effects in helicopter time-domain electromagnetic data: Field case studies. B49-B61 (82-2), Geophysics.

Macnae, J. 2016, 'Quantitative estimation of intrinsic polarization and superparamagnetic parameters from airborne electromagnetic data', Geophysics 81(6), E433-E446.

Oldenburg, D. W. and Kang, S. 2015, 'Recovering IP information in airborne-time domain electromagnetic data', 24th ASEG-PESA meeting - Perth, Extended Abstract.

Pelton W.H., Ward S.H., Hallof P.G., Sill W.R. and Nelson P.H. 1978. Mineral discrimination and removal of inductive coupling with multifrequency IP, Geophysics, vol. 43.

Smith R. and West G., 1988, TEM Coincident Loop Negatives and the Loop Effect: Exploration Geophysics, 19, 354 - 357

Viezzoli, A., V. Kaminski, and G. Fiandaca, 2017, Modeling induced polarization effects in helicopter time domain electromagnetic data: Synthetic case studies: Geophysics, 82, no. 2, E31–E50.

Viezzoli, A., Dauti, F., Devkurran, N., Pitts, B., 2021a. AIP effects in airborne em fixed wing systems: a spectrem theoretical study. AEGC expanded abstracts.

Viezzoli, A., Dauti, F., Wijns, C., 2021b, Robust scanning of AEM data for IP effects, Exploration Geophysics, 52 (5).

Viezzoli A., and Manca, G., 2020. On airborne IP effects in standard AEM systems: tightening model space with data space, Exploration Geophysics, 51:1, 155-169.

Viezzoli, A., Manca, G., Wijns, C., 2020, Causes and effects of the AIP trap in AEM data, Journal of Applied Geophsyics, 175.

Viezzoli A., Fiandaca, G., Sergio, S. 2013, Study on the potential of recovering IP parameters from Airborne TEM data in layered geology, Expanded abstract, 6th International AEM Conference & Exhibition.

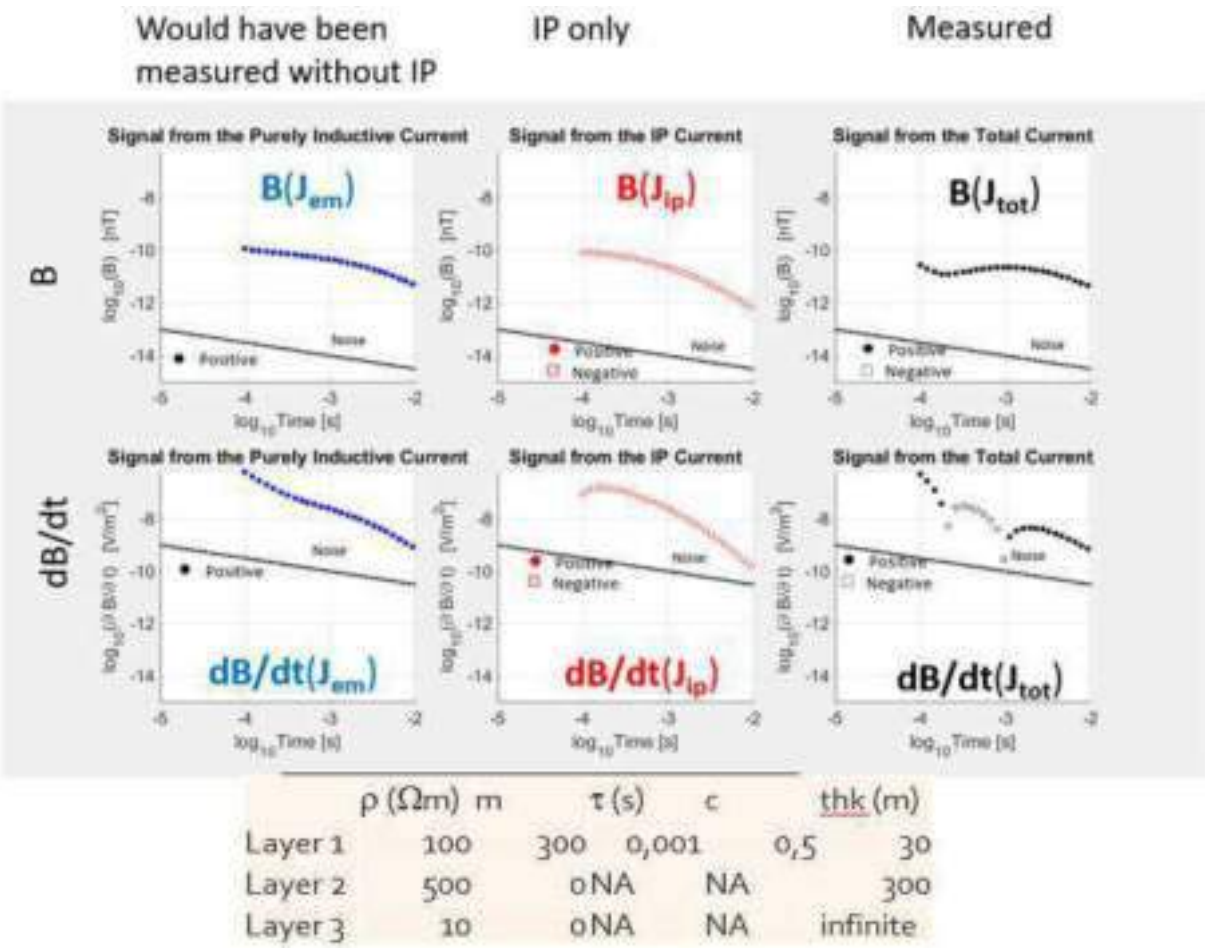

Figure 1. The effect of IP currents on measured transients of a nominal HTEM system, for the three-layer model described in the panel. The first layer is the only chargeable, the last represents a bedrock conductor

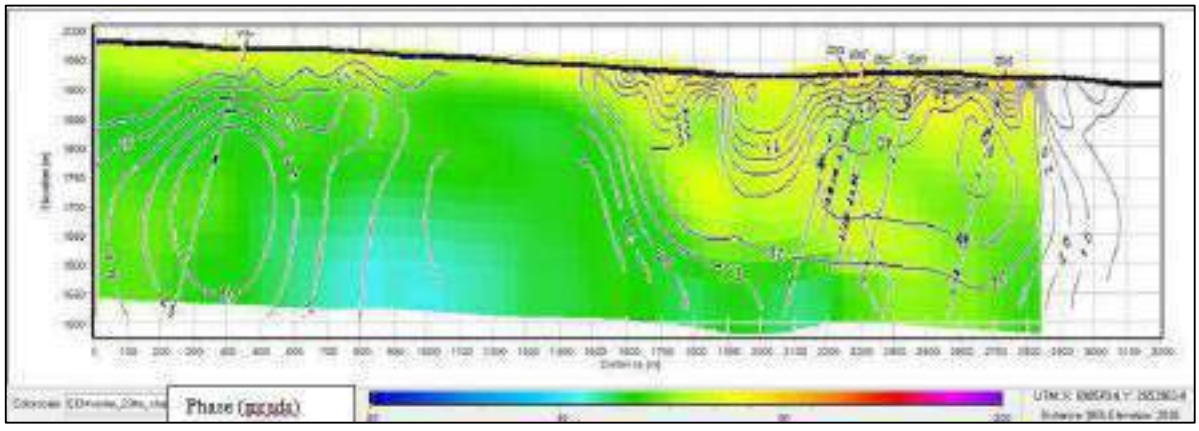

Figure 2. Phase (IP) derived fromn Galvanic (isolines) and AEM (bottom background colour) data, over coincident lines (edited from Fiandaca and Viezzoli, 2021)

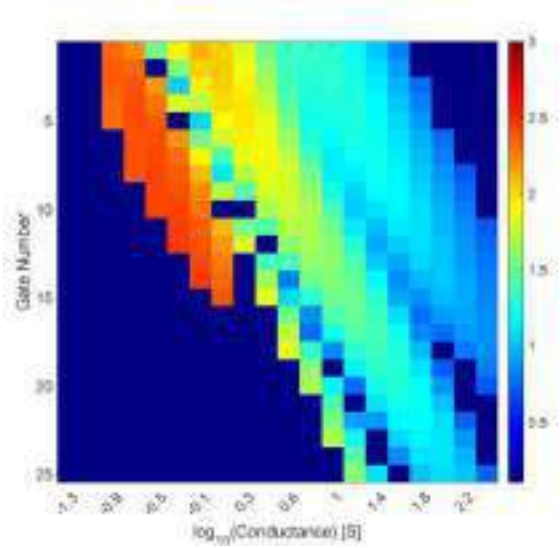

Figure 3. Distortions (cfr text for details) due to IP effects over individual gates of nominal HTEM system, as a function of cover's conductance.

Some comparisons of AEM systems for specific mineral exploration problems

Michael Whitford
IGO Ltd
PO Box 496 South Perth WA 6951
mike.whitford@igo.com.au

Andrew Fitzpatrick
IGO Ltd
PO Box 496 South Perth WA 6951
mike.whitford@igo.com.au

SUMMARY

Simple comparisons of airborne EM systems are limited, and those that are available have finite relevance of ~ 5-10 years due to ongoing improvements in current systems and new systems being offered. The comparisons are hindered by the myriad of system design features, but moreover each comparison must have a purpose, as no system is "the best", but there are many systems "suitable" to answer exploration questions. Several comparisons are presented here, where systems are compared for a specific application using mostly coincidentally acquired field data.

Key words: Airborne EM, SPECTREM, TEMPEST HeliTEM, VTEM.

INTRODUCTION

Since the widespread implementation of Airborne Electromagnetic (AEM) surveying as an exploration prospecting tool, comparisons between systems have been occurring. The design (and proprietary nature) of each AEM system is such that comparisons are not easily made. Factors such as transmitter waveform, dipole moment, windowing schemes, receiver noise levels, and more recently even the transmitted frequency needs to be considered. Data stacking routines for each of the AEM systems should also be included in any comparison, but these are rarely made publicly available. The sheer number of factors that need to be considered makes this a daunting task. Gilgallon et al (2019), demonstrate some comparisons of a variety of systems at the Forrestania test range where several well characterised basement conductors exist. Macnae (2007, 2011) demonstrated some tools that could be used to compare AEM systems through synthetic data and modelling. Each of these (and many others, Christensen et al., 2005, Viezzoli et al, 2018) has merits, though surely the answer for the appropriateness of the system will vary as their needs are considered.

As an airborne EM system is typically selected for a particular problem, this paper will provide example comparisons for several different exploration problems. The systems we have comparative data for are SkyTEM^{312}, HeliTEM^{2}, SPECTREM^{Plus}, TEMPEST, GeoTEM^{Deep} and VTEM^{plus}. Parameters describing each of these systems are given in Table 1.

Case 1: AEM for Geological Mapping in the Paterson Province

The Paterson province is known to host significant deposits of copper and gold, however the discovery of these deposits has been hampered by deep Phanerozoic cover overlying the strongly deformed Proterozoic sedimentary basins. IGO's strategy to explore this province is to build a geological model using integrated multi-scale geophysical data sets. In this project the objective of the AEM is to map the prospective host rocks of the Broadhurst Formation (containing numerous conductive shales) and produce a depth to basement surface (Huizi et al., 2023).

Over many years the numerous explorers of the province have taken a "piece meal" approach to exploration, resulting in an abundance of AEM data of many different varieties, however none of these surveys coherently overlapped. In 2022, while acquiring some HeliTEM^{2} data (utilising a frequency of 6.25Hz) IGO took the opportunity to re-fly a line of data previously acquired using a SkyTEM^{312} (25Hz) system. This repeat line encompasses a package of the Broadhurst Formation, along with covered Coolbro Sandstone, enabling a good opportunity to compare the differing system's ability to map the depth of cover, and the detail obtained from the conductive Broadhurst formation.

All AEM data have been inverted using the GA-LEI routine (Brodie, 2016), producing a standardised product to facilitate a depth of cover product across all datasets, additionally this product is useful in comparing the systems performance for the task (Ley-Cooper et al., 2013). Both systems have recovered very similar conductivity-depth models (Figure 1), clearly identifying varying resistive sand dune cover in the west, with a moderately conductive weathered regolith profile, progressing to deeper cover overlying the conductive Broadhurst formation in the east. However, the dual moment SkyTEM^{312} system appears to be producing a more geologically detailed result, with the system resolving many of the low, resistive sand dunes overlying the Broadhurst, and additionally providing resolution on two separate layers within the regolith profile. The layers in the regolith could be observed within the HeliTEM^{2} data but with much less confidence without prior knowledge.

The conductive Broadhurst formation is important for IGO's exploration efforts primarily because these reactive rocks represent good hosts for copper mineralisation, and as such they need to be able to be mappable in 3 dimensions. The layered-earth inversion (LEI) comparison above is suitable for a cover comparison (given the cover response we expect it to be a 1-D case), however, the Broadhurst formation certainly represents a 2-D case. To evaluate the suitability of the each of two systems to map in 3 dimensions, a representative line has been interpreted using plate models to define the conductors. For each system the latest delay time channels (in the case of the SkyTEM^{312}, the high moment data only) have been interpreted to understand the source of the response).

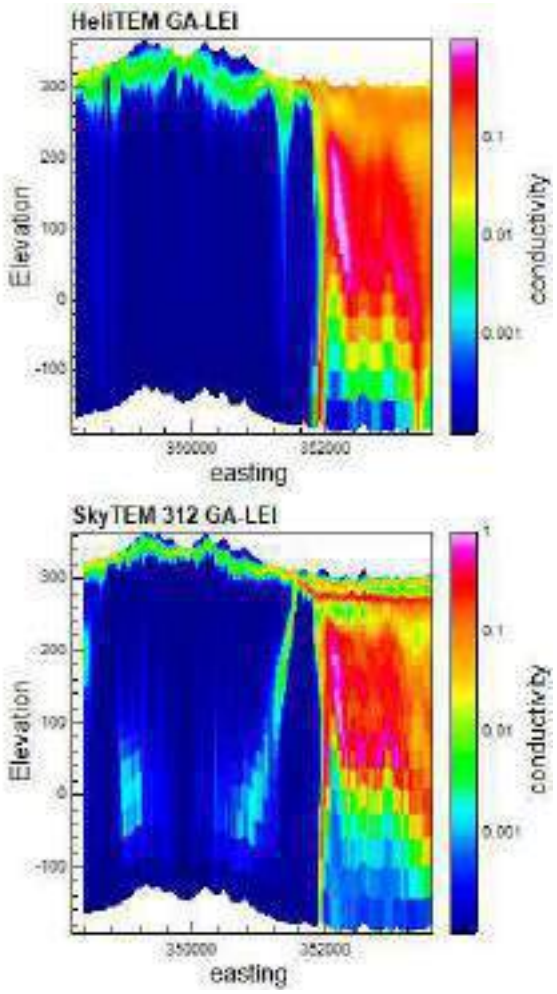

Figure 1. HeliTEM[2] Layer Earth inversion (top) and SkyTEM[312] LEI (bottom). Comparable results are achieved for the coincident line, greater detail is observed in the SkyTEM[312] inversion.

The modelling produces very similar plate models (and model fits) for both systems interpreted (Figure 2), despite the very different time channels used in the interpretation. In the case of the HeliTEM[2] delay times from 11.09-39.87ms were modelled, whereas for the SkyTEM[312] the delay times of 5.85-13.18ms were used. For this purpose, with both systems providing similar results, there was no clear advantage of one over the other.

The two systems compared here in the Paterson are both able to solve the exploration problem for which they are applied. In the case of the SkyTEM[312] system, the advantage of the additional low moment data increases the vertical shallow resolution which may be of value when considering geochemical sampling.

Case 2: AEM for Target Discrimination in the Kimberley

IGO has significant tenure in the Kimberley area of Western Australia. The tenure in the Kimberley spans a Proterozoic belt

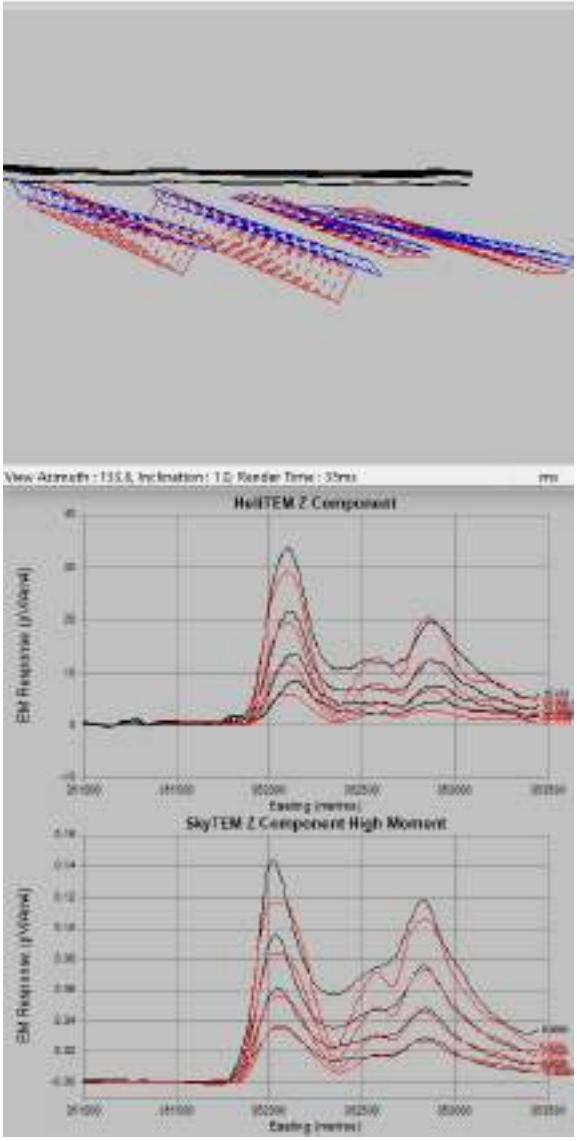

Figure 2. View from the SE (top) of interpreted HeliTEM[2] (red) and SkyTEM[312] (blue) plate models. Field (black) and model (red) response for HeliTEM[2] and SkyTEM[312] data using the latest delay times for both systems. Similar models are interpreted from both datasets.

that has proven magmatic nickel-copper-cobalt sulphide mineralisation that includes the Savanah mine in the East Kimberley, and the Merlin prospect in the west. The typical association of pyrrhotite with Ni-Cu-Co mineralisation mean these deposit styles respond well to electromagnetic methods, with the high conductivities associated with the pyrrhotite (and the expected thickness) generally providing unique conductance properties that enable the orebody's detection (King, 2007). Therefore, airborne EM is often used as a first pass direct detection method for systematic exploration as outlined by Fitzpatrick et al (2019).

Given the exceptionally rugged terrain in the Kimberley, the aim of the AEM is to both identify conductors, but also be able to discriminate higher conductance targets, and potentially save time and effort by not following up lower conductance targets.

With access to the Merlin prospect, which was initially identified in VTEM^{plus} data, a number of coincident lines have been subsequently flown with HeliTEM^2 and SPECTREM^{Plus} at 300m line spacing and an orientation of 045°/225° to evaluate the ability of each system to discriminate higher conductance targets. The VTEM^{plus} data is also available, however this was flown at a 0°/180° and a line spacing of 100m. In this example, the conductors identified have been quantified through ground EM and Maxwell plate modelling, with this result considered the "truth" allowing for a robust comparison. The ground EM was collected in a slingram or fixed loop configuration at 1Hz. The location of these surveys, and the target conductors are shown below in Figure 3.

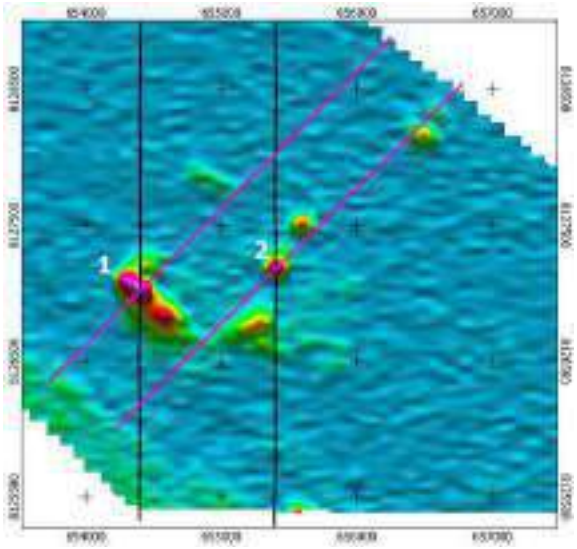

Figure 3. Plan view of the VTEM^{plus} Tau image, HeliTEM^2, SPECTREM^{Plus} (pink) and VTEM^{plus} (black) linepaths. The anomalies discussed are numbered from 1 and 2.

The conductor defined by "1" is characterised in the groundEM as being ~600m x 100m, dipping at ~70 to the SW, at a depth of 150m and conductance of 1500S. The conductor defined by "2" is characterised in the ground EM as being ~100m x 20m, dipping at 40 to the SW at a depth of 55m. with a high conductance of ~17000S. These two examples highlight the potential conductors we want to be able to discriminate.

All the systems flown over the known conductor 1 successfully identified the target in the data, with clear responses in all systems (Figure 4). Plate models have been interpreted for each of these datasets using the latest possible time channels to get a maximum conductance response. This generated conductance responses of 430S for the HeliTEM^2 and the SPECTREM^{Plus}, while the VTEM^{plus} produced an interpreted conductance of 100S.

The responses from all systems over conductor 2 are highlighted in Figure 5, where all systems clearly identify the known conductor. This is unsurprising given the depth, however, the response is clearly diminished in the SPECTREM^{Plus} data. This is interpreted to be likely due to the size of the target and the additional height that is required by the fixed-wing system. Despite the diminished amplitude response in the SPECTREM^{Plus}, a conductance of ~500S is interpreted here, the VTEM^{plus} interpreted with a conductance of 750S, and the HeliTEM^2 with a conductance of 1900S.

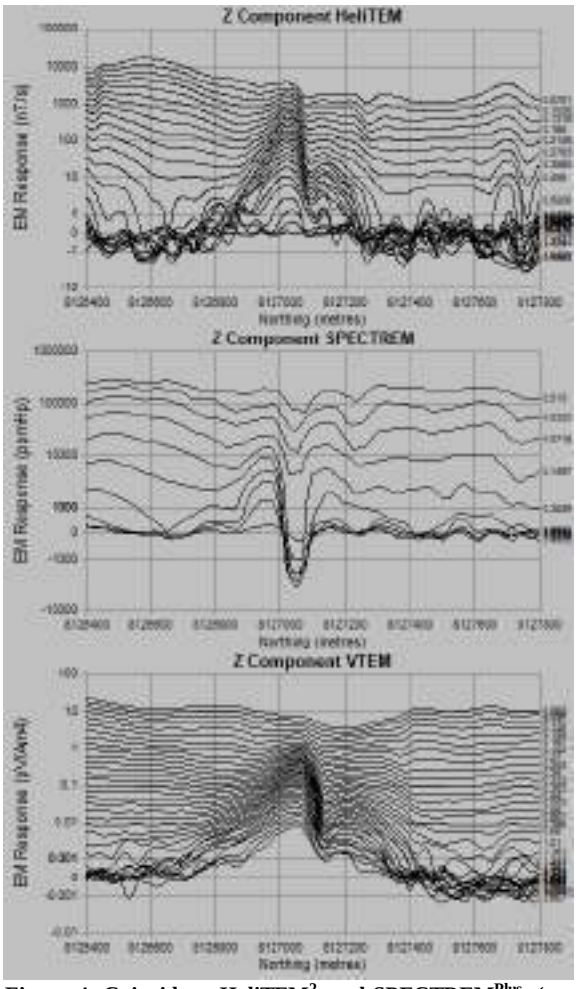

Figure 4. Coincident HeliTEM^2 and SPECTREM^{Plus} (top and centre) Z component response over target 1 and VTEM^{plus} (bottom) Z Component response over the corresponding target

In these two examples, unsurprisingly no system was able to recover an interpreted conductance similar to the ground EM result, due to their higher transmitter base frequency. However, the goal of these test lines was to ascertain if the airborne EM system could differentiate between high conductance and low conductance targets, albeit relative, and thus saving follow-up ground EM surveying over low conductance targets. The above example appears to show potential for the lower base frequency system to be able to achieve this. It should also be noted, given the small nature of the conductors here, tight line spacing is key to adequately characterising the target.

Case 3: Comparison of Historic and Modern AEM systems -Lake Mackay

The Lake Mackay project focuses on a continental-scale gravity ridge that straddles the crustal scale Centralian suture, separating the Paleoproterozoic Aileron and Warumpi provinces (McGloin et al, 2023). The project was identified by IGO as having the potential to host a significant iron oxide copper gold, intrusion-related gold, or intrusion-related Ni-Cu-PGE deposit, with early exploration at the Bumblebee, Springer

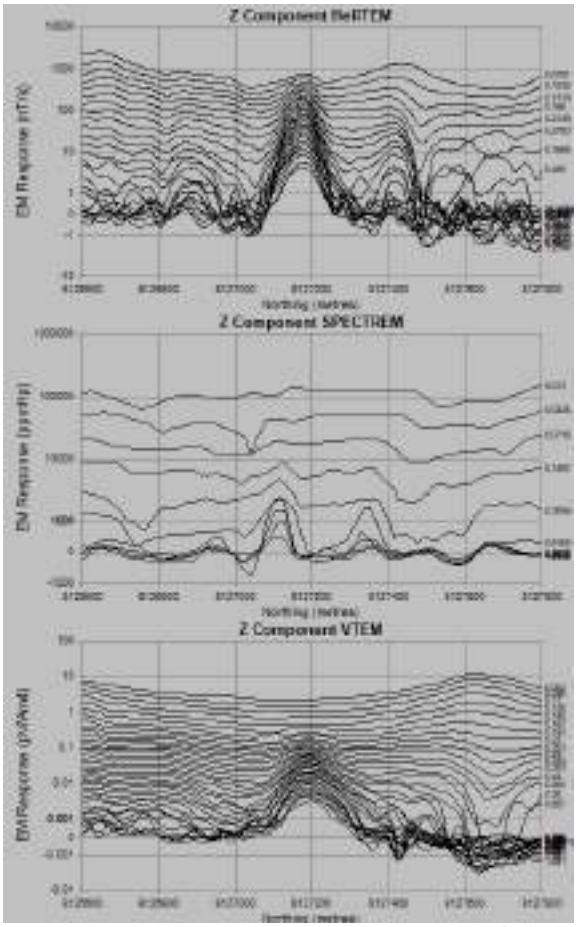

Figure 5. Coincident HeliTEM^{2} and SPECTREM^{Plus} (top and centre) Z component over target 2 with VTEM^{plus} (bottom) Z Component over the corresponding target

and Prowl prospects producing promising results (Winzar, 2016).

The previous exploration had covered parts of the tenure with the GeoTEM^{Deep} AEM system and identified several anomalies. Orientation ground EM surveying (Whitford, 2019) also identified areas of known mineralisation that did show a ground EM response with no response clearly identified in the GeoTEM^{Deep} survey. As such it was decided that an orientation survey would be conducted using the SPECTREM^{Plus} and TEMPEST systems to ascertain if these modern systems would detect potential mineralisation that had not been detected in the previous AEM survey, thus justifying the expense of re-flying the entire area. The SPECTREM^{Plus} and TEMPEST systems were chosen as the remote location of the project dictated that any economic discovery would need to be large, and as such fixed-wing systems would be suitable, while also offering the economic benefit of low-cost acquisition over a large survey area.

A number of lines were repeated from the GeoTEM^{Deep} survey, including over the Springer prospect (a known conductor not identified in the GeoTEM^{Deep}) and one flown over the Grapple mineralisation. Figure 6 shows plan images of all systems (including the ground EM) at similar delay times over Springer. The clearest response to the north west trending conductor is observed in the SPECTREM^{Plus} data I the TEMPEST does identify a response, and the GeoTEM^{Deep} had hints of an anomaly, though is not clearly evident. It should be noted here that the GeoTEM^{Deep} does have a wider line spacing, partly accounting for a lack of resolution.

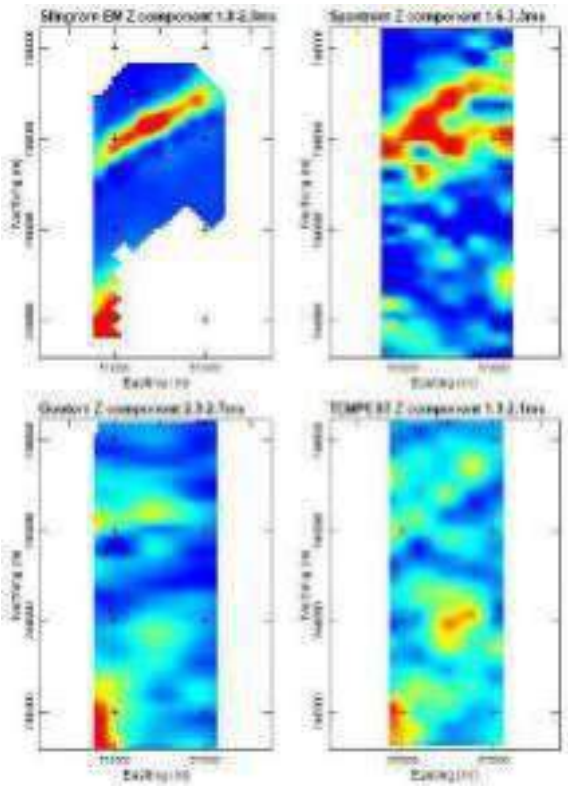

Figure 6. Coincident MLEM, SPECTREM^{Plus}. GeoTEM^{Deep}, and TEMPEST of similar time channels. The clear response in the MLEM is best represented in the PECTREM^{Plus}, with the GeoTEM^{Deep} and TEMPEST not clearly identifying the conductor at Springer.

The results of the repeated line at Grapple prospect are shown as profiles in Figure 7, where a clear response can be seen at the northern end of the line in all systems, though noticeably more pronounced in the TEMPEST and the SPECTREM^{Plus} data. A second anomaly is observed on the southern end of the line and shows a clear response in the TEMPEST and the SPECTREM^{Plus}, however the response is noticeably subdued in the GeoTEM^{Deep}. This response was not originally identified in the GeoTEM^{Deep} data, mainly due to the lack of X component response. Additional to this Z component response, both the TEMPEST and SPECTREM^{Plus} showed a significant X component response giving greater confidence in this target. Subsequently, this target was drill tested and intersected

significant Cu/Au mineralisation and is known as the Phreaker prospect.

The empirical data gained from the orientation survey, using numerous systems provided the confidence required to justify re-surveying a portion of the project that had been covered by an outdated system. The discovery of the Phreaker mineralisation further vindicates this decision.

CONCLUSIONS

A number of datasets are presented here that demonstrate empirical comparisons of systems to solve specific exploration objectives. In the Paterson, it is shown that the SkyTEM^{312} system provides the best solution for detailed cover mapping, while producing very similar results to the HeliTEM^{2} for a large stratigraphic conductor mapped at depth. In the Kimberley, it is shown that the HeliTEM^{2} system shows promise in being able to discriminate targets based on conductance, while all systems trialled successfully identified the known conductors. At the Lake Mackay project, orientation surveying highlighted that modern systems will certainly outperform historic systems and there is value to be realised by re-flying previously covered areas if the exploration proposition warrants it. In each of these examples, it is shown that there is a most appropriate system for each exploration problem.

ACKNOWLEDGMENTS

The Authors would like to thank and acknowledge the entire IGO exploration team and management. Without their support these examples would not be available.

REFERENCES

Brodie, R.C., 2016, User Manual for Geoscience Australia's Airborne Electromagnetic Inversion Software. Geoscience Australia

Christensen, N.B., Lawrie, K.C., 2012, Resolution analyses for selecting an appropriate airborne electromagnetic (AEM) system, Exploration Geophysics, 43:4, 213-227

Fitzpatrick A., and Whitford M., 2019, Strategic electromagnetic geophysical prospecting across a belt – an example over the Albany Fraser Orogen, Extended Abstracts, 2nd AEGC: From Data to Discovery, Perth, Australia

Gilgallon. K., Tomlinson, A., Mortimer, R., 2019, The Forrestania and Nepean electromagnetic test ranges, Western Australia – a comparison of airborne systems, ASEG Extended Abstracts

Huizi, A., Turley, N., Lindsey D., 2023, Integration of regional scale geophysical data to generate a 3D geological model of the Paterson Province, AEGC Extended Abstracts

King A., 2007, Review of Geophysical Technology for Ni-Cu_PGE deposits, Proceedings of Exploration 2007, Exploration in the New Millennium: Fifth Decennial Conference of the Geophysics and Geochemistry for Mineral Exploration, Toronto.

Ley-Cooper, A.J., and Munday, T.J., 2013, Groundwater Assessment and Aquifer Characterization in the Muscgarve Province, South Australia; Interpretation of SPECTREM Airborne Electromagnetic Data, Goyder Institute for Water Research Technical Report Series No. 13/7, Adelaide, South Australia

Macnae, J., 2007, Airborne Electromagnetic Systems, ASEG Extended Abstracts

Macnae, J., 2011, Airborne EM system comparison, Proceedings of the 10th SEGJ International Symposium, Kyoto

McGloin, M.,and Whitford M., 2023, Phreaker Prospect; in '*Annual Geoscience Exploration Seminar (AGES) Proceedings, Alice Springs, Northern Territory, 19–20 March 2023*'. Northern Territory Geological Survey, Darwin, 117–125

Viezzoli, A., Selfe, G., 2018, Comparing responses from different AEM systems and derived models at the Sunnyside nickel project, Botswana, ASEG Extended Abstracts

Whitford M, 2019. Application of electrical geophysics to exploration at the Lake Mackay Project: in '*Annual Geoscience Exploration Seminar (AGES) Proceedings, Alice Springs, Northern Territory, 19–20 March 2019*'. Northern Territory Geological Survey, Darwin, 114–118.

Winzar, D., 2016, Early indications of a copper-gold belt in the southwestern Aileron Province, in 'Annual Geoscience Exploration Seminar (AGES) Proceedings, Alice Springs, Northern Territory 15–16 March 2016'. Northern Territory Geological Survey, Darwin

Table 1. AEM System Specifications

	SkyTEM[312]	HeliTEM[2]	SPECTREM[Plus]	TEMPEST	GeoTEM[Deep]	VTEM[plus]
Transmitter Waveform	Trapezoidal	Square	Square	Square	Half Sine	Trapezoidal
Transmitter Duty Cycle	44% (LM) 25% (HM)	50%	100%	50% deconvolved to 100%	20%	36%
Transmitter Frequency (Hz)	275 (LM) 25 (HM)	6.26	25	25	25	25
Peak Dipole Moment (NIA)	4100 (LM) 51,400 (HM)	565,000	672,000	86,800	665,000	397,135
Transmitter On Time (ms)	0.8 (LM) 5 (HM)	40	20	10	4.108	7.32
Transmitter Off Time (ms)	1.018 (LM) 15 (HM)	40	20	10	15.892	12.68
Receiver Window Times (ms)	0.0016-0.877(LM) 0.04-13.156 (HM)	0.0781-35.873	0.013-10	0.013-16.2	0.501-13.985	0.096-10.717
Terrain Clearance (m)	35	35	50	68	55	50
Configuration	In-loop	In-loop	Slingram	Slingram	Slingram	In-loop

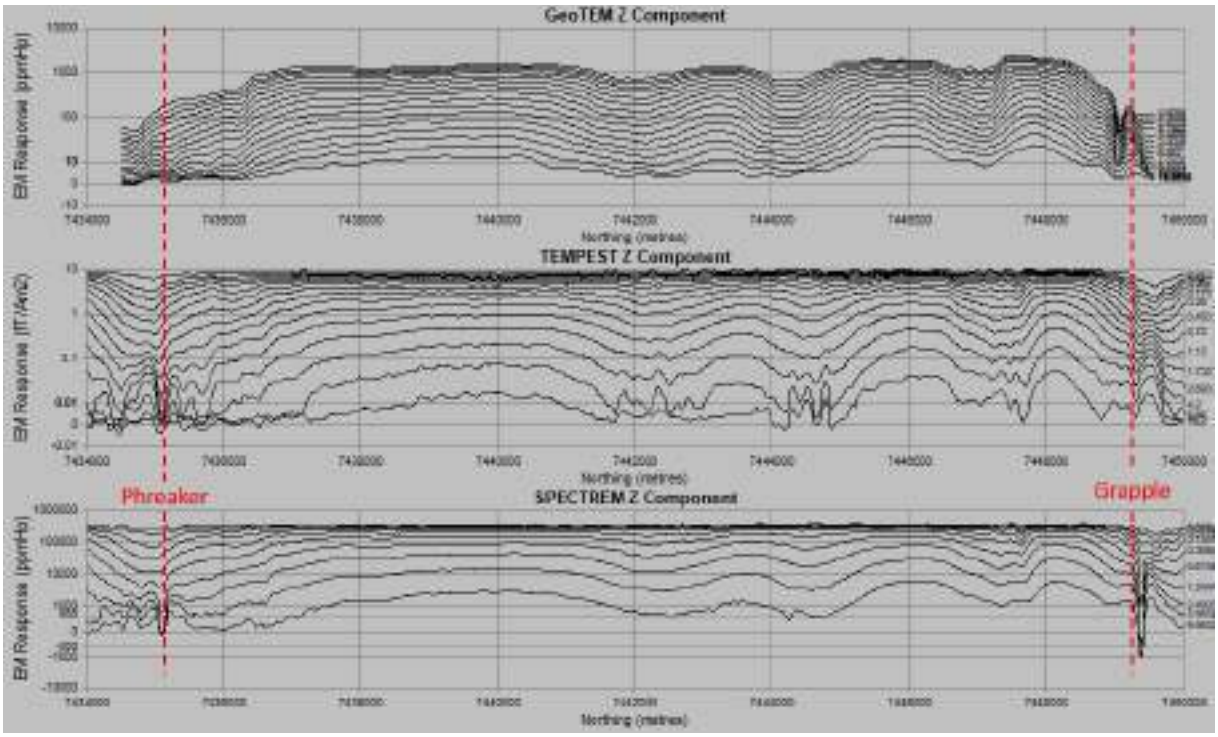

Figure 7. GeoTEM[Deep], Z component response (top), TEMPEST Z component response (centre) and SPECTREM[Plus] Z component response (bottom). The known Grapple conductor can clearly be identified in all datasets, while the conductor that became the Phreaker mineralisation can only clearly be recognised in the TEMPEST and SPECTREM[Plus] datasets.
data

Noise Considerations for TEMPEST Data

Peter Wolfgram*
Xcalibur Multiphysics
10 Compass Road
Jandakot, Perth
Western Australia
peter.wolfgram@xcaliburmp.com

Teo Hage
Xcalibur Multiphysics
10 Compass Road
Jandakot, Perth
Western Australia
teo.hage@xcaliburmp.com

Eric Steele
Xcalibur Multiphysics
10 Compass Road
Jandakot, Perth
Western Australia
eric.steele@xcaliburmp.com

SUMMARY

The noise characteristic of an AEM system is crucial not only for designing the signal processing strategy but more importantly for interpreting the data in terms of an earth model. Ad hoc estimates of noise are often all that is available to the user of an AEM data set, leaving noise as the "elephant in the room". We present a rigorous approach to estimating noise from first principles. We illustrate how such estimates may be obtained from high-altitude calibration data and then be applied to processing and interpretation of TEMPEST data.

Key words: TEMPEST, Noise Model, Data Processing, Conductivity Inversion.

INTRODUCTION

Noise estimates are no longer just "error bars" for display in pretty pictures, but they are being used in algorithms that further process the survey data either using weighted least squares solutions to systems of equations or iterative solutions of linear systems during conductivity inversion.

Noise estimates for conductivity inversions can be too generous which means large "error bars" and the possibility that the fitting model is not well determined. Jones' (2019) proposal to minimise the cross-correlation between the fitting residuals alleviates this problem to some extent, but better noise estimates are preferrable. Conversely, when error estimates are two tight, then the usual Chi-squared criterion will not achieve convergence because the fitting error will always be larger than the data error.

We have constructed a noise model for TEMPEST data from first principles and illustrated its features with examples. Narrow-band noise such as VLF and the spectral gaps resulting from the finite transmitter switching time are automatically down-weighted when the inverse standard deviation or variance are used as weights in signal processing algorithms. The noise estimates are also being used for improved conductivity depth transformation (CDT) and we tested them for improved layered earth inversion (LEI).

METHOD AND RESULTS

A Noise Model for TEMPEST

Using upper-case letters to indicate Fourier Transforms, the voltage measured in each receiver coil is:

$$V_r = -\frac{\mu_0 A_r A_t}{4\pi} R_{rf} R_c j\omega\{g + R_g\} I \qquad (1)$$

where A_r is the effective coil area, A_t is the transmitter loop area*turns, R_{rf} is the frequency response of the combined anti-alias filter and digitizer, R_c is the frequency response of the induction coil, g is the geometric coupling factor between the transmitter loop and the receiver coil, R_g is the frequency response of the ground, I is the transmitter current, and $j=\sqrt{(-1)}$, and $\omega=2\pi f$ with f being the frequency. Similarly, the voltage recorded from the transmitter monitoring device is

$$V_t = R_{tf} R_{tc} I \qquad (2)$$

where R_{tc} is the calibration factor of the current monitor device, R_{tc} is the frequency response of the anti-alias filter and digitiser, and I is the current. The transfer function T from the transmitter to the receiver is then

$$T = \frac{V_r}{V_t} = -\frac{\mu_0 A_r A_t}{4\pi} \frac{R_{rf}}{R_{tf} R_{tc}} R_c j\omega\{g + R_g\} \qquad (3)$$

The transfer function T_a for the high-altitude calibration run is the same but without the R_g ground response term. By forming the ratio T/T_a the quantity Ψ is obtained which constitutes the deconvolution of the system transfer function from the measured transfer function and was first published by Lane et al (2000):

$$\Psi(\omega, \mathbf{r}) := \frac{T(\omega, \mathbf{r})}{T_a(\omega)} = \frac{g(\mathbf{r})}{g_a} + \frac{R_g(\omega, \mathbf{r})}{g_a} \qquad (4)$$

The independent variables are included explicitly to highlight the dependence on location $\boldsymbol{r}$ and frequency ω. The data example in Figure 1 shows increased noise at the high frequency end of the spectrum.

Rasmussen et al (2017) investigate the effect of noise in TEM signals (ground and airborne) on the deconvolution. Their noise model consists of *external noise* (stationary and nonstationary components, e.g., from radio signals, spherics, and motion-induced noise, or nonlinear effects such as amplifier saturation due to a strong primary-field component in the on time), and *internal noise* (stationary components only, e.g., thermal noise, electronics noise from oscillators and power supplies, and quantization noise in the ADC). Their noise terms are complex functions of frequency and could in principle include bias spectra that have not been accounted for elsewhere. In particular, the noise model of Rasmussen et al (2017) does not allow for coupling variations between transmitter and receiver (g and g_a would be 1), it does not treat the deconvolution of high-altitude spectra from survey altitude spectra, and it also does not explicitly allow for an airframe response.

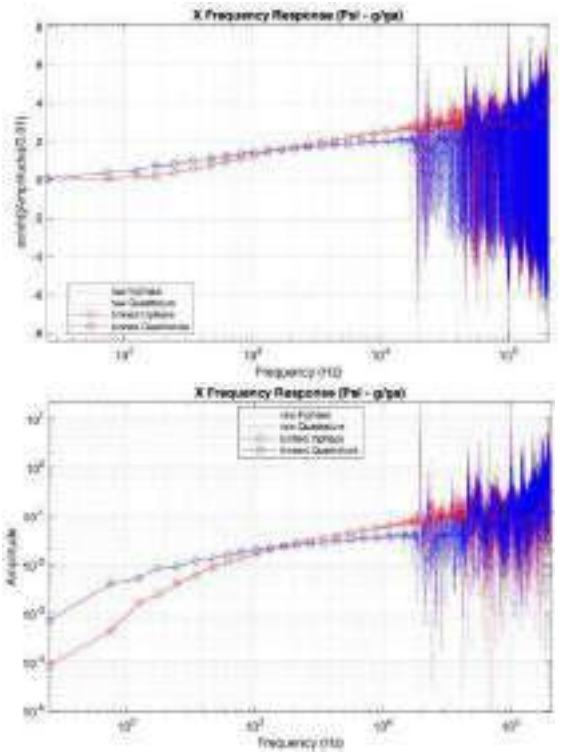

Figure 1: A snapshot of the frequency response at one location along a flightline showing the noise character with asinh scaling (upper panel) and with logarithmic scaling (lower panel). Dotted lines are the raw frequency response, the circles are weighted averages for logarithmically spaced frequency bins. The logarithmic scaling shows the transmitter nulls and VLF lines in the high frequencies more clearly but it hides the fact that the noise can go negative. The data are from a TEMPEST test flight with 25 Hz base frequency and 400 kHz acquisition rate.

All these noise features may be accounted for by including in equations 1 and 2 two extra terms representing complex spectra, one for the external noise $N_{ext}(\omega)$ (which is modified by the receiver parameters) and one for the internal noise $N_{int}(\omega)$. The receiver spectrum contains both whereas the transmitter spectrum contains only the internal kind (noted simply as N_t). Equations 1 and 2 then become

$$V_r = -\frac{\mu_0}{4\pi} A_t A_r R_{rf} R_c j\omega I\left(g + R_g + N_{ext}\right) + N_{int}$$
$$V_t = R_{tf} R_{tc} I + N_t \quad (5)$$

Forming the transfer functions T and T_a and then the frequency response Ψ is achieved with the help of Taylor expansion and neglecting second order terms. The main assumption for simplifying the final expression is that the noise does not change between the reference altitude and the survey altitude. Combining various noise terms into a single variable N_{mod} results in an expression for the *measured* Ψ_m equivalent to equation 4:

$$\Psi_m(\omega, \mathbf{r}) = \Psi(\omega, \mathbf{r}) + N_{mod}(\omega)\left(1 - \Psi(\omega, \mathbf{r})\right) + N_{add}(\omega) \quad (6)$$

where $N_{mod}(\omega)$ stands for the sum of internal and external complex noise spectra that have been modulated by coupling variations, and we have introduced $N_{add}(\omega)$ to allow for a complex bias and additive noise in Ψ_m. The ground response R_g is zero along any of the high-altitude lines resulting in an equation that may be used for determining the noise terms:

$$\Psi_m(\omega, \mathbf{r}_a) = \frac{g(\mathbf{r}_a)}{g_a} + N_{mod}(\omega)\left(1 - \frac{g(\mathbf{r}_a)}{g_a}\right) + N_{add}(\omega) \quad (7)$$

The complex term $N_{add}(\omega)$ can be estimated from the high-altitude *reference line*. This line is flown "straight and level" which minimizes any variations of the coupling ratio $g(\mathbf{r})/g_a$ so the round bracket is close to zero and the *modulated* noise term becomes negligible. The complex bias and standard deviation may then be estimated using the entire reference line:

$$N_{bias}(\omega) \approx \underset{\{\mathbf{r}=\mathbf{r}_{ref}\}}{mean}\left(\Psi_m(\omega, \mathbf{r}) - \frac{g(\mathbf{r})}{g_a}\right)$$
$$N_{std}(\omega) \approx \underset{\{\mathbf{r}=\mathbf{r}_{ref}\}}{stdev}\left(\Psi_m(\omega, \mathbf{r}) - \frac{g(\mathbf{r})}{g_a}\right) \quad (8)$$

Figure 2 illustrates the resulting noise spectra for a reference line flown with the standard TEMPEST system.

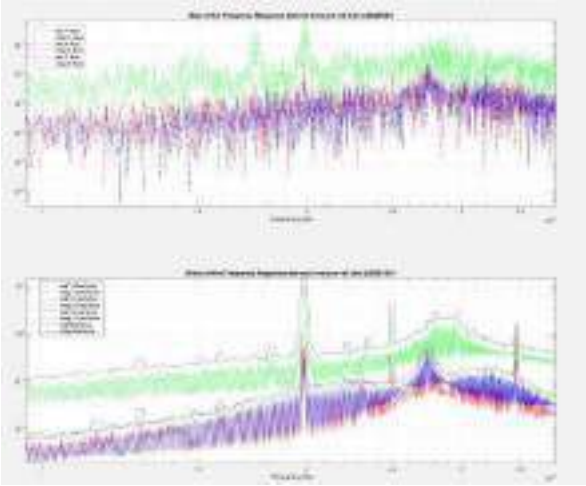

Figure 2: A high-altitude reference line showing the high frequency region of the complex bias of the Frequency Response (upper panel, solid lines for inphase, dashed for quadrature) and real-valued standard deviation (lower panel). The x,y,z components are red, green, blue respectively, and the black curves in the middle panel are the moving maximum over a sliding window with user-defined width. The Y component has higher noise because it is nearly null-coupled with the transmitter.

Figure 3 shows the windowed Bfield obtained from the high-altitude reference line. This is the result of processing the frequency response Ψ_m as if the line was a survey line. Although the noise estimates discussed here are for the frequency domain, the processed reference line may be used to derive noise estimates for the Bfield windows.

The modulated noise may be estimated from the high-altitude *swoop line*. The average is restricted to only those samples with strong geometrical coupling variations so that the denominator is different enough from zero.

$$N_{mod}(\omega) = \underset{\{\mathbf{r}=\mathbf{r}_{swoop}\}}{mean}\left(\frac{\Psi_m(\omega, \mathbf{r}) - N_{bias}(\omega) - \frac{g(\mathbf{r})}{g_a}}{1 - \frac{g(\mathbf{r})}{g_a}}\right) \quad (9)$$

This is not strictly "noise" because it includes any response from the metallic airframe that is sensed when the geometrical

coupling between transmitter and receiver changes. A correction for this effect is applied during processing of the survey lines as follows

$$\Psi(\omega, \mathbf{r}) = \frac{\Psi_m(\omega, \mathbf{r}) - N_{bias}(\omega) - \mathrm{N}_{mod}(\omega)}{1 - \mathrm{N}_{mod}(\omega)} \qquad (10)$$

Figure 4 illustrates the windowed Bfield processed along the swoop line without and with removing the airframe response, indicating that the effect of the airframe is typically small and below the overall noise level.

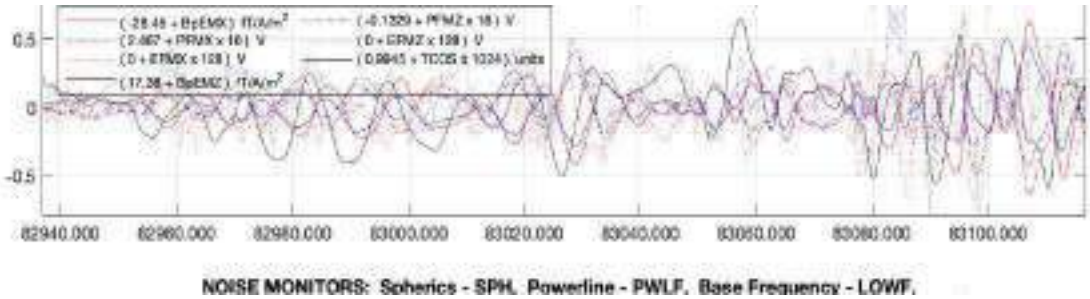

NOISE MONITORS: Spherics - SPH. Powerline - PWLF. Base Frequency - LOWF.

Figure 3: The X and Z components of the windowed, 100% duty-cycle Bfield obtained from processing a high-altitude reference line as if it was a survey line. This represents the noise during straight and level flight, and its variance may be used as noise estimate when working with windowed data.

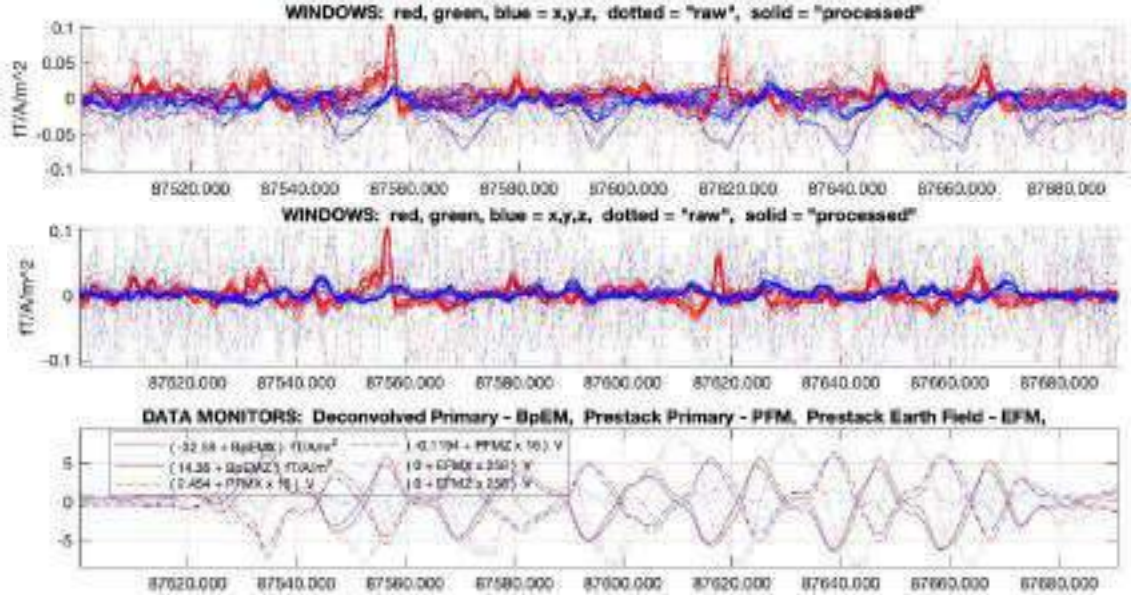

Figure 4: The "swoop line" before (top) and after (centre) the correction for the airframe response. The "before" data represent the noise during exaggerated aircraft manoeuvres. The lower panel shows the primary Bfield (BpEMX, BpEMZ) as solid lines, highlighting the swoop manoeuvres. The monitors have been scaled individually as indicated in the legend in order to fit onto a single plot.

Weighted Least Squares Solvers in Frequency Domain

Weighted least squares solvers may be employed to find the solutions to a linear system of equations (LSE): ***A*x=B***, where ***B*** is the data vector (the frequency response), ***x*** is the unknown vector and ***A*** is the LSE matrix. The weighted least squares solution minimizes

$$(B-A*x)^T * W * (B-A*x)$$

where the covariance matrix ***W*** may be constructed with the inverse of the standard deviation $N_{std}(\omega)$ from Equation 8 or the inverse of the variance on the diagonal.

We have established and solved such systems of equations for

- reducing the high-frequency noise in the frequency response (where ***A*** contains smoothness constraints and ***x*** is the smoothed data vector) before further processing, and for
- inverting the raw or binned frequency response data directly from the frequency domain to an earth conductivity model (where ***A*** contains constraints and regularization and ***x*** is the model vector).

Figure 5 shows the effect of fitting a piecewise cubic polynomial to the high (> 15 kHz) frequencies using weighted least squares. The high-frequency noise is successfully rejected.

Figure 6 illustrates how a wide (0.5 decades) weighted convolution filter has a stronger smoothing effect than the narrow (0.1 decades) binning shown by circles in Figures 1 and 5. It successfully extends the frequency response through the noisy high-frequency region.

Both examples result in a very similar windowed Bfield because the windowing further rejects high-frequency noise except in the very first few windows (not shown here).

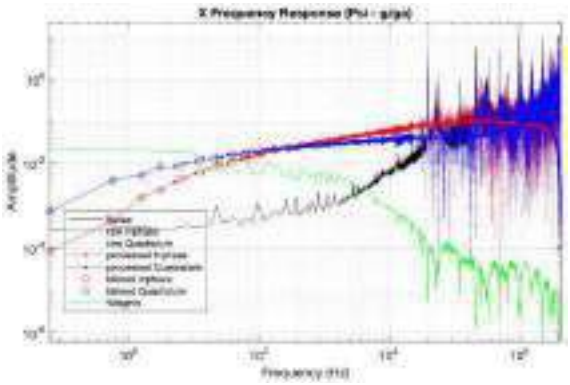

Figure 5: Same data as Figure 1 but including noise (black curve), weights (green), and processed data (red and blue with dot symbols) that were replaced by a weighted least squares fit above 15 kHz. The circles are the same as before: bins with a width of 0.1 decades.

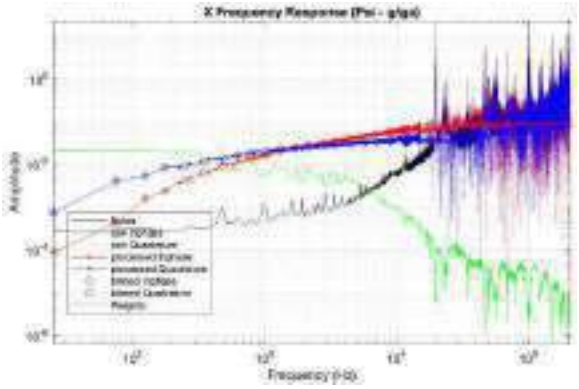

Figure 6: Same data as Figure 1 but including noise (black curve), weights (green), and processed data (red and blue with dot symbols) that were filtered above 15 kHz with a 0.5 decades width Hanning filter combined with data weights.

In order to calculate a Conductivity Depth Transform (CDT), the raw or binned frequency response is first fitted with a sum of complex basis functions using weighted least squares that also include constraints for stabilising the solution. Each basis function is the Fourier transform of an exponential decay. The resulting coefficients are then used to construct the step response which is in turn matched with the field of a receding image of the transmitter resulting in a conductivity versus depth function (Wolfgram and Karlik, 1995). The result compared well with conductivity sections generated in other ways.

As proof of concept only, we have also implemented and successfully tested a Layered Earth Inversion (LEI) that uses the raw or binned frequency response (dotted lines or circles in Figures 1, 5 and 6) together with the noise estimates as input.

Noise Estimates for Windowed Data in Time Domain

In the same manner as the noise and bias spectra were derived from the frequency response along high-altitude calibration lines, time-domain noise and bias may be derived from the final windowed Bfield calculated along these same lines (Figure 3). We have done this in order to derive quality control data (Figure 6) but the noise may also be converted to weights for further data processing or conductivity inversion in time domain.

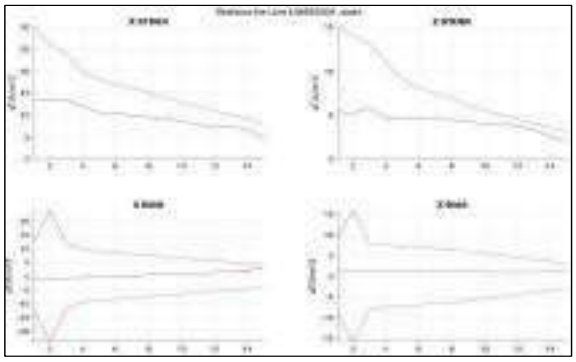

Figure 7: Statistics (black curves) for a high-altitude reference line. The red curves show noise bounds for quality control. The Window numbers are along the horizontal axis and atto-Teslas per Am^2 on the vertical axis.

CONCLUSIONS

We have captured the noise characteristic of TEMPEST data as complex noise and bias estimates for the raw frequency response and showed how this may be exploited for processing and interpretation. Data weights derived from the noise estimates effectively depress the major noise sources of VLF and transmitter spectral gaps when used in processing and inversion algorithms. Tests with CDT and LEI produced clean conductivity sections from the raw frequency response.

ACKNOWLEDGMENTS

New processing algorithms had become necessary to replace historic processing code that was no longer adequate for recent TEMPEST developments. None of this work would have been possible without the help and the patience of those in Xcalibur in Jandakot who are dealing with ‘real’ data on a daily basis.

REFERENCES

Jones, A.G., 2019, Beyond chi-squared: Additional measures of the closeness of a model to data. AEGC 2019, Perth, Extended Abstracts.

Lane, R., A. Green, C. Golding, M. Owers, P. Pik, C. Plunkett, D. Sattel, B. Thorn, 2000, An example of 3D conductivity mapping using the TEMPEST airborne electromagnetic system. *Exploration Geophysics* 31, 162-172.

Rasmussen, S., N.S. Nyboe, S. Mai, J.J. Larsen, 2017, Noise properties of Fourier deconvolution for time-domain electromagnetic soundings. *Geophysics* 82 (5), E257-E266.

Wolfgram, P., G. Karlik, 1995, Conductivity-depth transform of GEOTEM data. Exploration Geophysics 26, 179-185.

Australian continental-scale multilayered chronostratigraphic interpretation of airborne electromagnetics

Sebastian C. T. Wong[1], Ian C. Roach[1], Karen A. Connors[2], Juliana F. M. Vilhena[2], Liam Pitt[1], Malcolm G. Nicoll[1], Jackie A. Hope[1], Marie-Aude Bonnardot[1], Ross C. Brodie[1], Alan Yusen Ley-Cooper[1]

[1]Geoscience Australia, [2]University of Queensland
Corresponding author: Sebastian.Wong@ga.gov.au; GPO Box 378 Canberra ACT 2601 Australia

SUMMARY

A key issue for explorers in Australia is the abundant sedimentary and regolith cover obscuring access to underlying potentially prospective rocks. Multilayered chronostratigraphic interpretation of regional broad line-spaced (~20 km) airborne electromagnetic (AEM) conductivity sections have led to breakthroughs in Australia's near-surface geoscience. A dedicated/systematic workflow has been developed to characterise the thickness of cover and the depth to basement rocks, by delineating contact geometries, and by capturing stratigraphic units, their ages and relationships. Results provide a fundamental geological framework, currently covering 27% of the Australian continent, or approximately 2,085,000 km^2. Delivery as precompetitive data in various non-proprietary formats and on various platforms ensures that these interpretations represent an enduring and meaningful contribution to academia, government and industry. The outputs support resource exploration, hazard mapping, environmental management, and uncertainty attribution. This work encourages exploration investment, can reduce exploration risks and costs, helps expand search area whilst aiding target identification, and allows users to make well-informed decisions. Presented herein are some key findings from interpretations in potentially prospective, yet in some cases, underexplored regions from around Australia.

Key words: AusAEM, airborne electromagnetic interpretation, Exploring for the Future

INTRODUCTION

Australia is a major producer and exporter of natural resources. However, the Australian continent is vastly (~80%) covered by regolith and sedimentary basin cover, which obscures access to the underlying prospective rocks. It has been widely recognised that one of the greatest challenges hindering resource exploration in Australia is the lack of characterisation of the thickness and composition of this cover and the accessibility to the rocks beneath.

Historically, potential field geophysics, seismic and borehole data have been used to investigate the lithology and structure of the upper-crust through the cover. However, Geoscience Australia's (GA) Exploring for the Future program, in partnership with State and Territory geological surveys, has enabled the acquisition of the nominally 20 km line-spaced AusAEM surveys (Ley-Cooper et al., 2020). These surveys shed light on the geo-electrical properties of the subsurface geology to a depth of up to ~500 m. This provides a non-invasive and cost-efficient dataset that facilitates investigations on the regional lithostratigraphy, hydrostratigraphic characteristics, groundwater quality, basin configurations, structures, and presence of prospective rocks.

The modelled regional AEM data are interpreted using the multilayered chronostratigraphic AEM interpretation workflow (Wong et al., 2022). These interpretations provide seamless consistent data to help constrain the near-surface composition and architecture across both highly-explored and under-explored regions. Interpretation lines are converted to depth estimate points, and are stored alongside multidisciplinary depth estimates in the Estimates of Geological and Geophysical Surfaces (EGGS) database (Mathews et al., 2020). These points constitute important inputs to cover modelling (e.g. Bonnardot et al., 2020) These cover models are subsequently used as inputs into mineral potential mapping (Murr et al., 2020) and a resource extraction economic viability tool (Haynes et al., 2020).

Although the multilayered chronostratigraphic AEM interpretations cover large regions with homogenous line work, metadata and depth estimates, herein, several case studies have been selected to illustrate how AEM models may be interpreted to elucidate geological features with environmental, economic or community safety implications. These case studies include: the resource potential of the 1) Willowra Suture, 2) Dulcie Trough/Syncline, and 3) palaeovalleys, in the Northern Territory; the 4) hydrogen storage potential of salt-containing basins in Western Australia; and the 5) general exploration implications in underexplored areas.

METHODS

The majority of the AEM conductivity sections currently interpreted are from the AusAEM surveys (e.g. Ley-Cooper, 2020; Ley-Cooper, 2021; Ley-Cooper & Brodie, 2018), with selected sections from other surveys also interpreted (e.g. Brodie, 2021; Costelloe et al. 2012).

The AEM data were inverted using GA's Layered Earth Inversion Sample-By-Sample Time Domain Electromagnetics inversion (Brodie, 2015). The depth of investigation varies depending on the bulk electrical conductivity, with the depth of signal penetration estimated to be up to ~500 m in electrically resistive terrains.

The AEM models are interpreted in 2D space and then validated, and converted to 3D space and points, using code developed at GA (Wong et al., 2022). This workflow facilitates attribution of each interpretation line or point with large amounts of interpretation-specific metadata such as stratigraphic units, confidence and links to supporting datasets. Outputs meet strict EGGS database structure requirements and are available in multidimensional non-proprietary formats

across various delivery platforms. Integrated interpretation of AEM models with potential fields, boreholes, seismic sections and interpretations, surface and solid geology maps, ensures production of well-informed interpretations and confidence attribution.

RESULTS AND DISCUSSION

Chronostratigraphic interpretations produced by GA and its collaborators currently cover ~110,000 line km of AEM-derived conductivity sections, covering an area ~2,085,000 km^2 to a depth of up to ~500 m (Figure 1). . These interpretations have produced ~600,000 attributed depth estimate points, with ~300,000 already available through EGGS on the GA Portal (https://portal.ga.gov.au/).

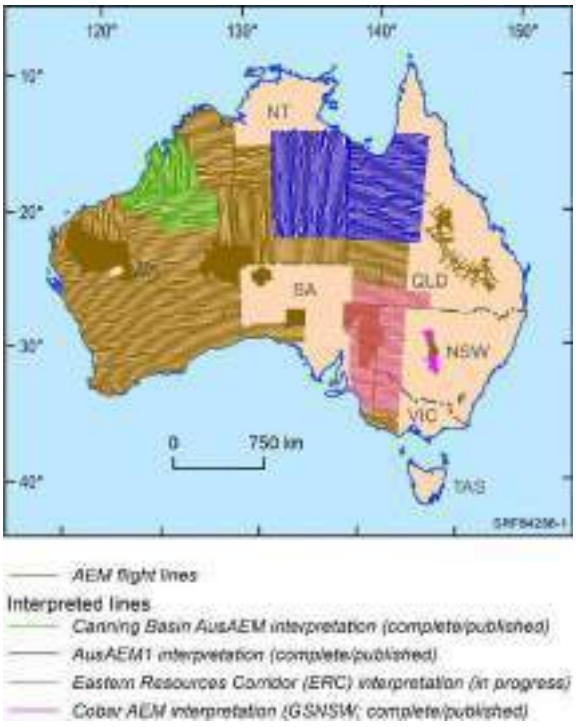

Figure 1 Current coverage of AEM interpretations made using the multilayered chronostratigraphic AEM interpretation workflow. Canning Basin AusAEM interpretation (Connors et al., 2022; Vilhena et al., 2023); AusAEM1 interpretation (Wong et al., 2020; Wong et al., 2021); Cobar AEM interpretation (Folkes et al., 2022; GSNSW = Geological Survey of New South Wales).

First-order structures and palaeovalleys

One key finding from the interpretation of regional AEM surveys is their ability to reveal first-order geological structures. In the central Northern Territory, the contact between the Proterozoic Aileron Province and the adjacent Paleozoic Lander Trough has been interpreted in the AusAEM models as a large-scale faulted contact (Figure 2a). This contact can be confidently mapped for hundreds of kilometres beneath thin (~5-10 m) Cenozoic cover. The location of the Willowra Suture (Korsch & Doublier, 2015), a south-dipping crustal-scale boundary that resulted from the collision of the Aileron and Tanami provinces at 1864-1844 Ma (Goleby et al., 2009; Korsch et al., 2011; Korsch & Doublier, 2015), correlates extremely well with this fault, suggesting that the interpreted fault is the near-surface expression of the Willowra Suture. Besides a change in the age of rare small scattered outcrops throughout the region, the presence of a major fault or the extent of the Willowra Suture reaching the near-surface was unknown. The near-surface geometry and distribution of this feature can now be well-constrained using AEM models.

Long-period magnetotellurics (MT) models have identified a major conductive zone at depth along this feature (Duan et al., 2019; Figure 2b). This significant crustal/mantle-scale feature could represent metasomatism along a major fluid flow pathway (Duan et al., 2022). Duan et al. (2022) noted that Au mines and deposits associated with the Tanami orogenic Au system are located directly above a conductivity anomaly, whereas Korsch & Doublier (2016) indicated that major crustal boundaries, such as the Willowra Suture, are conduits for mineralising fluids to upper-crustal levels. Structures potentially linked to these deeper fertile zones can now be mapped in the near-surface, and under thin cover, using AEM models, providing explorers additional data to refine and focus their exploration efforts.

Additionally, there is a significant elevation offset across this feature (Figure 2c), suggesting geologically recent movement, with the Aileron Province displaced upwards relative to the Lander Trough. This improved ability to precisely map the distribution of neo-tectonic structures allows for enhanced hazard mapping and community safety assessments.

Integration with palaeovalley maps (e.g. Bell et al., 2012) demonstrated that the regional AEM surveys are a powerful tool to refine such maps, by improving the capability to approximate under cover palaeovalley distribution and connectivity. Furthermore, these surveys can also be used to discover undocumented palaeovalleys. Importantly, the interpretations provide a depth dimension, which can be used to gauge thicknesses and volumes of the palaeovalley fill (Figure 2a). Determination of these properties is vital for explorers, land users and governments to make informed decision on policy, management of groundwater extraction, and management of groundwater dependent ecosystems.

Multilayered chronostratigraphic interpretation for resource exploration

The Dulcie Trough/Syncline in the central Northern Territory is an asymmetrical syncline with Neoproterozoic-Paleozoic Georgina Basin rocks in the hinge of the fold overlying Paleoproterozoic basement (Kruse et al., 2013). The Neoproterozoic-Paleozoic units are sedimentary fill of a Neoproterozoic depocentre, with the geometry of this structure being amplified by Upper Ordovician to Carboniferous Alice Springs Orogeny folding (Dunster et al., 2007; Kruse et al., 2013).

Interpretation of the AusAEM models has constrained the under cover geometry of the syncline by showing the thickness of the trough fill and depth to the underlying basement, as well as revealing internal structures, such as potential parasitic folding, faulting and/or separated depocentres (Figure 3). These observations have the potential to aid exploration, as the trough/syncline region is prospective for Au, base metals and phosphate (Huston et al., 2021; Kruse et al., 2013; Dunster, 2015).

In this example, as Au and base metal occurrences exist at or near the trough-basement boundary, the conductivity contrast between moderately conductive trough fill and resistive basement can help to extrapolate the distribution and depth of

prospective stratigraphy under cover. Delineation of this contact also helps to determine the thickness of overburden and the depth to prospective rocks. Similarly, the Georgina Basin stratigraphy is prospective for and hosts significant phosphate deposits. These deposits are typically covered by surficial sediments, are commonly situated on the Neoproterozoic-Paleozoic basin peripheries, and can occur proximal to palaeo-topographic highs (Khan et al., 2007; Howard, 1990). McCrow (2008) suggested that improved targeting of phosphate deposits would require additional structural interpretations, including identifying palaeo-topographic highs and embayments. Therefore, utilising AEM models to refine the basin boundary geometries, to identify the palaeo-topographies (e.g. the ridges separating possible depocentres in the Georgina Basin) and to develop the structural framework of the near-surface geology, is highly valuable in the design of exploration projects targeting phosphate deposits.

Multilayered chronostratigraphic AEM interpretations are currently occurring in the Eastern Resources Corridor of the Exploring for the Future program. These interpretations are providing a geological framework in areas including the Curnamona Craton, which hosts the world-class Broken Hill Pb-Zn-Ag deposit, as well as the Delamerian Orogen, which is prospective for Au, Cu, Pb, Ag, Ni, Zn and PGEs. These interpretations are also providing geological insight in agricultural areas in the western Murray Basin that rely heavily on groundwater resources. The AEM interpretations have been utilised in drilling programs to estimate cover thicknesses and identify basement highs. They help to support groundwater investigations by refining the subsurface basin boundaries and distribution of stratigraphic units. The interpretations are also crucial inputs into cover thickness modelling, and will be released as precompetitive data across various platforms.

The workflow has facilitated the delineation of individual stratigraphic units, by the interpretation of changes in electrical conductivities in the subsurface. The results can be extended to infer lithostratigraphic or hydrostratigraphic properties important to groundwater or hydrocarbon exploration, such as the presence or extrapolation of traps, seals, reservoirs and source rocks, and/or aquifers and aquitards.

Salt deposits

The AusAEM dataset has presented opportunities for using AEM models in unconventional ways to support exploration of subsurface salt deposits. Integration of the AEM models with a range of supporting information and datasets provided insight on the distribution of salt within various basins. This is important, as caverns made in underground salt deposits are cost effective storage sites for large quantities of hydrogen. New studies were undertaken to understand salt distribution in the Canning (Connors et al., 2022; Vilhena et al., 2023; Zhan, 2022) and Officer (Bradshaw et al., 2023) basins, in Western Australia, which are known for thick onshore salt accumulations. The multilayered chronostratigraphic AEM interpretation revealed disruption of the electrical conductivities in the shallow stratigraphy, likely caused by movement or dissolution of the salt at depth. As a result, the AEM models were found to be a powerful tool for targeting near-surface salt diapirs, and for mapping the regional distribution of bedded salt horizons under cover. Therefore, these studies provide insights into the geological hydrogen storage potential of the salt deposits within these basins by refining search areas.

CONCLUSIONS

Multilayered chronostratigraphic interpretations of regional AEM surveys have led to significant improvements in the understanding of near-surface geology in Australia. They help characterising the thickness and composition of the expansive cover, whilst providing insight into the underlying rocks at an unprecedented scale. They provide a foundational dataset that informs on Australia's subsurface geology and assists a variety of users in academia, government, industry and the public with environmental management, resource exploration and hazard mapping

The development of the integrated workflow presented here facilitates large quantities of interpretation-specific metadata to be captured and attributed to 2D and 3D line work and points. Large regions of Australia are now covered with precompetitive multidimensional interpretation data in non-proprietary formats, which are accessible across a variety of platforms.

ACKNOWLEDGEMENTS

The Authors acknowledge the AEM interpreters Millicent Crowe, Pauline English and Rosemary Hegarty. We thank AEM acquirers and processors in the Geophysical Acquisition and Processing section at GA. We acknowledge AEM interpreters from the Geological Survey of New South Wales for their collaboration and work on the Cobar AEM survey. We thank Andrew Clark and Michael Doublier for their peer reviews.

REFERENCES

Bell, J.G., Kilgour, P.L., English, P.M., Woodgate, M.F., and Lewis, S.J., 2012. WASANT Palaeovalley Map - Distribution of Palaeovalleys in Arid and Semi-arid WA-SA-NT. Geoscience Australia, Canberra. http://pid.geoscience.gov.au/dataset/ga/73980

Bonnardot, M., Wilford, J.R, Rollet, N., Moushall, B., Czarnota, K., Wong, S.C.T., and Nicoll, M.G. 2020. Mapping the cover in northern Australia: towards a unified national 3D geological model. Geoscience Australia, Canberra. http://dx.doi.org/10.11636/134507

Bradshaw, M.T, Rees, S., Wang, L., Szczepaniak, M., Cook, W., Voegeli, S., Boreham, C.J., Wainman, C., Wong, S.C.T., Southby, C., and Feitz, A. 2023. Australian salt basins – options for underground hydrogen storage. APPEA Journal 62(1)

Brodie, R.C., 2015. User manual for Geoscience Australia's airborne electromagnetic inversion software. https://github.com/GeoscienceAustralia/ga-aem.git

Brodie, R.C, 2021. MinEx CRC Mundi Airborne Electromagnetic Survey, NSW, 2021: XCITE® AEM data and conductivity estimates. Geoscience Australia, Canberra. http://pid.geoscience.gov.au/dataset/ga/145897

Connors, K.A., Wong, S.C.T., Vilhena, J.F.M., Rees, S., and Feitz, A. 2022. Canning Basin AusAEM interpretation: hydrogen storage potential and multilayered mapping. Geoscience Australia, Canberra. https://dx.doi.org/10.26186/146376

Costelloe, M.T., Roach, I.C., and Hutchinson, D.K., 2012. Frome Embayment TEMPEST AEM Survey: Inversion

Report and Data Package (200m). Geoscience Australia, Canberra. http://pid.geoscience.gov.au/dataset/ga/73838

Duan, J., Kyi, D., Kirkby, A., and Jiang, W. 2019. Resistivity model derived from magnetotellurics: AusLAMP-TISA project. Geoscience Australia, Canberra. http://dx.doi.org/10.26186/5d5e24d062977

Duan, J., Kyi, D., Jiang, W., Doublier, M.P., and Kirkby, A., 2022. Lithospheric resistivity structures and mineral prospectivity from AusLAMP data in northern Australia. Geoscience Australia, Canberra. https://dx.doi.org/10.26186/146312

Dunster, J.N., 2015. Partial relinquishment report for EL 24716, Patanella Phosphate Project. Rum Jungle Resources Ltd. GEMIS Report ID: CR2015-0558 https://geoscience.nt.gov.au/gemis/ntgsjspui/handle/1/86115

Dunster, J.N., Kruse, P.D., Duffett, M.L., and Ambrose, G.J., 2007. Geology and resource potential of the southern Georgina Basin. *Northern Territory Geological Survey, Digital Information Package* DIP007.

Folkes, C.B., Carlton, A., Eastlake, M., Deyssing, L., Trigg, S., Montgomery, K., Matthews, S., Spampinato, G., Roach, I.C., Gilmore, P., Ley-Cooper, A.Y., and Wong, S.C.T, 2022. The Cobar AEM Survey interpretation report. Geological Survey of New South Wales, Report GS2021/1592. MinEx CRC Record 2022/11.

Geoscience Australia, 2017. GEODATA 9 second DEM and D8: Digital Elevation Model Version 3 and Flow Direction Grid 2008; digital dataset, https://data.gov.au/data/dataset/geodata-9-second-dem-and-d8-digital-elevation-modelversion-3-and-flow-direction-grid-2008

Goleby, B.R., Huston, D.L., Lyons, P., Vandenberg, L., Bagas, L., Davies, B.M., Jones, L.E., Gebre-Mariam, M., Johnson, W., Smith, T. and English, L., 2009. The Tanami deep seismic reflection experiment: An insight into gold mineralization and Paleoproterozoic collision in the North Australian Craton. *Tectonophysics* 472(1-4):169-182.

Haynes, M.W., Walsh, S.D.C., Czarnota, K., Northey, S.A., and Yellishetty, M. 2020. Economic Fairways Assessments across Northern Australia. Geoscience Australia, Canberra. http://dx.doi.org/10.11636/133681

Howard, P.F., 1990. The distribution of phosphatic facies in the Georgina, Wiso and Daly River Basins, Northern Australia. *Geological Society of London, Special Publications* 52: 261-272.

Huston, D.L., Doublier, M.P., and Downes, P.M., 2021. Geological setting, age and endowment of major Australian mineral deposits - a compilation. Geoscience Australia, Canberra. http://dx.doi.org/10.11636/Record.2021.020

Khan, M., Ferenczi, P.A., Ahmad, M., and Kruse, P.D., 2007. Phosphate testing of waterbores and diamond drillcore in the Georgina, Wiso and Daly basins, Northern Territory. Northern Territory Geological Survey, Record 2007-003.

Korsch, R.J., and Doublier, M.P., 2015. Major crustal boundaries of Australia. Geoscience Australia, Canberra. http://dx.doi.org/10.4225/25/555C181CC0EAE

Korsch, R.J., and Doublier, M.P., 2016. Major crustal boundaries of Australia, and their significance in mineral systems targeting. *Ore Geology Reviews* 76: 211-228.

Korsch, R.J., Blewett, R.S., Close, D.F., Scrimgeour, I.R., Huston, D.L., Kositcin, N., Whelan, J.A., Carr, L.K., and Duan, J., 2011. Geological interpretation and geodynamic implications of deep seismic reflection and magnetotelluric line 09GA-GA1: Georgina Basin–Arunta region. Annual Geoscience Exploration Seminar (AGES) 2011, Record of Abstracts. Northern Territory Geological Survey, pp. 67–76 (Record, 2011-003).

Murr, J., Skirrow, R.G., Schofield, A., Goodwin, J., Coghlan, R.A., Highet, L., Doublier, M.P., Duan, J., Czarnota, K. 2020. Tennant Creek – Mount Isa IOCG mineral potential assessment. Geoscience Australia, Canberra. http://dx.doi.org/10.11636/134157

Ley-Cooper, A.Y., Brodie, R.C., and Richardson, M., 2020. AusAEM: Australia's airborne electromagnetic continental-scale acquisition program, *Exploration Geophysics* 51(1): 193-202, DOI: 10.1080/08123985.2019.1694393

Ley-Cooper, A.Y., 2020. AusAEM 02 WA/NT 2019-20 Airborne Electromagnetic Survey. Geoscience Australia, Canberra. http://pid.geoscience.gov.au/dataset/ga/140156

Ley-Cooper, A.Y., 2021. Exploring for the Future AusAEM Eastern Resources Corridor: 2021 Airborne Electromagnetic Survey TEMPEST® airborne electromagnetic data and GALEI inversion conductivity estimates. Geoscience Australia, Canberra. https://dx.doi.org/10.26186/145744

Ley-Cooper, A.Y., and Brodie, R.C., 2018. AusAEM Year 1 NT/QLD Airborne Electromagnetic Survey; GA Layered Earth Inversion Products. Geoscience Australia, Canberra. http://pid.geoscience.gov.au/dataset/ga/132709

Mathews, E.J., Czarnota, K., Meixner, A.J., Bonnardot, M., Curtis, C., Wilford, J., Nicoll, M.G., Wong, S.C.T., Thorose, M., and Ley-Cooper, A.Y., 2020. Putting all your EGGS in one basket: the Estimates of Geological and Geophysical Surfaces database. Geoscience Australia, Canberra. http://dx.doi.org/10.11636/132526

McCrow, B., 2008 Independent Geologists Report. Phosphate Australia Limited Prospectus. Accessed on 17/03/2023 at: http://www.gibbriverdiamonds.com/irm/PDF/efebe0bf-8d09-48a1-a877-f997301e0c5a/DisclosureDocumentPHOSPHATEAUSTRALIALTD

Vilhena, J.F.M., Connors, K.A., Wong, S.C.T., and Nicoll, M.G. 2023. Canning Basin AusAEM Airborne Electromagnetic Interpretation Data Package. Geoscience Australia, Canberra. https://dx.doi.org/10.26186/147597

Wong, S.C.T., Nicoll, M.G., Brodie, R.C., Hope, J.A., Bonnardot, M., Roach, I.C., and Ley-Cooper, A.Y., 2022. Multilayered chronostratigraphic airborne electromagnetic interpretation workflow. Record 2022/37. Geoscience Australia, Canberra. http://dx.doi.org/10.11636/Record.2022.037

Wong, S.C.T., Roach, I.C., Nicoll, M.G., English, P.M., Bonnardot, M., Brodie, R.C., Rollet, N., and Ley-Cooper, A.Y. 2020. Interpretation of the AusAEM1: insights from the world's largest airborne electromagnetic survey. Geoscience Australia, Canberra. http://dx.doi.org/10.11636/134283

Wong, S.C.T., Roach, I.C., Nicoll, M.G., English, P.M., Bonnardot, M., Brodie, R.C., Rollet, N., and Ley-Cooper, A.Y. 2021. AusAEM1 Interpretation Data Package. Geoscience Australia, Canberra. http://pid.geoscience.gov.au/dataset/ga/145120

Zhan, Y., 2022. Airborne electromagnetic survey, northern Western Australia: an integrated interpretation of selected features: Geological Survey of Western Australia, Report 234, 78p.

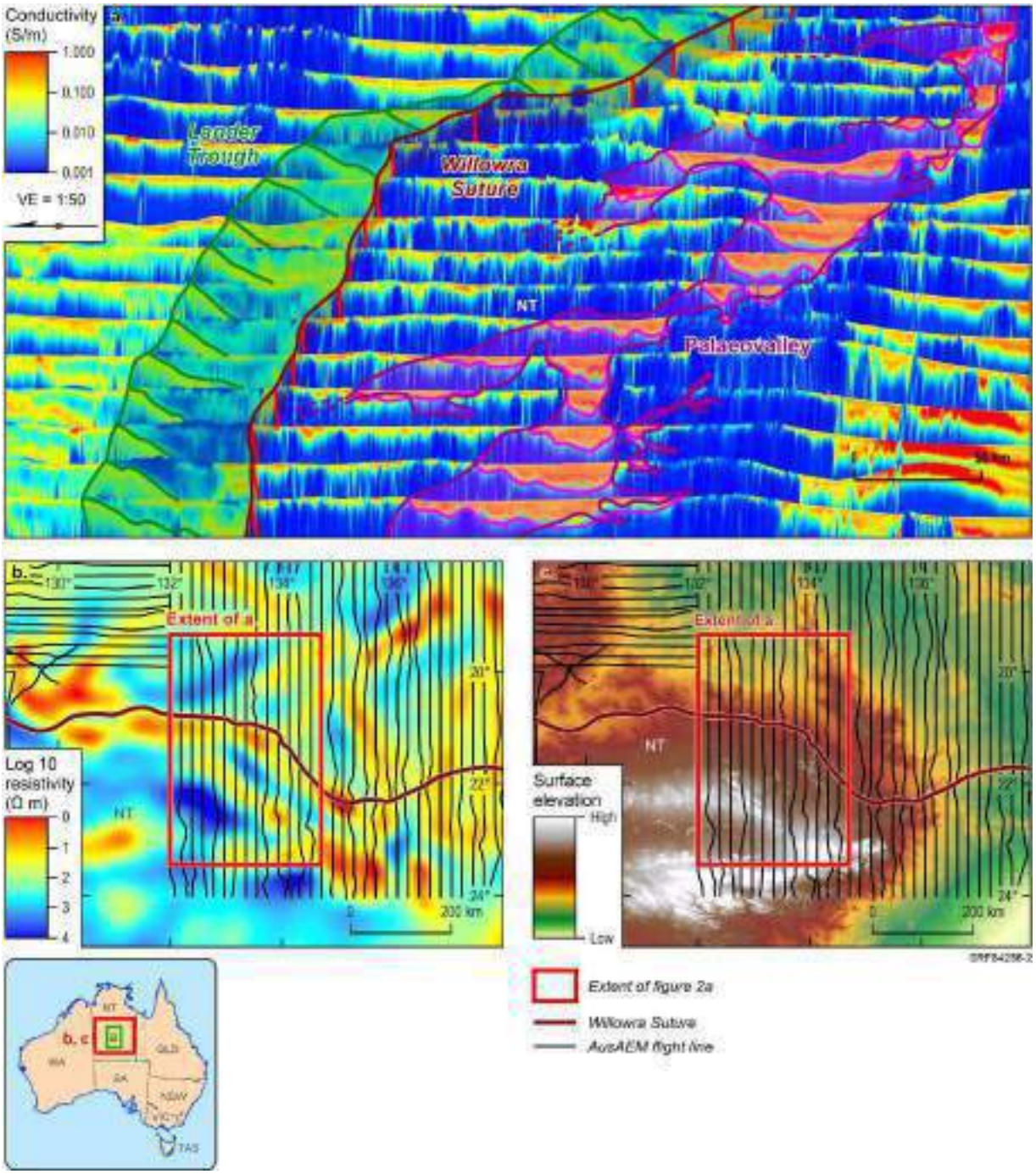

Figure 2 Palaeovalleys, first-order geological structures and sedimentary basins – examples of interpreted features in broadly-spaced AEM. a) Oblique view (looking east) of AusAEM conductivity sections (Ley-Cooper & Brodie, 2018) showing lithostratigraphic units in the Lander Trough of the Paleozoic Wiso Basin, first-order structural features, such as the near-surface expression of the Willowra Suture, and the connectivity and 3D geometry of palaeovalleys. b) AusLAMP long-period magnetotelluric 36 km depth slice (Duan, 2019) showing a deep conductivity anomaly that correlates with the distribution of the Willowra Suture. c) Digital elevation model (Geoscience Australia, 2017) illustrating a surface expression of the Willowra Suture. NT = Northern Territory

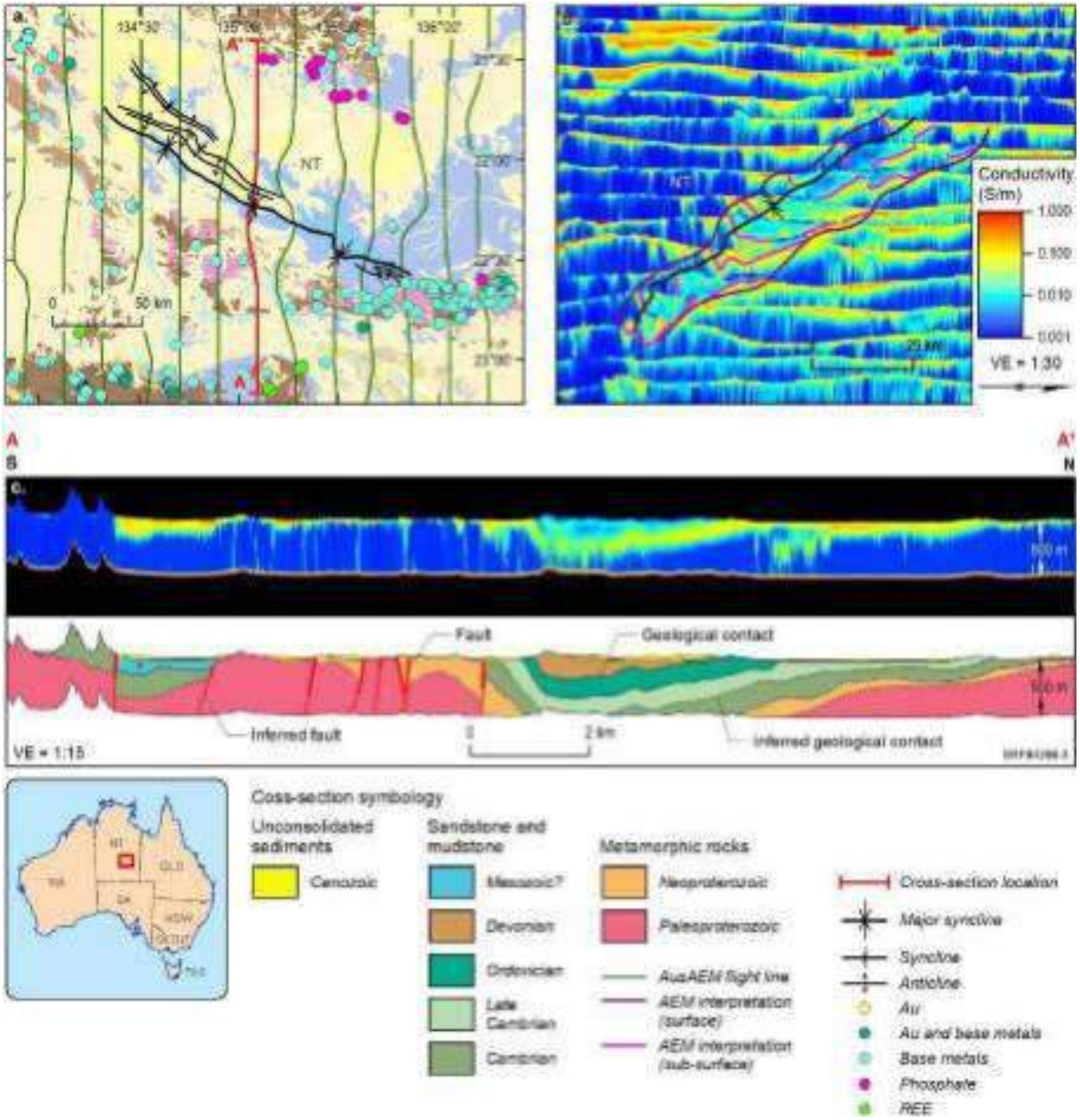

Figure 3 AusAEM interpretation in the Dulcie Trough/Syncline area. Internal structural geometries can be interpreted within the trough/syncline in the AEM. a) Map of the Dulcie Trough/Syncline area with interpretation of the major and minor fold axial traces observed in the AEM. The newly discovered minor folding in the northwest are examples of how the AEM can be used to refine 2D and 3D geological maps. b) Oblique view (looking west) of AusAEM conductivity sections (Ley-Cooper & Brodie, 2018) in the Dulcie Trough/Syncline area with basic interpretation delineating the conductivity contrast between Ordovician and Devonian stratigraphic units. This demonstrates the level of structural geometry that can be interpreted with the broadly-spaced surveys. c) Chronostratigraphic cross-section illustrating the level of detail that can be interpreted in this area, as a result of integrating the AEM with supporting geological and geophysical datasets. NT = Northern Territory

Enhanced Weathering and Oxidation Modelling in Coals by Integration of ATEM Results with Standard Coal Geoscience Data at Peak Downs Mine, Queensland, Australia

Amanda Zawada
BHP (BMA)
Brisbane, QLD
amanda.zawada1@bhp.com

Jonathan Lowe
BHP (BMA)
Brisbane, QLD
jonathan.lowe@bhp.com

Geoff Peters
SkyTEM
Perth, WA
gpe@skytem.com

SUMMARY

Geological processes of alteration such as oxidation and weathering lead to coal quality degradation. In the context of coal mining, this is significant because engineers must optimise mine plan designs with respect to waste rock and marketable coal. Airborne Transient Electromagnetic Methods (ATEM) can be useful in demarcating a coal seam's Limit of Oxidation (LOX) and add confidence to the related thickness of a weathered zone. This study demonstrates an attempt at using state of the art, high resolution ATEM data acquired over the Peak Downs Mine to improve upon the positioning of LOX 'lines', which can be notoriously difficult to model acutely where the coal seams are sub-parallel to the base of weathering estimate. The interpretation techniques applied throughout this study focus on using ATEM results visualized as X and Z component data profiles, compared to laterally constrained conductivity-depth inversions and borehole data. Such studies may enable geoscientists to better inform mine planning and development decisions.

INTRODUCTION

The primary focus of this study is to investigate if Airborne Transient Electromagnetic Method (ATEM) data can be analysed to improve the positional accuracy of a coal seam's Limit of Oxidation (LOX) line and the associated depth of Weathering (BHWE). The study uses data from the Peak Downs Mine (PDM) in the Bowen Basin of Queensland, approximately 31 km SSE of the town of Moranbah.

Within the context of coal mining, once a coal seam has undergone weathering and oxidation, the quality is lost and consequently, the resource wasted (Yang *et al.*, 2022). Therefore, it is important to identify the areas of coal which have been rendered worthless by these alteration processes (Lowe *et al.*, 2019). ATEM results are often used to facilitate the mapping of various geological features such as the BHWE and LOX lines, and can also help resolve coal seam architecture, structures & faults, igneous intrusives (e.g. basalts), hydrogeology or aquifer shape and thickness (Godber *et al.*, 2019).

The terms 'weathered' and 'oxidised' coals, are commonly discussed collectively as one (Yang *et al.*, 2022). However, in regards to the geo-modelling of coals, the limit of oxidation can be referred to as a 'LOX line' which is a boundary generated by intersecting a fresh coal seam's top with the Base of Weathering (BHWE). Improving upon LOX line positioning would also inherently result in an improved base of weathering estimate.

Current techniques for modelling LOX lines and BHWE are primarily based upon drilling data. However, the modelled position can be significantly offset by small errors in the depth of weathering where coal seam dips are very shallow.

Previous ATEM surveys conducted over various parts of the Bowen Basin have shown that the ATEM data can be effective for mapping the thickness of weathering (Godber *et al.*, 2019). Furthermore, electromagnetic (EM) methods may also assist with mapping LOX line positions, without the need to model them using the base of weathering estimate. This study shows partial success at generating such directly measured LOX lines for the purpose of better informing mine planning and development decisions.

METHOD AND RESULTS

EM methods have been employed widely across the minerals exploration industry for purposes of prospecting and detailed surveying (Telford *et al.*, 1990). In coal mining applications, ATEM is an attractive technique due to its ability to detect electrical conductors associated with the weathered overburden and heat affected (or 'coked') coals.

For the purposes of this study, a coal seam's LOX line is denoted as a conductor's edge, which can produce an observable and measurable EM anomaly in ATEM channel responses. This anomaly is caused by an electrical contrast at the contact between weathered (conductive) coal and fresh (generally resistive) coal. Therefore, when ATEM channel profile data is plotted, the LOX line of a coal seam can exhibit an EM profile with a particular amplitude and shape. This EM response is oftentimes consistent across a vast study area; therefore, it is mappable across closely spaced ATEM survey lines. The unique character of a coal seam's EM profile will vary depending on the architecture or dip of the seam, and the response may also appear suppressed or change shape between survey lines due to interference from any neighbouring conductors. Inter-seam conductive horizons can also mask the typically smaller response from the down-dip transition of the weathered seam to the fresh seam (Figure 1). As such, when interpreting, it can be helpful to model the conductive response as a 'plate'; either horizontal, vertical, or dipping, and compare this with the geology to determine the actual conductive sources and their relationship to the seams.

In attempts to achieve the optimal LOX line positioning for coal seams, the aforementioned technique has undergone initial

testing on a specific coal seam of interest at PDM, referred to as the 'P08'. The interpretation technique focused on visualising PDM's ATEM data displayed as conductivity-depth sections, which were carefully compared against the high moment (HM) X and Z component data channels. One of the key challenges in this study is assessing the potential for relying upon the HM X and Z data components (alongside EM conductivity–depth sections), for more accurate LOX line placement. An additional challenge is also determining how consistently traceable, and mappable the coal seam's EM response is, when attempting to correlate it across survey lines.

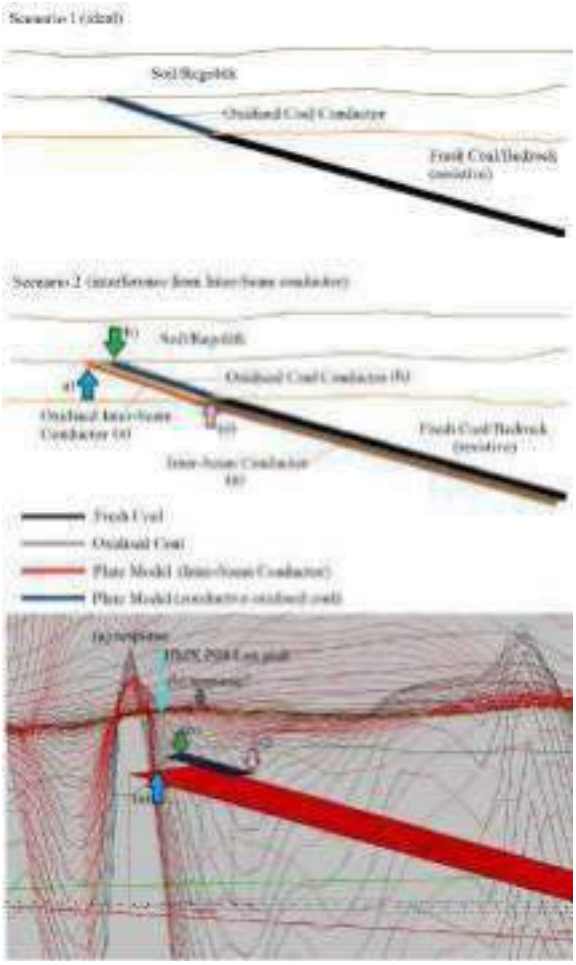

Figure 1. Two scenarios depicting the relationship of the EM plates to the geology. In the "ideal" scenario 1, weathered coal is the only conductor; In scenario 2, the relatively small response from the upper (b) and lower (c) edges of oxidised coal is masked by a much larger response from the upper edge of an inter-seam conductor (a).

The EM channel responses were plotted as profiles, and the P08's characteristic profile carefully analysed to determine a consistent 'edge' position for the LOX line. This edge was tracked across the EM survey lines throughout the study area, and each position validated using actual field LOX points which were uncovered during mining and reported by field geologists during pit inspections. For additional verification, the EM data has been compared against all other available coal geoscience data (Figure 2) such as topography, structural surfaces, and the geologists modelled coal seams, LOX lines, and BHWE (inferred mainly by drilling). Furthermore, the data for P08 was modelled as conductive plates using Maxwell, in attempts to more precisely position the P08 LOX edge on the EM profile.

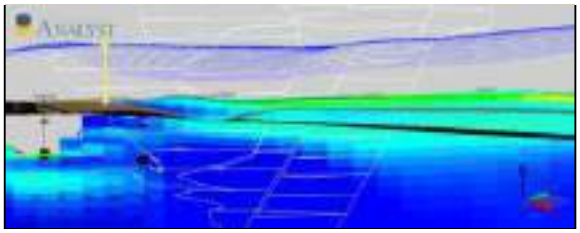

Figure 2. ATEM results displayed in 3D with other available coal geoscience data.

CONCLUSIONS

Several attempts have been made to clarify accurate placement of the P08 coal seams LOX line on EM channel profiles, using the HM X and Z data components. The consistency of the P08's EM response has also been assessed across the survey, and LOX line interpretations have been further validated using EM conductivity depth sections, as well as all other available geoscience data. While testing the reliability of this approach, the theorised LOX points were compared to the actual field LOX points as measured and reported by mine site geologists after the uncovering of the coal. Findings have confirmed that it is possible to approximate the P08 coal seams LOX line position on EM channel profiles, and consistently correlate the profile response across the survey's extent. However, Maxwell modelling suggests that the main HM X anomaly may be due to an inter-seam tuff horizon which is possibly obscuring the response from the weathered coal horizon above (Figure 1). The tuff may be a reliable marker horizon for the P08 seam, however further investigation is required to confirm. Further testing is also required to understand if the precise positioning of the LOX 'edge' on EM profiles is possible, and to determine if this approach is repeatable for other coal seams in PDM. Ongoing trials will evaluate the suitability of using this approach to enhance future modelling and interpretations of the LOX lines.

ACKNOWLEDGEMENTS

Thank you to BHP Mitsubishi Alliance (BMA) for allowing the publication of the data and results, as well as SkyTEM Australia Pty. Ltd. for acquiring and modelling data.

REFERENCES

Godber, K. E., Reid, J., Smith, G. L., 2019. Application of Airborne EM to Bowen Basin Coal Projects. Meeting, ASEG, Perth, Extended Abstracts: 1-4.

Lowe, J., Reid, J., Battig, E., Napier, S., Eremenco, D., 2019. Electromagnetic and electrical methods applied to mapping coked coal – A case study from the Bowen Basin, Eastern Australia. Meeting, ASEG, Perth, Extended Abstracts: 1-5.

Telford, W. M., Geldart, L.P., Sheriff, R.E., 1990. Applied Geophysics. 2nd ed. Cambridge University Press.

Yang, Y., Xiong, B., Peng, S., Liu, S., Chen, H., Zhang, T., 2022. Exploring weathered and oxidized zones of coal seams using the transient electromagnetic method. *Energy Exploration & Exploitation* 40:1634-1648.

Beyond conductive targets: Characterizing lithium-prospective lacustrine evaporite mineral systems of North America's Basin and Range Province with regional-scale AEM

Lyndsay B. Ball*
U.S. Geological Survey
Denver, Colorado USA
lbball@usgs.gov

Paul A. Bedrosian
U.S. Geological Survey
Denver, Colorado USA
pbedrosian@usgs.gov

Chloe D. Gustafson
U.S. Geological Survey
Denver, Colorado USA
cgustafson@usgs.gov

*presenting author

SUMMARY

The Basin and Range province of North America hosts substantial lacustrine evaporite mineral systems prospective for lithium, a critical mineral currently listed for mineral resource assessment by the U.S. Geological Survey. Airborne electromagnetic (AEM) surveys are being conducted to support these assessments by identifying shallow clays and brines, as well as through improving the shallow subsurface geologic framework of the regional fluid flow system. In 2022-2023, three focus areas with proven lithium resources or considered highly prospective for lithium are being surveyed. Results from this effort can help to improve our understanding of the geologic conditions and geophysical signatures associated with known resource regions and benefit future lithium resource assessments by identifying regions with similar geophysical and geologic characteristics.

Key words: airborne electromagnetic, critical minerals, lithium, brine, groundwater

INTRODUCTION

The Basin & Range Province of North America hosts a wealth of base, precious, and critical mineral resources, with Nevada serving as one of the top mineral producing states in the United States. (U.S. Geological Survey, 2023). The Basin and Range is a large extensional region in the arid and semi-arid southwestern United States with elevated heat flow, widespread Tertiary and Quaternary volcanism, and persistent grabens forming numerous closed intermountain basins. These conditions are consistent with potential lithium enrichment in lacustrine evaporite mineral systems (Bradley et al. 2013; Bradley et al. 2017; Hammarstrom et al. 2020). Lithium is key to the clean energy transition, with demand for rechargeable lithium-ion batteries driving recent increases in global consumption (U.S. Geological Survey, 2023). Lithium is also used in the manufacturing of ceramics, glass, and lubricants.

Lacustrine evaporite systems form in closed basins with arid climates where elements carried in surface water, groundwater, or geothermal fluids become concentrated in the shallow near-surface environment by evaporation. Brine deposits in these systems can potentially host economically viable lithium concentrations, and where lithium-enriched brines encounter lake sediments, lithium can become concentrated within clay deposits (Hammarstrom et al., 2020). These shallow clay and brine resources are obvious conductive targets for AEM methods. However, these evaporite systems are defined by the regional fluid flow system, and lithium prospectivity relies on the appropriate hydrogeologic conditions, presence of source materials, and basin history. As such, the potential contributions of AEM surveys to lithium resource assessments extend beyond simply identifying conductive brines and clays to improving the broader regional hydrogeologic and geologic framework.

The process model leading to viable lithium brine deposits has several characteristics (Bradley et al. 2013; Munk et al. 2016) where AEM surveys can provide improved hydrogeologic context (Figure 1):

1. An arid environment to facilitate evapoconcentration of surface water and shallow groundwater, and adequate aquifers to host brine.
    - Conductive brines indicate that substantial evapoconcentration has occurred; basin resistivity structure can provide additional information about the structure of aquifers and aquitards of the broader hydrogeologic framework.
2. Tectonically driven subsidence leading to persistent closed basins.
    - While modern surface watersheds may be closed, geophysical imaging of subsurface geologic structure can provide insights on fault structure, shallow low-permeability bedrock, and the potential for modern interbasin groundwater flow, with additional implications to improving our understanding of fault history, basin evolution, and groundwater basin closure.
3. Lithium bearing source rocks.
    - The extent of resistive silicic volcanic deposits in the near surface exposed to fluid flow can be identified where resistivity contrasts to underlying deposits are adequate. Improved characterization of bedrock aquifers may define deeper preferential groundwater flow paths or barriers influencing mountain block recharge from source rocks to evapoconcentration centers over time.
4. Igneous or geothermal fluids.
    - Improved definition of faults may inform our understanding of shallow connectivity to regional geothermal systems as a potential subsurface source of lithium-enriched fluids and may

also identify conductive hydrothermal features in the near-surface. This is particularly enhanced by supplemental deeper resistivity models from regional magnetotelluric surveys.

METHOD AND RESULTS

Under the Earth Mapping Resources Initiative (EarthMRI) program, the U.S. Geological Survey began conducting regional-scale AEM surveys of the Basin and Range Province in December 2022, with data acquisition continuing through the spring of 2023. The surveys consist of a total of 11,000 line kilometers distributed over three areas of interest (AOI) recently designated as lacustrine evaporite system focus areas (Hammarstrom et al. 2020) (Figure 2). The regional survey design uses a 5 km line spacing, where orientation shifts to remain perpendicular to the changing primary structural trends. Denser line spacing over areas undergoing detailed geologic mapping and alternate line orientations to explore secondary geologic trends and basin structure are also used. Data collection is being conducted by Xcalibur Multiphysics using multiple configurations of the HeliTEM^2 system to adapt to changing target depths, the need for shallow resolution, and the mountainous terrain; these systems use variations of airframe diameter, base frequency, transmitter moment and waveform (Burrows et al., 2023).

The 2022-2023 survey focuses on three proven and prospective regions for lithium resources (Figure 2):

- Region 1 encompasses a number of lithium-prospective closed basins in the South-Central Marshes area, including Clayton Valley, North America's only active lithium brine mining operation. A high-resolution infill survey in this region captures Silver Peak Range and the Rhyolite Ridge lithium clay deposit.
- Region 2 includes a high-resolution infill survey of McDermitt Caldera, a resurgent caldera associated with the Yellowstone Hot Spot with proven lithium resources associated with the Thacker Pass clay deposit, and regional coverage is extended into the surrounding basins.
- Region 3 encompasses Railroad Valley, a lithium-prospective closed basin with an extensive brine field undergoing active exploration, and the adjacent volcanic regions that contribute to its greater hydrogeologic system.

Results from these surveys can help to improve our understanding of the geologic conditions and geophysical signatures associated with these proven and prospective resource regions. This work can benefit future lithium resource assessments by identifying basins with geologic characteristics consistent with current process models, as well as by eliminating regions that lack substantial brine or clay deposits to host enriched lithium. The AEM surveys are also relevant to the geologic frameworks of several other mineral systems (Bedrosian et al., 2023) as well as groundwater, geothermal, and hazard studies.

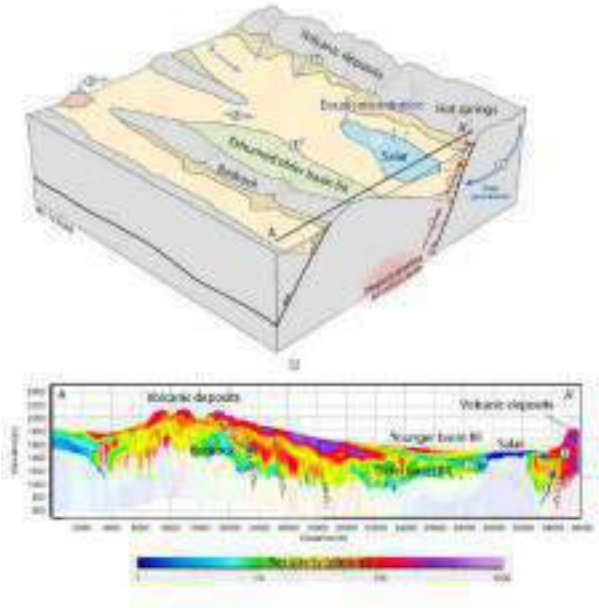

Figure 1. Conceptualization of the sources of lithium brine deposits in lacustrine evaporite systems in comparison to an example preliminary inverted resistivity section from survey region 1 in western Nevada (fig. 2). Preliminary results highlight substantial resistivity contrasts between brine, bedrock, basin fill, and volcanic units that define the geologic framework to depths of up to 500+ m. Numbers correlate to key aspects of the lithium brine process model described in the text (1, evapoconcentration resulting in conductive, high salinity groundwater; 2, basin hydrogeologic closure defined by the regional geologic structure; 3, lithium bearing source rocks exposed to fluid flow; 4, igneous and geothermal fluids and potential flow paths to the near surface along faults and other basin structures). Conceptual model modified from Bradley et. al (2017).

CONCLUSIONS

While the presence or absence of economical concentrations of lithium are not directly detectable by geophysical methods, AEM surveys can contribute to lithium resource assessments in several ways. Basins with substantial shallow conductive brine and clay deposits consistent with the potential for elevated lithium concentrations can be identified. In addition, improved and consistent detail in the regional geologic framework can help evaluate where other key conditions of mineral system process model are met, including geologic structure consistent with groundwater basin closure and potential regional fluid flow between evapoconcentration areas and lithium source materials. The 2022-2023 Basin and Range AEM surveys can help define the geophysical signatures of locations where lithium resources are known to occur and will provide improved regional geophysical imaging of the shallow geologic framework to better understand where similar conditions may exist that remain underexplored.

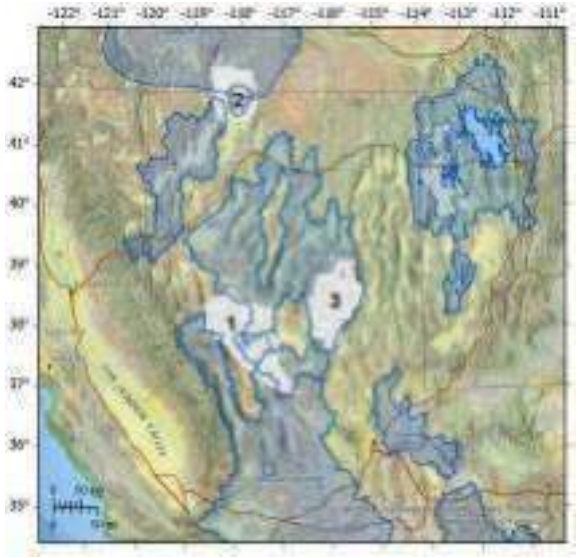

Figure 2. Map of 2022-2023 AEM survey areas (white lines) for the (1) Central Marshes, (2) McDermitt Caldera and (3) Railroad Valley regions. Lithium focus areas (blue shaded areas) modified from Hammarstrom et al. (2020).

ACKNOWLEDGMENTS

This work is funded by the U.S. Geological Survey's Earth Mapping Resources Initiative and the Mineral Resources Program. AEM surveys are being conducted by Xcalibur Multiphysics under contract to the U.S. Geological Survey through Fugro Earthdata Inc; Dwayne Beatty, Paris Cassidy, David Miles, and David Murray were instrumental to the execution of these surveys. Any use of trade, firm, or product names is for descriptive purposes only and does not imply endorsement by the U.S. government.

REFERENCES

Bedrosian, P. A., Ball, L. B., and Gustafson, C. 2023. Airborne electromagnetic imaging for critical minerals resource assessment. Intended for submission to the 8th International Airborne Electromagnetics Workshop, Fitzroy Island, QLD, Australia.

Bradley, D. C., Stillings, L. L., Jaskula, B. W., Munk, L. , and McCauley, A. D. 2017. Lithium. U.S. Geological Survey Professional Paper 1802-K. https://doi.org/10.3133/pp1802K.

Bradley, D. L. Munk, H. Jochens, S. Hynek, and K. A. Labay. 2013. A preliminary deposit model for lithium brines. U.S. Geological Survey Open-File Report 2013-1006. https://doi.org/10.3133/ofr20131006.

Burrows, D., Murray, D., and Plastow, G. 2023. Helitem^2 – system updates for broadband AEM data. Intended for submission to the 8th International Airborne Electromagnetics Workshop, Fitzroy Island, QLD, Australia.

Hammarstrom, J. M., C. L. Dicken, W. C. Day, A. H. Hofstra, B.J. Drenth, A.K. Shah, A. E. McCafferty, et al. 2020. Focus areas for data acquisition for potential domestic resources of 11 critical minerals in the conterminous United States, Hawaii, and Puerto Rico—aluminum, cobalt, graphite, lithium, niobium, platinum-group elements, rare earth elements, tantalum, tin, titanium, and tungsten. U.S. Geological Survey Open-File Report 2019-1023-B. https://doi.org/10.3133/ofr20191023B.

Munk, L., S. A. Hynek, D.C. Bradley, D. Boutt, K. Labay, and H.Jochens. 2016. Lithium brines: a global perspective. In Rare earth and critical elements in ore deposits, edited by P. L. Verplanck and M.W. Hitzman, 18:0. Society of Economic Geologists. https://doi.org/10.5382/Rev.18.14.

U.S. Geological Survey. 2023. Mineral commodity summaries 2023: U.S. Geological Survey, 210 p. https://doi.org/10.3133/mcs2023.

Airborne electromagnetic imaging for critical-minerals resource assessment

Paul A Bedrosian
U.S. Geological Survey
Denver, Colorado, USA
pbedrosian@usgs.gov

Lyndsay B Ball
U.S. Geological Survey
Denver, Colorado, USA
lball@usgs.gov

Chloe Gustafson
U.S. Geological Survey
Denver, Colorado, USA
cgustafson@usgs.gov

Patricia MacQueen
U.S. Geological Survey
Denver, CO, USA
pmacqueen@usgs.gov

SUMMARY

Mineral resource assessments are fundamentally grounded in data – specifically data that differentiate regions prospective for a resource from those that are not. The Earth Mapping Resources Initiative is collecting baseline geophysical data over targeted areas of the United States to support upcoming critical mineral assessments. Approximately 30,000 line-kms per year of airborne electromagnetic (AEM) data are being collected as part of this effort. In the first year, surveys in Nevada, Alabama and Alaska will be carried out to inform national-scale graphite and lithium assessments. AEM surveying for graphite is one of the few cases where geophysics can directly map the resource of interest; we describe AEM surveys to be flown over two of the primary graphite resources in the nation. We also describe a regional survey focused on lithium brines and clays, where AEM models will be used to constrain deposit genesis models and to narrow the currently vast region considered prospective for lithium. We highlight aspects of the survey design and show preliminary results for those surveys that have already begun flying.

Key words: airborne electromagnetic, critical minerals, lithium, graphite

INTRODUCTION

The Earth Mapping Resources Initiative (EarthMRI) is a partnership between the United States Geological Survey (USGS) and State Geological Surveys to modernize surface and subsurface geological mapping for the nation and to identify areas with potential for undiscovered critical minerals. Components of the program include airborne geophysical surveying, geologic mapping, and geochemical sampling. These data will ultimately be used to support mineral resource assessments and prospectivity mapping within a mineral-systems framework (Wyborn et al., 1994).

Geophysical surveying under EarthMRI, begun in 2019, was initially limited to aeromagnetic and radiometric data. Airborne electromagnetic (AEM) data acquisition began in 2022 and is currently acquiring ~30,000 line-km of data annually. AEM surveys to date have focused on lithium, a critical component of rechargeable batteries, and graphite, used for lubricants, batteries, and fuel cells.

Two AEM surveys are being flown over high-grade metamorphic terranes prospective for graphite: 1) the Alabama graphite-vanadium belt within the Southern Appalachian Mountains and 2) the Kigluaik, Bendeleben, and Darby Mountains of the Seward Peninsula, Alaska. The latter hosts the world-class Graphite Creek deposit, while the former is an area of both historic graphite mining and ongoing resource development. While graphite, with its enhanced electrical conductivity, is the primary electrical target, both survey areas host a wide range of other critical mineral commodities.

In addition, a multi-year regional AEM survey is being flown over the Basin and Range (B&R) province of Nevada and Oregon. This survey is focused on lithium contained within electrically conductive basin brines and clays. Worldwide lithium production comes primarily from pegmatites, but interest in sediment-hosted lithium resources has led to considerable exploration and development, predominantly in the B&R, which also includes the first lithium-brine mining operation in North America. As nearly half of the B&R is considered prospective for lithium, these surveys aim to better understand the components and controls on basin lithium formation, and in doing so reduce the exploration space for this class of deposits. Beyond lithium, the B&R province contains a range of deposits that may host critical minerals. Porphyry Cu-Mo-Au and Climax type deposits, for example, are known throughout the B&R and may contain beryllium, fluorine, tungsten, and gallium. These deposits are commonly characterized by conductive quartz-sericite-pyrite alteration halos, ideal targets for AEM.

METHOD AND RESULTS

The 11,000 line-km B&R survey spans several tectonic domains, requiring a flexible survey design with variable flight azimuth crossing different structural domains. To optimize survey design, Quaternary faults, mapped strike directions, and geologic cross-sections were examined to define three distinct flightline azimuths that vary throughout the survey area to best capture local structural trends (Figure 1). A nominal 5 km line spacing was chosen to balance the large survey area with a need for continuity between adjacent sections. In areas of known lithium resources, more densely spaced flightlines were flown to facilitate investigations into lithium process models (Ball et al., 2023; Bradley et al., 2013) and to support detailed geologic mapping activities. Finally, as the depth scale of interest ranges from ~5 m to 500 m (shallow sedimentary layers to deep

basement conductors), a hybrid system approach was employed using three systems with differing moment, loop size, waveform, and base frequency (Murray et al., 2023). This hybrid approach allows for superior depth-of-investigation in flat areas using a large, high-moment system while permitting better altitude control in areas of steep terrain using a lighter, smaller system.

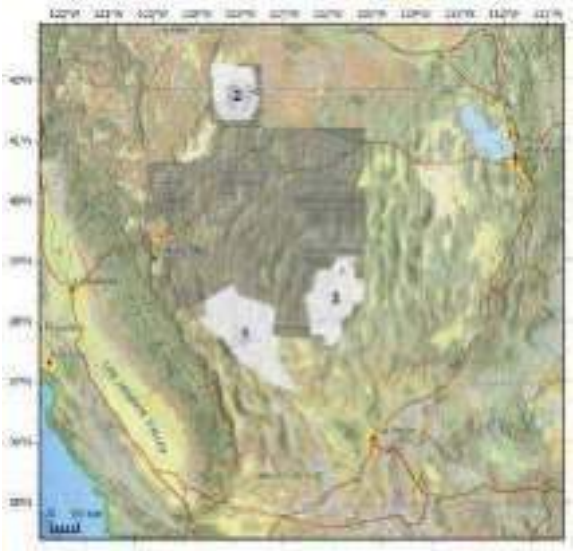

Figure 1. Nominal flight plan for regional AEM survey in Nevada. White lines in areas 1-3 were flown in 2023. Variable line azimuths capture changes in structural trend.

The dynamic range within the measured data is reflected in the model domain by a pronounced contrast between resistive basement and bedrock exposed in the ranges and thick conductive sedimentary packages in the intervening basins (Figure 2). Depth of investigation is ~500 m over the ranges, reducing to ~300 m in the basins, and as little as 100 m over clays and brines within closed basins. Induced polarisation (IP) effects are occasionally observed near range fronts, where thin conductive sediments overlie rocks. More pronounced are fault-bounded blocks of limestone and dolomite that exhibit strong IP effects including fully negative decay curves. As of this writing, flying is 2/3 completed, while another 10,000 line-km of flying is being contracted for 2024.

The AEM survey in Alabama is focused upon an area of historic mining and ongoing development in the graphite-vanadium belt but includes a halo of widely spaced lines designed to map the structural framework of this complex geologic terrane (Figure 3). The survey area, situated between the major metropolitan areas of Montgomery and Birmingham, is heavily built up, requiring a detailed survey design to both avoid airspace restrictions and minimise the impact of roads, powerlines, pipelines, and electrical substations. As of this writing, data collection has just begun. AEM data collected along a pair of test lines shows good agreement with ground geophysical data (transient electromagnetic and electrical resistivity tomography profiles) collected nearby. Inverted resistivity models from the AEM test line data show strong variability, with pronounced basement conductors (~1 Ω·m) over mapped graphite-bearing lithologies and a strong resistivity contrast at the edge of the mapped graphite belt (Figure 4).

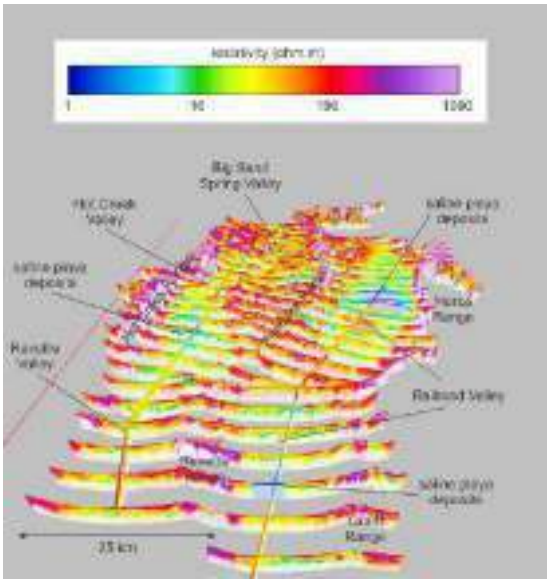

Figure 2. Perspective view of the Railroad Valley block looking north (area 3 in Figure 1). Strong conductors reflect clays and brines within closed valleys.

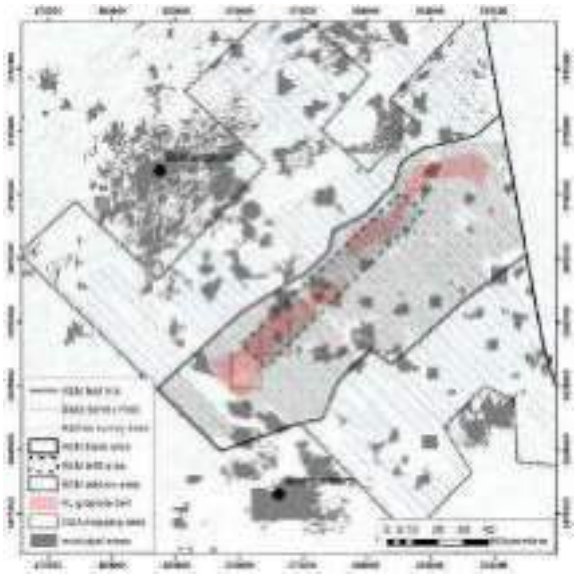

Figure 3. Flight plan for regional AEM survey in Alabama. Graphite-vanadium belt indicated in red.

The Alaska AEM survey, not contracted as of this writing, is the most remote of the surveys, covering a vast area of high-grade metamorphic rocks (Figure 5). Analogous to the Alabama belt, graphite in Alaska is contained within narrow, elongate stringers that can be traced for 10s of kilometers along strike. At the Graphite Creek deposit, these stringers contain lenses of massive graphite up to 1 m thick and with grades approaching 50% (Case et al., 2023). A commercial AEM survey over the Graphite Creek deposit area imaged several sub-vertical conductors aligned with regional faults and extending for more

than 15 km along strike. A goal of the Alaska AEM survey is to cover the entire region of high-grade metamorphic rocks (6,000 km^2) and to understand the geologic and tectonic controls on graphite formation and concentration in metamorphic terranes.

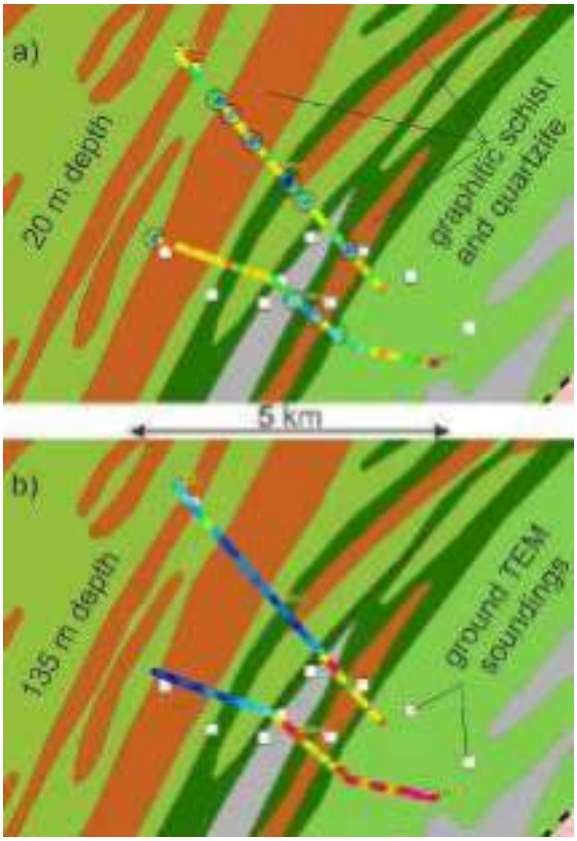

Figure 4. Inverted resistivity over the Alabama Graphite-Vanadium belt at (a) 20 m and (b) 135 m depth. Color scale is as in Figure 2. Note correspondence between graphitic schist and quartzite (brown) and shallow conductors in a) and abrupt change in resistivity along the eastern margin of the belt in b). Dark and light green units are amphibolite biotite gneiss, respectively. Gray unit is non-graphite bearing mica schist.

CONCLUSIONS

AEM surveys are an effective way to collect data at the scales needed to support regional and national-scale resource assessments. The initial AEM investment by EarthMRI has focused on 'low-hanging fruit,' including mapping graphite in metamorphic terranes and mapping areas prospective for lithium brines and clays, where imaging the lithologic and structural framework directly informs conceptual models for deposit formation. Future EarthMRI AEM surveys will expand upon these findings, both in terms of evaluating other regions for these same resources and in expanding to cover additional mineral systems (e.g., mafic magmatic and volcanogenic seafloor systems) known to host critical mineral commodities.

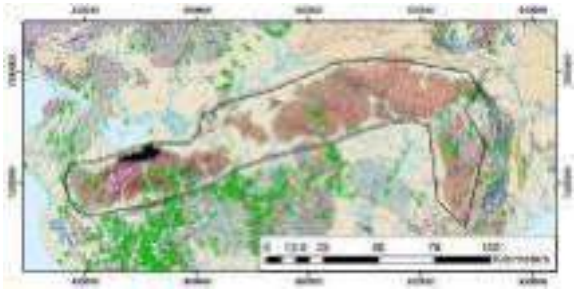

Figure 5. Alaska graphite survey area (black polygon). Filled black polygon denotes exploration AEM survey flown over the Graphite Creek deposit. Green symbols are mineral occurrences from the Mineral Resources Data System (primarily gold within the Nome mining district).

ACKNOWLEDGMENTS

This work is funded by EarthMRI and the USGS Mineral Resources Program. AEM surveys in Nevada and Alabama are being conducted by XCalibur Multiphysics and SkyTEM Surveys ApS, respectively, under subcontracts to the USGS through the Geospatial Products and Services Contracts. The successful execution of these surveys is thanks to the efforts of these contractors as well as the Geological Survey of Alabama, the Nevada Bureau of Mines and Geology, and the Alaska Division of Geological and Geophysical Surveys. Any use of trade, firm, or product names is for descriptive purposes only and does not imply endorsement by the U.S. government.

REFERENCES

Ball, L.B., Bedrosian, P.A. and Gustafson, C. 2023. Beyond conductive targets: the role for regional-scale AEM in understanding lithium-prospective lacustrine evaporite mineral systems of North America's Basin and Range Province, 8th Intl. Airborne Electromagnetics Wksp., Fitzroy, Il., Australia.

Bradley, D. L. Munk, H. Jochens, S. Hynek, and K. A. Labay. 2013. "A Preliminary Deposit Model for Lithium Brines."USGS Open-File Report 2013-1006. https://doi.org/10.3133/ofr20131006

Case, G.N.D., Karl, S.M., Regan, S.P. et al. Insights into the metamorphic history and origin of flake graphite mineralization at the Graphite Creek graphite deposit, Seward Peninsula, Alaska, USA. Miner Deposita (2023). https://doi.org/10.1007/s00126-023-01161-3.

Murray et al., 2023 - Comparison of HeliTEM variants, 8th Intl. Airborne Electromagnetics Wksp., Fitzroy, Il., Australia.

Wyborn, L.A.I., Heinrich, C.A. and Jaques, A.L. 1994. Australian Proterozoic mineral systems: essential ingredients and mappable criteria. In: Proc. Australasian Inst. Mining & Metallurgy An. Conf., Melbourne, 109–115.

AEM base frequency and depth of investigation

Magdel Combrinck
NRG
Unit 1, Stand 98, Tijger Vallei Office Park
Silver Lakes Rd, Pretoria
magdel.combrinck@nrgex.co.za

Richard Wright
NRG
Unit 1, Stand 98, Tijger Vallei Office Park
Silver Lakes Rd, Pretoria
richard.wright@nrgex.co.za

SUMMARY

Recent advances in time domain airborne electromagnetic (AEM) data acquisition include lower noise levels and subsequently the use of 12.5 Hz and even 6.25 Hz base frequencies instead of the dominant 25 Hz. The main advantages associated with lower base frequencies are increased depth of investigation (DOI) and improved conductor discrimination and detection in the high conductance range. A study was undertaken to quantify these improvements for the Xcite system that resulted from implementing a new suspension system.

A synthetic model study was done, evaluating the effect of base frequency and noise levels (utilising noise samples collected at high altitude) on a variety of conductance models. The results were displayed in different formats to illustrate the combined effects of conductance, base frequency and noise levels on DOI. There is no simple formula or correlation to quantify DOI as a function of all relevant parameters and visual analysis of model and inversion results for relevant conductance models is recommended to determine the best acquisition parameters for a survey.

The results highlighted the importance of noise levels compared to base frequency to achieve larger depths of investigation and the value of lower base frequencies when exploring for conductive targets in a relatively conductive host environment.

Key words: base frequency, depth of investigation, conductance, time domain electromagnetic, AEM

INTRODUCTION

In the first half of 2022, NRG has developed a new suspension system which reduced the Xcite 12.5 Hz noise levels by a factor of ten and made this acquisition choice very attractive for prospective clients. Making an informed decision on which base frequency to use requires a quantitative analysis of all the parameters that affect EM responses, including system specifications, base frequency, target conductance model and noise levels.

Lower base frequencies are associated with deeper DOI based on the ideas of wider pulse widths allowing for better target excitation, as well as longer off-times providing more time to measure at greater depths (Liu, 1998, Konieczny et al., 2016). The concept of later times being associated with greater depths can most likely be attributed to the ”smoke-ring” view of electric currents diffusing into the earth (Nabighian, M. N., 1979; Reid and Macnae, 1998). This is a useful model and allows us to understand the basic relationship between conductivity and DOI.

However, there are instances of good conductors in very resistive host rock environments where dominant currents stay concentrated in the conductor and don’t necessarily migrate deeper with time. Figure 1 illustrates this with a nomogram and comparative decay curves. This data was generated for a 400 m x 400 m plate model at 100 m depth and highlights a typical instance where more information is obtained from the 12.5 Hz base frequency with later time channels when compared to the 25 Hz response.

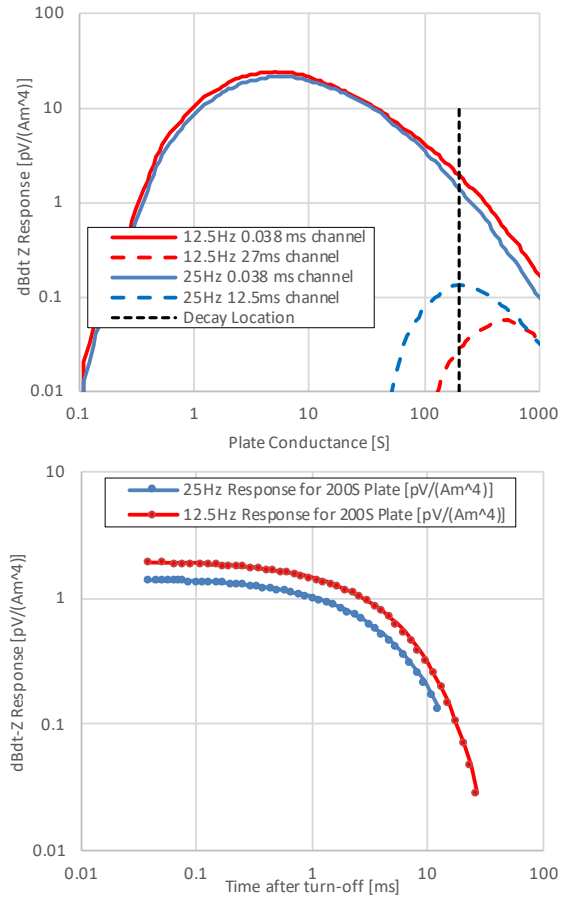

Figure 1: Conductance nomogram for a 400 m x 400 m plate at depth 100m. Only the first and last channels of each base frequency dBdt-Z is shown in the top panel nomogram, while all the channels for the 200 S response are shown in the bottom panel decay curves. Note the signal at later times in the 12.5 Hz that is completely unrelated to DOI.

However, this additional information does not imply a greater DOI; all currents are modelled at 100 m inside the conductive plate. Results from synthetic data are not meaningful without adding noise levels. For example, in Figure 1 a noise level of less than 0.01 pV/(Am^4) is implied, rendering all data useful. If the noise level was at 0.5 pV/(Am^4), there would be no benefit to measuring the later times in the 12.5 Hz because it would not contribute to any modelling or interpretation efforts.

In reality, geology is more complex than either a homogeneous half-space or simple plate model can represent and DOI has to be viewed from different perspectives, including as many parameters as possible.

For this study I calculated a number of layered earth models, plate models in free air and also plate models in a conductive environment for 25 Hz and 12.5 Hz base frequencies. The software used were GALEISBSTDEM (Brodie, 2016), Maxwell, and LeroiAir (Raiche, 1997). For noise samples I used Xcite data measured at high altitude with the different base frequencies using old and new suspensions. The results displayed the complexity of responses varying with depth, conductance and base frequency.

METHOD AND RESULTS

Table 1 lists the model types, descriptions and analysis strategy that were used. Not all results can be presented in this abstract, but a selection of the most important findings are shown in Figures 2 to 4.

Figure 2 illustrated the results from three different layered earth models that were inverted to recover the thickness of the first layer. As can be seen in rows 2 and 3, these are challenging models and even with no noise added the layer thickness cannot be recovered accurately, however, the 12.5Hz base frequency definitely has an advantage at depth.

Once the appropriate noise samples are added this picture changes. The 25 Hz results have a better DOI than either of the 12.5 Hz data options for model 1. For models 2 and 3 the 12.5 Hz with new suspension noise is superior to the 25 Hz results which in turn outperforms the 12.5 Hz inversion with old suspension noise. These images are presented as comparative visual examples; exact DOI will strongly depend on noise and altitude for any specific survey.

The results from Model 4 indicated good recovery of the conductive layer with conductance values up to 250 S for the 25 Hz base frequency, while the 12.5 Hz could discriminate up to 280 S and approximately 300 S respectively for the old and new suspension noise.

For models 5 and 6 the modelled data were represented as 3D conductance-depth nomograms. An example is shown in Figure 3 with EM responses of a 400 m x 400 m plate presented for a range of conductances and depths. Noise levels are implemented by clipping the traces at the appropriate response value.

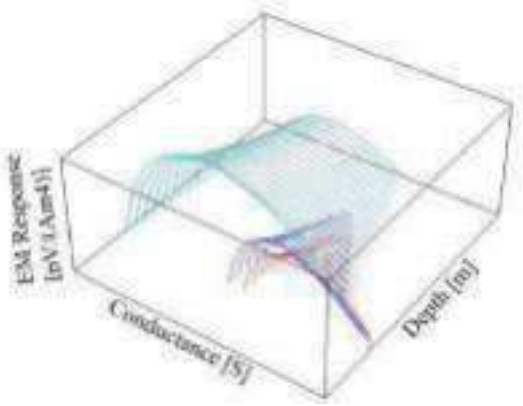

Figure 3: A 3D conductance-depth nomogram. The conductance varies from 0.1 to 106 S (log scale), depth varies from 20 to 500 m (linear scale) and EM response varies from 0-380 pV/(Am^4) (log scale). The cyan and blue traces are the first and last channels of 25 Hz data, while the light red (very close to cyan traces) and dark red traces are the first and last channels from 12.5 Hz modelled data.

A simplified parameter derived from the 3D nomograms were calculated to better compare data sets. For each base frequency and noise combination, the number of late time channels above noise levels are determined. Locations where 4-6 channels are above noise level are plotted on the same 3D view (Figure 4) to outline effective depth and conductance ranges for detecting the modelled targets 5 and 6.

Conductance ranges are bound to the left and right, while depths are bound at the top. This illustration of results is useful to compare the responses of different base frequencies and noise levels, while highlighting the complex relationship to conductance and depth. In figure 4 (top panel) we can see that 25 Hz data has better DOI in the range of 1 to 100 S. At higher conductances, the 12.5 Hz data with new suspension has a better chance of detecting conductors than the 25 Hz and up to a 200 m advantage over the old suspension. In Figure 4 (bottom panel) the results from model 6 is shown. The smaller target in a conductive host environment reduces the maximum DOI to 250 m compared to the 580 m for model 5. The general trend remains similar with 12.5 Hz base frequency outperforming the 25 Hz in the higher conductance range.

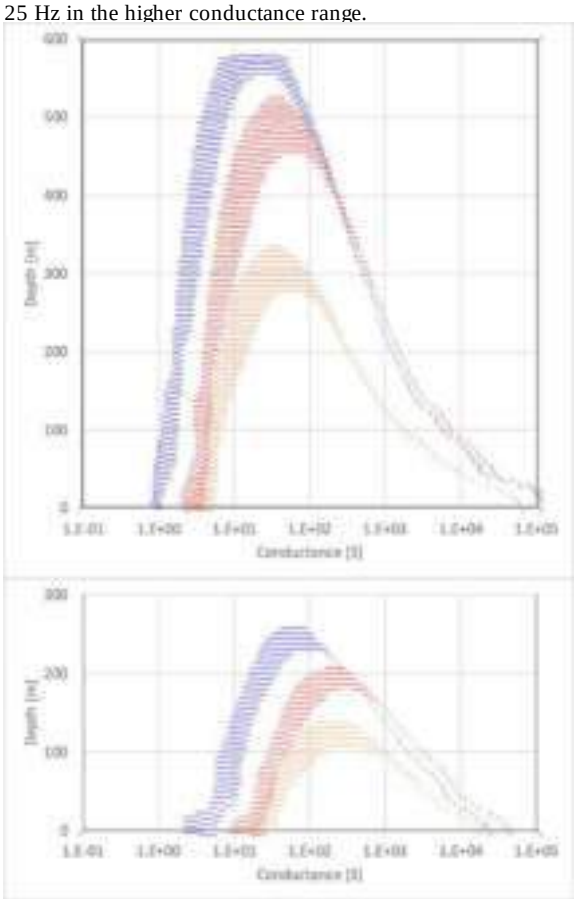

Figure 4: The conductance and depth ranges are mapped where 4-6 channels are higher than noise levels for two plate models at 25 Hz base frequency (blue), 12.5 Hz base frequency and old suspension noise (orange) and 12.5 Hz base frequency and new suspension noise (red). The top panel is for a 400 m x 400 m plate and the bottom panel is a 100 m x 100 m plate; both located in a conductive host environment.

CONCLUSIONS

The relationship between DOI and base frequency is strongly dependent on noise levels as well as the conductance range of the target and host environment.

12.5 Hz Data are advantageous in the higher conductance range (more than 200S) while 25 Hz data has a better range for more resistive targets. The improved suspension of the Xcite system resulted in a 10-fold decrease of noise levels for 12.5 Hz base frequency data and depending on the conductance range and type of model this translates to an improved DOI from 20 m to almost 200 m for the models included in this study.

In areas where the 25 Hz and 12.5 Hz DOIs are similar, the 12.5 Hz data offer better conductor discrimination and will add more value to interpretation.

ACKNOWLEDGMENTS

The NRG engineering squad deserve all credit for the noise improvements presented in this paper. This is a purely mechanical achievement and has not resulted from any difference in processing of the data.

REFERENCES

Brodie, R. C., 2016, GALEISBSTDEM: A deterministic algorithm for 1D sample by sample inversion of time-domain AEM data – theoretical details. Retrieved from https://github.com/GeoscienceAustralia/gaaem/docs/GALEISBSTDEM Inversion Algorithm Theoretical Details.pdf

Konieczny, G., Smiarowski, A., & Miles, P., 2016, Breaking through the 25/30 Hz barrier: Lowering the base frequency of the HELITEM airborne EM system. Seg Technical Program Expanded Abstracts.

Liu, G., 1998, Effect of transmitter current waveform on airborne TEM response. Exploration Geophysics, 29, 35-41. Nabighian, M. N., 1979, Quasi-static transient response of a conducting half-space: An approximate representation: Geophysics,44,1700-1705.

Raiche, A.P., 1997, LEROI-AIR, modelling program for sponsors of Australian Minerals Industry Research Association Project P223C

Reid, J.E., and Macnae, J.C., 1998, Comments of the electromagnetic "smoke ring" concept: Geophysics, 63, 1908-1913

Table 1. Model types, descriptions and analysis performed

Model Type	Number	Description	Analysis
Layered Earth (GALEISBSTDEM)	1	2 layer – resistive to conductive Layer 1 Conductivity: 0.001S/m Layer 2 Conductivity: 0.1S/m Layer 1 Thickness: Varying from 20-800m	Add noise, invert for thickness of layer 1 to estimate DOI for different base frequencies and noise levels
	2	2 layer – conductive to resistive Layer 1 Conductivity: 0.1S/m Layer 2 Conductivity: 0.001S/m Layer 1 Thickness: Varying from 20-800m	Add noise, invert for thickness of layer 1 to estimate DOI for different base frequencies and noise levels
	3	2 layer – very conductive to resistive Layer 1 Conductivity: 1S/m Layer 2 Conductivity: 0.001S/m Layer 1 Thickness: Varying from 20-800m	Add noise, invert for thickness of layer 1 to estimate DOI for different base frequencies and noise levels
	4	3 layer – resistive, conductive, resistive Layer 1 Thickness: 40m Layer 2 Thickness: 20m Layer 1, Layer 3 Conductivity: 0.001S/m Layer 2 Conductivity: varying from 1–50S/m	Invert for conductivity of layer 2 to estimate conductance discrimination
Plate (Maxwell)	5	400m x 400m horizontal plate Conductance varying from 0.1- 50,000S Depth varying from 20-800m	Construct 3D conductance-depth nomogram Plot depth and conductance range for 4 or more late channels above noise level
Plate in Conductive Environment (LeroiAir)	6	100x100m horizontal plate under 10m thick overburden (0.01S) in relatively conductive host rock (0.06S). Conductance varying from 0.1- 50,000S Depth varying from 20-400m	Calculate anomalous response compared to background Construct 3D conductance-depth nomogram Plot depth and conductance range for 4 or more late channels above noise level

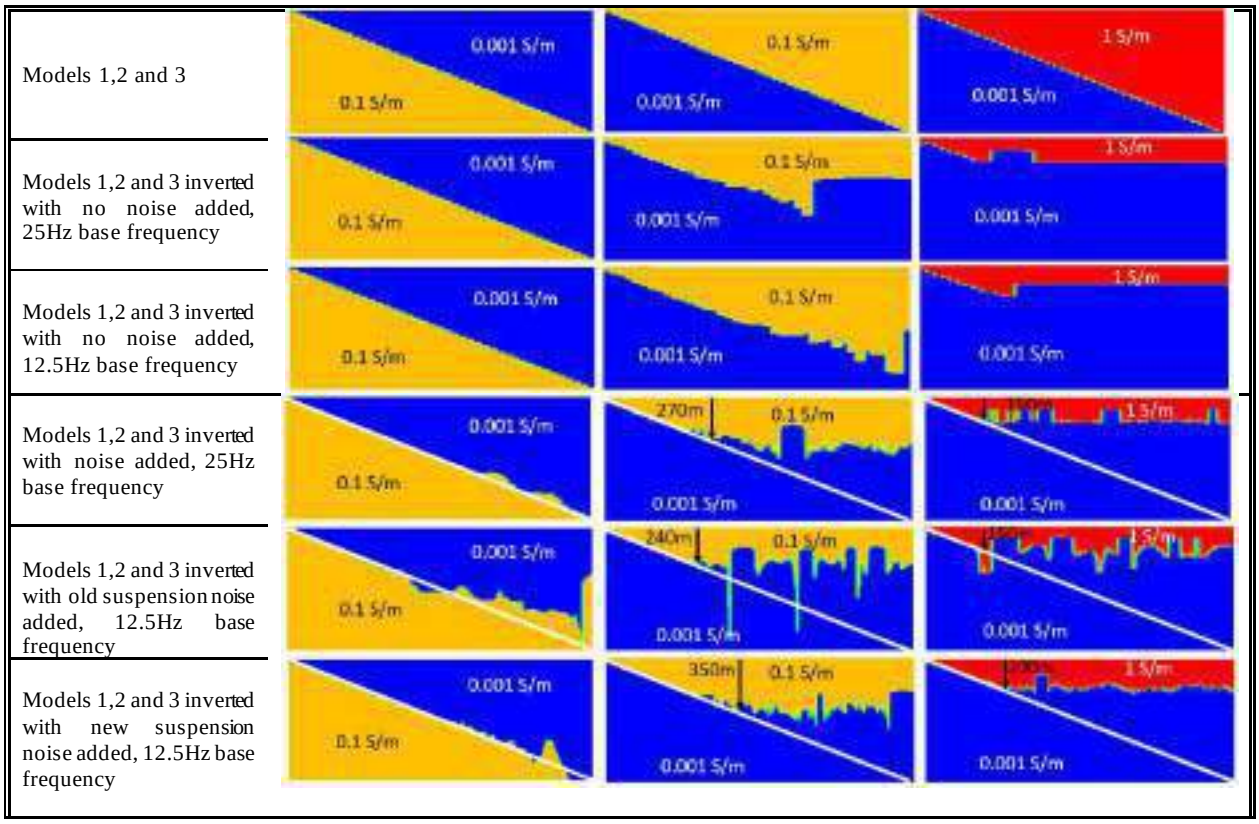

Figure 2: Models 1-3 (Row 1, left to right) and inversion results for 25 Hz (Row 2) and 12.5 Hz (Row 3) base frequency with no noise added. Even in the absence of noise, there are limitations to the DOI under conductive layers as in models 2 and 3. Row 4 shows 25 Hz data inverted with noise added. Rows 5 and 6 show 12.5 Hz data inverted after old suspension noise (Row 5) and new suspension noise (Row 6). The scales on all images represent 2000 m horizontally and 800 m vertically. Depths below surface are indicated with black arrows at points of interest.

TEMPEST Data System Bandwidth Comparisons

Nirocca Devkurran
Xcalibur Multiphysics
Pretoria, Gauteng, South Africa
nirocca.devkurran@xcaliburmp.com

Eric Steele
Xcalibur Multiphysics
Perth, Western Australia, Australia
eric.steele@xcaliburmp.com

David Murray
Xcalibur Multiphysics
Mississauga, Ontario, Canada
dave.murray@xcaliburmp.com

Mohamed Abubeker
Xcalibur Multiphysics
Perth, Western Australia, Australia
mohamed.abubeker@xcaliburmp.com

Kah Tho Lee
Xcalibur Multiphysics
Perth, Western Australia, Australia
kahtho.lee@xcaliburmp.com

SUMMARY

The TEMPEST fixed wing TDEM system continually undergoes evolutionary advancements, pushing the technical boundaries for meeting industry needs of improved accuracy and reliability. Higher speed data acquisition rates (increased bandwidth) have been one of the developments for improving resolution and imaging products that would benefit hydro geological exploration and reservoir characterization. Multiple sampling rate data will be acquired over a known (geologically mapped) setting and an assessment will be made against drill hole information, in order to understand the response as a function of varying bandwidth.

Key words: TEMPEST, Data Processing, Conductivity Inversion.

INTRODUCTION

Questions arise as to the validity of AEM data, and ways of improving the understanding the impact of data accuracy for various geological environments. One method to improve the quality of the result is by increasing the sampling rate and bandwidth of the TEMPEST system. In order to validate the various components required to increase system bandwidth, these upgrades have generally been done in a phased manner thereby alleviating the interdependence of each upgrade on different sub-systems. This paper only looks to investigate the prospective improvements based on higher acquisition rates of data compared to that of known geological formations.

METHOD AND RESULTS

Test lines of high and low sampling rate data will be acquired over a known geologically mapped setting and an assessment of this data against drill hole information will be performed using 1D inversions as well as standard interpretation products such as Conductivity Depth Transform (CDTs), as well as general processes of QA/QC and interpretation.

Figure 1: Calibration Range

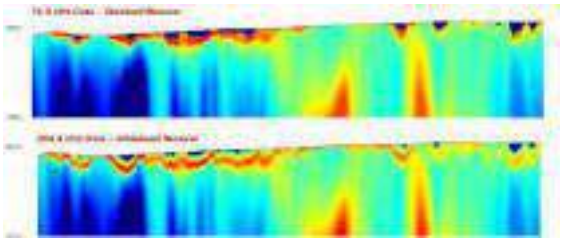

Figure 2: Conductivity Depth Images comparing two data sets that have been sampled at different acquisition rates; 76.8kHz and 204.8kHz.

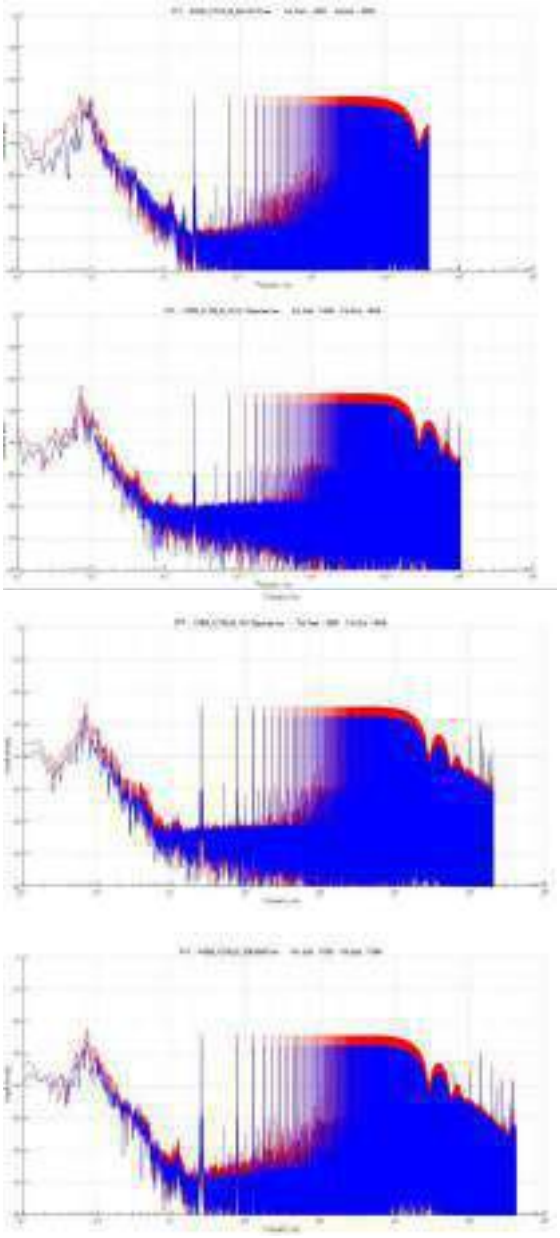

Figure 3: Spectra comparison of different bandwidths; 76.8kHz, 204.8kHz, 409.8kHz and 819.2kHz.

Accuracy will be assessed by analysing parameterisation variables of a known geological setting, in order to highlight the differences of high and low sampled airborne electromagnetic data. The sampling rates to be compared are primarily 76.8kHz and 204.6kHz and will be assessed against current system configurations of the TEMPEST system operating at a 25Hz base frequency.

Due to the limited availability of the TEMPEST system for internal research and development, we have been unable to assess high frequency rate data against known drillhole information to date and will endeavour as best we can to acquire this data during the commissioning stage of the next TEMPEST system coming online.

CONCLUSIONS

With the assessment of the high sampled data, the objective is to define and refine the following characteristics:

- higher sampling rate vs the improvement of near surface geological resolution.
- influence of data between high and low sampling rate at depth.
- accuracy of inversion outputs and parameterisation.
- added noise sources with increased bandwidth.
- relationship between sampling rate and its affect on the deconvolution process (if any).
- expanded options of windowing data.

ACKNOWLEDGMENTS

Thank you to Xcalibur Multiphysics and the processing and engineering teams, past and present who have contributed to the birthing and constant nurturing of the TEMPEST system.

Immense gratitude to Peter Wolfgram who has contributed a wealth of information of processing techniques and without whom this progression and analysis would not be possible. Reference to his currently unpublished work on “Noise Considerations for TEMPEST Data” will be made in this analysis.

Automated integration of AEM data, VES and borehole logs

Stefano Galli
The EEM Team for Hydro & eXploration,
Dep. of Earth Sciences A. Desio,
Università degli Studi di Milano,
Via Botticelli 23, Milano (Italy),
stefano.galli2@unimi.it

Frans Schaars
Artesia Water,
Korte Weistraat 12,
2871 BP Schoonhoven, the Netherlands
f.schaars@artesia-water.nl

Frank Smits
Waternet
Korte Ouderkerkerdijk 7
1096 AC Amsterdam (the Netherlands)
& Technical University of Delft
Frank.Smits@waternet.nl

Lucas Borst
PWN
Rijksweg 501
1991 AS Velserbroek
the Netherlands
lucas.borst@pwn.nl

Arianna Rapiti
Emergo S.r.l.,
Via XX Settembre 12, Cascina, PI (Italy)
arianna.rapiti@aarhusgeo.com

Gianluca Fiandaca
The EEM Team for Hydro & eXploration
Dep. of Earth Sciences A. Desio
Università degli Studi di Milano,
Via Botticelli 23, Milano (Italy)
gianluca.fiandaca@unimi.it

SUMMARY

Airborne electromagnetic (AEM) surveys are widely used for hydrogeological applications. The areas targeted for AEM campaigns may present a great deal of ancillary information (e.g. resistivity logs, lithology, etc.) and integrating it with AEM data is fundamental. Yet, using this information either as a-priori or a-posteriori may bring out conflict between different datasets, preventing reconciliation everywhere. For instance, some borehole drillings may have been logged inaccurately, AEM data may present bias, or data may have been acquired at different times, with variations occurring in between.
In this study we present a way to integrate AEM data and other types of resistivity data (boreholes electrical logging and vertical electrical soundings, in this case), through an inversion scheme that identify automatically conflicting data without preventing the general convergence of the process. To do so, we make use of a generalization of the minimum support norm, the asymmetric generalized minimum support (AGMS) norm, for defining the data misfit in the objective function of an iterative reweighted least squared (IRLS) gauss-newton inversion. The AGMS norm in the data misfit puts a cap on the weight of non-fitting data points, allowing for the inversion to focus on the data points that can be fitted. Outliers are identified after the AGMS inversion and excluded, in order to complete the inversion process with a classic L2 misfit.
We present an application of this method in the Netherlands, on a SkyTEM survey complemented with a vast and open-source database of ashore resistivity logs, as well as vertical electrical soundings (VES).

Key words: Airborne EM, minimum support, hydrogeology, interface fresh salt groundwater

INTRODUCTION

In areas rich with ancillary data, their integration in the inversion is a must, for validation as well as for enhancing sensitivity. However, data integration is a tricky process, for many reasons: data may be biased, their supporting volume may differ significantly, along with their location, or they may have been acquired in different periods, with variations occurred in between, for instance due to the depletion of groundwater resources or seawater intrusion.

Conflicting data in an inversion process can easily prevent the proper convergence of the inversion, but culling too much data out might throw out important information. The removal of conflicting information is even more difficult when there is a significant amount of ancillary information, acquired over a long period of time.

To solve this challenge, we propose to use a generalization of the minimum support norm (Last and Kubik, 1983; Portniaquine and Zhdanov 1999), namely the asymmetric generalized minimum support AGMS norm (Fiandaca et al., 2015), for identifying outliers in a joint inversion of AEM data, vertical electrical soundings (VES) and borehole resistivity logs. We test the method on a synthetic example, mimicking a joint inversion of AEM data and borehole logs, with both correct and incorrect logging, as well as real data. The field case consists of a SkyTEM survey carried out in 2022, complemented with a vast and open-source database of ashore resistivity logs, as well as VES, acquired over many decades.

METHOD AND RESULTS

The inversion of AEM, VES and borehole logs is carried out in EEMverter (Fiandaca et al., 2023), a new inversion algorithm in which different norms are applicable in the objective function for both data misfit and regularization through the iteratively reweighted least squared (IRLS) inversion scheme (Farquharson and Oldenburg, 1998).
In particular, the penalty of the data misfit $x = d - f$ between data and forward response is expressed through the AGMS norm (Fiandaca et al., 2015) as:

$$\phi(x) = \alpha^{-1}\left[(1-\beta)\frac{(x^2/\sigma^2)^{p_1}}{1+(x^2/\sigma^2)^{p_1}} + \beta\frac{(x^2/\sigma^2)^{p_2}}{1+(x^2/\sigma^2)^{p_2}}\right] \quad (1)$$

where

$$\beta = \frac{(x^2/\sigma^2)^{\max(p_1,p_2)}}{1+(x^2/\sigma^2)^{\max(p_1,p_2)}}. \quad (2)$$

In (1) and (2), σ is the data standard deviation, p_1 and p_2 control the shape of the norm before and after $\frac{x}{\sigma} = 1$ and α determines the total weight of the penalty. Figure 1 shows the comparison between the L2 penalty and the AGMS penalty with p1=1, and p2=0.5 and α = 0.5.

With this choice of values for the norm settings the AGMS norm gives misfit 1 for $\frac{x}{\sigma} = 1$ (i.e. the same value of the L2 norm), with similar penalty for low misfit (because of $p_1 = 1$)

and a slow growth of the penalty when $\frac{x}{\sigma} > 1$ (because of $p_2 = 0.5$). This slow growth allows for applying the AGMS norm in an iterative minimization process, because a decrease in $\frac{x}{\sigma}$ gives a measurable penalty reduction.

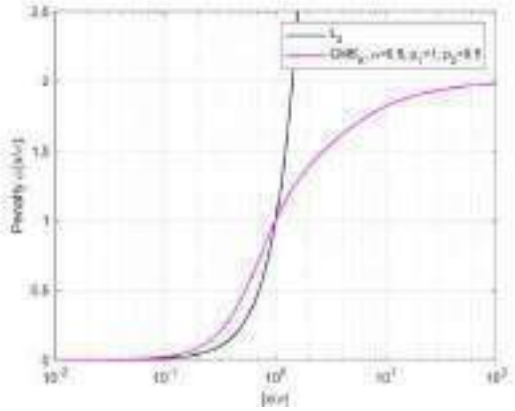

Figure 1. Penalty of the L2 and AGMS norms as a function of the difference $x = d - f$ between data and forward response, weighted by the data standard deviation σ.

This data norm is applied in a IRLS inversion composed of three inversion cycles (Fiandaca et al., 2023) with 1D forward/Jacobian computations: first a preliminary cycle which finds the best starting model without vertical variability of the parameters, through the use of a single-layer forward mesh; secondly, a cycle the AGMS norm is applied; lastly, the data norm is switched to the L2 norm, to reject the data with misfit above the set thresholds, and the inversion is carried out until the reach of the minimum misfit. In all cycles, borehole logs are treated as data, with the forward response of the logs consisting in the interpolation of the model resistivity at the log locations (Fiandaca et al., 2023).

Figure 2 presents a synthetic model mimicking a fresh aquifer comprised between an unsaturated sand dune and a brackish aquifer, and confined by clay layers. AEM data (Xcite system, New Resolution Geophysics) and three borehole logs are simulated and inverted with a classic L2 data norm and the AGMS norm, with three data scenarios:

- a first one, in which only AEM data are available (Fig. 2D and 2G);
- a second scenario, in which AEM data are complemented with the logs that bear correct information (Fig. 2E and 2H);
- a third scenario, in which one log contains wrong resistivity values (Fig. 2F and 2I).

Both L2 and AGMS inversions improve the model retrieval when correct log information is added, but a very different behaviour occurs when wrong data are fed to the inversions: the L2 inversion shows a significant artifact at the location of the wrong resistivity log, while the AGMS inversion is almost insensitive to the outliers.

The same inversion procedure was used on a SkyTEM dataset acquired in the Netherlands in 2022, around 25 kilometres west of Amsterdam (Fig. 3), together with 94 borehole resistivity logs, 91 VES, acquired in the same area over a period ranging many decades, in which the volume of the fresh groundwater has changed considerably. 'Excessive water abstraction from deep wells between 1903 to 1957 depleted the fresh groundwater. In 1957 the wells were stopped and infiltration with pretreated water from the river Rhine started. This enlarged the drinking water production capacity and restored the fresh water volume in the deep aquifer (Geelen et al., 2017; Olsthoorn and Mosch, 2020). The wells can still be used as a back-up system if the quality of the water in the river Rhine is not sufficient. For this reason, the integration of resistivity logs and VES with AEM data is particularly difficult: data will conflict not necessarily because of their different support volume or sensitivity, but because they were acquired over different periods of time. Consequently, with the AGMS inversion we aim at two distinct goals: improving the AEM inversion where borehole logs and VES information bring compatible information; identify the conflicting information, as a proxy of the variations that occurred on the fresh-sea water balance over the decades.

A 40 m x 80 m XY horizontal discretization and log-increasing depths from 5 to 400 m were used for the inversion, with the same three-cycle inversion scheme utilized for the synthetic case. Only borehole logs and VES data were rejected in the last cycle, the aim being to identify the information conflicting with the AEM data, which were carefully processed.

Figure 4 presents the rejection rate for both log data and VES data with the AGMS joint inversion, in comparison with the rejection rate computed after an AEM-only inversion, in which log and VES data do not concur in the model definition. The rejection of log data is not applied to entire logs, but value by value along the borehole depth. So the rejection rate indicates for each borehole log the fraction of values rejected. The overall rejection rates are presented also in Table 1.

Table 1. Comparison between rejection rates with AGMS joint inversion of AEM, VES and log data and with AEM-only inversion.

	Total data	Data rejected with AGMS	Rejection rate %	Data rejected with AEM-only	Rejection rate %
Borehole logs	33646	4399	13	12646	38
VESs	1815	1159	64	1475	81

As clearly shown by Fig. 4 and Table 1, the AGMS inversion has a much lower rejection rate, with very good compatibility between logs and AEM data, and poorer compatibility between the old VES data and the AEM ones. However, spatial patterns exist in the rejection fractions, which might be correlated with the variations occurred in the fresh-sea water interface. The AEM-only inversion has a much lower compatibility with the ancillary data, which is mostly due to equivalence problems instead of conflicting information.

Figure 5 shows in a 3-D view an example of data rejection in four borehole logs: most of the differences are only due to the vertical discretization of the inversion model, except for one of the logs in which the measured borehole data indicate a more conductive area at depth.

Finally, Figure 6 presents the comparison of the joint AGMS inversion and of the AEM-only inversion on an exemplary log, where AGMS inversion model fits much better the borehole information.

CONCLUSIONS

The inversion scheme proposed in this study allows an automated integration of AEM data and resistivity logs, as well as ground-based galvanic VES measurements, even in presence of conflicting information. The AGMS data norm puts a cap at the misfit penalty of outliers, and grants convergence to the inversion without culling valuable information out.

This approach allows to integrate to AEM surveys a great amount of ancillary data, without the need of careful and time-consuming data vetting: the accurate inspection of ancillary information could be reserved only to the data rejected by the automated scheme, with the kept data readily usable for further integration and interpretation.

Furthermore, this automated integration scheme is fully general, and can be applied not only to AEM data, but to any geophysical problem simply using the appropriate forward modelling.

ACKNOWLEDGMENTS

This work has been carried out within the project LakEMaging, funded by Acque Bresciane. The SkyTEM measurements are paid for by PWN, the municipality of Amsterdam, the waterboard Amstel, Gooi and Vecht, the Province of Noord-Holland and the Delta Programma Zoet Water (Delta Program for Fresh Water) of the Dutch Ministry of Infrastructure and Water Management.

REFERENCES

Farquharson, C.G. & Oldenburg, D.W., (1998). Non-linear inversion using general measures of data misfit and model structure, Geophysics, 134, 213–227.

Fiandaca, G., Doetsch, J., Vignoli, G., & Auken, E. (2015). Generalized focusing of time-lapse changes with applications to direct current and time-domain induced polarization inversions. Geophysical Journal International, 203(2), 1101-1112.

Fiandaca, G., Viezzoli, A., Schaars, F. (2021). Advanced Automated Integration of Aem and drilling data, *48th IAH Congress*, Brussels, Belgium, 6-10 september 2021.

Fiandaca, G., Zhang, B., Chen, J., Signora, A., Dauti, F., Galli, S., Sullivan, N.A.L., Bollino, A., Viezzoli, A. (2023). Closing the gap between galvanic and inductive methods: EEMverter, a new 1D/2D/3D inversion tool for Electric and Electromagnetic data with focus on Induced Polarization *AEM2023 - 8th International Airborne Electromagnetics Workshop, 3-7 September 2023, Fitzroy Island, QLD, Australia*.

Geelen, L. H. W. T., Kamps P. T. W. J., Olsthoorn T. N. (2017). "From overexploitation to sustainable use, an overview of 160 years of water extraction in the Amsterdam dunes, the Netherlands." *Journal of coastal conservation* 21.5: 657-668.

Last, B.J. & Kubik, K., 1983. Compact gravity inversion, Geophysics, 48, 713-721.

Olsthoorn, T. N., & Mosch, M. J. M. (2020). Fifty years artificial recharge in the Amsterdam dune area. In *Management of Aquifer Recharge for Sustainability* (pp. 29-33). CRC Press.

Portniaquine, O. & Zhdanov, M.S., 1999. Focusing geophysical inversion images, Geophysics, 64, 874-887.

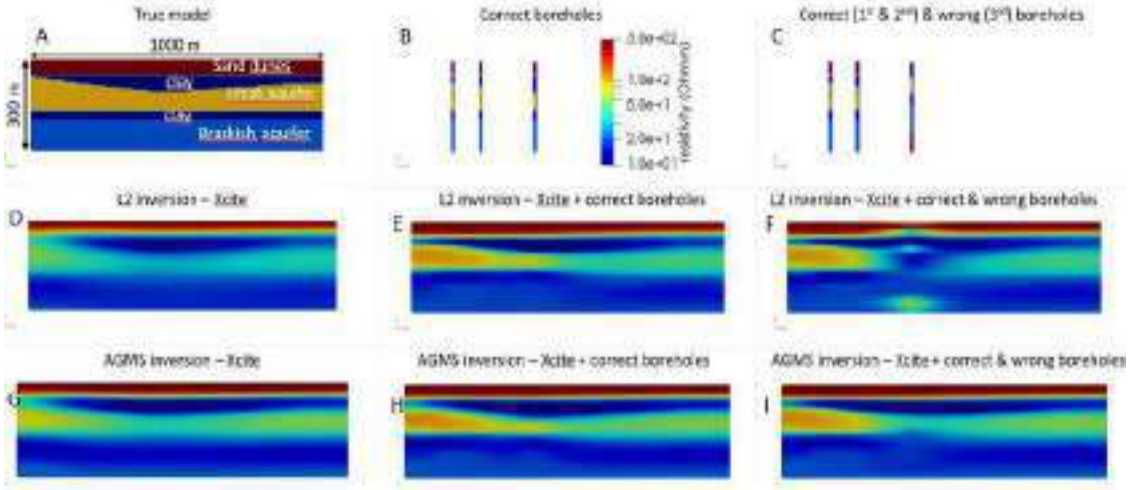

Figure 2. Conceptual model (A), boreholes information (all correct in B, one incorrect in C); model recovered by Xcite AEM data without drilling information using L2 norm (D) and AGMS norm (G); model recovered by Xcite with all correct drilling information using L2 norm (E) and AGMS norm (H); model recovered by Xcite with partially incorrect drilling information using L2 norm (F) and AGMS norm (I);

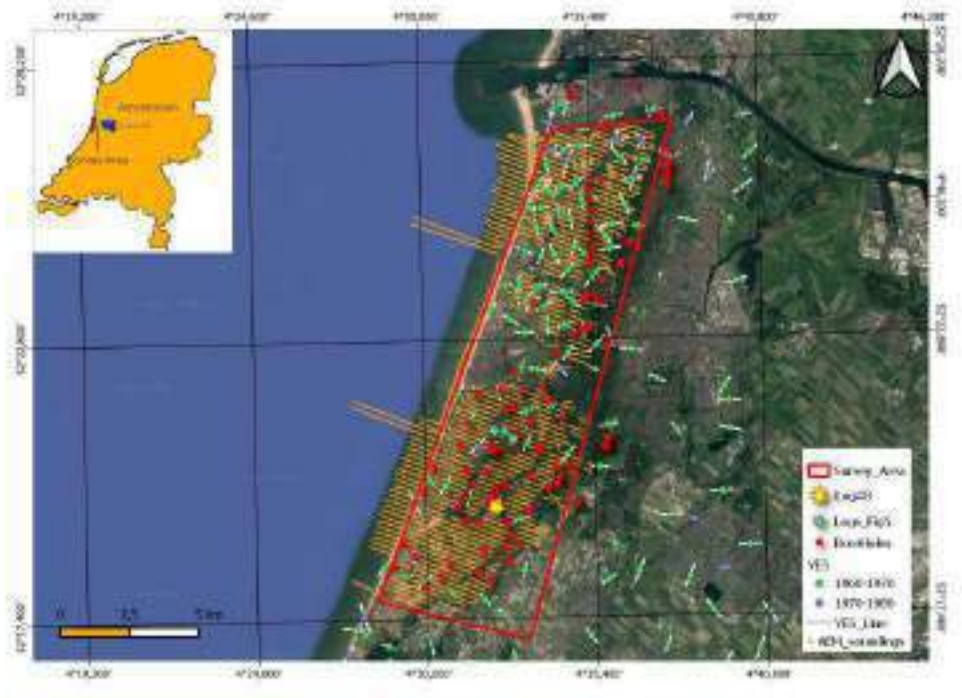

Figure 3. Survey area and sounding locations: red polygon – inversion area; orange dots – AEM soundings; red stars – borehole resistivity logs; yellow and green stars – logs presented in Fig. 5 and Fig. 6; green dots – VES soundings from the '60s; purple dots – VES soundings from the '70s; white bars: VES orientations.

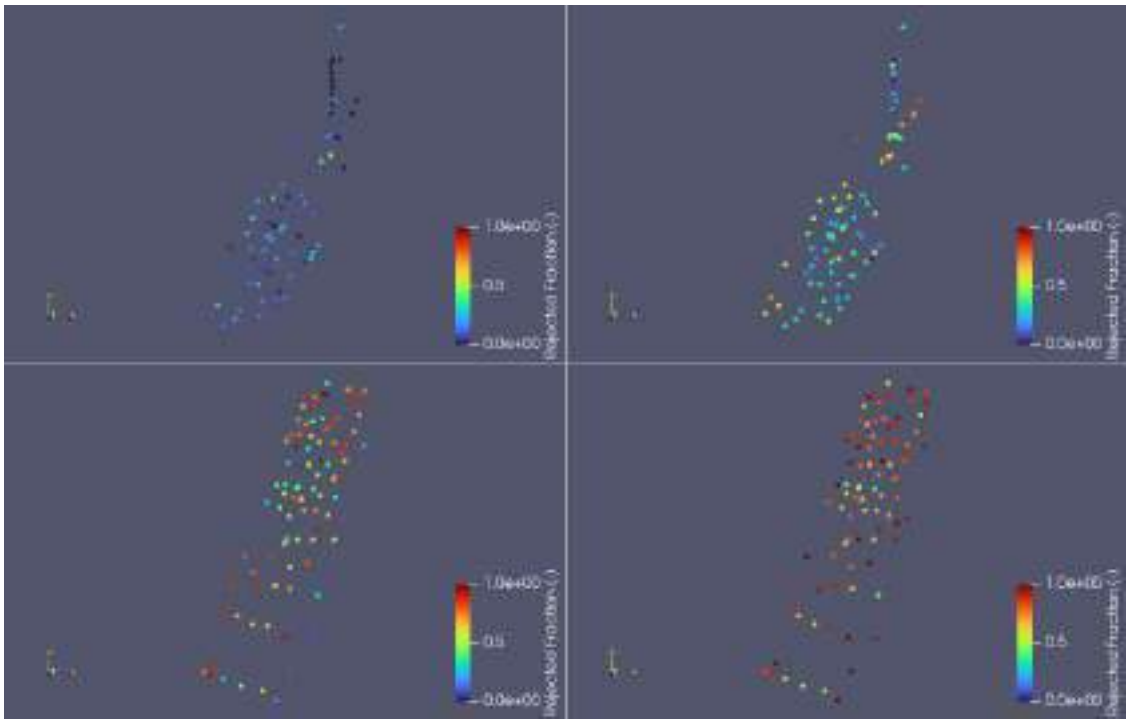

Figure 4. Plots of the fraction of rejected data with application of AGMS norm in joint inversion (left sections) and with AEM-only inversion (right sections); Top – rejections of log data; bottom – rejection of VES data.

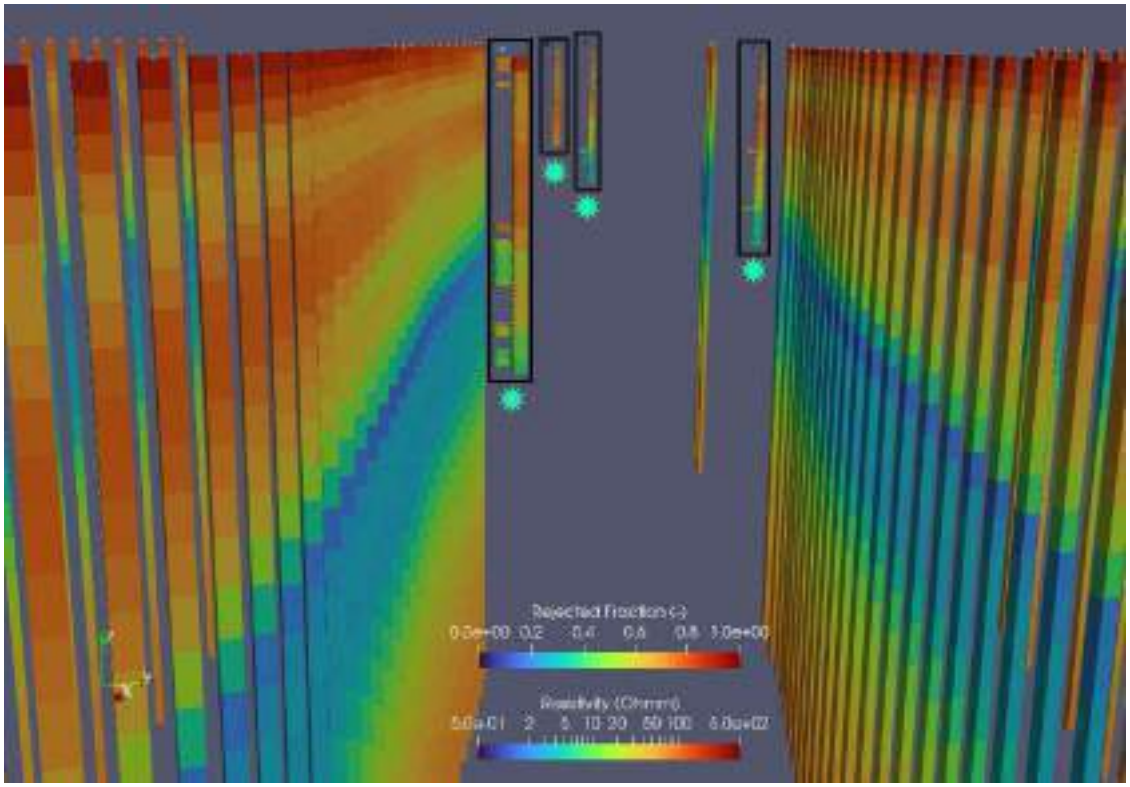

Figure 5. 3-D plot of 1-D forward models. Models framed in black: left – rejected log data; right – forward log model; dots – rejected fraction in colour code. All other columns represent AEM forward models. Locations of the framed logs are marked by green stars in Fig. 3.

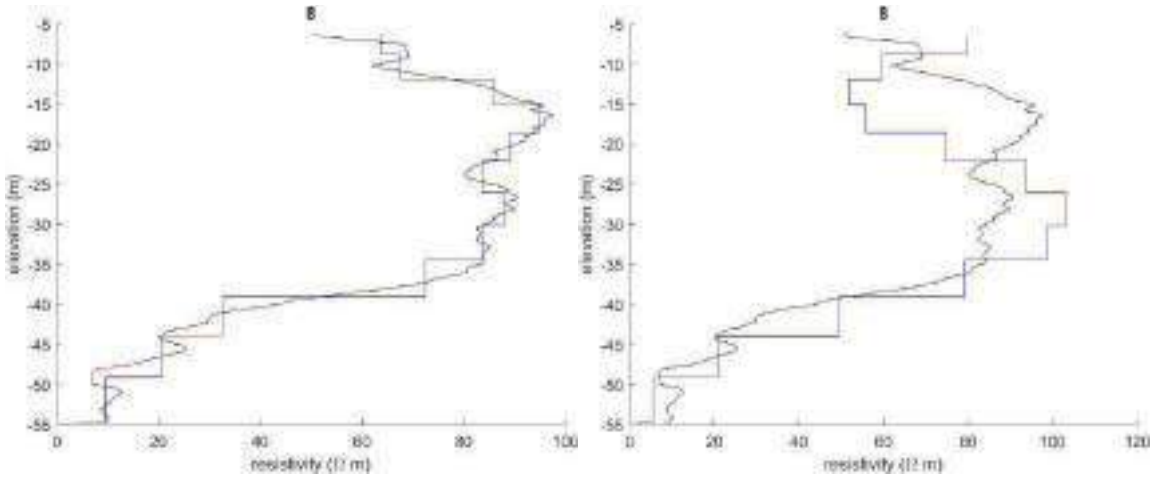

Figure 6. Comparison between Borehole#8 log (yellow star in Fig. 3) and inversion model. Left – AGMS joint inversion; right – AEM-only inversion. Blue lines – inversion model; black lines – resistivity logs; red lines – rejected data in resistivity log in the joint AGMS inversion.

An overview of SkyTEM surveys in New Zealand: data acquisition, community engagement, and results from Northland

Maïwenn Herpe
GNS Science
Wairakei, NZ
m.herpe@gns.cri.nz

Thomas Brakenrig
GNS Science
Wairakei, NZ
t.brakenrig@gns.cri.nz

Stewart Cameron
GNS Science
Wairakei, NZ
s.cameron@gns.cri.nz

Jane Frances
Saphron Consultancy
Wellington, NZ
jane.frances@saphron.co.nz

Richard Kellett
GNS Science
Lower Hutt, NZ
r.kellett@gns.cri.nz

Ben Pasco
Tetra Tech
Christchurch, NZ
ben.pasco@tetratech.com

Zara Rawlinson
GNS Science
Wairakei, NZ
z.rawlinson@gns.cri.nz

Tusar Sahoo
GNS Science
Lower Hutt, NZ
t.sahoo@gns.cri.nz

Rogier Westerhoff
GNS Science
Wairakei, NZ
r.westerhoff@gns.cri.nz

Chris Worts
GNS Science
Lower Hutt, NZ
c.worts@gns.cri.nz

Jesper Bjergsted Pedersen
HydroGeophysics Group
Aarhus C, Denmark
jesper.bjergsted@geo.au.dk

Nikolaj Foged
HydroGeophysics Group
Aarhus C, Denmark
nikolaj.foged@geo.au.dk

Andrew Kass
HydroGeophysics Group
Aarhus C, Denmark
andy.kass@geo.au.dk

SUMMARY

While the demand for groundwater has increased throughout New Zealand, there are still significant knowledge gaps in the understanding of most regional aquifer systems. To address those knowledge gaps, close to 30,000 line-km of airborne TEM data have been collected in New Zealand for groundwater characterisation over the past five years. GNS is currently involved in five regional projects (Hawke's Bay, Greater Wellington, Northland, Tairāwhiti (Gisborne) and Southland), working closely with local water managers and communities. The data interpretation and hydrogeological models resulting from those surveys will greatly improve the understanding of NZ's regional aquifers and inform opportunities for economic diversification in increasingly resource pressured environments. Extensive communication is undertaken in each region prior to the survey, ensuring engagement and interest of the general public. In Northland, the Te Hiku Water Study project is the result of an integrated, community-led water management and economic development plan. The project proposal was initially developed by the community and involved a significant level of community engagement. The team members' advocacy for the project in the community has been a valuable element of building local buy-in to the project. We are looking into expanding the use of SkyTEM to other regions of New Zealand, primarily to help inform water management, but also to subsequently contribute information to researchers in other disciplines (e.g., fault mapping, coastal depositional processes, geological mapping etc.).

Key words: Airborne TEM, groundwater, community engagement, New Zealand.

INTRODUCTION

The demand for groundwater to provide for economic growth has increased in all regions of New Zealand. Better understanding of the nation's groundwater systems will inform and support sustainable water use and regional economic development alongside the objectives of Te Mana o te Wai (the protection of the health and wellbeing of freshwater – MfE, 2020) in a setting of climate change and agricultural intensification.

There are still significant knowledge gaps in the understanding of most regional aquifer systems in New Zealand. GNS Science (GNS) is aiming to address those knowledge gaps by developing national hydrogeological maps and models within our Groundwater research programme (GNS, 2023). In priority areas, time-domain airborne electromagnetics (airborne TEM) data are being collected to improve hydrogeological understanding.

For the past ten years, GNS have been in discussion with water managers and funders to gather support for the use of airborne TEM to inform improved water management in New Zealand. In the past five years, close to 30,000 line-km of airborne TEM data have been collected in New Zealand for groundwater characterisation.

The application of airborne TEM to groundwater characterisation in New Zealand started in 2019, with Lincoln Agritech surveying two sub-catchment areas in Waikato as part of their Ministry of Business Innovation and Employment (MBIE) funded Critical Pathways Endeavour research programme (Stenger et al., 2019). The Provincial Growth Fund (PGF), administered by MBIE and established in 2018, has since provided a pathway to funding for five large-scale surveys in the following regions: Hawke's Bay (flown in 2020); Northland (flown in 2022); Southland (flown in 2022); Greater Wellington (flown in 2023); and Tairāwhiti/Gisborne (planned for summer 2023/2024).

This abstract presents an overview of the abovementioned five airborne TEM projects and will explain the engagement with local communities in more detail for one project (Te Aupōuri Peninsula in Northland).

AQUA INTEL AOTEAROA

AIA, a partnership between GNS and Kānoa Regional Economic Development and Investment Unit (Kānoa REDIU is the MBIE delivery arm of the PGF), is a national programme on regional water availability and storage. The programme began by identifying "areas where there is both water available and good-quality land that could be brought into higher-value production – in particular, to benefit Māori landowners" (Robert Pigou - AIA, 2021). AIA identified and is currently funded to work within four regions: Northland, Tairāwhiti (Gisborne), Otago, and Southland (Frances et al. 2021; White, Frances, et al. 2021; White, Mourot, et al. 2021; Cameron et al. 2021). The programme covers different water storage projects, corresponding to the specific needs of each region, with airborne TEM surveys funded in three of them (Northland, Tairāwhiti, and Southland) to streamline and improve cost efficiency on mobilisation (Figure 1). AIA contracted SkyTEM Australia to fly all three surveys. The Hawke's Bay and Greater Wellington SkyTEM projects were planned and funded before AIA was established.

REGIONAL SURVEYS OVERVIEW

Hawke's Bay

The HBRC 3D Aquifer Mapping project is a 4-year project (September 2019 – June 2023) co-funded between PGF, HBRC and GNS. SkyTEM Australia collected close to 8000 line-km of data over the Heretaunga plains (170 m line spacing), Ruataniwha plains (250 m line spacing) and Poukawa/Otane basins (200 m line spacing) using a SkyTEM 312 system (SkyTEM Australia Pty Ltd., 2020). Aarhus Workbench software was used for processing, early time gates added for additional near-surface resolution, and both sharp and smooth SCI inversion methodologies used to create final resistivity models (Rawlinson et al., 2021a., 2021b, 2022). Three boreholes were drilled with the aim to tie the airborne TEM data to lithological and hydrological data. Hydrogeological interpretations and numerical groundwater modelling are currently underway.

Prior to the data acquisition, the project team undertook communication with iwi (local indigenous communities), target groups and the general public to educate on the aims of the project and how it will relate to water resource management. An ESRI story map has been created as part of this project, to make the results publicly available (HBRC, 2022). Within this storymap, an embedded webmap provides user-selected 1D and 2D visualisations of the developed 3D models. These story maps are a means of educating the general public on the methodology and technology and for making the results more accessible for anyone to understand.

Greater Wellington

The SkyTEM survey across the Wairarapa valley in the Greater Wellington region was designed to provide detail on the distribution of aquifers and confining layers associated with the Ruamāhanga River in the southern part of North Island. The survey comprises 5800 line-km, split into five regions. Areas in the southern part of the valley adjacent to the coast are designed to map a complex pattern of raised terraces and older fluvial systems that might have potential aquifers or pathways for saltwater intrusion. Some areas, such as the shallow Lake Wairarapa, are covered at a wider line spacing (400 m) to provide more of a reconnaissance view of the aquifer systems. A 200 m line spacing was used in areas with a focus on connectivity between river gravels at surface and deeper paleo-channels, and the influences of faulting on aquifer connectivity. The SkyTEM 312 system was used, providing the balance between detailed shallow imaging with the low-moment signal, and a penetration of up to 400 m with the high moment signal.

Northland

The Aupōuri aquifer is the main aquifer system of the Northland region, sitting in the lower Aupōuri peninsula. It is one of the largest potential sources of freshwater and one of the most utilised groundwater areas in the region (Cameron et al. 2001). The populated eastern side of the peninsula battles with sufficient reliable water throughout the year. There are four key features typical of the Aupōuri Aquifer hydrogeological setting critical to the understanding of the system:

- Groundwater – surface water connectivity
- Presence of permeable shell beds
- Depth to hydrological basement
- Location and geometry of the saline interface

AIA undertook a feasibility study assessing the possibility to map those key features with airborne TEM. This feasibility assessment included collection of ground-based TEM measurements and simulation of airborne TEM signal for realistic hypothetical scenarios encompassing the four criteria (Westerhoff et al. 2022). The results of this feasibility study concluded that, by using a combination of other geophysical and hydrogeological methods (e.g. drilling, aquifer testing, etc.), airborne TEM data will provide significant amounts of continuous subsurface information that will reveal aquifer properties with unmatched quality and consistency. They also concluded that some of the criteria could be harder to image with airborne TEM data alone (e.g. differentiation of basement types, presence of thin shell beds).

SkyTEM collected 6000 line-km of airborne TEM data over the entire Aupouri Peninsula using the SkyTEM 306HP system. With the main part of the aquifer system sitting in the lower peninsula, the southern block of the survey was covered with a 200 m line spacing allowing for a good understanding of the aquifer. The Northern block, where no known groundwater resources are currently utilized, was collected with a wider line spacing of 300 m to still enable identification of potentially poorly understood groundwater sources.

Tairāwhiti (Gisborne)

In Tairāwhiti, AIA is planning to map regional aquifers to provide a greater certainty about water quantity and inform and support future regulatory decisions. The mapping of the Poverty Bay Flats aquifers is a priority for the region because of the high water demand, uncertainty about groundwater availability, and to give the community greater confidence in the potential to bring land into sustainable production. The Tairawhiti survey area is comprised of the Poverty Bay Flats area and four smaller exploration areas where very little is known about the groundwater resource potential (Hicks Bay, Te Araroa, Waiapu and Tolaga Bay). SkyTEM has been contracted to fly 3500 line-km of airborne TEM data with a line spacing between 175 and 200 m, depending on the area, using the SkyTEM 306 HP system.

Although originally planned for collection in February 2023, due to severe impacts of cyclone Gabrielle on the region, the SkyTEM survey has been delayed to summer 2023/2024.

Southland

The Northern Plains survey area in Southland, is set in a highly allocated complex aquifer system with often thin and very shallow alluvium unconfined aquifers overlaying fault separated confined aquifers (Cameron et al. 2021). In 2022, SkyTEM collected 5225 line-km of data with a 200 m line spacing using a SkyTEM 312 system. AIA plans to interpret these data to better understand the hydrogeological complexity and interactions between groundwater systems in the region. It will improve the understanding of the availability of water across Southland and will help support future regulatory decisions.

COMMUNITY ENGAGEMENT IN NORTHLAND

The Te Hiku Water Study project is the result of an integrated, community-led water management and economic development plan in the Far North area of New Zealand. The plan identified a sustainable increase in use of water as a way to lift the economic and social outcomes in the region and to create resilience to droughts – a challenge faced by the region. The plan brought together 4 local iwi (Ngāi Takoto, Ngāti Kuri, Te Aupōuri, Te Rarawa), landowners, the local ratepayers association, the Northland Regional Council and the Far North District Council.

The proposal for the Te Hiku airborne TEM project was initially developed by the community and involved a significant level of community engagement. To reflect the importance of community buy-in for undertaking the aquifer mapping, a project oversight team was established that included representatives of these local groups. The project team also included GNS as science lead and the Ministry of Business Innovation and Employment as funder.

The engagement and importance of the project seen by the Te Hiku community is well described by councillor Penetaui Kleskovic, from Te Aupōuri iwi, who explains that "the name of this aquifer itself is the Te Aupōuri Aquifer. We need to be able to access our own resource to implement better strategies that allow our people to live healthier lifestyles. This includes access to wai [water], especially in times of drought, a pandemic and of course in the creation of job opportunities, especially in horticulture and farming. Our research rōpū [team/committee] work well together. There is a vast range of expertise within and by working together we can build a well-rounded result for the betterment of the people" (Te Hiku, 2022).

The objective of the project team is to achieve improved sustainable use of the water in the Te Hiku Peninsula:

- through science, that is trusted by the community and others, that informs our understanding of the impacts on the aquifer and of water security for the people of Te Hiku
- through informed input to the regulatory process, including spatial planning

On the basis of this overarching objective, the project team worked together to determine the objectives for the science in relation to connectivity, presence of shell beds, saline interface and basement. The team members also led the communication with the community about the project's activities. Their advocacy for the project in the community has been a valuable element of building local buy in to the project. Communication involved town hall meetings, social media, interviews with the media and provision of information through project team member's channels.

The inaugural SkyTEM flights in Northland were marked with a blessing/launch event (Figure 2). A local kaumatua (elder) opened proceedings with a karakia (prayer) for the SkyTEM activities and representatives of all parts of the project team were present to observe the helicopter begin to undertake the flights. In the run up to the blessing/launch event and the flights, a dedicated effort to communications was undertaken, to ensure the public understood the purpose of the helicopter's activities.

The project team will continue to oversee the project's activities. During the life of the project this will involve the processing and interpretation of the data and carrying out any associated borehole drilling. Beyond this, the project team (particularly iwi representatives) will remain involved in decisions about the use and re-use of data. The project team is exploring the principles and processes to be applied to requests for use of the data, with a focus on ensuring that making the data available to others does not undermine the interests of the community groups involved.

CONCLUSIONS

GNS is currently involved in five regional projects using airborne TEM data applied to groundwater mapping, working closely with local water managers and communities. The data interpretation and hydrogeological models resulting from those surveys will greatly improve the understanding of NZ's regional aquifers and inform opportunities for economic diversification in increasingly resource pressured environments.

Extensive communication is undertaken in each region prior to the survey, ensuring engagement and interest of the general public. As part of the Hawke's Bay 3D Aquifer Mapping project, a story map illustrating the acquisition process and an interactive visualisation of the results, was made available to everyone. This has been essential in ensuring the findings are made accessible for anyone to understand and use.

We are looking into expanding the use of SkyTEM to other regions of New Zealand, primarily to help inform water management, but also to subsequently contribute information to researchers in other disciplines (e.g., fault mapping, coastal depositional processes, geological mapping etc.).

ACKNOWLEDGMENTS

The projects are funded by Kānoa Regional Economic Development and Investment Unit (part of the New Zealand Ministry of Business, Innovation and Employment), GNS Science Groundwater Strategic Science Investment Fund, Northland Regional Council, Far North District council, Te Aupōuri iwi, Ngāi Takoto iwi, Hawke's Bay Regional Council,

Gisborne District Council, Masterton District Council, Carterton District Council, South Wairarapa District Council and Greater Wellington Regional Council.

As part of the Northland project, the authors would like to acknowledge Ngāi Takoto iwi, Ngāti Kuri iwi, Te Aupōuri iwi, Te Rarawa iwi, landowners, the ratepayers association, Far North district Council and Northland Regional Council for their contributions as part of the Te Hiku Water Project team.

As part of the Southland, Gisborne, Hawke's Bay and Greater Wellington projects, the authors would like to thank Environment Southland, Te Ao Marama Inc., Ngāi Tamanuhiri iwi, Ngāti Porou iwi, Rongowhakaata iwi, Te Aitanga a Mahaki iwi, Hawke's Bay Regional Council, Greater Wellington Regional Council and Rangitane-o-Wairarapa, for their contributions to the corresponding projects.

Finally, the authors would like to thank the SkyTEM and HeliA1 crews for the data acquisition and Latitude Strategy and Communication, and Earth Environmental Science for their contributions on communications across the different projects.

REFERENCES

AIA, 2021. Aqua Intel Aotearoa media release. Investment to help inform regions about water resources. https://www.aquaintel.co.nz/_files/ugd/99451c_c5b379b5eb4e4ba0b6308220d053f363.pdf

AIA, 2022. Aqua Intel Aotearoa media release. Aerial surveying of Aupōuri aquifer gets green light. https://www.aquaintel.co.nz/_files/ugd/99451c_1ddc69d35c87479181fc973f0d9475f2.pdf

Cameron, S., S., Osbaldiston, G., Skuse, and C., Revfern. 2001. Northland. In: rosen MR, White PA, editors. Groundwaters of New Zealand. Wellington (NZ): New Zealand Hydrological Society. P. 291-302.

Cameron, S.G., P.A., White, A.P., Lovett, M.W., Taves, D., Hamilton, K., Scott, J., Frances, R., Austen-Falloon, and R., Westbury. 2021. Southland water storage : options and opportunities assessment. Aqua Intel Aotearoa report 2021/03; GNS Science consultancy report 2021/96. 63 p.

Frances, J., P.A., White, M.W., Taves, and C., Frost. 2021. Northland water storage : options and opportunities assessment. Aqua Intel Aotearoa report 2021/01; GNS Science consultancy report 2021/94. 57 p.

GNS, 2023. GNS Science Groundwater Strategic Science Investment Fund programme webpage. https://www.gns.cri.nz/research-projects/groundwater-strategic-science-investment-fund/

HBRC, 2022. Hawke's Bay Regional Council storymap https://storymaps.arcgis.com/stories/ea328f3a17f64daeae58d516d4433511

MfE, 2020. Ministry for the Environment, Essential freshwater Te Mana O Te Wai factsheet. https://environment.govt.nz/assets/Publications/Files/essential-freshwater-te-mana-o-te-wai-factsheet.pdf

Rawlinson, Z.J., R.S., Westerhoff, R.L., Kellett, J.B., Pederson, P.K., Maurya, and N., Foged. 2021a. Hawke's Bay 3D Aquifer Mapping Project: Poukawa and Otane Basin SkyTEM data processing and resistivity models. Wairakei (NZ): GNS Science. 76 p. Consultancy Report 2020/138.

Rawlinson, Z.J., N., Foged, R.S., Westerhoff, and R.L., Kellett. 2021b. Hawke's Bay 3D Aquifer Mapping Project: Heretaunga Plains SkyTEM data processing and resistivity models. Wairakei (NZ): GNS Science. 90 p. Consultancy Report 2021/93.

Rawlinson, Z., R., Reeves, R., Westerhoff, N., Foged, J., Pedersen, and Kellett, R. 2022. Hawke's Bay 3D Aquifer Mapping Project: Ruataniwha Plains SkyTEM data processing and resistivity models. Consultancy Report 2022/38, 79.

Stenger, R., A., Rivas, S., Wilson, M., Friedel, G., Barkle, J., Clague, T., Wöhling, B., Moorhead, L., Lilburne, A., Eger, R., McDowell, U., Morgenstern, R., Fuller, P., Journeaux, and I., Kusabs. 2019. Critical Pathways Programme: unravelling sub-catchment scale nitrogen delivery to waterways. In: *Nutrient loss mitigations for compliance in agriculture.* (Eds L.D. Currie and C.L. Christensen). http://flrc.massey.ac.nz/publications.html. Occasional Report No. 32. Fertilizer and Lime Research Centre, Massey University, Palmerston North, New Zealand. 8p.

SkyTEM Australia Pty Ltd. 2020. Data acquisition and processing report SkyTEM Helicopter EM and Magnetic Survey Hawke's Bay, NZ. Doc. No: AUS 10056 Hawkes Bay v1.1, 33.

Te Hiku, 2022. Te Hiku Media news article. Ground-breaking research used in Te Hiku Water Study. https://tehiku.nz/te-hiku-radio/tautinei/30595/ground-breaking-research-used-in-te-hiku-water-study

Westerhoff, R.S., M., Herpe, Z.J, Rawlinson, M.E., Santamaria Cerrutti, T., Brakenrig, and S.G., Cameron. 2022. Feasibility of aquifer investigation with the SkyTEM method in the Aupōuri Peninsula, Northland. Wellington (NZ): Aqua Intel Aotearoa. 85p. Report 2021/06.

White, P.A., J., Frances, M.W., Taves, M., Moreau, T., Howatson, and L.B., Clarke. 2021. Gisborne water storage : options and opportunities assessment. Aqua Intel Aotearoa report 2021/04; GNS Science consultancy report 2021/97. 63 p.

White, P.A., F., Mourot, M.W., Taves, J., Frances, R., Austeen-Falloon, R., Westbury, D., Hamilton, and K., Scott. 2021. Otago water storage: options and opportunities assessment. Aqua Intel Aotearoa report 2021/02; GNS Science consultancy report 2021/95. 77 p.

Figure 1. Location of airborne TEM surveys flown and contracted in New Zealand, since 2019. GNS Science is involved in five regional surveys: Hawke's Bay (flown 2020), Greater Wellington (flown 2023), Northland (flown 2022), Southland (flown 2022) and Tairawhiti (planned for 23/24).

Figure 2. Picture of the people present at the blessing/launch event of the Te Hiku Water Study data acquisition. The present group is consisting of local iwi (Ngāi Takoto, Ngāti Kuri, Te Aupōuri, Te Rarawa), landowners, local ratepayers association representative, Northland Regional Council representatives, GNS Science representatives and the field crew consisting of HeliA1 pilots and SkyTEM crew.

Airborne electromagnetics: dealing with the aircraft speed

Evgeny Karshakov
V.A. Trapeznikov Institute of Control Sciences, Russian Academy of Sciences
65, Profsoyuznaya street, Moscow 117997, Russia
karshakov@ipu.ru

SUMMARY

It is no secret that the solution of Maxwell's equations depends on the coordinate system. But in current studies, the dependence of the solution on both the speed of the transmitter and the speed of the receiver is usually not discussed.

In this article, I present an analysis of such an effect on the readings of an alternating magnetic field receiver and on the secondary field. I have found that the effect of the receiver's motion is critical. I have proposed a compensation method now implemented in some systems, after which the measurements of a moving receiver can be considered as signals of an equivalent stationary receiver at the current position.

It is also shown that the field distortions proportional to the aircraft speed are related to the flight altitude and the electrical conductivity of the medium. I analyzed data from the EQUATOR airborne electromagnetic system obtained over the sea surface. It is shown that the influence of speed is much less than the influence of restrictions on the environment model, which are imposed during the inversion of airborne electromagnetic data.

Key words: airborne electromagnetic survey; aircraft speed, EQUATOR.

INTRODUCTION

In my experience the question about the speed influence appeared twice. The first time was related to the very first flight of the AEM time-domain system EQUATOR in 2010 (Moilanen et al., 2013). While we were trying to analyze AEM data in frequency domain, it was necessary to get high quality measurements on-time, during the pulse of the primary field. After all possible compensations there was still a valuable signal which was obviously related to the receiver angular motion. A solution was founded and it is presented in this paper.

The second time was quite recently, during the Neretva river AEM surveying in 2021, again with EQUATOR system. I found that when approaching the Adriatic sea coastline from the water area, the residuals of the obtained solution for the 1D inversion increase noticeably. Possible causes needed to be explored. Since the electrical conductivity of the sea water is very high, a hypothesis arose about the influence of the speed of the AEM system. Indeed, according to Landau et al. (1984), Maxwell's equations depend on the reference frame in which they are written:

$$\nabla \times (\mathbf{E} - \mathbf{B} \times \mathbf{v}) = -\frac{\partial \mathbf{B}}{\partial t},$$
$$\nabla \times (\mathbf{B} + \mu_0 \varepsilon_0 \mathbf{E} \times \mathbf{v}) = \sigma \mu_0 \mathbf{E} - \mu_0 \rho \mathbf{v} + \mu_0 \varepsilon_0 \frac{\partial \mathbf{E}}{\partial t} + \mu_0 \mathbf{J}^{st}. \quad (1)$$

Here σ is the conductivity, ε_0 is the permittivity, μ_0 is the magnetic permeability, ρ is the charge density, **v** is the coordinate system velocity vector, $\mathbf{J}^{st}$ denotes the external currents density, **E** is the electric field strength vector, and **B** is the magnetic field induction vector.

However, when considering publications related to AEM, the only aspect in which the influence of speed is considered is the possibility of missing a small target. This applies to the basic works of the last quarter of the 20th century, when the AEM method had already become established all over the world (Won and Smits , 1987, Becker and Cheng, 1988). Little has changed in the 21st century. In works considered to be a general overview of methods and tasks of AEM, the direct influence of speed on the measurements is not considered (Christiansen et al., 2006, Macnae, 2007, Kamenetsky et al., 2010, Legault, 2015, Moilanen, 2022).

Thus, the problem turns out to be unexplored. Further, I present the studying results of the influence of the movement of the receiver and transmitter separately. At the end, I give some examples of data processing for the EQUATOR system.

SPEED INFLUENCE INVESTIGATION

Receiver motion

To analyze the influence of the receiver movement, let's use the Faraday's law written in the coordinate system associated with the receiver:

$$Emf_k = -\frac{d\Phi}{dt} = -\frac{d}{dt}\iint_{S_k} \mathbf{B} \cdot \mathbf{n}_k ds \approx -\frac{dB_k}{dt} \cdot S_k. \quad (2)$$

Here on the left side is the electromotive force in the *k*-th frame of the inductive sensor, Φ is the magnetic flux through this frame, calculated via the induction vector **B** and the frame area S_k, $\mathbf{n}_k$ is a unit vector orthogonal to the corresponding frame surface.

In case of a harmonic field $B_k = B_k^0(t) \cdot e^{i\omega t}$:

$$\frac{dB_k(t)}{dt} = i\omega B_k^0(t) \cdot e^{i\omega t} \left\{ + \frac{dB_k^0(t)}{dt} \cdot e^{i\omega t} \right\}. \quad (3)$$

The second term in equation (3) is usually not considered. However, with the characteristics of EQUATOR we have:

- receiver oscilation frequency in flight $u \sim 2\pi$ 0.5 rad/s;
- amplitude of oscillations in flight $A \sim 0.02$ rad;
- field frequency $\omega \sim 2\pi \cdot 100$ rad/s;

and this term will be approximately 10^{-4} with respect to the first one ($\sim A \cdot u/\omega$). It means that if the sensitivity level is better than 10^{-4}, the receiver motion cannot be neglected. For

this reason, in the EM4H system (Vovenko et al., 2013) it is not necessary to take into account the effect of the receiver motion, since the maximum sensitivity level for it is about this value. And for the EQUATOR it is necessary, as we can see in Figure 1. By introducing a correction into the measured signal proportional to the change in the corresponding harmonic amplitude

$$B_k^m(\omega) = -\frac{i}{\omega S_k} Emf_k(\omega) = B_k^0(\omega) - \frac{i}{\omega}\frac{dB_k^0(\omega)}{dt} \Rightarrow \\ B_k^c(\omega) = B_k^m(\omega) + \frac{i}{\omega}\frac{dB_k^m(\omega)}{dt} \quad (4)$$

the motion influence can be excluded (Figure 1). The error of the substitution $dB_k{}^0/dt$ by $dB_k{}^m/dt$ in (4) is about 10^{-8}.

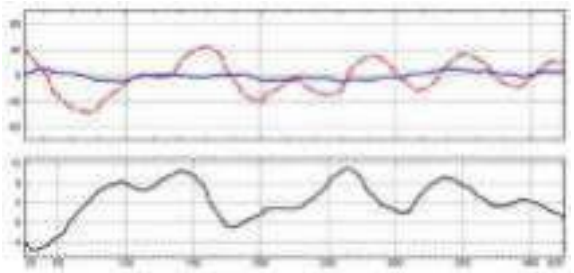

Figure 1. In the absence of the secondary field: measured (red) and corrected (blue) values in ppm as a function of time in samples (~ 10 Hz) for one of the EQUATOR's harmonics (230 Hz). The bottom chart is the receiver axis inclination in degrees.

Transmitter motion

Let's rewrite Maxwell's equations in the quasistatic approximation in the coordinate system associated with the Earth in the following form:

$$\nabla^2 \mathbf{B}^p + \mu_0 \sigma \frac{\partial \mathbf{B}^p}{\partial t} = 0. \quad (5)$$

$\mathbf{B}^p$ is the primary field, which can be expressed via dipole moment vector $\mathbf{M}$:

$$\mathbf{B}^p = \frac{\mu_0}{4\pi|\mathbf{r}|^3}\left(3\frac{\mathbf{r}\mathbf{r}^T}{|\mathbf{r}|^2} - \mathbf{I}\right)\mathbf{M} = \Omega(\mathbf{r})\mathbf{M}. \quad (6)$$

$\mathbf{r}$ is the radius vector of the point with respect to the transmitter, $\mathbf{I}$ is the 3×3 identity matrix, $\mathbf{r}\mathbf{r}^T$ is the 3×3 matrix of the component wise products. Then the derivative of the primary field contains two terms:

$$\frac{\partial \mathbf{B}^p}{\partial t} = \underbrace{\frac{\partial \Omega(\mathbf{r}(t))}{\partial t}\mathbf{M}}_{\text{(I)}} + \underbrace{\Omega(\mathbf{r})\frac{\partial \mathbf{M}(t)}{\partial t}}_{\text{(II)}}. \quad (7)$$

The first term is

$$\text{(I)} = \frac{\partial \mathbf{B}^p(\mathbf{r})}{\partial \mathbf{r}} \cdot \frac{\partial \mathbf{r}(t)}{\partial t} = \nabla \mathbf{B}^p \mathbf{v}. \quad (8)$$

Thus, the velocity of the field source is a coefficient at the gradient of the primary field. The second term, in turn, has two components ($\boldsymbol{\upsilon}$ is the angular velocity of rotation of the transmitter frame, the value of $|\mathbf{M}|$ does not change):

$$\text{(II)} = (\boldsymbol{\upsilon} \times \mathbf{M})e^{i\omega t} + i\omega \mathbf{M} e^{i\omega t}. \quad (9)$$

Usually in AEM only the second part of the second term in equation (9) is taken into account. But in will be more accurate to write Maxwell's equations for the frequency ω in the following form:

$$\nabla^2 \mathbf{B}^p + i\omega\mu_0\sigma\mathbf{B}^p\{+\mu_0\sigma[\nabla \mathbf{B}^p \mathbf{v} + \Omega(\mathbf{r})(\boldsymbol{\upsilon} \times \mathbf{M})]\} = 0. \quad (10)$$

Using the characteristics of the EQUATOR system, namely:

- loop oscilation frequency in flight $u \sim 2\pi$ 0.1 rad/s;
- amplitude of oscillations in flight $A \sim 0.1$ rad;
- field frequency $\omega \sim 2\pi \cdot 100$ rad/s;
- flight speed $v = |\mathbf{v}| \sim 40$ m/s;
- loop height over ground $h \sim 40$ m;

the contribution of each term can be estimated. Thus, the contribution of the term, which includes the flight speed, is $v/(\omega h) \sim 10^{-3}$ with respect to the first, main term. Here it is taken into account that the dipole field near the surface is proportional to $1/h^3$, while the gradient is proportional to $1/h^4$. The contribution from the angular motion of the transmitting loop is $(A u)/\omega \sim 10^{-4}$.

Further, the last term of the equation (10) will not be taken into account. However, it should be kept in mind that at lower frequencies (~10 Hz) the angular motion of the transmitter loop can no longer be neglected.

The form of the influence of the speed-related term of the equation (10) is somewhat similar to the form of the field of a horizontal dipole directed in the direction of flight. However, the field under consideration decays faster with distance because it is related to the gradient. Figure 2 shows three components of the secondary magnetic field appeared due to the transmitter speed at the altitude of the transmitter – 40 m. They are presented as the parts of the stationary component. It can be seen that the horizontal component of the field is distorted by 0.2% on the transmitter axis (point(0,0)). The vertical component is distorted when moving in the flight direction (up to 0.25%).

Data analysis

I considered signals in the frequency domain in the range from 77 Hz to 14 kHz. I performed vertically constrained 1D inversion (Guillemoteau et al., 2011) with fixed layers having thickness of 4 meters and thicker. Over the shallow sea a large residual was obtained, about 5–10 units of the signal RMS, which was increasing with approaching to the coastline. To solve this problem, in addition to the resistivity the altimeter readings error was also estimated. Despite the fact that the solution obtained almost never differs from the measurements by more than 3 RMS, serious doubts arose, since the adequacy of the altimeter was checked many times. However, the height correction turned out to be up to 3 meters. Moreover, it correlates with the electrical conductivity of the medium.

To check if the transmitter speed is the cause of these distortions, the two lowest frequencies, 77 and 231 Hz, were excluded from processing. For higher frequencies the contribution of the speed-related part is negligible. As a result, in terms of height correction, the solution improved, but did not improve completely. As before, as the water depth decreases, the height correction began to increase, and its maximum value, as before, reached 3 meters.

Figure 3 shows the results of the inversion for the same set of frequencies (without two lowest), but not adjusting the height correction. The top graph shows the residuals calculated for

the two frequencies not involved in processing. It can be seen that the residuals for 77 Hz are much larger than for 231 Hz, which is consistent with the conclusions about the effect of speed. However, the magnitude of the residual (up to 4000 ppm) is almost two orders higher than the magnitude the estimate of the speed effect, which at a secondary field strength of about 20000 ppm in this case will be up to 0.25%, i.e. about 50 ppm. It should be noted that the measurement noise at this frequency is about 10 ppm. Thus, the speed of the transmitter at this stage of interpretation does not affect the result, while the layers grid obliviously does: height correction value never exceeds 4 meters – the thickness of the 1st layer.

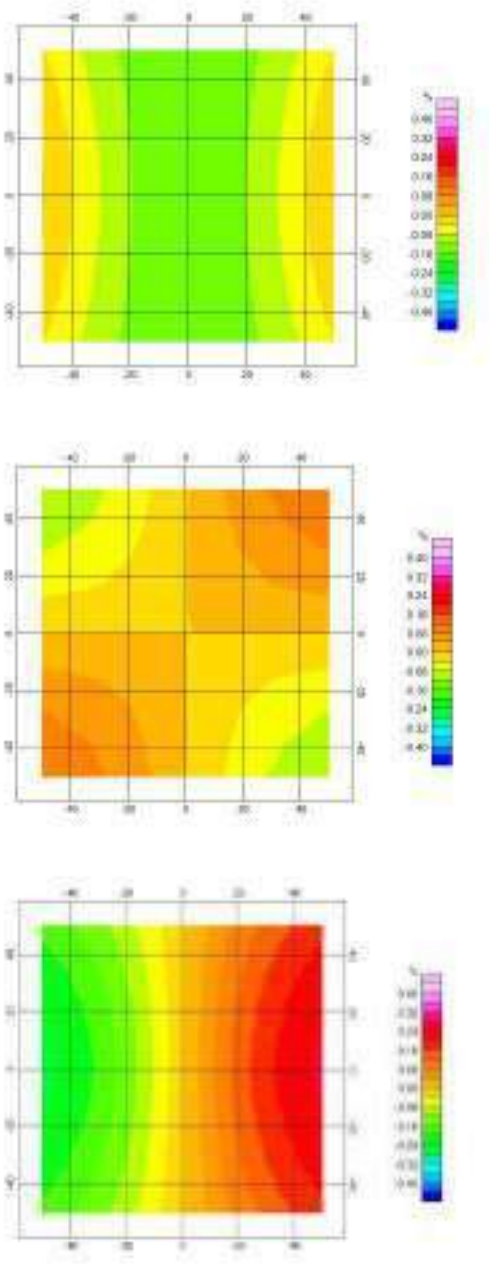

Figure 2. X, Y and Z components of the speed-induced field with respect to the stationary part.

CONCLUSIONS

With the existing level of sensitivity of the AEM equipment, it is necessary to take into account the movement of the receiver. The easiest way is to introduce a correction proportional to the change in the amplitude of the corresponding field harmonic.

Accounting for the transmitter speed for the EQUATOR system is not critical. The residuals obtained by 1D inversion of AEM data are explained by the grid spacing of the resistivity distribution model. Four meters thickness turned out to be too much in this specific case. The resulting height correction compensates for misadjustment of the boundary position between the conductor (sea water) and the more resistive base. It is for this reason that the height correction nowhere exceeds 4 meters.

Nevertheless, calculations show that when the frequency of the primary field signal decreases by an order (from 100 Hz to 10 Hz), it becomes necessary to take into account the aircraft speed.

ACKNOWLEDGMENTS

I want to thank my dear colleague, Dr. Pavel Aleksandrov, who has always emphasized the difference between mobile and stationary EM systems.

REFERENCES

Becker, A., and G. Cheng, 1988. Detection of repetitive electromagnetic signals. In *Electromagnetic* methods in applied geophysics, vol. 1: 442–466.

Christiansen, A.V., Auken, E., and K. Sørensen, 2006. The transient electromagnetic method. In *Groundwater* geophysics. A tool for hydrogeology: 179-225.

Guillemoteau, J., Saihac, P. and M. Behaegel, 2011. Regularization strategy for the layered inversion of airborne TEM data: application to VTEM data acquired over the Basin of Franceville (Gabon). *Geophysical Prospecting* 59 (6): 1132-1143.

Kamenetsky, F.M., Stettler, E.H., and G.M. Trigubovich, 2010. Transient geo-electromagnetics. Ludwig-Maximilian-Univercity of Munich.

Landau, L.B., Lifshitz, E.M., and L.P. Pitaevskii, 1984. Electrodynamics of continuous medea. 2nd ed. Butterworth-Heinemann.

Legault, J.M., 2015. Airborne electromagnetic systems – state of the art and future directions. *CSEG recorder* 40 (6): 38-49.

Macnae, J., 2007. Developments in broadband airborne electromagnetics in the past decade. 5th decennial international conference on mineral exploration "Exploration 07", Toronto, Canada, Proceedings: 387-398.

Moilanen, J., 2022. Modern methods of airborne electromagnetic survey. *Izvestiya, Physics of the Solid Earth* 58 (5): 755-764.

Moilanen, J., Karshakov, E., and A. Volkovitsky, 2013. Time-domain helicopter EM System "Equator": resolution, sensitivity, universality. 13th SAGA biennial and

6thInternational AEM conference AEM-2013, Mpumalanga, South Africa, Expanded Abstracts: 1-4.

Vovenko, T., Moilanen, E., Volkovitsky, A., and E. Karshakov, 2013. New abilities of quadrature EM systems. 13th SAGA biennial and 6th international AEM conference AEM-2013, Mpumalanga, South Africa, Expanded Abstracts: 1-4.

Won, I.J., and K. Smits, 1987, Airborne electromagnetic bathymetry. U.S. Geological Survey Workshop on Developments and Applications of Modern Airborne Electromagnetic Surveys, USA, Proceedings: 155-164.

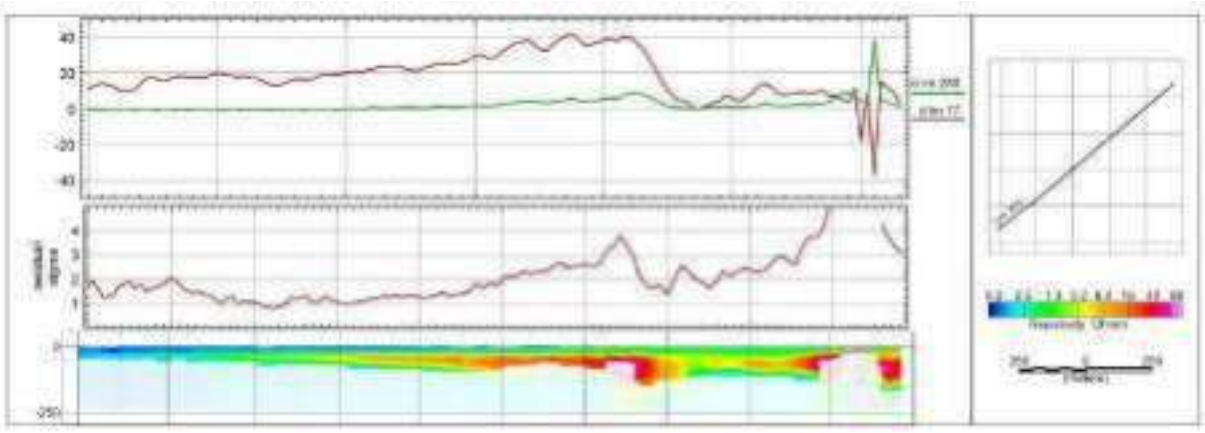

Figure 3. Inversion result in frequency domain without 77 and 230 Hz. Upper chart: d Im 77 – residual for 77 Hz, d Im 230 – residual for 230 Hz, both in ppm*100. Central chart: solution residual calculated for all other frequencies, normalized by the signal RMS. Bottom: the resistivity section.

Adaptive correction for airborne electromagnetic measurements

Andrey Volkovitsky
Institute of Control Sciences
65 Profsoyuznaya street, Moscow
avolkovitsky@yandex.ru

Evgeny Karshakov
Institute of Control Sciences
65 Profsoyuznaya street, Moscow
karshakov@ipu.ru

SUMMARY

We present results of development and practical implementation of the adaptive correction method and algorithm. They ensure high accuracy and stability of the airborne low-frequency inductive electromagnetic measurements. We describe the theoretical foundations of the method and the basic schemes of the algorithm, and consistently consider the stages of computational transformations. We provide several examples of experimentally obtained data proving the effectiveness of the method. The main result achieved is the possibility of functioning of the airborne electromagnetic system without calibration during the entire flight.

Key words: measurements transformations; frequency domain; adaptive correction.

INTRODUCTION

Modern trends of development of the AEM technologies set ever higher demands on the detail and accuracy of measurements (Legault, 2015). It is directly related to the problem of suppression of distortions of various kinds during the measurements processing. The influence of the measurement distortions is especially strong for inductive low-frequency AEM systems. The impact is harmful because the induced field at the location of the receiver overwhelms the response from the conductive layers of the medium. And the receiver registers both these fields simultaneously. Under these conditions, the inherent instability of the measurement conversion parameters has a decisive influence.

The interpretation reliability, as well as the productivity of the survey, are significantly limited since the required accuracy is achievable only in a time interval between calibration procedures. Calibration is usually done at a high enough altitude where the secondary field can be neglected. Reducing the number of such procedures during the flight is our main goal.

It is assumed that modern AEM systems must solve very complex problems, such as estimation of induced polarization and superparamagnetic parameters (Macnae, 2016). And for this we need to carefully eliminate all possible noises. The survey of existing approaches can be found in Wu et al. (2019). From their work, it can be concluded that it is necessary to ensure the sensitivity of the receiver at a level of the order of 10^{-6} with respect to the primary field. The authors considered various noises, including motion-induced noise, nearby or moderately distant sferics noise, power-line noise, background electromagnetic noise etc. They proved that sensitivity at this level is achievable.

At the same time it is absolutely impossible to ensure the stability of measurements with such an accuracy at the hardware level even using the most modern electronic elements. Here we propose a method and an algorithm for stabilizing the measurement accuracy.

THE ADAPTIVE CORRECTION IDEA

We can ensure the accuracy and stability of measurement transformations by digital filtering, applied during registration,which may significantly reduce noises (Hemming, 2013). In frequency domain having a continuous sounding field the measurement results are usually presented in the form of coherent accumulation:

$$U(t_0, j\omega_k) = \frac{1}{2N+1} \sum_{n=-N}^{N} f_n \cdot e^{j\omega_k t_n} u(t_0, t_n). \qquad (1)$$

Here $U(t_0, j\omega_k)$ are the complex amplitudes for all sounding frequencies ω_k, $t_n = t_0 + n\Delta\tau$, $\Delta\tau$ is the time step of analog to digital conversion, $2N+1$ is the number of samples in the averaging interval.

Coherent accumulation, or synchronous detection, has an important feature of frequency selectivity as applied to AEM signals processing. The detection results turn out to be insensitive not only to signals that are significantly far from the detection frequency in frequency domain, but also to signals with frequencies that are separated from it by a strictly defined frequency interval, which depends entirely on the shape of the weight function f_n (Figure 1). In the figure δ is the frequency interval strickely defined by the form of f_n. Signals at frequencies $\omega_k \pm \delta$ close to the main one ω_k turn out to be invisible after applying (1).

At these invisible frequencies a set of reference signals can be added to the input of the system, since it will not affect the results of detecting the main frequencies.

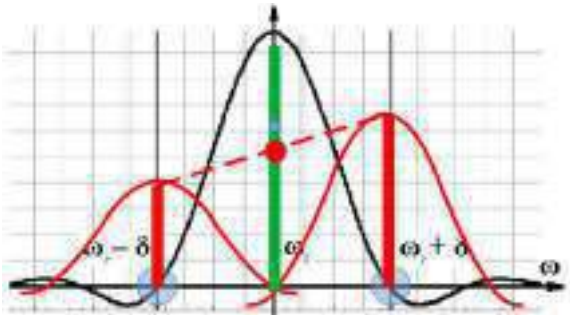

Figure 1. Selectivity of coherent accumulation main signal (green), reference signals (red), frequency response of the filter f_n

Then, by accumulating each reference signal on the system output and assuming the frequency band of the resulting triplet is narrow, we are able to get the value of the frequency response of the conversion at the main frequency. Figure 1 shows the form of the frequency response of coherent accumulation, the spectral lines of the reference process, the scheme of calculating the conversion coefficient for main detection frequency.

ALGORITHM OF ADAPTIVE CORRECTION FOR FREQUENCY DOMAIN AEM

Let us consider the operation of the adaptive correction method and algorithm for a harmonic field of a frequency ω_k. Having equation (1) we can also consider the result in the following form:

$$U(t, j\omega_k) = W(t, j\omega_k) \cdot X(t, j\omega_k), \qquad (2)$$

where $W(t, j\omega_k)$ is the measurement transformation applied to the input signal $X(t, j\omega_k)$.

Applying (1) at the frequencies $\omega_k \pm \delta$ we will not see the input signal $X(t, j\omega_k)$, while ω_k is shifted by δ. Nevertheless, we will be able to see the left (L) and the right (R) reference signals:

$$\begin{aligned} U_L(t, j\omega_k) &= W(t, j(\omega_k - \delta)) \cdot X_L(j\omega_k), \\ U_R(t, j\omega_k) &= W(t, j(\omega_k + \delta)) \cdot X_R(j\omega_k). \end{aligned} \qquad (3)$$

We have to note that $X_L(j\omega_k)$, $X_R(j\omega_k)$ are actually related to the frequencies $\omega_k - \delta$, and $\omega_k + \delta$ respectively. But while these signals are associated with the main frequency ω_k, we will not write δ in the argument. Also these signals supposed to be stationary, so they do not depend on time. So, only W contains t as an argument in the last two equations.

It is important that the proposed method allows us to obtain for the same coherent accumulation interval both the value of the complex amplitude of the signal and the parameters of the measurement transformation W for the known stationary signal. So, using the reference signals X_L and X_R the approximate value of W can be calculated as

$$\tilde{W}(t, j\omega_k) = \frac{1}{2}\left(\frac{U_L(t, j\omega_k)}{X_L(j\omega_k)} + \frac{U_R(t, j\omega_k)}{X_R(j\omega_k)}\right). \qquad (4)$$

This makes it possible to track the variability of measurement transform coefficient and correct the main signal as follows:

$$\tilde{X}(t, j\omega_k) = \frac{U(t, j\omega_k)}{\tilde{W}(t, j\omega_k)}. \qquad (5)$$

So, for the same accumulation interval, both the approximate value of the conversion coefficient $\tilde{W}(t, j\omega_k)$ for the frequency ω_k and the corrected value of the complex amplitude of the main signal $\tilde{X}(t, j\omega_k)$ for this frequency are obtained.

ALGORITHM OF ADAPTIVE CORRECTION FOR TIME DOMAIN AEM

For AEM methods the sounding field is usually periodic and its frequency spectrum is discrete. When the sounding signals sequentially switching polarity pulses, spectrum has only odd harmonics (Figure 2).

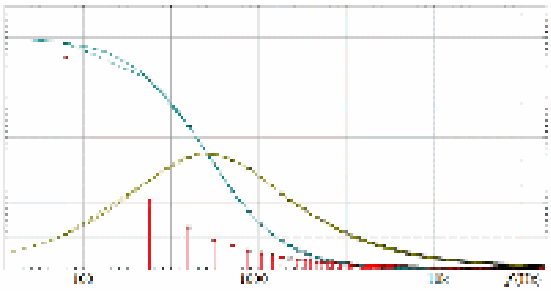

Figure 2. Structure of the sounding spectrum

For the spectrum structure, each of the lines can have its own pair of reference frequencies. It becomes a set of triplets, and for each one correction can be performed according to the above scheme (4)–(5).

In case of time domain measurements we are able to apply Fourier transform to the measured data. After that we can deal with them as with frequency domain data, including adaptive correction. While both digital filtering and Fourier transform are linear operations, we can switch the summation order to separate main and reference signals. Obviously, having in (1)

$$u(t_0, t_n) = \frac{1}{K}\sum_{k=1}^{K} U(t_0, j\omega_k) \cdot e^{j\omega_k t_n}, \qquad (6)$$

we can apply all the described techniques to each frequency separately. But to add the reference signals, we recommend using the following method for generating them

$$X_{LR}(t_n) = \cos(\delta t_n) \sum_{k=1}^{K} A_k \cdot \cos(k\omega_0 t_n). \qquad (7)$$

In this case it is easy to show that $X_{LR}(t_n) = (X_L(t_n) + X_R(t_n))/2$. In frequency domain for each frequency $k\omega_0$, $k = 1,...,K$, $X_L(jk\omega_0) = X_R(jk\omega_0) = X_{LR}(jk\omega_0)$. The value of ω_0 is the base frequency of the system – the lowest frequency of the primary field spectrum.

We can note, that formula (7) approximates an impulse function. But it works for any other. The key idea here is to modulate it with the frequency δ to make it invisible for filtering with f_n.

To extract the reference signal, we modulate the measured signal $u(t)$ with the frequency δ of the interval between the main and the reference harmonics.

$$u_M(t_0) = \frac{1}{2N+1}\sum_{n=-N}^{N} f_n \cdot \cos(\delta t_n) u(t_0, t_n). \qquad (8)$$

Due to the mentioned properties of the filter f_n the detection result will not contain the signal at any of main frequencies $k\omega_0$, $k = 1,...,K$.

Indeed, using (7) as a signal, we'll get $\cos^2(\delta t_n)$ in (8), so the result will be similar to $X_{LR}(t_n)$ with a scale factor. A stationary non modulated signal containing only $k\omega_0$ harmonics will give zero as the result, while any of those harmonics after multiplying by $\cos(\delta t_n)$ gives a sum of harmonics of $k\omega_0 \pm \delta$ frequencies.

Using Fourier transform, frequency domain shape of the output signals can be obtained for both the main signal and the reference signals. Due to selectivity of the coherent accumulation in spectral form the detection result gives the frequency response of measuring conversion up to a known factor X_{LR}:

$$U_M(t, j\omega_k) = \frac{W(j(\omega_k - \delta)) + W(j(\omega_k + \delta))}{2} X_{LR}(j\omega_k), \qquad \bar{W}(j\omega_k) = \frac{U_M(t, j\omega_k)}{X_{LR}(j\omega_k)}. \tag{9}$$

Now, for the main signal at all frequencies of the spectrum, according to (5), a correction can be performed, after which, using the inverse Fourier transform, the original time domain form for the main process is restored:

$$\bar{X}(t, j\omega_k) = \frac{U(t, j\omega_k)}{\tilde{W}(t, j\omega_k)}, \qquad \tilde{x}(t, t_n) = \frac{1}{K} \sum_{k=1}^{K} \bar{X}(t, j\omega_k) \cdot e^{j\omega_k t_n}. \tag{10}$$

PRACTICAL IMPLEMENTATION

Let's consider the results of the adaptive correction method on the example of data obtained for the EQUATOR AEM system (Moilanen *et al.*, 2013).

To implement the method and the algorithm, an additional transmitter dipole as a source of the reference magnetic field is built into the receiver. The current in this dipole is induced using a precise digital-to-analog conversion. Time-domain form of the reference field is formed according to (7).

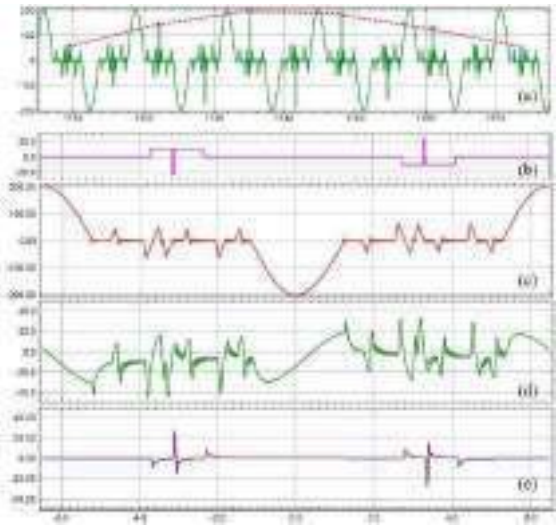

Figure 3. Processes and signals before and after measuring conversion

Figure 3 shows the sequence of signal transformations: (a) – linear superposition at the measuring system input of the reference (b) and main (c) processes, the dotted line shows the modulation of the reference process; at (d) and (e) we can see time-domain forms of the main and reference processes after separation respectively.

Figure 4 explains the calculation according to (9) for the frequency response of the measuring conversion. There are spectra for both known reference process at the input (a) and for the signal obtained at the output of the measuring transformations (b). The graph (c) in the spectral form shows the shape of measuring system frequency response (only the amplitude part of spectrum is shown).

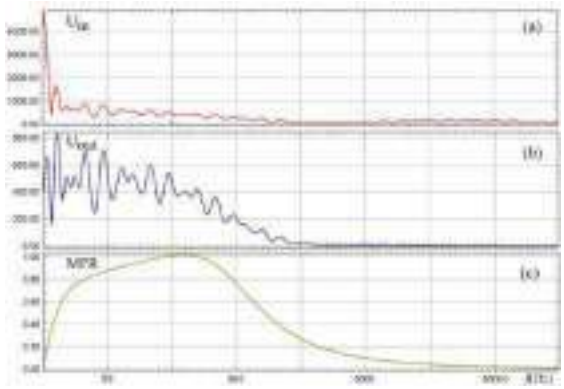

Figure 4 . Calculation of the frequency domain response of the measurement conversion

Figure 5 shows in time-domain the result of the correction performed according to (9)–(10) for all significant harmonics of the spectrum. In the figure: (a) is the input process, (b) is the output signal after the measurement conversion immediately, (c) is the result of the correction.

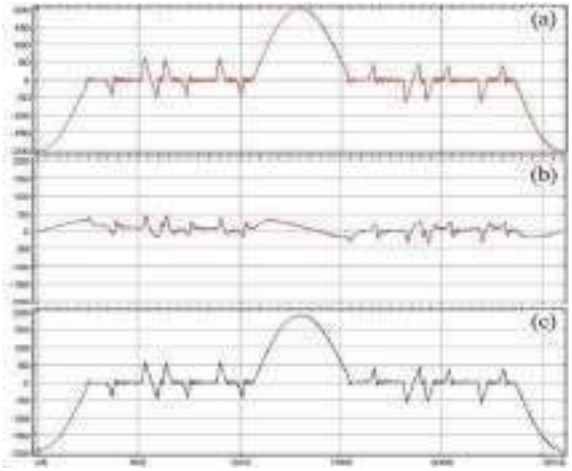

Figure 5. The result of the correction, obtaining the original time domain shape of main process

Figure 6 shows the results of adaptive correction method and algorithm. There are three groups of graphs related to the start, to the survey and the end of the same flight. The upper graphs are the inphase components of the secondary field at 20 harmonics from 77 Hz to 10 kHz (at high altitude must be zero). Under them there are the quadrature components (also zero at high altitude). Next there are 14 channels of *dB*/*dt* for the big pulse in figure 5 in time domain. The lowest graphs show the flight altitude above the ground. We can see that the values of the secondary field both in time an frequency domain at high altitude equal zero, and due to use of the adaptive correction after six hours flight the phase of the measured signal remain the same.

CONCLUSIONS

We have presented the results of development and implementation of the adaptive correction method and algorithm. We have shown functioning stability of AEM system EQUATOR provided by suggested approach. In our opinion, the versatility of the approach and the simplicity of technical implementation make it possible to apply the proposed method and algorithm in many well known AEM systems.

REFERENCES

Hamming, R., 2013. Digital filters. Dover Publications.

Legault, J.M., 2015. Airborne electromagnetic systems – state of the art and future directions. CSEG recorder 40 (6): 38-49.

Macnae, J., 2016. Quantitative estimation of intrinsic induced polarization and superparamagnetic parameters from airborne electromagnetic data. Geophysics 81 (6): E433-E446.

Wu, X., Xue, G., He, Y., and J. Xue, 2019. Removal of the multi-source noise in airborne electromagnetic data based on deep learning. Geophysics 85(6): 1-72.

Moilanen, J., Karshakov, E., and A. Volkovitsky, 2013. Time-domain helicopter EM System "Equator": resolution, sensitivity, universality. 13th SAGA biennial and 6thInternational AEM conference AEM-2013, Mpumalanga, South Africa, Expanded Abstracts: 1-4.

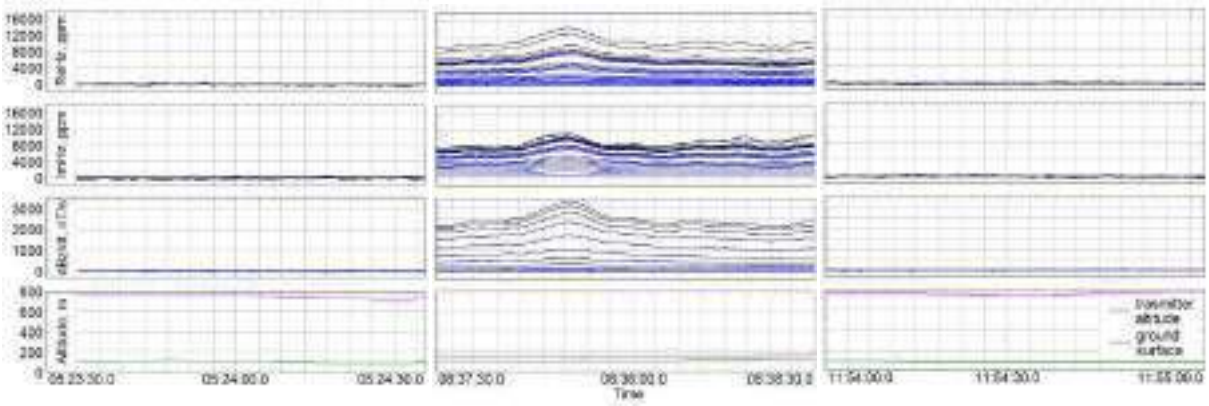

Figure 6. Effectiveness of applying adaptive correction, long-time stability

Targeting epithermal Au-Ag using helicopter TDEM, magnetic, and radiometric data at Lawyers Project, North-Central BC, Canada.

Jean M. Legault
Geotech Ltd.
Aurora ON CAN
Jean.legault@geotechairborne.com

Karl Kwan
Geotech Ltd.
Aurora ON CAN
karl.kwan@geotechairborne.com

Jim Greig
Benchmark Metals Inc.
Vancouver BC CAN
jim.greig@benchmark.ca

Ewan Webster
Benchmark Metals Inc.
Vancouver BC CAN
Ewan.webster@benchmark.com

Mark Hanki
Apex Geoscience Ltd.
Vancouver BC CAN
mark.hanki@apexgeoscience.com

SUMMARY

In September 2018, Geotech Ltd. completed a VTEM helicopter time-domain electromagnetic, magnetic and radiometric survey on behalf of Benchmark Metals Inc. over the Lawyers property, in northcentral BC. The magnetic results reveal a strong spatial relationship between sharp magnetic lineaments and the known mineralization. Radiometric results show that mineralization is characterized by hydrothermal alteration resulting in potassium enrichment, manifested as K/Th highs. The VTEM electromagnetic results identified local EM anomalies representing both discrete and structural conductors. However, none of the EM anomalies making up conductive zones coincide with the known epithermal mineralization, instead all the known Au-Ag deposits and occurrences are located in zones of high apparent resistivity.

Subsequent analysis of the VTEM data analysed using AIIP mapping revealed that all the known Au-Ag mineralized zones coincide with moderate to high Cole-Cole time constant (TAU) anomalies, consistent with relatively coarse-grained polarizable material, such as disseminated sulphides or hydrothermally altered clays.

The previous targeting approach focused on individual analyses of magnetic, structural, radiometric, EM resistivity and AIIP results, then arriving at a targeting model, based on geologically and geophysically based considerations. A new approach for targeting uses a semi-automated, machine-learning (ML) assisted approach that includes: Structural Complexities (SC), Self-Organizing Map (SOM) classifications, and Supervised Deep Neural Network (SDNN) targeting of the geophysical data. The new targeting approach has further reduced the number of priority targets from previous five (5) to three (3), which includes most of the known epithermal Au-Ag occurrences, as well as two areas for follow-up.

Key words: Epithermal gold-silver, airborne time domain electromagnetics, resistivity, magnetics, mineral exploration targeting (MET.

INTRODUCTION

Benchmark Metals' Lawyers Gold-Silver Project, situated 45 km northwest of Kemess South Mine in BC's Golden Horseshoe region (Figure 1) of north-central British Columbia, is host to a large, low sulphidation epithermal system known as the Lawyers Trend that contains a total indicated mineral resource of 40.3 Mt at 1.19 g/t Au and 38.7 g/t Ag. At the heart of the Lawyers Trend are the structurally-controlled Cliff Creek, Dukes Ridge, Phoenix and AGB zones that are located within a large 5 km by 8 km radiometric anomaly that is coincident with potassic alteration associated with the low-sulphidation epithermal system. The property straddles an important stratigraphic horizon between the Upper Triassic Stuhini Group and Lower Jurassic Hazelton Group that defines an important geological unconformity that hosts many of the deposits in the Golden Horseshoe.

Figure 1: Lawyers Project property location, and schematic of Golden Horseshow mineral district in northwestern British Columbia (modified after www.benchmark metals.com).

Originally explored in the late 1960's, mineralization at Lawyers was identified by the 1980's and lead to the development of the Lawyers gold-silver mine that operated from 1989-1992 and produced 171,200 oz gold and 3.6 million oz silver in that 4 year period. In the years following, exploration had focused on targeting high grade veins within the large epithermal system. Benchmark Metals has been actively exploring the Lawyers property since 2018, with a low-

grade bulk tonnage targeting model approach, using extensive geological mapping, drilling, soil and rock geochemistry, ground, drone and airborne geophysics, which led to a NI 43-101 compliant mineral resource estimate in 2021 (Stone et al., 2021). The Stone et al. (2021) report documented the targeting approach on helicopter TDEM, aeromagnetic and spectrometric data (Khaled et al., 2018) performed by Kwan et al. (2019), which was subsequently presented in Legault et al. (2022). This paper presents a new targeting approach that uses a semi-automated, machine-learning (ML) assisted approach that includes: Structural Complexities (SC), Self-Organizing Map (SOM) classifications, and Supervised Deep Neural Network (SDNN) approach to mineral targeting.

Geology and Mineralization

Lawyers property is predominantly underlain by a shallow northwest-dipping sequence of volcanic and sedimentary rocks of the Lower Jurassic Toodoggone Formation (Hazleton Gp). The Lower cycle Toodoggone rocks are comprised of thick sequences (>300 m) of dacitic and andesitic tuffs and flows. The most dominant structural features are NW-NNW (310-340°) striking faults that are subvertical to steeply SW or NE dipping. These host the mineralized epithermal systems. NW structures and associated mineralization are locally offset by E-W and SW-NE trending strike-slip faults (Stone et al., 2021).

Lawyers rocks are typically weakly altered, but gold-silver mineralization is associated with intense silicification and potassic alteration. Advanced argillic and qtz-sericite also present in some zones. Mineralization includes both low sulphidation (LS) in central & east (AGB, Cliff Ck, Duke Ridge) parts of the property, & high sulphidation (HSE) in the western (Silver Pond) part of the block (Stone et al., 2021).

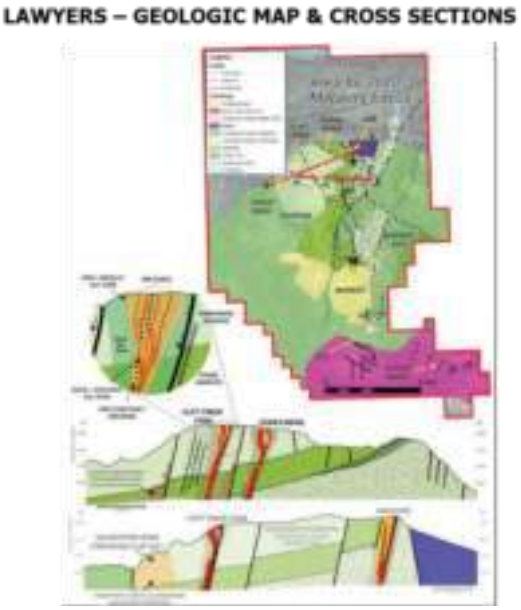

Figure 2: Lawyers Project geologic map (top) and schematic geologic cross sections (modified after www.benchmarkmetals.com).

METHOD AND RESULTS

Helicopter TDEM, Magnetic and Magnetic Surveys

In September 2018, Benchmark contracted Geotech Ltd. to complete a VTEM (Witherly et al., 2003) helicopter time-domain electromagnetic, magnetic and radiometric survey over the central and northern parts of the Lawyers property (Khaled et al., 2018). A total of 1,272 line-km were flown over a 115 km^2 area along 100 m spaced EW lines and 1 km spaced NS tie-lines. The VTEM Terrain system consisted of a 17.6m diameter, 4-turn transmitter loop (250k NIA @ 30Hz), a coincident-coplanar Z-component receiver (40ch 0.036-9.3ms), a caesium magnetometer, and RSX-5 spectrometer. The survey objectives were to map resistivity, magnetic susceptibility, and gamma radiation related to low to high sulphidation epithermal gold and silver targets in Lawyers camp.

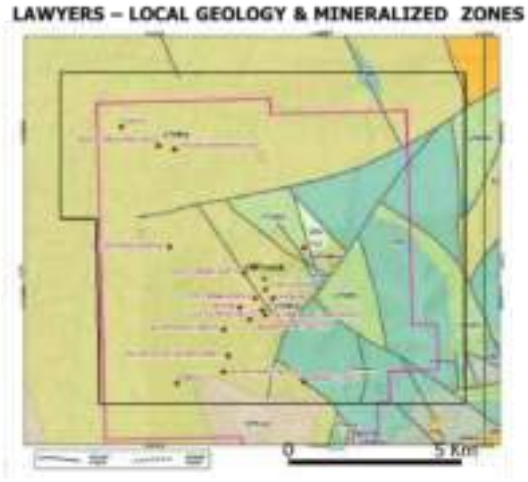

Figure 3: Lawyers Project local geology, mineral occurrences, and deposits, and known faults (modified after

VTEM, Magnetic & Radiometric Results

The total field magnetic results (Figure 4) reveal a strong spatial relationship between sharp magnetic lineaments, magnetic lows, and the known mineralization. In order to quantify the structural elements, the magnetic data were subjected to a structural complexity (SC) analysis, using the Geosoft CET (Center for Exploration Targeting) grid analysis extension (www.seequent.com). The magnetic ridges are derived using the method described in Holden et al. (2012). The structural complexity highs are in the SW region concentrated with known Au-Ag occurrences.

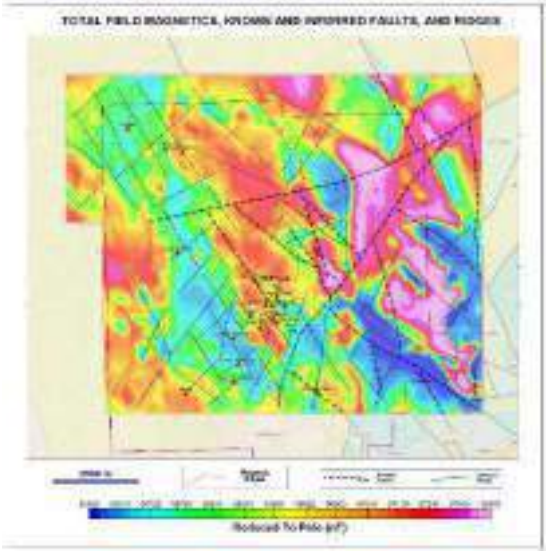

Figure 4: Total field magnetic intensity, over mineral occurrences & known/inferred faults (dashed lines), and magnetic ridges.

The faults and ridges are used to compute the structural complexity (SC) data (Holden et al., 2012), as shown in Figure 5. The structural complexity highs are in the SW region concentrated with known Au-Ag occurrences.

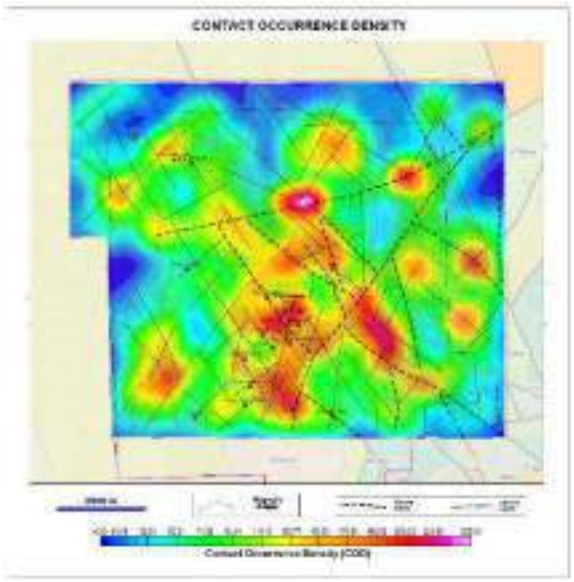

Figure 5: Structural complexity (SC) analysis of magnetic data, showing the Contact Occurrence Density (COD), over mineral occurrences & known/inferred faults (dashed lines), and magnetic ridges.

Radiometric results show that the Lawyers Property mineralization is characterized by hydrothermal alteration resulting in potassium enrichment, commonly manifested as K/eTh highs (Figure 6).

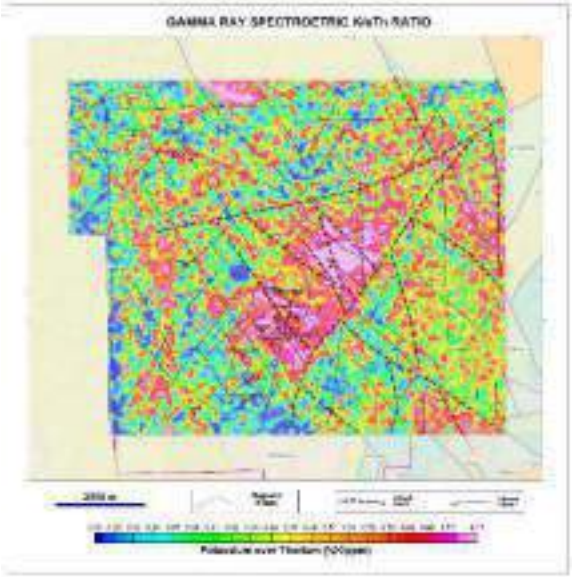

Figure 6: Gamma Ray Spectrometric K/eTh Ratio, over mineral occurrences & known/inferred faults (dashed lines), and magnetic ridges.

The VTEM dBz/dt EM decay constant map in Figure 7 includes the location of local EM anomalies centres represented by both large area and structural conductors. However, as shown, none of the EM anomalies making up conductive zones coincide with the known epithermal mineralization. Instead, all the known Au-Ag deposits and occurrences are located in zones of low TAU corresponding to high apparent resistivity (Figure 8).

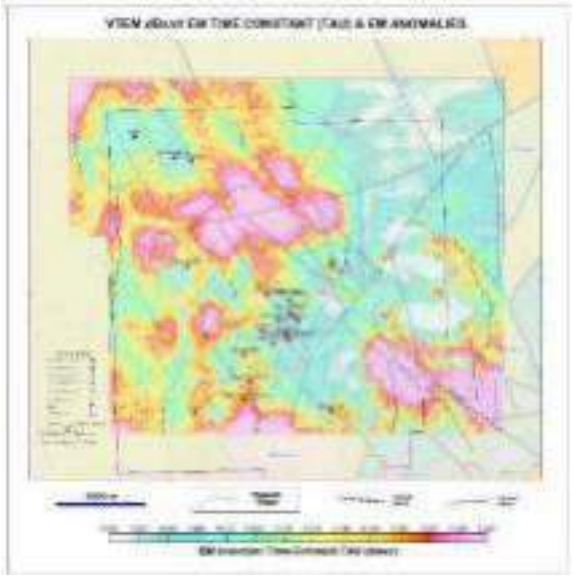

Figure 7: VTEM dBz/dt EM time constant TAU and EM anomaly picks, over mineral occurrences & known/inferred faults (dashed lines), and magnetic ridges.

VTEM AIIP and 1D Inversion Results

Layered Earth (LE) 1D inversions of the VTEM data were carried out using GALEI code. The VTEM data were analysed using AIIP (airborne inductively induced polarization) mapping tool (Kwan et al., 2015, 2016, 2018). The 1D resistivity -100 m depth slice and the AIIP Cole-Cole apparent resistivity data are displayed in Figure 8a & b, respectively. The two resistivity maps are different because the 1D inversions do not account of AIIP effects in the VTEM data.

The AIIP mapping revealed that all the known Au-Ag mineralized zones coincide with moderate to high Cole-Cole time constant (TAU) anomalies in resistive zones (Figure 9) that are consistent with relatively coarse-grained polarizable material, such as disseminated sulphides or hydrothermally altered clays. The product of the AIIP apparent resistivity and the Cole-Cole TAU (termed ResTau), presented in Figure 9, has proven to be a useful parameter for identifying low sulphidation epithermal Au-Ag mineralization elsewhere on the property.

Targeting Epithermal Au-Ag

Self-Organizing Maps (SOM) are a potent tool in analysing and classifying multiple datasets. The SC data, the K/eTh, and the AIIP apparent resistivity and Cole-Cole Tau products are classified using the Geosoft SOM GX tool (https://geosoftgxdev.atlassian.net). The SC data, the K/eTh, and the AIIP apparent resistivity and Cole-Cole Tau products are classified using SOM. Most of the anomalous SOM classes (9 to 17) coincide with the known Au-Ag mineralization in the SW and central regions of the Lawyers property (Figure 10).

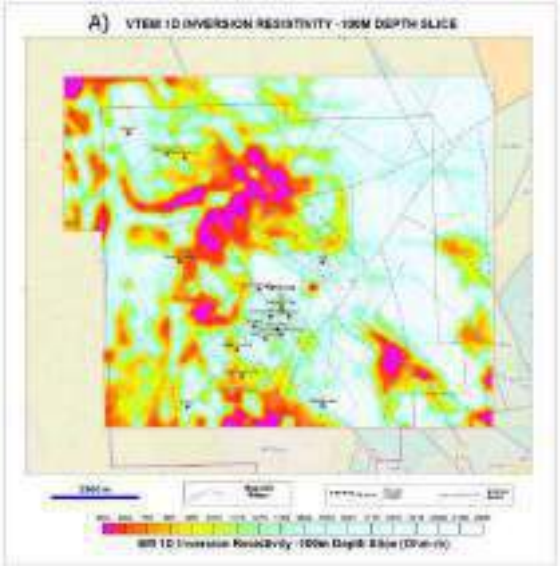

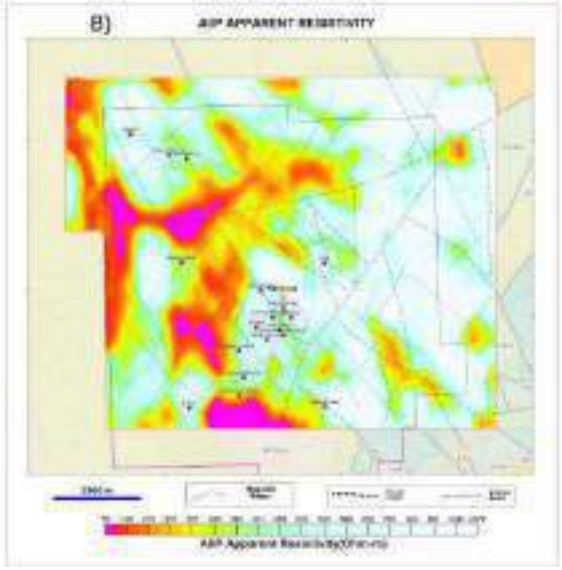

Figure 8: (A) VTEM 1D Inversion resistivity depth slice (-100m), and (B) AIIP Cole-Cole apparent resistivity, over mineral occurrences & known/inferred faults (dashed lines), and magnetic ridges.

The final targeting preparation was done using the Google TensorFlow version TF 2.30 (https://www.tensorflow.org/) and its Supervised Deep Neural Network (SDNN) module. The training of the SDNN was performed using the SC, SOM, K/eTh, and AIIP apparent resistivity-tau product from an area with known Au-Ag deposit (Cliff Creek), Figure 11A. The top 6% probability is selected for Au-Ag targeting, Figure 11B.

The SDNN targeting process was then reapplied to the Lawyers survey area. The results showing the top 6% targeting probabilities are presented over the DEM data, and the selected targets, LET_1 to LET_3 are presented in Figure 12. The selected targets all occur in topographic highs.

CONCLUSIONS

Previous targeting of VTEM results at Lawyers (Kwan et al., 2019; Legault et al., 2022) focused on individual analyses of magnetic, structural, radiometric, EM resistivity and AIIP results, then arriving at a targeting model, based on geologically and geophysically based considerations, resulting in five (5) priority targets. A new approach for targeting, presented here, uses a semi-automated, machine-learning (ML) assisted approach that includes: Structural Complexities (SC), Self-Organizing Map (SOM) classifications, and Supervised Deep Neural Network (SDNN) targeting of the geophysical data. Structural complexity analyses of the magnetic data at Lawyers Project have identified a strong spatial relationship between the known and inferred faults and calculated ridges and the known mineralization EM results have shown that the known mineral occurrences are located in zones of high resistivity.

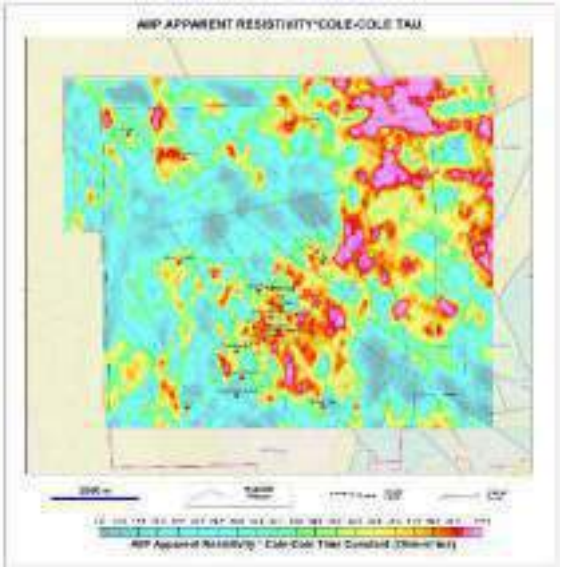

Figure 9: VTEM AIIP ResTau (Resistivity*Time Constant) Product, over mineral occurrences & known/inferred faults (dashed lines), and magnetic ridges.

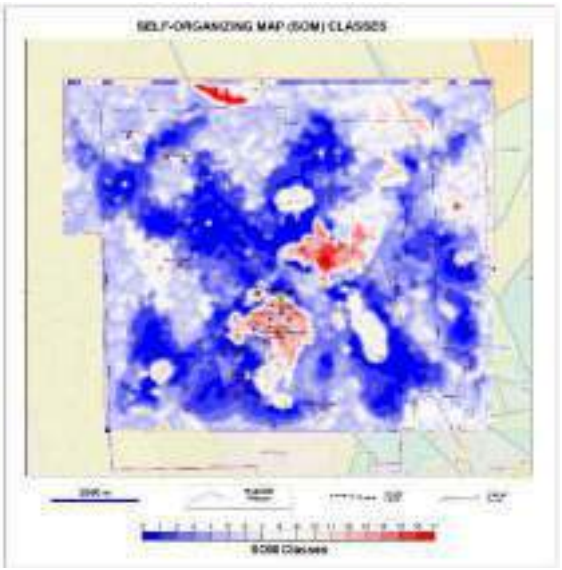

Figure 10: The anomalous SOM classes cover most of the known Au-Ag occurrences.

Gamma ray spectrometric results have shown that the known mineral occurrences are located in high to moderate K/eTh ratio anomalies. AIIP results at Lawyers Project suggest that the product of AIIP apparent resistivity and Cole-Cole time constant (Res*Tau) could be a useful targeting tool. Using SOM and SDNN results, the previous five (5) have been reduced to just three (3) priority targets, which include most of the known epithermal occurrences and include other areas for follow-up. It is also worth noting that the targeting of epithermal Au-Ag mineralization is done by a semi-automated processes which require little human intervention or bias. Importantly, the structural complexities, computed using known and inferred faults, also played a critical role in targeting.

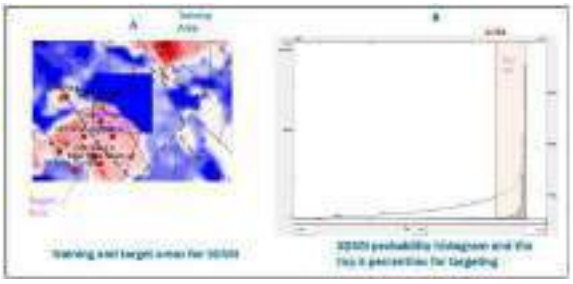

Figure 11: (A) Training area for SDNN, (B) top 6% target probability cut-off for targeting.

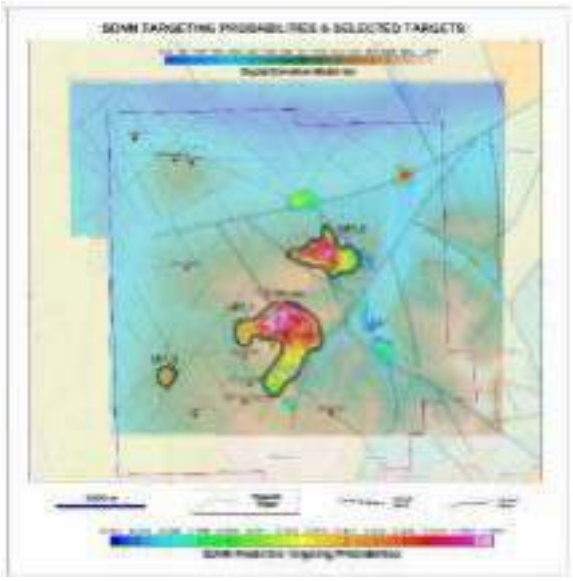

Figure 12: The SDNN top 6% probabilities over the DEM data and the selected potential epithermal Au-Ag targets.

ACKNOWLEDGMENTS

The authors wish to thank Benchmark Metals, Apex Geoscience and Geotech for allowing us to present these results.

REFERENCES

Holden, E.-J., Wong, J. C., Kovesi, P., Wedge, D., Dentith, M., Bagas, L., 2012. Identifying structural complexity in aeromagnetic data: An image analysis approach to greenfields gold exploration. Ore Geology Reviews 46: 47–59.

Khaled, K., Shei, T.C., Prikhodko, A., and Orlowski, K., Report on helicopter-borne versatile time domain electromagnetic (VTEM), aeromagnetic and gamma-ray spectrometry geophysical survey, over Lawyers Project, Kemess Creek, BC, for Benchmark Metals Ltd.: Internal report (GL180180), 62 p.

Kratzer, T. and Macnae, J.C., 2012: Induced polarization in airborne EM, Geophysics, 77, E317-327.

Kwan, K., Legault, J.M., Johnson, I., Prikhodko, A. and Plastow, G., 2018: Interpretation of Cole-Cole parameters

derived from helicopter TDEM data – Case studies, Extended Abstract, SEG Anaheim 2018 International Exposition and 88th Annual Meeting.

Kwan, K., A. Prikhodko, J.M. Legault, G. Plastow, J. Kapetas, and M. Druecker, 2016: Airborne EM, aeromagnetic and gamma-ray spectrometric data over the Cerro Quema high sulphidation gold deposits, Panama, *Exploration Geophysics*, 47, 179-190.

Kwan, K., Prikhodko, A., Legault, J.M., Plastow, G., Xie, J. and Fisk, K., 2015: Airborne Inductive Induced Polarization Chargeability Mapping of VTEM data, ASEG-PESA 24th International Geophysical Conference and Exhibition, Perth, Australia.

Kwan, K., Han, Z., Khaled, K. and Prikhodko, A., 2018: Interpretation report on a helicopter-borne versatile time domain electromagnetic (VTEM), aeromagnetic and gamma-ray spectrometry geophysical survey, over Lawyers Project, Kemess Creek, BC, for Benchmark Metals Inc. Internal report (GL180180) for Benchmark Metals Inc., 52 p.

Legault, J.M., Kwan, K., Greig, J., Webster, E., Hanki, M., and Wilson, R., 2022: Helicopter Time Domain EM-AIIP, Magnetic and Radiometric Case Study over the Lawyers Epithermal Gold-Silver Project, North-Central BC, Canada. SAGA, Extended Abstracts, 4 p.

Stone, W., Wu., Y., Barry, J., Puritch, E, Ray, B., Wright, F., and Mioska, M., 2021: Technical Report and Updated Mineral Resource Estimate of the Lawyers Gold-Silver Property, Omineca Mining Division, British Columbia, Canada, NI 41-101 Technical Report for Benchmark Metals Inc. by P&E Mining Consultants Inc., 478 p.

Witherly, K., Irvine, R. and Morrison, E., 2004:The Geotech VTEM time-domain helicopter EM system, 74th Meeting SEG, Expanded Abstracts, 1217-1220.

An Airborne Heterodyne Sulphide Exploration Test at Kempfield

James Macnae
CD3D Pty Limited
jcm@c3dmap.com

Terry Kratzer
BIPTEM
terry@biptem.com

SUMMARY

We continue to investigate an ancillary method to Induced Polarization for sulphide exploration, using analysis to measure heterodyne effects in time-domain Airborne Electromagnetic data. We investigate how a parameter named mixabiity can characterise these effects in terms of frequency content and composition, finding that with sufficiently low noise levels, heterodyne effects could theoretically be observable in time-domain AEM data.

Analysing existing AEM survey data, we earlier found no spatial correlation between known sulphide distribution and mixability. We postulated that this is because potential heterodyne effects due to sulphides were being masked by two different limitations of the survey dataset we used; firstly, variable transmitter waveform asymmetry; and secondly, the decreasing signal levels from the fixed a ground-loop transmitter resulting in increasing relative noise levels away from the transmitter. We therefore conducted a airborne Slingram EM/IP survey with the BIPTEM system to address the identified limitations of existing test data.

We present results from an airborne test at Kempfield, the test site for definitive ground tests of the heterodyne method for sulphide detection. The small mixability anomalies detected in the airborne data were not consistent with either drilled sulphides or mapped IP anomalies.

Key words: Induced Polarization Heterodyne Sulphide Airborne Electromagnetic Kempfield

INTRODUCTION

The non-linear electronic behaviour of sulphides has been well-studied in the laboratory (Shuey, 1975). Most sulphides are semiconductors, and electrical conduction between grain boundaries will usually show evidence of a directional bias, identical in concept to the physics of semiconducting p and n junctions in transistors. Recent papers (White et al., 2018; Oertel et al., 2018, Collins et al., 2022, White et al., 2023) present evidence that the known non-linear behaviour of sulphides may be detected in the field to discriminate sulphides with semiconducting grains from graphitic rocks.

The ground studies reported by White et al, used two separate injected currents at different frequencies; injected into the ground by pure sine-wave generators. Heterodyne effect detection relied on non-linear effects from frequency mixing to detect th8isa distinctive sulphide conductivity behaviour. In his talk in 2022, Steve Collins suggested that since the heterodyne effects were independent of frequency, the methodo logy could usefully be used in airborne electromagnetic geophysical methodology.

SULPHIDES, SEMICONDUCTORS, HETERODYNE

Sulphides are semiconductors (Shuey, 1975), and ores usually contain billions of grain boundary junctions (Figure 1). Individual grains may have different impurities and be effectively p or n "doped". In bulk, these junctions may preferentially favour current flow in one direction rather than the other, leading to asymmetric current flow and voltage responses to symmetric, alternating, background electrical fields (Figure 2).

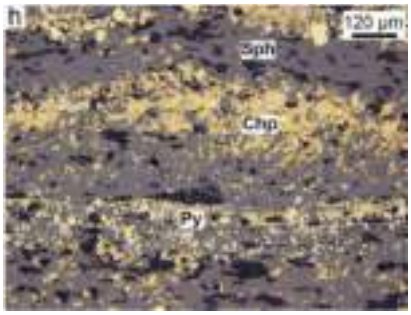

Figure 1: Example massive Sulphide structures. (Maslennikov et al, 2019)

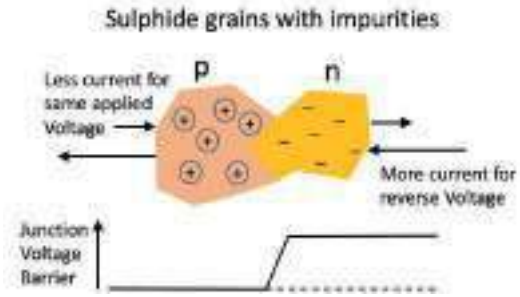

Figure 2: Semiconductor conductivity physics

The physics of semiconductor junctions has seen extensive use in radio, where the term heterodyne was used when two separate signals at different frequencies were used to create a beat. The term superheterodyne is used when frequency mixing and band-limited amplification extracts a signal at a fixed intermediate frequency. In the ground, the methodology used by White et al and Collins et al to detect non-linearities in sulphides transmits two low frequency signals into separate electrodes and looks for responses at mixed frequencies. Laboratory studies (Oertel et al, 2018, Oertel, 2019) confirm that mixed frequency signals are located when significant sulphides are present, but not otherwise (Figure 3, at end of abstract).

Sulphides have frequency-dependent conductivities usually modelled with the Cole-Cole equation. When this behaviour is

combined with the effect of junction non-linearities, some of the mixed frequency responses are reduced in amplitude (Figure 4). The largest secondary amplitudes (at 10 and 100 Hz) mixed from the source frequencies being 55 and 45 Hz are somewhat affected by including a Cole-Cole response as well as the heterodyne mixing, but still remain the optimum search targets from a frequency analysis for the presence of heterodyne effects.

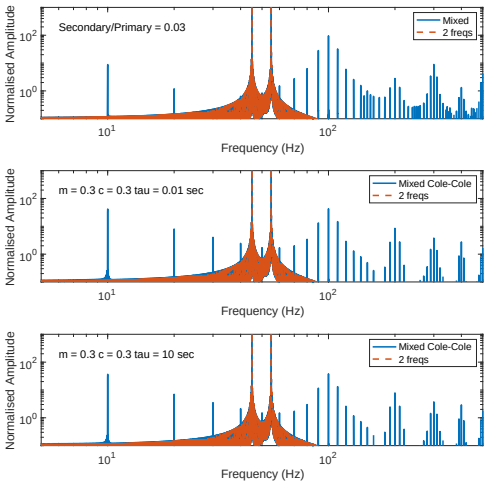

Figure 4: Relative amplitude modulations of the 'pure' mixed frequencies (top) are modified if Cole-Cole IP effects are also present. Source frequencies of 45 and 55 Hz in this simulation.

HETERODYNE EFFECTS IN TIME DOMAIN

Collins et al (2020) suggested that the lab and ground survey concepts could be extended to AEM as they are frequency independent at local grain level. To do so on existing data, we investigated what the time domain equivalent to the mixing in a superheterodyne response might be.

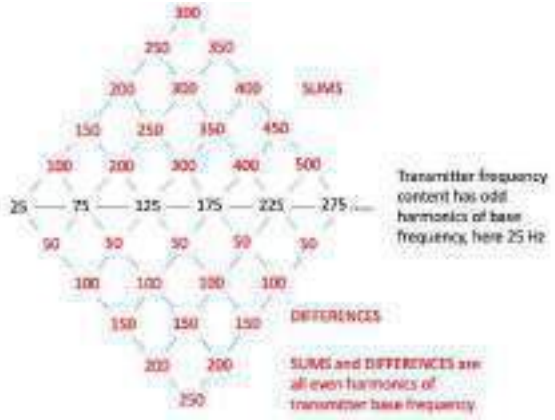

Figure 5: Mixed additive and subtractive frequencies from non-linear response to a 25 Hz repetitive waveform. The heterodyne frequencies in this case are all harmonics of the 50Hz powerline frequency, and as such not a useful detection frequency in Australia.

Taking the Fourier transform of 25 Hz base frequency data shows that the waveform consists only of odd harmonics of the base frequency, i.e. 25, 75, 125, 175 … Hz. In an fft, there is an upper limit to the odd harmonics just less than the Nyquist (sampling) frequency. A non-linear process is expected to produce new frequencies at the sums/differences of the transmitter waveform's odd harmonics. Figure 5 shows that all the simple sums and differences lie at the even harmonics of the transmitter base frequency. More convoluted differences such as f3 = (2f2 – f1) lie on odd harmonics. It was clear to us that in Australia, 50 Hz and its harmonics are undesirable frequencies to look for small effects, so ubiquitous 25 Hz airborne AEM data unless located far from infrastructure was likely to be of limited value. We therefore looked for some 12.5 Hz data. Note that as implemented in frequency domain, the mixing frequencies are not harmonics of either of the primary frequencies.

In the simple case of a 50% duty-cycle square wave current, a perfect p-n junction inhomogeneity appears as a reduction in amplitude on one half of a secondary in-phase with the primary B field. Taking the fft of this modified response for a 12.5 Hz base (Figure 6) leads to a very interesting result. When phase information is included, half of the predicted even harmonics are not evident. The primary field is evident at 12.5, 37.5, 62.5, 97.5 … Hz, and the heterodyne effects are seen at 25, 75, 125, 175 … Hz. This is a set of odd harmonics of the first even harmonic of the base frequency, called even-odd harmonics later in the paper.

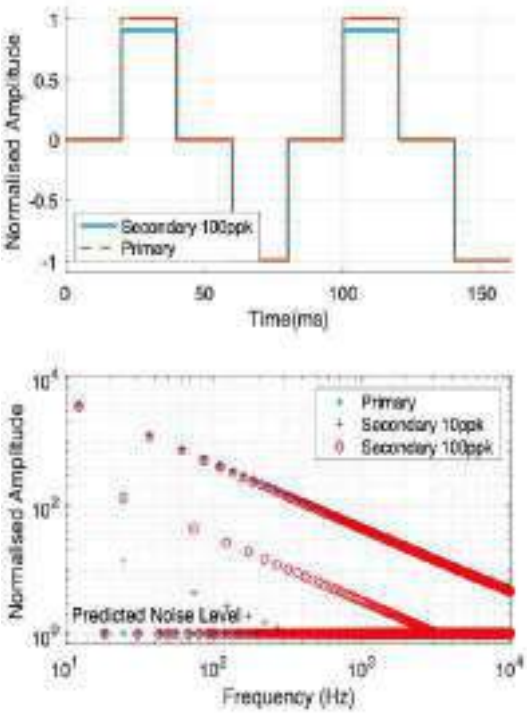

Figure 6: (Top) Plot of time domain 50% duty cycle with 12.5 Hz base frequency. A non-linear secondary B field of amplitude 10% (100 parts per thousand) of the primary field is plotted and reduces the observed field on the positive transmitter cycle. (Between harmonics at 25, 75, 125, 175 … Hz These signals do not compete with the powerline harmonics and should be detectable in data if (a)

superheterodyne effects exist and (b) the noise level is low enough.

FIELD TEST

During testing of the BIPTEM system at Kempfield, we had the opportunity to use the acquired data to measure mixability over 4 profiles. Similarly to the ground field results of Collins et al (2023), our airborne data did not show any evidence of significant mixability effects. While small variations (between 0.3 and 0.5 ppk above background are seen, these did not correspond to sulphides in the initial analysis,. Whose intrinsic mixabilities were in the 10 to 100 ppk range.

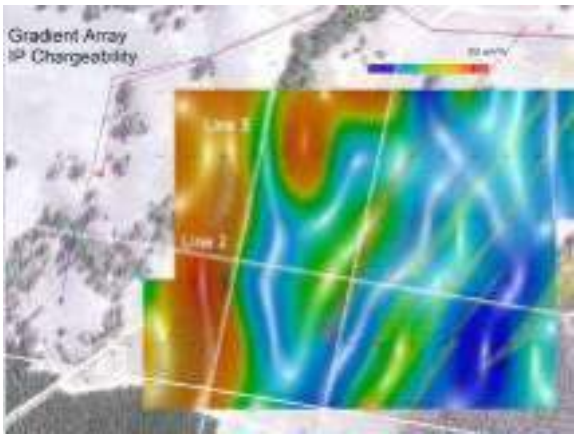

Figure 7: Gradient Array IP (Collins et al., 2022) with location of BITTEM flightlines 2 and 3.

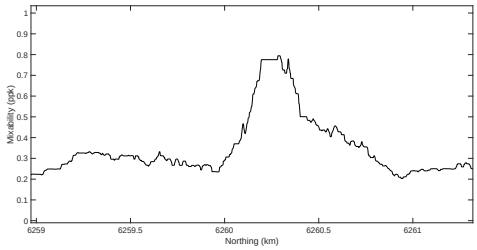

Figure 8. Mixability of the 25 Hz signal on Line 3 at Kempfield. All measured values are less than 1 part per thousand and do not correspond to IP responses or drilled sulphides.

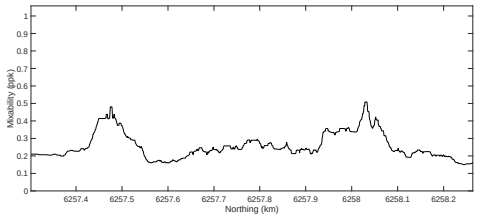

Figure 9. Mixability of the 25 Hz signal on Line 2 at Kempfield shows lower amplitude than on Line 3.

CONCLUSIONS

Mixability (a measure of non-linearity in electrical response) clearly occurs in Kempfield drill-core samples, but measurements using streamed airborne data did not show any useful characterisation of known sulphides or mapped IP effects.

ACKNOWLEDGMENTS

We thank Steve Collins, Bob White and Keith Leslie for stimulating this research, and Duncan Massie (Monex Geoscope), Paul Rogerson (Thomson Air), Chris Wilkinson (Argent) and Greg Walker (Newmont) for assistance with / funding for the Kempfield test flight using the BIPTEM system

REFERENCES

Collins, S., White, R., Leslie, K., & Sloot, A., 2022, A completely different geophysical way to explore for sulphides. Heterodyne method - latest progress and field results, Presentation, ASEG-SMERDG

Hine, K. and Macnae, J., 2016, Comparing induced polarization responses from airborne inductive and galvanic ground systems: Lewis Ponds, New South Wales, Geophysics 81(6):B179-B188.
DOI: 10.1190/geo2016-0204.1

Macnae, J., 2018, B field measurements for AEM and AIP: the BIPTEM system. AEM2018 –June 17-20,Kolding, Denmark, extended Abstract www.conferencemanager.dk/aem2018.

Macnae J. and Kratzer, T., 2023, An Airborne Heterodyne Sulphide Exploration Test, AEGC Extended abstract 185, Brisbane, Australia

Maslennikov , V., Ayupova , N., Safina, N., Tseluyko, A., Yu, I., Melekestseva, Large, R., Herrington, R., Kotlyarov, V., Blinov, I., Maslennikova, S., & Tessalina , S., 2019 Mineralogical Features of Ore Diagenites in the Urals Massive Sulfide Deposits, Russia; Minerals 2019, 9(3), 150; https://doi.org/10.3390/min9030150

Oertel, AWhite, R., Collins, C., Leslie, K> and Spyridis, B., , 2018, Frequency and current analysis of non-linear electrical effects in mineralised rocks: 1st Australian Exploration Geoscience Conference, Extended Abstracts https://doi.org/10.1080/22020586.2019.12073239

Oertel;, A., 2019, Biased Heterodyne Method; a future technique for sulphide exploration, Laboratory study & Kempfield field trials. SMEDG presentation;
https://smedg.org.au/wp-content/uploads/2020/07/Alan%20Oertel%20Biased%20Heterodyne%20Method.pdf

Shuey, A., 1975, Semiconducting Ore Minerals, Elsevier, eBook ISBN: 9780444601421

White, R., Collins, S., Leslie, K., Oertel, A., & Sloot, A., 2018, Field trials of the Biassed Heterodyne Method of Exploration for Sulphide Minerals. ASEG expanded abstracts, https://doi.org/10.1071/ASEG2018abM3_2F.

White, R., Collins, S., Leslie, K., & Sloot, A., 2018, Heterodyne Method of Sulphide detection. Latest field results. AEGC Extended abstract 36, Brisbane, Australia

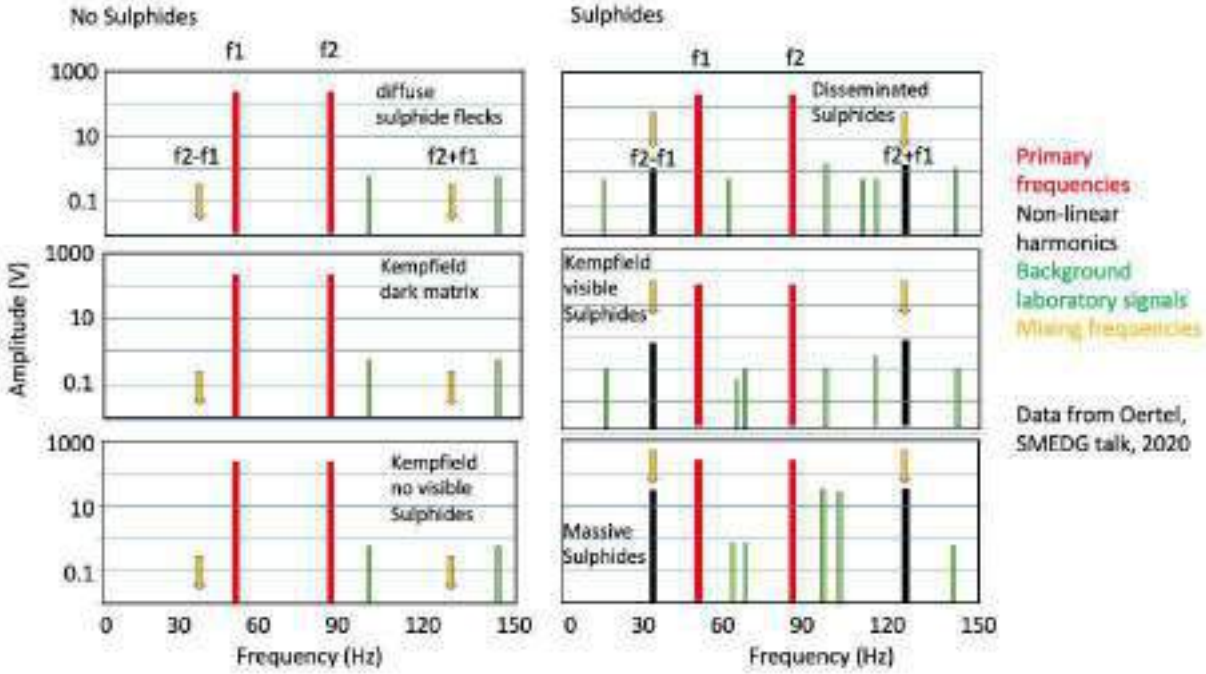

Figure 3. Figure 3: Laboratory testing of cores by Oertel (2020) shows that significant mixing responses at the difference and sum of the two source frequencies inly occur when significant sulphides are present. Note that the vertical logarithmic scale has 5 decades so covers a 100,000 to 1 amplitude range. Mixability values between 10 and 100 ppk (parts per thousand) were seen in sulphides.

Using airborne electromagnetics to improve depth to bedrock estimates in Wisconsin

Burke J. Minsley
U.S. Geological Survey
Denver, Colorado, USA
bminsley@usgs.gov

Jade Crosbie
U.S. Geological Survey
Denver, Colorado, USA
jcrosbie@usgs.gov

Jim Duncker
U.S. Geological Survey
Champaign, Illinois, USA
jduncker@usgs.gov

Daniel Feinstein
U.S. Geological Survey
Madison, Wisconsin, USA
dtfeinst@usgs.gov

Lisa Haas
WI Geological and Natural History Survey
Madison, Wisconsin, USA
ldhaas@wisc.edu

Dave Hart
WI Geological and Natural History Survey
Madison, Wisconsin, USA
david.hart@wisc.edu

Randy Hunt
U.S. Geological Survey
Madison, Wisconsin, USA
rjhunt@usgs.gov

Matt Komiskey
U.S. Geological Survey
Madison, Wisconsin, USA
mjkomisk@usgs.gov

SUMMARY

Depth to bedrock is often an important factor in hydrologic systems because hydraulic properties of bedrock and overlying sediments are typically appreciably different. For example, the thickness of glacial sediments overlying bedrock in Wisconsin controls the routing of groundwater in surficial aquifers and its connection with surface water bodies such as lakes and wetlands. In fractured bedrock environments, shallow bedrock can be vulnerable to degraded water quality when contaminants at the surface infiltrate quickly through permeable formations. Here, airborne electromagnetic surveys were acquired in three different parts of Wisconsin, totalling more than 5,700 flight line-kilometers, to improve understanding of depth to bedrock, the lithologic composition of overlying sediments, and as input structure for groundwater model development.

Key words: airborne electromagnetic, bedrock, groundwater resources, Wisconsin

INTRODUCTION

Improved estimates of the depth to sedimentary bedrock units and the composition of overlying materials are needed to characterize groundwater systems and support their protection in Wisconsin. Glacial sediments overly Ordovician to Silurian-age bedrock units in southwest, southeast, and northeast parts of the state where airborne electromagnetic (AEM) surveys were conducted in 2021 and 2022 in support of shallow geologic mapping studies (Figure 1). Electrical resistivity models derived from the AEM data are used to distinguish the top of bedrock, spatial variability of glacial sediment and bedrock lithology, and deeper shale units beneath the shallow bedrock. This work involved collaboration across several USGS projects along with the Wisconsin Geological and Natural History Survey (WGNHS), the Wisconsin Department of Agriculture, Trade, and Consumer Protection (DATCP), and the Wisconsin Department of Natural Resources (WDNR).

Figure 1. Airborne electromagnetic survey flight lines acquired in Wisconsin from 2021 to 2022.

Depth to Silurian bedrock is the metric used in the state of Wisconsin to control mechanical application of manure to cropland and pasture areas. Because the dolomite bedrock is fractured and highly permeable, technical standards on verification of depth to bedrock are implemented to help prevent pathogens from reaching groundwater. Manure application is prohibited where depth to bedrock is less than two feet, and application restrictions apply where depths are 20 feet or less. In the northeast 2021 study area, an AEM survey was conducted over an area of about 2,600 square kilometers to provide a systematic approach for mapping bedrock depth beneath glacial sediments. Semi-automated picks of the top-bedrock elevation were made at over 80,000 AEM model locations, and picks were used to generate a gridded depth to bedrock map over the survey area (Figure 2).

The 2022 southeast Wisconsin survey covered an area along the Fox River, in the uppermost part of the Illinois River Basin where additional AEM surveys extended in early 2023. This study area partly overlaps an existing inset groundwater model of the Mukwonago Basin that focused on characterization of the glacial aquifer system and its importance to surface water and wetlands (Feinstein et al. 2020). Here, AEM-derived interpretations of the depth to bedrock were used to refine the

thickness and geometry of the overlying glacial aquifer system in the groundwater model. The existing model allows comparison of model outputs with and without the refined bedrock geometry to test the value of new AEM information in groundwater model performance.

METHOD AND RESULTS

AEM data were acquired in northeast Wisconsin (3,170 line-kilometers) during January and February 2021, and in southwest (1,381 line-kilometers) and southeast (1,171 line-kilometers) Wisconsin during February and March 2022 (Figure 1). Both surveys used the SkyTEM 304 system, with a modified system configuration where an increased high-moment base frequency was implemented to improve early-time responses given the particular focus on resolving shallow bedrock. The higher base frequency resulted in some compromise with reduced depth of investigation, given the last time gate around 3 ms as opposed to 9 ms for the standard SkyTEM 304 configuration. One-dimensional electrical resistivity models were recovered for using Aarhus Workbench laterally constrained inversions (Auken et al. 2015).

Northeast Wisconsin depth to Silurian bedrock

Inverted resistivity models for northeast Wisconsin (Minsley et al. 2022) were imported into Geoscene3D (I-GIS, Denmark) where semi-automated picks of the top-bedrock elevation were made by evaluating the shallow transition to high resistivity at over 80,000 locations along AEM flight lines (Figure 2A). Picks were interpolated into maps of bedrock elevation (Figure 2B) and bedrock thickness (Figure 2C) by differencing the elevation from a Lidar digital elevation model. Bedrock thicknesses are displayed within several classes that are relevant to the state technical standards.

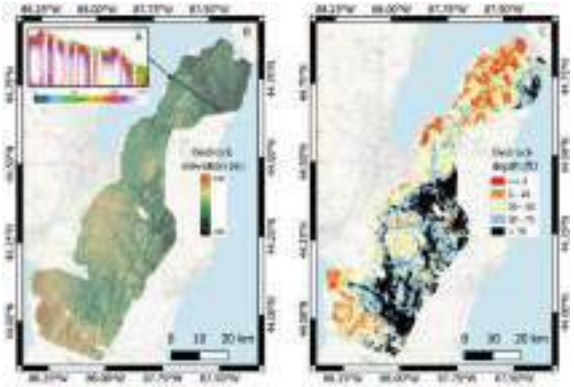

Figure 2. AEM interpretations of shallow bedrock. (A) Bedrock elevation was interpreted at over 80,000 locations along AEM flight lines, where were interpolated into a bedrock elevation surface (B). (C) Map of depth to bedrock classes relevant to state technical standards produced by subtracting the bedrock elevation from a lidar DEM.

Although AEM is effective in identifying bedrock depth using a systematic approach, small-scale details can be missed between flight lines separated by 800 m and regions outside the AEM footprint are not included. For this reason, we augmented the AEM-only maps using a statistical approach that incorporated both AEM picks along with other ground-based datasets of bedrock depth (over 170,000 points). Empirical Bayesian kriging with regression prediction was implemented using Esri ArcGIS Pro 2.9.1 (Esri, Redlands, California) to assimilate all available AEM and ground-based data into a map of bedrock elevation over a larger area in eastern Wisconsin (Hart et al. 2022). Updated bedrock maps will be incorporated in publicly available maps used to apply state technical standards.

At one location where AEM interpretations of bedrock depth were significantly greater than previous maps derived from manual probing, detailed ground-truthing was undertaken to understand this difference. Digging of a shallow trench with an excavator confirmed that bedrock depth was greater than indicated by manual probing, which was likely misinterpreted when shallow cobbles were hit in coarse grained glacial layers.

Groundwater model improvements with refined aquifer thickness

We followed a similar process in southeast Wisconsin to refine interpretations of depth to bedrock, corresponding here to the thickness of a glacial aquifer system, by using Geoscene3D to make bedrock picks guided by resistivity transitions along AEM flights (Crosbie et al. 2023). Refining the geometry of the glacial aquifer provided an opportunity to evaluate the value of this information in performance of an existing groundwater model in the Mukwonago Basin (Figure 3A; Feinstein et al. 2020).

Although AEM survey lines do not cover the entire model domain because of populated areas, new interpretations most notably enhanced representation of a bedrock valley that intersects the southern part of the model domain (Figure 3B-C). The bedrock valley is apparent as a transition to a resistive layer at depth that can be tracked in cross-section view (Figure 3D). Although its general location and pattern remain similar, interpreted depths can vary by more than 25 m, with the updated bedrock surface being narrower than in the original version.

Analysis compared groundwater model fit and performance between the original groundwater model (Feinstein et al. 2020) and a re-run with refined estimates of depth to bedrock, both calibrated with the parameter estimation code PEST (Doherty 2022). Addition of the AEM data improved overall model fit by 17%. More importantly, however, significant improvements were observed in simulation of wetland fens (114% improvement in fen count) and distribution of groundwater discharge to non-fen surface water features (72% improvement). Estimates of total basin discharge worsened somewhat (-26%).

Better assessment of groundwater interaction with fens and other surface water features is achieved through including more realistic aquifer geometry and associated distribution of groundwater flow between the bedrock and overlying unconsolidated sediments. This insight, in turn, improves the ability to inform decisions about water resource management in this basin. Future efforts will aim to further improve model performance and predictions by incorporating additional details interpreted from the AEM data beyond just bedrock depth estimates: (1) refine the geometry of different subcropping bedrock units beneath the glacial aquifer, which have different hydrologic properties; and (2) inform lithologic changes within the model's glacial aquifer that are likely important for local groundwater flow.

CONCLUSIONS

AEM surveys can contribute in various ways to support decision making, land use management, and understanding of groundwater resources. Model-independent information such as depth to bedrock is directly useful in informing land management practices in agricultural areas where shallow fractured bedrock is vulnerable to contamination. In other areas, basic interpretations of depth to bedrock are shown to improve groundwater model predictions when more representative aquifer geometry is assigned from AEM interpretations.

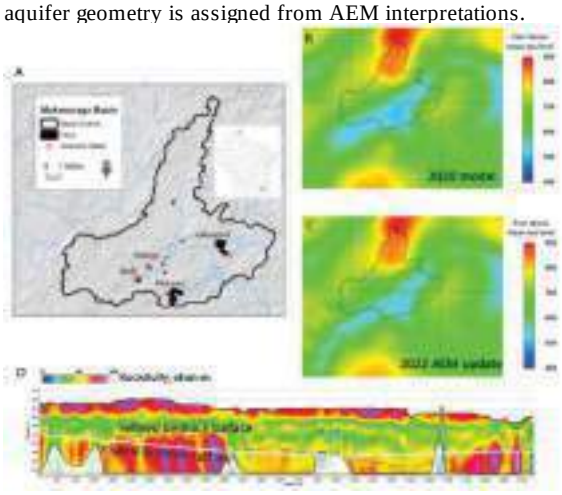

Figure 3. Groundwater model area bedrock surface interpretations. (A) Mukwonago Basin model domain and area of mapped fens. (B) Bedrock elevation for the original 2020 model (Feinstein et al. 2020) and (C) and revised 2022 update based on AEM interpretations. (D) Example resistivity cross-section along an AEM flight line shows interpretation of the bedrock surface and difference compared to the original model

ACKNOWLEDGMENTS

This study was funded through U.S. Geological Survey State Cooperative Matching funds and the Next Generation Water Observing Systems project, together with support from multiple Wisconsin State agencies (WGNHS, DATCP, WDNR), and a U.S. Department of Agriculture Natural Resources Conservation Service (NRCS) grant. Airborne geophysical data were acquired by SkyTEM through a competitive open solicitation. Any use of trade, firm, or product names is for descriptive purposes only and does not imply endorsement by the U.S. government.

REFERENCES

Auken, E., A. V. Christiansen, C. Kirkegaard, G. Fiandaca, C. Schamper, A. A. Behroozmand, A. Binley, et al. 2015. "An Overview of a Highly Versatile Forward and Stable Inverse Algorithm for Airborne, Ground-Based and Borehole Electromagnetic and Electric Data." *Exploration Geophysics* 46 (3): 223–35. https://doi.org/10.1071/EG13097.

Crosbie, J. W., B. J. Minsley, D. J. Hart, W. Fitzpatrick, M. A. Muldoon, E. K. Stewart, R. J. Hunt, M. J. Komiskey, and J. J. Duncker. 2023. "Airborne Electromagnetic (AEM) Survey in Southwest and Southeast Areas, Wisconsin, 2022." *U.S. Geological Survey Data Release*. https://doi.org/10.5066/P90K1CRG.

Doherty, John. 2022. "PEST, Model-Independent Parameter Estimation User Manual, 7th Ed." Brisbane, Australia.

Feinstein, Daniel T., David J. Hart, Sarah Gatzke, Randall J. Hunt, Richard G. Niswonger, and Michael N. Fienen. 2020. "A Simple Method for Simulating Groundwater Interactions with Fens to Forecast Development Effects." *Groundwater* 58 (4): 524–34. https://doi.org/10.1111/gwat.12931.

Hart, D. J., L. Haas, M. Rehwald, B. J. Minsley, and C. Calkins. 2022. "Statistical Models of Depth-to-Bedrock across Eastern Wisconsin, USA Using AEM Data." In *Abstract H25J-1229 Presented at 2022 AGU Fall Meeting, 12-16 Dec.*

Minsley, B. J., B. R. Bloss, D. J. Hart, W. Fitzpatrick, M. A. Muldoon, E. K. Stewart, R. J. Hunt, S. R. James, N. L. Foks, and M. J. Komiskey. 2022. "Airborne Electromagnetic and Magnetic Survey Data, Northeast Wisconsin (Ver. 1.1, June 2022)." *U.S. Geological Survey Data Release*. https://doi.org/10.5066/P93SY9LI.

EEMstudio: an open-source freeware QGIS plugin for processing, modelling and inversion of electric and electromagnetic data

Nicole Anna Lidia Sullivan
The EEM Team for Hydro & eXploration, Dep. of Earth Sciences A. Desio, Università degli Studi di Milano, Via Botticelli 23, Milano (Italy)
nicole.sullivan@unimi.it

Andrea Viezzoli
EMergo S.r.l., Via XX Settembre 12, Cascina, (Pisa, Italy)
andrea.viezzoli@em-ergo.it

Gianluca Fiandaca
The EEM Team for Hydro & eXploration, Dep. of Earth Sciences A. Desio, Università degli Studi di Milano, Via Botticelli 23, Milano (Italy)
gianluca.fiandaca@unimi.it

SUMMARY

The typical workflow in electric and electromagnetic methods includes the acquisition of the data, processing of the received signal and inversion to achieve a model of the electrical properties of the ground. The data processing is a crucial step that defines the outcome of the resulting model. The electromagnetic method, in fact, as well as the induced polarization in galvanic acquisitions, is particularly susceptible to the systematic noise caused by anthropogenic infrastructures. Therefore, it is mandatory to remove the noised data in order to retrieve reliable models. The standard method for this task is the visual culling of the data that are most affected by noise and interferences (the so-called outliers), through software with graphical user interfaces designed with this specific aim.

EEMstudio is a QGIS plugin that allows to visualize electric and electromagnetic data, to select and remove outliers, as well as modelling data and launch inversions though the modelling and inversion kernel EEMverter, keeping always a link to the map during the process.

EEMstudio is composed by a docked widget in QGIS where the soundings are plotted, a main window for data processing, equipped with ad hoc plots to visualize the data, and other windows for launching forward modelling on synthetic data as well as inversions, having all the useful tools in a minimum space. Furthermore, EEMstudio is distributed as a freeware and open-source tool, accessible to anyone and editable to suit new necessities, under the EUPL 1.2 free software licence.

Key words: QGIS, processing, modelling, inversion, QC.

INTRODUCTION

In electric and electromagnetic (EM) methods, the processing phase between data acquisition and inversion is a crucial step in the workflow. Without a proper evaluation of the data included in the inversion, outliers may generate erroneous inversion models that do not reflect geology. This is especially relevant with EM and induced polarization (IP) measurements that are particularly affected by coupling with man-made metal structures, altering the response of the ground and producing artifacts in the models if not properly removed.

Furthermore, IP measurements in environmental applications are often characterized by a low signal-to-noise ratio, making the processing step crucial to retrieve the desired results.
Despite the existence of automatic processing algorithms, the preferred method to process data and perform a quality control remains the visual inspection and culling of the data. Hence the need to have an interface to perform this task.

Nowdays the market is very well stocked with inversion softwares and tools for electric and electromagnetic data: among the most used for EM data we can mention AarhusInv (Auken et al., 2015), SimPEG (Cockett et al., 2015), the GA-AEM programs (Brodie, 2016) and EMagPY (McLachlan et al., 2021); for galvanic data examples are RES2DINV/RES3DINV (Loke, 2004), ResIPy (Blanchy et al., 2020) and pyGIMLi (Rücker et al., 2017).
However, fewer choices are available for data processing. The most complete option both for electromagnetic and electric data is Aarhus Workbench (Auken et al., 2009b), which uses AarhusInv as inversion kernel (Auken et al., 2015) and uses an integrated GIS for data inspection. However, Aarhus Workbench is an expensive commercial software that does not allow modifications by the users.

EEMstudio has been developed to be a freeware and open-source Graphic User Interface (GUI) in the form of a QGIS plugin for processing, modelling and inversion of electric and electromagnetic data, all in one place. It has been developed to be available for academic, teaching and professional use, and being open source, under license EUPL 1.2, it is possible to interrogate, adapt and customize the source code to the user's need. In the following, the sources of systematic noises are described, together with the typical processing steps; subsequently, EEMstudio is illustrated in all its parts.

DATA PROCESSING

The EM method, as well as galvanic induced polarization, are particularly susceptible to inductive coupling. Inverting raw data, keeping the coupled data distorted by the presence of anthropogenic infrastructure, produces artifacts in the resulting models, with the risk of being erroneously interpreted as geological features. In particular, the presence of metallic man-made structures causes buried conductors in the models; the random noise instead causes spotted appearance at depth or deep conductors, affecting also the resistivity of the intermediate parts of the model because of the vertical constraints that are used in the inversions (Viezzoli et al., 2013). Therefore, it is essential to recognize these interferences and carefully remove their effect in order to achieve reliable models.

Typically, an AEM dataset requires a three-step processing: i) automatic processing (averaging and filtering) of the navigation data; ii) automatic processing of voltage data and calculation of standard deviations based on data stacks; iii) manual refinement and quality control of the automatic processing. A fourth step can consist in a fast inversion using a smooth model to improve the previous ones (Auken et al., 2009).

In areas with extensive man-made infrastructures (power lines, metal fences, roads, pipes) voltage data need a careful manual evaluation with the support of the georeferenced map to remove coupling effects before being averaged. Coupling is either galvanic or capacitive: galvanic coupling happens when the conductor is in galvanic contact with the ground and behaves like a LR circuit; capacitive coupling is due to the presence of buried insulated conductors that leaks current in the subsoil through displacement currents, forming a LCR circuit (Danielsen et al., 2003). Galvanic coupling shows up as a local rise in the voltage data, while capacitive coupling as oscillations and possibly change of sign (Auken et al., 2009). Usually, all the data that are included within a distance of 100-150 m from the infrastructure have to be removed (Auken et al., 2009). More specifically, in the case of power lines, their effect depends on the resistivity of the ground pathway between the base of the power-line poles, as well as on the quality of the grounding of the poles themselves (Kang et al., 2021).

The other feature to be careful about in the processing step is the late-time noise. It represents the ambient noise, which is evident when the signal drops below the noise level and starts to oscillate toward the ends with changes of sign. (Viezzoli et al., 2013). Before removing this final part of the soundings (referred as denoising), averaging filters with a trapezoid shape, narrow at early times and wider at late times, are applied to the decoupled dataset (Auken et al., 2009). This operation ensures an increase of the S/N (signal-to-noise) ratio at depth, reducing the high-frequency features caused by background noise.

EEMstudio

EEMstudio has been designed to have in the same place a processing tool, an interface to launch inversions and visualize them and an app to forward model data, all while having a connection to a georeferenced map.

GIS

The link between the data and where it was acquired is a key feature, on which a large part of the quality of the processing depends. We chose QGIS as the base of the tool, as it is the most widespread open-source Geographic Information System (GIS) software available. In QGIS, EEMstudio starts as a docked widget (Figure 1), where the user can upload the processing and inversion files. It automatically loads the positions of the soundings in a QGIS project. Additionally, also the positions of the soundings that are shown in the plots are constantly shown in QGIS map as temporary layers, to locate them in real time.

Processing

For the processing, it has been developed a graphic interface (GUI) to visualize data and to perform an accurate processing of various kinds of data, such as transient EM data (airborne and ground-based), time-domain induced polarization data and galvanic data.
EEMstudio was created after experiencing processing with other codes and adapting it to the needs and experience of the research group. Therefore, the user is provided with many plots, linked to the QGIS map, to have a better overview of the data. Processing is made by the usage of a vast range of shortcuts that reflects all the necessities that could arise during processing, based on personal experience and other user's feedbacks, ensuring a quick and optimized processing phase.

EEMstudio processing window (Figures 2 and 3) is composed by the plots in which the data are visualized, selected and processed. The plots in the central part of the widow can be changed with different configurations.

The plot in the upper part of the window is Positions, where the elevation or flight altitude is shown. Additionally, measures of pitch, roll and yaw can be added to the plot.
Under this plot there are Patchwork (Figure 2) and Data Stripe (Figure 3) plot types. Both plot types show the decays' values gate-by-gate for a number of soundings. In Patchwork the sounding number (or the flight time, depending on the setting choice) is plotted on x axis, the gate number on y axis, with data values represented in colour scales. Culled-out data are coloured in grey (no culled data are shown in Figures 2 and 3, to highlight the noised data).

In Patchwork visualization (Figure 2), raw data does not provide direct information about conductivity or depth, because it is dependent by the resistivity of the layers that are investigated, but it's useful to observe spatial patterns of the measured response and possibly identify where the signal is affected by infrastructures or noise (Viezzoli et al., 2013).
In Data Stripe (Figure 3) the sounding number (or the flight time) is plotted on x axis, and $\frac{(dB/dt)}{(NiA)}$ (other choices are ρ_a or dB/dt) values on y axis Positive data are plotted in blue, negative in red, culled-out in grey. The plot on the right panel shows the $\frac{(dB/dt)}{(NiA)}$ (or ρ_a or dB/dt) decays that can be selected in the Data Stripe/Patchwork. Like in Data Stripe, positive data are plotted in blue, negative in red, culled-out in grey.

Modelling

Within EEMstudio an interface to manage easily modelling and inversion will be provided. The modelling part will be useful for educational purposes, like the modelling software EMMA (Auken et al., 2002) but also to build or modify 1D/2D/3D starting models for the inversions.

For the inversions part, it will be possible to launch 1D/2D/3D and joint inversions using EEMverter (Fiandaca et al., 2023), the freeware software for electric and electromagnetic methods developed by the EEM Team for Hydro & eXploration.

CONCLUSIONS

EEMstudio brings to the scientific community a tool for visualization, processing, modelling and inversion of AEM data, ground EM and galvanic data. It is a free alternative to the commercial software that dominate the field. Being open source, the user has also the opportunity to modify and improve it, with huge development possibilities. Functioning within QGIS, it allows to use the most widespread open-source GIS software during the processing, keeping all the main workflow in one place.

The processing app is equipped with a variety of plots to have a well-rounded understanding of the data and is optimized for a

quick and straightforward processing. Furthermore, from the modelling app is possible to launch easily inversions with an intuitive and user-friendly GUI.

EEMstudio is a recently born project, still in development but ready to accommodate new modules, making it a canvas for everyone idea.

ACKNOWLEDGMENTS

This study has been partially carried out within the Horizon Europe project SEMACRET. We thank PanGlobal resources to allow us in using the airborne IP data in our data visualizations.

REFERENCES

Auken, E., Nebel, L., Sørensen, K., Breiner, M., Pellerin, L., & Christensen, N. B. (2002). EMMA—a geophysical training and education tool for electromagnetic modeling and analysis. *Journal of Environmental & Engineering Geophysics*, *7*(2), 57-68.

Auken, E., Christiansen, A. V., Westergaard, J. H., Kirkegaard, C., Foged, N., & Viezzoli, A. (2009). An integrated processing scheme for high-resolution airborne electromagnetic surveys, the SkyTEM system. *Exploration Geophysics*, *40*(2), 184-192.

Auken, E., Viezzoli, A., & Christensen, A. (2009b). A single software for processing, inversion, and presentation of AEM data of different systems: The Aarhus Workbench. *ASEG Extended Abstracts*, *2009*(1), 1-5.

Auken, E., Christiansen, A. V., Kirkegaard, C., Fiandaca, G., Schamper, C., Behroozmand, A. A., ... & Vignoli, G. (2015). An overview of a highly versatile forward and stable inverse algorithm for airborne, ground-based and borehole electromagnetic and electric data. *Exploration Geophysics*, *46*(3), 223-235.

Blanchy, G., Saneiyan, S., Boyd, J., McLachlan, P., & Binley, A. (2020). ResIPy, an intuitive open source software for complex geoelectrical inversion/modeling. *Computers & Geosciences*, *137*, 104423.

Brodie, R. C., 2016, User Manual for Geoscience Australia's Airborne Electromagnetic Inversion Software. Online: https://github.com/GeoscienceAustralia/ga-aem.git.

Cockett, R., Kang, S., Heagy, L. J., Pidlisecky, A., & Oldenburg, D. W. (2015). SimPEG: An open source framework for simulation and gradient based parameter estimation in geophysical applications. *Computers & Geosciences*, *85*, 142-154.

Danielsen, J. E., Auken, E., Jørgensen, F., Søndergaard, V. H., and Sørensen, K. I., 2003, The application of the transient electromagnetic method in hydrogeophysical surveys: *Journal of Applied Geophysics*, 53, 181–198.

Fiandaca, G., Zhang, B., Chen, J., Signora, A., Dauti, F., Galli, S., Sullivan, N.A.L., Bollino, A., Viezzoli, A. (2023). Closing the gap between galvanic and inductive methods: EEMverter, a new 1D/2D/3D inversion tool for Electric and Electromagnetic data with focus on Induced Polarization. *AEM2023 - 8th International Airborne Electromagnetics Workshop, 3-7 September 2023, Fitzroy Island, QLD, Australia*.

Kang, S., Dewar, N., & Knight, R. (2021). The effect of power lines on time-domain airborne electromagnetic dataThe effect of power lines on AEM data. *Geophysics*, 86(2), E123-E141.

Loke, M. H. (2004). Tutorial: 2-D and 3-D electrical imaging surveys.

McLachlan, P., Blanchy, G., & Binley, A. (2021). EMagPy: Open-source standalone software for processing, forward modeling and inversion of electromagnetic induction data. *Computers & Geosciences*, *146*, 104561.

Rücker, C., Günther, T., & Wagner, F. M. (2017). pyGIMLi: An open-source library for modelling and inversion in geophysics. *Computers & Geosciences*, 109, 106-123.

Viezzoli, A., Jørgensen, F., & Sørensen, C. (2013). Flawed processing of airborne EM data affecting hydrogeological interpretation, *Groundwater*, 51, 191–202.

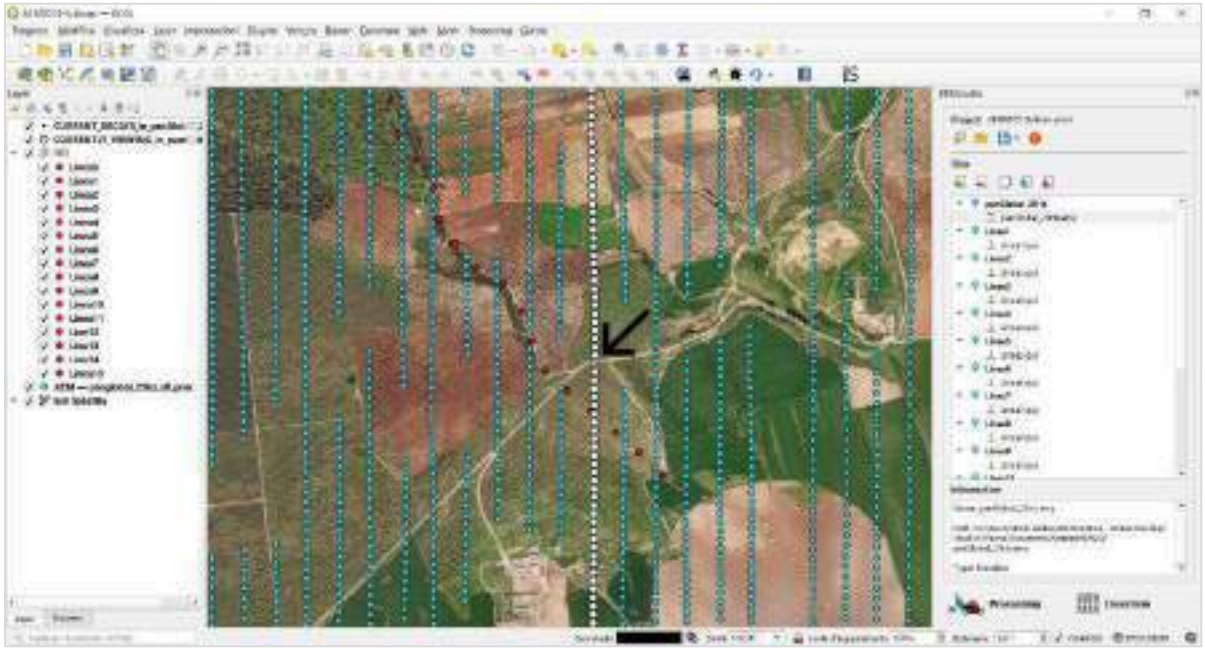

Figure 1. QGIS main window with EEMstudio plugin on the right, i.e. the docked widget. There the user can upload the processing and inversion files. The layers containing the acquisition positions are automatically added to the QGIS project. Blue dots are AEM soundings, red dots are electrodes of galvanic soundings. The white dots are all the AEM soundings shown in EEMstudio processing window and the ones with a smaller black dot inside (where the arrow points) are the soundings shown in Decays (right panels in Figure 2 and Figure 3).

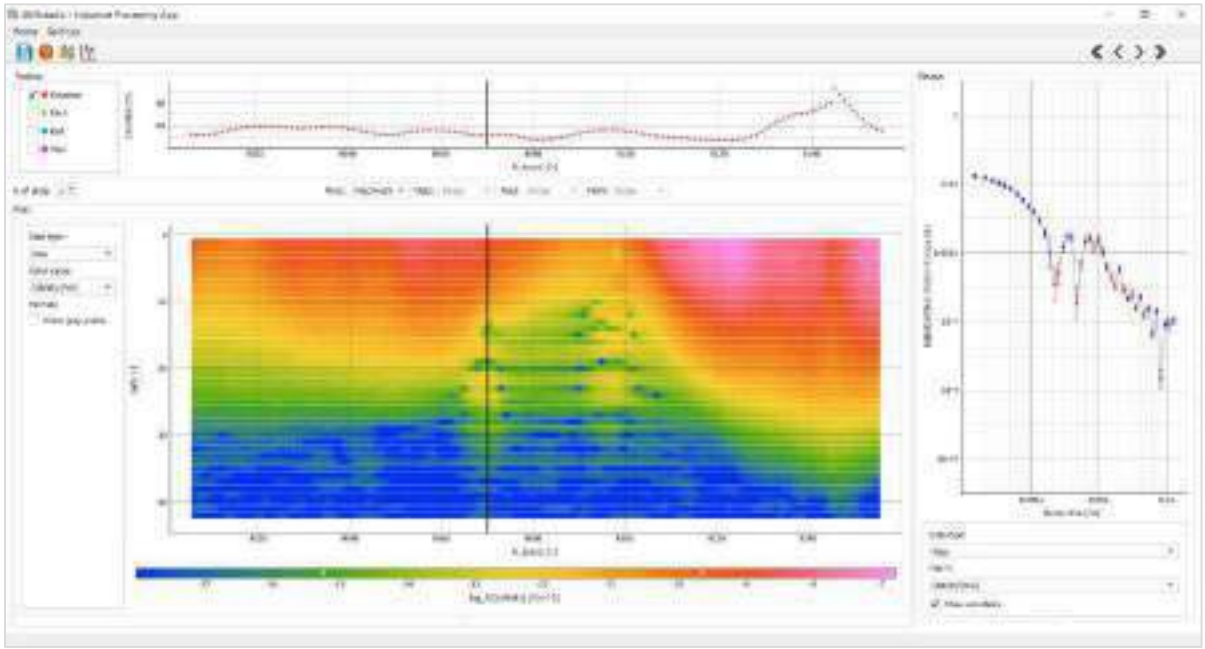

Figure 2. EEMstudio processing window – Patchwork view. In the plot in the centre top the elevation of the acquisition points is plotted against the sounding number or acquisition time. In the bottom plot the decays are plotted gate by gate against sounding number or acquisition time, and represented with a colour scale that indicates the value of $\frac{(dB/dt)}{(NiA)}$ or dB/dt or ρ_a (in this figure the data are not culled out to highlight the noise). The plot on the right are the decays of $\frac{(dB/dt)}{(NiA)}$ or dB/dt or ρ_a. All the soundings that are present in the Patchwork are plot with white dots in the QGIS map; the decays shown in the right panel with an additional black dot inside (Figure 1).

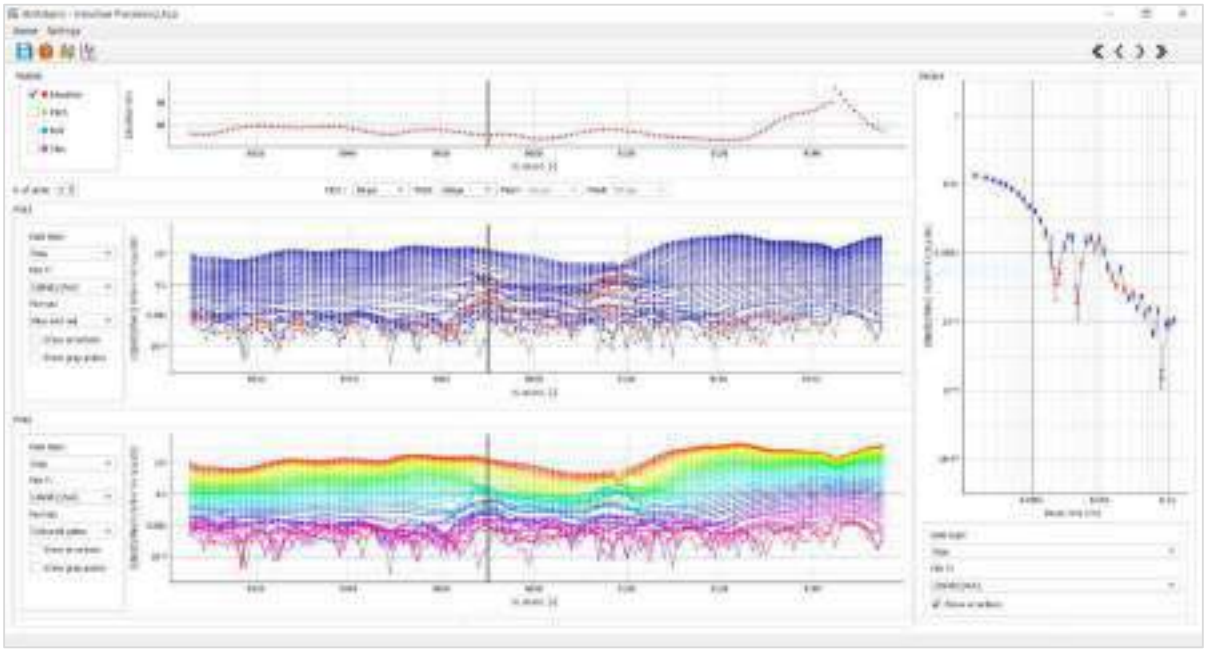

Figure 3. EEMstudio processing window – Data Stripe view. In the plot in the centre top the elevation of the acquisition points is plotted against the sounding number or acquisition time, as in Patchwork view. In the centre and bottom plots the decays are plotted gate by gate against sounding number or acquisition time, with two choices of representation: in the centre plot as blue dots if positive, red if negative and grey if culled out; in the bottom plot with gate-by-gate colouring. The plot on the right panel shows the decays selected in the Data Stripe as $\frac{(dB/dt)}{(NiA)}$ or dB/dt or ρ_a. All the soundings that are present in the Data Stripe are plot with white dots in the QGIS map; the decays in the right panel with an additional black dot inside (Figure 1).